frontiers | Research Topics

Advances in artificial intelligence application in data analysis and control of smart grid

Edited by
Xin Ning, Imr Fattah, Praveen Kumar Donta
and Mohamed M. F. Darwish

Published in
Frontiers in Energy Research

ISSN 1664-8714
ISBN 978-2-8325-3956-9
DOI 10.3389/978-2-8325-3956-9

About Frontiers

Frontiers is more than just an open access publisher of scholarly articles: it is a pioneering approach to the world of academia, radically improving the way scholarly research is managed. The grand vision of Frontiers is a world where all people have an equal opportunity to seek, share and generate knowledge. Frontiers provides immediate and permanent online open access to all its publications, but this alone is not enough to realize our grand goals.

Frontiers journal series

The Frontiers journal series is a multi-tier and interdisciplinary set of open-access, online journals, promising a paradigm shift from the current review, selection and dissemination processes in academic publishing. All Frontiers journals are driven by researchers for researchers; therefore, they constitute a service to the scholarly community. At the same time, the *Frontiers journal series* operates on a revolutionary invention, the tiered publishing system, initially addressing specific communities of scholars, and gradually climbing up to broader public understanding, thus serving the interests of the lay society, too.

Dedication to quality

Each Frontiers article is a landmark of the highest quality, thanks to genuinely collaborative interactions between authors and review editors, who include some of the world's best academicians. Research must be certified by peers before entering a stream of knowledge that may eventually reach the public - and shape society; therefore, Frontiers only applies the most rigorous and unbiased reviews. Frontiers revolutionizes research publishing by freely delivering the most outstanding research, evaluated with no bias from both the academic and social point of view. By applying the most advanced information technologies, Frontiers is catapulting scholarly publishing into a new generation.

What are Frontiers Research Topics?

Frontiers Research Topics are very popular trademarks of the *Frontiers journals series*: they are collections of at least ten articles, all centered on a particular subject. With their unique mix of varied contributions from Original Research to Review Articles, Frontiers Research Topics unify the most influential researchers, the latest key findings and historical advances in a hot research area.

Find out more on how to host your own Frontiers Research Topic or contribute to one as an author by contacting the Frontiers editorial office: frontiersin.org/about/contact

Advances in artificial intelligence application in data analysis and control of smart grid

Topic editors
Xin Ning — Institute of Semiconductors, Chinese Academy of Sciences (CAS), China
Imr Fattah — University of Technology Sydney, Australia
Praveen Kumar Donta — Vienna University of Technology, Austria
Mohamed M. F. Darwish — Aalto University, Finland

Citation
Ning, X., Fattah, I., Donta, P. K., Darwish, M. M. F., eds. (2023). *Advances in artificial intelligence application in data analysis and control of smart grid*. Lausanne: Frontiers Media SA. doi: 10.3389/978-2-8325-3956-9

Table of contents

frontiers | Frontiers in Energy Research

TYPE Original Research
PUBLISHED 12 January 2023
DOI 10.3389/fenrg.2022.1058378

EDITED BY
Mohamed M. F. Darwish,
Aalto University, Finland

REVIEWED BY
Mohamed H. A. Hassan,
Benha University, Egypt
Manal M. Emara,
Kafrelsheikh University, Egypt
Xuguang Hu,
Northeastern University, China

*CORRESPONDENCE
Xiangli Deng,
xiangli_deng@163.com

SPECIALTY SECTION
This article was submitted to Smart Grids,
a section of the journal
Frontiers in Energy Research

RECEIVED 30 September 2022
ACCEPTED 27 October 2022
PUBLISHED 12 January 2023

CITATION
Deng X, Zhang Z, Zhu H and Yan K (2023), Early fault diagnosis of transformer winding based on leakage magnetic field and DSAN learning method.
Front. Energy Res. 10:1058378.
doi: 10.3389/fenrg.2022.1058378

Early fault diagnosis of transformer winding based on leakage magnetic field and DSAN learning method

Xiangli Deng*, Zhan Zhang, Hongye Zhu and Kang Yan

School of Electric Power Engineering, Shanghai University of Electric Power, Shanghai, China

Aiming at the problem of lack of training samples and low accuracy in transformer early winding fault diagnosis, this paper proposes a transformer early faults diagnosis method based on transfer learning and leakage magnetic field characteristic quantity. The method uses the leakage magnetic field waveform on the measuring point of the simulated transformer winding to draw the Lissajous figure to calculate the characteristic quantity. The characteristic quantity of the simulation model is used to train the convolutional neural network (CNN) faults classification model. The CNN fault classification model is transferred to the actual transformer fault detection through the improved deep subdomain adaptive network (DSAN), so as to realize the fault diagnosis of the actual transformer by the classification model trained by the simulation data. The test examples of the actual transformer early fault experimental platform and the leakage magnetic field measurement platform are established, and the feasibility of the transfer learning method based on the leakage magnetic field feature quantity proposed in this paper is verified.

KEYWORDS

transformer early fault, leakage magnetic field, CNN-convolutional neural network, transfer learning (TL), self-attention mechanism

1 Introduction

The power transformer is one of the most important electrical equipment in the power network. When the transformer is impacted by the external force or repeatedly impacted by the short-circuit fault current outside the region, it is easy to cause the deformation of the transformer winding (Hang and Butler, 2002). The long-term operation of the transformer under overload condition and insulation aging will cause the decrease of the insulation performance of the transformer winding, which further leads to the inter-turn short-circuit faults (Liu et al., 2003). The transformer internal winding fault occurs above and does not have huge impact, we call this fault for the transformer early fault. Early faults of transformers are often difficult to detect. The cumulative effect of long-term operation of transformers under potential early faults will eventually lead to serious accidents. Therefore, the accurate detection of transformer early faults is of great significance to ensure the stable operation of power system (Naseri et al., 2018).

At present, the detection methods for transformer faults are mainly divided into offline detection methods and online monitoring methods. Off-line detection commonly used oil chromatography (Gao and He, 2010; Alshehawy, et al., 2021; Emara et al., 2021; Wu et al., 2021), frequency response method (Shamlou et al., 2021), the technology is relatively mature, but the maintenance is limited by the operation cycle cannot be real-time monitoring and timely detection of faults. The method of real-time online monitoring is the main research direction at present. Transformer winding deformation fault can be diagnosed online by using leakage inductance parameters of transformer winding (Deng et al., 2014). The inter-turn short-circuit fault of transformer can be identified by constructing the fitness function of resistance and leakage inductance parameters (Wang and Zeng, 2021). An article paper proposes an online fault detection method for transformers based on an IoT platform (Elsis et al., 2022). All of the above studies have achieved some results. However, one parameter can only detect a single fault and has the disadvantages of low parameter calculation accuracy and unclear fault relationship (Chen et al., 2019). Therefore, it is necessary to find a leakage magnetic field characteristic which can not only reflect the internal winding deformation of the transformer but also identifies the inter-turn short circuit and reflect more quickly as the early fault monitoring of the transformer. Using leakage magnetic field to monitor early faults of the transformer is a feasible online monitoring scheme.

The leakage magnetic field data of the transformer can directly reflect the operation state of the transformer (Wang and Han, 2021). When the transformer winding is deformed, the leakage magnetic field around the winding is asymmetrically distributed in space. When inter-turn short circuit occurs in the transformer, the iron core may be partially saturated, which increases the leakage magnetic field around the winding (Zhang, 2019). The winding deformation of the transformer can be monitored based on the asymmetry of the distribution of the leakage magnetic field (Zhou and Wang, 2017; Pan et al., 2020; Zhang et al., 2021). At the same time, the mutation of the leakage magnetic field can be used to diagnose the inter-turn short circuit faults (Cabanas et al., 2007). However, when the leakage magnetic field data are used to segment the fault types of transformers, there are problems such as small differences between different fault characteristics and difficult to distinguish manually.

In recent years, with the development of artificial intelligence technology, data-driven transformer fault classification methods have been widely employed because they can effectively identify small data differences. Machine learning can effectively classify transformer faults and identify early faults in transformers (Haghjoo et al., 2017; Li et al., 2022). Recent studies have shown that the distribution of the magnetic field leakage changes when the transformer has an early fault. Online monitoring of the early fault of the transformer can be realized by using the magnetic field leakage data and artificial intelligence methods. However, there are several problems worthy to solve.

(1) When using magnetic field leakage data to diagnose transformer faults, the change in transformer load has a greater impact on fault classification, and the fault classification accuracy is low.
(2) Is difficult to obtain actual transformer fault data in field applications, and there is a lack of labeled training data.

Based on the deficiencies in the existing literature, this study proposes the following innovations:

(1) The Faraday magneto-optical effect was used to measure the leakage magnetic field of the transformer, and current information was used to normalize the leakage magnetic field waveform to eliminate the influence of load changes on fault classification. The leakage magnetic field waveform was used to draw Lissajous figures and extract the characteristic quantities for the early fault classification of transformer windings, which enhances the classification accuracy.
(2) Through the improved DSAN, the transfer learning can reduce the difference between the actual transformer and the simulation model data, so as to realize the fault diagnosis of the actual transformer using the neural network trained by the simulation data, and solve the problem of insufficient training data.

In this study, a fault diagnosis test was performed on the measured data of an actual transformer. The results reveal that the proposed method can effectively transfer the transformer fault classification model and has high classification accuracy.

2 Transformer fault classification method based on deep subdomain adaptive network

For a new transformer we cannot obtain data on early winding faults, but we can use simulation software to simulate different fault types and obtain a large amount of fault data, but there are deviations between the simulation data and the actual data before. We first use the simulation data to train a CNN fault classification model, and then use the DSAN transfer learning method to achieve early fault diagnosis of the actual transformer.

2.1 Convolutional neural network classification model

The convolutional perceptual features of CNN can fully extract various features of the input image and have strong transferability. In this study, the classic LeNet-5 in CNN was used for the feature extraction of images. The parameters for each layer of the designed CNN are presented in Supplementary Appendix A1. The convolution layer in a CNN is composed of several convolution kernels. Different convolution kernels can extract different image features. Convolution operations can extract low-level to complex features from the input image data. The mathematical expression of the convolution layer is expressed in Eq. 1 (Lecun et al., 1998):

$$g^l(\gamma) = ACT\left[\sum_{i=1}^{G}\sum_{j=1}^{H}\boldsymbol{W}_{i,j}^{l} * \boldsymbol{\gamma}_{i,j}^{l} + \boldsymbol{E}_{i,j}^{l}\right] \tag{1}$$

In the formula, l indicates the number of layers, ACT indicates the activation function, G, H denotes the size of the current layer node matrix, γ indicates the number of nodes in the node matrix, $\boldsymbol{W}_{i,j}^{l}$ corresponds to the weight matrix of the convolution kernel, $\boldsymbol{\gamma}_{i,j}^{l}$ indicates the input value of the convolution layer, and $\boldsymbol{E}_{i,j}^{l}$ denotes the bias of the current node.

Using a nonlinear Rectified Linear Activation Function (ReLU) activation function can solve the problem of low expression ability of linear models (Wang et al., 2019). Using the maximum pooling layer to scale and map the convolution image can simplify the parameters and reduce the data dimensions. The mathematical expression is as follows Eq. 2 (Wang et al., 2019):

$$g^{l+1}(\gamma) = MP\left\{g^l(\gamma)\right\} \tag{2}$$

MP indicates the maximum pooling function, $g^l(\gamma)$ represents convolution computes the eigenvalues of the output. After the convolution-pooling network, the transformer fault classification stage is composed of a full connection layer, and the last fully connected layer is used as the classifier. The transformer winding is divided into different states using one-hot coding form to calculate the classification probability of one sample for each state and take the state with the maximum probability as the classification result. Cross-entropy loss is used as the loss function of the classifier, as expressed in the following Eq. 3 (Jang et al., 2017):

$$J(\theta(\boldsymbol{x}_i), \boldsymbol{y}_i) = -\sum_{c=1}^{C}\{\boldsymbol{y}_i \mid= c\}\log\theta(\boldsymbol{x}_i) \tag{3}$$

In the formula, $J(\cdot,\cdot)$ denotes the cross-entropy loss function, $C = \{1, 2, \cdots, c\}$ indicates the type of classification, and $\theta(\boldsymbol{x}_i)$ represents the probability that the network attaches the current type label $\boldsymbol{y}_i$ to the sample $\boldsymbol{x}_i$. The empirical error of the CNN classification model is given by the Eq. 4 (Jang et al., 2017):

$$\min_{\theta}\frac{1}{n}\sum_{i=1}^{n}J(\theta(\boldsymbol{x}_i), \boldsymbol{y}_i) \tag{4}$$

In the formula, n represents the total number of samples. In the form represents a collection of parameters for each layer of CNN.

2.2 Transfer learning

Based on the theory of transfer learning (Ghifary et al., 2014), this study applies the knowledge learned in one field to another similar field. More specifically, a machine learning algorithm is utilized to transfer the transformer fault classification model trained by the simulation model from the fault diagnosis of the simulation transformer to the fault diagnosis of the actual transformer. In field applications, actual transformer fault data are often difficult to obtain and the fault process causes irreversible damage to the transformer. Actual transformers take the initiative to produce fault data at a high cost. For an actual transformer that needs to be diagnosed, there is almost no available labeled data. Although a large amount of sample data can be generated using the transformer simulation model, there are still some differences between the simulation data and actual data. The classification model trained using simulation data cannot be directly applied to the fault diagnosis of an actual transformer.

Owing to the lack of actual transformer data with labels, this study adopted the method of model transfer. We define the dataset generated by the transformer simulation model as the source domain data, which is a labeled system $\boldsymbol{D}_{\mathrm{S}} = \{(\boldsymbol{x}_1^S, \boldsymbol{y}_1^S), \cdots, (\boldsymbol{x}_s^S, \boldsymbol{y}_s^S)\}$, the actual transformer data set as target domain data, and the target domain data as unlabeled system $\boldsymbol{D}_{\mathrm{T}} = \{(\boldsymbol{x}_1^T), \cdots, (\boldsymbol{x}_t^T)\}$. The simulation data and the actual data are mapped from the original feature space to the new feature space. In the new feature space, the data distribution of the simulated data and the actual data are similar, so that the existing labeled data samples of the simulated data can be better used in the new space for classification testing of the actual transformer data. We place the description of transfer learning schematic in Supplementary Appendix B1. The probability distributions p and q are obtained by sampling the transformer simulation data $\boldsymbol{D}_{\mathrm{S}}$ and the actual transformer data $\boldsymbol{D}_T$. The goal of using transfer learning in this study is to design a neural network to eliminate the difference between simulated transformer data and real data by learning the transferable characteristics of distribution p and q to minimize the target risk.

2.3 Deep subdomain adaptive network based on multi-core local maximum mean difference

To minimize the distance between the source domain data $\boldsymbol{D}_{\mathrm{S}}$ and target domain data $\boldsymbol{D}_{\mathrm{T}}$, and align the edge distribution of the simulation and actual transformer data, a multiple kernel variant of the maximum mean discrepancy (MK-MMD) is used to measure the distance between the source domain data and the target domain data (Long and Wang, 2015). MK-MMD is an extension of MMD and is a non-parametric method used to measure the distribution differences between datasets in different domains. MMD uses a single kernel for transformation, and it is difficult to determine an optimal kernel for different datasets. The optimal kernel of the MK-MMD is obtained by a linear combination of several kernels, which can be adapted to different datasets. MK-MMD is defined to map the source domain data distributed and the target domain data distributed as to the reproducing kernel Hilbert space (RKHS) and calculate the mean distance as follows Eq. 5 (Ghifary et al., 2014):

$$M_k^2(p,q) \triangleq \left\| E_{\boldsymbol{x}^S \sim p}[\phi(\boldsymbol{x}^S)] - E_{\boldsymbol{x}^T \sim q}[\phi(\boldsymbol{x}^T)] \right\|_{\hbar}^2 \tag{5}$$

In the formula, $\| \cdot \|_{\hbar}^2$ represents the two norms of RKHS, $E_{\boldsymbol{x}^S \sim p}[\cdot]$, and $E_{\boldsymbol{x}^T \sim q}[\cdot]$ represents the mathematical expectation of distribution p and q, $\phi(\cdot)$: $\boldsymbol{x} \rightarrow \hbar$ denotes the infinite order nonlinear feature map of vector $\boldsymbol{x}$ in $\hbar$.

Assuming that a characteristic kernel in RKHS is k, and the mean value of distribution p in kernel space $\hbar$ is an element $\mu_k(p)$, all the key statistical features in distribution p are coded into $\mu_k(p)$, so that all the mapping functions satisfying $f \in \hbar$ satisfy the expectation $E_{\boldsymbol{x} \sim p} f(\boldsymbol{x}) = \langle f(\boldsymbol{x}), \boldsymbol{\mu}_k(p) \rangle_{\hbar}$, so we can learn through $\mu_k(p)$ rather than distribution p, so as to eliminate the incalculable density estimation in distribution p. The empirical estimation of the MK-MMD is given by the following Eq. 6 (Long and Wang, 2015):

$$\begin{aligned} M_{\mathrm{K}}^2(\boldsymbol{D}_S, \boldsymbol{D}_T) \triangleq \\ \frac{1}{n_s^2} \sum_{i=1}^{n_s} \sum_{j=1}^{n_s} k\left(\boldsymbol{x}_i^S, \boldsymbol{x}_j^S\right) + \frac{1}{n_t^2} \sum_{i=1}^{n_t} \sum_{j=1}^{n_t} k\left(\boldsymbol{x}_i^T, \boldsymbol{x}_j^T\right) \\ -\frac{2}{n_s n_t} \sum_{i=1}^{n_s} \sum_{j=1}^{n_t} k\left(\boldsymbol{x}_i^S, \boldsymbol{x}_j^T\right) \end{aligned} \tag{6}$$

In the above formula, n_s, n_t denote the sample size of $\boldsymbol{D}_S, \boldsymbol{D}_T$. $k(\boldsymbol{x}, \boldsymbol{x}') = \langle \phi(\boldsymbol{x}), \phi(\boldsymbol{x}') \rangle$ is considered as the correlation between vectors $\boldsymbol{x}$ and $\boldsymbol{x}'$, and the kernel function $k(\boldsymbol{x}, \boldsymbol{x}')$ is a convex combination of k Gaussian kernels. The composition of kernel is as follows Eq. 7 (Long and Wang, 2015):

$$\left\{ k = \sum_{i=1}^{K} \beta_i k_i : \sum_{i=1}^{K} \beta_i = 1, \beta_i \geqslant 0, \forall U \right\} \tag{7}$$

Constraints are imposed on coefficient β to ensure that each core k combination has unique characteristics. K denotes the total number of the kernel. Using kernel k with different bandwidths to obtain the mean value of the distribution at different scales can give distribution p and q an optimal kernel.

The regularization based on MK-MMD can effectively align the probability distribution of the sample; however, DSAN considers the fine-grained information of the label of the sample and defines the label weight $w_{i,c}$ as shown in Eq. 8 (Zhu et al., 2021):

$$w_{i,c} = \frac{\boldsymbol{y}_{i,c}}{\sum_{y_{j,c} \in \{D_S, D_T\}} \boldsymbol{y}_{j,c}} \tag{8}$$

$y_{i,c}$ denotes the probability that sample $\boldsymbol{x}_i$ belongs to category c, and $y_{j,c}$ denote the category of the current sample label. The source domain data uses the actual annotation to calculate the $w_{i,c}^S$, the target domain samples data uses the CNN prediction probability calculate $w_{j,c}^T$. The regularization formula (8) of MK-LMMD use the activation vectors $\{\boldsymbol{z}_i^S\}_{i=1}^{n_s}$ and $\{\boldsymbol{z}_j^T\}_{j=1}^{n_t}$ of the full connection layer as features to calculate the distance, as follows Eq. 9 (Zhu et al., 2021):

$$\begin{aligned} M_{\mathrm{KL}}^2(\boldsymbol{D}_S, \boldsymbol{D}_T) \triangleq \\ \frac{1}{C} \sum_{c=1}^{C} \left[\begin{array}{l} \sum_{i=1}^{n_s} \sum_{j=1}^{n_s} w_{i,c}^S w_{j,c}^S k\left(\boldsymbol{z}_i^S, \boldsymbol{z}_j^S\right) + \\ \sum_{i=1}^{n_t} \sum_{j=1}^{n_t} w_{i,c}^T w_{j,c}^T k\left(\boldsymbol{z}_i^T, \boldsymbol{z}_j^T\right) \\ -2 \sum_{i=1}^{n_t} \sum_{j=1}^{n_t} w_{i,c}^S w_{j,c}^T k\left(\boldsymbol{z}_i^S, \boldsymbol{z}_j^T\right) \end{array} \right] \end{aligned} \tag{9}$$

In the expression $\boldsymbol{z}_i^S$, $\boldsymbol{z}_j^T$ represent the activation vectors of the source domain and target domain samples.

Convolutional layers in a CNN are transferable; therefore, there is no need to add MK-LMMD regularizers to these layers. When migrating, we freeze the convolution and pooling layers to maintain the effectiveness of collaborative adaptation. In a CNN, the deep features transition from general to specific features in the last layer of the network. The transferability of the neural network decreases with an increase in the difference between the source and target domains, and the transferability of data between different domains decreases through the full connection layer. Therefore, we only compute the distance difference between the source and target domains in the full connection layer, and the transfer learning loss function as follows Eq. 10:

$$\min_{\theta} \frac{1}{n} \sum_{i=1}^{n} J\left(\theta(\boldsymbol{x}_i^S), y_i^S\right) + \lambda \sum_{l=l_1}^{l_2} M_{\mathrm{KL}}^2\left(\boldsymbol{D}_s^l, \boldsymbol{D}_t^l\right) \tag{10}$$

λ symbolizes a penalty factor, l_1 and l_2 denote the number of layers based on MK-LMMD regularization, $M_{kL}^2(\boldsymbol{D}_s^l, \boldsymbol{D}_t^l)$ represents the local maximum mean difference value of the current layer.

2.4 Improvement of deep subdomain adaptive network

Considering the different correlations between the simulation data and the actual measurement data, to further improve the generalization ability of the DSAN, it is proposed to add the self-attention mechanism to the

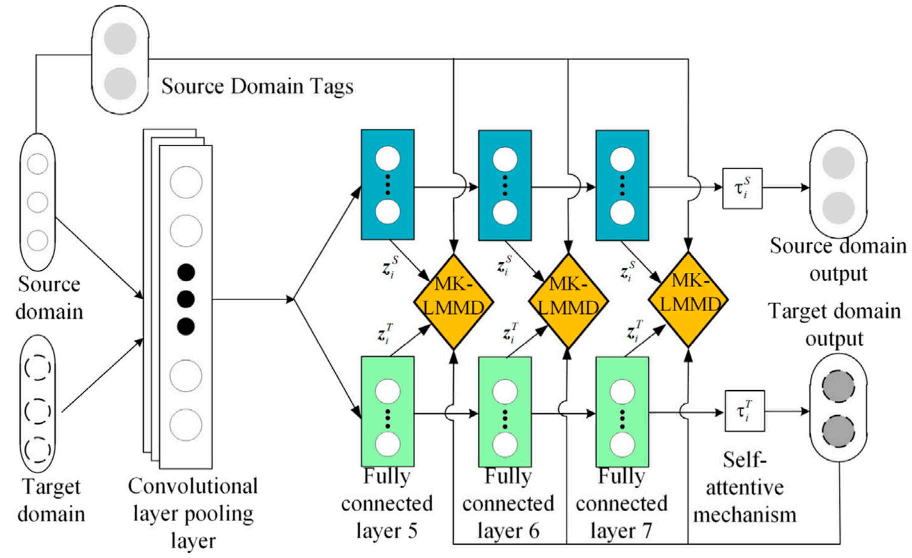

FIGURE 1
DSAN model based on self-attentive mechanism.

traditional DSAN (Bo et al., 2021). Based on the regional characteristics, the full connection layer and sigmoid are used to estimate the importance of the sample and provide the weight value. The input sample is divided into several features, and the full connection layer data obtained by the convolution of each sample is input into a sigmoid function to obtain different weights. The correlation between the simulation data and actual measurement data is too large to obtain higher weights, and *vice versa*. This allows the neural network to automatically focus on samples with significant weights. The sigmoid function is shown in the following Eq. 11 (Bo et al., 2021):

$$\tau_i = SIG\left(\boldsymbol{x}_i^S,\ cov\left(\boldsymbol{x}_i^S\right)\right) \tag{11}$$

$cov(\boldsymbol{x}_i^s)$ represents the parameter feature of the full connection layer after the convolution layer. τ_i corresponds to the importance weight parameter of $i-\mathrm{th}$, SIG represents the sigmoid function. The improved DSAN loss function is given by Eq. 12:

$$\min_{\theta} \frac{1}{n}\sum_{i=1}^{n} J\left(\theta\left(\boldsymbol{x}_i^S\right), \tau_i \boldsymbol{y}_i^S\right) + \lambda \sum_{l=l_1}^{l_2} M_{\mathrm{KL}}^2\left(\boldsymbol{D}_s^l,\ \boldsymbol{D}_t^l\right) \tag{12}$$

The DSAN model, based on the self-attention mechanism, is presented in Figure 1. From the perspective of the construction process of the transfer model, although feature extraction is not necessarily able to completely eliminate the difference between the actual transformer simulation model and the actual transformer data distribution, according to the statistical principle, MK-LMMD regularization can reduce this difference as much as possible and can obtain a better classification effect in theory. Simultaneously, a DSAN with a self-attention mechanism can weight the sample data, which can further improve the accuracy of classification.

3 Transformer fault diagnosis based on magnetic field leakage characteristic

3.1 Load normalization of magnetic flux leakage

In this study, leakage magnetic field information is used to diagnose transformer faults. Because the load change of the transformer affects the current of the secondary winding and subsequently affects the amplitude and phase angle of the leakage magnetic field waveform, it will adversely affect the accuracy of fault classification. Previous papers have selected several different load conditions to analysis of leakage fields for different load conditions. In this paper, we propose a method based on real-time load normalization of the current on the first and second sides of the transformer.

To eliminate the influence of load changes on fault diagnosis, in this study, the amplitude and phase angle of the leakage magnetic field waveform are normalized using the currents at the primary and secondary windings of the transformer. The magnetic line of the leakage flux of the primary and secondary windings is closed along the nonferromagnetic material and is linear with the primary and secondary side currents (Gu, 2010). The resistive inductive load is the common load of a transformer. The change in load simultaneously affects the waveform of the leakage magnetic field amplitude and phase angle. The linear function between the leakage magnetic field and the response of the transformer primary and secondary side currents is as Eq. 13 (Gu, 2010):

$$\dot{B}_L = \dot{p}\dot{I}_1 + \dot{q}\dot{I}_2 \tag{13}$$

$\dot{B}_L$ Indicates leakage magnetic field. $\dot{p}, \dot{q}$ is constant coefficient, $\dot{I}_1, \dot{I}_2$ is the primary and secondary side current. When the transformer operates in any two different load states, the Eq. 14 shows:

$$\begin{aligned} \dot{B}_a^* &= \dot{p}\dot{I}_{a1}^* + \dot{q}\dot{I}_{a2}^* \\ \dot{B}_b^* &= \dot{p}\dot{I}_{b1}^* + \dot{q}\dot{I}_{b2}^* \end{aligned} \tag{14}$$

$\dot{B}_a^*, \dot{B}_b^*$ indicates the leakage magnetic field under two different loads. $\dot{I}_{a1}^* \dot{I}_{a2}^* \dot{I}_{b1}^* \dot{I}_{b2}^*$ is the primary and secondary side current under two different loads. When the transformer operates under the rated load, as shown in the Eq. 15:

$$\dot{B}_f^* = \dot{p}\dot{I}_{f1}^* + \dot{q}\dot{I}_{f2}^* \tag{15}$$

$\dot{B}_f^*$ Indicates leakage magnetic field under the rated load. $\dot{I}_{f1}^*, \dot{I}_{f2}^*$ is the primary and secondary side current under the rated load. Eq. 16 can be obtained from Eq. 14, 15:

$$\dot{B}_f^* = \left[\dot{I}_{f1}^* \, \dot{I}_{f2}^* \right] \begin{bmatrix} \dot{I}_{a1}^* & \dot{I}_{a2}^* \\ \dot{I}_{b1}^* & \dot{I}_{b2}^* \end{bmatrix}^{-1} \begin{bmatrix} \dot{B}_a^* \\ \dot{B}_b^* \end{bmatrix} \tag{16}$$

Eq. 16 shows that under any two load conditions, the leakage magnetic field intensity of any measuring point can be normalized to the rated load condition, which avoids the interference of load fluctuation on the fault classification.

3.2 Extraction of Lissajous figure feature quantity of magnetic field leakage

The transformer used in this experiment was a toroidal core transformer, which is widely used in electronic equipment with high technical requirements, and it primarily serves as a power transformer. From the perspective of straightening the iron core, the radial magnetic field leakage is equivalent to the axial direction of the core transformer, and the tangential direction is equivalent to the radial direction of the core transformer. This is called the radial direction and the tangential direction is called the axial direction. In this study, the primary and secondary-side windings of the A-phase Y/Y connection of the three-phase transformer are used as an example for testing.

When an early fault occurs in the transformer, it can be found by analyzing the waveform of the leakage magnetic field that the change in the leakage magnetic field at the end and central positions of the transformer is the most evident, and there are distinct differences in different fault types. To distinguish the different fault types of the winding, it is proposed set a measuring point at the two ends and central positions of the winding to measure the axial and radial leakage magnetic fields. The measurement point position of the transformer leakage magnetic field is illustrated in Figure 2.

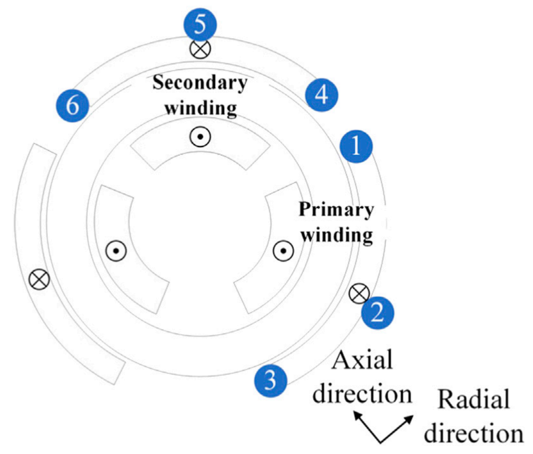

FIGURE 2
Schematic diagram of transformer measurement points.

Previous studies have only used the amplitude and phase angle of the leakage field at individual measurement points, but for transformer faults it is the internal leakage field balance that changes. The relationship of the leakage field between the measurement points is also important information. We propose a method that uses the Lissajous image of the leakage field signal to better integrate the information between these measurement points. The transformer leakage magnetic field waveform is a harmonic signal and the Lissajous figure is widely used in harmonic signal processing (Zhao et al., 2019). When the transformer fails, the symmetry of the magnetic field leakage at both ends of the winding changes. The Lissajous figure drawn by the leakage magnetic field waveform at measuring points 1, 3 and 4, 6 can reflect the change in the symmetry of the winding at the time. The leakage magnetic field in the middle of the fault winding changes; however, that of the non-fault winding remains unchanged. The Lissajous figure drawn by the leakage magnetic field waveform at 2, 5 measuring points can reflect this mutation. To make the fault characteristics more intuitive, this work deduces the length, swing angle, area, least square radius, and roundness of the long and short axes of the Lissajous figure as characteristic parameters that reflect the change in the leakage magnetic field amplitude and phase angle. Considering the leakage magnetic field waveform of 1, 3 measuring points as an example, the characteristic quantity of the leakage magnetic field is calculated. Assuming that the leakage magnetic field waveform of measuring points 1, 3 is as shown in Eq. 17:

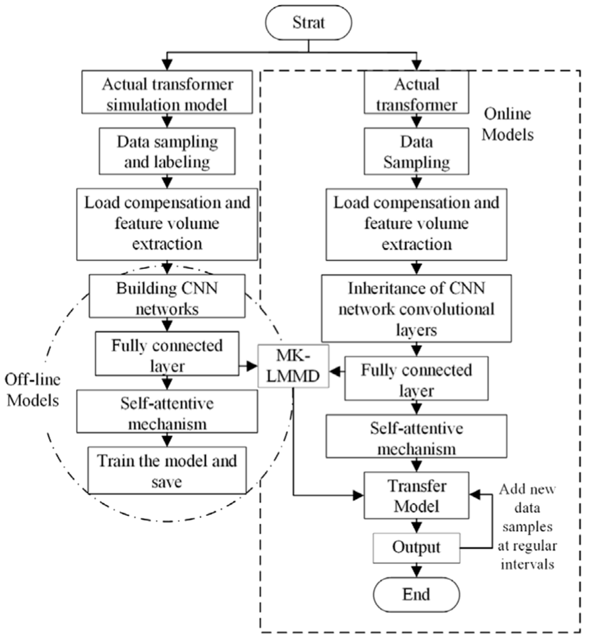

FIGURE 3
System operation flowchart.

$$\begin{cases} B_1 = M\cos(\omega t + \psi_1) \\ B_3 = N\cos(\omega t + \psi_3) \end{cases} \tag{17}$$

M, N indicate the amplitude of the magnetic field leakage, and $\xi = \psi_1 - \psi_3$ is defined as the phase angle difference between points 1, 3 measuring points. Solve the equation, we obtain the length of the long- and short-axis a、b of the Lissajous figure, as follows Eq. 18:

$$a^2 \text{or} b^2 = \frac{(M^2 + N^2) \mp \sqrt{(M^2 + N^2)^2 - 4M^2N^2\sin^2\xi}}{2} \tag{18}$$

According to the elliptic area formula, the area of the Lissajous figure is calculated using $S = \pi ab$.

The coordinates are rotated to calculate the swing angle of the Lissajous figure as follows Eq. 19:

$$\theta_Q = \frac{1}{2}\arctan\frac{2MN\cos\xi}{N^2 - M^2}, N \neq M \tag{19}$$

It is evident from the above formulas that the long-short axis, area, and swing angle of the leakage magnetic field Lissajous figure are functions of the amplitude and phase difference of measuring points 1, 3, and the fault information of the leakage magnetic field represented by it is more abundant, which is conducive to improving the accuracy of classification.

Assuming that u、v is divided into m points of u_i、$v_i\,(i = 1, 2, \ldots, m)$ following sampling, then the center coordinate of the least square circle is $(u_0 = \frac{2}{m}\sum_i^m u_i$; $v_0 = \frac{2}{m}\sum_i^m v_i)$. The radius of the least square circle of Lissajous figure is $r_0 = \frac{1}{m}\sum_{i=1}^m \sqrt{(u_i^2 + v_i^2)}$, and the distance between the first point and the least square center is as follows Eq. 20:

$$r_i = \sqrt{(u_i - u_0)^2 + (v_i - v_0)^2} \tag{20}$$

The circularity of the Lissajous graph is $e = \max(r_i) - \min(r_i)$.

The change in the least square radius of the Lissajous figure reflects the change in the amplitude of the leakage magnetic field waveform, and the change in the roundness reflects the change in the phase difference of the leakage magnetic field waveform. It can also be used as a characteristic quantity of the magnetic field leakage for transformer fault diagnosis.

3.3 Transformer early fault diagnosis process

First, the CNN classification model was constructed by offline learning the fault leakage magnetic field characteristics of the simulation transformer model. Second, the actual transformer fault is diagnosed by online measurement and extraction of the magnetic field leakage characteristics of the actual transformer. The early fault diagnosis process of the transformer is as follows.

3.3.1 Simulation model construction and actual transformer experimental platform construction

1) Measured actual transformer structure data and electrical parameters on the nameplate to establish a 1: 1 actual transformer simulation model.

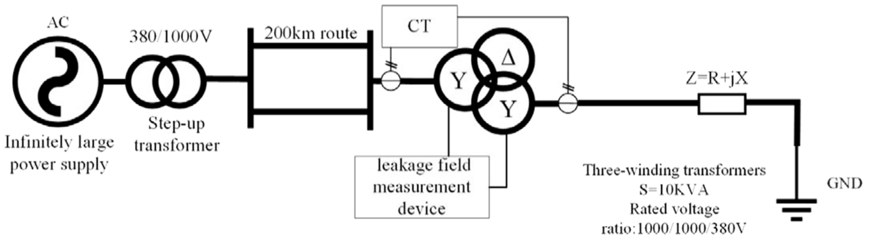

FIGURE 4
Transformer leakage magnetic field measurement.

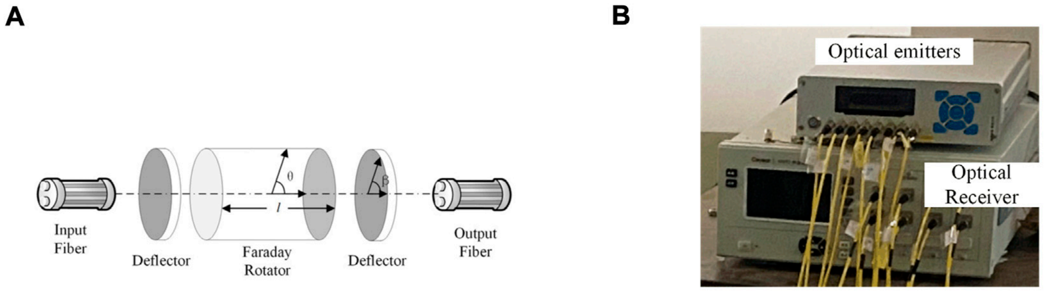

Schematic diagram of fiber optic leakage magnetic field sensor

Optical signal transmitter and receiver Instrument

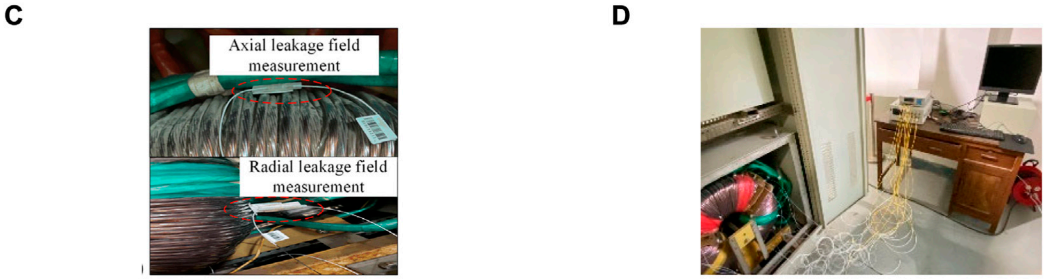

Leakage magnetic field measurement sensor installation

Field measurement device for leakage magnetic field

FIGURE 5
Transformer leakage magnetic field measurement device and installation schematic. **(A)** Schematic diagram of fiber optic leakage magnetic field sensor. **(B)** Optical signal transmitter and receiver Instrument. **(C)** Leakage magnetic field measurement sensor installation. **(D)** Field measurement device for leakage magnetic field.

2) Develop the actual transformer fault simulation and magnetic field leakage measurement platform.

3.3.2 Data generation

1) An actual transformer simulation model was used to simulate the possible faults in the transformer under different load conditions. The current on the primary and secondary windings of the transformer and the waveform data of the leakage magnetic field at each measuring point were recorded. The measured current data are normalized by the formula in Section 3.1, and the characteristic quantity of the magnetic field leakage is calculated. The gray image formed by the characteristic quantity of the magnetic field leakage is considered as the sample data $\boldsymbol{x}_s$, and the label $\boldsymbol{y}_s$ is added according to the fault type to generate the training sample $\boldsymbol{D}_S$. Part of the data was randomly divided into training dataset $\boldsymbol{D}_{\text{train}}$, and another part of the data was randomly divided into validation dataset $\boldsymbol{D}_{\text{valid}}$.
2) Normal operation, inter-turn short circuit, and winding deformation experiments of the actual transformer experimental platform were performed, and the data were recorded. The measured data from the actual transformer are used to constitute the test sample. $\boldsymbol{D}_T$.

3.3.3 Network structure and acceleration algorithm

Because the input image is small, to fully extract its feature information, the kernel functions of the convolution and pooling layers in the CNN are both large. The momentum-updating stochastic gradient descent (SGD) acceleration algorithm was used to improve the network training speed. Offline model training was terminated when the error was less than the set value. The online detection model inherits the convolution layer parameters completed by offline training, and its full connection layer parameters are randomly initialized.

3.3.4 Parameter update and stop

1) The loss function of the offline CNN model is calculated according to the actual label data and label output predicted by the classifier and stops after the error reaches the set value.
2) The online model uses direct transfer learning. After calculating the transfer loss and classification loss by MK-LMMD regularization, the full connection layer parameters in the CNN model were retrained until the set number of training was reached.

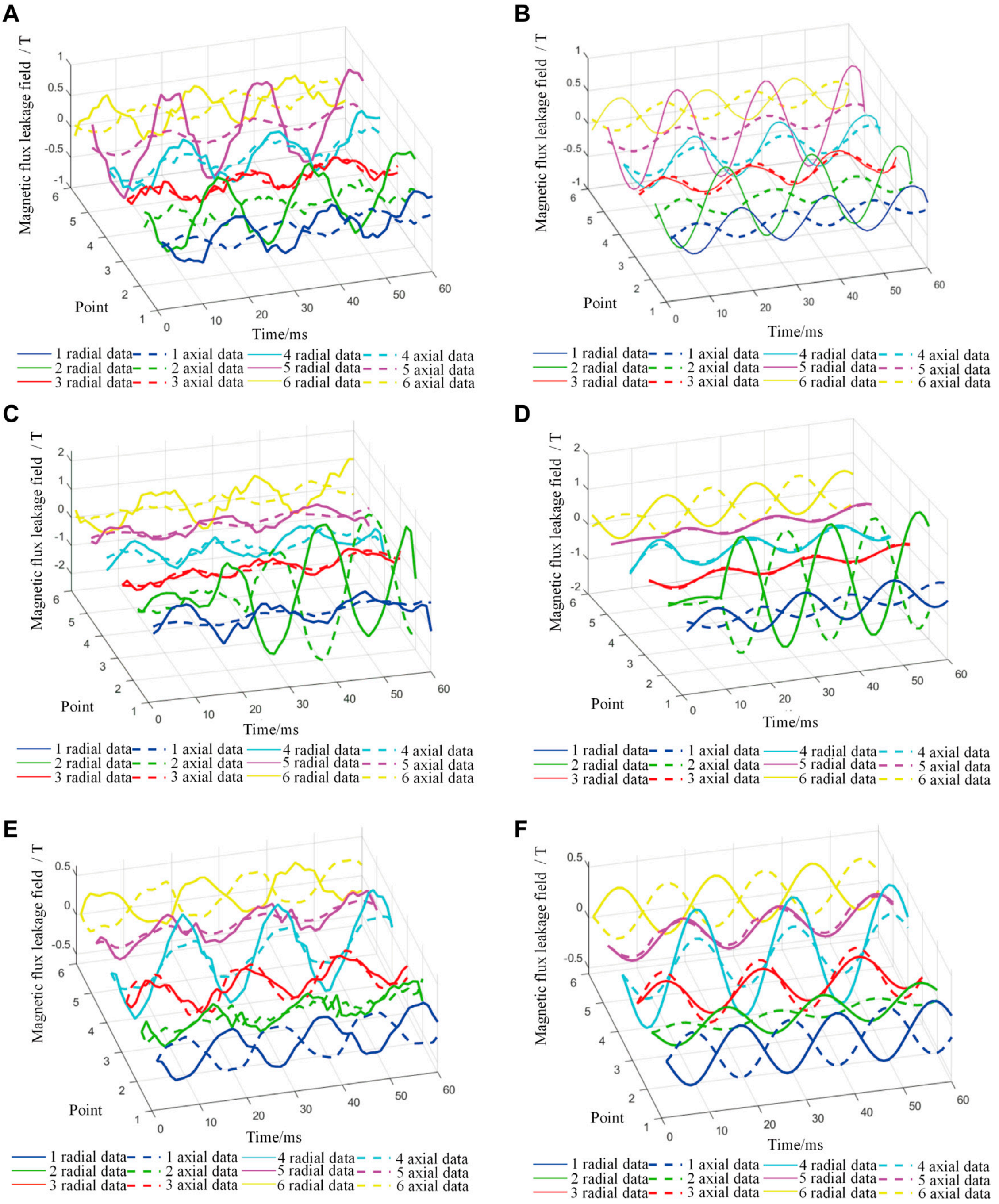

FIGURE 6

Measured waveform of transformer leakage magnetic field. **(A)** Measured waveform of normal Operation leakage magnetic field. **(B)** Simulation waveform of normal operation leakage magnetic field. **(C)** Measurement Waveform of Interturn Short Circuit leakage magnetic field. **(D)** Simulation waveform of interturn short circuit leakage magnetic field. **(E)** The Measured waveform of winding deformation leakage magnetic field. **(F)** Simulation waveform of winding deformation leakage magnetic field.

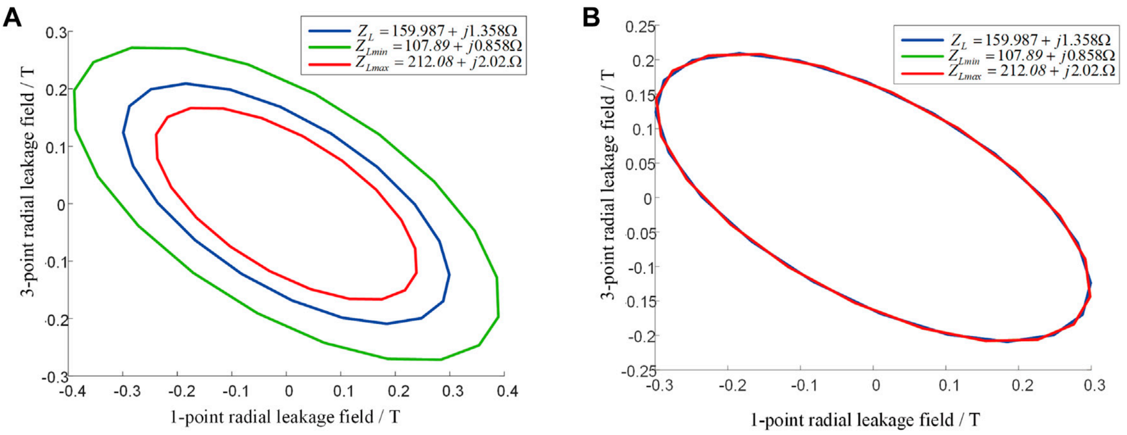

FIGURE 7
Lissajous figure before and after load normalization. **(A)** Before normalization. **(B)** After normalization.

3) Online model parameter updating refers to online model updating by re-labelling the monitored fault data following manual verification after each running period of online detection.

The overall flowchart of the transformer early fault diagnosis model based on CNN transfer learning is illustrated in Figure 3.

4 Example analysis

4.1 The establishment of simulation model and actual transformer experimental platform

4.1.1 Transformer simulation model

The ANSYS MAXWELL software used in this study simulated an actual transformer. In the actual measurement, the sensor only measure the axial and radial leakage magnetic field waveforms in the transformer section. To reduce the generation time of the simulation data, only the two-dimensional (2D) section model of the ring core transformer is established. The solution area of the model was set according to the actual box size, and the primary and secondary windings were connected using a star connection. The 2D model of the transformer was set up, as shown in Supplementary Appendix B2, and the grid value was set according to the empirical value.

4.1.2 The construction of the actual transformer early fault experimental platform

A wiring diagram of the actual experimental platform system is shown in the Figure 4. Infinite power $E = 380V$, with no internal resistance, passes through the high-voltage bus *via* the boost transformer. The test transformer was a three-phase, three-winding transformer. Primary and secondary windings with a Y-shaped connection were used for the experiment. Secondary windings with angular connections were unloaded. The structural and electrical parameters of the transformer are listed in Supplementary Appendix A2. The rated load parameter is $Z_L = 159.98 + j1.35\Omega$. The load adjustment ranges were $Z_{\text{Lmin}} = 107.89 + j0.858\Omega$, $Z_{\text{Lmax}} = 212.08 + j2.02.\Omega$.

4.1.3 Transformer leakage magnetic field measurement platform

We developed a fiber optic leakage magnetic field sensor based on a magneto-optical crystal to collect the actual transformer magnetic field leakage waveform according to the Faraday magneto-optical effect. A sensor probe was installed on the transformer winding. The laser emitter emitted a light signal through the optical signal polarizer and Faraday rotator, and the other end detected the deflection angle of the optical signal through the optical signal receiver and converted it to leakage magnetic field intensity. A leakage magnetic field measurement platform was built on an actual transformer experimental platform, as displayed in Figure 5.

4.2 Generation and processing of leakage magnetic field experimental data

4.2.1 Training sample generation

During the normal operation of the transformer, several groups of normal operation state data of the transformer were generated according to the different load values, and several groups of data were generated by changing the number of turns, the position, and the load of the primary and secondary side winding short circuits, respectively. The minimum number of short-circuit turns is two, and the maximum is 40 turns. In the simulation of the winding axial deformation fault, the axial deformation degree of the upper or double ends of the primary and secondary side windings were changed, the axial

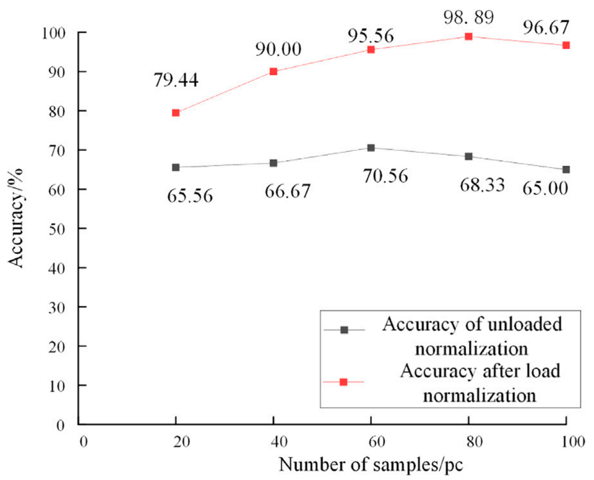

FIGURE 8
Effect of different number of simulation sample data and load normalized on detection accuracy.

compression ratio ranged from 1% to 40%, and several groups of data were generated by changing the load. In the fault simulation of the radial deformation of the winding, the proportion of the radial deformation of the primary- and secondary-side windings changes from 3% to 25%. Different training data were generated according to different radial deformation ratios, the position of the radial deformation line cake, and the load. Each state type of the simulation model generated 125 groups of sample data and a total of 1,125 groups of training sample data.

4.2.2 Test sample generation

The test samples were generated by the actual transformer, and several groups of data for normal operation under different loads were generated by the actual transformer. In the inter-turn short-circuit test of the primary and secondary windings, the minimum is 6 turns and the maximum is 24 turns, and several groups of data were obtained under different loads. Winding deformation test on transformer to change the degree of axial and radial deformation of the primary and secondary windings to form training samples. Each state type generated 20 groups of sample data with 180 groups of test-data waveforms.

4.2.3 Comparison between simulation model and actual transformer normal operation and inter-turn short circuit

A sampling frequency of 1 kHz was used for all samples in this study. Except for the actual measured waveforms, the data were filtered. A comparison of the measured and simulated waveforms of the transformer leakage field is shown in Figure 6.

TABLE 1 Effect of different characteristic quantity on detection accuracy.

Number of features	R_m/%	F_1/%	A_c/%
0	92.19	91.79	92.22
1	93.24	88.12	90.00
2	91.59	91.15	91.11
3	92.60	92.59	92.78
4	94.37	94.30	94.44
5	96.84	96.59	96.67
6	**98.94**	**98.87**	**98.89**

TABLE 2 Effect of different regularizer layers on accuracy.

Add MK-MMD regularizer layers	R_m/%	F_1/%	A_c/%
CNN only	89.78	84.93	85.56
A layer of MK-LMMD regularizer	94.92	94.91	95.00
Two layer MK-LMMD regularizer	96.28	96.03	96.11
Three layer MK-LMMD regularizer	**98.94**	**98.87**	**98.89**

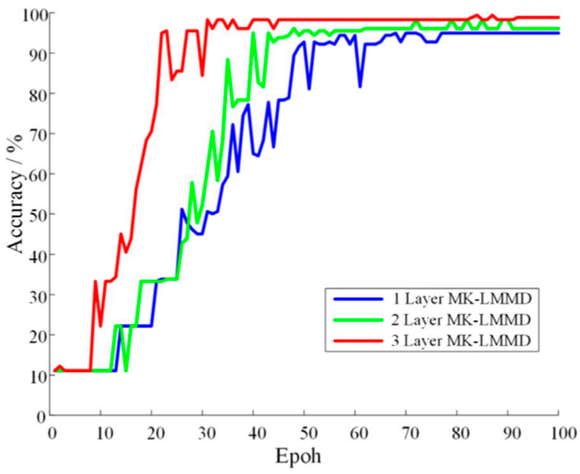

FIGURE 9
Transfer learning training correct rate curve.

It can be observed from Figure 6, the amplitude and phase angle of the leakage field at our selected measurement points change to different degrees when the transformer is in normal condition and a fault occurs. We use the Lissajous curve proposed in Section 3.2 to extract the changes in the characteristic quantities at the time of the fault as input to the CNN and use artificial intelligence techniques to analyze the differences for transformer winding fault classification. Meanwhile, there is still a gap between the simulation waveform and the actual waveform difference. DSAN realizes domain adaptation by aligning its distribution difference and

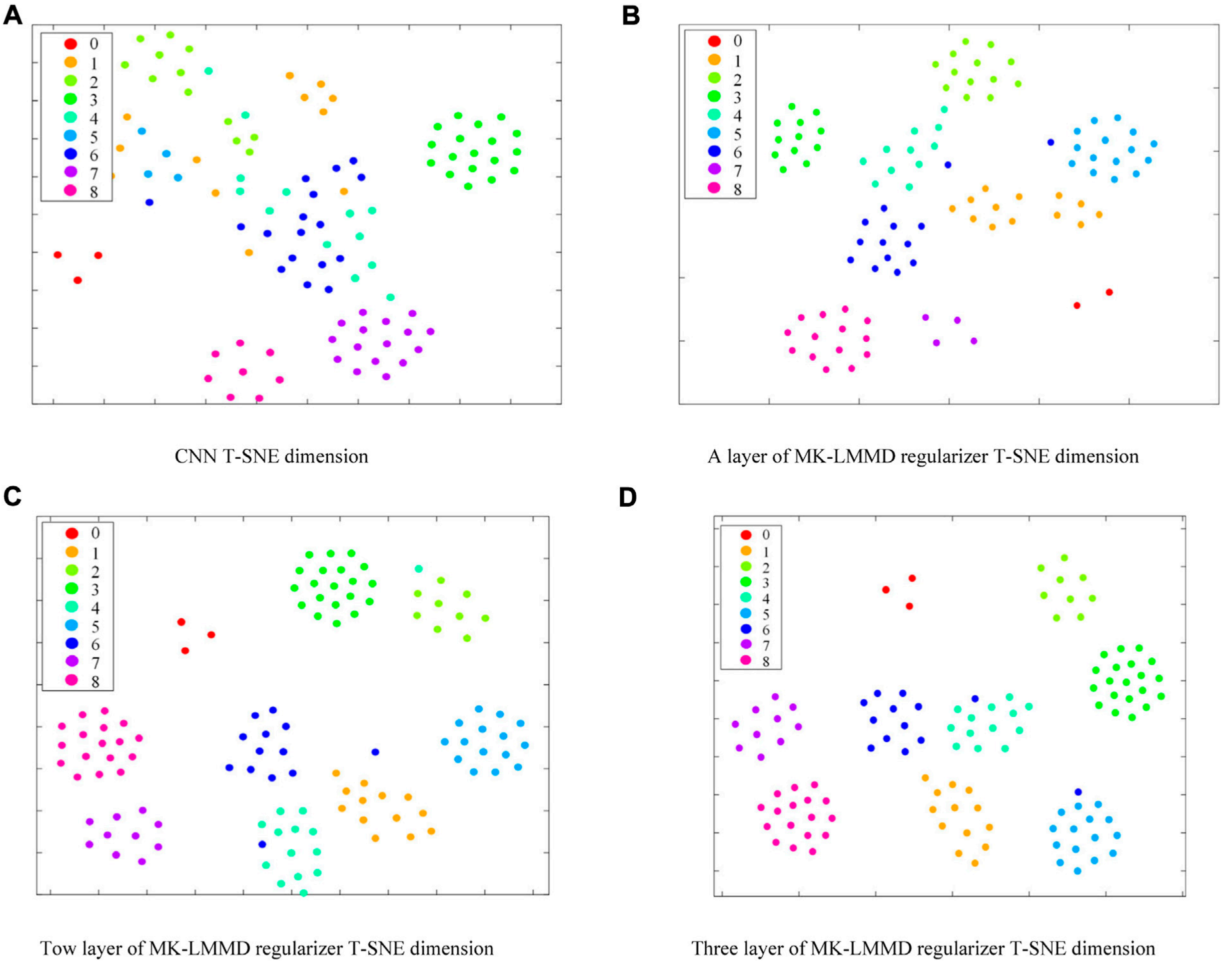

FIGURE 10
Comparison of T-SNE scatter plots under different training models. **(A)** CNN T-SNE dimension. **(B)** A layer of MK-LMMD regularizer T-SNE dimension. **(C)** Tow layer of MK-LMMD regularizer T-SNE dimension. **(D)** Three layer of MK-LMMD regularizer T-SNE dimension.

achieves the ability to diagnose actual transformer faults using simulation data.

4.2.4 Lissajous figure comparison before and after load normalization

The measured radial leakage magnetic fields at 1, 3 are plotted as Lissajous figures under the rated load, respectively, as shown in Figure 7A. It is evident that the Lissajous figures change with the change in load, which adversely affects the classification accuracy. Figure 7B illustrates the Lissajous figures of measuring points 1, 3 after load normalization. It is evident that after load normalization, the change of Lissajous figure caused by the change of transformer load is eliminated, and the characteristic quantity of leakage magnetic field is not affected by the load.

4.2.5 Lissajous figure feature extraction and gray image generation

The characteristic quantity of the Lissajous figure formed by the leakage magnetic field was extracted, and the data were transformed into gray image data of 6 × 6. The gray image formed by the characteristic quantity of the transformer winding is shown in Supplementary Appendix B3, B4.

4.3 Example analysis

The transfer neural network prepared in this study is based on Python 3.6 version and Pytorch version 1.2.0. CPU training was then performed. The CPU of the computer was an AMD Ryzen 7 4800 H, and the main frequency was 2.90 GHz. A batch

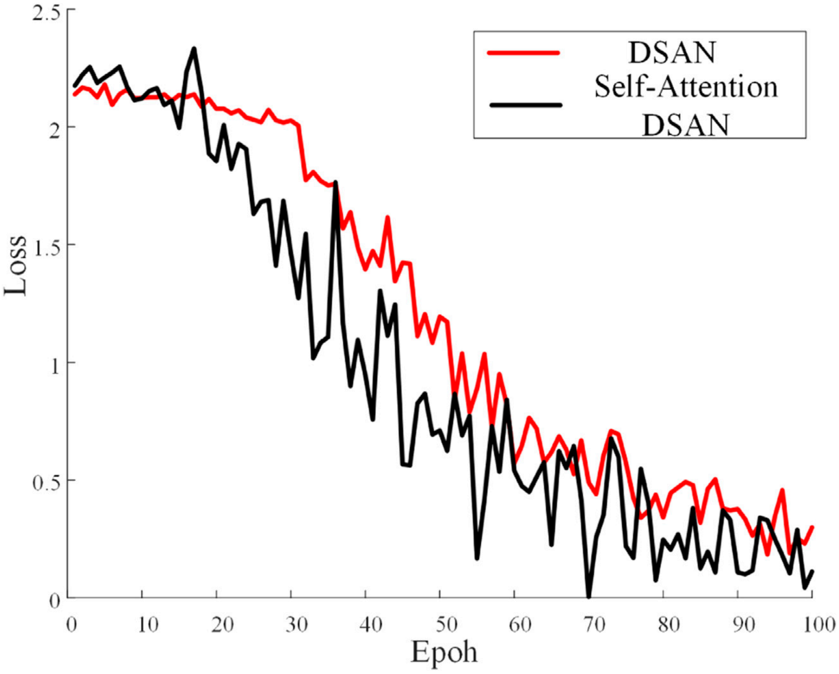

FIGURE 11
DSAN error curve of self-attentive mechanism.

of 10 sets of data, initial learning rate 0.4, training 100 Epohs, MK-LMMD regularizer penalty factor initial value $\lambda = 1$. The transformer states in this paper are divided into normal operation, winding deformation and inter-turn short circuit. The inter-turn short circuit is subdivided into primary winding inter-turn short circuit and secondary winding inter-turn short circuit. The winding deformation is subdivided into nine states, namely, the axial deformation at the upper end of primary and secondary side winding, the axial deformation at the two ends of primary and secondary side winding, and the radial deformation of primary and secondary side winding. The operation state of the transformer is coded as shown in Supplementary Appendix A3.

4.3.1 Load normalization and simulation sample number experiments

To test the influence of load balances and the number of simulation samples participating in training on transformer fault diagnosis, we also generated gray images for training and testing the data without load normalization. Simultaneously, to detect the influence of the number of simulation samples on the detection effect, different numbers of simulation samples were selected for offline training. To ensure that the data of the offline training test set were unchanged, a certain number of simulation samples were randomly selected as the training set, and samples without and after load normalization were tested. The accuracy results are presented in Figure 8.

TABLE 3 Identification accuracy of different transfer methods in case of transformer faults.

Transfer method	R_m/%	F_1/%	A_c/%
DAN	91.34	91.06	91.11
Deep-CORAL	95.62	95.55	95.56
GAN	96.21	96.12	96.11
DSAN	96.84	96.66	96.67
Model in this paper	**98.94**	**98.87**	**98.89**

It is evident from the above diagram that load normalization has a significant impact on overall accuracy. Load normalization can significantly improve the transformer detection accuracy. Compared with the unnormalized load data, the highest accuracy increased by 28.33%. Simultaneously, the number of training sets also affects the detection accuracy. Increasing the number of simulation samples did not always improve the accuracy of the test. When the number of simulation samples is too large, the model focuses on the detection of simulation samples, which reduces the accuracy of the actual transformer

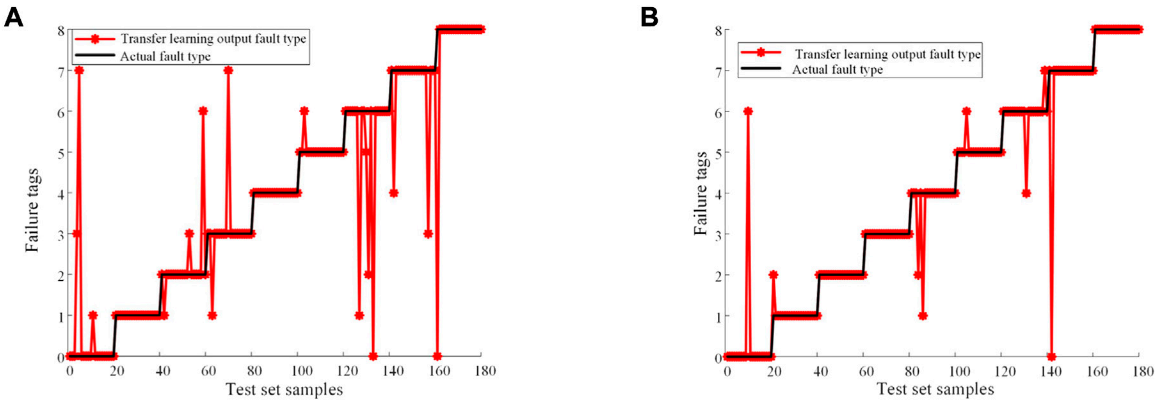

DAN transfer learning model diagnosis result graph

CORAL transfer learning model diagnosis result graph

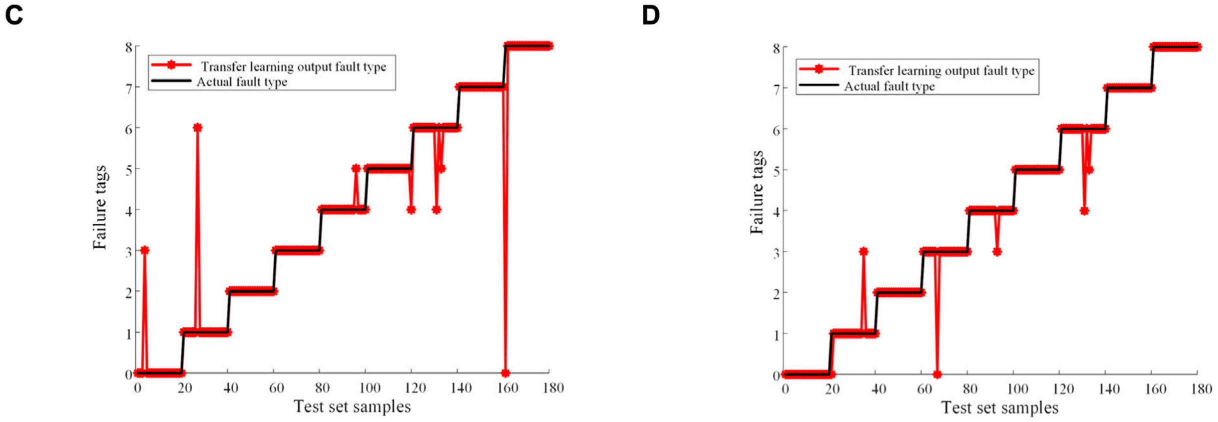

GAN transfer learning model diagnosis result graph

DSAN transfer learning model diagnosis result graph

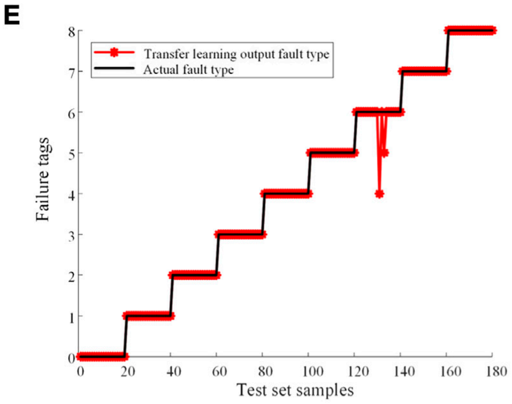

Diagram of the diagnostic results of the model in this paper

FIGURE 12
Comparison of diagnostic results of four different transfer models. **(A)** DAN transfer learning model diagnosis result graph. **(B)** CORAL transfer learning model diagnosis result graph. **(C)** GAN transfer learning model diagnosis result graph. **(D)** DSAN transfer learning model diagnosis result graph. **(E)** Diagram of the diagnostic results of the model in this paper.

detection. When the number of simulation samples was 80 in each state, the accuracy was the highest, and the accuracy did not increase again when the number of training samples increased.

4.3.2 Experiment on the quantity of characteristic quantities of magnetic field leakages

To test the influence of the leakage magnetic field characteristics on the accuracy of the transformer fault diagnosis, different quantities of characteristics were selected for training and testing, and the accuracy of classification was compared. For the experimental group without feature parameters, we directly used the amplitude and phase angle data of the six measuring points to load balance and convert them into gray images for testing. Recall rate R_m, stability comprehensive index F_1, and accuracy A_c were used as evaluation indexes. Table 1 presents the results.

It can be observed from Table 1 that the method of using the characteristic quantity has a positive effect on enhancing the accuracy of transformer diagnosis. Compared with the method of using only the amplitude and phase angle of the leakage magnetic field to diagnose faults, the accuracy of this method was improved by 6.67%.

4.3.3 MK-LMMD regularizer layer experiment

The data of the 80 simulation groups for each fault state were used as training samples, and the measured waveform was used as the test sample. To test the effect of adding different numbers of MK-LMMD regularizers on the test results, the training results of adding MK-LMMD regularizers in the last layer, last two layers, and three layers of the full connection layer were tested and compared with the results of the CNN classification model without transfer learning. The results are as follows. Table 2 presents that the accuracy curve of the classification model with different numbers of MK-LMMD regularizer layers increases with the number of iterations, as shown in Figure 9.

Table 2 indicates that the difference between the simulation data and the actual transformer data cannot be overcome when the non-transfer CNN fault classification model is directly used for actual transformer detection, resulting in unsatisfactory accuracy of the actual transformer fault classification. As shown in Figure 9, the classification model with three-layer MK-LMMD regularization has the highest accuracy and fastest convergence rate, which is 13.33% higher than that with only CNN.

The transformer fault features extracted from the model with MK-LMMD regularizers of different layers were reduced to 2D visualization by T-SNE, as shown in Figure 10.

In high-dimensional spatial data, the points with closer distances remain close when they are projected to 2D by T-SNE dimension reduction. The farther the distance of each cluster, the greater the difference and the better the classification effect. The results in Figure 10 reveal that the transfer learning model using three-layer MK-LMMD regularization has a better discrimination for different fault types of the actual transformer, indicating that increasing the adaptability of the high-order feature layer can effectively improve the transfer effect.

4.3.4 Self-attention mechanism deep subdomain adaptive network experiment

To verify the effect of the DSAN network with the self-attention mechanism, the data from 80 simulation groups for each fault state were used as training samples, and the measured waveform was used as the test sample. The error iteration curve obtained using training is illustrated in Figure 11.

Figure 11 shows that in the training process without giving training samples self-attention weights, some samples deviate too much from the test sample, resulting in large transfer error of MK-LMMD regularization, resulting in oscillation of error curve. The self-attention DSAN proposed in this paper can speed up the network training speed, reduce the error level, has good stability and reduce the training loss.

4.4 Comparative experiments with other transfer networks

To compare the proposed method with other transfer neural networks, the existing DAN transfer learning (Long and Wang, 2015), CORAL transfer learning (Sun and Saenko, 2016), GAN transfer learning (Hu et al., 2021), and traditional DSAN models are used for comparison (Zhu et al., 2021). In the experiments, the data of 80 simulation groups for each fault state were used as the simulation samples. The test results for the 20 groups of experimental samples in each group are listed in Table 3. The classification of the test samples is depicted in Figure 12. In Figure 12, the black solid line represents the true value of the fault type and the red circle represents the diagnostic value of the model for the fault. When the red circle coincides with the black line, it indicates that the diagnosis is correct; otherwise, the diagnosis is incorrect.

Figure 12 illustrates that the method used in this study has the best classification effect. In addition to the misjudgment of the upper end winding deformation of the secondary side, the classification effect of the fault is superior. Compared with the other three transfer models, the MK-LMMD regularization and self-attention mechanism used in the proposed transfer model effectively reduced the distribution distance between the simulated transformer data and the actual transformer data, and realized the transfer from the simulated transformer to the actual transformer with high accuracy.

5 Conclusion

This paper eliminates the effect of transformer load variations on leakage field measurements by negative normalization and improves the utilization rate of the leakage magnetic field information. Meanwhile, transfer learning to reduce the difference between the simulation model and the actual transformer data and realizes the fault classification model trained by the simulation data to early diagnosis of actual transformer faults. The influence of load change in transformer leakage magnetic field detection is eliminated, and the characteristic quantity of the leakage magnetic field is extracted to diagnose transformer faults, which improves the utilization rate of the leakage magnetic field information. The accuracy of the method proposed in this paper reaches 98.89%, which is suitable for detecting and diagnosing the internal faults of transformer windings promptly *via* real-time acquisition of transformer faults and provides a reference for reasonable periodic shutdown maintenance of transformers. However, only one structure of transformer transfer learning ability is studied in this paper, for other structures of transformer simulation and transfer learning between actual transformers and mutual transfer between the different structure of transformers is our next research direction.

Data availability statement

The original contributions presented in the study are included in the article/Supplementary Material, further inquiries can be directed to the corresponding author.

Author contributions

The XD wrote the original draft. ZZ, KY, and HZ provided the supervision, review, and editing of the draft. All authors contributed to theatrical and approved the submitted version.

Funding

Funded by the National Nature Fund (51777119).

Conflict of interest

The authors declare that the research was conducted in the absence of any commercial or financial relationships that could be construed as a potential conflict of interest.

Publisher's note

Supplementary material

The Supplementary Material for this article can be found online at: https://www.frontiersin.org/articles/10.3389/fenrg.2022.1058378/full#supplementary-material

References

Alshehawy, A. M., Mansour, D. E. A., Ghali, M., Lehtonen, M., and Darwish, M. M. F. (2021). Photoluminescence spectroscopy measurements for effective condition assessment of transformer insulating oil. *Processes* 9 (5), 732. doi:10.3390/pr9050732

Bo, Z., Xza, B., Zza, B., and Wu, Q. (2021). Deep multi-scale separable convolutional network with triple attention mechanism: A novel multi-task domain adaptation method for intelligent fault diagnosis. *Expert Syst. Appl.* 2021, 115087. doi:10.1016/j.eswa.2021.115087

Cabanas, M. F., Melero, M. G., Pedrayes, F., Rojas, C. H., Orcajo, G. A., Cano, J. M., et al. (2007). A new online method based on leakage flux analysis for the early detection and location of insulating failures in power transformers: Application to remote condition monitoring. *IEEE Trans. Power Deliv.* 22 (3), 1591–1602. doi:10.1109/TPWRD.2006.881620

Chen, Y. M., Liang, J., and Zhang, J. W. (2019). Method of online status monitoring for windings of three-winding transformer based on improved parameter identification. *High. Volt. Eng.* 45 (5), 1567–1575. doi:10.13336/j.1003-6520.hve.20190430029

Deng, X. l., Xiong, X. F., and Gao, L. (2014). On line monitoring method of transformer winding deformation based on parameter identification CSEE. *Proc.*34 (28), 4950–4958. doi:10.13334/j.0258-8013.pcsee.2014.28.023

Elsis, M., Minh, Q. T., Karar, M., Diaa-Eldin, A. M., Matti, L., and Darwish, M. M. F. (2022). Effective IoT-based deep learning platform for online fault diagnosis of power transformers against cyberattacks and data uncertainties. *Meas. (. Mahwah. N. J).* 2022, 110686. doi:10.1016/j.measurement.2021.110686

Emara, M. M., Peppas, G. D., and Gonos, I. F. (2021). Two graphical shapes based on DGA for power transformer fault types discrimination. *IEEE Trans. Dielectr. Electr. Insul.* 28 (3), 981–987. doi:10.1109/TDEI.2021.009415

Gao, J., and He, J. J. (2010). Application of quantum genetic ANNs in transformer dissolved gas-in-oil analysis. *Proc. CSEE* 30 (30), 121–127. doi:10.13334/j.0258-8013.pcsee.2010.30.020

Ghifary, M., Kleijn, W. B., and Zhang, M. (2014). "Domain adaptive neural networks for object recognition," in *Pacific rim international conference on artificial intelligence* (Cham: Springer), 898–904. doi:10.1007/978-3-319-13560-1_76

Gu, C. L. (2010). *Electrical engineering*. Wuhan: Huazhong University of Science and Technology.

Haghjoo, F., Mostafaei, M., and Mohammadi, H. (2017). A new leakage flux-based technique for turn-to-turn fault protection and faulty region identification in transformers. *IEEE Trans. Power Deliv.* 33, 671–679. doi:10.1109/TPWRD.2017.2688419

Hang, W., and Butler, K. L. (2002). Modeling transformers with internal incipient faults. *IEEE Trans. Power Deliv.* 17 (2), 500–509. doi:10.1109/61.997926

Hu, X., Zhang, H., Ma, D., and Wang, R. (2021). A tnGAN-based leak detection method for pipeline network considering incomplete sensor data. *IEEE Trans. Instrum. Meas.* 70, 1–10. doi:10.1109/TIM.2020.3045843

Jang, E., Gu, S. S., and Poole, B. (2017). Categorical reparameterization with gumbel-softmax. Available at: http//:ArXiv.org/abs/1611.01144. doi:10.48550/arXiv.1611.01144

Lecun, Y., Bottou, L., Bengio, Y., and Haffner, P. (1998). Gradient-based learning applied to document recognition. *Proc. IEEE* 86 (11), 2278–2324. doi:10.1109/5.726791

Li, H., Huang, Z. Y., and Tian, Y. (2022). Research on transformer fault diagnosis method based on deep neural network. *Transformer* 59 (04), 35–40. doi:10.19487/j.cnki.1001-8425.2022.04.014

Liu, N., Liang, G. D., Wang, L. F., Gao, W. S., and Tan, K. X. (2003). Construction and analysis of fault tree for large-scalepower transformer. *Electr. Power* 36 (11), 33–36. doi:10.13336/j.1003-6520.hve.2003.02.002

Long, M., and Wang, J. (2015). "Learning transferable features with deep adaptation networks," in International conference on machine learning. PMLR 2015, 97–105. doi:10.1109/TPAMI.2018.2868685

Naseri, F., Kazemi, Z., Arefi, M. M., and Farjah, E. (2018). Fast discrimination of transformer magnetizing current from internal faults: An extended kalman filter-based approach. *IEEE Trans. Power Deliv.* 33 (1), 110–118. doi:10.1109/TPWRD.2017.2695568

Pan, C., Shi, W. X., and Meng, T. (2020). Study on electromagnetic characteristics of interturn short circuit of single-phase transformer. *High. Volt. Eng.* 46 (05), 1839–1856. doi:10.13336/j.1003-6520.hve.20200515040

Shamlou, A., Feyzi, M. R., and Behjat, V. (2021). Winding deformation classification in a power transformer based on the time-frequency image of frequency response analysis using Hilbert-Huang transform and evidence theory. *Int. J. Electr. Power & Energy Syst.* 129 (5), 106854. doi:10.1016/j.ijepes.2021.106854

Sun, B., and Saenko, K. (2016). *Deep CORAL: Correlation alignment for deep domain adaptation*. Berlin, Germany: Springer International Publishing.

Wang, G., Giannakis, G. B., and Chen, J. (2019). Learning ReLU networks on linearly separable data: Algorithm, optimality, and generalization. *IEEE Trans. Signal Process.* 67 (9), 2357–2370. doi:10.1109/TSP.2019.2904921

Wang, K., and Zeng, J. L. (2021). Simulation study of leakage field of power transformer under different operation modes based on field-path coupling. *J. Harbin Inst. Technol.* 26 (04), 28–37. doi:10.15938/j.jhust.2021.04.005

Wang, X., and Han, T. (2021). Transformer fault diagnosis based on Bayesian optimized random forest. *Electr. Meas. Instrum.* 58 (6), 167–173.

Wu, Z. H ., Zhou, M. B., Lin, Z. H., Chen, X. J., and Huang, Y. H. (2021). Improved genetic algorithm and XGBoost classifier for power transformer fault diagnosis. *Front. Energy Res.* 2021, 9. doi:10.3389/fenrg.2021.745744

Zhang, B. Q., Xian, R., and Yu, Y. (2021). Analysis of physical characteristics of power transformer windings UnderInter-turn short circuit fault. *High. Volt. Eng.* 47 (06), 2177–2185. doi:10.13336/j.1003-6520.hve.20201178

Zhang, J. C. (2019). *Analysis of transformer winding leakage field and short-circuit electromotive force*. Shenyang, China: Shenyang University of Technology.

Zhao, X., Yao, C., Zhou, Z., Li, C., Abu-Siada, A., Zhu, T., et al. (2019). Experimental evaluation of transformer internal fault detection based on V–I characteristics. *IEEE Trans. Ind. Electron.* 67, 4108–4119. doi:10.1109/TIE.2019.2917368

Zhou, Y. C., and Wang, X. (2017). The on-line monitoring method of transformer winding deformation based on magnetic field measurement. *Electr. Meas. Instrum.* 54 (17), 58–63.

Zhu, Y. C., Zhuang, F. Z., Wang, J. D., Ke, G., Chen, J., Bian, J., et al. (2021). Deep subdomain adaptation network for image classification. *IEEE Trans. Neural Netw. Learn. Syst.* 32 (4), 1713–1722. doi:10.1109/TNNLS.2020.2988928

frontiers | Frontiers in Energy Research

TYPE Original Research
PUBLISHED 03 February 2023
DOI 10.3389/fenrg.2023.1092673

OPEN ACCESS

EDITED BY
Xin Ning,
Institute of Semiconductors (CAS), China

REVIEWED BY
Imran Khan,
University of Engineering and Technology,
Peshawar, Pakistan
Prayag Tiwari,
Halmstad University, Sweden

*CORRESPONDENCE
Huanghai Xie,
✉ 201908080011006@ctgu.edu.cn

SPECIALTY SECTION
This article was submitted to Smart Grids, a section of the journal Frontiers in Energy Research

RECEIVED 08 November 2022
ACCEPTED 17 January 2023
PUBLISHED 03 February 2023

CITATION
Tang B, Xie H, Liu G, Zhang L and Shang Z (2023), Radar echo simulation of dynamically rotating wind turbine blades based on 3D scattering center.
Front. Energy Res. 11:1092673.
doi: 10.3389/fenrg.2023.1092673

Radar echo simulation of dynamically rotating wind turbine blades based on 3D scattering center

Bo Tang, Huanghai Xie*, Gang Liu, Longbin Zhang and Zhiyu Shang

College of Electrical Engineering and New Energy, Three Gorges University, Yichang, China

Introduction: High-fidelity simulation of the radar echo from the wind turbine (WT) for accurate acquisition of Doppler features, is the key issue in addressing radiation interference from the wind farm on the nearby radar station. In view of the limitation of the conventional scattering center-based equivalent model to reflect the complex surface of blades, it is difficult to simulate the rotating blades'echo accurately with the existing algorithm. Therefore, we proposed a simulation method based on a 3D scattering center extraction to deal with it.

Methods: Therefore, we proposed a simulation method based on a 3D scattering center extraction to deal with it. First, the method of scattering center equivalence to blade scattering is used in order to reduce the modelling as well as the solution of electromagnetic scattering from the multi-space attitude of the blade, which is different from the existing algorithm. Since the geometry affects the parameters of the scattering center, an orthogonal matching pursuit greedy algorithm is used to extract the parameter of the 3D scattering center model.

Results: Therefore, the temporal correspondence between the scattering center and the blade motion characteristics is established, resulting in a reconstruction of the scattered field data of the rotating blades. Consequently, the real-time simulation and Doppler characteristic of blades echoes are achieved using the Short Time Fourier Transform (STFT).

Discussion: A comparison of the results with the data obtained from the GTD scattering center model verififies the accuracy of the proposed method.

KEYWORDS

wind turbine, wind farm, short-time Fourier transform, radar echo, three-dimensional scattering center

1 Introduction

With the large-scale construction of wind farms in China, the interference from wind farms on adjacent radar stations are becoming more and more serious (He et al., 2017b; Steven et al., 2017). Engineering practice shows that with the stimulation of radar incident electromagnetic waves, the radar echoes scattered by WT blades possess micro-Doppler characteristics, quite different from static targets. Accordingly, the accurate acquisition of WT radar echoes to identify the wind farm targets for radar filtering is the key problem to calculate the interference on radar stations from wind farms.

The current methods for obtaining WT Doppler echoes can be divided into two categories, namely the experimental measurement and the numerical simulation (Pooria et al., 2017; He et al., 2021). Experimental measurement which is the most reliable is difficult to perform widely

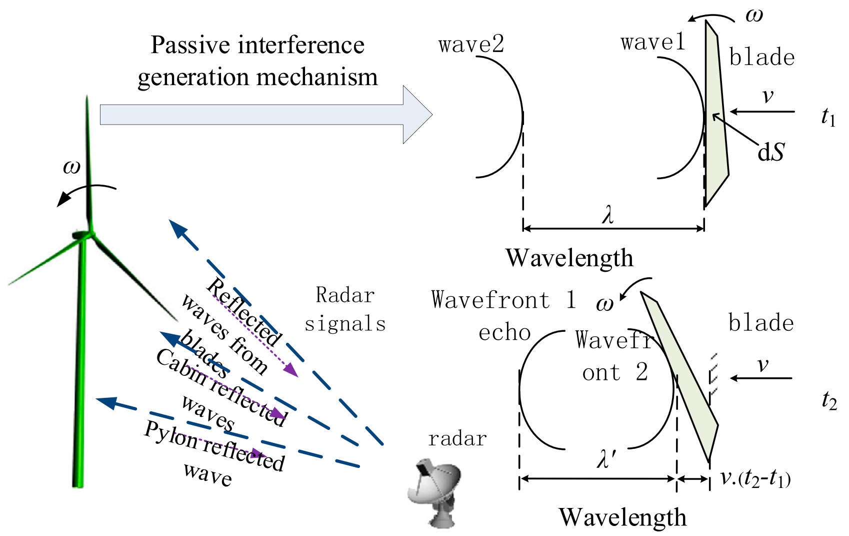

FIGURE 1
Schematic diagram of passive interference of WT to radar signal.

due to its high cost and rather complicated procedures (Chen, 2011; Crespo-Ballesteros et al., 2017). In consequence, increasing efforts have been devoted to the numerical simulation of WT Doppler echoes (Chen et al., 2017; He et al., 2017a).

The earliest numerical method adopt the scattering point model (Tang et al., 2019a; Tang et al., 2019b). However, as the discreteness of scattering point spacing is neglected, the obtained echo is too ideal to represent the real echo (Sun et al., 2016). The method of moments (MoM) can accurately calculate the echo by means of an accurate and intricate geometric model, but the calculation time and resources of MoM increase dramatically with frequency, which is unacceptable in the high-frequency band (Dunoon and Brown, 2013). With the aim of improving calculation efficiency, high-frequency electromagnetic algorithms (Tang et al., 2011; Yan et al., 2011) have been used to calculate the echo, such as the physical optics method (PO) (Zheng et al., 2020a), geometrical theory of diffraction (GTD) (Dai et al., 2020), and others that allow for very fast calculations. However, these. methods neglect the contribution of the edge's diffraction field of the WT during the calculation. So the calculation results are in a poor accuracy, when solving such electromagnetic scattering problems of complex shaped surface like the WT blade.

From the present point of view, scattering centers are used in radar echo analysis of rotating targets such as missiles, which are introduced into the electromagnetic scattering solution of WT blades. In (Zheng et al., 2020b), the scattering center model was used to calculate the scattered electric field of WT blades, laying the groundwork for the solution of the echo. Then Tang *et al.* (Tang et al., 2019c) combined the GTD scattering center model with the radar echo equation to calculate the echo. Although the introduction of the scattering center provides new ideas for calculating the echo simulation, the calculation accuracy was still relatively low. That's because the existing scattering center models are based on a two-dimensional plane for equivalent model reconstruction, so the existing equivalent models neglect the scattering center occultation and anisotropy caused by the geometric properties of WT blades (Gao et al., 2016). Therefore, the equivalent model built from the current scattering center model is too rough to represent the scattering properties from the actual shape of blades. As a result, the simulation results are quite different from the real echo, and the echo cannot be accurately obtained.

To address the problem that the conventional method is difficult to obtain accurate WT radar echoes, a new simulation method using scattering center parameters is proposed which could be considers the influence on the variation of from the blades' three-dimensional geometric configuration. And then an echo simulation method based on 3D scattering center extraction is proposed to solve the anisotropy problem of the traditional scattering center model and finally achieve a high-fidelity echo simulation.

2 WT radar echoes and scattering center

2.1 Radar echoes of WT

The WT is mainly composed of three parts: tower, nacelle, and blades. The tower and nacelle are stationary parts and their echoes are zero-frequency components that can be easily filtered out using the high-pass filter. On the contrary, the rotating blades will generate complex electromagnetic scattering problems.

As shown in Figure 1, this is the process of the Doppler effect caused by WT blades, where d**S** is the scattering face element on the blades and v is the radial velocity vector. At a time of t_1, wave 1 reaches the surface of the blades, at the same time the radar emits wave 2; at a time of t_2, the radar receives an echo of wave 1, at which time wave 2 arrives the surface of the blades. Due to the rotation of the blades with the velocity of ω, there is a difference between the time when the radar receives the wave 1 and wave 2 echoes, making it possible to change the number of blade echoes received by the radar per unit time, thereby changing the frequency of the blades echoes. Therefore, the rotating blades will modulate the echo signal (Bo et al., 2016).

The modulated echo signal is affected by the radar observation point position, the complex heterogeneous surface of the blades, and the dynamic

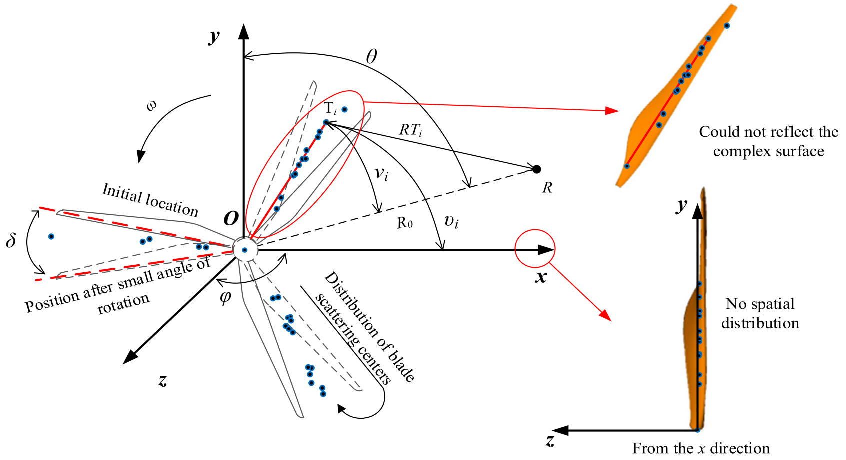

FIGURE 2
Diagram of integral algorithm based on scattering center.

blade speed (Ding et al., 2017; Tang et al., 2017). So accurately obtaining the echoes of blades is a prerequisite for filtering out WT clutter.

2.2 Existing blades echoes simulation methods

At present, the numerical simulation algorithms of WT blades radar echoes mainly include integral algorithm based on scattering point model, scattering field algorithm based on precise geometry model, and integral algorithm based on scattering center. According to the results of echo simulation, the scattering point integration algorithm is simple to calculate. Yet, owing to the theoretical defects of the algorithm, the simulated echo lacks precision, and can only be used for qualitative analysis. The scattered field algorithm, although computationally accurate, relies on complex electrical large size models and a large number of calculations.

The integral algorithm based on scattering center is a new algorithm proposed in the literature (Zheng et al., 2020b) to overcome the defects of the above 2 algorithms. The mathematical model used in this algorithm is shown in Figure 2. The blade is rotated on the *z*-axis, the rotation plane lies in the *xoy* plane, the radar is located at point *R*, and the included angle between the radar incident wave and the blades rotation plane is $\varphi = 0^{\circ}$. Considering that the blades of WT are electrode large size electromagnetic scatter, a scattering center model based on GTD was used.

The method equates the entire blades' scattering entity as a series of scattering point sources by using the scattering field of the blades. And these scattering point sources are represented by the set of scattering center parameters. After the blades scattering center is obtained, the point target radar echo equation is introduced in literature (Zheng et al., 2020b) to simulate the blades radar echoes. Considering that the echo equation contains the position coordinates of the target point and the scattering intensity coefficient, only the position coordinates and the scattering intensity factor are applied to the echo equation.

In terms of the echo simulation process, the integral algorithm based on GTD scattering center discarded the scattering center type parameter α_i when using the radar echo equation for echo simulation. Equivalence of complex curved blade to isotropic scattering center (Li and Du, 2017). Meanwhile, it is considered that the scattering center exists only in the *xoy* plane, ignoring the anisotropy of the scattering center caused by the 3D complex surface of the blades. Subsequently, the scattering center-based integration algorithm still lacks accuracy in the simulated echo signal.

2.3 Key steps to achieve accurate simulation of blades echoes

Starting from Section 1, it can be concluded that to accurately simulate the high-fidelity echo signal of dynamic blades, the following two 2 key problems need to be solved: firstly, the selection of a more accurate scattering center to accurately describe the scattering characteristics of a complex blade; and secondly, how to simulate a dynamic blade echo based on the dynamic scattering center.

Following electromagnetic scattering center theory, a complete scattering center dataset is required when the scattering center is used to equate a target scattering entity with a complex special shape structure (Li and Du, 2017). As a result, a length parameter L and type parameter α_i will be introduced in this paper as quantitative indicators of the 3D geometry of WT blades compared to the traditional GTD scattering center model. Moreover, the 3D scattering center model based on physical optics and geometric diffraction theory is used to distinguish the various scattering structures of the blades, to realize the accurate characterization of the scattering characteristics of the blades.

On this basis, considering that the scattering center parameters of dynamic blades are closely related to the radar aspect, the rotation angle of the blade throughout its motion cycle is divided into multiple aspects, under which the 3D scattering center parameters of each aspect are solved. In addition, according to the idea of accurately solving the echo based on the scattered electric field, the obtained blades scattering centers are used to reconstruct the scattered electric field distribution corresponding to the real-time dynamic rotation of the blades, and the short-time Fourier transform is performed on the obtained scattered electric field vector. Finally, the real-time and fidelity simulation of blades echoes is achieved.

3 Simulation of WT blades radar echoes based on 3D scattering center

3.1 3D scattering center mode

According to the 3D scattering center model and the scattering characteristics of the blades, the total scattered electric field of the blades $\boldsymbol{E}(f,\theta,\varphi;\boldsymbol{\Psi})$ can be represented by a coherent superposition oif the P scattering center responses $\boldsymbol{E}_i(f,\theta,\varphi;\boldsymbol{\Psi}_i)$ (Xie et al., 2019).

$$\begin{aligned}\boldsymbol{E}(f,\theta,\varphi;\boldsymbol{\Psi}) &= \sum_{i=1}^{P}\boldsymbol{E}_i(f,\theta,\varphi;\boldsymbol{\Psi}_i)\\ &= \sum_{i=1}^{P}A_i\cdot\left(\mathrm{j}\frac{f}{f_c}\right)^{\alpha_i}\cdot\exp\left[-\mathrm{j}\frac{4\pi f}{c}r_i\right]\\ &\quad\cdot\operatorname{sinc}\left(\frac{2\pi f}{c}L_i\sin(\theta-\bar{\theta}_i)\right)\cdot\exp(-2\pi f\gamma_i\sin\theta)\end{aligned}\tag{1}$$

where: f_c is the central frequency of the radar electromagnetic wave; L_i is the length of the scattering center, where is the localized scattering center when $L_i = 0$ and the distributed scattering center when $L_i \neq 0$; γi is the orientation-dependent term of the scattering center, of order 10^{-10}, which can be approximated to 0; $\boldsymbol{\Psi}^T = [\boldsymbol{\Psi}_1^T, \boldsymbol{\Psi}_2^T, \cdots, \boldsymbol{\Psi}_i^T, \cdots \boldsymbol{\Psi}_P^T]$ is the attribute scattering center is the parameter matrix of the p attribute scattering centers, complete with information on the scattering properties of the target entity, where Ψ_i is the scattering center parameter set $\{x_i, y_i, z_i, \alpha_i, L_i, \bar{\theta}_i, A_i\}$, $(\cdot)^T$ denoting the transpose; c is the velocity of light; position relation between the blades and radar is shown in Figure 2, r_i is the distance from the ith scattering center to the scene origin, assuming that radar is in the far-field, the range r_i can be obtained by

$$r_i = x_i\cos\theta\cos\varphi + y_i\sin\theta\cos\varphi + z_i\sin\theta \tag{2}$$

3.2 Extraction of 3D scattering center of WT blades

It is necessary to build a large parametric dictionary to estimate those parameters simultaneously. As the 3D scattering center includes eight target parameters and three radar parameters, the dimension of the parameterized dictionary is very high, which greatly increases the cost of computation and storage.

According to Eq. 1, the total scattering from blades in the frequency domain is a vector superposition of the electromagnetic scattering from multiple attribute scattering centers, so by creating an over-complete dictionary and dividing each column of the dictionary into an atom (a parameter set representing a scattering center), the total scattering from solid blades is a linear combination of these atoms. Firstly, let the dictionary $\boldsymbol{D}$ be given by the following equation.

$$\boldsymbol{D}(f,\theta,\varphi;\boldsymbol{\Theta}_i) = \boldsymbol{d}_{x,y,z}\cdot\boldsymbol{d}_{L,\bar{\theta}} \tag{3}$$

where: $\boldsymbol{D}(\boldsymbol{\Theta}_i)$ is the $\{\Theta_i \mid x_i, y_i, z_i, L_i, \bar{\theta}_i\}$ dictionary of partial parameter sets for the ith scattering center; $\boldsymbol{d}_{x,y,z}$ is the scattering center position information term $\exp[-\mathrm{j}\frac{4\pi f}{c}r_i]$; $\boldsymbol{d}_{L,\bar{\theta}}$ is the scattering center orientation information term $\operatorname{sinc}(\frac{2\pi f}{c}L_i\sin(\theta-\bar{\theta}_i))$.

Due to $\boldsymbol{D}(\boldsymbol{\Theta})$ the high spatial dimensionality, a direct solution would lead to a sharp increase in the number of atoms in the dictionary. Therefore, to reduce the dimensionality of the dictionary processing, dictionary scaling and alternate optimization methods are used to $\{\boldsymbol{\Theta} \mid x, y, z, L, \bar{\theta}\}$ decompose the high-dimensional joint dictionary into two sub-dictionaries $\{\boldsymbol{\Gamma} \mid x, y, z\}$, $\{\mathrm{H} \mid L, \bar{\theta}\}$, containing the scattering center coordinates and orientation information, i.e., we have

$$\begin{cases}\boldsymbol{D}(\boldsymbol{\Gamma})^T &= [\boldsymbol{\Gamma}_1, \boldsymbol{\Gamma}_2, \cdots, \boldsymbol{\Gamma}_j, \cdots, \boldsymbol{\Gamma}_n]^T\\ \boldsymbol{D}(\mathrm{H})^T &= [\boldsymbol{H}_1, \boldsymbol{H}_2, \cdots, \boldsymbol{H}_j, \cdots, \boldsymbol{H}_n]^T\\ \boldsymbol{\Gamma}_{pq} &= \operatorname{vec}(\boldsymbol{d}_{x,y,z})/\operatorname{vec}(\|\boldsymbol{d}_{x,y,z}\|_2)\\ \boldsymbol{H}_{pq} &= \operatorname{vec}(\boldsymbol{d}_{L,\bar{\theta}})/\operatorname{vec}(\|\boldsymbol{d}_{L,\bar{\theta}}\|_2)\end{cases}\tag{4}$$

where: n, j is the number of parameters quantized $\{x_i, y_i, z_i, L_i, \bar{\theta}_i\}$, respectively; $\operatorname{vec}(\cdot)$ denotes the vector straightened into columns; $\|\cdot\|$ denotes the vector parametrization.

According to the principles of the OMP algorithm, after constructing the atomic dictionary, the problem of estimating the scattering center parameters is transformed into an optimal solution of the sparse representation, as follows.

$$\begin{cases}\boldsymbol{\Psi} = \arg\min\limits_{\boldsymbol{\Psi}}\|\boldsymbol{s}-\boldsymbol{DA}\|_0\\ \text{s.t.}\|\boldsymbol{A}\|_2 \leq \|\boldsymbol{n}\|_2\end{cases}\tag{5}$$

where: $\boldsymbol{\Psi}$ is the estimated sparse vector of scattering center parameters; $\boldsymbol{s}$ is the column vectorisation of the observed data $\boldsymbol{E}(f,\theta,\varphi)$; $\boldsymbol{A}$ is the amplitude of the observed data in the dictionary; $\boldsymbol{n}$ is the noise level.

For the acquisition of the observed data $\boldsymbol{E}(f,\theta,\varphi)$, a well-established high-frequency hybrid algorithm can be used to calculate it, as described in the literature (Xie et al., 2019), and will not be repeated here.

In the process of estimating the scattering center parameters using the OMP algorithm, it is considered that the performance of the OMP algorithm is disturbed by the scattering centers of neighboring WT blades. For this reason, the RELAX algorithm is introduced to correct the scattering center parameters calculated by the OMP algorithm for each iteration and to determine the termination conditions that satisfy the iterative process, then Eq. 5 is transformed into

$$\boldsymbol{\Psi}_i = \arg\min_{\boldsymbol{\Psi}_i}\|\boldsymbol{s}_i - A_i\boldsymbol{D}_i\|_2^2 \tag{6}$$

The procedure for the joint solution using the OMP and RELAX algorithms can be found in the literature (Xie et al., 2019). Once the parameter set is obtained $\{x_i, y_i, z_i, L_i, \bar{\theta}_i\}$, the type parameter α_i can be determined from the length parameter L_i of the scattering center, thus giving a complete estimate of the set of parameters $\boldsymbol{\Psi}$ of the attribute scattering center of the WT.

3.3 Simulation process of WT echoes

After obtaining the scattering centers of all the blades, the scattering center parameters derived from the above steps $\boldsymbol{\Psi}_\beta$ are

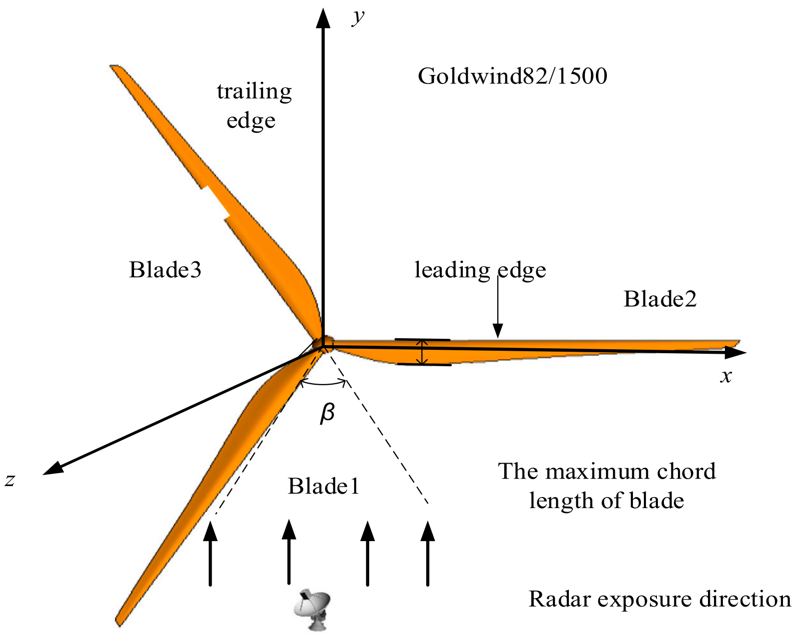

FIGURE 3
Geometry model of Goldwind82/1500 WT blades.

used as local data, and according to the sub-aspect range of the blades rotation angle at different time t, the scattering center parameter of the corresponding sub-aspect is substituted into the 3D scattering center model. According to the relationship between the blades motion characteristics and the 3D scattering center in each aspect, the scattering electric field distribution corresponding to the rotation of the blades can be reconstructed, as follows Eq.

$$\boldsymbol{E}(f,\omega t)=\sum_{i=1}^{P}A_{ji}\cdot\left(\mathrm{j}\frac{f}{f_c}\right)^{\alpha_{ji}}\cdot\exp\left[-\mathrm{j}\frac{4\pi f}{c}\left(x_{ji}\cos\theta\cos\varphi+y_{ji}\sin\theta\cos\varphi+z_{ji}\sin\theta\right)\right]\tag{7}$$

Where: ω is the angular velocity of the WT blades rotation; j is the jth sub-angle domain to which the rotating WT blades belong at moment t, where $j=[\frac{M\cdot\omega t}{2\pi}]+1$, $[\cdot]$ denotes rounding.

On this basis, in order to achieve the time-frequency characteristics of the dynamic blade echo and Doppler characteristic analysis, the scattered electric field vector obtained needs to be processed by Short Time Fourier Transform (STFT), that is, there are

$$rect(t,f)\Big|_{t=m\Delta t,f=\frac{r}{MN\Delta t}}=STFT(\boldsymbol{E}(\omega t,f))=\sum_{k=0}^{MN-1}\boldsymbol{E}(k\Delta t)w^{*}(k\Delta t-m\Delta t)\mathrm{e}^{-\mathrm{j}2rk\pi/MN}\tag{8}$$

where: Δt is the sampling interval associated with the amount of time, i.e. the scattered electric field under the reconstructed continuous time series is taken after each interval of Δt time to facilitate time-frequency characterization; $m, k, r = 0,1,2,3,\ldots, (t/\Delta t\text{-}1)$, where $t/\Delta t$ is the number of angular sampling points for the entire rotation period of the blades; $\boldsymbol{E}(k)$ is the reconstructed scattered electric field data. $w(t)$ is the window function; "*" denotes the complex conjugate.

4 Verification of echo simulation method for 3D scattering center

The algorithm proposed in Section 2.1 for parameter estimation in terms of the scattering center of blade properties was compared with existing algorithms and the actual measurement experiments given in reference (Tang et al., 2019c) in order to verify the accuracy of the equivalent modelling of the blade 3D scattering center. Due to the fact that the actual measured wind turbine model and parameters are missing in the literature (Tang et al., 2019c), the typical Goldwind GW82/1,500 wind motor is taken as an example.

The full-size model of the blades and their position in relation to the radar is shown in Figure 3. To compare with the research results in the literature (Tang et al., 2019c), the incident Angle of radar electromagnetic wave is adopted by literature (Tang et al., 2019c), that is, the incident wave is set parallel to the blades rotation plane, the incident point is set on the y-axis, and the included Angle φ is 0° between the incident wave and blades rotation plane xoy. The initial frequency of electromagnetic wave f_0 is 2.5 ghz, the center frequency f_c is 3 GHz, the step frequency is 10 MHz, the bandwidth is 1 GHz, and the intensity is 1 V/m. The incidence direction of electromagnetic waves of radar is fixed and unchanged. Given the single blade length L of Goldwind GW82/1,500 wind motor is 41 m.

The electromagnetic scattering source data $\boldsymbol{E}(f,\theta,\varphi)$ of static blades were obtained using FEKO. The 3D scattering center extraction method described in Section 2.1 was adopted to process the original simulation data $\boldsymbol{E}(f,\theta,\varphi)$ and obtain the scattering center distribution of blades, as shown in Figure 4.

The 3D scattering centers of the blades are point-like or lamellar, including local scattering centers and distributed scattering centers. The uneven distribution of the scattering center is mainly related to the shape and structure of the blades, being densely distributed at the front and rear edges, axes and tips of the WT.

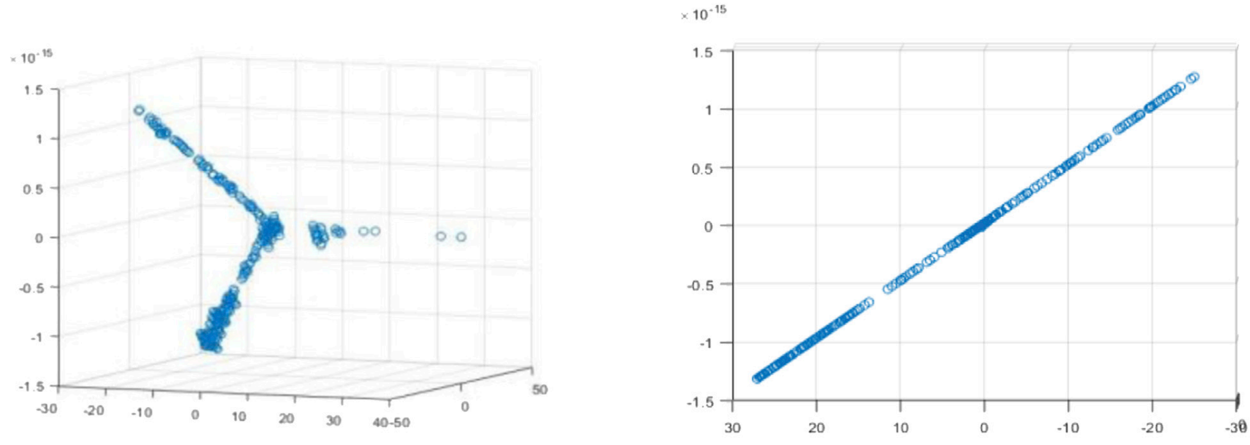

3-D Scattering center

Left view

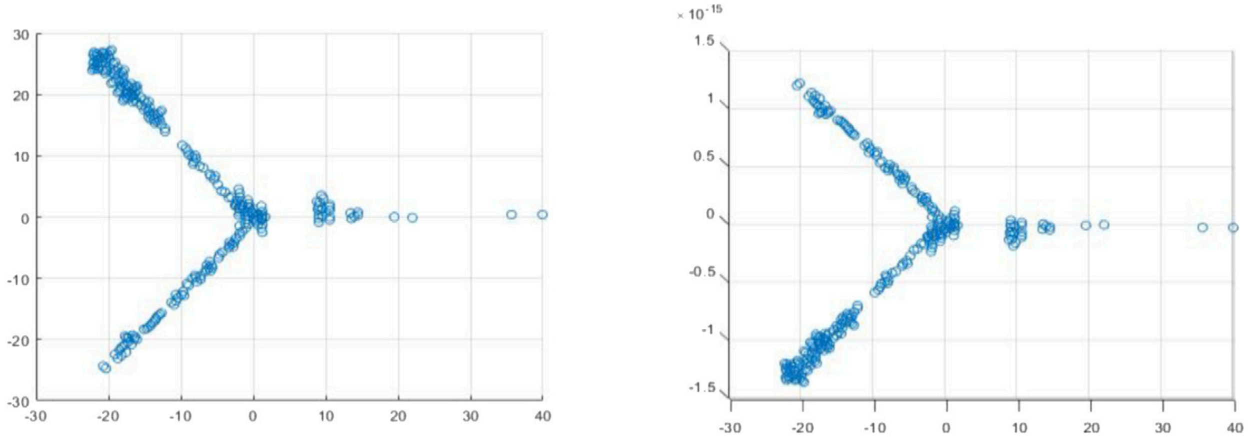

Plan view

Front view

FIGURE 4
Equivalent model of the 3-D scattering center.

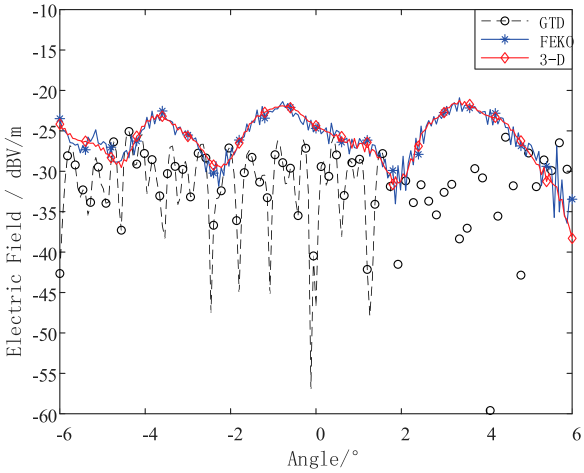

FIGURE 5
The distribution of the scattered electric field of the blade.

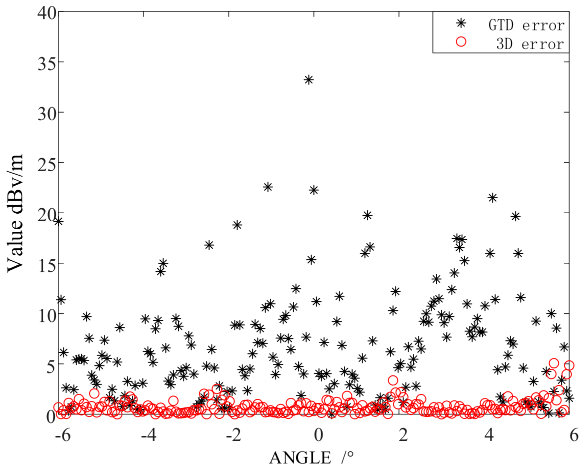

FIGURE 6
Distribution of scattered electric field error results.

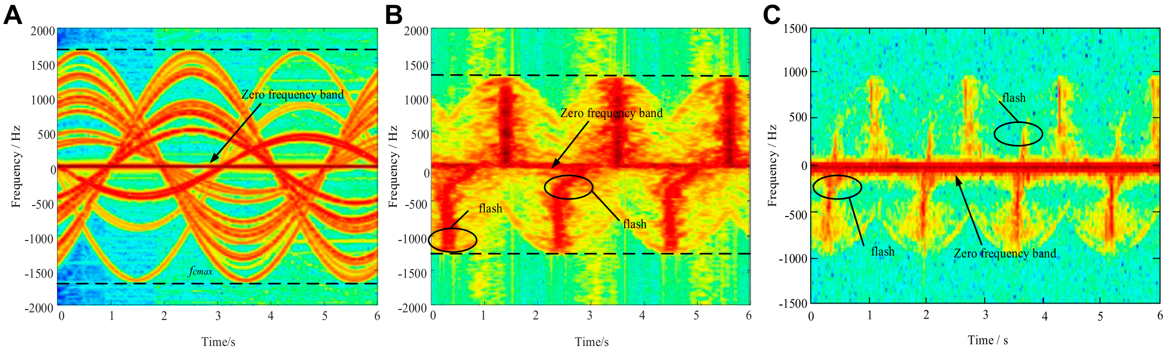

FIGURE 7
Comparison of time and frequency domain echo of blades obtained by different methods. **(A)**Integral algorithm based on scattering center, **(B)** proposed method, **(C)** measured data.

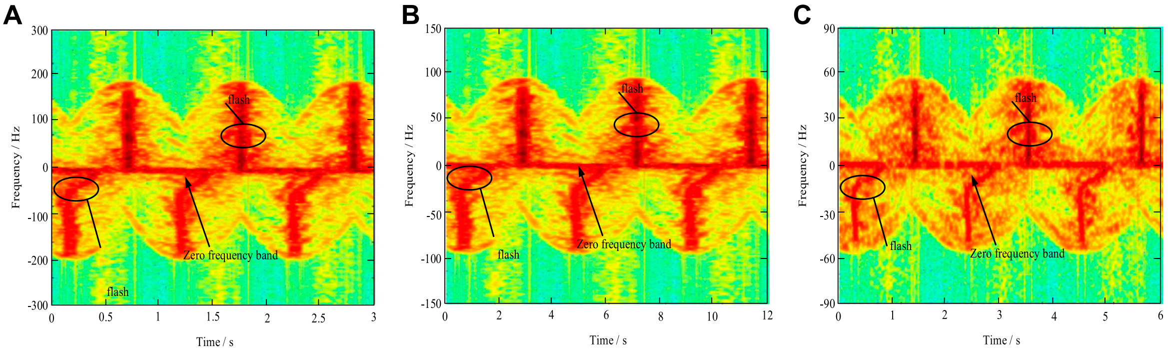

FIGURE 8
Comparison of time-frequency echoes of blades at a different speed. **(A)**Time-frequency domain of echoes with a frequency of 1 GHz and the speed of π/3 rad/s, **(B)** Time-frequency domain of echoes with a frequency of 1 GHz and the speed of π/6 rad/s, **(C)** Time-frequency domain of echoes with a frequency of 1 GHz and the speed of π/12 rad/s.

It is evident from Figure 4 that the estimated scattering center is consistent with the appearance profile of the body of the blades. However, as a further step towards a more accurate quantitative analysis of the equivalent modelling of the three-dimensional scattering centers of the blade, the GTD scattering center and 3D scattering center obtained were reconstructed respectively to obtain the scattering electric field distribution of the blades, using the FEKO simulation data as standard data. Figure 5 shows the error distribution of the scattering electric field reconstructed by the two scattering centers and the standard data.

It can be seen from Figure 5 that the distribution of the scattering electric field reconstructed by the attribute scattering center is in good agreement with the original scattering electric field data simulated by the FEKO. While the distribution of the scattering electric field reconstructed by the GTD scattering center algorithm is in bad agreement with the original scattering electric field.

As can be seen from Figure 6, out of a total of 401 data, only 5 scattered electric field data reconstructed by attribute scattering center have an error of more than 3dB, while 144 scattered electric field data reconstructed by GTD scattering center have an error of more than 3dB, with a precision difference of 34.7%.

It can be seen from Figure 6 that among the total 12,001 sampling points, there are 9,751 points with a difference less than 3 dB V/m, that is, the rotating WT scattering electric field reconstructed by the attribute scattering center method is 81.26% similar to the original data. The average error between the electric field data obtained by the algorithm proposed in this paper and the original electric field data obtained by Feko is 3.16 dB V/m. For the convenience of calculation while retaining the calculation accuracy, the value of 3 dB V/m is taken as the criterion for the accuracy of the algorithm. It shows that the extracted 3D scattering center can better replace the scattering characteristics of the real rotating WT, which verifies the correctness and accuracy of the equivalent modeling of the WT based on the 3D scattering centers.

The 3D scattering centers of the blades are point-like or lamellar, including local scattering centers and distributed scattering centers. Non-uniform distribution of scattering centers is mainly related to the shape and structure of the blade, with scattering centers of the blade densely distributed at the front and back. As described in Section 1.2 of the paper, the blades GTD scattering center is equivalent to the point-like scattering center shown in Figure 2 for the blades of a complex profiled surface, ignoring a large number of dihedral Angle reflections and straight edge reflections of the front and rear edges of the blades. And 3D scattering center model of leaf blades length, the curvature of the scattering entities such as quantitative three-dimensional structure, thus distinguishing the various scattering structures of the blade and allowing a more accurate description of the scattering effects of straight blades, so that the accuracy of the scattering field strength calculation using the three-dimensional scattering center method is much higher than that of the GTD scattering center.

5 WT blades radar echoes simulation and analysis

5.1 Echo simulation of WT blades

On this basis, the same blade model and its specific parameters as in Section 3.1 are used to obtain the corresponding scattered electric field data. We also set the rotation of the blades angular velocity for 2π/3 rad/s, the pulse repetition frequency PRF for 4000 Hz and the observation time t for 3 s, by using Equation 7 to process the scattered electric field data obtained *via* the method proposed in this paper and the traditional single-view scattering center method respectively, which can obtain the time-frequency characteristics. The radar echo with time-frequency characteristics are obtained and compared with the blades radar time-frequency echo maps obtained from experimental measurements, as shown in Figure 6.

Comparing Figures 7A,B, it is observed that the maximum Doppler frequency appears at the same time in the blade time-frequency echogram, and both appear in the zero frequency band with stronger energy. According to the literature (Zheng et al., 2020b), the maximum Doppler frequency of the simulated blade can be found to be consistent with the calculated value $f_{dmax} = 2f_c\omega l/c = 1717.36$ Hz.

Meanwhile, the measured results in Figure 7C show that the time-frequency echo of the actual wind motor blades should also have the following characteristics: 1) positive and negative time-frequency flicker with energy difference; 2) time-frequency scintillation with bending phenomenon (Zheng et al., 2020b). These features are not shown in Figure 7A, but the simulation results of the proposed method are in complete agreement with the measured features.

The proposed algorithm uses a desktop computer, the CPU model is Intel(R) Core(TM) i5-9,500, the CPU frequency is 3.00GHz, the memory is 8GB, and the simulation software is matlab 2020B. The algorithm needs to complete the calculation of the scattering center for about 660 s. This algorithm can guarantee the calculation accuracy and simulate the radar echo of wind turbines without consuming a lot of computing time and computer memory.

5.2 Echo simulation analysis

An in-depth analysis of the Doppler characteristics shown in Figure 6B shows that for the Doppler characteristic of positive and negative time-frequency scintillation with energy difference appearing alternately in Figure 7B, combined with the analysis of the initial position of WT and the incident radar wave in Figure 3, it can be seen that when WT and the incident wave direction it is vertical, the effective irradiation range of the received electromagnetic wave will reach the maximum. In one rotation period, each blade will be vertically irradiated by electromagnetic waves twice, and the WT will have larger energy. As a result, the time-frequency echo of WT appears six times with energy difference in a single rotation period. The positive and negative alternating flicker is caused by the blades approaching or away from the incident electromagnetic wave.

The bending flash appears in Figure 7B and is due to the complex heterogeneous curved surface of the blade, considering the three-dimensional structure of the blade, so that the scattering energy provided by the blade surface is different when the electromagnetic wave is directed vertically at the front and rear edges of the blade. Combined with the 3D scattering center model, when the values of the scattering center parameter α and the length parameter L are different, the scattering forms of different structures can be characterized. Consequently, the time-frequency echoes obtained by the method in this paper shows the phenomenon of bending and flashing (Tang et al., 2021).

According to the above analysis, the proposed method in this paper can be seen to be superior to the traditional scattering center-based integration algorithm.

5.3 Analysis of generalizability

In engineering practice making full use of wind energy, the rotational plane of the WT blades will change accordingly with the wind direction of the natural wind, while the electromagnetic wave parallel to the blade rotational plane in Section 3.2 above belongs to a very special state, in most cases, there will be a certain angle between the radar incident electromagnetic wave and the blade rotational plane. Therefore, it is necessary to carry out echoes simulations of WT blades at different incidence angles β of the electromagnetic waves to further illustrate the universality of the method proposed in this paper.

Using the same blades model and radar parameters in Section 3.2, and setting the speed of the WT as π/3 rad/s,π/6 rad/s, π/12 rad/s, the radar echoes of the WT blades simulated by the method in this paper are shown in Figure 8.

The maximum value of Doppler frequency in the blade time-frequency echo is 250 Hz, 125 Hz and 50 Hz respectively when the speed v is π/3 rad/s,π/6 rad/s, π/12 rad/s, as can be seen from Figure 8, and the sub-flash phenomenon gradually disappears. The reason for the above phenomenon is that, as the angle between the radar incident electromagnetic wave and the blades rotating plane increases, the incident electromagnetic wave in the blades rotating plane irradiation component gradually decreases, making the effective modulation effect of the blades on the incident wave decreases, thus finally leading to the blades' maximum Doppler frequency of the time-frequency echoes is presented as a zero frequency band.

Conclusion

(1) Considering the hidden and anisotropic nature of the scattering center caused by geometric properties and rotation angle, an equivalent calculation model for the WT blades based on 3D

scattering centers is proposed, which solves the problem that exists algorithms cannot accurately simulate echoes.

(2) Taking the GW82/1,500 as an example, the equivalent modelling accuracy of the blade scattering center is improved by 34.7% compared with the scattering center-based integration algorithm, achieving an accurate echo simulation and providing a theoretical reference for the next research on wind turbine array echoes.

Data availability statement

The raw data supporting the conclusion of this article will be made available by the authors, without undue reservation.

Author contributions

BT and HX participated in the design of this study, and they both performed the statistical analysis. GL carried out the study and collected important background information. LZ and ZS drafted the manuscript. All authors read and approved the final manuscript.

Funding

This work was supported by project Supported by National natural Science Foundation of China (51977121), Research Fund for Excellent Dissertation of China Three Gorges University (2021BSPY011).

Conflict of interest

The authors declare that the research was conducted in the absence of any commercial or financial relationships that could be construed as a potential conflict of interest.

Publisher's note

References

Bo, T., Bin, H., Li, H., and Jiawei, Y. (2016). "Radar echo signal simulation of wind turbine blades," in 2018 IEEE International Conference on Applied Superconductivity and Electromagnetic Devices (ASEMD). 06 December 2018, (Tianjin, China: IEEE), 8–14. doi:10.1109/ASEMD.2018.8559006

Chen, V. C. (2011). *The micro-Doppler effect in radar[M]*. Boston: Artech House, 56–60.

Chen, Y., Li, S., Yang, J., and Cao, F. (2017). Rotor blades radar echo modeling and its mechanism analysis. *Acta Phys. Sin.* 65 (13), 138401. doi:10.7498/aps.65.138401

Crespo-Ballesteros, M., Antoniou, M., and Cherniakov, M. (2017). Wind turbine blade radar signatures in the near field: Modeling and experimental confirmation. *IEEE Trans. Aerosp. Electron. Syst.* 53 (4), 1916–1931. doi:10.1109/taes.2017.2675241

Dai, C., Huang, L., Tang, B., Liu, G., and Xie, H. (2020). "Simulation and characteristic analysis of wind turbine radar echo based on improved multipath model," in 2020 IEEE International Conference on High Voltage Engineering and Application (ICHVE), 15 December 2020 (Beijing, China: IEEE), 2–24. doi:10.1109/ICHVE49031.2020.9279549

Ding, B., Wen, G., Yu, L., and Ma, C. (2017). Matching of attributed scattering center and its application to synthetic aperture radar automatic target recognition[J]. *J. Radars* 6 (2), 157–166. doi:10.12000/JR16104

Dunoon, L. R., and Brown, A. K. (2013). Modeling methodology for computing the radar cross section and Doppler signature of wind farms. *IEEE Trans. Antennas Propag.* 61 (10), 5166–5174. doi:10.1109/tap.2013.2272454

Gao, Y., Li, Z., Sheng, J., and Xing, M. (2016). Extraction method for anisotropy characteristic of scattering center in wide-angle SAR imagery[J]. *J. Electron. Inf. Technol.* 38 (8), 1956–1961.

He, W., Shi, Y., Guo, S., Wang, X., and Wu, R. (2017a). Simulation on wind turbine radar scattering characteristics and its micro-Doppler analysis[J]. *Chin. J. Radio Sci.* 32 (1), 103–111.

He, W., Liu, A., Wang, X., Zhang, Y., and Chen, M. (2021). Modeling and analysis of wind turbine echoes for airborne array radar[J]. *Syst. Eng. Electron.* 43 (3), 666–675.

He, W., Wu, R., Wang, X., Guo, S., and Ma, C. (2017b). The review and prospect on the influence evaluation and interference suppression of wind farms on the radar equipment [J]. *J. Electron. Inf. Technol.* 39 (7), 1748–1758. doi:10.11999/JEIT161004

Li, T., and Du, L. (2017). SAR automatic target recognition based on attribute scattering center model and discriminative dictionary learning. *IEEE Sensors J.* 19 (12), 4598–4611. doi:10.1109/jsen.2019.2901050

Pooria, P., Louis, L. S., Margaret, C., Andrew, H., and Matthew, F. (2017). Multipulse adaptive coherence for detection in wind turbine clutter[J]. *IEEE Trans. Aerosp. Electron. Syst.* 53 (6), 3091–3103. doi:10.1109/TAES.2017.2727825

Steven, I. K., Monica, M., Vincent, A., and Paul, B. (2017). Wind turbine interference mitigation using a waveform diversity radar[J]. *IEEE Trans. Aerosp. Electron. Syst.* 53 (2), 805–815. doi:10.1109/TAES.2017.2665143

Sun, H., Du, L., and Liang, G. (2016). Antenna model of MMC-HVDC converter valve system and its radiated electromagnetic disturbance analysis[J]. *Proc. CSEE* 36 (3), 879–888.

Tang, B., Chen, H., Huang, L., Yuan, F., Feng, P., and Li, Y. (2019c). Simulation and analysis of wind turbine blades radar echo based on electromagnetic scattering center[J]. *Proc. CSEE* 39 (24), 7375–7384.

Tang, B., Hao, B., Huang, L., and Yang, J. (2019b). Simulation of the Doppler echoes from wind turbine based on scattered electric field calculation. *IET Radar,Sonar Navigation* 13 (11), 2055–2062. doi:10.1049/iet-rsn.2018.5482

Tang, B., Hao, B., Zhang, J., Huang, L., Gan, Z., and Yang, J. (2019a). Simulation of wind turbine echoes based on electromagnetic scattering point spacing[J]. *High. Volt. Eng.* 45 (8), 2652–2661.

Tang, B., Liu, G., Xie, H., Huang, L., Dai, C., and Li, F. (2021). Radar echo simulation of dynamic wind turbine blade based on multi view attribute scattering center[J]. *Proc. CSEE* 41 (18), 6449–6460.

Tang, B., Liu, R., Zhang, J., Liu, X., Sun, R., and Jiang, H. (2017). Doppler characteristics of wind turbine blades based on dynamic RCS[J]. *High. Volt. Eng.* 43 (10), 3435–3442.

Tang, B., Wen, Y., Zhao, Z., and Zhang, X. (2011). Three-dimensional surface computation model of the reradiation interference from UHV angle-steel tower[J]. *Proc. CSEE* 31 (4), 104–111.

Xie, J., Liu, Y., Liu, L., Tang, L., Wang, G., and Li, X. (2019). A partial discharge signal denoising method based on adaptive weighted framing fast sparse representation[J]. *Proc. CSEE* 39 (21), 6428–6438.

Yan, H., Chen, Y., Li, S., Hu, L., Li, H., and Yin, H. (2011). A fast algorithm for establishing 3-D scattering center model for ship targets over sea surface using the shooting and bouncing ray technique[J]. *J. Radars* 8 (1), 07–116. doi:10.12000/JR18078

Zheng, X., Tang, B., Liu, G., Xie., H., and Dai, C. (2020). "Scattering electric field solution of wind turbine blade based on scattering center," in 2020 IEEE International Conference on High Voltage Engineering and Application (ICHVE), 15 December 2020 (Beijing, China: IEEE), 1–4. doi:10.1109/ICHVE49031.2020.9279800

Zheng, X., Tang, B., Xie, H., Liu, G., and Dai, C. (2020). "Simulation and analysis of radar echo of wind turbine blades based on shooting and bouncing ray technique," in 2020 IEEE International Conference on High Voltage Engineering and Application (ICHVE), 15 December 2020 (Beijing, China: IEEE), 3–34. doi:10.1109/ICHVE49031.2020.9279841

Frontiers in Energy Research

TYPE Original Research
PUBLISHED 07 February 2023
DOI 10.3389/fenrg.2023.1113384

OPEN ACCESS

EDITED BY
Praveen Kumar Donta,
Vienna University of Technology, Austria

REVIEWED BY
Vinit Gunjan,
CMR Institute of Technology, India
William Tichaona Vambe,
Walter Sisulu University, South Africa

*CORRESPONDENCE
Jianfei Chen,
✉ jianghai166@163.com

This article was submitted to Smart Grids, a section of the journal Frontiers in Energy Research

RECEIVED 01 December 2022
ACCEPTED 11 January 2023
PUBLISHED 07 February 2023

CITATION
Chen J, Zhao L, Sun Q and Zhang C (2023), Security feedback trust model of power network demand response terminal triggered by hacker attacks.
Front. Energy Res. 11:1113384.
doi: 10.3389/fenrg.2023.1113384

Security feedback trust model of power network demand response terminal triggered by hacker attacks

Jianfei Chen[1]*, Lina Zhao[2], Qiang Sun[3] and Cheng Zhang[4]

[1]State Grid Shandong Electric Power Company, Jinan, China, [2]Information and Communications Company, State Grid Shandong Electric Power Company, Jinan, China, [3]State Grid Weihai Wendeng Power Supply Company, Weihai, China, [4]State Grid Juxian Power Supply Company, Rizhao, China

With the rapid expansion of power system scale, demand response business is promoted to develop. More and more demand response terminals are connected to the smart grid, smart grid is an intelligent system that allows the grid to effectively perform its functions. Its data can be used in intelligent decision-making during grid operation, which may be attacked by hackers in practical applications, causing security problems of demand response terminals of the power network. The security feedback trust model establishes trust relationship through trust mechanism, which can effectively ensure the security of interaction between nodes and demand response terminals of the smart grid. Therefore, a security feedback trust model of power network demand response terminal triggered by hacker attacks is proposed. Analyze the role of smart grid in power grid, and use convolutional neural network in artificial intelligence technology to enhance the flexibility of smart grid. Aiming at the security problem of the demand response terminal of the power network being attacked by hackers, based on the trust theory, the security feedback trust model of the demand response terminal of the power network is designed through the main services provided by the security feedback trust model, the trust information storage of the power network nodes and the summary of the main work. Establish the identity trust relationship, adopt the distributed verifiable signature scheme, update the power grid node certificate, update the identity trust relationship, and revoke the identity trust relationship based on the trust evaluation and threshold value to prevent hackers from attacking the power grid demand response terminal. Based on information theory, trust is established and measured. Entropy is used to represent the trust value. Behavior trust evaluation and composition mechanism are introduced into the security feedback trust model of power network demand response terminals to achieve the credibility of identity and behavior among power network nodes. The experimental results show that the proposed method can judge the hacker attacks, reduce the impact of hacker attacks on the trust of power grid nodes, and improve the interaction security between power grid demand response terminals and power grid nodes.

KEYWORDS

hacker attacks, power network, trust assessment, node certificate, demand response terminal, security feedback trust model, artificial intelligence, smart grid

1 Introduction

At present, the energy revolution is further integrated with the digital revolution, vigorously promoting the innovative development of the energy industry and the Internet. The power system is an important part of the energy network. With the continuous improvement of the intelligent degree of the power system, the coupling degree between the power network and the information network is constantly improving. They are interdependent and interact with each other. The normal operation of the information network cannot be separated from the power support of the power network. The switching and adjustment operations of each node in the power network need to be realized through the information network (Li et al., 2021a; Zhang et al., 2021a; Sun et al., 2022). Considering that the demand for interactive regulation responds to the increase in the number of service deployed terminals, which is different from the previous terminals, which are mostly accessed by dedicated lines or deployed sporadically through pilot projects. Without the security test of the external network, a large number of demand response terminals are connected to the power network. At the same time, according to the protection requirements, the data, and control information transmitted by the terminal connected to the power network are blurred in the horizontal isolation boundary of the security zone, which may be attacked by hackers in practical applications, resulting in a large area of power failure and interruption of communication between devices. The security feedback trust model is to establish the trust prediction value of external entities through a reasonable trust system model, and correctly judge the trust degree of the other entity, so as to promote the safe, high-speed and harmonious development of the entire power network demand response terminal, which can effectively solve the security problems of the power network demand response terminal attacked by hackers (Jiang et al., 2019; Liu et al., 2020). Therefore, it is of great significance to establish the security feedback trust model of power network demand response terminal.

At present, scholars in related fields have studied the power trust model. Zhang et al. (2019a) proposed a master-slave chain architecture model for cross domain trusted authentication of power services. With the gradual complexity of China's electricity information, the current power business is diversified, and multi business integration is increasingly becoming the direction of power business development. However, the integration of commercial trust and mutual trust has not been effectively solved, which will bring huge economic losses to the power grid. Therefore, while effectively isolating multiple services, how to ensure the integration and reliability of multiple services is an urgent security issue. This paper introduces a master-slave chain architecture based on blockchain, which is used for cross domain trusted authentication of power services. Use slave chains to isolate multiple services. The trunk ensures the trust of the business and minimizes the untrusted security risks. Alagappan et al. (2022) proposed a zero trust network architecture to enhance the security of virtual power plants. In order to prevent and contain network threats or network crimes, considering the ability of the architecture, a single damaged endpoint in a zero trust network is unlikely to spread horizontally, thus infecting the entire network. This provides the ability to adopt the architecture in the energy sector. The popularity of distributed generators enables consumers to supply power to the grid. These small generators form a virtual power plant. Through this arrangement, its network also faces security challenges and needs to protect these physical systems, data protection and information privacy. However, the above methods still have the problem of low security of power network demand response terminals. In order to establish the trust relationship between power grid nodes and improve the security of interaction between power grid nodes and demand response terminals, a comprehensive zero trust security architecture needs to be built to help power grid reduce system risk and protect data privacy under hacker attacks.

In order to improve the security of power network node interaction and demand response terminal, a security feedback trust model of power network demand response terminal triggered by hacker attacks is proposed. Based on the definition of trust theory, the security feedback trust model of power network demand response terminal is designed. By establishing, updating and revoking the identity trust relationship, the trust is established and measured based on information theory, and the trust value is expressed by entropy. The behavior trust evaluation and composition mechanism is introduced into the security feedback trust model of power network demand response terminals to achieve the identity trust and behavior trust between power network nodes. The security feedback trust model of power grid demand response terminal is constructed by trust theory, and the behavioral trust evaluation and synthesis mechanism are input into the model, can judge the hacker attacks, reduce the impact of hacker attacks on the trust of power grid nodes, and improve the interaction security between power grid demand response terminals and nodes.

2 Literature review

Cherukuri et al. (2022) designed Raspberry Pi to develop a family safety framework. After the intruder is identified, the intrusion detection system will pay attention to the image of the intruder. After the intrusion is identified, the mobile owner/administrator will be sent an alarm email with the recognizable and visible images of the attacker (facial view). The owner can also watch the real-time monitoring through the camera head on the intelligent device in the settings used to view the surrounding environment of the house.

Karthik et al. (2022a) uses visual encryption technology to hide original information such as images and texts. In VC, the basic principle is to segment the image and recreate it. According to the size, quality, pixel expansion, and nature of the image, the image is encrypted and improved to an 8-bit key.

Karthik et al. (2022b) used the deep transfer learning strategy to find network attacks in a simple way, and with the help of Analytics, collected information from IOT devices to be obtained. The nine current data sets of IOT are comprehensively tested, and the output results show that the proposed model significantly improves the accuracy of identifying IOT attacks.

Das and Mukherjee, (2022) analyzed the spying and security vulnerability cases that endanger user privacy and proposed blockchain technology. Blockchain distributed ledger is a new technology system, which can easily solve the security vulnerability problem with the help of the Internet of Things system. It can be used in energy, health, entrepreneurship, finance, and other fields. It has huge benefits and innovation potential.

Gunjan et al., (2014) studies data protection based on digital and cloud computing systems. Data protection is to build a data security system covering the whole life cycle of data from the perspective of assets, intrusion and risk under the guidance of zero trust architecture. In order to improve the work efficiency more accurately, it requires not only technical expertise to crack it, but also to improve the security of users. Through this study, we will check the level of consciousness of cyber crime and security profession, and propose the necessary methods that really help to make the cyber environment safe, stable and credible.

Prasad et al., (2022) proposed a blockchain based medical image privacy access control mechanism and collaborative analysis. Image privacy refers to the process of protecting the information that involves individuals or organizations and should not be disclosed in the image during data collection, data storage, data query and analysis, and data distribution. Build a system model based on two stages of data cleaning and disease classification, write the model obtained after training into the blockchain, use the model with the best performance on the chain to identify the image quality when cleaning data, and transfer high-quality images to the disease classification model for use.

3 Security feedback trust model of power network demand response terminal

As the power network demand response terminal is connected to the external network, it may be attacked by hackers in the process of information transmission. Hacker attack is an unauthorized illegal access. The malicious acts of hackers attacking the internal nodes of the power grid will cause catastrophic damage to them (Wang et al., 2021; Group, 2022; Xu and Hong, 2022). It is mainly through the occupation of power network bandwidth, CPU, memory, and other resources, resulting in network performance degradation, or even failure, thus affecting the normal access of users. Therefore, establish a unified trust management model based on trust theory to form a formal description and measurement method of trust and privacy (Ren et al., 2020), improve the overall operation ability and anti attack ability of the power grid, then, the security feedback trust model of power network demand response terminal is designed.

3.1 Overall design of model

Convolution neural network is a feedforward neural network with convolution calculation and depth structure, which is one of the representative algorithms of depth learning (Li et al., 2021b; She et al., 2021). Convolutional neural network has the ability of representation learning. It can translate and classify the input information according to its hierarchical structure, and effectively identify hacker attacks in the power network.

The original members who participate in the establishment of a social group have the highest power and are called managers. New members need their approval to join, which is called general members. Managers can enjoy the benefits and services of members of other social groups preferentially. Under this incentive, each member works hard to serve the group to improve the trust of other members. Members who are unwilling to cooperate with other members will not be trusted by other members and will eventually be abandoned by the group. By referring to the level of trust, management members can develop general members into managers, or can exclude untrustworthy managers from the group.

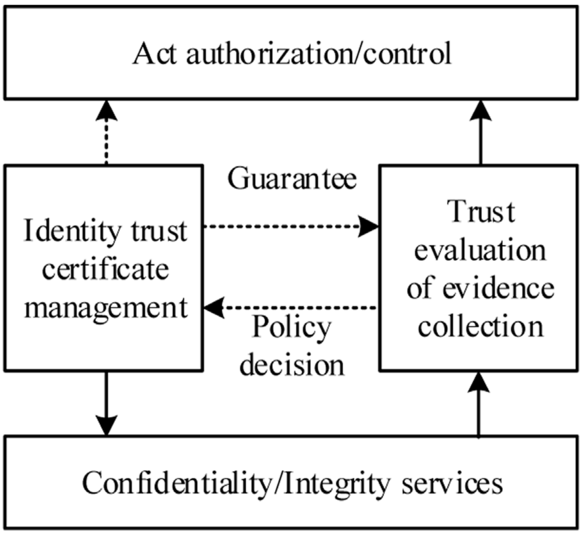

FIGURE 1
Overall structure of security feedback trust model of power network demand response terminal.

According to the characteristics of open network computing environment and networked software applications, trust theory systematically studies its requirements for trust management models and technologies. Based on the unified formal model of trust management, it breaks through two core technologies: trust can be established and privacy can be protected. By establishing a unified trust management model, the formal description and measurement methods of trust and privacy are formed, the dynamic construction algorithm of distributed trust chain, the collusion boycott protocol of malicious entities, the privacy protection policy and disclosure protocol, and the anonymous communication mechanism are studied. Finally, the security of the power network is analyzed based on the overall structure of the established power network demand response terminal security feedback trust model. Based on the research on trust theory (Zhang et al., 2019b; Moelker, 2021), trust is divided into identity trust and behavior trust. The security feedback trust model of power grid demand response terminal is also constructed according to this principle (Charis et al., 2021), which is divided into two main parts: identity trust relationship management module and evidence collection and trust evaluation module. The overall structure is shown in Figure 1.

These two parts are also the focus of this paper. Among them, identity trust is the basis of confidentiality and integrity services, and confidentiality and integrity services provide security for behavioral trust assessment and confidential communication. At the same time, the updating and revoking of trust relationship are all based on behavioral trust evaluation.

(1) The main services provided by the security feedback trust model of power grid demand response terminals: the main services provided by the two modules of the security feedback trust model of power grid demand response terminals: identity trust

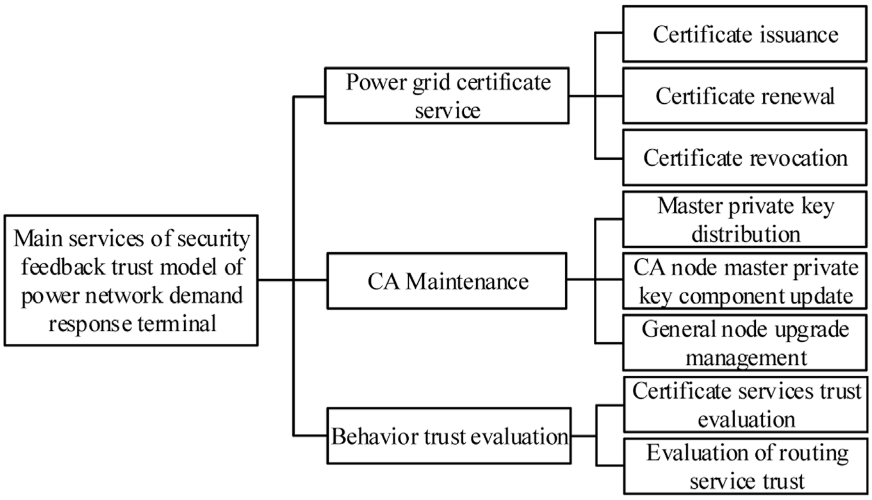

FIGURE 2
Main services of security feedback trust model of power network demand response terminal.

relationship management and evidence collection and trust evaluation include: power grid certificate service, CA maintenance and behavior trust evaluation (Tung et al., 2021). The main services of the security feedback trust model of power grid demand response terminals are shown in Figure 2.

Power gridcertificate service is responsible for establishing, updating and revoking the identity trust relationship between power grid nodes. The specific operations can be expressed as certificate issuing, updating and revoking. CA maintenance mainly includes the distribution of master and private key components in the initialization phase of the power grid (Hu et al., 2021), approving the upgrading of trusted general nodes to CA nodes, allocating master and private components to them, periodically updating the master and private key components of CA nodes, and depriving untrusted CA nodes of the authority to issue certificates. The services provided by behavior trust evaluation are mainly based on direct observation and trust recommendation of other nodes. The CA node's certificate service behavior and routing forwarding behavior of all nodes are evaluated. The trust value obtained is used as the basis for certificate revocation, master private key component update, routing, and other decisions.

(2) Storage method of power grid node trust information: In order to ensure the normal operation of power grid demand response terminal security feedback trust model, each power grid node needs to store three information bases: local information base, trust information base and certificate base.

The local information base mainly stores the node's own identity ID_{c_i}, public/private key pair PK_i/SK_i and the corresponding certificate version number m_i, the demand response terminal's primary public key PSK, the local time T_i, the demand response terminal's primary private key component S_i and the corresponding primary private key component version number. The local time is used as the standard for power grid nodes to determine whether the certificates of other nodes are expired. Therefore, after node c_i certificate is updated, other nodes will not immediately obtain c_i latest certificate, and may still use c_i old public key to communicate with it. c_i only when other nodes are aware that they are still using their old public key, will they notify the other party of their latest certificate. To ensure that c_i can decrypt the information encrypted by the old public key, c_i still retains the certificate information of the previous version after the certificate is updated.

The trust information base mainly stores some data related to identity trust and behavior trust as the basis for trust evaluation and certificate decision (Liu et al., 2019; Goyat et al., 2021). In theory, the local trust information base needs to store the information of all nodes in the power network, so it does not store large bit data information. After the power grid node interacts with a new node, the identity ID of the new node will be added to the local trust information base, and the corresponding information will be refreshed continuously according to the status and behavior of the new node.

The certificate store mainly stores the public key, session key and other information of other power network nodes that communicate with the local node. The certificate store mechanism reduces the number of certificate exchanges and communication between nodes. Because the storage space of nodes is limited, the certificate library does not store the information of all nodes in the power grid, but refreshes the certificate library according to the policy cycle.

(3) The main work of the security feedback trust model (Zhang et al., 2021b) of power network demand response terminal can be summarized as: providing three services: power network certificate management, CA maintenance and behavior trust evaluation.

The whole life cycle of power network can be divided into two stages (Huang et al., 2022): initialization and normal operation. In order to establish a secure communication environment in the power network, the first step is to realize the identity trust between communication nodes, that is, to conduct identity authentication. The process of authentication is also the process of establishing the initial trust relationship between nodes. In the initialization phase of the power network, the trusted management center randomly generates the master public/private key pair of the demand response terminal, decomposes the master private key, distributes it to all CA nodes in the power network, and then publishes the master public key and master private key verification parameters of the demand response terminal to exit the power network. Each power grid node needs to apply to a trusted management center offline to obtain a signature certificate binding identity and public key before it can successfully enter the power grid. After the initialization phase of the power network is completed, the power network can enter the normal operation phase.

In the normal operation stage of power network, the main work of the security feedback trust model of power network demand response terminal is as follows: CA nodes cooperate to periodically update public key certificates for each node; Revoke the certificate of the illegal node, that is, remove the trust relationship with the illegal node; CA nodes cooperate to approve the trusted general node to be upgraded to CA node, and calculate and allocate the master private key component of the demand response terminal for the node that approved the upgrade; Periodically update the master and private key components of the demand response terminal mastered by each CA node; Evaluate the behavior trust of other nodes.

Power grid nodes establish identity trust relationship with other nodes by using signature certificates bound by identity and public key. Public key encryption is computationally complex and expensive. Therefore, after the nodes of the power network mutually authenticate their identities by exchanging public key certificates, they negotiate a session key each session, and use symmetric cryptographic algorithm for secure communication. In this way, the confidentiality of communication between power grid nodes is realized, which fundamentally prevents malicious acts such as eavesdropping, impersonation and tampering from hackers, and also provides basic security guarantees for trust evaluation.

During the validity period, the certificate of a power grid node may become invalid for various reasons, such as the node is damaged or the private key of the node is obtained by hackers. Therefore, certificate revocation mechanism must be provided for certificate service of power grid. The trust based command and control mechanism is used to revoke the node certificate of power network. After the power grid node discovers the malicious behavior of node c_i, it broadcasts an accusation against c_i certificate to the power grid. After node c_i receives an accusation about c_i, it first judges whether the node issuing the accusation is credible. If so, it accepts the accusation. When c_j receives a valid accusation about c_i that reaches the threshold value, c_j marks c_i certificate as invalid in the local trust repository, that is, revokes c_i certificate locally.

The main work of CA maintenance of power network demand response terminal security feedback trust model is to approve trusted general power network nodes to be upgraded to nodes, and regularly update the master and private key components of CA nodes. This is also the two main mechanisms to realize the dynamic change of CA node set based on trust. A general power network node can apply to CA node for upgrading after it has survived in the power network for a period of time. Each CA node determines whether to generate a master private key sub component for it according to the trust value of this node. The threshold number of master private key sub components can be combined to generate a new master private key component.

The above certificate service and CA maintenance of power grid are guaranteed by behavior trust evaluation mechanism. At the same time, the behavior trust evaluation mechanism can also solve the routing security problems from within the power network. The method of probability theory is used to realize behavior trust evaluation mechanism. Power network nodes can evaluate the credibility of CA node's certificate service behavior and all node's routing and forwarding behavior. The nodes of power network dynamically select routing and certificate services based on behavior trust value.

3.2 Establishing, updating and revoking identity trust relationships

The establishment of identity trust relationship and the confidential transmission of information in the security feedback trust model of power network demand response terminals enhance the security and credibility of the trust evaluation process (Hongal and Shettar, 2020; Zhang et al., 2021c). Behavioral trust evaluation can not only achieve secure routing and improve power network performance, but also further improve the security and reliability of the verification process.

The security feedback trust model of power network demand response terminal is mainly divided into two stages in the entire life cycle of the power network: the initialization stage of the power network and the normal operation stage of the power network, as shown in Figure 3.

The demand response terminal of the whole power network has a master public/private key pair (PSK, SSK), which is generated by the offline trusted management center and provides the binding service of power network node identity ID and public key signature. The master private key SSK is shared by CA nodes in the (z, x) threshold mode. Any node smaller than z cannot recover any information of the master private key. Each node generates a user public/private key pair PK_i/SK_i, which is used for authentication and secure exchange of session keys between power grid nodes. The power grid node c_i can successfully join the power grid only after obtaining the signature certificate bound by ID and PK_i offline, and the certificate update is completed by the CA node in the power grid. The node adds a serial number to the communication message to prevent hacker attacks in the power network.

3.2.1 Establishment of identity trust relationship

The power grid node generates public/private key pair (PK_i, SK_i) by itself, obtains the binding certificate of identity and public key through the offline management center, and joins the power grid with the legal certificate. The trusted management center G assigns a globally unique ID to the new node c_i of the power network, issues a certificate with the master private keys SSK and c_i of the demand response terminal, and finally transmits the latest set of power network nodes ID to c_i.

Power grid nodes can enter the power grid by carrying the binding certificate of identity ID and public key issued by the master private key of the demand response terminal. They can obtain each other's public key and establish the identity trust relationship by exchanging signature certificates with other nodes. At the same time, the power network node identity ID is distributed by the trusted management center and signed by the master private key of the demand response terminal, which ensures the uniqueness of ID in the power network and effectively prevents hackers from impersonating the power network node identity and denying the identity of the node.

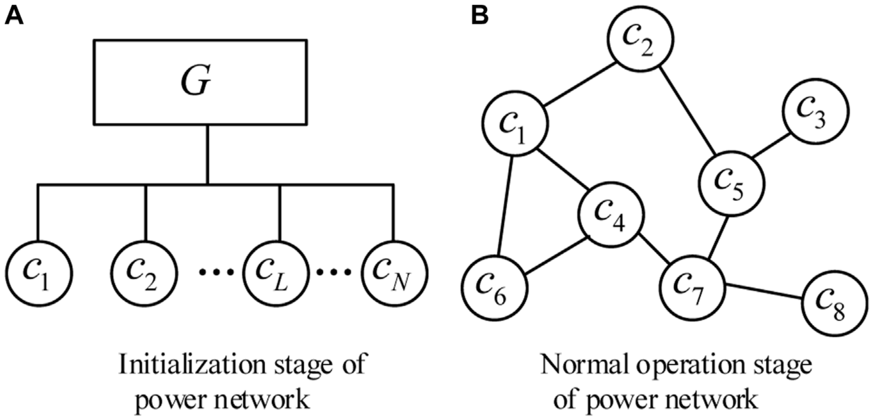

FIGURE 3
(A) Initialization stage and **(B)** normal operation stage of power network.

3.2.2 Update of identity trust relationship

It is insecure for power network nodes to use a certificate throughout the life of the power network, that is, the public/private key pair of power network nodes will not change all the time (Sui et al., 2020; Li et al., 2021c; Moorthy et al., 2021). The longer a node uses the same certificate, the greater the probability of hacker attack. Therefore, the security feedback trust model of power network demand response terminal must have the mechanism of node certificate update.

The distributed verifiable signature scheme (Han et al., 2019) is adopted to update the certificate of power grid nodes. The specific steps are as follows:

Step 1: Power grid node c_i applying for certificate update sends a certificate update request to its trusted CA node c_j. The content of the new certificate is signed with $SK_i^{(T)}$ to verify the identity of c_i, and ensure that c_i really owns the $CERT_{c_i}^{(T)}$ it claims. All contents are encrypted with $PK_j^{(T)}$, which is to authenticate the identity of CA node and prevent other hackers from damaging the contents of the new certificate.

Step 2: CA node c_j receiving the certificate application first retrieves the local trust information table. If it is determined that c_i certificate has not been revoked and c_i behavior trust value is greater than the threshold value, it will sign the certificate using its master private key component S_j, and the resulting signature certificate component is:

$$cert_{ij} = S_{S_j L_j(0)}\left(ID_{c_i}, PK_i^{(T+1)}, CM_i^{(T+1)}\right) \tag{1}$$

Then send $S_{PK_i^{(T+1)}}\left(cert_{ij}, H\left(cert_{ij}, J^{S_j}\right)\right)$ to c_i. At the same time, broadcast the primary private key verification parameters J and V. The certificate components are transmitted with $PK_i^{(T+1)}$, preventing hackers from damaging the certificate components.

Step 3: After power grid node c_i receives the $\left(cert_{ij}, H\left(cert_{ij}, J^{S_j}\right)\right)$ sent by CA node S_j, it needs to verify the correctness of $cert_{ij}$. c_i is calculated by using the mastered verification parameters J and V:

$$J^{S_j} = J^{SSK + a_1 c_j + \cdots + a_{k-1} c_j^{k-1}} \equiv J^{SSK} \cdot \left(J^{a_1}\right)^{c_j} \cdots \left(J^{a_{k-1}}\right)^{c_j^{k-1}} \pmod c \tag{2}$$

c_i is obtained by calculating J^{S_j} from $cert_{ij}$ provided by c_j and himself, and then $validate_i = H\left(cert_{ij}, J^{S_j}\right)$ is obtained. If $validate_i$ is equal to $H\left(cert_{ij} + J^{S_j}\right)$ sent by S_j, $cert_{ij}$ is accepted, and the trust degree of power grid nodes is improved; Otherwise, discard $cert_{ij}$ and reduce the trust of S_j.

Step 4: Power grid node c_i combines k verified signature certificate components collected to finally obtain the certificate issued by SSK:

$$CERT_i^{(T+1)} = \prod_{j=1}^{k} cert_{ij} = \left(ID_{c_i}, PK_i^{(T+1)}, CM_i^{(T+1)}\right)^{SSK} \tag{3}$$

3.2.3 Revocation of identity trust relationship

The certificate of a power network node may become invalid during its validity period for various reasons. Therefore, the security feedback trust model of power network demand response terminals must have a certificate revocation mechanism. The security feedback trust model of power grid demand response terminal mostly adopts the distributed storage of CRL list, that is, each power grid node maintains its own CRL list. However, this method takes up a lot of storage resources of power grid nodes. Therefore, the revoked certificate is marked with the certificate revocation identifier.

If the power grid node finds the hacker attack of node c_i, it marks c_i certificate as revoked in the local trust information base, clears c_i revocation count, and broadcasts a charge against node c_i certificate to the power grid. The revocation of identity trust relationship based on trust evaluation and threshold value can effectively prevent malicious accusations of hackers attacking nodes.

3.3 Behavior trust evaluation and synthesis

In the security feedback trust model of power network demand response terminal, the establishment, update, and revocation of identity trust relationship and the security routing of power network are all based on behavior trust evaluation. The accuracy and rationality of trust evaluation will directly affect the security and efficiency of the security feedback trust model of power network demand response terminals.

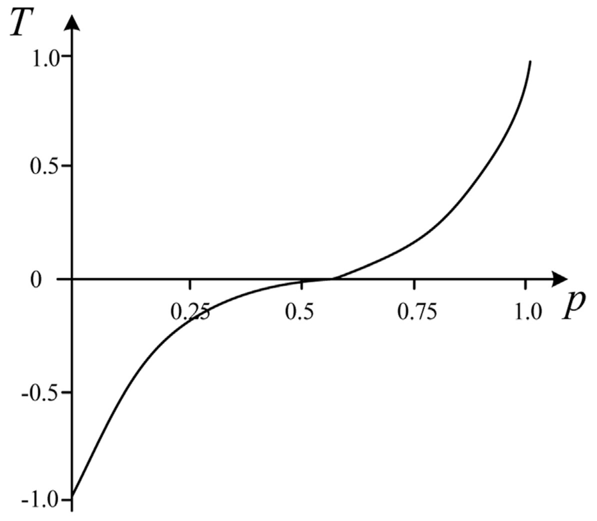

FIGURE 4
Value of $T\{c_i\colon c_j, action\}$

3.3.1 Behavior trust measurement

It can be seen from the definition of trust that it is an uncertain measurement standard. Therefore, it lacks theoretical support to directly express trust with probability value or mathematical expectation. On the basis of information theory, trust is established and measured, and the value of trust is expressed by entropy.

Trust is the relationship established between two entities (power grid nodes) to perform a specific behavior. Suppose $\left\{c_i\colon c_j, action\right\}$ represents entity c_i, trust entity c_j will perform behavior *action*, and $T\left\{c_i\colon c_j, action\right\}$ represents trust degree, that is, trust degree.$p = P\left\{c_i\colon c_j, action\right\}$ represents the probability that c_i believes c_j will perform action *action*. According to the concept of entropy in information theory, there are:

$$T\left\{c_i : c_j, action\right\} = \begin{cases} 1 - W(p), & 0.5 \le p \le 1 \\ W(p) - 1, & 0 \le p < 0.5 \end{cases} \tag{4}$$

In Formula (4), $W(p) = -p\log_2(p) - (1-p)\log_2(1-p)$. The value of $T\left\{c_i\colon c_j, action\right\}$ is shown in Figure 4.

It can be seen that the trust degree is a continuous real value between $[-1, 1]$ and increases with the increase of *a posteriori* probability p.

3.3.2 Behavior trust evaluation and synthesis

The overall trust T_T of power grid node c_i to c_j mainly comes from the direct trust D_T established through the observation of c_j behavior and the recommendation of other entities to c_j, that is, the indirect trust R_T to c_j. In essence, trust recommendation is a process of trust transmission, and trust recommendation between different power grid nodes also realizes trust transmission.

(1) Direct trust value calculated according to observation: establish a direct mutual trust relationship with neighboring nodes through observation, and the goal is to obtain the direct trust value for the node according to the previously observed behavior of neighboring nodes.

Use *a posteriori* probability to calculate the direct trust. Suppose c_i has requested c_j to execute action *action* for N_u times and c_j has executed action *action* for K_u times during the u observation, then:

$$P\left\{c_i : c_j, action\right\} = \frac{1 + \alpha^{T_c - T_m} K_m}{2 + \alpha^{T_c - T_m} N_m} \tag{5}$$

In Formula (5), $\alpha \in [0, 1]$ is a forgetting factor determined by the speed of c_j behavior change. The worse the stability of c_j, the lower the value of α. T_c represents the current time point, while T_m represents the time of each observation.

(2) Indirect trust value is calculated based on trust transfer and composition (Ding et al., 2020; Xu, 2021): when a power grid node just joins the power grid or changes its location, in order to establish trust with the target node without interactive experience with the target node, the recommendation of other nodes is mainly used to obtain the trust value of the target entity. Recommendation is essentially a process of trust transmission.

Let $R_{c_ic_c} = T\{c_i\colon c_c, recommendation\} = T_{Tc_ic_c}$ and $T_{Tc_cc_j}$ be the overall trust value of c_c to c_j. Among them, trust transfer includes:

$$R_{Tc_ic_cc_j} = R_{c_ic_c} T_{Tc_cc_j} \tag{6}$$

Trust composition is the process of synthesizing the recommended trust values from two or more channels to the target node into indirect trust values to the target node according to certain rules. On this basis, using the weight maximization algorithm (Yang et al., 2022), the trust value of the intermediate node on each recommended path is taken as the trust weight, and the trust composition is performed. Then we can use Formula (7) to calculate c_i indirect trust value of c_j obtained through c_C and c_D recommendation:

$$R_{Tc_ic_j} = \frac{R_{c_ic_C}\left(R_{c_ic_C} T_{Tc_Cc_j}\right) + R_{c_ic_D}\left(R_{c_ic_D} T_{Tc_Dc_j}\right)}{R_{c_ic_C} + R_{c_ic_D}} \tag{7}$$

When there are more than two trust recommendation paths, expand Formula (7) to comprehensively recommend the trust value from multiple trust recommendation paths as follows:

$$R_{Tc_ic_j} = \sum\nolimits_{L=1}^{K} R_{Tc_ic_Lc_j} = \frac{\sum_{L=1}^{K} R_{c_ic_L}^2 T_{Tc_Lc_j}}{\sum_{L=1}^{K} R_{c_ic_L}} \tag{8}$$

In Formula (8), C_L represents the different nodes that provide c_i with the recommended value of c_j, and K represents the number of recommended paths. When c_i just joined the power grid or changed its location, it did not establish behavioral trust relationship with other nodes. In this case, to obtain the indirect trust value of the target node of the power grid, it can only request the neighbor node of the power grid to provide it. When c_i gradually establishes trust relationship with other power network nodes in the power network, it can obtain the recommended trust value of the target node through the most trusted node, and finally obtain the indirect trust of the target node.

(3) Overall trust evaluation: the overall trust $T_{Tc_ic_j}$ of power grid node c_i to c_j, the recommended trust of other nodes to c_j, and the direct trust, the indirect trust value is as follows:

TABLE 1 Parameter setting of simulation experiment.

Project	Parameter
T_m	50/s
J	0.02
V	0.01
α	0.8
β	0.5

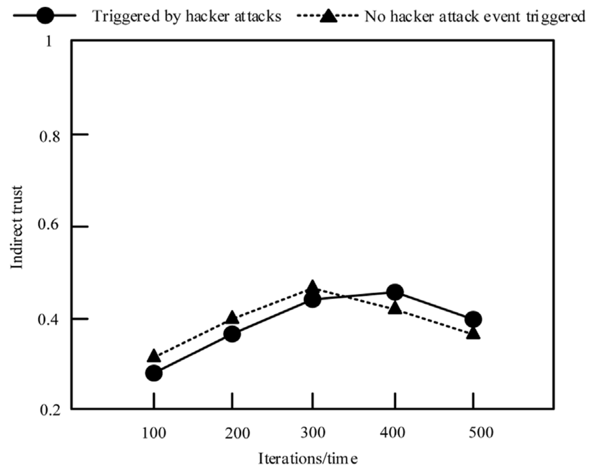

FIGURE 5
Impact of hacker attacks on power network node trust.

$$T_{Tc_ic_j} = \beta D_{Tc_ic_j} + (1-\beta) R_{Tc_ic_j} \tag{9}$$

In Formula (9), $\beta \in [0, 1)$ is the confidence coefficient. Confidence coefficient controls the proportion of direct trust and indirect trust in the overall trust. If c_i is newly added to the power grid or its location has just changed, and there is no direct interaction experience with c_j, then c_i trust in c_j mainly comes from the trust recommendation of other nodes to T, and Y is very small at this time. With the continuous interaction between c_i and c_j, direct trust accounts for more and more of the overall trust, and β also increases until it reaches a value less than 1.

Through the above steps, the security feedback trust model of power network demand response terminal triggered by hacker attacks is realized.

3.4 Simulation experiment and analysis

3.4.1 Setting the simulation experiment environment

In order to verify the validity of the security feedback trust model of power network demand response terminal triggered by hacker attacks, this paper uses PeerSim1.0.5 simulation software to simulate it. On this basis, it is assumed that the total number of nodes in the power network is 100 and the trust degree of each node is 0.5. Each node in the power grid has 50 files in total, and each node selectively downloads 30 times from other nodes. Each group of experiments is simulated for 10 times, and each simulation cycle is 30 times. The results of simulation experiments are average results. The simulation experiment parameter settings are shown in Table 1.

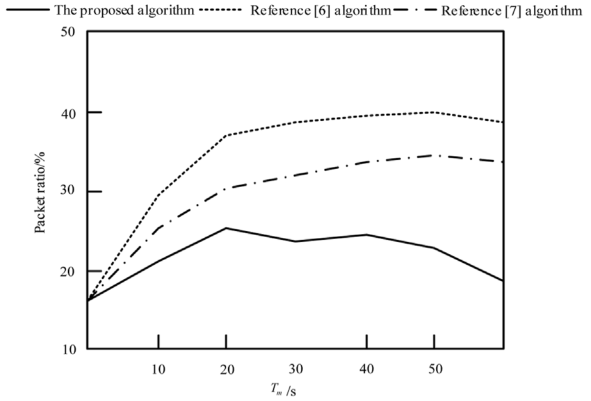

FIGURE 6
Packet ratio of malicious nodes triggered by hacker attack events in different methods.

3.4.2 Analysis of the impact of hacker attacks on the trust of power grid nodes

In order to verify the validity of the security feedback trust model of power network demand response terminals, the impact of hacker attacks on the trust of power network nodes is analyzed. It is assumed that 50% of the power network has transacted with the target node, and two conditions are set under whether there is a hacker attack event triggered. The influence results on the trust level of the power network node are shown in Figure 5.

According to Figure 5, as the number of iterations increases, the impact of hacker attacks on the indirect trust of power grid nodes decreases. The reason is that the more iterations, the more similar the hacker attack ID is, and the trust given by nodes with similar IDs is roughly the same. Therefore, the security feedback trust model of power network demand response terminals can judge the hacker attacks, thereby reducing the impact of hacker attacks on the trust of power network nodes.

3.4.3 Security analysis of power network demand response terminal

On this basis, the security of the power network demand response terminal of the proposed method is verified, and the packet ratio of malicious nodes triggered by hacker attacks is taken as the evaluation index. The lower the packet ratio, the higher the security of the power network demand response terminal of the method. The calculation formula is as follows:

$$\gamma = \frac{\kappa}{\mu} \times 100\% \tag{10}$$

In Formula (10), κ is the number of malicious node packets triggered by hacker attacks, and μ is the total number of packets

TABLE 2 Comparison results of packet loss rates of different methods.

T_m/s	The proposed method/%	Reference (Zhang et al., 2019a) method/%	Reference (Alagappan et al., 2022) method/%
10	0.6	1.5	2.6
20	1.2	2.7	4.7
30	2.4	3.9	5.6
40	3.7	5.2	7.4
50	4.4	6.1	8.9

transmitted by the power network. By comparing the methods of literature (Zhang et al., 2019a), the methods of literature (Alagappan et al., 2022) and the proposed methods, we can get the packet ratio of malicious nodes triggered by hacker attacks in different methods, as shown in Figure 6.

According to Figure 6, when there is a malicious node triggered by a hacker attack event in the power grid using the methods of literature (Zhang et al., 2019a), the methods of literature (Alagappan et al., 2022) in the power grid demand response terminal, the packet rate of the malicious node triggered by the hacker attack event will increase from 16% to 40%. With the increase of the number of malicious nodes triggered by hacker attacks in the power grid, the packet ratio of malicious nodes triggered by hacker attacks will also rise rapidly. However, in the power network demand response terminal, using the proposed method, the trust of malicious nodes triggered by hacker attacks drops rapidly, and normal nodes will bypass these malicious nodes triggered by hacker attacks when routing. Therefore, the packet rate of malicious nodes triggered by hacker attacks will decrease. It can be seen that the proposed method has a high security of power network demand response terminal.

3.4.4 Mutual security analysis between power grid nodes

Further verify the interaction security between power grid nodes of the proposed method, and take packet loss rate as the evaluation index. The lower the packet loss rate, the higher the interaction security between power grid nodes of the method. The calculation formula is as follows:

$$\tau = \frac{\lambda}{\mu} \times 100\% \tag{11}$$

In Formula (11), λ is the total number of packets dropped by power grid nodes. The methods of literature (Zhang et al., 2019a), the methods of literature (Alagappan et al., 2022) and the proposed methods are compared, and the comparison results of packet loss rates of different methods are shown in Table 2.

According to Table 2, the packet loss rate of different methods increases with the increase of observation time. When the observation time reaches 50 s, the packet loss rate of the methods of literature (Zhang et al., 2019a) is 6.1%, and that of the methods of literature (Alagappan et al., 2022) is 8.9%. The packet loss rate of the proposed method is only 4.4%. It can be seen that the packet loss rate of the proposed method is low, indicating that the interaction security between nodes of the power network of the proposed method is high.

4 Discussion

In the experimental test, the proposed method can judge the hacker attacks, reduce the impact of hacker attacks on the trust of power grid nodes, and improve the interaction security between power grid nodes. Reference (Zhang et al., 2019a) method and Reference (Alagappan et al., 2022) method are based on the master-slave chain architecture of the blockchain and the zero trust network architecture to enhance the security of virtual power plants, respectively, to reduce security risks. No identity trust relationship has been established, resulting in low security between power grid nodes. But the proposed method uses convolutional neural network method in artificial intelligence technology to effectively improve the flexibility of smart grid and effectively enhance the overall anti-interference capability of power grid.

5 Conclusion

This paper proposes a security feedback trust model of power network demand response terminals triggered by hacker attacks. By analyzing the role of smart grid in power grid, the flexibility of smart grid is enhanced based on convolutional neural network in artificial intelligence technology. Aiming at the security problem of demand response terminal of power network being attacked by hackers, a security feedback trust model of demand response terminal of power network is designed based on trust theory. The distributed verifiable signature scheme is adopted to update the certificate of power network nodes. Based on information theory, trust is established and measured. The behavior trust evaluation and composition mechanism is introduced into the security feedback trust model of power network demand response terminals to achieve the credibility of power network node identity and behavior. The following conclusions are drawn:

(1) As the number of iterations increases, the impact of hacker attacks on the indirect trust of power grid nodes decreases, which indicates that the proposed method can judge the hacker attacks, thereby reducing the impact of hacker attacks on the trust of power grid nodes.
(2) The proposed method can improve the security of power network demand response terminals because of the low packet rate of malicious nodes triggered by hacker attacks.
(3) The low packet loss rate of the proposed method indicates that the interaction security between nodes of the power network is high.

The subsequent research will deeply study the storage mode and hash mapping mode of trust information on the device access network to improve the search efficiency of resources and reduce the cost of proxy servers.

Data availability statement

The original contributions presented in the study are included in the article/Supplementary Material, further inquiries can be directed to the corresponding author.

Author contributions

Each author made significant individual contributions to this manuscript. JC: methodology, data analysis, and writing; LZ: data analysis, writing-reviewing, and editing; QS: article review and intellectual concept of the article; CZ: research and investigation, consult materials and references.

Conflict of interest

JF was employed by State Grid Shandong Electric Power Company. LZ was employed by Information and Communications Company, State Grid Shandong Electric Power Company. QS was employed by State Grid Weihai Wendeng Power Supply Company. CZ was employed by State Grid Juxian Power Supply Company.

Publisher's note

References

Alagappan, A., Venkatachary, S. K., and Andrews, L. J. B. (2022). Augmenting Zero Trust Network Architecture to enhance security in virtual power plants. *Energy Rep.* 8, 1309–1320. doi:10.1016/j.egyr.2021.11.272

Charis, G., Danha, G., Muzenda, E., and Nhubu, T., (2021). Modeling a sustainable, self-energized Pine Dust Pyrolysis system with staged condensation for optimal recovery of bio-Oil. *Front. Energy Res.* 8, 594073. [J].

Cherukuri, S., Chenniboyena, R., Yarlagadda, D., Kolluru, V. R., and Razia, S., (2022). *Development of Raspberry pibot surveillance security system, confidential computing*. Singapore: Springer, 79–86.

Das, T., and Mukherjee, S. (2022). *Data privacy in IoT network using blockchain technology, intelligent systems for social good*. Singapore: Springer, 117–137.

Ding, Y., Zhao, Y., and Zhang, R. (2020). "A secure routing algorithm based on trust value for micro-nano satellite network," in Proceedings of the 2020 2nd International Conference on Information Technology and Computer Application (ITCA), Guangzhou, China, December 2020 229–235. [C]//.

Goyat, R., Kumar, G., Alazab, M., Saha, R., Thomas, R., and Kumar, R. M. (2021). A secure localization scheme based on trust assessment for WSNs using blockchain technology. *Future Gener. Comput. Syst.* 125, 221–231.

Group, R. (2022). Hacker attack on deutsche windtechnik. *Renew. Energy Monit.* 21, 10–11.

Gunjan, V. K., Kumar, A., and Rao, A. A. (2014). "Present & future paradigms of cyber crime & security majors-growth & rising trends," in Proceedings of the 2014 4th International Conference on Artificial Intelligence with Applications in Engineering and Technology, Kota Kinabalu, Malaysia, December 2014 89–94.

Han, S., Xie, M., Yang, B., Lu, R., Bao, H., Lin, J., et al. (2019). A certificateless verifiable strong designated verifier signature scheme. *IEEE Access* 7, 126391–126408. doi:10.1109/access.2019.2938898

Hongal, R. S., and Shettar, R. B. (2020). A power-efficient and quantum-resistant N-bit cryptography algorithm. *Int. J. Nat. Comput. Res. (IJNCR)* 9 (4), 18–33. doi:10.4018/ijncr.2020100102

Hu, W., Yang, Z., Chen, C., Wu, Y., and Xie, Q. (2021). A weibull-based recurrent regression model for repairable systems considering double effects of operation and maintenance: A case study of machine tools. *Reliab. Eng. Syst. Saf.* 213, 107669. doi:10.1016/j.ress.2021.107669

Huang, Z. F., Soh, K. Y., Islam, M. R., and Chua, K. (2022). Digital twin driven life-cycle operation optimization for combined cooling heating and power-cold energy recovery (CCHP-CER) system. *Appl. Energy* 324, 119774. doi:10.1016/j.apenergy.2022.119774

Jiang, W., Wang, Y., Jiang, Y., Chen, J., Xu, Y., and Tan, L. (2019). Research on mobile internet mobile agent system dynamic trust model for cloud computing. *China Commun.* 16 (7), 174–194. doi:10.23919/jcc.2019.07.014

Karthik, R., Baji, V. M. M., Kumar, M. P., Anjum, S. A., Suresh, M., et al. (2022). *Image security based on rotational visual cryptography, confidential computing*. Singapore: Springer, 87–96.

Karthik, R., Shukla, P., Lavanya, S., Naga Satish, L. L., and Sai, R. K. J. (2022). *Deep transfer learning for detecting cyber attacks, confidential computing*. Singapore: Springer, 113–124.

Li, C., Qu, Q., Gao, W., Xiao, X., Yuan, P., and Wang, X. (2021). "Heterogeneous network selection strategy based on power wireless communication system," in Proceedings of the 2021 5th International Conference on High Performance Compilation, Computing and Communications, Guangzhou China, June 2021 1–6.

Li, J., Liu, H., Wang, D., and Bi, T., (2021). Classification of power quality disturbance based on S-transform and convolution neural network. *Front. Energy Res.* 9, 325.

Li, S., Lu, D., Wu, X., Han, W., and Zhao, D. (2021). Enhancing the power grid robustness against cascading failures under node-based attacks. *Mod. Phys. Lett. B* 35 (09), 2150152. doi:10.1142/s0217984921501529

Liu, G., Yang, Q., Wang, H., and Liu, A. X. (2019). Trust assessment in online social networks. *IEEE Trans. Dependable Secure Comput.* 18 (2), 994–1007. doi:10.1109/tdsc.2019.2916366

Liu, Z., Fan, Y., Wang, Y., Miao, Z., Sun, Y., and Miao, X. (2020). Evaluation trust model of block chain information capacity based on subjective logic. *J. Hebei Univ. Nat. Sci. Ed.* 40 (2), 431–437.

Moelker, R. (2021). *SHAPE we trust! Trust theory put to the test within an ambidexterious headquarters. The yin-yang military*. Cham, Switzerland: Springer, 213–224.

Moorthy, R. S. K., Liu, G., Chinthavali, M., Choi, J., and Starke, M., (2021). Architecture of a residential solid state power substation (SSPS) node Proceedings of the 2021 IEEE power & energy society innovative smart grid technologies conference (ISGT). Washington, DC, USA, February 2021 , 1–5.

Prasad, P. S., Beena Bethel, G. N., Singh, N., Kumar Gunjan, V., Basir, S., and Miah, S. (2022). Blockchain-based privacy access control mechanism and collaborative analysis for medical images. *Secur. Commun. Netw.* 2022, 9579611–9579617. doi:10.1155/2022/9579611

Ren, H., Hou, Z. J., Vyakaranam, B., Wang, H., and Etingov, P. (2020). Power system event classification and localization using a convolutional neural network[J]. *Front. Energy Res.* 8, 607826.

She, J., Shi, T., Xue, S., Zhu, Y., and Cao, H., (2021). Diagnosis and prediction for loss of coolant accidents in nuclear power plants using deep learning methods. *Front. Energy Res.* 10, 186.

Sui, B., Chen, X., Li, Z., Zhao, J., and Tian, J. (2020). Research on multi-node frame early warning system of power grid based on abnormal data extraction[C]//Journal of physics: Conference series. *IOP Publ.* 1654 (1), 012020. doi:10.1088/1742-6596/1654/1/012020

Sun, M., Wang, Q., He, J., Huang, H., Huang, Y., Shen, X., et al. (2022).Research on automatic scanning method of network vulnerabilities in power system *J. Phys. Conf. Ser.*, 2290. 112036. doi:10.1088/1742-6596/2290/1/012036

Tung, N. T., Nam, P. M., and Tin, P. T. (2021). Performance evaluation of a two-way relay network with energy harvesting and hardware noises. *Digital Commun. Netw.* 7 (1), 45–54. doi:10.1016/j.dcan.2020.04.003

Wang, W., Wang, C., Guo, Y., Yuan, M., and Gao, Y. (2021). Industrial control malicious traffic anomaly detection system based on deep autoencoder. *Front. Energy Res.* 8, 555145. [J].

Xu, Q. (2021). Wireless sensor networks secure routing algorithm based on trust value computation. *Int. J. Internet Protoc. Technol.* 14 (1), 10–15. doi:10.1504/ijipt.2021.10036582

Xu, X., and Hong, L. (2022). Instantaneous and limiting behavior of an n-node blockchain under cyber attacks from a single hacker. *arXiv Prepr. arXiv* 13 (2), 352–359.

Yang, C., Ma, B., Yin, B., and Chen, Y. (2022). Model predictive control for compound power supply based on fuzzy weight. *Comput. Simul.* 39 (04), 103–109.

Zhang, M., Zhao, W., Shi, W., and Zhou, H. (2021). Privacy protection method of electric power network based on blockchain[C]//Journal of physics: Conference series. *IOP Publ.* 1744 (2), 022009. doi:10.1088/1742-6596/1744/2/022009

Zhang, N., Dai, H., Wang, Y., Zhang, Y., Yang, Y., Lund, P., et al. (2021). Power system transition in China under the coordinated development of power sources, network, demand response, and energy storage. *Wiley Interdiscip. Rev. Energy Environ.* 10 (2), e392. [J].

Zhang, N., Dai, H., Wang, Y., Zhang, Y., and Yang, Y. (2021). Power system transition in China under the coordinated development of power sources, network, demand response, and energy storage. *Wiley Interdiscip. Rev. Energy Environ.* 10 (2), 392–399. doi:10.1002/wene.392

Zhang, X., Gong, Y., and Spece, M. (2019). Trust decision model for online consumer evaluation: Deeper uncertainty integration in evidence theory approach. *J. Intelligent Fuzzy Syst.* 36 (5), 4257–4264. doi:10.3233/jifs-169983

Zhang, Z., Zhong, C., Guo, S., and Wang, F. (2019). “A master-slave chain architecture model for cross-domain trusted and authentication of power services,” in Proceedings of the 2019 7th International Conference on Information Technology: IoT and Smart City, Shanghai China, December 2019 483–487.

frontiers | Frontiers in Energy Research

TYPE Original Research
PUBLISHED 15 February 2023
DOI 10.3389/fenrg.2023.1135741

OPEN ACCESS

EDITED BY
Xin Ning,
Institute of Semiconductors (CAS), China

REVIEWED BY
Sahraoui Dhelim,
University College Dublin, Ireland
Luyang Hou,
Beijing University of Posts and
Telecommunications (BUPT), China
Achyut Shankar,
University of Warwick, United Kingdom

*CORRESPONDENCE
Yang Liu,
✉ liuyang42467452@163.com

SPECIALTY SECTION
This article was submitted to
Smart Grids, a section of the journal
Frontiers in Energy Research

RECEIVED 01 January 2023
ACCEPTED 30 January 2023
PUBLISHED 15 February 2023

CITATION
Xu F, Liu Y and Wang L (2023), An
improved ELM-WOA–based fault
diagnosis for electric power.
Front. Energy Res. 11:1135741.
doi: 10.3389/fenrg.2023.1135741

An improved ELM-WOA–based fault diagnosis for electric power

Feifei Xu[1], Yang Liu[2]* and Lei Wang[3]

[1]Department of Marketing, State Grid Yantai Fushan Power Supply Company, Yantai, China, [2]Teaching and Research Support Center, Naval University of Engineering, Wuhan, China, [3]College of Weaponry Engineering, Naval University of Engineering, Wuhan, China

Due to its fast learning speed, the extreme learning machine (ELM) plays a very important role in the real-time monitoring of electric power. However, the initial weights and thresholds of the ELM are randomly selected, therefore it is difficult to achieve an optimal network performance; in addition, there is a lack of distance selection when detecting faults using artificial intelligence algorithms. To solve the abovementioned problem, we present a fault diagnosis method for microgrids on the basis of the whale algorithm optimization–extreme learning machine (WOA-ELM). First, the wavelet packet decomposition is used to analyze the three-phase fault voltage, and the energy entropy of the wavelet packet is calculated to form the eigenvector as the data sample; then, we use the original ELM model coupled with the theory of distance selection to locate faults and compared it with the SVM method; finally, the whale algorithm is used to optimize the input weight and hidden layer neuron threshold of the ELM, i.e., the WOA-ELM model, which solves the problem of the random initialization of the input weight and hidden layer neuron threshold that easily affects the network performance, further improves the learning speed and generalization ability of the network, and is conducive to the overall optimization. The results show that 1) the accuracy of selecting the data according to the fault distance is twice that of not selecting data according to it; 2) compared with the BP neural network, RBF neural network, and ELM, the fault diagnosis model based on the WOA-ELM has a faster learning speed, stronger generalization ability, and higher recognition accuracy; and 3) after optimization of the WOA, the WOA-ELM can improve 22.5% accuracy in fault detection when compared to the traditional ELM method. Our results are of great significance in improving the security of smart grid.

KEYWORDS

smart grid, ELM, fault diagnosis, support vector machine, wavelet transform, WOA-ELM

1 Introduction

With the rapid development of modern economy, the consumption of energy is increasing high (Zhang et al., 2023). The direct consumption and waste of non-renewable energy are particularly serious. The direct consumption and waste of non-renewable energy are particularly serious. People's demand for the energy, power quality, and power company services are growing (Chang et al., 2023). For the traditional power grid, with the continuous extension of transmission lines, the occurrence rate of faults is also constantly improving (Lei et al., 2022). There are many reasons for the large-scale blackout of the power grid due to fault in transmission, for example, extreme weather events and aggravating anthropogenic activities (Lei et al., 2022; Liu et al., 2022). However, faults cannot be completely avoided, as they are not only affected by human factors, but also by nature. Therefore, it is very meaningful to detect, classify, and locate faults in smart grid (Liu et al., 2022; Waldrigues et al., 2022).

Unified power fault detection methods bring huge costs (Chen et al., 2022a; Wang, 2022; Yan et al., 2022), so now, many works use artificial intelligence methods to detect, classify, and locate power faults (Hou et al., 2022; Li et al., 2022; Ma et al., 2022). For example, Yuvaraja et al. (2022) examined the effect of smart grid systems by implementing the artificial intelligence technique with application of renewable energy sources (Yuvaraja et al., 2022). Chen et al. (2022a) used the CNN-LSTM model to solve the problem of the slow transmission rate of high-frequency information in smart grid and improve the efficiency of information transmission (Xin, 2022). Because the distance of the transmission line is relatively long, the probability of failure of the transmission line is increased (Ayushi et al., 2022; Xin, 2022; Yuvaraja et al., 2022). Some scholars use neural networks to detect whether there is a current that is directly grounded (Xin, 2022). In their results, the decision tree and neural network have a good effect in the fault classification and location of electric wires (Ayushi et al., 2022). Moreover, some studies have used the neural network coupled with wavelet transforms to detect faults—specifically, some signals of the layer are extracted through wavelet transforms to judge whether there is a fault and then the neural network or regression decision tree is used to judge what the fault is (Ayushi et al., 2022; Singhal et al., 2022; Xin, 2022). Generally, the collected data are trained and located by simulating the fault type and fault location of the wire (Chen et al., 2022b; Singhal et al., 2022). Furthermore, a complex neural network is specially designed for the complex of power grid data.

The data used in fault detection are divided into two categories: one, the data that are collected at only one end and the other, the data that are collected at both ends (Chen et al., 2022b). If data from only one end is used, it will be easier to collect than when collecting data from both the ends at the same time. However, data from only one end usually show either poor accuracy or incomplete detection. Some researchers have suggested using the K-nearest neighbor (KNN) to solve the above problem (Fang et al., 2022). For KNN, Euclidean distance was calculated, and the smaller one as the similar standard. Also, the KNN when combined with the wavelet transform can classify and locate wire faults more efficiently, with the data at one end being used to calculate the wavelet transform before classification and location. In the past, some scholars have compared the data only used at one end with that from both ends (Shafiullah et al., 2022). In these two cases, the accuracy of fault location estimation is similar. However, since it is more difficult to collect data to measure the data at both ends, it has been recommended to use only the data at one end (Fang et al., 2022; Jia et al., 2022; Shafiullah et al., 2022). Data collection at both ends has certain requirements for data collection instruments. Because the data at both ends have to be synchronized, GPS satellites are now used for synchronization (Jia et al., 2022). However, there are also some researchers who have recommended using the data at both ends that can to some extent obtain good performance in fault detection (You et al., 2021; Dac and Trung, 2023; Ma et al., 2023).

The ELM is the new type of neural network proposed by Professor Huang Guangbin of Nanyang University of Technology in Singapore in 2004. It has been widely used in many fields in recent years. The limit learning machine randomly selects hidden node parameters (such as input weights and deviations) and analyzes and judges the output weights of the single hidden layer feedforward neural network (SLFN). In this way, when the minimum training error is reached, the training burden can be significantly reduced. It is a simple and effective SLFN learning algorithm. It not only has the characteristics of a simple mathematical model and fast learning speed but also a good generalization performance. At present, it is being successfully applied to handwritten font recognition, weather prediction, voice and image recognition, and other fields. However, since the initial weights and thresholds of the traditional ELM are randomly selected, the best network performance is difficult to achieve. Furthermore, the fault location would be affected by the compensation equipment, but due to the uncertainty of these models, there would be some deviation when estimating the error. These shortcomings have currently not been solved by researchers.

In this article, therefore, a method is proposed to roughly judge whether the fault may be in the first half or second half with regard to the data at both ends and then locate the fault with the data at the end close to the fault. We also use the learning method of artificial intelligence (the extreme learning machine, ELM) to locate the fault location. Then, a smart grid fault diagnosis method based on the whale optimization algorithm (WOA) and extreme learning machine (ELM) is proposed to improve the ELM method in fault detection. If the data at the far end is used, the artificial intelligence method cannot locate the fault location well. This is because the data collected at the detection data end must pass through more power components at the end farther from the fault location. These components have an impact on the transmission of electrical signals. In order to reduce the unnecessary effects, the data collected at the nearest end can be selected as the input feature of the classifier. The methodology in this article is to first use the data at both ends of the classifier to determine the end at which the fault is likely to occur and then select the data at the nearest end to locate fault. Furthermore, because the initial weights and thresholds of the ELM are randomly selected, it is difficult to reach the optimum network performance. In order to overcome the abovementioned shortcomings, a fault diagnosis model is established by using the whale algorithm optimized–extreme learning machine (WOA-ELM). The whale algorithm has the characteristics of a simple parameter setting, fast learning speed, high optimization accuracy, and strong global optimization ability. It can solve the problem of manually setting the initial weights and hidden layer thresholds of the limit learning machine and is conducive to further improve the recognition accuracy.

Therefore, we 1) first use the ELM to define the fault line and then analyze its results. At the same time, the support vector machine classifier and wavelet transforms are used to process the signal for location; 2) analyze the three-phase fault voltage by wavelet packet decomposition, and the energy entropy of wavelet packet is calculated to form the eigenvector as the data sample; 3) finally, use the whale algorithm to optimize the input weight and hidden neuron threshold of the ELM, which solves the problem of random initialization of the input weights and hidden neuron thresholds that easily affect network performance, which can further improve the learning speed and generalization ability of the network and is conducive to global optimization. Some data of these simulated wire faults are obtained as samples for experimental learning.

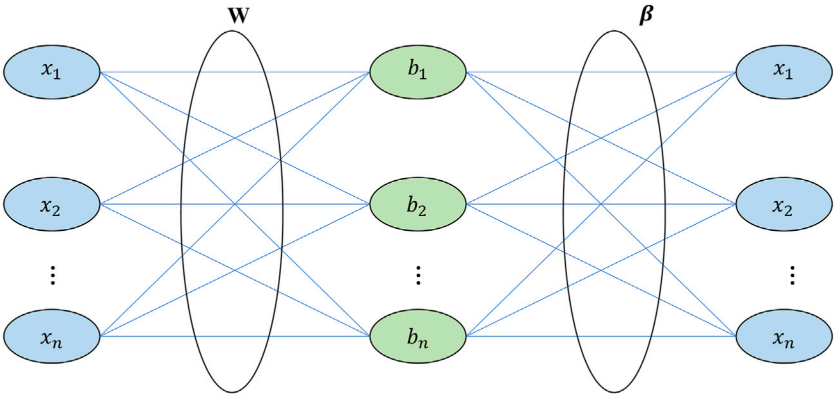

FIGURE 1
Structure of extreme learning machine. W is input weight, β is output weight.

This study is organized as follows. We summarize the related works in Section 2; then, we introduce the ELM methodology, WOA approach, and data process in Section 3; in Section 4, a model of the high-voltage transmission system is established; and in the Results section, the ELM, WOA-ELM, and SVM are used to locate the fault line, and the results are analyzed.

2 Related works

Compared with the traditional fault diagnosis method, the fault diagnosis method based on AI technology has a higher diagnosis accuracy and faster diagnosis speed. Many experts and scholars have proposed a large number of fault diagnosis methods on the basis of the AI algorithm, such as the expert system method, method based on the optimization model, method based on the graph theory model (such as the Petri net, Bayesian network, spike neural network (SNP) system, and artificial neural network (ANN).

The method based on the expert system is the earliest AI method to be applied for power grid fault diagnosis. This method establishes an expert rule base by simulating the logical experience of experts when dealing with faults. During diagnosis, the current fault information is compared with the rules of the expert base, and the diagnosis results are obtained according to the matching situation. Due to its good reasoning ability and fault interpretation ability, this method has become the most widely adopted and applied method in the field of power grid fault diagnosis in the early stages. Fukui and Kawakami (1986) proposed for the first time applying the expert system to the field of power grid fault diagnosis, using concepts and simplified information to estimate fault components and realizing smart grid fault diagnosis. However, due to the simple rule base, it can deal only with simple fault situations. The essence of this method based on the analytical model is a mathematical model built according to the power grid protection configuration and the action rules of protection and circuit breaker in case of faults. This method represents the fault diagnosis problem as a 0-1 integer programming problem and then uses the intelligent optimization algorithm to find out the fault hypothesis that can best explain the fault information. Because the theoretical basis is rigorous and has a mathematical basis, and the diagnosis process has explanatory power and is concise and clear, a large number of optimization algorithms are applied for power grid fault diagnosis. Xiong et al. (2018) proposed a brainstorming algorithm for binary coding optimization, established a fast fault diagnosis for large power grids, and solved the 0-1 integer programming problem using binary vector coding instead of the algorithm, thus improving the efficiency of the diagnosis model. The power grid fault diagnosis method based on the graph theory has strong explanatory power. The general process of such algorithms is to first establish a causal model, directly representing the causal relationship between protection and the circuit breaker through a clear and intuitive graphical process and then use their respective reasoning methods to diagnose the fault components. The graphical process makes it unnecessary to extract the representative fault samples, while the "transparent" diagnosis process (the diagnosis process conforms to logical reasoning) enables dispatchers to understand the whole fault diagnosis process in a very short time, which is conducive to the subsequent power recovery. The method based on Petri net is the most widely studied graphical fault diagnosis model. This method uses the repository/transition of weighted directed network to clearly restore the knowledge logic in fault diagnosis. The reverse reasoning process is simple and clear and the speed is fast, but the ability to deal with complex problems is low. Since then, researches in terms of diagnosis detection are mainly concentrated in high level high-level Petri net (Lcfcbvre, 2014). The method is based on the Bayesian network and conditional probability reasoning to realize power grid fault diagnosis. The diagnosis model is intuitive and can diagnose effectively even when the alarm information is wrong, but it is difficult to obtain the prior probability of component fault in a complex power grid (Ji et al., 2022). The SNP system is essentially a directed graph composed of multiple neurons and synapses connecting the neurons, in which the neurons are the nodes and synapses are the directed arcs of the graph (Wang et al., 2011). In the SNP system, the transmission of data information is realized through

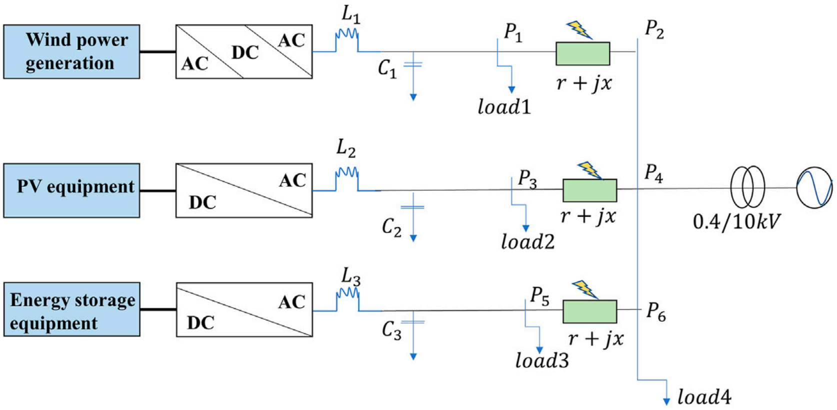

FIGURE 2
Structure of microgrid system. L_1, L_2, and L_3 are filter inductances; C_1, C_2, and C_3 are filter capacitors; Load1, Load2, Load3, and Load4 are electrical loads; r is line resistance; x is line reactance.

the excitation of pulse potentials in the neurons. All pulses are represented by characters and considered undifferentiated. The data information in the SNP system can be transferred from the presynaptic neurons to postsynaptic neurons according to specific excitation rules. According to the excitation rules, new pulses are generated after the consumption of a part of the pulses. These new pulses are transmitted to all the neurons connected after the synapse. The fault diagnosis method based on the neural network has the characteristics of distributed storage, adaptive learning, high fault tolerance rate, and fast diagnosis speed and a certain development prospect in the field of power grid fault diagnosis (Luo et al., 2014). At present, there are three types of fault diagnosis methods based on the neural network: one is the centralized diagnosis method that takes the whole power grid as a whole and directly diagnoses; the second is the partition diagnosis method which divides the large-scale power grid into several regions for diagnosis; and the third is the component-oriented diagnosis method of establishing diagnosis network for faults of various power grid components (lines, buses, and transformers).

Chang et al. (2023) proposed a fault identification method on the basis of a unified inverse-time characteristic equation to aim at the problems of large setting workload and easy mis-operation of the inverse-time overcurrent relay after distributed generation access (Chang et al., 2023); Lei et al. (2022) proposed the multi-population particle swarm optimization algorithm and compared it with single-population particle swarm algorithm on the IEEE 69-node model, they proved that the new algorithm can find fault locations faster; meanwhile, they verified the effectiveness of the algorithm in a variety of distribution network fault location scenarios (Lei et al., 2022). Liu et al. (2022) considered the randomness and uncertainty of the output of the solar and wind power, as well as the bidirectional characteristic of current flow and because the faults in the microgrids being difficult to identify using the traditional fault detection methods, they proposed a machine learning–based fault identification method for microgrids. Waldrigues et al. (2022) proposed an improved method after Brazil (2020) to verify the feasibility of using time-series forecasting models for fault prediction; they also evaluated the long short-term memory (LSTM) model to obtain a forecast result that an electric power utility can use to organize maintenance teams. Wang (2022) presented a fault line selection approach on the basis of the modified artificial bee colony optimization–deep neural network (ACB-DNN) to address the difficulties in choosing a fault line in electric current grounding systems for small electric currents. Chen et al. (2022a) put forward a novel fault recovery method for Automatic driving network (ADN) on the basis of an improved binary particle swarm optimization (BPSO) algorithm, and the topology constraints were specially considered to accelerate the recovery operation.

The extreme learning machine (ELM) is a single implicit feedforward network learning method derived from the neural network (NN). Because the weight value between the input and hidden layer and the hidden layer threshold of the algorithm are randomly generated without adjustments and training and the output can be obtained only by setting the number of hidden layer neurons, the algorithm has a good learning efficiency and high generalization (Luo et al., 2017). However, the ELM has the following shortcomings: the ELM uses the least squares method to learn, only considers the empirical risk of the model, and is prone to over-fitting. Especially, when the training data cannot express the characteristics of the learning data set, the over-fitting phenomenon is particularly serious. The accuracy of the ELM is significantly affected by the number of neurons in the hidden layer. The calculation error of the ELM depends heavily on the large number of hidden layers and easily causes dimension disaster, seriously affecting the practical application of the ELM (Kasun et al., 2013).

In order to overcome the abovementioned shortcomings, a fault diagnosis model is established by using the whale algorithm optimized–extreme learning machine (WOA-ELM). The whale algorithm has the characteristics of simple parameter setting, fast learning speed, high optimization accuracy, and strong global optimization ability. It can solve the problem of manually setting the initial weight and hidden layer threshold of the limit learning machine and is conducive to further improve the recognition accuracy.

3 Methods and data

3.1 ELM and WOA-ELM

In the single hidden layer feedforward networks (SLFNs), many parameters have to be adjusted because the weights of the neurons in the different layers are interdependent. In the past few decades, the gradient-based learning algorithm has been generally used in feedforward neural networks. The method is slow and easy to fall into the local minimum. Different from the traditional feedforward neural network, the extreme learning machine (ELM) has to adjust all the parameters of the feedforward neural network (for the structure of the ELM, see Figure 1). This method randomly gives the input weight and threshold value of the neuron weight and then calculates the output weight by solving the generalized inverse (Dac and Trung, 2023). It has been proved that random selection of the node parameters of the feedforward neural network of a single hidden layer does not affect the convergence ability of the neural network, which makes the network training speed of the ELM thousands of times higher than that of the traditional network (Ma et al., 2023). Therefore, we first let SLFN have one hidden node. For the feedforward neural network with a single hidden layer, its standard model is

$$\sum_{i=1}^{\tilde{N}} g(w_i \cdot x_j + b_i)\beta_i = o_j, j = 1, 2, 3, \ldots, N, \tag{1}$$

where $w_i \cdot x_j$ is the inner product of vector $w_i$and x_j, N is the training sample, $\tilde{N}$ is the number of hidden layer units, o_j is the actual input value. $g(x)$ is the activation function. Using sigmoid function as the activation function, if let Eq. 2 is the infinite approximation at 0 with existing W, β, b:

$$\min\sum_{j=1}^{N} \| o_j - t_j \|, \tag{2}$$

$$\sum_{i=1}^{\tilde{N}} g(w_i \cdot x_j + b_i)\beta_i = t_j, j = 1, 2, 3, \ldots, N. \tag{3}$$

Eq. 3 can be written compactly as

$$H\beta = T, \tag{4}$$

where $T \in R^{N\times m}$ and $\beta \in R^{N\times m}$.

$$H = (W, b) = \left(h_{ij}\right)_{N\times\tilde{N}} \tag{5}$$

where $h_{ij} = g(w_i \cdot x_j + b_i)$, and H is the output matrix of the hidden layer of the neural network. When the number of hidden layer elements is the same as the total number of training samples, and the matrix is invertible, Eq. 4 has a unique solution. That is, Eq. 2 is satisfied. However, in many cases, when the number of hidden layer elements is far less than the total number of training samples, H is a rectangular matrix at this time and W, β, b does not necessarily exist and makes Eq. 2 hold, so it can be equivalent to finding the minimum value of Eq. 5 as the solution of Eq. 2.

$$E = \sum_{j=1}^{N} \| \sum_{i=1}^{\tilde{N}} g\left(w_i \cdot x_j + b_i\right)\beta_i - t_j \|^2. \tag{6}$$

If Eq. 5 is solved by the gradient learning method, it can be used to represent all parameters, and the iteration can be written as given in Eq. 7.

TABLE 1 **Test error in the experiments (%).**

Number	B1	B2	B1B2	Present study
1	3.96	1.85	6.83	0.59
2	4.76	0.95	1.78	0.31
3	4.73	1.20	1.61	0.50
4	4.99	1.68	4.06	0.36
5	4.74	1.39	2.53	0.67
6	4.46	1.38	2.28	0.27
7	4.73	1.98	8.17	0.59
8	4.77	1.60	1.76	0.66
9	4.65	1.44	4.18	0.51
10	4.11	1.30	6.78	0.29
Average	4.59	1.48	4.01	0.48

$$\theta_k = \theta_{k-1} - \eta\frac{\partial E(\theta)}{\partial\theta}, \tag{7}$$

where η is the learning efficiency. For feedforward neural networks, back-propagation neural networks are generally used. The neural network is a multilayer feedforward network trained according to error (You et al., 2021). The neural network includes input layer nodes, output layer nodes, and one or more hidden layer nodes. First, the input signal reaches the hidden layer node, where it passes through the excitation function and the output signal of the hidden layer node is then transmitted to the output node to finally get the output result. (Fukui and Kawakami, 1986). The learning process is that the neural network constantly changes the connection weight of its own network in the case of external input samples, so as to make the output result of the network closest to the expected output value (Xiong et al., 2018). If the output results differ greatly from the expected values, backpropagation can be carried out, and then the weights of each neuron can be modified again, and finally, a good classifier can be trained through continuous iteration. If the learning rate is too small, the learning speed is very slow. If the selection is too large, it is difficult to obtain network convergence. If Eq. 6 is a non-convex function, it is easy to fall into a local minimum by continuously iterating and adjusting parameters. Repeated iteration is not only time consuming but also easily falls into the situation of learning and fitting (Lcfcbvre, 2014).

In SLFNs, W and b are given at the beginning of the algorithm and can be arbitrarily specified. Then, H is calculated, while the value remains unchanged. In this way, only the parameter β that can be changed is left, and this shows that the given W and b do not affect the results.

When W and b are fixed, Eq. 4 is solved by replacing it with Eq. 8:

$$\| H\hat{\beta} - T \| = min \ \| H\beta - T \| . \tag{8}$$

The least squares solution can be obtained by solving the Eq. 8.

In some large-scale projects, the learning process usually uses all the data and these learning times are very long. If new samples are added at this time, they have to learn together with the original data.

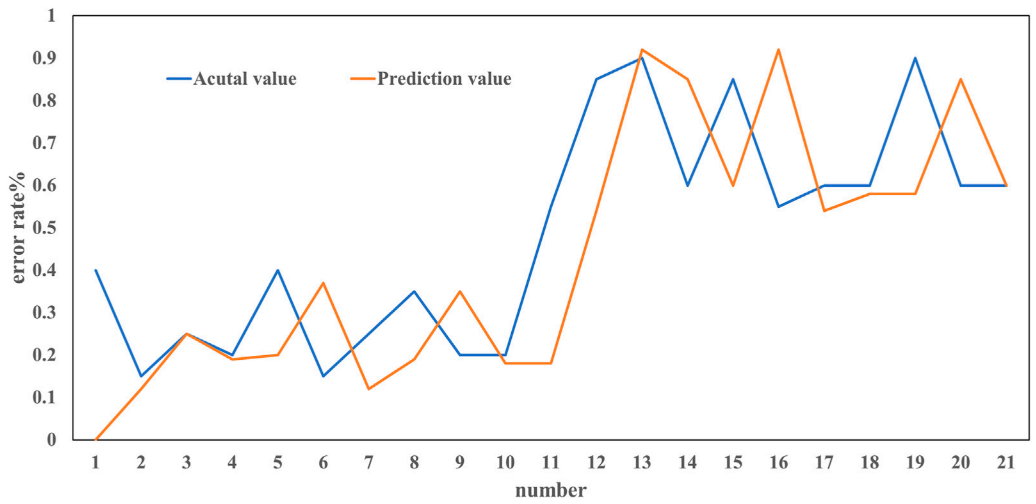

FIGURE 3
Comparison between actual values and predictive value.

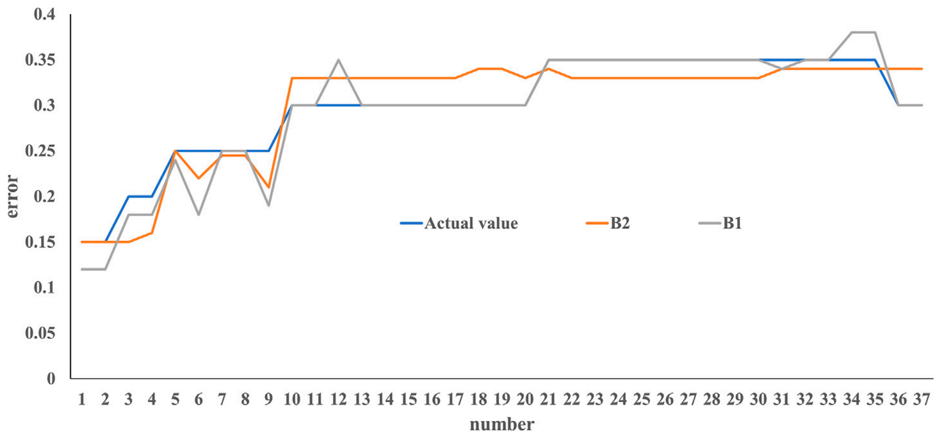

FIGURE 4
Comparison of experimental values with B1 and B2 data when fault is close to B1 end.

In this way, it is a waste of time to relearn all the data. The online sequential learning neural network (OS-LNN) does not have to learn the previous data, but only has to add the new data to the learned network. However, the OS-LNN has to set network weights, and the training speed is also very slow. Although the training is completed, the online sequential learning–extreme learning machine (OS-ELM) can not only learn data one by one but also learn them batch by batch. The least squares solution of $H\beta - T \; is \; \hat{\beta} = H^{*}T$, and we considered that $Rank\ (H) = \tilde{N}$ is the number of hidden layer units, and H^{*} is the left pseudo inverse of H, $H^{*}H = I_N$.

$$H^{*} = \left(H^{T}H\right)^{-1}H. \tag{9}$$

By substituting equation (9) into equation (8), we get

$$\hat{\beta} = \left(H^{T}H\right)^{-1}HT. \tag{10}$$

According to previous studies (Dac and Trung, 2023; Ma et al., 2023), the least square root is $\beta^{(0)} = K_0^{-1}H_0T$, where $K_0 = H_0^{T}H_0$. When adding the new data (k + 1), $N_{k+1} = \{x_i, t_i\}_{i=\left(\sum_{j=0}^{k}N_j\right)+1}^{\sum_{j=0}^{k+1}N_j}$, $k \geq 0, N_{k+1}$ is (k+1)th data, $K_{k+1} = K_k + H_{k+1}^{T}H_{k+1}$, and

$$\beta^{(k+1)} = \beta^{(k)} + K_{k+1}^{-1}H_{k+1}^{T}\left(T_{k+1} - H_{k+1}\beta^{(k)}\right). \tag{11}$$

With the help of the Sherman-Morrison-Woodbury (SMW) equation, $\beta^{(k+1)}$ can be calculated by

$$\beta^{(k+1)} = \beta^{(k)} + P_{k+1}H_{k+1}^{T}\left(T_{k+1} - H_{k+1}\beta^{(k)}\right). \tag{12}$$

where $P_{k+1} = K_{k+1}^{-1} = P_k - P_kH_{k+1}^{T}\left(I + H_{k+1}P_kH_{k+1}^{T}\right)^{-1} \times H_{k+1}P_k$.

TABLE 2 Distance interval testing error through B1 data.

Experiment	0%–33%	33%–66%	66%–100%
1	0.0021	0.0046	0.045
2	0.0027	0.0072	0.039
3	0.0021	0.0173	0.042
4	0.0002	0.0173	0.035
5	0.0006	0.0042	0.039
6	0.0017	0.0144	0.032
7	0.0007	0.0081	0.0344
8	0.0025	0.0088	0.0356
9	0.0017	0.0094	0.0401
10	0.0017	0.0103	0.0395

When the OS-ELM faces the new data, it does not have to relearn the old data, which makes it faster than the other neural network methods. When selecting the network parameters, it becomes only necessary to determine the number of neural units in the hidden layer, which also reduces the dependence on the network layers.

The whale optimization algorithm is mainly divided into three steps: surround prey, spiral bubble net attack method, and randomly search for prey.

Surround prey: because the location of the target prey is unknown *a priori*, the WOA algorithm treats the location of the best candidate in the current whale group as the location of the target prey, and the other individuals in the whale group update the location according to the location of the best candidate:

$$D = |C \cdot X^{*}(t) - X(t)|, \tag{13}$$

$$X(t+1) = X^{*}(t) - A \cdot D, \tag{14}$$

$$A = 2ar - a, \tag{15}$$

$$C = 2r, \tag{16}$$

where X is the position vector of the current solution; t is the number of iterations; A and C are coefficient vectors; X^{*} is the position vector of the optimal solution in the current whale population. a decreases linearly from 2 to 0 as the number of iterations increases; r is an arbitrary vector between 0 and 1.

Spiral bubble net attack method: the WOA algorithm first calculates the distance between the individual whale and the target prey, and then simulates the spiral movement of humpback whales for hunting behavior:

$$D' = |X^{*}(t) - X(t)|, \tag{17}$$

$$X(t+1) = D' e^{bl}\cos(2\pi l) + X^{*}(t), \tag{18}$$

where b is the constant coefficient defining the spiral shape, and l is a random number in the interval [−1, 1].

Randomly search for prey: in the process of predation, when A is greater than 1 or less than −1, the individuals in the whale group randomly select a prey with reference to each other's position to improve the global search ability of the algorithm, namely,

$$D = |CX_{rand} - X|, \tag{19}$$

$$X(t+1) = X_{rand} - AD, \tag{20}$$

where X_{rand} is a randomly selected position vector for the current whale group.

The steps for WOA to optimize the ELM are as follows:

(1) Parameter initialization. Set the WOA parameters, namely, the number of whales, maximum iterations, variable dimensions, and upper and lower limits of variables;
(2) Population initialization. Randomly initialize the position values of each dimension of all whale individuals, and the position values of each dimension of each whale individual representing the input weights or thresholds;
(3) Calculate the fitness value. Select the objective function to calculate the fitness value of each whale individual;
(4) Update the optimal solution. According to the fitness value of each whale individual, find the position of the optimal solution in all solutions and update the position of each whale individual according to the position of the optimal solution;
(5) The position of each individual whale is updated. When the probability $p < 0.5$ and $|A| < 1$, the location is updated according to Equation 16. If $|A| \geq 1$, a location vector X_{rand} is randomly selected and the location is updated according to Equation 19. when the probability $p \geq 0.5$, the location is updated through Equation 20.

3.2 Wavelet packet energy entropy extraction

The structure of the wind solar storage microgrid system is shown in Figure 2.

The internal line faults of the microgrid can be divided into single-phase ground short circuit (AG, BG, and CG), two-phase short circuit (AB, AC, and BC), two-phase ground short circuit (ABG, ACG, and BCG), three-phase short circuit (ABC), and three-phase ground short circuit (ABCG) faults.

When processing the signal, wavelet packet decomposition can decompose the low-frequency component and high-frequency component of the signal at the same time; higher the resolution, more detailed the decomposition and better the effect. The square-integrable function *f(t)* can be decomposed into a scaling function $\phi(t)$ and wavelet function $\varphi(t)$; $\phi(t)$ is low frequency of *f(t)*, $\varphi(t)$ is high frequency of *f(t)*, and their relationship includes

$$\begin{cases} \delta_{2n}(t) = \sqrt{2}\sum_{k\epsilon z} h(k)\delta_n(2t-k) \\ \delta_{2n+1}(t) = \sqrt{2}\sum_{k\epsilon z} g(k)\delta_n(2t-k) \end{cases}, \tag{21}$$

where $h(k)$ is low pass filter coefficient, and $g(k)$ is high pass filter coefficient.

When $n = 0, \delta_0(t) = \phi(t), \delta_1(t) = \varphi(t)$, the set of functions defined above $\{\delta_n(t)\}$ (n = 0,1,2,...) is determined by $\delta_0(t) = \phi(t)$ determined wavelet packet. According to the fast algorithm of orthogonal wavelet transform, the recursive formula of wavelet packet coefficients can be obtained as follows:

$$\begin{cases} \lambda_{i+1}^{2i} = \sum_{k\epsilon z} h(k-2t)\lambda_i^j(k) \\ \lambda_{i+1}^{2i+1} = \sum_{k\epsilon z} g(k-2t)\lambda_i^j(k) \end{cases}, \tag{22}$$

TABLE 3 Experimental results of SVM (%).

Number	B1+SVM	B1+RF	B1+RNN	B2+SVM	B2+RF	B2+RNN	B1B2+SVM	B1B2+RF	B1B2+RNN	Our method + SVM	Our method + RF	Our method + RNN
1	4.1	5.2	4.2	1.7	2.3	2.1	0.9	1.5	1.2	0.8	1.0	0.9
2	3.06	2.1	4.0	1.5	2.0	1.9	0.9	1.2	1.0	0.8	1.2	1.1
3	4.2	5.3	5.6	1.7	1.6	1.8	1.1	1.1	1.1	1.0	0.9	1.2
4	4.3	5.4	5.2	1.8	1.9	1.9	1.1	1.0	0.8	0.8	0.8	1.1
5	3.6	4.2	4.8	1.6	2.5	1.9	0.9	1.6	0.8	0.7	0.8	1.0
6	3.7	4.3	3.6	1.4	1.0	0.9	0.8	1.6	0.9	0.9	1.3	0.8
7	3.7	4.0	3.2	1.9	1.8	2.1	1.1	0.8	2.0	0.8	1.0	0.8
8	4.3	4.8	3.9	1.4	2.3	2.3	0.9	0.8	1.0	0.7	0.7	1.5
9	3.4	3.6	3.3	1.7	2.2	2.5	1.0	2.1	1.2	0.8	0.7	1.5
10	3.4	3.9	4.0	1.5	1.8	2.2	0.9	2.1	1.3	0.7	0.6	1.6
Average	3.9	4.3	3.8	1.6	1.9	2.0	0.9	1.4	1.1	0.8	0.9	1.2

where $\lambda_i^j(k)$ is the *kth* coefficient corresponding to the *jth* node of layer *i* after wavelet packet decomposition.

Wavelet packet energy entropy is a description of signal uncertainty, which can reflect the degree of random change of signals. When a fault occurs in the internal lines of the microgrid, because the voltage signal contains non-stationary signal components, the wavelet packet voltage reconstruction signal waveform will immediately fluctuate at the time of the fault. The wavelet packet decomposition and reconstruction technology can make accurate and rapid localization analysis of the voltage signal, which is reflected in the wavelet packet energy entropy, so the wavelet packet energy entropy can well reflect the fault characteristics of the voltage signal. According to information entropy theory, wavelet packet energy entropy can be defined as

$$WPEE = -\sum_{i=1}^{L} P\left(X_{i,j}\right) log_2\, P\left(X_{i,j}\right), \tag{23}$$

where L is the original signal length; $X_{i,\ j}$ is the *jth* decomposition signal of layer *i*; $P\ (X_{i,\ j})$ is the frequency band energy probability density, and the mathematical expression is

$$P\left(X_{i,j}\right) = \frac{E_{i,j}}{\sum_{j=1}^{2^i} E_{i,j}}, \tag{24}$$

where $E_{i,j}$ is the energy of the *jth* decomposed signal of the *ith* layer, defined as

$$E_{i,j} = \sum_{k=1}^{N} \left|\lambda_i^j(k)\right|^2, \tag{25}$$

where N is the length of the *j*th frequency band.

3.3 Data

According to Figure 2, a microgrid model that includes wind turbine (10 kW), photovoltaic cell (10 kW), and battery (10 Ah) is built in the MATLAB simulink environment. The filter inductances L_1, L_2, and L_3 are $3.6e^{-3}$ H; the filter capacitors C_1, C_2, and C_3 are $200e^{-6}$ F; the electrical loads Load1, Load2, Load3, and Load4 are 10 kVA, 10 kVA, 5 kVA, and 15 kVA, respectively; the line resistance r is 0.175 Ω/km; and the line reactance x is 0.070 Ω/km. Simulate each type of line fault at 10%, 20%, 30%, 40%, 50%, 60%, 70%, 80%, and 90% of the lines between P_1 and P_2 on the microgrid side. The db6 wavelet is selected as the wavelet base, and the simulated A-phase fault voltage is analyzed by three-layer wavelet packets to obtain 2^3 sub signals in different frequency bands, which are reordered from low frequency to high frequency. The wavelet packet signal reconstruction is carried out for each frequency band, and a total of eight wavelet packet reconstruction signals are obtained. The energy entropy of the reconstructed signal of each wavelet packet is calculated, and a set of eigenvectors are constructed from the energy entropy of eight wavelet packets. By the same processing of phase B and phase C voltage signals, a eigenvector containing 24 wavelet packet energy entropy can be obtained $X = [x_1, x_2, \ldots, x_{24}]^T$. Taking $X = [x_1, x_2, \ldots, x_{24}]^T$ as the input sample of the network, and the output sample of the network is $T = [t_1, t_2, \ldots, t_4]^T$, t_1, t_2 and t_3, respectively, representing the line status of phase A, phase B, and phase C, and t_4 representing whether the fault phase is grounded

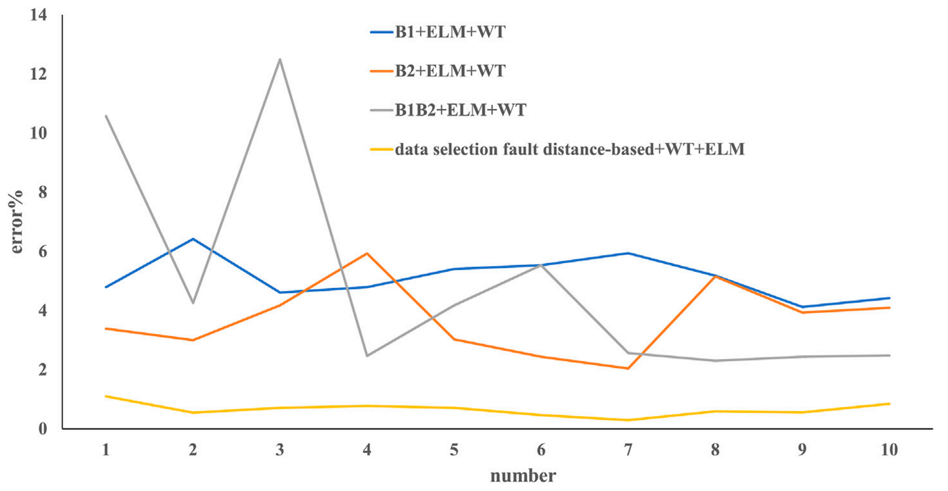

FIGURE 5
Data are located by ELM after wavelet transform.

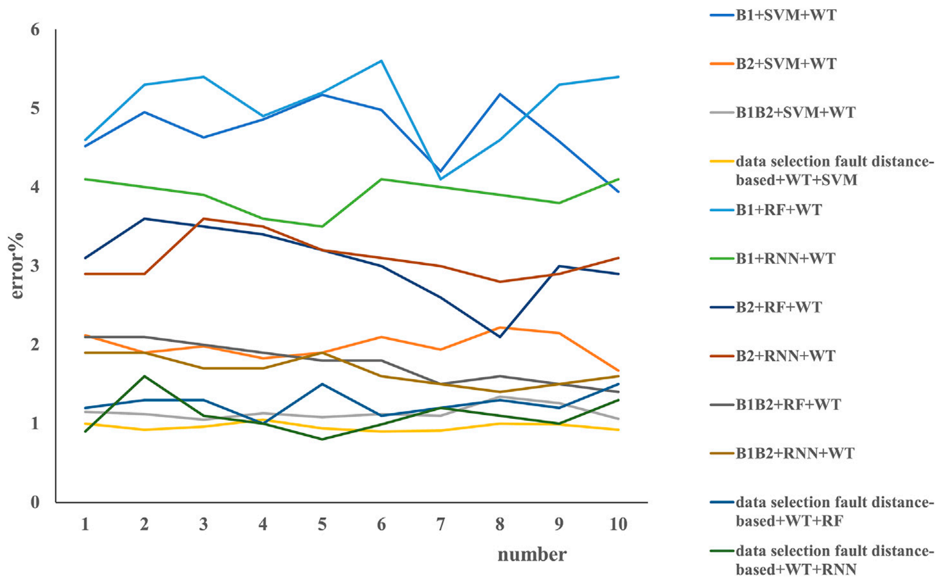

FIGURE 6
Data are located by SVM, RF, and RNN after wavelet transform.

when the line fails. When it is 0, it means there is no fault or the fault phase is not grounded at this time; when the output is 1, it means the fault phase is grounded.

The data samples at 10%, 20%, 40%, 60%, 80%, and 90% of the line positions are taken as training samples, and the data samples at 30%, 50%, and 70% are taken as test samples. The number of neurons in the input layer of ELM is 24, the number of neurons in the output layer is 4, the number of neurons in the hidden layer is determined to be 35 according to the trial and error method, the number of whales in WOA is 30, the maximum number of iterations is 200, and the variable dimension is 875.

4 Results and discussion

4.1 Fault detection based on original ELM coupled with distance selection

As shown in Table 1, the method proposed in this article is nearly twice (mean error is 0.47%) as good as the method using B2 data only (mean error is 1.48%). The performance based on B2 only is better than that based on B1 (4.58%), it should be noted that the performance using combined B1B2 data (4.0%) is the poorest among the all methods.

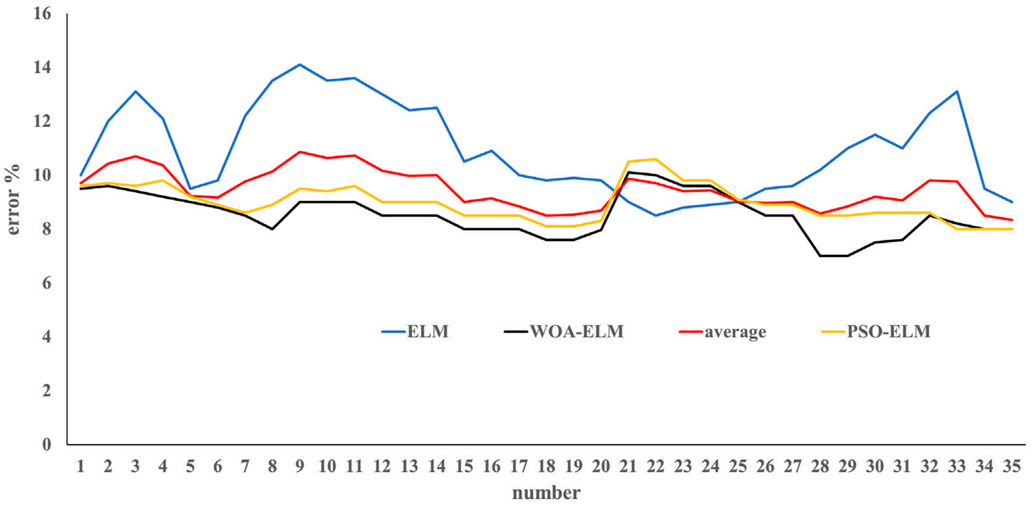

FIGURE 7
Comparative results of WOA-ELM, PSO-ELM, and traditional ELM models.

TABLE 4 Error between ELM and WOA-ELM methods in training and testing data sets.

	Training set			Testing set		
Error	ELM	WOA-ELM	PSO-ELM	ELM	WOA-ELM	PSO-ELM
MSE	6.374×10^{-6}	7.615×10^{-9}	8.96×10^{-8}	4.215×10^{-5}	8.759×10^{-8}	9.65×10^{-7}
RMSE	0.0052	0.00210	0.0039	0.0079	0.0035	0.0045
MAE	0.0096	0.0017	0.0041	0.017	0.021	0.036

We compared the results between actual and predictive in Figure 3, a total of samples of 209 are used for testing. Only 21 samples is not completely positioned accurately, that is, 10% samples have positioning errors, and the predicted values of the remaining test samples are identical to the actual values. The maximum error is that the actual value is 85% of the fault point that away from B1 and the predicted value is 92% of the fault point, with 7% error.

We did a comparative experiment, and the results are presented in Figure 4, when the B1 fault occurs, the data of B1 and B2 are used to locate the fault location. Through comparison, it can be found that the data on the B1 side should be accurate to the data on the B2 side. Table 2 divides the fault distance into three sections: 0%–33%, 33%–66%, and 66%–100%, respectively. Then, only the data of B1 is used to locate the fault, and it is found that the farther away from B1, the greater the test error. We demonstrated that it is more effective to use data close to the fault point. From the experimental results, it is shown that using the data points at the near end has better results. The farther the signal is transmitted, the greater is the resistance affected by various electrical components.

The experiment in Table 3 uses the SVM classifier, random forest (RF), and recurrent neural network (RNN) to test the method proposed in this article. Moreover, we choose to use libsvm and genetic the algorithm to optimize C and gamma parameters. The range of C is 0–1,000, the range of gamma is 0–1,000, the maximum evolutionary algebra is 200, and the maximum data of the population is 20. We can see that, in our methods, the selection of data based on the fault distance coupled with SVM can improve the accuracy of detection of fault in smart grids, with an average error of 0.86%, followed by RF with a mean error of 0.91% and B1B2-SVM with a mean error of 0.98%. Keeping the results of Figure 4 in mind when coupling with the SVM algorithm, the B1B2 method can obtain substantial accuracy with an average error of 0.98%, B1+SVM has the poorest performance with a mean error of 3.87%, B2+SVM has a moderate performance with a mean error of 1.61% (ranking of performance in Figure 4 is B2 > B1B2 > B1), which means that the artificial intelligence algorithm (SVM here) can substantially improve the detection of fault in the smart grid. the SVM can improve accuracy of fault detection more robustly than RF and RNN, for example, B1+RF has an error of 4.3%, followed by B1+RNN with 3.8%, and 1.9% and 2.0% for B2+RF and B2+RNN, respectively; 1.4% and 1.1% for B1B2+RF and B1B2+RNN, respectively. Fault distance–based data selection can substantially improve accuracy of fault detection on the basis of not only SVM but also RF and RNN, for example, 0.8%, 0.9%, and 1.2% for SVM, RF, and RNN, respectively, which means the fault distance–based data selection is useful for fault diagnoses.

TABLE 5 Error between BP and RBF methods in training and testing data sets.

	Training set		Testing set	
Error	BP	RBF	BP	RBF
MSE	9.110×10^{-4}	4.392×10^{-17}	7.889×10^{-4}	0.0321
RMSE	0.0302	2.001×10^{-9}	0.0285	0.0512
MAE	0.0181	1.401×10^{-9}	0.0190	0.021

After processing the data with Daubechies wavelet, the data output of the first layer is selected as the feature of the input classifier. The results obtained after positioning with ELM and with SVM, RF, and RNN are shown in Figures 5, 6, respectively. It can be seen that the method proposed in this article still has a good effect, with an average error of 0.66%. The method of B1+ELM after wavelet transform is the poorest with a mean error of 5.12%, followed by B1B2+ELM with of mean error of 4.93% and B2+ELM with a mean error of 3.72. Performance of the SVM, RF, and RNN methods after wavelet transform is better than that of the ELM method, and the SVM has the best performance. As we can see in Figure 6, B1+SVM, B2+SVM, or B1B2+SVM has smaller errors in fault detection, specifically, B1+SVM has the poorest performance with a mean error of 4.7%, followed by B2+SVM (1.98%), B1B2+SVM (1.14%), and our method, i.e., fault distance–based data selection + SVM (0.96%), which means that our fault distance–based method to detect faults is robust. The methods of both RF and RNN are poorer than SVM; B1+RF and B1+RNN are the poorest with a mean 5.04% and 3.9%, respectively. However, RF and RNN substantially improve the accuracy of fault detection, which is still poorer than SVM, for example, a mean error of 1.099% and 1.26% for the fault distance–based data selection + RNN and fault distance–based data selection + RF, respectively, while the mean error was 0.959% for our method, which means that improvement of SVM is robust.

4.2 Fault detection based on WOA-ELM method

In order to verify the superiority of the WOA-ELM diagnostic model and improve the recognition accuracy, the WOA-ELM diagnostic model is compared with the traditional ELM diagnostic model and optimized ELM by Quantum PSO, i.e., PSO-ELM. The results are shown in Figure 7. The error of WOA-ELM and WOA-ELM diagnostic faults are nearly 8.5% and 8.9%; separately, they are higher than the traditional ELM model with an error of 11%. We further compared the results of the three models using the mean square error (MSE), root mean square error (RMSE), and mean absolute error (MAE) (Table 4). The WOA-ELM model is largely better than the PSO-ELM and ELM models both in the training and testing data sets in fault detection. The WOA-ELM model uses WOA algorithm to optimize the input weight and hidden layer node threshold of the ELM, overcomes the shortcomings of random initialization of the input weight and hidden layer node threshold of the ELM, improves the global search ability of the network, and makes the network have better recognition accuracy.

Compared with the research results of others, the literature (Ji et al., 2022) proposes a basic network architecture design, using a simplified residual connection technology, using focal loss as the objective function for supervised training, adding a BatchNormalization layer to the network for optimization, reducing parameters based on ShuffleNet network, and improving accuracy on the basis of the attention mechanism, a process that can automatically determine the appropriate CNN architecture for fault diagnosis problems. Wang et al. (2011) proposed a new method for fault identification on the basis of parameter optimized variational mode decomposition (VMD) and convolutional neural network (CNN). Luo et al. (2014) proposed a real-time deep learning algorithm to classify and localize the faults that occurred in the system based on measured data. Luo et al. (2017) presented a method on the basis of gated graph neural network for automatic fault localization on distribution networks. The method aggregates problem data in a graph where the feeder topology is represented by the graph links and nodes attributes that can encapsulate any selected information such as operated devices, electrical characteristics, and measurements at the point. Kasun et al. (2013), Zhibin et al. (2019), and Xue and Dola (2022) proposed a multi-fault diagnosis model of distribution network on the basis of the fuzzy optimal convolutional neural network. In order to compare their results with ours, we used the RBF neural network and BP neural network to detect fault location in the smart grid and used indicators of MSE, RMSE, and MAE to evaluate accuracy; the results are provided in Table 5.

The three training errors of the WOA-ELM model are about one order of magnitude smaller than those of the BP neural network model and ELM model, while the three training errors of the RBF neural network model are 6–13 orders of magnitude smaller than those of the WOA-ELM model. The training effect of RBF neural network is the best. However, it can be seen from Table 6 that the three test errors of the WOA-ELM model are significantly smaller than those of the RBF neural network model. It shows that the RBF neural network model has a phenomenon of over-fitting, and its generalization ability is weak and cannot accurately identify the untrained fault types.

4.3 WOA-ELM performance in microgrid fault diagnoses

In substituting the data samples into the WOA-ELM fault diagnosis model for training and testing, the line fault diagnosis results of the test samples at 50% of the line position are shown in Table 6.

It can be seen from Table 6 that the absolute value of the error between the expected output and the actual output of the WOA-ELM fault diagnosis model does not exceed 0.015 at the most. The error is small, the accuracy is high, and the approximation ability is strong. It can accurately identify the fault types of microgrid lines.

In order to verify that WOA-ELM diagnostic model has better performance and higher recognition accuracy than the other models, the BP neural network, RBF neural network, and ELM were selected to establish the diagnostic models for comparative analysis. The expected output and actual output results of all training samples (72) are shown in Figure 8A. It can be seen

TABLE 6 Fault diagnosis results of test samples at 50% of line.

Types of faults	Expected output	Actual output
Normal	(0,0,0,0)	(−0.001 1, 0.008 6, −0.000 5, 0.001 1)
AG	(1,0,0,1)	(0.995 6, −0.002 5, 0.002 0, 0.987 4)
BG	(0,1,0,1)	(−0.001 0, 0.997 5, −0.002 6, 0.998 0)
CG	(0,0,1,1)	(−0.002 1, 0.001 5, 0.998 3, 0.996 5)
AB	(1,1,0,0)	(1.004 2, 0.995 7, 0.002 3, 0.009 1)
AC	(1,0,1,0)	(1.002 5, −0.007 9, 0.995 7, 0.002 3)
BC	(0,1,1,0)	(0.001 7, 0.988 4, 0.993 8, −0.003 6)
ABG	(1,1,0,1)	(1.000 2, 0.995 9, −0.010 7, 0.989 4)
ACG	(1,0,1,1)	(1.004 6, 0.000 4, 0.992 4, 1.001 3)
BCG	(0,1,1,1)	(−0.006 6, 0.994 9, 1.010 3, 1.004 8)
ABC	(1,1,1,0)	(1.004 8, 1.004 5, 0.999 1, 0.000 1)
ABCG	(1,1,1,1)	(1.014 8, 1.012 5, 0.994 2, 1.004 4)

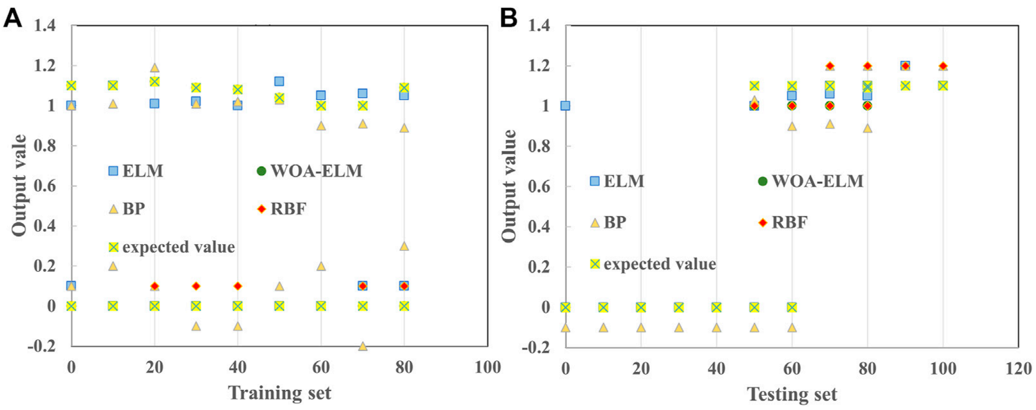

FIGURE 8
Desired output and actual output of 72 training samples **(A)** and testing samples **(B)**.

from Figure 8A that the training error of the BP neural network model is large; the training results of the other three models can well approximate the expected output; the error between the actual value and expected value is small; and the training accuracy is high.

The expected output and actual output results of all test samples (36) are shown in Figure 8B. It can be seen from Figure 8B that the test results of the BP neural network model, RBF neural network model, and the non-optimized ELM model have large errors, while the test accuracy of the WOA-ELM model is the highest.

5 Conclusion

In this article, a microgrid fault diagnosis method based on the whale algorithm optimization limit learning machine was proposed. The whale algorithm has the characteristics of fast convergence speed and strong global optimization ability. It optimizes the input weights and hidden layer neuron threshold of the ELM, effectively avoids the shortage of random initialization of network input weights and hidden layer threshold, enhances the approximation ability of the model, and significantly improves the recognition accuracy of the network. The results show that the selection of data based on the fault distance is twice as effective as the useless real data. The ELM method was proved to have a good location result by using the support vector machine classifier and wavelet transform to process the signal. After the ELM is improved by the WOA algorithm, the accuracy of fault detection is improved by nearly 22.5%. The simulation results show that the WOA-ELM model has a higher recognition accuracy than the BP neural network model, RBF neural network model, and ELM model and can more accurately identify the fault types of internal lines in the microgrid, which verifies the effectiveness and reliability of the WOA-ELM model.

The power system simulated in this article may be different from the complex power grid in reality. The actual power system wires are more complex, and the accuracy of the detection data may not be as high. Now, the method proposed in this article is to choose which end of the data to use on the basis of the distance. In fact, in the power system model, the information of the power components on both sides is not equal, which leads to a worse situation when using only the B1 end data than when using only the B2 end data. In this article, we use distance 1:1 to select data. Next, we can select data at B1 or B2 on the basis of a certain proportion, such that the effect of adding distance to power components is equivalent to 1:1. In fault location, many articles use wavelet transform to analyze because when a fault just occurs, the power system will produce transient signals, which is also one of the directions of future research. How to select data for fault location? Is it a half cycle or one cycle after fault? How long to choose is also something that can be further studied in the future.

Data availability statement

The original contributions presented in the study are included in the article/Supplementary Material; further inquiries can be directed to the corresponding author.

Author contributions

Conceptualization: FX and YL; methodology: YL; software: FX; validation: FX and YL; formal analysis: LW; investigation: LW; resources: FX; data curation: LW; writing—original draft preparation: FX; writing—review and editing: YL; visualization: FX; supervision: FX; project administration: YL; funding acquisition: YL; all authors have read and agreed to the published version of the manuscript.

Acknowledgments

The authors of the present study thank the reviewers for their contribution in improving the study.

Conflict of interest

Author FX was employed by State Grid Yantai Fushan Power Supply Company.

The remaining authors declare that the research was conducted in the absence of any commercial or financial relationships that could be construed as a potential conflict of interest.

Publisher's note

References

Ayushi, C., Preeti, G., Singh, G. N., and Moy, C. J. (2022). Performance analysis of an optimized ANN model to predict the stability of smart grid. *Complexity* 2022, 1–13. doi:10.1155/2022/7319010

Chang, N., Song, G., Hou, J., and Chang, Z. (2023). Fault identification method based on unified inverse-time characteristic equation for distribution network. *Int. J. Electr. Power Energy Syst.* 20, 213–223. doi:10.1016/J.IJEPES.2022.108734

Chen, B., Yu, L., Luo, W., Wu, C., Li, M., Tan, H., et al. (2022). Hybrid tree model for root cause analysis of wireless network fault localization. *Web Intell.* 20 (3), 213–223. doi:10.3233/web-220016

Chen, L., Jiang, Y., Deng, X., Chen, H., and Zheng, S. (2022). A novel fault recovery method of active distribution networks oriented to improving resilience. *Energy Rep.* 8 (S15), 456–466. doi:10.1016/j.egyr.2022.10.152

Dac, Q. H., and Trung, H. H. (2023). Solving partial differential equation based on extreme learning machine. *Math. Comput. Simul.* 205, 697–708. doi:10.1016/j.matcom.2022.10.018

Fang, J., Wang, H., Yang, F., Yin, K., Lin, X., and Zhang, M. (2022). A failure prediction method of power distribution network based on PSO and XGBoost. *Aust. J. Electr. Electron. Eng.* 19 (4), 371–378. doi:10.1080/1448837x.2022.2072447

Fukui, C., and Kawakami, J. (1986). An expert system for fault section estimation using information from protective relays and circuit breakers information from protective relays and circuit breakers. *IEEE Trans. Power Deliv.* PER-6 (04), 83–90. doi:10.1109/tpwrd.1986.4308033

Hou, S., Xu, Y., and Guo, W. (2022). Distribution network fault-line selection method based on MICEEMDAN–recurrence plot–yolov5. *Processes* 10 (10), 2127. doi:10.3390/pr10102127

Ji, Q., Hu, Z., and Liu, X. (2022). Fault Diagnosis algorithms of distribution network based on convolutional neural network. *J. Phys. Conf. Ser.* 2301 (1), 012009. doi:10.1088/1742-6596/2301/1/012009

Jia, Y., Liu, Y., Wang, B., Lu, D., and Lin, Y. (2022). Power network fault location with exact distributed parameter line model and sparse estimation. *Electr. Power Syst. Res.* 212, 108137. doi:10.1016/j.epsr.2022.108137

Kasun, L. L. C., Zhou, H., Huang, G., and Vong, C.-M. (2013). Representational learning with extreme learning machine for big data. *IEEE Intell. Syst.* 28 (06), 31–34.

Lcfcbvre, D. (2014). On-line Fault Diagnosis with partially observed Petri ncts. *IEEE Transaction Automatic Control* 59 (07), 1919–1924. doi:10.1504/IJISE.2018.10016217

Lei, J., Guo, Y., Luo, D., Xu, Z., and Wang, R. (2022). Fault Location of distribution network based on multi-population particle swarm optimization algorithm. *J. Phy. Conf. Ser.* 2360 (1), 012024. doi:10.1088/1742-6596/2360/1/012024

Li, Z., Qiao, J., Wang, Y., and Yin, X. (2022). A faulty section location method for distribution grid based on grounding fault transfer device. *Energy Rep.* 8 (S8), 81–89. doi:10.1016/j.egyr.2022.09.088

Liu, Y., Zhang, S., Li, L., Wang, S., Lu, T., Yu, H., et al. (2022). A machine learning-based fault identification method for microgrids with distributed generations. *J. Phy. Conf. Ser.* 2360 (1), 012019. doi:10.1088/1742-6596/2360/1/012019

Luo, J., Vong, C. M., and Wong, P. K. (2017). Sparse bayesian extreme learning machine for multiclassification. *IEEE Trans. Neural Netw. Learn. Syst.* 25 (04), 836–843. doi:10.1109/TNNLS.2013.2281839

Luo, Y., Ling, S., and Cao, Y. (2014). Fault diagnosis of electric power grid based on improved RBF neural network. *TELKOMNIKA Indonesian J. Electr. Eng.* 12 (09), 4777–4784. doi:10.11591/telkomnika.v12i9.4642

Ma, T., Hu, Z., Xu, Y., and Dong, H. (2022). fault location based on comprehensive grey correlation degree analysis for flexible DC distribution network. *Energies* 15 (20), 7820. doi:10.3390/en15207820

Ma, Z., Wang, X., and Hao, Y. (2023). Development and application of a hybrid forecasting framework based on improved extreme learning machine for enterprise financing risk. *Expert Syst. Appl.* 215, 119373. doi:10.1016/j.eswa.2022.119373

Shafiullah, M., AlShumayri Khalid, A., and Alam, M. S. (2022). Machine learning tools for active distribution grid fault diagnosis. *Adv. Eng. Softw.* 173, 2022. doi:10.1016/J.ADVENGSOFT.2022.103279

Singhal, D., Ahuja, L., and Seth, A. (2022). An insight into combating security attacks for smart grid. *Int. J. Perform. Eng.* 18 (7), 512. doi:10.23940/ijpe.22.07.p6.512520

Waldrigues, B. N., Matos, C. M. S., Frizzo, S. S., and Quietinho, L. V. R. (2022). Wavelet LSTM for fault forecasting in electrical power grids. *Sensors* 22 (21), 8323. doi:10.3390/s22218323

Wang, J., Zhou, L., Hong, H., and Zhang, G. X. (2011). An extended spiking neural P system for fuzzy knowledge representation. *Int. J. Innovative Comput. Inf. Control* 7 (7A), 3709–3724. doi:10.1049/iet-cta.2010.0325

Wang, N. (2022). Fault line selection of power distribution system via improved bee colony algorithm based deep neural network. *Energy Rep.* 8 (S12), 43–53. doi:10.1016/j.egyr.2022.10.070

Xin, C. (2022). Research on high-frequency information-transmission method of smart grid based on CNN-LSTM model. *Information* 13 (8), 375. doi:10.3390/info13080375

Xiong, G., Shi, D., and Zhang, J. (2018). A binary coded brain storm optimization for fault section diagnosis of power systems for fault section diagnosis of power systems. *Electr. Power Syst. Res.* 163 (01), 441–451. doi:10.1016/j.epsr.2018.07.009

Xue, W., and Dola, S. (2022). "KNEW: Key generation using NEural networks from wireless channels," in Proceedings of the 2022 ACM Workshop on Wireless Security and Machine Learning (WiseML '22) (New York, NY, USA: Association for Computing Machinery), 45–50.

Yan, X., Liu, R., Tu, N., and Xing, J. (2022). Research on fault location of distribution network with DG based on HHO. *Sci. Discov.* 10 (5). doi:10.11648/J.SD.20221005.19

You, B., Qi, H., Ding, L., Li, S., Huang, L., Tian, L., et al. (2021). Fast neural network control of a pseudo-driven wheel on deformable terrain. *Mech. Syst. Signal Process.* 152, 107478. doi:10.1016/j.ymssp.2020.107478

Yuvaraja, T., Irina, K., Hariprasath, M., Ramya, K., Ravi, A., and Ramesh, T. A. (2022). Diminution of smart grid with renewable sources using support vector machines for identification of regression losses in large-scale systems. *Wirel. Commun. Mob. Comput.* 2022, 1–11. doi:10.1155/2022/6942029

Zhang, X., Ding, R., Wang, Z., Guo, Z., Liu, B., and Wei, J. (2023). Power grid fault diagnosis model based on the time series density distribution of warning information. *Int. J. Electr. Power Energy Syst.*, 146. doi:10.1016/J.IJEPES.2022.108774

Zhibin, Z., Liping, S., and Xuan, C. (2019). Labeled box-particle CPHD filter for multiple extended targets tracking. *J. Syst. Eng. Electron.* 30 (1), 57–67. doi:10.21629/JSEE.2019.01.06

frontiers | Frontiers in Energy Research

TYPE Original Research
PUBLISHED 20 February 2023
DOI 10.3389/fenrg.2023.1140685

OPEN ACCESS

EDITED BY
Xin Ning,
Institute of Semiconductors (CAS), China

REVIEWED BY
Yassine Himeur,
Qatar University, Qatar
Bing Yan,
Rochester Institute of Technology,
United States
Wang Wei,
Chiba University, Japan

*CORRESPONDENCE
Min Xia,
✉ xiamin@nuist.edu.cn

SPECIALTY SECTION
This article was submitted to Smart Grids, a section of the journal Frontiers in Energy Research

RECEIVED 09 January 2023
ACCEPTED 08 February 2023
PUBLISHED 20 February 2023

CITATION
Yu F, Wang Z, Zhang X and Xia M (2023), DRA-net: A new deep learning framwork for non-intrusive load disaggregation. *Front. Energy Res.* 11:1140685.
doi: 10.3389/fenrg.2023.1140685

DRA-net: A new deep learning framwork for non-intrusive load disaggregation

Fang Yu[1], Zhihua Wang[2], Xiaodong Zhang[3] and Min Xia[3]*

[1]China Electric Power Research Institute, Nanjing, China, [2]State Grid Shanghai Municipal Electric Power Company, Shanghai, China, [3]Jiangsu Key Laboratory of Big Data Analysis Technology, Nanjing University of Information Science and Technology, Nanjing, China

The non-intrusive load decomposition method helps users understand the current situation of electricity consumption and reduce energy consumption. Traditional methods based on deep learning are difficult to identify low usage appliances, and are prone to model degradation leading to insufficient classification capacity. To solve this problem, this paper proposes a dilated residual aggregation network to achieve non-intrusive load decomposition. First, the original power data is processed by difference to enhance the data expression ability. Secondly, the residual structure and dilated convolution are combined to realize the cross layer transmission of load characteristic information, and capture more long sequence content. Then, the feature enhancement module is proposed to recalibrate the local feature mapping, so as to enhance the learning ability of its own network for subtle features. Compared to traditional network models, the null-residual aggregated convolutional network model has the advantages of strong learning capability for fine load features and good generalisation performance, improving the accuracy of load decomposition. The experimental results on several datasets show that the network model has good generalization performance and improves the recognition accuracy of low usage appliances.

KEYWORDS

non-intrusive, load disaggregation, deep learning, feature extraction, energy efficiency, residential electricity

1 Introduction

With the development trend of smart grid, the traditional intrusive load monitoring method has many problems, such as high construction cost and difficult application, which makes the non-invasive load monitoring method a unique way to solve these problems. Non-intrusive load decomposition can help power companies more easily obtain the power consumption of users and understand the power consumption of various electrical appliances. Non-intrusive load decomposition can more accurately predict the distribution of residential power consumption and the total amount of residential load by providing the power consumption of each electrical appliance of users, reduce planning investment, save budget, and avoid unnecessary waste of power resources. It is also conducive to the scientific formulation of relevant policies for dynamic demand response by power companies, the adjustment of electricity prices, the evaluation of relevant projects and the more reasonable allocation of power resources, and the formation of a more benign and friendly interaction between users and power companies, so as to achieve the results of peak shaving and valley filling, mutual benefit and win-win results. On the other hand, if a family can know more details about electricity consumption, it will consciously reduce energy waste. For example, most American and British families install smart meters in their homes to facilitate users to learn about the low peak electricity price information in time, promote users to use electricity at night or at low prices, alleviate the pressure of peak electricity consumption, avoid power loss, and indirectly improve the economic benefits of power sources (Zhao et al., 2019). In 1992, Hart proposed non-invasive load monitoring (NILM). Its essence is non-invasive load decomposition NILD (Hart, 1992), that is, the total energy consumption is decomposed into a single device to analyze the electricity consumption behavior of residential users. This provides effective feedback on residential electricity consumption, helping users save energy and reduce electricity charges (Paterakis et al., 2017). Hart's method is mainly to extract steady-state features for power decomposition. Based on Hart's algorithm, a simple non-invasive charge load monitoring system can be designed. However, this algorithm can only be used for a small number of electrical appliances, and the number of types of features extracted is small. When there are many types and numbers of electrical appliances, the decomposition accuracy of this algorithm decreases significantly (Dash and Sahoo, 2022).

In view of the problems in the above non-invasive load decomposition, Inagaki et al. (2011) and others used the integer programming method to monitor the load of household power equipment, but it is only applicable to equipment in discrete operation mode. Kolter et al. (2010) studied sparse coding algorithm to improve decomposition performance, but this method is only applicable to data sets containing low resolution data types. Lin Y. and Tsai (2014) and Chang et al. (2013) used particle swarm optimization algorithm to carry out non-invasive charge load decomposition experiments for a small number of several electrical appliances. This algorithm can decompose the total power data to each electrical equipment at the same time, but the error of the decomposition results is still large. The optimization method is based on load characteristic analysis. First, the static and dynamic characteristics of the load should be modeled. The total load curve is the superposition of multiple loads. The objective of optimization is to obtain the optimal load coefficient (i.e., the contribution of each load), so as to minimize the residual between the superimposed total load and the actual load. Piga et al. (2016) proposed a sparse optimization algorithm for non-invasive charge load decomposition, which reduced the decomposition error to a certain extent. Ahmadi and Marti (2015) proposed a non-invasive charge load decomposition experiment based on feature matching (also called load information matching), which effectively solved the problem of high similarity between load features. Johnson and Willsky (2013); Luan et al. (2022); Xia et al. (2021) used the Hidden Markov Model to perform non-invasive charge load decomposition. Similar to the combination optimization algorithm, these algorithms first obtain the state power of electrical appliances through clustering. Its encoding and decoding process is the process of optimizing the power values obtained by these clustering, and the decomposition results are also the combination of power values obtained by clustering, which cannot obtain more accurate electrical power consumption values (Himeur et al., 2020a; Fan et al., 2021). Compared with hidden Markov algorithm, Tsai and Lin (2012) proposed a method achieves more accurate non-invasive load decomposition through K-nearest neighbor regression algorithm. However, when the power consumption difference between appliances is large, this algorithm cannot achieve accurate decomposition. Other researches, such as algorithms based on Adaboost algorithm (Hassan et al., 2014), 2D phase encoding algorithm (Himeur et al., 2020b; Himeur et al., 2021a), fuzzy algorithm (Lin Y. H and Tsai, 2014), bagging tree algorithm (Himeur et al., 2020c), histogramming descriptor algorithm (Himeur et al., 2021b) and neural network algorithm, have made certain achievements in non-invasive charge load decomposition tasks. For the machine learning model, non-intrusive load decomposition is to take the total power time series data as the input, take the power data of each electrical appliance as the output (fitting method) or take the electrical appliance category as the output (classification). These two tasks are consistent in nature, although it is more difficult to take the power data of each electrical appliance as the output. For machine learning methods, a large number of sample data are needed for training. Non-intrusive load decomposition based on machine learning is to fit the machine learning model through training of a large number of samples, so as to obtain the power distribution of various loads under different total power conditions, which has no essential difference from traditional machine learning fitting and classification. For 1/60 Hz sampling data, it can meet the needs of non-intrusive load decomposition very well. In Lin's work, the fuzzy C-means algorithm based on particle swarm optimization is combined with the fuzzy neural algorithm for non-invasive charge load decomposition experiments. This algorithm can identify the state of an electrical appliance at a certain time, and also solve the problem of high similarity between the power consumption characteristics of electrical appliances. Park et al. (2019) proposed an equipment status recognition algorithm based on neural network, which is simple and fast in decomposition. Welikala et al. (2019) proposed a NILD method, which combines the application usage patterns (AUPs) of equipment to improve the state recognition performance of high-frequency appliances. Himeur et al. (2021c) proposed a histogram post-processing of 2D local binary patterns for smart grid applications. Guo et al. (2021) proposed a multi-model combination model for non-intrusive load disaggregation, which It can integrate the advantages of various methods and improve the accuracy of decomposition. The traditional methods mainly use artificial features to realize the identification of electrical appliances by optimizing methods, but it is difficult to extract effective artificial features. The algorithm is highly sensitive to noise and has low decomposition accuracy.

Traditional load feature extraction needs manual design, so it is difficult to extract effective features, and it is difficult to analyze the features of time series. Recently, deep learning technology has been widely used in various fields (Qu et al., 2021; Chen et al., 2022; Gao et al., 2022; Song et al., 2023). The application of deep learning in non-invasive load decomposition has gradually attracted researchers' attention. So far, there are a large number of load record data for model training. For model training, we need to record the power data of a household user and each load. At present, there are many data sets, such as UK-DALE public data set and WikiEnergy data set, which provides a data basis for the application of deep learning. Different from traditional pattern recognition, deep learning can automatically extract features without manual extraction. In Kelly's experiment (Kelly and Knottenbelt, 2015), it is proved that AutoEncoder method has the best effect in sequence pair sequence method. Singh and Majumdar (2018), Singh and Majumdar (2019) proposed deep sparse coding for non-intrusive load monitoring, improved decomposition efficiency. Xia et al. (2019) constructed a deep dilated residual network for load feature extraction, it can improve feature utilization. Jia et al. (2021) used bidirectional dilated residual network to realize the sequence to point non-intrusive load decomposition. At present, there are two main load decomposition methods: sequence to sequence and sequence to point. Sequence-to-sequence refers to the direct decomposition of the input sequence into different load sequences. Instead of training a network to predict a window, the sequence to point method is only to predict the midpoint element of input window. The idea is that the input of the network is a mains window, the output is the power at one point of various electrical devices. Zhang et al. (2016) realized sequence to sequence and sequence to point non-invasive charge load decomposition using convolutional neural network. In Zhang's experiment, sequence to point decomposition method has achieved good results in the decomposition of most electrical equipment. Compared with other deep learning methods, convolutional neural network has been proved to be more effective in the application of non-invasive load decomposition. However, Zhang's experiment uses a relatively shallow convolutional neural network, which is prone to the phenomenon of gradient disappearance, and cannot extract the deep level charge load characteristics. It is difficult to capture the relationship between long time series data. Xia et al. (2020) constructed a deep LSTM model to realize the decomposition of sequences into multiple sequences, and improved the decomposition accuracy through depth feature extraction. However, the current deep learning model is prone to model degradation and other problems, resulting in insufficient fitting ability. In addition, because it is difficult to extract the features of low usage appliances, the weight of low usage appliances in deep learning training is too small. Therefore, the existing deep learning model has poor decomposition effect on low utilization rate appliances.

To solve above problem, a dilated-residual aggregation network (DRA-Net) is constructed and applied to non-invasive load disaggregation. The network model increases the receptive field of convolution kernel through hole convolution to capture more features. In addition, a feature enhancement module is proposed to improve the learning ability of the model to fine load features, and further improve the generalization performance of non-invasive load decomposition. In conclusion, our contributions are as follows: 1) The differential processing of raw power data enhances the ability of data expression. 2) A structure combining residual structure and dilated convolution is proposed to realize cross-layer transmission of load characteristic information and capture more long sequence content. 3) A feature enhancement module is proposed to recalibrate the local feature mapping to enhance the learning ability of network for fine features.

2 Dilated-residual aggregation convolutional neural network

Since different load devices in residential houses have different electrical characteristics and some other influencing factors such as interference noise, this work realizes the optimization and improvement of the common convolutional network structure, and proposes a new network model, Dilated-residual Aggregation Convolutional Neural Network (DRAnet) to realize Non-intrusive power load disaggregation, whose overall structure is shown in **Figure 1**.

As shown in **Figure 1**, the network model includes the ordinary convolutional layer, the Dilated Resblock, Feature Enhancement Module (FEM), Information Fusion Module (IFM), and Fully Connected Layer (FC). There are a total of three void residual modules, namely, Dilated Resblock1, Dilated Resblock2, and Dilated Resblock3. There are a total of three feature enhancement modules, namely, FEM1, FEM2, and FEM3. The total load power is differentially processed and then recombined with the original data as the input side, which enriches the edge information of residential power data. The convolutional layer of the Dilated-residual Aggregation Convolutional Neural Network enhances the extraction of load features of different residential electrical devices by combining multiple convolutional kernels to retain the basic load characteristic information. The initial convolutional layer for load disaggregation feature mapping is followed by three void residual modules. The non-intrusive power load disaggregation

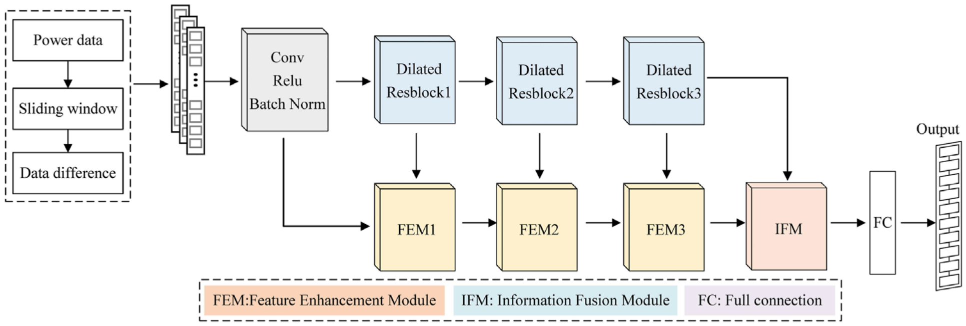

FIGURE 1
Structure of the dilated-residual aggregation convolutional neural network.

task enhances the model's ability to fit the load features without increasing the number of parameters through these three cavity residual modules. At the same time, it ensures that the signal passed layer by layer in the network will not be lost when back propagation is performed. The dilated residual module is based on the idea of "cross-layer connection" and uses the residual connection to further extract features from the low-order load features Hu et al. (2022). The higher-order residential load feature mapping contains more abstract load characteristics and timing information.

To enhance the disaggregation performance of the network for load, a feature enhancement module is proposed to process the output mapping of different stages in the network to obtain the attention weight matrix. This matrix is multiplied and summed with the corresponding vectors with the output of the dilated residual module. This module facilitates the integration and strengthening of the base load characteristics extracted by the first three void residual modules, and fully utilizes the load characteristics and timing information of each network stage, which makes the fitting ability of the whole network structure enhanced, especially for the load devices with low usage frequency like washing machines and dishwashers, and has a great disaggregation improvement effect. The output dilated residual convolutional feature mapping and the feature-enhanced load feature mapping both contain a large amount of different higher-order load information. Using the dimensional splicing in the information fusion module and conventional convolutional operation processing, these two parts are then integrated, and finally the power prediction results of the electrical equipment are output by the full-connected operation. Dilated-residual Aggregation Convolutional Neural Network constructed in this section is mainly designed to make up for the defects of insufficient utilization of residential load characteristics, poor disaggregation of low-use appliances and disappearance of gradients, reflecting the more excellent feature extraction capability and learning ability of the dilated residual aggregation convolutional network.

2.1 Dilated resblock

The dilated convolution uses the parameter Dilated Factor (DF) to adjust the size of the dilated convolution (Miao et al., 2022). Since loads like washing machines and dishwashers are used less frequently and have sparse temporal features, the proposed dilated convolution allows resampling of the underlying load feature mapping. Pooling and down-sampling operations cause the loss of temporal information of the load, while the advantage of the dilated convolution is that it can both replace the pooling effect and increase the field of sensation exponentially (field of sensation refers to the corresponding size of the convolution kernel, that is, the range of the convolution for the load series.), allowing each convolution output to capture a larger range of feature information, which has a good feature extraction effect for load appliances like washing machines without adding extra redundant number of parameters.

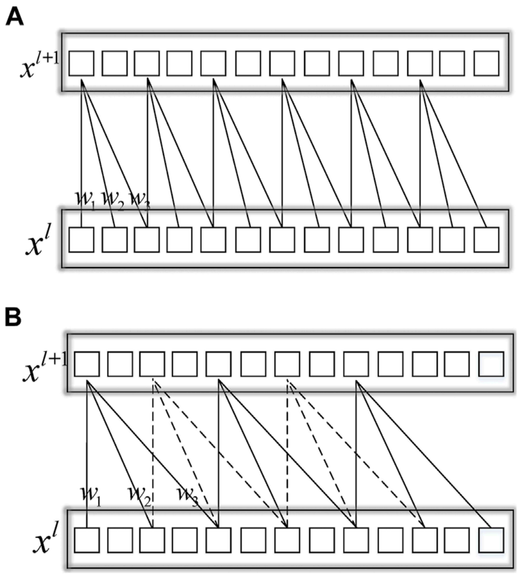

FIGURE 2
Comparison of ordinary convolution and dilated convolution. **(A)** Normal convolution. **(B)** Dilated convolution.

The dilated convolution kernel in the Dilated-residual Aggregation Convolutional Neural Network is shown in **Figure 2B**. **Figure 2A** shows the ordinary convolutional kernel convolution, where x_l and x_{l+1} are the input and output of $l+1$ layer respectively. Assuming that the convolutional kernel size *kernel* is a and the step *stride* is 1, when the hole rate d is 1, i.e., the number of filled "0" weights is 0. From the calculation of Eq. 1, we can see that the mapping range length of layer $l+1$ (L_{l+1}) and layer l (L_l) is the same.

$$L_{l+1} = \frac{[L_l + 2 \times padding - kernel - (kernel - 1) \times (d - 1)]}{stride} + 1, \quad (1)$$

where *padding* is the number of padding zeros. The dilated rate d is 2 in **Figure 2B**, and the perceptual field is expanded to 5×1. So, the advantage of the dilated convolution lies in the ability to increase the local receptive field during the convolution operation and capture more information about the load characteristics without introducing additional parameters. For load feature extraction, dilated convolution can control the receptive field without changing the size of the feature map, so as to extract multi-scale information and effectively improve the accuracy of load decomposition. The combination of the three-layer dilated convolution and the residual connection constitutes a dilated residual module, as shown in **Figure 3**.

The feature mapping is performed sequentially using the dilated convolution kernel with convolution of the dilated rate of 1, 2, and 3, including Leaky-Relu (Leaky ReLU is the commonly used activation function of convolution neural network at present), Batch Normalization (Similar to common data standardization, it is a way to unify scattered data and a common method to optimize neural network at present.), and other operations for processing, and the reason why Relu is not used as a non-linear activation function is that when the input value of the convolution layer is negative, the learning speed of Relu will be slow (Wang et al., 2022), even deactivating the neurons and preventing them from updating weights, resulting in the disappearance of the network gradient. Leaky-Relu activation function can correct the distribution of load data and retain the negative values in the gradient calculation process (Lu et al., 2022), which indirectly improves the

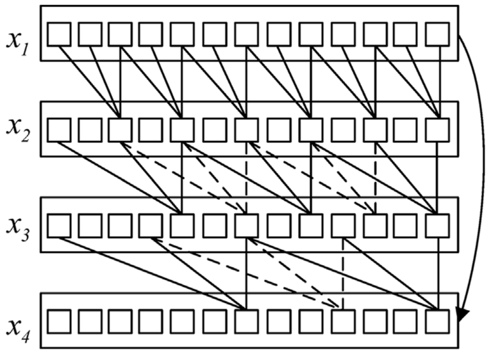

FIGURE 3
Structure of dilated resblock.

retention of power load timing information in the network. The residual connection also solves the problem of network degradation caused by the gradual disappearance of information in the reverse transmission of network layers, so the dilated residual module enhances the fitting ability of the network itself to the load samples and improves the disaggregation accuracy of the model.

2.2 Feature enhancement module

The structure of the feature enhancement module proposed in this work is shown in Figure 4. The two input mappings of the internal structure of the null residual aggregated convolutional network are used as the input side of the feature reinforcement module, which are feature map1 and feature map2. Where feature map1 is the output feature map of the current null residual module, while feature map2 is the output feature map of the previous stage. As known from Figure 4, there are two optimization branches of the feature reinforcement module, the first branch includes operations such as Convolution, GlobalAvgPooling (GAP), FC, Sigmoid, Reshape, etc. The second branch contains operations such as tensor multiplication of feature maps, i.e., feature rescaling. Feature map1 and feature map2 are processed by the feature reinforcement module to obtain the output mapping feature map3.

The specific process of the enhancement module in loading information is shown in Figure 5. In Figure 5, feature map2 is the previous stage feature mapping, so it is not consistent with the dimensionality of the output mapping feature map1 of the null residual module, and the dimensionality of feature map2 is C. The number of convolution kernels of the convolution is 1×1×C. The convolution operation of this 1×1 convolution makes the two dimensions consistent, which is convenient for subsequent processing. The weight vector1 (weight vector1 in the figure) is obtained after the GlobalAvgPooling layer operation, which compresses the pre-multi-dimensional load feature map to a one-dimensional feature map. Weight vector1 is essentially a one-dimensional vector containing low-order load feature information, which characterizes the global information on the feature layer, and its dimension is 1×C. weight vector1 is then processed by FC layer, Relu non-linear activation function to obtain weight vector2 (weight vector2 in the figure), weight vector2 is a high-dimensional vector of higher-order global features obtained on the basis of weight vector1, whose dimension is also 1×C. Through this series of operations, the weight vector2 further represents the change in dimensional response of residential housing load characteristics as described as follows:

$$W_1 = GAP(conv(F_1)), \tag{2}$$

$$W_2 = FC(Relu(W_1)), \tag{3}$$

Where $F1$ is the feature mapping of feature map1, $GAP(\cdot)$ is global average pooling, $FC(\cdot)$ is fully connection. W_1 and W_2 is the weight vector 1 and weight vector 2, respectively.

Sigmoid non-linear activation processing is similar to a gated filtering mechanism to achieve a filtering function on load information. Sigmoid processes each feature of the weight vector2 to generate a different weight variable. When the load feature of a channel is more effective, its corresponding weight variable is closer to 1; when the load feature of a channel is invalid, its corresponding weight variable is closer to 0. In this way the feature reinforcement module filters the useless information effectively. Then after Reshape operation to complete the dimensional change, the weight vector2 processed by the above operation is multiplied with feature map2 to complete the feature rescaling of feature map2, and finally the reinforced output mapping feature map3 is obtained, the specific calculation is as Eq. 4.

$$F_3 = F_2 \cdot Sigmoid(W_2), \tag{4}$$

Where F_3 is the feature mapping of feature map3, $Sigmoid(\cdot)$ is the Sigmoid fuction. The main role of the feature enhancement module is to integrate and optimize the features of the output mapping feature map1 of the dilated residual module and the output load feature mapping feature map2 of the previous part to complete the rescaling of the weights. This module makes use of the feature maps obtained at different stages of the network model, thus enabling the discrimination of the importance of the load features. The feature reinforcement module of the null residual aggregated convolutional network learns the dependencies of load timing information through the weight vector weight vector1 and weight vector weight vector2 and learns the importance of each load feature in the network accurately. Feature mappings that are favorable to the load decomposition task are given biased weight vectors, which serve to improve the decomposition accuracy, and conversely are given biased weight vectors that are small, which suppress irrelevant load features and achieve filtering of invalid information.

In summary, the null residual aggregated convolutional network model improves the decomposition accuracy of low-use appliances by completing the rescaling operation of load features through the feature reinforcement module.

2.3 Information fusion module

The structure of the information fusion module proposed in this work is shown in Figure 6. In total, it is composed of Add

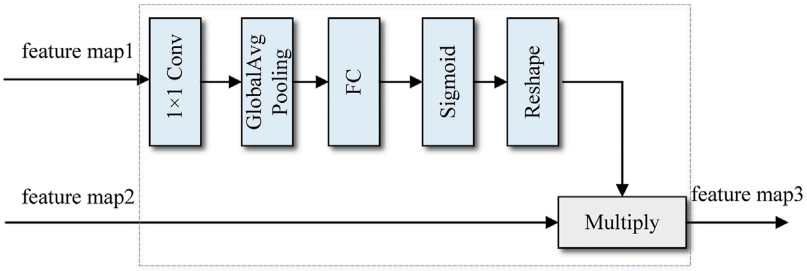

FIGURE 4
Structure diagram of feature enhancement module.

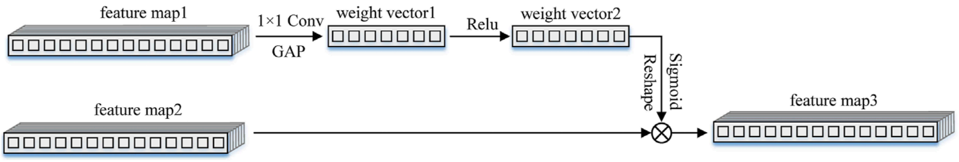

FIGURE 5
Schematic diagram of the process of the feature enhancement module.

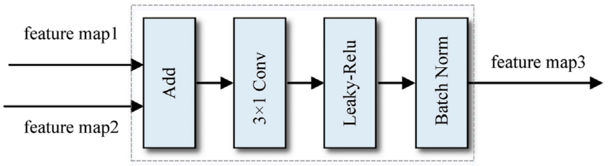

FIGURE 6
Information fusion module structure diagram.

operation, 3 × 1 Conv, Leaky-Relu non-linear activation function, and Batch Normalization. The output feature mapping of the null residual module is different from the output feature mapping of the feature reinforcement module, so the two parts are fused using the information fusion module. The dimensionality of feature map1 and feature map2 of Figure 6 is made consistent using the base convolution, and the dual input feature mappings are fused by Add operation, and feature re-extraction is performed using 3× 1 convolution. After that, the load feature mapping is further adjusted and optimized using Leaky-Relu activation function, Batch Normalization and other operations. Finally the output feature mapping of the information fusion module is a one-dimensional vector, and then the prediction results of residential load devices are obtained by the full join operation.

The null residual aggregated convolutional network uses multiple null residual blocks to extract the electric load features of residential houses, which improves the network model's ability to encode and decode load information, and also uses residual connections to transfer feature information to further ensure the effectiveness of load transfer between layers and avoid problems such as gradient disappearance of the network model. The non-intrusive load decomposition based on DRAnet uses the combined power data X as input samples and the power data Y of individual load devices as output labels to train and tune the network model. When tested on the test set, the decomposition results will be predicted based on the mapping relationship between X and Y during the training of the network. The model's feature enhancement module and information fusion module achieve optimal integration of load features extracted at different stages, thus improving the accuracy of the network model for load decomposition applications, especially improving the decomposition and identification of low-use appliances.

3 Simulation and analysis

3.1 Data sets

In this paper, two datasets [UK-DALE public data set and WikiEnergy data set (Kelly and Knottenbelt, 2015)] are used to verify the algorithm. WikiEnergy data set is a research power data set released by Pecan Street, and it is the most abundant residential power energy database in the world to study power load decomposition. It contains power data collected by nearly 600 household users over a period of time, including single load and total household power consumption. The active power of all loads and residential buildings is obtained at the sampling frequency of 1/60 Hz. The collection of power data began in 2011, but it has not stopped. The database is still expanding, providing a good data support for the research of non-intrusive load decomposition. The UK-DALE public data mainly contains the information of single load and total household power consumption of five household

TABLE 1 **Load decomposition evaluation metrics comparison on WikiEnergy data sets.**

Index	Method	Air condition	Fridge	Microwave	Washing machine	Dish washer
MAE	KNN	38.484	43.014	26.928	16.677	30.630
	DAE	36.964	39.520	17.015	12.081	25.107
	FHMM	40.212	22.898	12.787	12.787	19.782
	CNN s-p	39.635	13.760	13.155	11.959	11.624
	CNN s-s	61.129	38.413	9.973	18.497	19.084
	CD-LSTM	39.921	19.989	7.898	10.989	9.989
	D-ResNet	38.881	16.787	8.878	12.762	9.727
	DRAnet	**36.388**	**10.841**	**4.879**	**1.894**	**1.948**
SAE	KNN	0.0006	0.096	2.160	2.323	1.121
	DAE	**0.0001**	0.071	2.317	2.835	1.405
	FHMM	0.004	0.076	0.452	1.002	0.926
	CNN s-p	0.006	0.074	0.319	2.467	0.098
	CNN s-s	0.013	0.051	0.060	3.925	0.886
	CD-LSTM	0.065	0.045	0.172	1.190	0.158
	D-ResNet	0.011	0.021	0.182	1.022	0.152
	DRAnet	0.011	**0.019**	**0.133**	**0.08**	**0.084**

Bold indicates the best result.

users. The number of load devices in each household is up to 9, but the sampling period of each household is different. In the experimental, 70% of the sequences are used for training and 30% for testing.

In deep learning, artificially adding some noisy "dummy samples" combined with real data is beneficial to improve the robustness of the model and the generalization performance of the model. In this work, differential processing is performed on the raw power data. The load power signal is essentially a set of time-varying data, similar to a set of linear time-series information, and the total power samples are subjected to first-order differential processing, where the differential signal is a representation of the difference between two data. After the processing, the performance state of each non-zero-valued load device in the time dimension changes. Main purposes: 1) Each non-zero value power is changed to eliminate data fluctuation of load power signal and make the data tend to smoothness. 2) Combining raw data and differential data as the data input side enhances the data expression capability. The equation for differential processing is shown as follow Equation.

$$\Delta X_t = X_t - X_{t-1}, \tag{5}$$

where X_t represents the instantaneous total power data at the current moment t, X_{t-1} represents the instantaneous total power data at the moment point $t-1$, ΔX_t is the result of differential processing.

3.2 Analysis of experimental results for the WikiEnergy dataset

For the network model proposed in this work, experimental simulations and analyses are performed using several load devices, namely, air conditioner, refrigerator, microwave oven, washing machine, and dishwasher in WikiEnergy data set. DRAnet conducts non-invasive load decomposition experiments on the corresponding load devices on the WikiEnergy dataset, and compares K-Nearest Neighbor (KNN) algorithm, factorial hidden Markov model (FHMM), Denoising AutoEncoder (DAE) algorithm, CNN Sequence to Sequence (CNN s-s) algorithm, and CNN Sequence to Point (CNN s-p) algorithm, composite deep long short-term memory network (CD-LSTM) (Xia et al., 2020), and deep dilated residual network (D-ResNet). In this work, the input size of the network is 100. For the sequence-to-sequence method, the output size is 100. For the sequence to point method, the output size is 1. The average absolute error (MAE) and the comprehensive absolute error (SAE) are used to evaluate the performance of the algorithm. **Table 1** and **Figure 8** shows the comparison between the load decomposition effects of the above algorithms and the real power data on the WikiEnergy dataset.

The experimental results show that the KNN algorithm has the worst load decomposition effect on the following loads, such as microwave oven, washing machine and dishwasher. Because these loads have the characteristics of low frequency use, the KNN algorithm cannot effectively identify and decompose the sudden change point of load power due to its own algorithm structure. All algorithms can effectively decompose the air conditioning load with periodic laws. From the decomposition results of refrigerators, it can be found that D-Resnet algorithm and DRAnet network model proposed in this paper can be decomposed better, mainly because they can accurately identify the peak area of load power. In fact, for load decomposition, the most important thing is to improve the decomposition ability at high power consumption. For the moment of very low power, although all methods are different, they have little

TABLE 2 **Load operating state index comparison on WikiEnergy data sets.**

Index	Method	Air condition	Fridge	Microwave	Washing machine	Dish washer
Recall	KNN	0.998	0.996	0.759	0.290	0.561
	DAE	0.999	0.996	**1**	0.451	0.833
	FHMM	0.999	0.996	0.912	0.174	0.674
	CNN s-p	0.999	1	0.987	0.129	0.596
	CNN s-s	0.999	0.990	0.949	0.290	0.868
	CD-LSTM	0.999	0.994	0.957	0.453	0.856
	D-ResNet	1	0.997	0.947	0.675	0.887
	DRAnet	**1**	**1**	0.988	**0.880**	**0.982**
Precision	KNN	0.987	0.870	0.198	0.236	0.336
	DAE	0.987	0.853	0.050	0.229	0.281
	FHMM	0.991	0.966	0.061	0.132	0.421
	CNN s-p	0.995	0.996	0.050	0.047	0.414
	CNN s-s	0.939	0.847	0.033	0.428	0.391
	CD-LSTM	0.976	0.902	0.213	0.562	0.415
	D-ResNet	0.986	0.976	0.453	0.612	0.568
	DRAnet	**0.999**	**0.997**	**0.712**	**0.758**	**0.823**
Accuracy	KNN	0.991	0.889	0.967	0.993	0.978
	DAE	0.991	0.872	0.812	0.992	0.967
	FHMM	0.987	0.877	0.854	0.993	0.971
	CNN s-p	0.997	0.980	0.816	0.986	0.982
	CNN s-s	0.958	0.864	0.729	0.995	0.978
	CD-LSTM	0.976	0.978	0.821	0.995	0.968
	D-ResNet	0.975	0.981	0.942	0.987	0.971
	DRAnet	**0.999**	**0.986**	**0.979**	**0.996**	**0.996**

Bold indicates the best result.

impact on practical applications. Therefore, effective decomposition of load peaks is particularly important. The experiment shows that the DAE algorithm has certain advantages in identifying and decomposing regions with zero power consumption. For low frequency load equipment such as microwave ovens, washing machines and dishwashers, CNN s-s and CNN s-p convolutional neural networks can not accurately realize power decomposition. In terms of MAE and SAE, decomposition errors are relatively large. The main reason is that the number of layers of these two network models is small, and the load feature extraction is insufficient. D-ResNet's performance is better than CNN s-s and CNN s-p, but it still cannot accurately realize the decomposition. That is because, although the residual structure makes the network deeper and improves the feature extraction ability, the feature extraction of electrical appliances with less frequency of use is still insufficient. Due to the structural advantages of the model, DRAnet uses dilated convolution to deepen the receptive field of convolution kernel, capture more time series information of fine load characteristics, and improve the decomposition effect. Compared with the existing decomposition algorithms, the DRAnet network model has better decomposition effect and better decomposition performance. In particular, the load decomposition curve is closer to the real power consumption curve on the load of microwave oven, washing machine, dishwasher and other low-frequency use.

After the load is decomposed, the start and stop status of the electrical appliances can be distinguished by the threshold value. The threshold values of five kinds of appliances are: air conditioner 100 W, refrigerator 50 W, washing machine 20 W, microwave oven 200 W, dishwasher 100 W. Table 2 shows the comparison of the evaluation indexes of load operation status after load decomposition by each algorithm. In Precision and Accuracy indexs, the DRAnet network model achieves the best decomposition performance in each appliance. In Recall metrics, good metrics performance was also achieved on Air Wither, Refrigerator, Washing Machine and Dishwasher. For CNN s-s, CNN s-p, DAE, CD-LSTM and D-ResNet, combining the decomposition results of microwave oven, washing machine and dishwasher in Figure 7 with the load operation state metrics Recall and Precision analysis, the actual power consumption of these three loads is significantly less in the proportion of samples in the on state compared to the other two loads. Therefore, from the indexes, for these low-frequency use load devices, none of them can accurately identify the operating state of the load switch. The

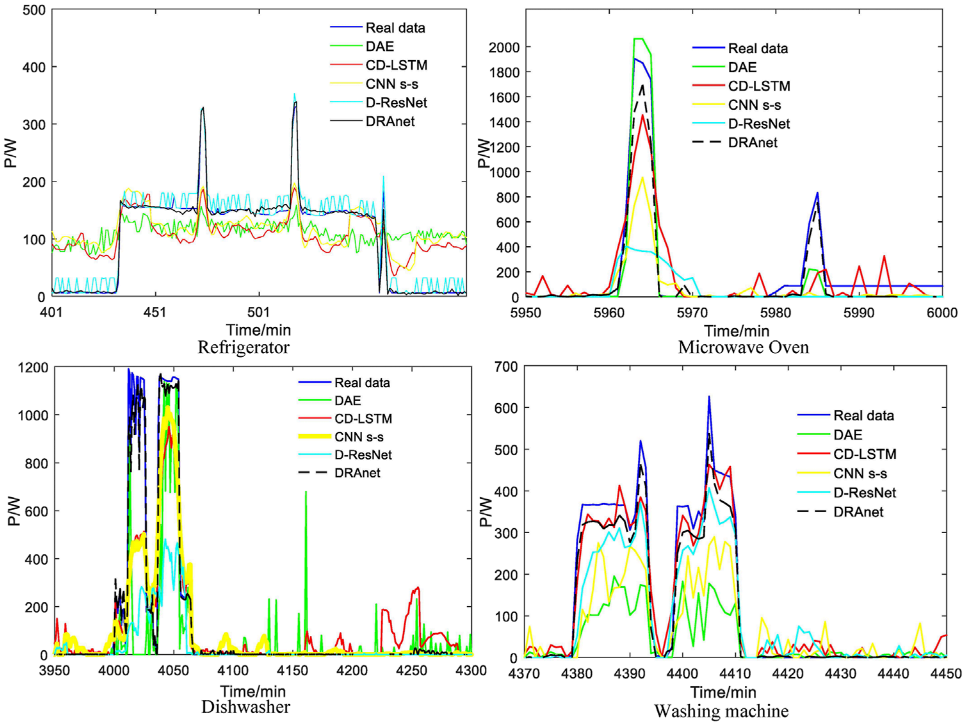

FIGURE 7
Partial view of load decomposition for WikiEnergy dataset.

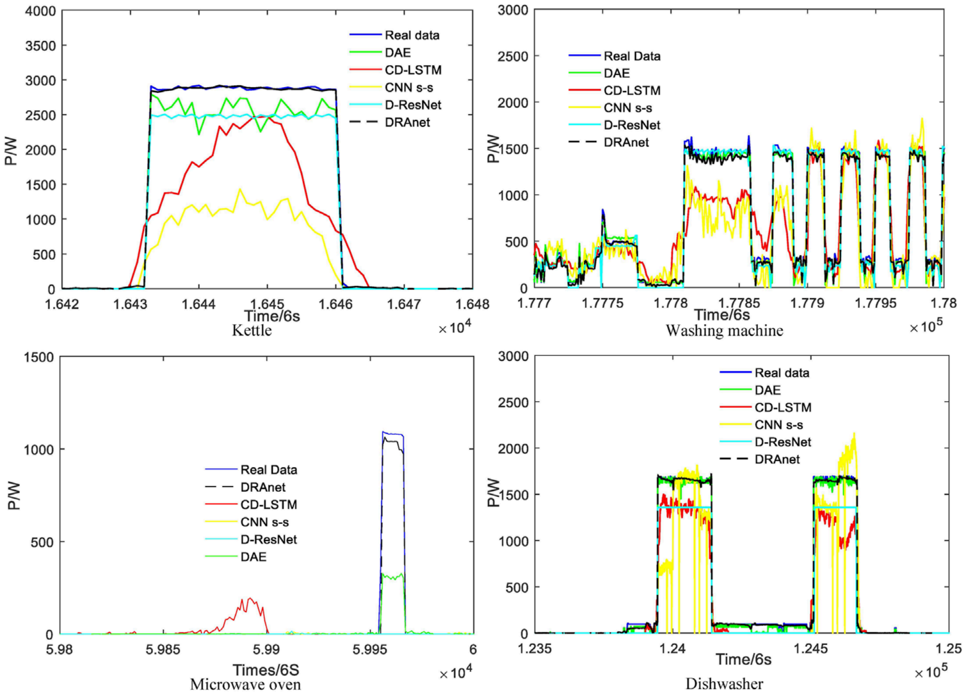

FIGURE 8
Partial view of load decomposition for UK-DALE dataset.

TABLE 3 **Load Decomposition Evaluation Metrics Comparison on UK-DALE data sets.**

Index	Method	Kettle	Fridge	Microwave	Washing machine	Dish washer
MAE	KNN	1.413	2.407	1.078	4.032	3.274
	DAE	8.867	8.218	1.226	14.920	12.756
	FHMM	9.432	6.432	1.123	15.773	12.722
	CNN s-p	4.002	4.517	1.159	23.881	9.747
	CNN s-s	8.829	3.866	1.125	20.696	9.101
	CD-LSTM	3.139	3.762	1.021	17.622	7.653
	D-ResNet	3.028	2.862	0.972	14.526	6.525
	DRAnet	**0.703**	**2.133**	**0.811**	**3.618**	**2.403**
SAE	KNN	0.076	0.015	0.054	0.018	0.001
	DAE	0.377	0.021	0.748	0.006	0.340
	FHMM	0.004	0.076	0.452	1.002	0.926
	CNN s-p	0.242	0.024	0.845	0.302	0.154
	CNN s-s	0.522	0.032	0.880	0.315	0.213
	CD-LSTM	0.271	0.020	0.421	0.102	0.061
	D-ResNet	0.121	0.014	**0.226**	0.081	0.052
	DRAnet	**0.002**	**0.011**	0.237	**0.0007**	**0.020**

Bold indicates the best result.

best load identification is the network model proposed in this work, which is most capable of accurately predicting the operating state of such load switches. In general, the power of the refrigerator is relatively regular, that is, it will stay at a relatively high power position for a period of time after starting. Although there is a power peak during the period, this does not affect the judgment of the start and stop of the electric appliance.

3.3 Analysis of experimental results for the UK-DALE dataset

In order to verify the generalization performance of the network model in this paper, relevant comparative experiments were carried out in UK-DALE. In the electric power data, five typical loads of kettle, refrigerator, microwave oven, washing machine and dishwasher are selected for experiment and analysis. As shown in Table 3, the above five algorithms can achieve effective power decomposition for frequently used load equipment such as air conditioners and refrigerators. For loads such as washing machines, microwave ovens and dishwashers, KNN algorithm, FHMM algorithm, CNN s-s algorithm and CNN s-p algorithm are far less effective than CD-LSTM algorithm, D-ResNet algorithm and DRAnet network model. This is mainly due to the advantages of the proposed network structure, which can better detect the peak state of power consumption and the operating state change of load switch.

Figure 8 shows the local load decomposition of UK-DALE data samples. Observe the decomposition curves of other methods. It is not well represented in the peak area of load power consumption, and the curve has some burrs. But it performs well in the range of power close to zero. To sum up the four local decomposition renderings, the load decomposition result of DRAnet network model is the closest to the real power consumption compared with other algorithms, indicating that DRAnet decomposition performance is superior to other algorithms.

The decomposition performance of the algorithm is further evaluated by using the evaluation indexes of load start and stop operation states such as recall, accuracy and precision. As shown in Table 4, it is the comparison of load switch operation status indicators of five algorithms in UK-DALE data set. From the index point of view, DRAnet network model achieves the best numerical performance on these types of loads, and can accurately identify the operation status of load startup and shutdown. From the Recall index and Precision index, other algorithms perform well on kettles, dishwashers and refrigerators, and can also judge the start and stop status of electrical appliances, but they do not perform very well on other microwave ovens and washing machines. The accuracy of non-invasive load decomposition based on DRAnet is obviously superior to other methods.

On the two experimental results of WikiEnergy dataset and UK-DALE dataset, the dilated residual aggregated convolutional network based on its own structural advantages, the proposed dilated residual module enhances the network's ability to extract low-frequency load features, rescale the features using the feature enhancement module, filter the useless information, and reinforce the useful load features, thus to be have better decomposition effect and generalization performance than other methods.

TABLE 4 Load operating state index comparison on UK-DALE data sets.

Index	Method	Air condition	Fridge	Microwave	Washing machine	Dish washer
Recall	KNN	0.987	0.988	0.254	0.911	0.968
	DAE	0.985	0.944	0.345	0.921	0.938
	FHMM	0.992	0.937	0.362	0.931	0.941
	CNN s-p	0.993	0.923	0.425	0.838	0.928
	CNN s-s	0.969	0.990	0.463	0.857	0.904
	CD-LSTM	0.964	0.978	0.429	0.862	0.914
	D-ResNet	0.973	0.992	0.653	0.902	0.934
	DRAnet	**1**	**0.996**	**0.947**	**0.926**	**0.969**
Precision	KNN	0.998	0.974	0.933	0.617	0.799
	DAE	0.650	0.932	0.421	0.471	0.813
	FHMM	0.991	0.966	0.061	0.132	0.421
	CNN s-p	1	0.968	0.435	0.701	0.829
	CNN s-s	0.946	0.944	0.632	0.663	0.835
	CD-LSTM	0.964	0.964	0.643	0.673	0.801
	D-ResNet	0.973	0.976	0.732	0.701	0.823
	DRAnet	**1**	**0.996**	**0.989**	**0.771**	**0.850**
Accuracy	KNN	0.982	0.954	0.956	0.981	0.934
	DAE	0.997	0.955	0.949	0.967	0.976
	FHMM	0.972	0.954	0.954	0.943	0.965
	CNN s-p	0.987	0.981	0.967	0.936	0.967
	CNN s-s	0.988	**0.987**	0.966	0.955	0.974
	CD-LSTM	0.987	0.977	0.964	0.954	0.971
	D-ResNet	0.988	0.985	0.952	0.962	0.976
	DRAnet	**0.999**	0.986	**0.979**	**0.985**	**0.998**

Bold indicates the best result.

4 Summary

This work firstly introduces the overall structure of the dilated residual aggregated convolutional network, which mainly has the differential processing of data, the dilated residual module, the feature enhancement module, and the information fusion module. The differential data enhances the expressiveness of the data and improves the robustness of the network model, and then the null residual module, feature reinforcement module, and information fusion module are proposed for the characteristics of sparse features of low-usage load devices. In this work, the dilated residual aggregated convolutional network is trained and tested on the WikiEnergy dataset and UK-DALE dataset samples. Through experimental simulations and result analysis, the proposed method is significantly better than other methods. In terms of load sequence decomposition, the method proposed in this paper has significantly improved on MAE and SAE indicators compared with the existing deep learning decomposition method, and in terms of electrical start and stop judgment, the method in this paper is superior to the existing method in three indicators. The fundamental reason is mainly that the dilated residual aggregated convolutional network model has a stronger extraction capability for higher order load features, and therefore has better decomposition results for low usage appliances. However, there are still many problems in non-intrusive load decomposition that need further study. 1) In order to improve the decomposition accuracy of load equipment, it is often to train the corresponding model for each load equipment. The process is complex and the time cost is high. Therefore, we can further study the deep neural network model with adaptive learning ability, such as the confrontation network model, which can be transplanted to the application of non-invasive load decomposition. 2) The decomposition of low power electrical appliances is more susceptible to noise interference and is not easy to decompose. The decomposition of low power loads needs further research. 3) The non-intrusive load decomposition algorithm based on deep learning in this paper has certain requirements for computing resources, and cannot be integrated with smart meters at present. In the future research work, we can consider further improvement of the algorithm, so that the algorithm can be directly used on embedded platforms and other hardware devices.

Data availability statement

Publicly available datasets were analyzed in this study. This data can be found here: https://paperswithcode.com/dataset/uk-dale.

Author contributions

FY: methodology, conceptualization, investigation; ZW: writing review and editing, methodology, validation; XZ: formal analysis, validation, resources; MX: supervision, funding acquisition, project administration.

Funding

This work was supported by the Science and Technology Project of SGCC, named Research on the Construction Technology of Artificial Intelligence Application Verification Platform for Power Grid Dispatching in Typical Scenarios (SGSH0000DKJS2200274).

Conflict of interest

Author ZW was employed by State Grid Shanghai Municipal Electric Power Company.

The remaining authors declare that the research was conducted in the absence of any commercial or financial relationships that could be construed as a potential conflict of interest.

Publisher's note

References

Ahmadi, H., and Marti, J. R. (2015). Load decomposition at smart meters level using eigenloads approach. *IEEE Trans. Power Syst.* 30, 3425–3436. doi:10.1109/tpwrs.2014.2388193

Chang, H. H., Lin, L. S., Chen, N., and Lee, W. J. (2013). Particle-swarm-optimization-based nonintrusive demand monitoring and load identification in smart meters. *IEEE Trans. Industry Appl.* 49, 2229–2236. doi:10.1109/tia.2013.2258875

Chen, B., Xia, M., Qian, M., and Huang, J. (2022). Manet: A multi-level aggregation network for semantic segmentation of high-resolution remote sensing images. *Int. J. Remote Sens.* 43, 5874–5894. doi:10.1080/01431161.2022.2073795

Dash, S., and Sahoo, N. (2022). Electric energy disaggregation via non-intrusive load monitoring: A state-of-the-art systematic review. *Electr. Power Syst. Res.* 213, 108673. doi:10.1016/j.epsr.2022.108673

Fan, W., Liu, Q., Ahmadpour, A., and Gholami Farkoush, S. (2021). Multi-objective non-intrusive load disaggregation based on appliances characteristics in smart homes. *Energy Rep.* 7, 4445–4459. doi:10.1016/j.egyr.2021.07.033

Gao, J., Weng, L., Xia, M., and Lin, H. (2022). MLNet: Multichannel feature fusion lozenge network for land segmentation. *J. Appl. Remote Sens.* 16, 1–19. doi:10.1117/1.jrs.16.016513

Guo, Y., Xiong, X., Fu, Q., Xu, L., and Jing, S. (2021). Research on non-intrusive load disaggregation method based on multi-model combination. *Electr. Power Syst. Res.* 200, 107472. doi:10.1016/j.epsr.2021.107472

Hart, G. W. (1992). Nonintrusive appliance load monitoring. *Proc. IEEE* 80, 1870–1891. doi:10.1109/5.192069

Hassan, T., Javed, F., and Arshad, N. (2014). An empirical investigation of v-i trajectory based load signatures for non-intrusive load monitoring. *IEEE Trans. Smart Grid* 5, 870–878. doi:10.1109/tsg.2013.2271282

Himeur, Y., Alsalemi, A., Bensaali, F., and Amira, A. (2020a). Effective non-intrusive load monitoring of buildings based on a novel multi-descriptor fusion with dimensionality reduction. *Appl. Energy* 279, 115872. doi:10.1016/j.apenergy.2020.115872

Himeur, Y., Alsalemi, A., Bensaali, F., and Amira, A. (2020b). An intelligent nonintrusive load monitoring scheme based on 2d phase encoding of power signals. *Int. J. Intelligent Syst.* 36, 72–93. doi:10.1002/int.22292

Himeur, Y., Alsalemi, A., Bensaali, F., and Amira, A. (2020c). Robust event-based non-intrusive appliance recognition using multi-scale wavelet packet tree and ensemble bagging tree. *Appl. Energy* 267, 114877. doi:10.1016/j.apenergy.2020.114877

Himeur, Y., Alsalemi, A., Bensaali, F., Amira, A., and Dimitrakopoulos, G. (2021a). "On the applicability of 2D local binary patterns for identifying electrical appliances in non-intrusive load monitoring," in *Intelligent systems and applications*. Editor K. Arai (Berlin: Springer Nature), 188–205.

Himeur, Y., Alsalemi, A., Bensaali, F., and Amira, A. (2021b). Smart non-intrusive appliance identification using a novel local power histogramming descriptor with an improved k-nearest neighbors classifier. *Sustain. Cities Soc.* 67, 102764. doi:10.1016/j.scs.2021.102764

Himeur, Y., Alsalemi, A., Bensaali, F., and Amira, A. (2021c). "Appliance identification using a histogram post-processing of 2d local binary patterns for smart grid applications," in International Conference on Pattern Recognition, Milan, Italy, 10-15 January 2021.

Hu, K., Li, M., Xia, M., and Lin, H. (2022). Multi-scale feature aggregation network for water area segmentation. *Remote Sens.* 14, 206. doi:10.3390/rs14010206

Inagaki, S., Egami, T., Suzuki, T., Nakamura, H., and Ito, K. (2011). Nonintrusive appliance load monitoring based on integer programming. *Electr. Eng. Jpn.* 174, 18–25. doi:10.1002/eej.21040

Jia, Z., Yang, L., Zhang, Z., Liu, H., and Kong, F. (2021). Sequence to point learning based on bidirectional dilated residual network for non-intrusive load monitoring. *Int. J. Electr. Power & Energy Syst.* 129, 106837. doi:10.1016/j.ijepes.2021.106837

Johnson, M. J., and Willsky, A. S. (2013). Bayesian nonparametric hidden semi-markov models. *J. Mach. Learn. Res.* 14, 673–701.

Kelly, J., and Knottenbelt, W. (2015). "Neural nilm: Deep neural networks applied to energy disaggregation," in 2nd ACM International Conference on Embedded Systems For Energy-Efficient Built Environments, Seoul, South Korea, November 4 - 5, 2015, 55–64.

Kolter, J. Z., Batra, S., and Ng, A. Y. (2010). "Energy disaggregation via discriminative sparse coding," in International Conference on Neural Information Processing Systems, British Columbia, Canada, 6-9 December 2010.

Lin, Y., and Tsai, M. (2014). Development of an improved time–frequency analysis-based nonintrusive load monitor for load demand identification. *IEEE Trans. Instrum. Meas.* 63, 1470–1483. doi:10.1109/tim.2013.2289700

Lin, Y. H., and Tsai, M. S. (2014). Non-intrusive load monitoring by novel neuro-fuzzy classification considering uncertainties. *IEEE Trans. Smart Grid* 5, 2376–2384. doi:10.1109/tsg.2014.2314738

Lu, C., Xia, M., and Lin, H. (2022). Multi-scale strip pooling feature aggregation network for cloud and cloud shadow segmentation. *Neural Comput. Appl.* 34, 6149–6162. doi:10.1007/s00521-021-06802-0

Luan, W., Yang, F., Zhao, B., and Liu, B. (2022). Industrial load disaggregation based on hidden markov models. *Electr. Power Syst. Res.* 210, 108086. doi:10.1016/j.epsr.2022.108086

Miao, S., Xia, M., Qian, M., Zhang, Y., Liu, J., and Lin, H. (2022). Cloud/shadow segmentation based on multi-level feature enhanced network for remote sensing imagery. *Int. J. Remote Sens.* 43, 5940–5960. doi:10.1080/01431161.2021.2014077

Park, S. W., Baker, L. B., and Franzon, P. D. (2019). Appliance identification algorithm for a non-intrusive home energy monitor using cogent confabulation. *IEEE Trans. Smart Grid* 10, 714–721. doi:10.1109/tsg.2017.2751465

Paterakis, N. G., Erdinc, O., Bakirtzis, A. G., and Catalao, J. (2017). Optimal household appliances scheduling under day-ahead pricing and load-shaping demand response strategies. *IEEE Trans. Industrial Inf.* 11, 1509–1519. doi:10.1109/tii.2015.2438534

Piga, D., Cominola, A., Giuliani, M., Castelletti, A., and Rizzoli, A. E. (2016). Sparse optimization for automated energy end use disaggregation. *IEEE Trans. Control Syst. Technol.* 24, 1044–1051. doi:10.1109/tcst.2015.2476777

Qu, Y., Xia, M., and Zhang, Y. (2021). Strip pooling channel spatial attention network for the segmentation of cloud and cloud shadow. *Comput. Geosciences* 157, 104940. doi:10.1016/j.cageo.2021.104940

Singh, S., and Majumdar, A. (2019). Analysis co-sparse coding for energy disaggregation. *IEEE Trans. Smart Grid* 10, 462–470. doi:10.1109/tsg.2017.2743763

Singh, S., and Majumdar, A. (2018). Deep sparse coding for non-intrusive load monitoring. *IEEE Trans. Smart Grid* 9, 4669–4678. doi:10.1109/tsg.2017.2666220

Song, L., Xia, M., Weng, L., Lin, H., Qian, M., and Chen, B. (2023). Axial cross attention meets cnn: Bibranch fusion network for change detection. *IEEE J. Sel. Top. Appl. Earth Observations Remote Sens.* 16, 32–43. doi:10.1109/jstars.2022.3224081

Tsai, M. S., and Lin, Y. H. (2012). Modern development of an adaptive non-intrusive appliance load monitoring system in electricity energy conservation. *Appl. Energy* 96, 55–73. doi:10.1016/j.apenergy.2011.11.027

Wang, Z., Xia, M., Lu, M., Pan, L., and Liu, J. (2022). Parameter identification in power transmission systems based on graph convolution network. *IEEE Trans. Power Deliv.* 37, 3155–3163. doi:10.1109/TPWRD.2021.3124528

Welikala, S., Dinesh, C., Ekanayake, M., Godaliyadda, R. I., and Ekanayake, J. (2019). Incorporating appliance usage patterns for non-intrusive load monitoring and load forecasting. *IEEE Trans. Smart Grid* 10, 448–461. doi:10.1109/tsg.2017.2743760

Xia, D., Ba, S., and Ahmadpour, A. (2021). Non–intrusive load disaggregation of smart home appliances using the ippo algorithm and fhm model. *Sustain. Cities Soc.* 67, 102731. doi:10.1016/j.scs.2021.102731

Xia, M., Liu, W., Wang, K., Song, W., Chen, C., and Li, Y. (2020). Non-intrusive load disaggregation based on composite deep long short-term memory network. *Expert Syst. Appl.* 160, 113669. doi:10.1016/j.eswa.2020.113669

Xia, M., Liu, W., Wang, K., Zhang, X., and Xu, Y. (2019). Non-intrusive load disaggregation based on deep dilated residual network. *Electr. Power Syst. Res.* 170, 277–285. doi:10.1016/j.epsr.2019.01.034

Zhang, C., Zhong, M., Wang, Z., Goddard, N., and Sutton, C. (2016). Sequence-to-point learning with neural networks for nonintrusive load monitoring. Available at: https://arxiv.org/abs/1612.09106.

Zhao, H., Yan, X., and Ren, H. (2019). Quantifying flexibility of residential electric vehicle charging loads using non-intrusive load extracting algorithm in demand response. *Sustain. Cities Soc.* 50, 101664. doi:10.1016/j.scs.2019.101664

frontiers | Frontiers in Energy Research

TYPE Original Research
PUBLISHED 22 February 2023
DOI 10.3389/fenrg.2023.1103038

OPEN ACCESS

EDITED BY
I. M. R. Fattah,
University of Technology Sydney, Australia

REVIEWED BY
Ali Riza Yildiz,
Bursa Uludağ University, Türkiye
Thang Trung Nguyen,
Ton Duc Thang University, Vietnam
Xiangyu Kong,
Tianjin University, China

*CORRESPONDENCE
Yi Zhang,
✉ whdzy2000@vip.sina.com

SPECIALTY SECTION
This article was submitted to Smart Grids, a section of the journal Frontiers in Energy Research

RECEIVED 19 November 2022
ACCEPTED 17 January 2023
PUBLISHED 22 February 2023

CITATION
Zhang Y and Lv Y (2023), Research on electrical load distribution using an improved bacterial foraging algorithm.
Front. Energy Res. 11:1103038.
doi: 10.3389/fenrg.2023.1103038

Research on electrical load distribution using an improved bacterial foraging algorithm

Yi Zhang* and Yang Lv

Jilin Jianzhu University, Changchun, China

This paper proposes an improved bacterial foraging algorithm for electrical load distribution to impro-ve power plants' efficiency and reduce energy consumption costs. In the chemotaxis stage, the adaptive step size is introduced to accelerate the random search speed compared with the traditional algorithm. In the replication stage, a hybrid crisscross operator is proposed to replace the traditional binary replication method in the algorithm to ensure the diversity of the population and improve the efficiency of the algorithm. The adaptive dynamic probability is used instead of the initial fixed probability to improve the global search performance of the algorithm. The mathematical model of electrical load distribution in a natural power plant is established, and the improved bacterial foraging algorithm is used to solve the model. Through comparative analysis of two power plant unit experiments, it is proved that the results of the improved algorithm can reduce 3.671% and 1.06% respectively compared with the particle swarm optimization algorithm, and 7.26% and 1.37% respectively compared with the traditional bacterial foraging algorithm, which can significantly reduce the coal consumption of the power plant.

KEYWORDS

bacterial foraging algorithm, crisscross operator, electrical load distribution, economic benefits of power plant, self-adaption

1 Introduction

The adjustment of electric power and energy structure is a hot topic. Germany proposes to realize the energy structure adjustment in 2035 so that the proportion of renewable energy generation can reach or even exceed half (Kopiske et al., 2017). Although the optimization of the power energy structure in China started late, it is also being optimized and adjusted constantly. With the integration of more and more distributed new energy into the power grid, the stability of the power grid faces many challenges due to the uncertainty brought by power generation methods such as wind photovoltaic power. As the main output method of my country's power resources, thermal power generation is of great significance to the stable operation of the power grid. The energy consumption problem caused by thermal power generation gradually becomes

---

Abbreviations: CSO, Crisscross Algorithm; BFO, Bacterial Foraging Algorithm; PSO, Particle Swarm Optimization; ELD, Electrical Load Distribution; ICSBFO, Improved Crisscross Algorithm Mixed Bacterial Foraging Algorithm; EBO, Ecogeography-based Optimization Algorithm; HGSO, Henry Gas, Solubility Optimization Algorithm; HTTSA, Hybrid Taguchi Salp Swarm Algorithm; HSSA-NM, Hybrid Salp Swarm-Nelder-Mead; COOA, Coot Optimization Algorithm; IEO, Improved Equilibrium Optimizer; ECSA, Effective Cuckoo Search Algorithm.

prominent with the increasing demand for power resources in recent years. Some achievements have been made in reducing the energy consumption of thermal power generation by upgrading traditional industrial equipment (Wu et al., 2019). However, it also faces a bottleneck period. It is essential to reduce energy consumption through electrical load distribution (ELD) among thermal power units. Therefore, optimizing coal consumption can not only improve the competitiveness of thermal power resources but also contribute significantly to the goal of "carbon neutrality" while ensuring the stability of the power production process and reducing the cost of thermal power.

Meta heuristic algorithms, such as [sine cosine algorithm (Aye et al., 2019) (Yildiz et al., 2020), seagull algorithm (Panagant et al., 2020), grasshopper algorithm (Yildiz et al., 2022a; Yildiz et al., 2022b) (Yildiz et al., 2021a; Yildiz et al., 2021b)], are widely used to solve various problems depending on their excellent convergence effects. In recent years, the optimization of heuristic algorithms has also become increasingly mature and improved. The efficiency of heuristic algorithms and their vulnerability to local optima are gradually improving with the optimization process. Ref (Premkumar et al., 2021) proposed a new multi-objective arithmetic optimization algorithm (MOAOA), which uses distance mechanism and elite sorting to optimize and upgrade the single objective arithmetic optimization algorithm, and can be applied to multiple scenarios in reality. Ref (Yildiz et al., 2021a; Yildiz et al., 2021b) proposed a political optimization algorithm (POA), which has better search ability and computational efficiency than other algorithms. In Ref (Yildiz et al., 2021c), an EBO algorithm is proposed. Compared with the slime mold algorithm, marine predator algorithm and other novel algorithms, this algorithm is not only simpler, but also more robust and has better design results. Ref (Yildiz et al., 2022a; Yildiz et al., 2022b) applies the idea of chaotic mapping to HGSO algorithm, which can effectively improve the convergence speed and robustness of the algorithm. In Ref (Yildiz and Erdas 2021), a new hybrid algorithm HTSSA is proposed, which can better jump out of the local optimum. Compared with some new algorithms, this algorithm has more advantages. In Ref (Yildiz et al., 2022c), chaotic map is used to mix Levy flight, which effectively improves the convergence speed of the algorithm. A new algorithm HSSA-NM is proposed in Ref (Yildiz 2020), which can effectively optimize engineering design problems through the hybrid salp swarm algorithm.

Meta heuristic algorithm is widely used in the power field (Chi et al., 2022). Used COOA algorithm to apply to the distribution network with photovoltaic generators. Compared with other algorithms, it proved that this method can not only effectively reduce the active power loss, but also significantly reduce the solution time. In Ref (Nguyen et al., 2022), an IEO algorithm is proposed to select the location and scale of photovoltaic power generation in the distribution network. The algorithm is improved by updating the concentration. Compared with a large number of meta heuristic algorithms, the improved method can effectively reduce the loss. In Ref (Pham et al., 2022), ECSA is used to solve the generation cost of integrated power system. Compared with equilibrium optimizer and marine predator algorithm, this method has the lowest cost. The ELD refers to achieving maximum economic benefits under the conditions of meeting production needs and power constraints from the perspective of an electric power producer. The methods of Unit Commitment (UC) can be divided into four categories: Mixed Integer Linear Programming (MILP), dynamic programming, decomposition method, and heuristic method. In the past, the optimization of thermal power units was usually done by mixed integer linear programming or dynamic programming. However, with the development of swarm intelligence algorithms in recent years, more and more swarm intelligence algorithms have been applied to ELD. (Jianjun et al., 2021) proposed an improved invasive weed algorithm for the non-linear programming model of thermal power units. Traditional swarm intelligence algorithms, represented by particle swarm optimization (PSO), cuckoo algorithm (CS) and genetic algorithm (GA), are widely used in ELD problems because of their stability and simplicity. However, they are all faced with problems such as easy to fall into local optimal solution, slow convergence, high iteration number requirements, and low efficiency, which are also some defects of swarm intelligence algorithms themselves. With the deepening of research, the application of swarm intelligence algorithm in ELD mainly focuses on solving the above problem. (Zou et al., 2019) improves and optimizes the selection, crossover, and mutation of the GA algorithm and applies it to the economic dispatch model of cogeneration. The results show that the improved method can improve the convergence speed and result from accuracy. In (Mahdi et al., 2018), a quantum-inspired particle swarm optimization algorithm is used to improve the robustness and efficiency of ELD processing. (Al-Bahrani and Patra 2018) proposes a multi-gradient PSO, which solves the problem that global particle swarm optimization with inertia weight (GPSO-w) is not efficient in the optimization process of large-scale thermal power units. It is found that the performance of this method is better than several improved PSO algorithms through experimental comparison. The other group of intelligent algorithms is also gradually being developed is applied to the ELD problems. (Hatata and Hafez 2019) is optimized by the ant lion algorithm (ALO) compared with the PSO algorithm and artificial immune system (AIS). The results found that the ALO in dealing with ELD has higher efficiency and convergence precision. In addition, (Kumar et al., 2021) also uses the improved Slap Swarm algorithm to optimize the load problem of large-scale power plants, and the experimental results confirm the high efficiency of its solving process. (Carmen et al., 2021) compares the advantages and disadvantages of various methods used in current UC optimization for the Italian power market application scenarios.

Bacterial Foraging Optimization (BFO) (de et al., 2022), (Chen et al., 2021) and (Farshi and Orujpour 2021) has been an emerging swarm intelligence algorithm in recent years. BFO is a bionic algorithm to simulate the foraging behavior of *Escherichia coli*. Bacterial foraging algorithms are widely used, such as image segmentation, path planning, power system, parameter optimization and identification. The improvement of bacterial foraging in the existing research mainly focuses on the chemotaxis and dispersion of bacteria, as shown in the reference (Hu et al., 2020), (Chen et al., 2017), (Wang et al., 2019), (Ramaporselvi and Geetha 2021) and (Devi and Srinivasan 2021). The contributions of this paper mainly focus on the improvement of the three key steps of the algorithm. The improvements are aimed at the characteristics of the bacterial foraging algorithm, such as slow convergence speed, low efficiency, and easily falling into local optimum.

(1) The adaptive modified step is used instead of the traditional fixed step to solve the problem of slow solution speed in the chemotaxis stage.
(2) The traditional fitness value ranking dichotomous replication optimization method was improved by using a crisscross algorithm mixture in the process of bacterial replication.
(3) Adaptive dynamic probability is used to replace the traditional fixed dispersal probability to avoid the optimal result elimination problem and ensure the algorithm's efficiency in the dispersal stage.

Through two case studies and comparison of different algorithms, it is proved that the improved hybrid bacteria foraging algorithm proposed in this paper has better results.

This paper consists of five sections. The first section establishes the mathematical model of ELD. Section 2 describes the improvement of chemotaxis, replication and dispersal of the bacterial foraging algorithm. In Section 3, an improved hybrid bacterial foraging algorithm is used to solve the ELD problem, and the pseudo-code is given. The fourth section is the experimental part, which analyzes the case of 10 units of a medium power plant and 3 units of a small power plant and proves that the improved algorithm can significantly reduce coal consumption. The fifth section is the summary of this paper.

2 Mathematical model of ELD

Coal consumption characteristics and valve-point effect of generating units are taken as objective functions, and unit output and load balance are taken as mathematical models with constraints in the model of ELD.

2.1 Objective function

The characteristic of coal consumption refers to the curve of coal consumption of a thermal power unit changing with the load. It is the critical basis for analyzing energy consumption and load optimization scheduling of a thermal power plant. When a load of a single unit decreases with the generation condition, its coal consumption rate will increase, and the formula is as follows:

$$F\left(P_g(x)\right) = a(x) + b(x) * P_g(x) + c(x) * P_g(x)^2 \tag{1}$$

In Eq. 1, $F(P_g(x))$ represents the coal consumption of the thermal power unit; $a(x)$, $b(x)$, $c(x)$ represents the coal consumption characteristic parameters of the x unit; and $P_g(x)$ represents the x unit's power.

The influence of the valve-point effect on UC should be considered in the unit operation process. The leakage of steam causes the valve-point effect at the opening moment of the regulating valve of the steam turbine, which is reflected as the pulsation influence at high load in the coal consumption characteristic curve of the unit. The formula is as follows:

$$G(P(x)) = |d(x) * \sin(e(x) * (P_{\min}(x) - P(x)))| \tag{2}$$

In Eq. 2, $d(x)$, and $e(x)$ represent the valve-point coefficient $P_{\min}(x)$ represents the lowest power value of the x unit.

The mathematical model of the objective function can be expressed as the compound superposition function in summary. In the model, the quadratic function and the sine function of the valve-point effect are set for solving the minimum coal consumption characteristic. It can be expressed as follows:

$$\min f(P(x)) = \sum_{x=1}^{N} (F(P(x)) + G(P(x))) \tag{3}$$

2.2 Constraint function

Capacity constraint function is the prerequisite for the standard and safe operation of the thermal power unit. Its formula is as follows:

$$P_{\min}(x) \le P(x) \le P_{\max}(x) \tag{4}$$

Where $P_{\max}(x)$ denotes the upper limit of capacity constraint and $P_{\min}(x)$ the lower limit of capacity constraint. This paper ignores power flow loss and assumes that only thermal power units participate in power generation in the network. Load balance constraint means that the sum of the power of each unit needs to be consistent with the total load, and its formula is as follows:

$$\sum_{x=1}^{N} P(x) = Load \tag{5}$$

In Eq. 5, *Load* represents the total load of the system.

2.3 Penalty function

The purpose of adding a penalty function is to consider some other constraints or ignored losses, and its formula is as follows:

$$h(P(x)) = \varepsilon * \left| \sum_{x=1}^{N} P(x) - Load \right| \tag{6}$$

In Eq. 6, ε represents the penalty coefficient which can be fixed or changed to an adaptive value according to the characteristics of the algorithm. Thus, the mathematical model of ELD can be expressed as follows:

$$\min F = f(P(x)) + h(P(x)) \tag{7}$$

3 Improved crisscross algorithm mixed bacterial foraging optimization (ICSBFO)

3.1 The improve the chemotactic process with adaptive modification of step size

Chemotaxis is to simulate the motion part of *E. coli* foraging behavior. The process includes forward and reverses in two parts. *E. coli* runs along the vector direction with a random vector until the fitness value cannot continue to be smaller. In (Long et al., 2020), the cost function of the A* algorithm is used to improve the chemotaxis process to solve the path planning problem under different working conditions effectively. In the process of chemotaxis, the step length C is an essential factor affecting the movement process of *E. coli*. The step length *C* of chemotaxis is a fixed value in the traditional BFO algorithm. It will bring some disadvantages. The minor *C* value can improve the search accuracy, but it will reduce the search efficiency of the algorithm and easy to fall into the local optimal. The larger value of *C* can improve the search speed of the algorithm, but it will reduce the accuracy of the search results and lead to search misjudgment. Therefore, the value of step size dramatically affects the excellence of the algorithm. Inspired by the fish swarm algorithm, (Yufang and Jianwen 2021) uses an exponential function to modify the step size. Adaptive modified step size is used to replace the traditional fixed value in this paper.

$$C(x) = \exp\left(-\left(N_c * N_{re} * N_{ed} - \frac{\tau}{j + (k-1) * N_c (l-1) * N_{re} * N_{ed}}\right)^{\frac{1}{\alpha}}\right) * C \tag{8}$$

In Eq. 8, N_c, N_{re}, N_{ed} respectively represent the number of chemotactic restrictions, replication restrictions, and dispersal restrictions in BFO algorithm. α denoted as the step coefficient. j, k and l represent the current times of chemotaxis, replication and dispersion respectively. τ is a dynamic change. The BFO algorithm can search for optimization with giant steps in the early stage of the search to accelerate the algorithm's convergence through the adaptive step correction exponential formula. And search for optimization with a small step in the late stage of search to improve the accuracy of the algorithm.

3.2 The replication process of the hybrid crisscross algorithm to optimize

The replication process is a process that simulates biological evolution and survival of the fittest. The *E. coli* are arranged in ascending order according to the cumulative fitness value. The first half of the high-quality *E. coli* is copied instead of the second half of the poor *E. coli*. The total number is unchanged in this process. Although this method reduces the algorithm's complexity, it also brings some disadvantages. The diversity of the population is greatly decreased to ensure the diversity of the population and ensure that high-quality bacteria individuals are not lost. (Jufeng et al., 2020) used single individual ranking and crossover operations to replace the cumulative health ranking method. In this paper, the Crisscross Algorithm (Xiongmin et al., 2022), (Shaowei et al., 2021) and (Anbo et al., 2022) is a novel population random search algorithm that is proposed to improve the replication process. The Crisscross Algorithm includes two parts, horizontal crisscross, and longitudinal crisscross. Compared with the previous generation, the method achieves the optimal effect through each iteration of the crisscross process. Horizontal crossover is like the crossover process in GA, but it also has a comparison process with the previous generation.

$$\begin{aligned} MS_{hc}(x,d) = r_1 * X(x,d) + (1-r_1) * X(y,d) \\ + c_1 * (X(x,d) - X(y,d)) \end{aligned} \tag{9}$$

$$\begin{aligned} MS_{hc}(y,d) = r_1 * X(y,d) + (1-r_1) * X(x,d) \\ + c_1 * (X(y,d) - X(x,d)) \end{aligned} \tag{10}$$

The parameters x and y in Eqs. 9, 10 represent individual bacteria, d represents dimension solved by the algorithm, and $r_1 c_1$ both represent random numbers. The former is between 0 and 1, and the latter is between −1 and 1. This formula represents the offspring of bacteria x and y after horizontal crossing in the d dimension. Longitudinal crossover is similar to the mutation process in a genetic algorithm, and longitudinal crossover is the crossover of different dimensions of the same bacterium. After each crossover, a progeny with different dimensions from the previous generation is produced. The progeny produced each time should be compared with the previous generation to retain the optimal value.

$$MS_{vc}(x,d_1) = r * X(x,d_1) + (1-r) * X(x,d_2) \tag{11}$$

According to Eq. 11, bacteria x can produce a progeny by crossing dimensions $d_1 d_2$. The crisscross algorithm was used to cross-optimize the chemotactic population. Compared with the traditional sequencing and replication method, the optimization and replication process of the crisscross algorithm not only retained high-quality bacterial individuals but also ensured the diversity of the population.

3.3 Adaptive dispersal probability to improve dispersal process

The random dispersal optimization of *E. coli* individuals was carried out according to a fixed dispersal probability. In this process, certain high-quality individuals were also dispersed to random areas. Although the global search performance of the algorithm was ensured in principle, the fitness value of the algorithm would also deteriorate, which would decrease the efficiency of the algorithm. In this paper, we use the adaptive dispersal probability instead of the traditional fixed value to avoid falling into the local optimum and ensure the global search performance of the algorithm.

$$P(x) = P_{ed} * \frac{J_{worst} - J_x}{J_{worst} - J_{best}} \tag{12}$$

In Eq. 12, J_{worst} represents the worst fitness value, J_{best} represents the optimal fitness, and J_x is the real-time fitness value of the xth bacterium. The dispersal probability of *E. coli* was modified adaptively by this fraction. The fitness value of bacteria individuals with good fitness was small, and the dispersal probability was reduced while the dispersal probability of individuals with poor fitness was increased. In this way, the loss of high-quality individuals is avoided and the efficiency and performance of the algorithm are guaranteed.

3.4 Flowchart of ICSBFO

The parameters need to be initialized first in the algorithm. It includes the number of iterations *maxgen*, the dimension *p* of the search range, the number of bacteria s, the maximum number of chemotaxis N_c, the maximum number of steps of one-way movement in chemotaxis operation N_s, the maximum number of replication N_{re}, the maximum number of dispersal N_{ed}, and the fixed probability of bacterial dispersal P_{ed}, the number of attractive factors and the release speed $d\_attract$, $ommiga\_attract$, the number of repellant factors and the release speed $h\_repellant$, $ommiga\_repellant$. Then the population is initialized. The population of this algorithm is generated according to the lower limit of unit load plus the difference between the upper and lower limits of unit load multiplied by a random number. Initialize the population as a high-dimensional array. After the population initialization is completed, the cycle is carried out. The maximum number of dispersals, replication, and chemotaxis, are determined first, and the chemotaxis operation is carried out after the requirements are met. In the chemotaxis process in this paper, N_c is 60; N_s is 4. After determining the adaptive correction step and the repulsive attraction between the bacteria, the fitness value was calculated. The bacteria turn over and then proceed with dynamic steps in the direction of the randomly generated vector until the maximum swimming limit is reached or the fitness value is updated to the optimal value. During this period, the bacterial constraint should be considered, namely the upper and lower limits of the unit output constraint. After the chemotactic process, the fitness value is updated to enter the replication stage. During replication, bacteria are sorted according to their cumulative fitness values, and new populations are formed in ascending order. Replicate 2 times in total. The longitudinal and horizontal crossover operators were used to update the fitness value, retain the perfect result and eliminate the wrong result. Finally, the bacteria were dispersed according to the adaptive dispersal probability when it came to the dispersal stage. The dispersal probability of the perfect result was tiny, while the dispersal probability of the impaired result was extensive. After the dispersal, the bacteria died out, and the new bacteria re-determined the random position. The algorithm ends when the maximum number of dispels reaches 4, and the algorithm iterates 480 times in total. The flow chart of bacterial foraging algorithm is shown in Figure 1.

4 ICSBFO addresses ELD issues

4.1 ELD based on ICSBFO

In the process of solving the ELD problem by ICSBFO, the control variable is the initial population of *E. coli*, and the dependent variable is the coal consumption of the unit. Use the algorithm to solve Eq. 7, first, it is necessary to tune the relevant parameters of the ICSBFO algorithm in solving the ELD problem. The initial population of *E. coli* is generated with the upper and lower limits of the power load, and the number of units is set as the solution dimension. Then we need to determine the load and solve the ELD model. The fitness value in the solving process is the objective function proposed above after considering the penalty coefficient. If there is no new load command or percentage load requirement, each unit's optimal load distribution and optimal coal consumption can be output.

4.2 ICSBFO solves ELD model pseudo code

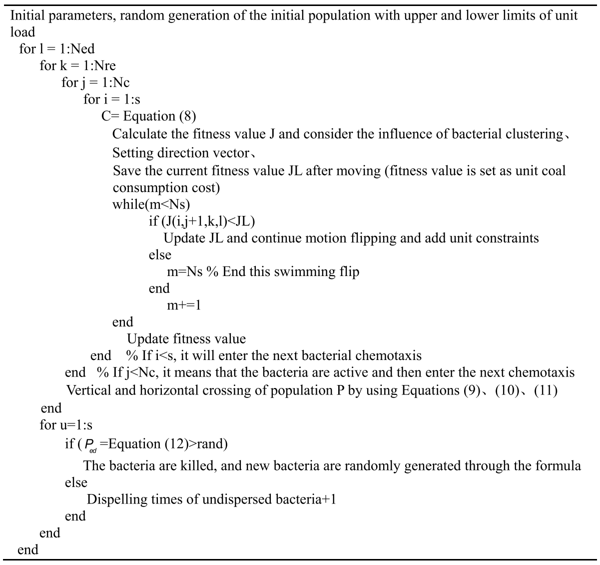

```
Initial parameters, random generation of the initial population with upper and lower limits of unit
load
  for l = 1:Ned
      for k = 1:Nre
          for j = 1:Nc
              for i = 1:s
                  C= Equation (8)
                    Calculate the fitness value J and consider the influence of bacterial clustering、
                    Setting direction vector、
                    Save the current fitness value JL after moving (fitness value is set as unit coal
                    consumption cost)
                    while(m<Ns)
                           if (J(i,j+1,k,l)<JL)
                              Update JL and continue motion flipping and add unit constraints
                           else
                               m=Ns % End this swimming flip
                           end
                               m+=1
                    end
                       Update fitness value
              end   % If i<s, it will enter the next bacterial chemotaxis
          end  % If j<Nc, it means that the bacteria are active and then enter the next chemotaxis
          Vertical and horizontal crossing of population P by using Equations (9)、(10)、(11)
      end
      for u=1:s
          if ( $P_{ed}$ =Equation (12)>rand)
             The bacteria are killed, and new bacteria are randomly generated through the formula
          else
              Dispelling times of undispersed bacteria+1
          end
      end
  end
```

5 Analysis of two cases

This paper uses the case of 10-unit medium-sized and 3-unit small-scale power plants, respectively, to prove the feasibility of the ICSBFO algorithm. The experimental environment is Windows7, Intel Core i5 quad-core 1.70 GHz processor, 8 GB physical memory, and Matlab 2018a simulation platform. Case 1 Using the ICSBFO, CSO, BFO, and PSO to solve the ELD problem of the 10-unit model, the experimental results show that the ICSBFO algorithm has the smallest coal consumption. Experiments are carried out with different load conditions, and the ICSBFO and BFO algorithms are compared. We find that the lower the load, the more pronounced the optimization effect of ICSBFO. Case 2 Using ICSBFO, BFO, and PSO to solve the ELD problem of the 3-unit model, the experimental results demonstrate that ICSBFO has the best optimization results and point out the limitations of bacterial foraging algorithms when dealing with small-scale unit data.

5.1 Case of 10 units

In Case 1, taking 10 units in a power plant (Basu 2016) as an example, the coal consumption characteristic parameters of the unit and the upper and lower limits of the unit load are shown in the following Table 1:

In the case of a 10-unit medium-sized power plant, this paper uses the improved crisscross hybrid bacterial foraging algorithm (ICSBFO), the crisscross algorithm (CSO) (Meng et al., 2015), the bacterial foraging algorithm (BFO), and the particle swarm algorithm (PSO) (Hatata and Hafez 2019) to solve the 10-unit load optimization distribution model of a medium-sized power plant. Since different unit parameters and valve point effect parameters greatly influence the results of unit load economic dispatch, this paper uses the methods proposed by them in their

TABLE 1 Coal consumption characteristic parameters of a 10-unit power plant and upper and lower limits of unit load.

	a_i	b_i	c_i	d_i	e_i	$P_{\min}$/MW	$P_{\max}$/MW
G1	26.97	−0.3975	0.002176	0.02697	−3.975	100	250
G2	118.4	−1.269	0.004194	0.1184	−12.69	50	230
G3	−95.14	0.4864	0.00001176	−0.05914	4.864	200	500
G4	266.8	−2.338	0.005935	0.2668	−23.38	99	265
G5	−53.99	0.4462	0.0001498	−0.05399	4.462	190	490
G6	266.8	−2.338	0.005935	0.2668	−23.38	85	265
G7	−43.35	0.3559	0.0002454	−0.04335	3.559	200	500
G8	266.8	−2.338	0.005935	0.2668	−23.38	99	265
G9	14.23	−0.0182	0.0006121	0.01423	−0.1817	130	440
G10	−61.13	0.5084	0.0000416	−0.06113	5.084	200	490

respective articles to simulate the unit parameters of the same case. In the process of PSO testing, a mutation strategy is introduced to improve the problem that PSO is easy to fall into the local optimum. Since the test algorithms all contain a random search mechanism, each group is tested 30 times in this experiment, and the experimental results are taken as the average value of the tests. During the test, the population size was 50, the dimension was 10, the load was 2,700 MW, and the total number of iterations of various algorithms is 480.

In the process of dealing with ELD problems, PSO is widely used because of its fast convergence speed, but its disadvantage is poor robustness. CSO shows good convergence efficiency and accuracy in the ELD process due to its independent update iterations in the horizontal and vertical directions, and a simplified algorithm process characterizes it. It can be seen from Figure 2 that the improved bacterial foraging algorithm has faster convergence speed and convergence results than the previous two, which is due to the improvement of the convergence speed by the adaptive correction step size and the mixing in the replication process. Compared with traditional BFO, improvement optimization is more significant. In taking the average value of multiple experiments, we also found that ICSBFO has better robustness and the smallest variance of its optimal coal consumption. Research on the high-quality robustness of ICSBFO is expected to be carried out in the future.

It can be seen from the above Table 2 that the optimal coal consumption of ICSBFO is the smallest. Compared with the CSO, the coal consumption reduced by the ICSBFO algorithm is 4.6317 $g \cdot kW^{-1} \cdot h^{-1}$. The percentage reduction is 0.707%. Compared with the PSO, the coal consumption optimization results are more prominent, decreasing 24.0534 $g \cdot kW^{-1} \cdot h^{-1}$. The percentage reduction is 3.671%. Compared with the unimproved traditional BFO algorithm, the effect is more prominent, ICSBFO reduces coal consumption by 47.5621 $g \cdot kW^{-1} \cdot h^{-1}$. The percentage reduction is 7.26%. The resulting significant reduction in coal consumption can improve the efficiency of the power plant, reduce the economic cost of the power plant and reduce the pollution to the environment. (From the load distribution of each unit solved by the ICSBFO algorithm, since the upper and lower limits of a load of units 9 and 10 are both high, the outputs of units 9 and 10 are the most, which are 413 and 479 MW respectively.)

To test the influence of different loads on the performance and solution quality of the algorithm, this paper uses 90%, 80%, and 70% of the rated load to solve the load optimization distribution model of the 10-unit case of the medium-sized power plant. This experiment compares the ICSBFO and unimproved traditional BFO.

Affected by the valve-point effect, traditional methods often perform poorly in low-load optimization of processing units. For example, in the traditional BFO algorithm, it can be seen from the above Figure 3 that the optimization of coal consumption by BFO in reducing the load is not very obvious. In this process, the coal consumption at 70% load is higher than 80% load, which shows that BFO can no longer effectively optimize the ELD problem at low load. However, ICSBFO can solve the problem of adapting to low-load optimization. As seen from the above Figure 3, as the load rate decreases, the convergence speed of ICSBFO gradually slows down, but the optimization result of ICSBFO is still significantly better than that of BFO. It can be seen from Table 3 that under the condition of 90% load rate, under the load of 2430 MW, the optimized reduction is 66.2689 $g \cdot kW^{-1} \cdot h^{-1}$. The percentage reduction is 12.624%. Under the load rate of 80%, the load of 2160MW, the coal consumption is saved by 90.4748 $g \cdot kW^{-1} \cdot h^{-1}$.The percentage reduction is 21.183%. Under the load rate of 70% and the load capacity of 1890MW, the optimized amount is 220.1997 $g \cdot kW^{-1} \cdot h^{-1}$. The percentage reduction is 65.357%. From the analysis of the load optimization distribution of different units, the ICSBFO algorithm can give full play to the output advantages of different units. In this case, the two units G9 and G10, with higher upper and lower load limits, have the most output under different load ratios. From this, it can also be concluded that ICSBFO has an excellent performance in optimizing the load of 10 units. By comparing different load rates, it can be found that under high load rates, the optimized amount of ICSBFO is small, and as the load rate decreases, the

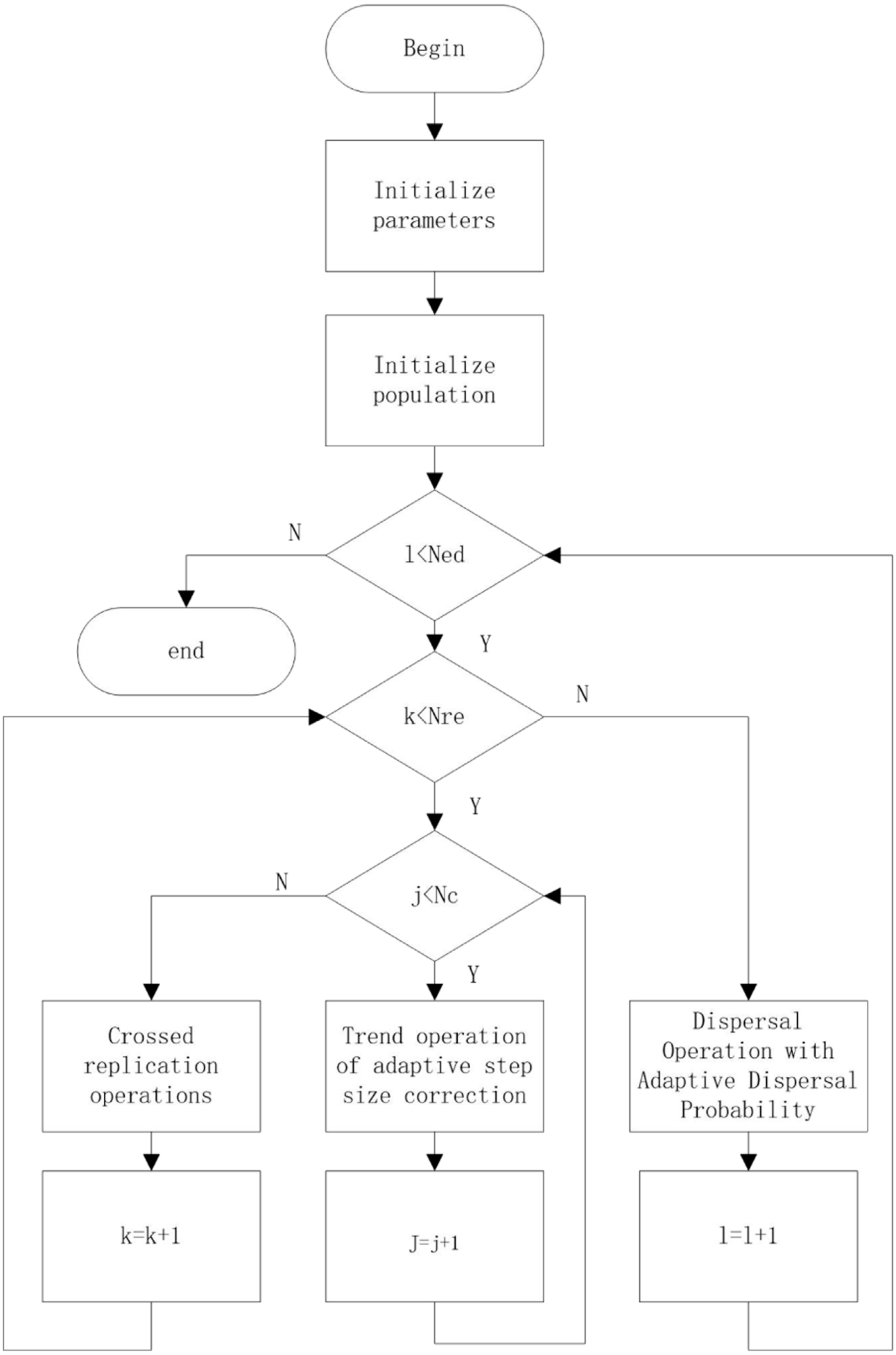

FIGURE 1
Flowchart of ICSBFO.

optimized coal consumption gradually increases. The traditional BFO algorithm has a poor unit optimization effect in the case of low load, but ICSBFO still has an excellent optimization effect in the case of low load rate. Therefore, the algorithm is expected to have good application scenarios during the low-peak electricity consumption period in spring and autumn.

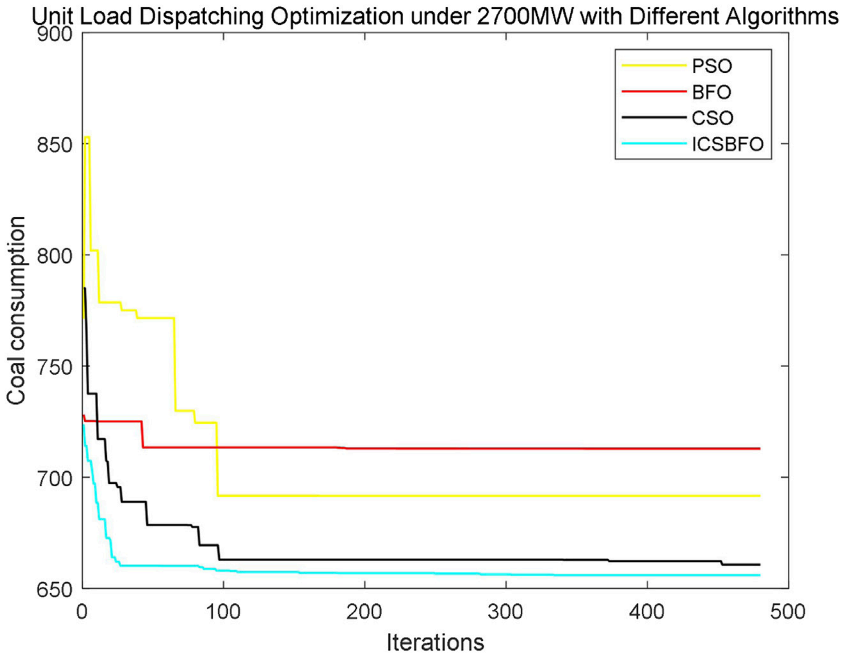

FIGURE 2
Convergence curve of unit economic dispatch of case 1.

TABLE 2 Load optimization results of units under 2700 MW load with different algorithms.

Algorithms	Load distribution of each unit/MW (integer is reserved for the result)										Optimal coal consumption $g \cdot kW^{-1} \cdot h^{-1}$
	G1	G2	G3	G4	G5	G6	G7	G8	G9	G10	
ICSBFO	193	199	227	235	191	233	280	228	413	479	655.0957
CSO	205	209	240	228	255	223	308	231	402	357	659.7274
PSO	211	215	200	254	401	212	200	247	291	468	679.1500
BFO	184	170	238	255	476	196	298	209	326	269	702.6578

TABLE 3 Comparison results of ICSBFO and BFO under different loads.

Load (%)	Algorithm	Load distribution of each unit/MW (integer is reserved for the result)										Optimal coal consumption $g \cdot kW^{-1} \cdot h^{-1}$
		G1	G2	G3	G4	G5	G6	G7	G8	G9	G10	
90	ICSBFO	219	205	238	241	194	236	224	240	422	208	524.9383
90	BFO	207	146	215	216	315	209	358	203	210	357	591.2072
80	ICSBFO	160	195	196	223	204	212	211	229	342	207	427.1072
80	BFO	228	150	202	250	202	212	205	132	181	206	517.5820
70	ICSBFO	110	146	200	211	196	221	202	222	184	200	336.8949
70	BFO	122	63	334	173	227	156	205	234	262	226	557.0746

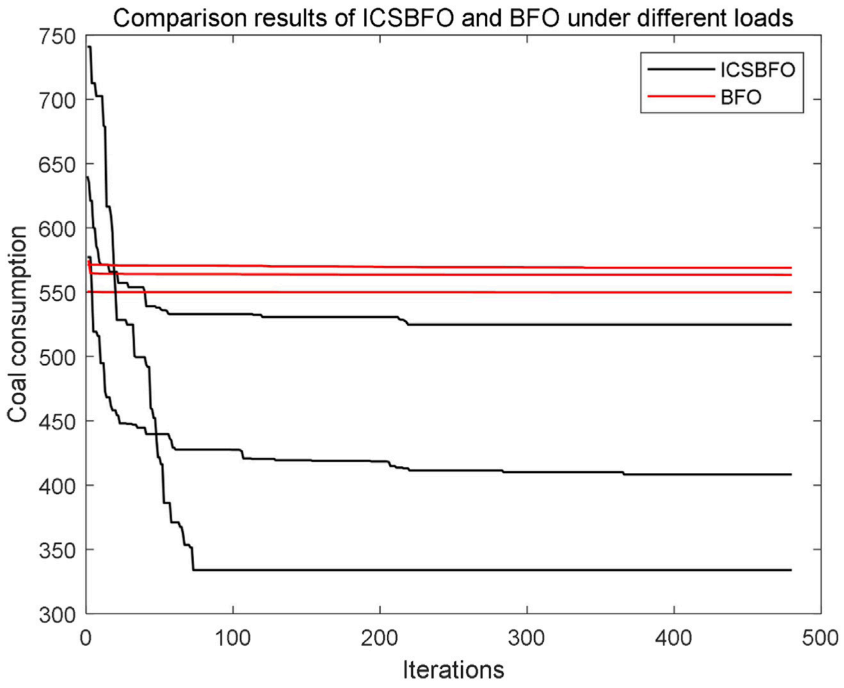

FIGURE 3
Comparison of ICSBFO and BFO under different load factors in Case 1.

TABLE 4 Coal consumption characteristic parameters and upper and lower limits of unit load in a particular 3-unit power plant.

	a_i	b_i	c_i	d_i	e_i	$P_{\min}$/MW	$P_{\max}$/MW
G1	358.0643	−0.1438	0.0001	0.1716	0.9776	170	350
G2	420.4021	−0.5391	0.0008	0.9610	1.0080	170	350
G3	196.7672	1.1705	−0.0024	5.1336	1.0314	170	350

5.2 Case of 3 units

In case 2, taking 3 units of a miniature thermal power plant as an example, the coal consumption characteristic parameters of the units and the upper and lower limits of unit load are shown in the following Table 4:

In the case of a small power plant with 3 units, this paper uses ICSBFO, BFO and PSO to solve and compare the load distribution optimization model of the same unit data. In this experiment, each group was tested 30 times, and the average was taken. The population size was 50, the dimension was 3, the load was 900 MW, and the total number of iterations of various algorithms is 480.

This experiment sets the number of units as the solution dimension. The crisscross algorithm used in this paper in the replication process, its horizontal crossover operator is the crossover of dimensions, while the dimension of this experimental case is 3, and the crossover dimension is too small, resulting in The offspring after crossover are highly similar to the previous generation, so the horizontal crossover operator is omitted in this experiment, and only the vertical crossover operator is used to improve the replication process, so as to ensure the diversity of the population. Although the energy consumption coefficients of the three units in this experiment are different, the upper and lower limits of the unit load are the same. It can be seen from Figure 4 that the result of ICSBFO is significantly better than that of PSO and BFO, but the convergence rate will be slightly lower. Under the condition of 900 MW load, the optimal coal consumption of ICSBFO is 975.23 $g \cdot kW^{-1} \cdot h^{-1}$, which is 1.37% lower than that of BFO algorithm and 1.06% lower than that of PSO. Combining the low load rate in the 10-unit case and the 3-unit case, it can be concluded that the traditional bacterial foraging algorithm generally performs in processing the optimization data of small-scale units, and the solution time is slightly longer. However, the improved bacterial foraging algorithm can overcome such problems. Given this characteristic, follow-up research will be carried out on the case of large-scale power plant units. In addition, in the future work, we will also study the dynamic ELD problem with multiple constraints, not limited to the valve-point effect constraint.

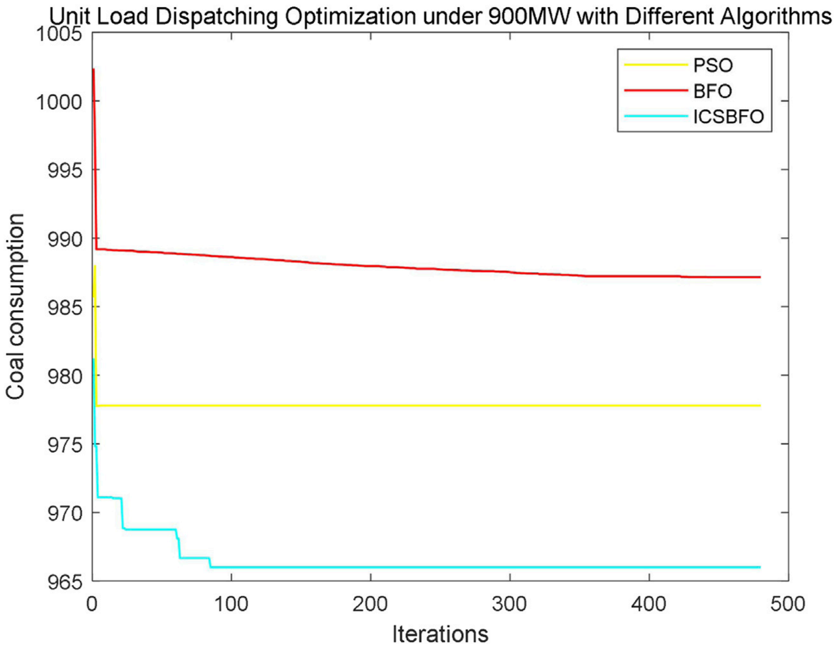

FIGURE 4
Economic dispatch curve of units in case 2.

6 Conclusion

In this paper, we improve the three main steps of bacterial foraging in dealing with slow speed problems in the ELD process. The step size is a key factor affecting the speed of the BFO algorithm. Therefore, in this paper, an improved adaptive correction step size is used to replace the fixed step size in the chemotaxis process to speed up the convergence speed of ICSBFO. Given the excellent hybridization of the CSO algorithm, we propose to use the CSO operator to hybridize the population in the replication process to ensure the diversity of the population; in the dispersal part, the adaptive dynamic dispersal probability is used instead of the fixed probability to solve the problem that the traditional BFO algorithm easily leads to the loss of the optimal solution, and the algorithm efficiency is guaranteed. The mathematical model of the ELD problem is established. By comparing with other algorithms, it is proved that the ICSBFO proposed in this paper has excellent performance, which can significantly reduce coal consumption and improve the economic benefits of the power plant. At the same time, through the case study of small-scale units, it is found that ICSBFO can also solve the problem that BFO is not good at processing the scheduling data of small-scale units. In the follow-up research, we will try to apply ICSBFO to the problems of multi-objective microgrid scheduling optimization and multi-region joint dynamic economic scheduling and add disturbances to the population initialization and dispersal stage of ICSBFO to test the performance of the algorithm.

Data availability statement

The original contributions presented in the study are included in the article/supplementary material, further inquiries can be directed to the corresponding author.

Author contributions

Conceptualization and Methodology, YZ; Data curation and Investigation, YL.

Funding

This work is supported by the fund of the education department of Jilin province No. JJKH20210257KJ, the fund of the Science and Technology Development Project of Jilin Province No. 20220203190SF.

Conflict of interest

The authors declare that the research was conducted in the absence of any commercial or financial relationships that could be construed as a potential conflict of interest.

Publisher’s note

References

Al-Bahrani, L. T., and Patra, J. C. (2018). Multi-gradient PSO algorithm for optimization of multimodal, discontinuous and non-convex fuel cost function of thermal generating units under various power constraints in smart power grid. *Energy* 147, 1070–1091. doi:10.1016/j.energy.2017.12.052

Anbo, M., Cong, Z., Xuancong, X., Weifeng, D., Shiyun, L., De, C., et al. (2022). Decentralized power economic dispatch by distributed crisscross optimization in multi-agent system. *Energy* 246, 123392. doi:10.1016/j.energy.2022.123392

Aye, C. M., Pholdee, N., Yildiz, A. R., Bureerat, S., and Sait, S. M. (2019). Multi-surrogate-assisted metaheuristics for crashworthiness optimisation. *Int. J. Veh. Des.* 80 (2-4), 223–240. doi:10.1504/ijvd.2019.109866

Basu, M. (2016). Quasi-oppositional group search optimization for multi-area dynamic economic dispatch. *Int. J. Electr. Power Energy Syst.* 78, 356–367. doi:10.1016/j.ijepes.2015.11.120

Carmen, F. M., Stefano, P., Mauro, C., and Federico, Q. (2021). A review on unit commitment algorithms for the Italian electricity market. *Energies* 15 (1), 18. doi:10.3390/en15010018

Chen, G., Heng, T., and Ben, N. (2021). Evolutionary state-based novel multi-objective periodic bacterial foraging optimization algorithm for data clustering. *Expert Syst.* 39 (1). doi:10.1111/exsy.12812

Chen, Y.-P., Li, Y., Wang, G., Zheng, Y.-F., Xu, Q., Fan, J.-H., et al. (2017). A novel bacterial foraging optimization algorithm for feature selection. *Expert Syst. Appl.* 83, 1–17. doi:10.1016/j.eswa.2017.04.019

Chi, K. L., Thi, B. N. T., Minh, P. T., and Trung, N. T. (2022). Coot optimization algorithm for optimal placement of photovoltaic generators in distribution systems considering variation of load and solar radiation. *Math. Problems Eng.* 2022, 1–17. doi:10.1155/2022/2206570

de, M. C. H. V., de, V. B. J. L., Germano, L., de, A. G. C. C., and Almeida, C. C. I. d. (2022). Intelligent power distribution restoration based on a multi-objective bacterial foraging optimization algorithm. *Energies* 15 (4), 1445. doi:10.3390/en15041445

Devi, J. A., and Srinivasan, V. P. (2021). A two-fold optimization framework using hybrid B2 algorithm for resource allocation in long-term evolution based cognitive radio networks system. *Int. J. Commun. Syst.* 35 (3). doi:10.1002/dac.5023

Farshi, T. R., and Orujpour, M. (2021). “A multi-modal bacterial foraging optimization algorithm,” in *Journal of ambient intelligence and humanized computing*. (prepublish).

Hatata, A. Y., and Hafez, A. A. (2019). Ant lion optimizer versus particle swarm and artificial immune system for economical and eco-friendly power system operation. *Int. Trans. Electr. Energy Syst.* 29 (4), e2803. doi:10.1002/etep.2803

Hu, J., Jin, N., Li, P., and Zhang, H. (2020). *An improved bacterial foraging algorithm for multi-modal problems*. 中国湖北武汉.

Jianjun, W., Shuo, Z., Jikun, H., Yan, Z., Li, L., and Taoya, H. (2021). Dispatch optimization of thermal power unit flexibility transformation under the deep peak shaving demand based on invasive weed optimization. *J. Clean. Prod.* 315, 128047. doi:10.1016/j.jclepro.2021.128047

Jufeng, W., Chunfeng, L., and MengChu, Z. (2020). Improved bacterial foraging algorithm for cell formation and product scheduling considering learning and forgetting factors in cellular manufacturing systems. *IEEE Syst. J.* 14, 3047–3056. doi:10.1109/jsyst.2019.2963222

Kopiske, J., Spieker, S., and Tsatsaronis, G. (2017). Value of power plant flexibility in power systems with high shares of variable renewables: A scenario outlook for Germany 2035. *Energy* 137, 823–833. doi:10.1016/j.energy.2017.04.138

Kumar, C. V., and Babu, M. R. (2021). An exhaustive solution of power system unit commitment problem using enhanced binary salp swarm optimization algorithm. *J. Electr. Eng. Technol.* 17, 395–413. (prepublish). doi:10.1007/s42835-021-00889-0

Long, Y., Zuo, Z., Su, Y., Li, J., and Zhang, H. (2020). An A*-based bacterial foraging optimisation algorithm for global path planning of unmanned surface vehicles. *J. Navigation* 73, 1247–1262. doi:10.1017/s0373463320000247

Mahdi, F. P., Vasant, P., Abdullah-Al-Wadud, M., Watada, J., and Kallimani, V. (2018). A quantum-inspired particle swarm optimization approach for environmental/economic power dispatch problem using cubic criterion function. *Int. Trans. Electr. energy Syst.* 28 (3), e2497. doi:10.1002/etep.2497

Meng, A., Hu, H., Yin, H., Peng, X., and Guo, Z. (2015). Crisscross optimization algorithm for large-scale dynamic economic dispatch problem with valve-point effects. *Energy* 93, 2175–2190. doi:10.1016/j.energy.2015.10.112

Nguyen, T., Trung, N., Thanh, T., and Quan, M. (2022). “An improved equilibrium optimizer for optimal placement of photovoltaic systems in radial distribution power networks,” in *Neural computing and applications*. (prepublish).

Panagant, N., Pholdee, N., Bureerat, S., Yildiz, A. R., and Sait, S. M. (2020). Seagull optimization algorithm for solving real-world design optimization problems. *Mater. Test.* 62 (6), 640–644. doi:10.3139/120.111529

Pham, L., Huu, D., Hoang, N. B., and Trung, T. (2022). “Optimal power flow for an integrated wind-solar-hydro-thermal power system considering uncertainty of wind speed and solar radiation,” in *Neural computing and applications*. (prepublish).

Premkumar, M., Jangir, P., Kumar, B. S., Sowmya, R., Alhelou, H. H., Abualigah, L., et al. (2021). A new arithmetic optimization algorithm for solving real-world multiobjective CEC-2021 constrained optimization problems: Diversity analysis and validations. *IEEE ACCESS* 9, 84263–84295. doi:10.1109/access.2021.3085529

Ramaporselvi, R., and Geetha, G. (2021). Congestion management in deregulated power system using adaptive moth swarm optimization. *COMPEL - Int. J. Comput. Math. Electr. Electron. Eng.* 41, 334–356. doi:10.1108/compel-06-2021-0198

Shaowei, W., Wenlong, T., Bo, O., and Jeng-Shyang, P. (2021). Reversible data hiding method for multi-histogram point selection based on improved crisscross optimization algorithm. *Inf. Sci.* 549, 13–33. doi:10.1016/j.ins.2020.10.063

Wang, Y., Cui, Z., and Li, W. (2019). A novel coupling algorithm based on glowworm swarm optimization and bacterial foraging algorithm for solving multi-objective optimization problems. *Algorithms* 12 (3), 61. doi:10.3390/a12030061

Wu, T., Wei, H., Ge, Z., Yang, L., and Du, X. (2019). Cooling water mass flow optimization for indirect dry cooling system of thermal power unit under variable output load. *Int. J. Heat Mass Transf.* 133, 1–10. doi:10.1016/j.ijheatmasstransfer.2018.12.097

Xiongmin, T., Zhengshuo, L., Xuancong, X., Zhijun, Z., Tianhong, J., Wenrui, F., et al. (2022). Multi-objective economic emission dispatch based on an extended crisscross search optimization algorithm. *Energy* 244, 122715. doi:10.1016/j.energy.2021.122715

Yildiz, A. R., and Erdas, M. U. (2021). A new Hybrid Taguchi-salp swarm optimization algorithm for the robust design of real-world engineering problems. *Mater. Test.* 63 (2), 157–162. doi:10.1515/mt-2020-0022

Yildiz, B. S., Kumar, S., Pholdee, N., Bureerat, S., Sait, S. M., and Yildiz, A. R. (2022c). A new chaotic Levy flight distribution optimization algorithm for solving constrained engineering problems. *EXPERT Syst.* 39 (8). doi:10.1111/exsy.12992

Yildiz, B. S., Patel, V., Pholdee, N., Sait, S. M., Bureerat, S., and Yildiz, A. R. (2021c). Conceptual comparison of the ecogeography-based algorithm, equilibrium algorithm, marine predators algorithm and slime mold algorithm for optimal product design. *Mater. Test.* 63 (4), 336–340. doi:10.1515/mt-2020-0049

Yildiz, B. S., Pholdee, N., Bureerat, S., Erdas, M. U., Yildiz, A. R., and Sait, S. M. (2021a). Comparision of the political optimization algorithm, the Archimedes optimization algorithm and the Levy flight algorithm for design optimization in industry. *Mater. Test.* 63 (4), 356–359. doi:10.1515/mt-2020-0053

Yildiz, B. S., Pholdee, N., Bureerat, S., Yildiz, A. R., and Sait, S. M. (2022a). Enhanced grasshopper optimization algorithm using elite opposition-based learning for solving real-world engineering problems. *Eng. Comput.* 38 (5), 4207–4219. doi:10.1007/s00366-021-01368-w

Yildiz, B. S., Pholdee, N., Bureerat, S., Yildiz, A. R., and Sait, S. M. (2021b). Robust design of a robot gripper mechanism using new hybrid grasshopper optimization algorithm. *EXPERT Syst.* 38 (3). doi:10.1111/exsy.12666

Yildiz, B. S., Pholdee, N., Bureerat, S., Yildiz, A. R., and Sait, S. M. (2020). Sine-cosine optimization algorithm for the conceptual design of automobile components. *Mater. Test.* 62 (7), 744–748. doi:10.3139/120.111541

Yildiz, B. S., Pholdee, N., Panagant, N., Bureerat, S., Yildiz, A. R., and Sait, S. M. (2022b). A novel chaotic Henry gas solubility optimization algorithm for solving real-world engineering problems. *Eng. Comput.* 38 (2), 871–883. doi:10.1007/s00366-020-01268-5

Yildiz, B. S. (2020). Robust design of electric vehicle components using a new hybrid salp swarm algorithm and radial basis function-based approach. *Int. J. Veh. Des.* 83 (1), 38–53. doi:10.1504/ijvd.2020.10037481

Yufang, D., and Jianwen, T. (2021). Knowledge worker scheduling optimization model based on bacterial foraging algorithm. *Future Gener. Comput. Syst.* 124, 330–337. doi:10.1016/j.future.2021.05.028

Zou, D., Li, S., Kong, X., Ouyang, H., and Li, Z. (2019). Solving the combined heat and power economic dispatch problems by an improved genetic algorithm and a new constraint handling strategy. *Appl. Energy* 237, 646–670. doi:10.1016/j.apenergy.2019.01.056

Nomenclature

S The number of bacteria

N_c Maximum number of chemotaxis

N_s Maximum number of steps of one–way movement in chemotaxis operation

N_{re} Number of replication

N_{ed} Maximum number of dispersal

P_{ed} The fixed probability of bacterial dispersal

d_attract, ommiga_attract The number of attractive factors and the release speed

h_repellant, ommiga_repellant The number of repellant factors and the release speed

P Population

C Step size

J Fitness value

Frontiers in Energy Research

TYPE Original Research
PUBLISHED 02 March 2023
DOI 10.3389/fenrg.2023.1144785

OPEN ACCESS

EDITED BY
Xin Ning,
Institute of Semiconductors (CAS), China

REVIEWED BY
Gabriel Gomes,
State University of Campinas, Brazil
Tomasz Górski,
University of Gdansk, Poland
Rui Wang,
Northeastern University, China

*CORRESPONDENCE
Qiang Li,
liqiang1@ehv.csg.cn

SPECIALTY SECTION
This article was submitted to Smart Grids, a section of the journal Frontiers in Energy Research

RECEIVED 15 January 2023
ACCEPTED 10 February 2023
PUBLISHED 02 March 2023

CITATION
Wu J, Li Q, Chen Q, Zhang N, Mao C, Yang L and Wang J (2023), Fault diagnosis of the HVDC system based on the CatBoost algorithm using knowledge graphs.
Front. Energy Res. 11:1144785.
doi: 10.3389/fenrg.2023.1144785

Fault diagnosis of the HVDC system based on the CatBoost algorithm using knowledge graphs

Jiyang Wu[1], Qiang Li[1]*, Qian Chen[1], Nan Zhang[2], Chizu Mao[2], Litai Yang[3] and Jinyu Wang[3]

[1]EHV Power Transmission Company, China Southern Power Grid Co., Ltd., Guangzhou, China, [2]Maintenance and Test Center of CSG EHV Power Transmission Company, China Southern Power Grid Co., Ltd., Guangzhou, China, [3]EHV Power Transmission Company, China Southern Power Grid Co., Ltd., Dali, China

In order to overcome the difficulty of fault diagnosis in the high-voltage direct current (HVDC) transmission system, a fault diagnosis method based on the categorical boosting (CatBoost) algorithm is proposed in this work. To make the research conform to the actual situation, three kinds of measured fault data in the HVDC system of the Southern Power Grid are selected as the original data set. First, the core role and significance of fault diagnosis in knowledge graphs (KGs) are given, and the characteristics and specific causes of the four fault types are explained in detail. Second, the fault dates are preprocessed and divided into the training data set and the test data set, and the CatBoost algorithm is employed to train and test fault data to realize fault diagnosis. Finally, to verify the progressiveness and effectiveness of the proposed method, the diagnostic results obtained by CatBoost are compared with those obtained by the BP neural network algorithm. The results show that the diagnostic accuracy of the CatBoost algorithm in the three test sets is always higher than that of the BP neural network algorithm; the accuracy rates in the three case studies of the CatBoost algorithm are 94.74%, 100.00%, and 98.21%, respectively, which fully proves that the CatBoost algorithm has a very good fault diagnosis effect on the HVDC system.

KEYWORDS
HVDC, CatBoost, fault diagnosis, knowledge graph, BP

1 Introduction

With the development of the human society, the issues of environmental pollution and resource shortage are becoming more and more serious (Mohamed et al., 2020; Tanmay et al., 2020). Energy conservation and emission reduction, and recycling of resources have widely attracted the attention of all countries in the world (Yang et al., 2017; Mehdi and Mehdi, 2020). The emergence of electric energy has greatly changed the way of energy consumption; using electric energy to replace bulk coal, fuel oil, and other energy sources can effectively alleviate the energy crisis and reduce environmental pollution (Yang et al., 2019). In particular, the development and utilization of renewable energy sources, such as wind and solar energy, have greatly improved the energy structure and promoted the development of contemporary new power systems (Yang et al., 2018; Li R. S et al., 2020; Wang et al., 2021; Wang et al., 2022). In recent years, in the process of social and economic development, many advanced technologies have been applied to further improve the quality and efficiency of

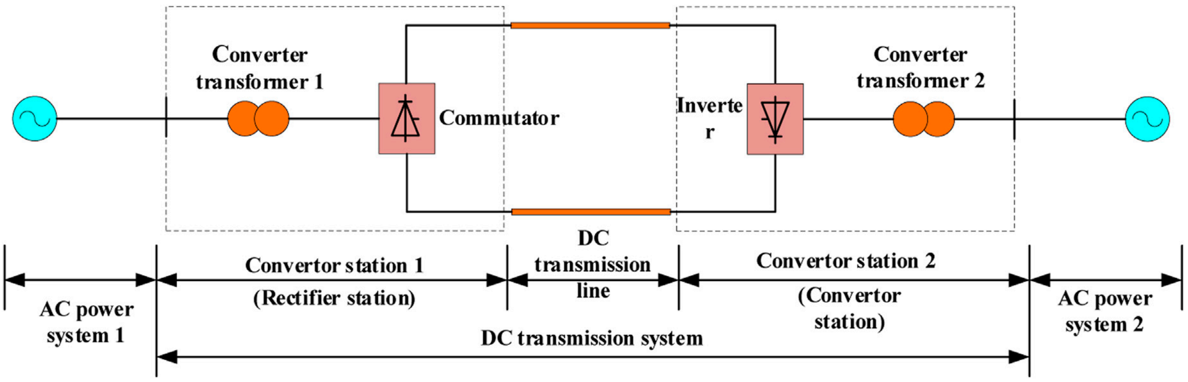

FIGURE 1
Block diagram of the HVDC system.

power transmission, thus promoting the growth of social economy. At present, there are three main transmission methods in the power system: high-voltage direct current (HVDC), high-voltage alternating current (HVAC), and low-frequency alternating current (LFAC) transmissions (Reed et al., 2013; Zhang et al., 2013; Yao et al., 2015; Meng et al., 2021). Among them, the application of HVDC technology has not only effectively improved the quality of power resource transmission to meet the requirements of people's daily life but also further optimized the operation performance of the power grid system (Li, 2010; Ma et al., 2022). In order to accelerate the transformation of the development mode of electric power and enhance the ability of the grid to optimize the allocation of resources on a large scale, the State Grid Corporation has proposed the strategic goal of building a strong smart grid with an ultra-high vacuum grid as the backbone.

HVDC has a large transmission capacity, fast and flexible power regulation, and is widely used in long-distance high-capacity transmission projects. However, with the increase in voltage levels, the problem of commutation failure in the transmission system is becoming increasingly prominent (Zeng et al., 2016; Li G et al., 2020). As shown in Figure 1, the HVDC system is composed of three parts, namely, the rectifier station, inverter station, and direct current (DC) line, which can convert three-phase AC power into DC power through rectification of the converter station and then send it to another converter station through the DC transmission line to reverse into three-phase AC power. Structurally, it is a power electronic rectifier circuit in the form of alternating current (AC)–DC–AC. In HVDC systems, AC-side faults, lightning faults, short-circuit faults, and inverter phase change failures bring great challenges to the normal operation of the transmission system.

The converter station is often compared to the heart of the DC system. As the most important component in the DC transmission system, its controllability and the characteristics of single conduction also constitute as important features of the fault behavior of the DC transmission system. These characteristics are mainly expressed in the triggering, conduction, and shutdown of the converter valve (Zheng and Peng, 2019; Li G et al., 2020). The converter failure can be divided into main circuit failure and control system failure. The converter main circuit failure is divided into the short circuit of the converter valve, DC-side outlet short circuit, DC-side ground short circuit, AC-side phase short circuit, and AC-side ground short circuit (Chen et al., 2022). The control system fault refers to whether the converter valve is opening or not opening (Zhou et al., 2022). Furthermore, commutation failure is the most common system fault in HVDC systems, which can lead to DC voltage drop and DC increase for a short period of time, and may lead to system shutdown in serious cases. Commutation failure is very similar to the transient process of DC and DC voltage during the DC line short circuit, and if the type of fault cannot be accurately distinguished, it will cause the protection device to operate incorrectly. Therefore, after a fault occurs on a high-voltage DC transmission line, it is critical to make a quick and accurate diagnosis of the fault, isolate the faulty element after the accident, and adopt an appropriate control and protection strategy (Torres-Olguin and Garces, 2017; Zhang et al., 2021).

At present, the main methods used for phase change failure fault diagnosis include the minimum voltage drop method and the phase comparison method. An improved morphological filter used to decompose the DC signal in different faults is proposed in the literature (Vidlak et al., 2021), which can extract accurately the morphological spectrum under each scale and calculate the energy entropy and singular entropy of the decomposed morphological spectrum. Meanwhile, wavelet scale energy statistics and wavelet scale energy entropy can be utilized to correctly identify the commutation failure of the HVDC system (Xiong et al., 2019). In the issue of current sharing/voltage regulation, Wang et al. (2022) proposed an adaptive dynamic programming approach based on the Bellman principle, which facilitates the analysis and treatment of AC and DC faults in the system. Furthermore, in order to overcome the small-signal instability problem in the power system, Wang et al. (2021) proposed a droop coefficient stability region analysis approach based on the generalized incidence matrix, which can help in information extraction from the fault diagnosis model in the system. Faced with the massive transmission system equipment alarm information, the maintenance personnel cannot expressly and accurately locate the cause of the fault that generates the alarm, which leads to the inefficiency of fault handling and, in turn, cannot meet the growing demand for intelligent management of the power grid. In the past, the main power system fault reasoning and diagnosis included expert systems (Xiao et al., 2021), configurable rules (Trondoli et al., 2022), fuzzy reasoning (Lokanadham and Subbaiah, 2021), and neural network (Giljum et al., 2021). The research ideas of fault diagnosis are mainly used to sort, train, classify, and identify the historical fault data, and the most important idea is to train the diagnosis model according to the data set so that it can use the data features as much as possible for classification. Górski (2022) proposed a smart contract testing pattern for the symmetric array, which can significantly limit the needed number of test cases and save the calculation cost. However, in the actual power system, most of the fault data are asymmetric, so the follow-up research work is mainly based on the fault data on the asymmetric array. Wang et al. (2023) proposed a robust diagnosis method of photovoltaic (PV) array faults considering label errors in training data, which can effectively improve the efficiency of fault diagnosis. Both of these methods can effectively train the original data set, which is highly important for regression testing. The difference is that the training data set used by Górski (2022) is symmetric, and research focused on reducing the calculation cost, while the data set used by Wang et al. (2023) simulated the actual PV array data and focused on improving the accuracy of fault diagnosis.

In this context, the development and utilization of the HVDC system knowledge graph (KG) (Li et al., 2021) enable data collection, data processing, problem analysis, application services, and data analysis functions for the entire HVDC system. With the rapid development of artificial intelligence, KG has become one of the core driving technologies to drive the development of cognitive intelligence, while the widespread application of deep learning techniques and distributed word vector representation of natural language words provide a new basis for the in-depth application of different artificial intelligence methods in natural language processing.

Almost all traditional intelligent fault identification methods use shallow learning models, which are difficult to represent the complex relationships that exist between transmission system faults and the signals to be detected, making it difficult to deal with complex pattern recognition problems. Therefore, there is an urgent need to develop new methods that can automatically extract features. In this work, a fault diagnosis of the HVDC system based on the categorical boosting (CatBoost) algorithm is proposed, which can effectively extract fault data features for accurate identification of various types of HVDC faults based on fault data knowledge mapping. Compared with the existing studies, the fault diagnosis model proposed in this paper combines the mechanism of the knowledge map, and the results can be visually designed. At the same time, the transmission network and data set are from the actual framework and fault data on the Southern Power Grid, which have certain authenticity and reliability. Moreover, this study uses the backpropagation (BP) neural network as a comparison method to diagnose HVDC system faults. The test results show that the proposed method shows good performance and high accuracy in fault diagnosis of the HVDC system. The main contributions and innovations of this work are listed as follows:

1. According to the application of the knowledge atlas in the power system, based on the transmission system of a power grid in southwest China, a fault diagnosis model of the HVDC system based on the CatBoost algorithm is proposed, and the accuracy of fault diagnosis can be up to 94%.
2. The fault types mainly include the AC fault, DC fault, converter valve fault, and commutation failure. The causes of these four types of faults are specifically analyzed in this paper. The fault data mainly come from the measured data on a power grid in southwest China, which has certain authenticity and reliability.
3. In order to verify the progressiveness and effectiveness of the proposed method, BP is used as the comparison algorithm in the case of the same data set. The experimental results show that the CatBoost algorithm fault diagnosis accuracy is higher than BP in the three data sets.
4. To improve the readability of this paper and the reference value of power system fault diagnosis, three constructive prospects for future research studies are presented.

The rest of this work is structured as follows: the HVDC system KG is established in Section 2. Section 3 introduces the four common faults of HVDC, namely, the AC fault, DC fault, converter valve fault, and commutation failure. The principle, framework, and execution process of CatBoost are provided in Section 4 and Section 5. In Section 6, case studies and statistical analysis are carried out. The main discussion and limitations to this study are discussed in Section 7. Finally, conclusions and future developments are given in Section 8.

2 HVDC system knowledge graph

Knowledge mapping relational reasoning is an effective means to solve knowledge verification, prediction, and inference. By combining KG with text, entities and relations can be mapped to a specific vector space to establish logical relationships between entities and relations, thus realizing knowledge reasoning and meeting the needs of intelligent diagnosis and decision-making for complex relational scenarios in grid fault diagnosis. The construction of the HVDC system KG mainly includes six steps, as shown in Figure 2. It mainly includes knowledge acquisition, knowledge analysis, knowledge base establishment, graph construction, knowledge service, and knowledge application. It mainly includes three parts, namely, the knowledge system construction layer, knowledge service layer, and knowledge application layer (Wu et al., 2022). In the face of massive data, including images, text, and electrical signals, it is necessary to establish a knowledge map of fault diagnosis of the HVDC transmission system. Through the sorting and classification of historical fault data sets, the type and time of fault occurrence can effectively be predicted, thus reducing the losses caused by faults in the power system.

2.1 Knowledge acquisition

In the HVDC system, the knowledge sources are extremely complex. Some data included are the operation and maintenance data on the HVDC system, as well as some engineering data or technical breakthrough data. Due to the diversity of knowledge source paths, it is necessary to classify various knowledge sources in the process of building the graph. In addition, there are various ways to carry data. In the HVDC system, some data are in the text format

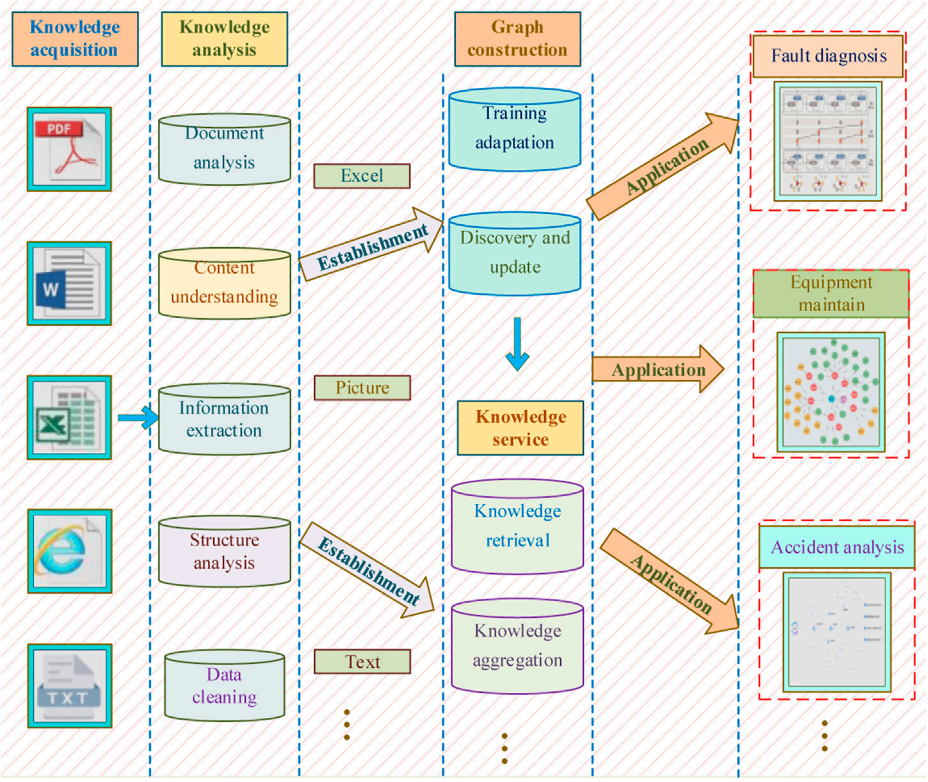

FIGURE 2
HVDC system KG construction diagram.

(Chen et al., 2020), such as various technical research materials, while some data are in the excel format, such as the temperature and humidity of some equipment, and some data are in some picture types, such as the fault waveform obtained using the fault recorder. Due to the diverse ways of carrying data, it is necessary to establish a corresponding knowledge base for storage; this can improve the efficiency of the whole KG.

2.2 Knowledge graph reasoning

The inference of the KG mainly refers to relational inference, the core of which is to infer unknown entities or relations based on existing entities or relations and can help achieve the complementation of the KG and the prediction of entities and relations. The core idea of the KG relational inference is to find a mapping function that graphs symbolic representations to vector spaces for numerical representations, extracts implicit associations between entities and relations, and uses associative knowledge for inference. TransE is inspired by the translation invariance in word vectors and represents both entities and relations as vectors, and for a specific relation. The TransE model performs well for simple entity relationships but does not perform well for mappings of multiple relationships (Zeng et al., 2022).

The training process of the KG relies on a collection of triples derived from existing data, each of which is a training sample of the KG containing the relationships between the head and tail entities, to build a semantic network of the KG for high-voltage DC transmission systems using a translation-based model.

2.3 Knowledge base establishment

In order to realize the fault diagnosis of the HVDC system with limited fault feature data available, this paper proposes a method based on knowledge mapping CatBoost decision tree technology to construct fault diagnosis of the HVDC system, using theoretical analysis and experimental research to realize the safety state assessment and fault analysis and prediction of the HVDC system. By sending requests to the knowledge base of the HVDC system, fault record data are obtained; then, data are extracted from the key record segments, and the processed fault data are inputed into the risk analysis model of the HVDC system for fault classification. Figure 3 shows the fault handling and risk analysis framework of the KG-based HVDC system. Finally, the effectiveness and accuracy of the proposed method are verified by the real historical data set of an actual operation of a substation in the Southern Power Grid.

3 Fault classifications

There are many common faults in the HVDC system, such as the AC fault, DC fault, inverter commutation fault (Nanayakkara et al., 2012), converter valve fault (Narendra et al., 1998), single-phase

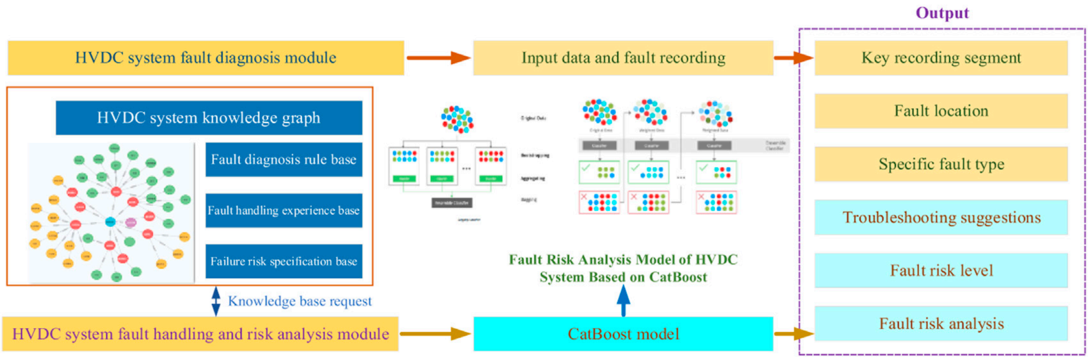

FIGURE 3
Flow chart of KG-based DC transmission system fault handling and the risk analysis module.

fault (Vidal et al., 2015), interphase fault, and lightning stroke fault (Pauli et al., 1988). According to the statistics of a substation in the Southwest China Power Grid, since the converter station was put into operation in 2010, the average number of annual occurrences of the AC fault, DC fault, converter valve fault, and commutation failure is 11.6, 16.2, 14.2, and 16.8, respectively, which caused a hidden danger to the safe and stable operation of the system. Therefore, this paper mainly studies these four types of faults, and the fault diagnosis model based on the CatBoost algorithm is constructed by taking the measured data on a substation in the Southwest China Power Grid as the original data set.

3.1 AC fault

The power regulation of DC transmission is fast and flexible. It does not have the stability problem of synchronous operation. Therefore, it is considered an ideal ultra-high voltage and long-distance transmission mode (Li et al., 2007; Zheng et al., 2020). However, the failure rate of the DC system is relatively high, and AC and DC parallel operations also have the problem of interaction between AC and DC. In particular, the main grid of the power transmission from the west to the east of the China Southern Power Grid presents the characteristics of strong DC and weak AC: the proportion of DC transmission is large, while the AC system running in parallel with it is relatively weak. When DC system fails, the power angle may be stable due to a large range of power transfer voltage stability failure, which, to a certain extent, affects the safety and stability of the system and the performance of the transmission channel capacity (Guo et al., 2018). Similarly, for the multi-infeed DC system, if the AC fault cannot be removed in time, it may also lead to the simultaneous locking of multiple DC lines, resulting in system stability failure. The schematic diagram of the AC fault in the HVDC system is shown in Figure 4A.

3.2 DC fault

The HVDC transmission system is often considered in long-distance transmission projects, but long lines also bring many safety problems, and the probability of failure caused by long distance is high. The probability of short circuit to ground is the largest in the DC transmission system, accounting for more than 80% of the DC transmission system line faults, most of which is flashover discharge. Generally, the ground flashover of the DC transmission system is mainly caused by damage to the insulation between the transmission line and the ground. The common causes are the breakdown of the air caused by lightning, the reduction of the insulation level caused by pollution, and the ground flashover caused by the shortening of the insulation distance caused by tree branches. The schematic diagram of the DC fault in the HVDC system is shown in Figure 4B. The DC line fault includes the grounding fault on a single pole, broken wire fault, and short-circuit fault caused by an abnormal connection between two poles. The permanent fault of the DC transmission system is generally believed to exist for a long time. In practical engineering, the fault should be prevented from further expanding and endangering the power supply reliability of the system (Guo et al., 2018).

3.3 Converter valve fault

During the commutation of the inverter-side converter valve, the single valve of the converter valve appears to be turned off when the positive voltage is too high or has a certain positive voltage when the thyristor is not fully turned off, and the gate is applied with a trigger pulse; the thyristor will be turned on again, causing the converter valve that is turned on to fail to conduct, and the commutation of the converter valve fails (Liu et al., 2015). The turn-off time of the thyristor is usually slightly less than 1 ms. When the converter valve is in inverse operation, the forward voltage will appear after the thyristor bears approximately 1 ms of reverse voltage after the turn-off. When the AC system voltage disturbance or other factors make the thyristor in commutation again, commutation failure may occur. The schematic diagram of the converter valve fault in the HVDC system is shown in Figure 4C. When the converter valve operates at the rectifier side of the DC transmission project, the thyristor bears a continuous reverse voltage greater than 5 ms after it is turned off, and the thyristor can be turned off reliably. Therefore, the converter valve will not

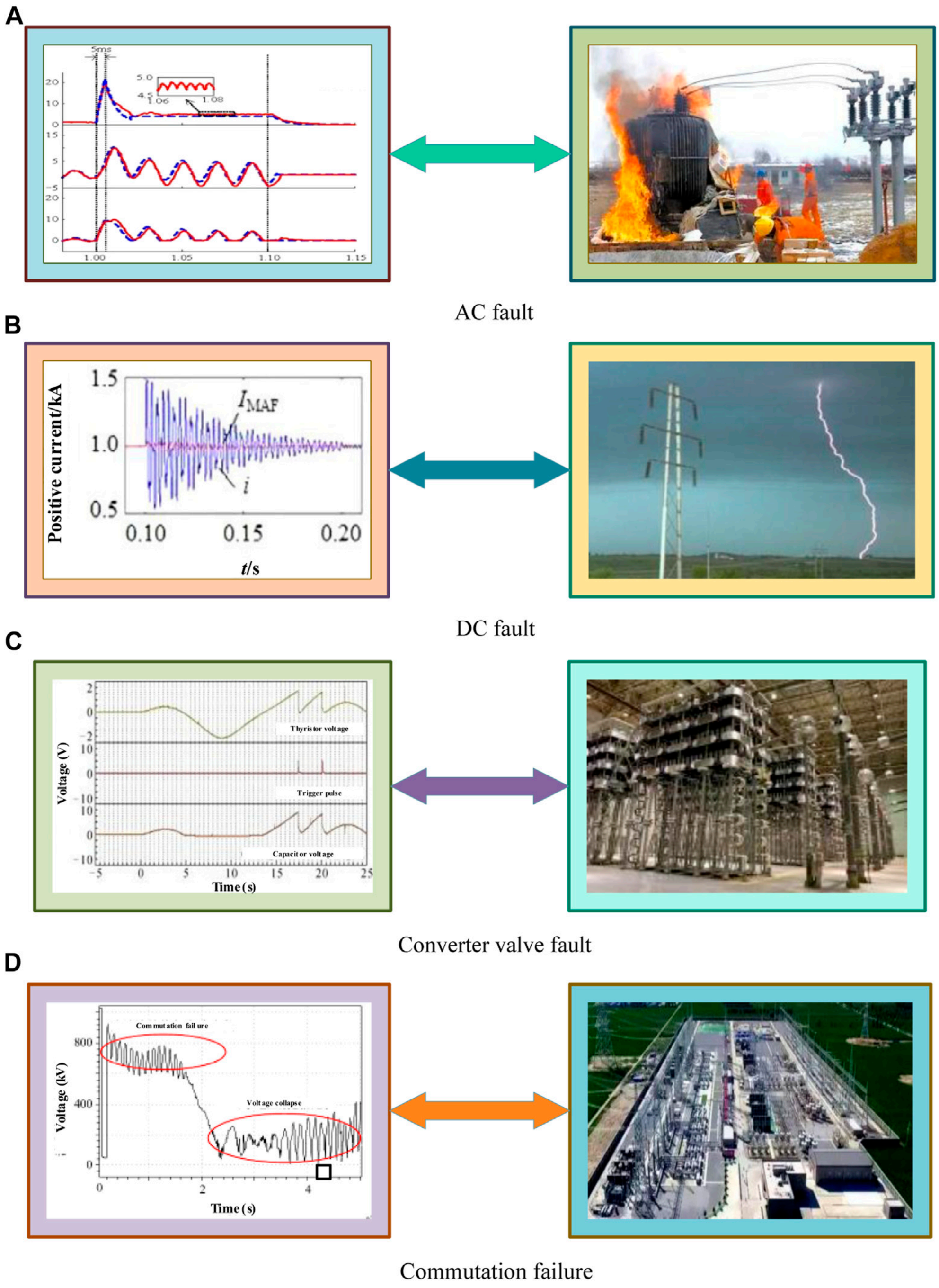

FIGURE 4
Four fault diagrams of the HVDC system. **(A)** AC fault. **(B)** DC fault. **(C)** Converter valve fault. **(D)** Commutation failure.

have a commutation failure fault when it operates at the rectifier side.

3.4 Commutation failure

In the converter, the valve that is out of conduction fails to recover its blocking capacity within a period of time under the action of reverse voltage, or the commutation process is not completed during the reverse voltage, resulting in the valve voltage becoming positive; the commutation valve will reverse the phase of the valve that was originally scheduled to be out of conduction, which is called commutation failure. The schematic diagram of commutation failure in the HVDC system is shown in Figure 4D. The commutation failure is due to a short circuit on the DC side and the open circuit on the AC side of the converter valve that should be turned off but is not turned off, resulting in power fluctuations. In essence, commutation failure is caused by the characteristic that the thyristor is a semi-controlled device, which cannot be completely ignored under the existing technical conditions (Wei et al., 2006).

The commutation failure is essentially caused by external or internal factors that lead to the inverter turn-off angle to be γ. If the voltage is too small, the thyristor will be completely turned off when the online voltage changes from negative to positive, and there will be phase reversal.

The calculation formula of the turn-off angle γ is as follows:

$$\gamma = \arccos\left(\frac{\sqrt{2}\, I_d X_c}{U_L} + \cos\beta\right), \tag{1}$$

where U_L is the AC system line voltage at the inverter side; I_d is the DC system current; β and γ are the lead trigger angle and the turn-off angle of the inverter, respectively; X_c is the equivalent reactance from the power supply to the converter, particularly composed of the converter leakage reactance, which is a fixed value.

4 Principle of the CatBoost algorithm

The handling of category features is a key feature of the CatBoost algorithm, hence its name. The CatBoost algorithm improves the regular target variable statistics method by adding priors to it. In addition, the CatBoost algorithm considers using different combinations of category features to expand the data set feature dimension.

In a set of samples $D = \{(X_k, y_k)\}_{k=1,\ldots,n}$, including $X_k = (x_k^1, \ldots, x_k^m)$, there are m characteristics of random vectors and $y_k \in \mathbb{R}$ as the target; this can be a binary or digital response. For example, (X_k, y_k) is independent and follows some unknown distribution P. The goal of the learning task is to train a function $F\colon \mathbb{R}^m \to \mathbb{R}$ to minimize the expected loss $\mathcal{L}(F) = \mathbb{E}L(y, F(X))$. Here, $L\,()$ is a smoothing loss function, and (X, y) is a test example sampled from P independent of the training set D.

The gradient enhancement procedure iteratively builds an approximate sequence $F^t\colon \mathbb{R}^m \to \mathbb{R}, t = 1, 2, \ldots$ in an insatiable manner. F^t is approximately additive to the previous F^{t-1}: $F^t = F^{t-1} + \alpha h^t$, where a is the step size, and the function $h^t\colon \mathbb{R}^m \to \mathbb{R}$ is selected from the family of functions h to minimize the expected loss:

$$h^t = \underset{h \in H}{argmin}\, \mathcal{L}\left(F^{t-1} + h\right) = \underset{h \in H}{argmin}\, \mathbb{E}L\left(y, F^{t-1}(X) + h(X)\right). \tag{2}$$

The minimization problem is usually treated by Newton's method using the quadratic approximation of $\mathcal{L}(F^{t-1} + h)$ at F^{t-1} or by using the (negative) gradient step. Both of these methods are functional gradient descent. In particular, the choice of the gradient step h^t makes $h^t(X)$ akin to $-g^t(X, y)$. The $g^t(X, y)$ and least squares approximation are usually used.

$$g^t(X, y) = \frac{\partial L(y, s)}{\partial s}\Big|_{s=F^{t-1}(X)}, \tag{3}$$

$$h^t = \underset{h \in H}{argmin}\, \mathbb{E}\left(-g^t(X, y) - h(X)\right)^2. \tag{4}$$

The CatBoost algorithm is a gradient-enhanced implementation that uses a binary decision tree as a basic predictor. The decision tree is based on the values of some split attribute a. The model is built by recursively dividing the feature space R^m into several disjoint regions (tree nodes). Properties are typically binary variables that identify a feature that exceeds some threshold t, that is, $a = |x^k > t|$, where x^k is either a numerical feature or a binary feature, the latter being $t = 0.5$. The decision tree h is as follows:

$$h(X) = \sum_{j=1}^{J} b_j \left[X \in R_j\right], \tag{5}$$

where R_j is the disjoint region corresponding to the leaves of the tree.

4.1 Target statistics

Using target statistics as a new numerical feature seems to be the most efficient way to deal with class features with minimal information loss. Target statistics is widely used and plays a crucial role in classifying features.

One of the biggest purposes of the CatBoost algorithm design is to better handle the category features of GBDT features. The most direct approach of the conventional TS method is to replace the average value of the label corresponding to the category. In the process of GBDT constructing the decision tree, the average value of the replaced category labels is used as the standard for node splitting, which is also known as greedy target-based statistics (Greedy TS), and the calculation formula can be expressed as follows:

$$x_k^i = \frac{\sum_{j=1}^{n} \left[x_j^i = x_k^i\right] \cdot y_j}{\sum_{j=1}^{n} \left[x_j^i = x_k^i\right]}. \tag{6}$$

The aforementioned method has an obvious defect. If the average value of the label is used to represent the feature, the condition deviation problem will occur when the data structure and distribution of the training data set and the test data set are different.

One way to improve greedy target-based statistics is to add a prior distribution so as to reduce the impact of noise and low-frequency category data on data distribution. The formula is as follows:

$$x_k^i = \frac{\sum_{j=1}^{n} \left[x_j^i = x_k^i\right] \cdot y_j + a \cdot p}{\sum_{j=1}^{n} \left[x_j^i = x_k^i\right] + a}, \tag{7a}$$

where p is the added prior term and a is usually a weight coefficient greater than 0.

4.2 Combination features

Another innovation in CatBoost's treatment of category features is that any combination of any number of category features can be built into a new feature. The CatBoost algorithm considers combining these two classification features to form a new classification feature.

Therefore, the CatBoost algorithm uses a greedy strategy to consider the combination of features when building new split nodes. The CatBoost algorithm combines all combination and category-type features of the current tree with all category-type features in the data set and dynamically converts new category-combined features into numerical features.

TABLE 1 Ordered boosting calculation.

```
Algorithm: Ordered boosting
Input: ${(X_k, y_k)}_{k=1}^{n}, I$;
$\sigma \leftarrow$ random permutation of $[1, n]$;
$M_i \leftarrow 0$ for $i = 1...n$; for $t \leftarrow 1$to $I$ do
    for $i \leftarrow 1$ to $n$ do
        $r_i \leftarrow y_i - M_{\sigma(i)-1}(X_i)$
    for $i \leftarrow 1$ to $n$ do
        $\Delta M \leftarrow$ LearnModel $((X_j, r_j): \sigma(j) \le i)$;
        $M_i \leftarrow M_i + \Delta M$
return $M_n$
```

4.3 Prediction shift and ordered boosting

4.3.1 Prediction shift

The so-called prediction shift is the deviation between the distribution of training samples and the distribution of test samples.

CatBoost first reveals the problem of prediction deviation in the gradient lift. It is considered that the predicted deviation, like the TS treatment method, is caused by a special characteristic of target leakage and gradient deviation.

As in the case of TS, the prediction shift is caused by a particular kind of target leak. An ordered enhancement similar to the ordered TS approach is used to solve this problem. The following formula is used:

$$h^t = \underset{h \in H}{\text{argmin}} \frac{1}{n} \sum_{k=1}^{n} \left(-g^t(X_k, y_k) - h(X_k)\right)^2. \tag{7b}$$

4.3.2 Ordered boosting

CatBoost adopted an ordered boosting method based on ordered TS to deal with predicted migration. The sorting promotion algorithm flow is shown in the following figure.

For the training data, ordered boosting first becomes a random arrangement and the random collocation column is used for the subsequent model training. However, the practice of training individual models will greatly increase memory consumption and time complexity; the operability is not strong. Therefore, CatBoost improves this sort of lifting algorithm based on the gradient lifting algorithm based on decision tree learning.

CatBoost offers two boosting modes, ordered and plain. The plain mode simply has to sort the TS operation built into the standard GBDT algorithm, while the ordered mode improved the sorting promotion algorithm.

The complete ordered mode is described as follows: CatBoost generates an independent random sequence of the training set to define and evaluate the splitting of the tree structure and to calculate the value of the leaf node, resulting from the splitting. CatBoost uses a symmetric tree as a base learner, meaning that the splitting criteria are the same at the same level of the tree. A symmetric tree is balanced, not easy to over-fit, and can greatly reduce the test time.

The pseudocode of the CatBoost algorithm is shown in Table 1. It is not difficult to see that when the original data set is input, CatBoost can output the trained data set after training. CatBoost has two enhancement modes, ordered and normal. The latter mode is a standard GBDT algorithm with built-in ordered TS, and the former mode is an effective improvement of Table 1.

CatBoost generates a random arrangement of $s + 1$ independent training data sets. The permutation $\sigma_1, \ldots, \sigma_s$ is used to evaluate the splitting of the defined tree structure (i.e., the internal nodes), while σ_0 serves for choosing the leaf values σ_j of the obtained tree.

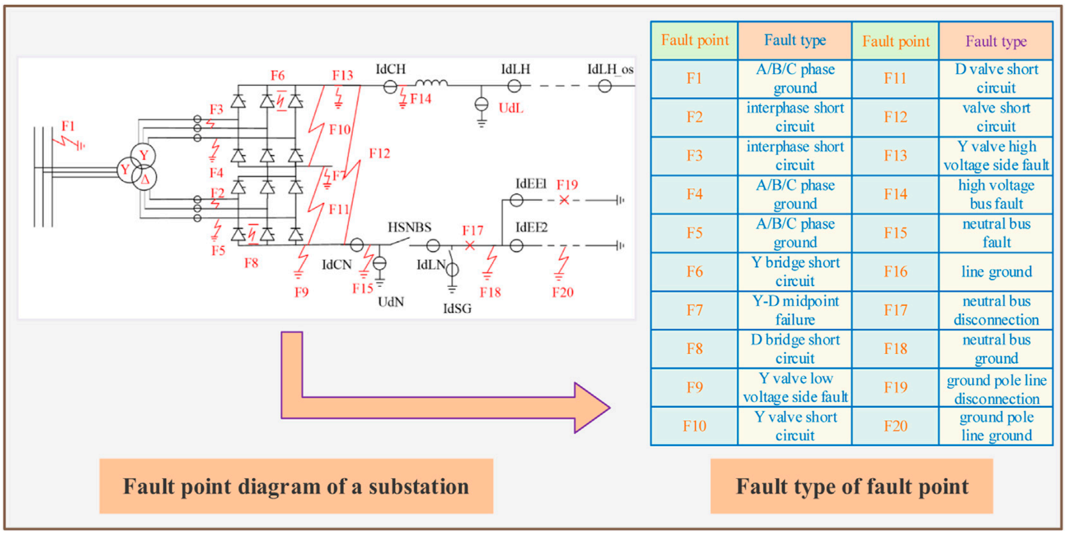

Fault point	Fault type	Fault point	Fault type
F1	A/B/C phase ground	F11	D valve short circuit
F2	interphase short circuit	F12	valve short circuit
F3	interphase short circuit	F13	Y valve high voltage side fault
F4	A/B/C phase ground	F14	high voltage bus fault
F5	A/B/C phase ground	F15	neutral bus fault
F6	Y bridge short circuit	F16	line ground
F7	Y-D midpoint failure	F17	neutral bus disconnection
F8	D bridge short circuit	F18	neutral bus ground
F9	Y valve low voltage side fault	F19	ground pole line disconnection
F10	Y valve short circuit	F20	ground pole line ground

FIGURE 5
Fault type diagram corresponding to fault points of the HVDC system.

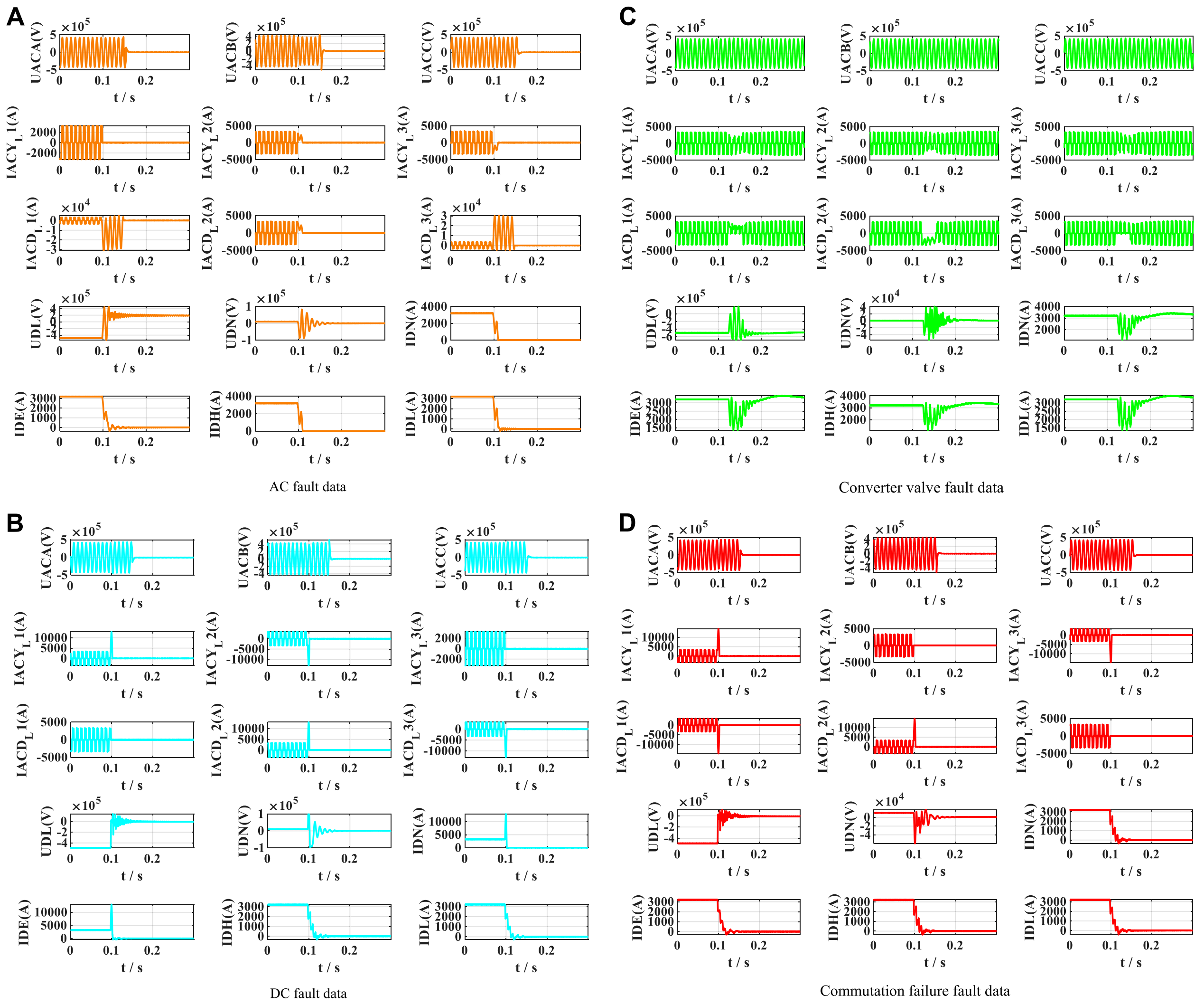

AC fault data

DC fault data

Converter valve fault data

Commutation failure fault data

FIGURE 6
Waveforms of the HVDC system four types of faults. **(A)** AC fault data. **(B)** DC fault data. **(C)** Converter valve fault data. **(D)** Commutation failure fault data.

5 Fault diagnosis model

In this section, according to the four types of fault data measured in the substations of the Southwest Power Grid, the electrical diagram of the transmission system and the corresponding fault types of the fault points are shown in Figure 5. There are 20 fault points in the electrical wiring diagram, and the type represented by each fault point is clearly explained in the right figure. In the original data set, the recorded data on 15 cycles before and after the fault is extracted; the extraction duration of the recorded data is 0.5 s, as shown in Figure 6. Also, the specific meaning of each channel can be referred to from Table 2. It is easy to observe that the 15 channel data mainly record the current and voltage signals of the fault points, and the 15 channel waveforms of the four types of faults are intuitively different, so the characteristics of the data can be used for fault classification and identification. Furthermore, the elements in the data samples of the AC fault, DC fault, converter valve fault, and commutation failure are $N_1 = 10$, $N_2 = 14$, $N_3 = 14$, and $N_4 = 18$, respectively.

After determining the original data, the CatBoost algorithm is used to process and train the four types of fault data, and finally, the fault is diagnosed and the accuracy is calculated. The specific steps are as follows:

First, 15 channel data on each sample in each type of fault data are connected in series to conduct data preprocessing and then stacked according to the number of samples to form a full fault data set. Then, 70% of the total fault data set is randomly selected as training data and 30% as test data. Second, integrated learning is used to extract the features of fault data, and 70% of the data is intensively trained. After determining the number of data classifiers and training data, finally, the remaining 30% of data will be used as test samples for fault diagnosis and classification. The CatBoost classifier is used to train and recognize the training data set, and the accuracy of various fault diagnosis results is

TABLE 2 Channel name and meaning.

Signal	Description meaning	Signal	Description meaning
UACA(V)	A-phase AC voltage	IACD_L$_3$(A)	C-phase AC current of the D-bridge valve side
UACB(V)	B-phase AC voltage	UDL(V)	DC line voltage
UACC(V)	C-phase AC voltage	UDN(V)	Neutral bus voltage
IACY_L$_1$(A)	A-phase AC of the Y-bridge valve side	IDN(A)	Neutral bus current
IACY_L$_2$(A)	B-phase AC of the Y-bridge valve side	IDE(A)	Grounding pole bus current
IACY_L$_3$(A)	C-phase AC of the Y-bridge valve side	IDH(A)	High-voltage bus current
IACD_L$_1$(A)	A-phase AC of the D-bridge valve side	IDL(A)	DC line current
IACD_L$_2$(A)	B-phase AC of the D-bridge valve side		

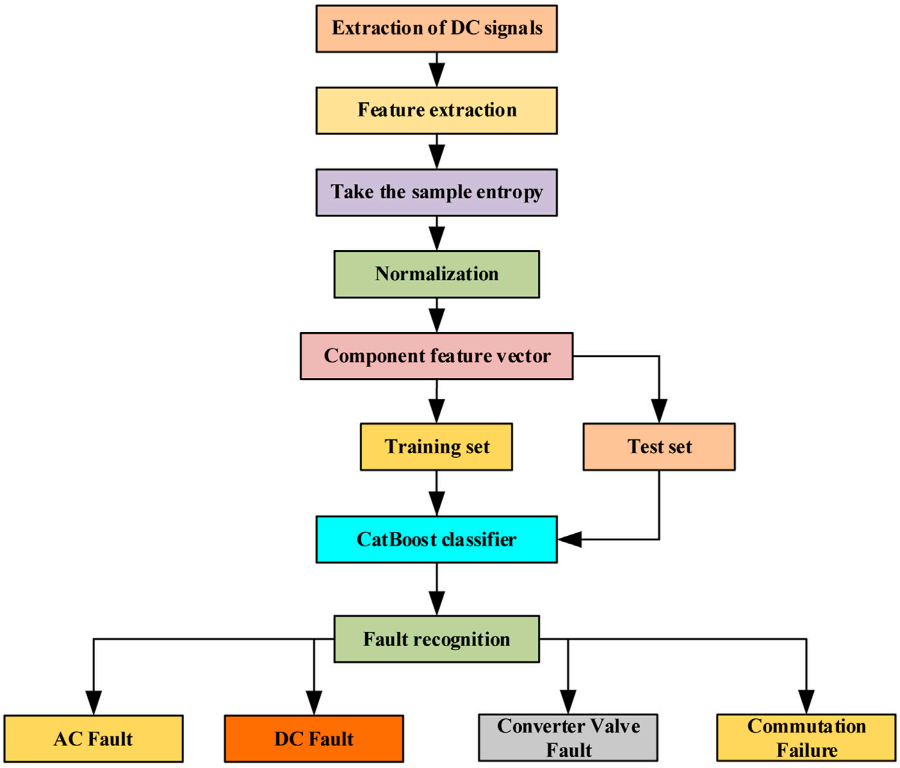

FIGURE 7
CatBoost algorithm fault diagnosis flow chart.

counted. The flow chart of the CatBoost-based fault diagnosis model is shown in Figure 7.

6 Case study

First, the training samples from the fault data are input into the model, and then, the test samples are input. In this paper, in order to reflect the scientific nature of fault diagnosis, the test data are divided into three groups to verify the model. The first group of test data is Y_1 ($n_1 = 3$, $n_2 = 5$, $n_3 = 5$, and $n_4 = 6$), and the second group of test data is the training data itself Y_2 ($n_1 = 7$, $n_2 = 9$, $n_3 = 9$, and $n_4 = 12$). After training the model, the training data itself are substituted into the model for verification. The third group of test data is all the fault data Y_3 ($n_1 = 10$, $n_2 = 14$, $n_3 = 14$, and $n_4 = 18$). In this paper, in order to reflect the effectiveness, diagnostic accuracy, and effectiveness of the CatBoost algorithm in small sample fault diagnosis, the BP neural network algorithm is used for comparison, and the fault diagnosis accuracy of the two methods is compared under the same training set and test set. Finally, in order to intuitively reflect the fault diagnosis accuracy of the two methods for the test set, this paper uses the confusion matrix to visually express the fault diagnosis accuracy.

After the two methods have trained their respective fault diagnosis models, the confusion matrix of fault diagnosis results

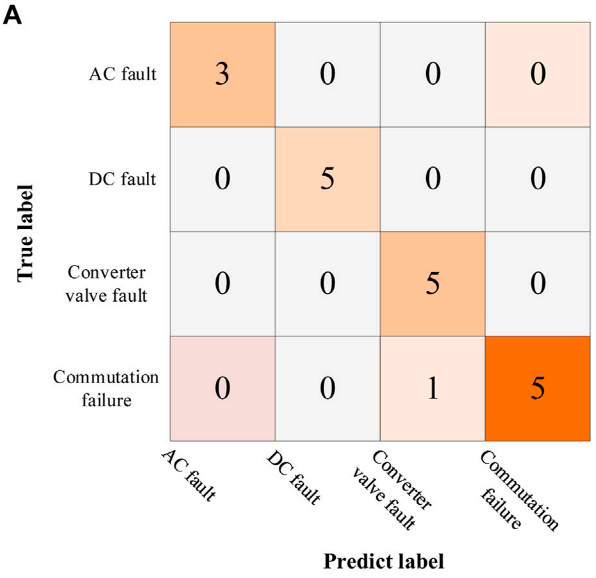

	AC fault	DC fault	Converter valve fault	Commutation failure
AC fault	3	0	0	0
DC fault	0	5	0	0
Converter valve fault	0	0	5	0
Commutation failure	0	0	1	5

CatBoost model test result diagram

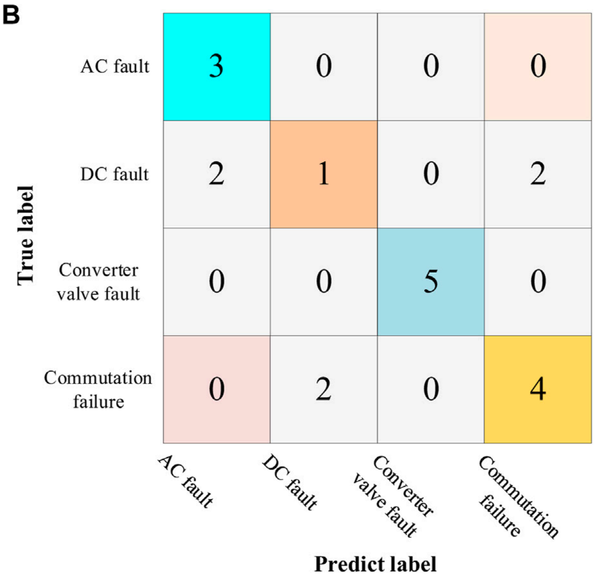

	AC fault	DC fault	Converter valve fault	Commutation failure
AC fault	3	0	0	0
DC fault	2	1	0	2
Converter valve fault	0	0	5	0
Commutation failure	0	2	0	4

BP model test result diagram

FIGURE 8
Confusion matrix of experimental results for the test set Y_1. **(A)** CatBoost model test result diagram. **(B)** BP model test result diagram.

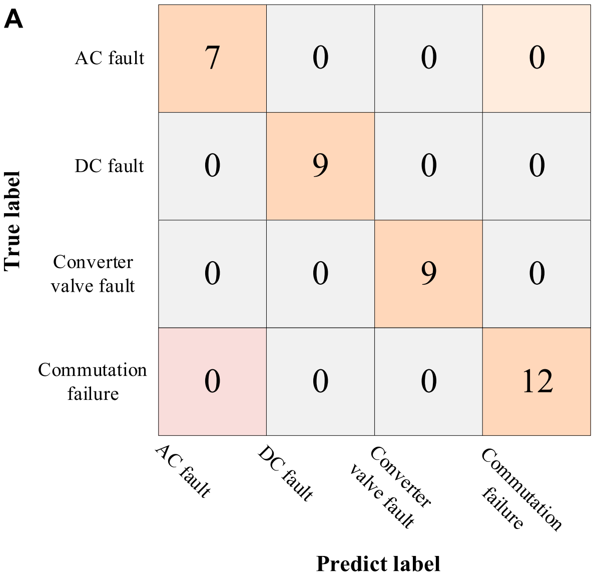

	AC fault	DC fault	Converter valve fault	Commutation failure
AC fault	7	0	0	0
DC fault	0	9	0	0
Converter valve fault	0	0	9	0
Commutation failure	0	0	0	12

CatBoost model test result diagram

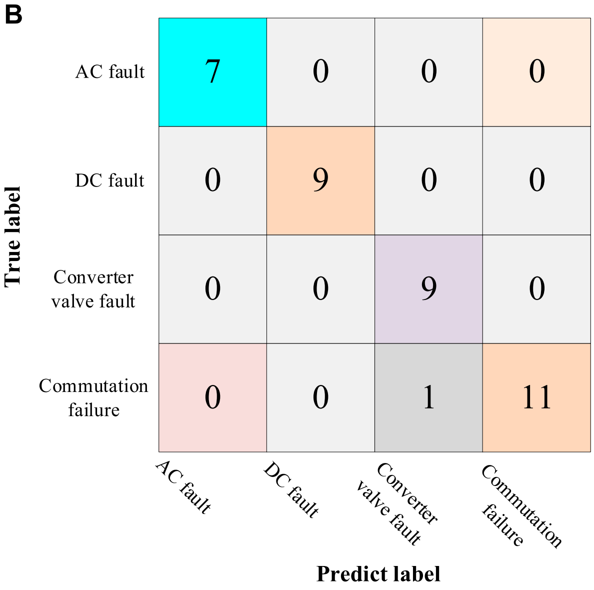

	AC fault	DC fault	Converter valve fault	Commutation failure
AC fault	7	0	0	0
DC fault	0	9	0	0
Converter valve fault	0	0	9	0
Commutation failure	0	0	1	11

BP model test result diagram

FIGURE 9
Confusion matrix of experimental results for the test set Y_2. **(A)** CatBoost model test result diagram. **(B)** BP model test result diagram.

of the Y_1 test set is shown in Figure 8. It is easy to see that when the test set is Y_1, in the diagnosis result of the CatBoost algorithm, a date group of commutation failure faults are misdiagnosed as converter valve faults, and the fault diagnosis rate of the CatBoost algorithm is as high as 94.74%. However, in BP's diagnosis results, four groups of DC faults are misdiagnosed as AC faults and commutation failures, respectively. At the same time, two groups of commutation failures are also misdiagnosed as DC faults. BP's overall fault diagnosis accuracy cannot reach a satisfactory level, only reaching 68.42%. The CatBoost algorithm has the highest classification accuracy of the two methods, although it has diagnostic errors when diagnosing converter valve faults.

The confusion matrix of fault diagnosis results for the Y_2 test set is shown in Figure 9. It is easy to see that under the condition that the test set is Y1, the four types of faults can be accurately identified through the CatBoost algorithm and the accuracy rate of fault diagnosis of the CatBoost algorithm is as high as 100%, which proves that the CatBoost algorithm can effectively extract fault data and accurately identify according to the characteristics. However, it

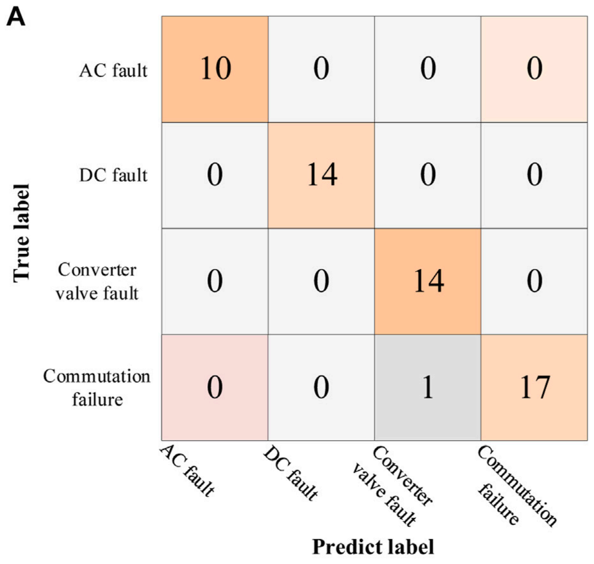

	AC fault	DC fault	Converter valve fault	Commutation failure
AC fault	10	0	0	0
DC fault	0	14	0	0
Converter valve fault	0	0	14	0
Commutation failure	0	0	1	17

CatBoost model test result diagram

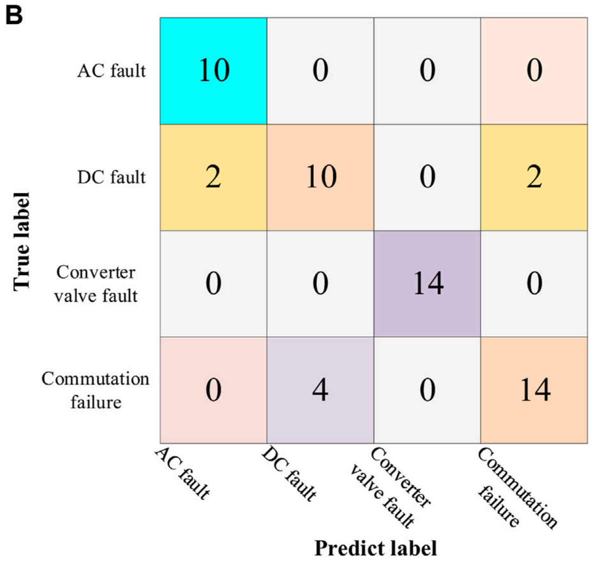

	AC fault	DC fault	Converter valve fault	Commutation failure
AC fault	10	0	0	0
DC fault	2	10	0	2
Converter valve fault	0	0	14	0
Commutation failure	0	4	0	14

BP model test result diagram

FIGURE 10
Confusion matrix of experimental results for the test set Y_3. **(A)** CatBoost model test result diagram. **(B)** BP model test result diagram.

is not difficult to find from the BP diagnosis results that one of the commutation failure faults was misdiagnosed as a valve fault, and its accuracy reached 97.3%.

The results of the two algorithms under the Y_3 test set are shown in Figure 10. It is obvious that CatBoost has the highest diagnostic accuracy, although a group of inverter commutation failure is misdiagnosed as converter valve fault in the CatBoost fault diagnosis model. However, in the fault diagnosis model of the BP neural network algorithm, four groups of DC faults are misdiagnosed as AC faults and commutation failures, respectively, and four groups of commutation failure data are misdiagnosed as a DC fault. According to the confusion matrix, the accuracy of fault diagnosis of CatBoost and BP neural network algorithms can be calculated to be 98.21% and 85.71%, respectively. Furthermore, the fault diagnosis iteration curve of the two algorithms for Y_3 is shown in Figure 11. It can be seen that the CatBoost algorithm converges after 30 iterations, while algorithm B converges after 41 iterations, which indicates that CatBoost has a faster diagnosis speed.

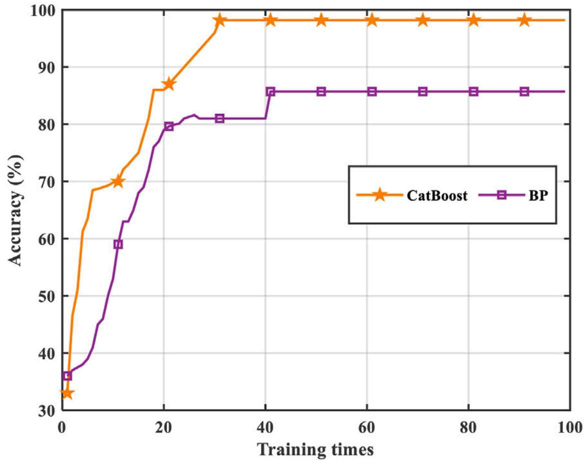

FIGURE 11
Accuracy curve of experimental results for the test set Y_3.

Finally, according to the confusion matrix, the accuracy rates of three groups of fault diagnosis experiments are obtained, as shown in Table 3. In test sets Y_1, Y_2, and Y_3, the number of negative data on the CatBoost fault diagnosis model is 1, 0, and 1, respectively, and the BP neural network fault diagnosis model is 6, 1, and 8, respectively. Also, in the CatBoost fault diagnosis model, the DC fault and AC fault can be accurately identified, and misdiagnosis mainly occurs in commutation failure and the converter valve fault. In addition, it is obvious that the CatBoost algorithm has the highest accuracy rate of fault diagnosis in the three groups of data, which can be guaranteed between 94% and 100%, which reflects that CatBoost is applicable to data classification in small sample data sets. However, the accuracy rate of the BP neural network can reach 64% at the lowest. To sum up the aforementioned analysis, it can be seen that algorithm B is superior to algorithm A in terms of convergence speed and fault diagnosis accuracy, which verifies the effectiveness and progressiveness of the method proposed in this paper.

7 Discussion and limitations

7.1 Discussion

Fault diagnosis of the HVDC transmission system is important research to ensure the reliable power supply of the whole power system. In the past, the fault diagnosis and inspection of the power system mainly depended on image recognition or acoustic theory, but this kind of method has a huge workload and cannot get timely feedback and maintenance when the system fails. In recent years,

TABLE 3 Experimental accuracy of three test sets.

Test sample	Number of samples	Number of positive samples		Number of negative data		Accuracy (%)	
		CatBoost	BP	CatBoost	BP	CatBoost	BP
Y_1	19	18	13	1	6	94.74	68.42
Y_2	37	37	36	0	1	100.00	97.30
Y_3	56	55	49	1	8	98.21	85.71

with the development of artificial intelligence technology, such as machine learning, reinforcement learning, and KG, these technologies have been applied in fault diagnosis technology of the power system to further improve the speed and accuracy of fault diagnosis. The CatBoost fault diagnosis method proposed in this paper belongs to this kind of technology. On the basis of obtaining historical fault data, the data features are extracted and recognized, and the accuracy is better. The BP neural network algorithm is relatively common in many studies, but it does not show good results in this data set.

7.2 Limitations

The fault diagnosis model of the HVDC transmission system proposed in this paper only contains four types of faults in the data set, so the data set does not cover all faults in the HVDC transmission system to a certain extent, such as the transformer fault and generator fault. In addition, the current work is mainly carried out under small samples, and the number of data sets is not large. Therefore, the data sets need to be improved and enriched. Since fault diagnosis is based on historical fault data to predict the system, the method proposed in this paper has certain limitations for fault prediction in some special cases.

8 Conclusion

In this paper, a novel fault diagnosis method for the HVDC system is proposed, and the significance of fault diagnosis for the later fault analysis and processing of the HVDC system is described by combining with the KG of the HVDC system. In this paper, the CatBoost algorithm is fully proven to be very effective, accurate, and fast in fault diagnosis of the HVDC system through relevant data validation and analysis. Four common faults of the HVDC system are introduced and analyzed in this work: the AC fault, DC fault, converter valve fault, and commutation failure, and the fault data are sorted out. The representative 15 channel data in the fault recording system are selected, and then, the data are summarized and sorted as the experimental data on this study. Furthermore, a fault diagnosis model of the HVDC system based on the CatBoost algorithm is proposed. Three test sets are used in the experiment to verify the model. The final structure proves that the method can effectively, quickly, and accurately realize the fault diagnosis of the HVDC system. Then, the fault diagnosis effect is compared with the BP neural network algorithm. Finally, the obtained results are visualized and the algorithm convergence curve and confusion matrix are drawn. From the figure, it can be seen that the CatBoost algorithm has a short diagnosis time and high fault diagnosis accuracy. Under the three test sets, its diagnosis accuracy is 94.74%, 100%, and 98.21%, respectively. However, the diagnostic accuracy of the BP neural network algorithm under three test sets is low, which is 68.42%, 97.30%, and 85.71%, respectively.

In the application of new generation AI in the power system, the method proposed in this paper has a certain reference value for the stable operation of the power system. Future studies might focus on the following three aspects:

(1) At present, the proposed fault diagnosis model is mainly applied to the HVDC transmission system. In the future research work, the effectiveness and progressiveness of the proposed method will be tested using the AC/DC hybrid system;
(2) The data set will be further enriched and improved, and more types of HVDC transmission fault data will be considered in the data set, such as the transformer fault, lightning fault, and noise impact on the system;
(3) The proposed algorithm will be further improved and integrated into more effective mechanisms in the KG. At the same time, more algorithms will be tested to analyze the speed and accuracy of system fault diagnosis under a large data set.

Data availability statement

The original contributions presented in the study are included in the article/Supplementary Material, further inquiries can be directed to the corresponding author.

Author contributions

JWu: writing the original draft and editing. QL, QC, and NZ: conceptualization. CM, LY, and JWa: visualization and contributed to the discussion of the topic.

Funding

This work was supported by the Technology Project of China Southern Power Grid (CGYKJXM20210309 and

CGYKJXM20220343). The funder was not involved in the study design, collection, analysis, interpretation of data, the writing of this article, or the decision to submit it for publication.

Conflict of interest

Authors JWu, QL, and QC were employed by the company China Southern Power Grid Co., Ltd. Authors NZ and CM were employed by the company China Southern Power Grid Co., Ltd. Authors LY and JWa were employed by the company China Southern Power Grid Co., Ltd.

Publisher's note

References

Chen, C. P., Chen, S. L., Bi, G. H., Gao, J. Y., Zhao, X., and Li, L. (2022). Fault diagnosis of weak receiving DC transmission system based on parallel CNN-LSTM. *Mot. Control Appl.* 49 (6), 83–91. doi:10.12177/emca.2022.022

Chen, X., Jia, S., and Xiang, Y. (2020). A review: Knowledge reasoning over knowledge graph. *Expert Syst. Appl.* 141, 112948. doi:10.1016/j.eswa.2019.112948

Giljum, A., Liu, W., Li, L., Weber, R., and Kelly, K. F. (2021). General neural network approach to compressive feature extraction. *Appl. Opt.* 60 (25), 217–223. doi:10.1364/AO.427383

Górski, T. (2022). The k + 1 symmetric test pattern for smart contracts. *Symmetry* 14 (8), 1686. doi:10.3390/sym14081686

Guo, X. S., Li, T., Li, G. W., Wei, Z., Yuan, B., and Chen, D. (2018). Converter valve fault ride through strategy and protection setting optimization in Zhang-Bei flexible DC power grid. *Automation Electr. Power Syst.* 42 (24), 196–202. doi:10.7500/AEPS20180506004

Li, G., An, T., Liang, J., Liu, W., Joseph, T., Lu, J., et al. (2020). Studies of commutation failures in hybrid LCC/MMC HVDC systems. *Glob. Energy Interconnect.* 3 (3), 193–204. doi:10.1016/j.gloei.2020.07.001

Li, J. X., Li, X., Gao, T. L., Zhang, J., and Zhang, B. Y. (2021). Research and application of fault handling based on power grid multivariate information knowledge graph. *Power Inf. Commun. Technol.* 19 (11), 30–38. doi:10.16543/j.2095-641x.electric.power.ict.2021.11.005

Li, J. X., Qian, J., Li, J. J., and Shan, J. S. (2007). Influence of AC side fault of converter station on HVDC system. *Yunnan Electr. Power* 35 (3), 10–12. doi:10.3969/j.issn.1006-7345.2007.03.005

Li, R. S., Wong, P., Wang, K., Li, B., and Yuan, F. F. (2020). Power quality enhancement and engineering application with high permeability distributed photovoltaic access to low-voltage distribution networks in Australia. *Prot. Control Mod. Power Syst.* 5 (3), 18–189. doi:10.1186/s41601-020-00163-x

Li, Z. Q. (2010). Research on a new method of HVDC system fault diagnosis based on auto disturbance rejection controller. *Telecom Power Technol.* 27 (6), 39–43. doi:10.19399/j.cnki.tpt.2010.06.014

Liu, X., Dai, D., Rao, H. L., Cheng, C., Ai, L., and Wu, S. (2015). Common faults and treatment methods of converter valve in DC system. *Electron. World* 21, 115–117. CNKI: SUN: ELEW.0.2015-21-068.

Lokanadham, D., and Subbaiah, K. V. (2021). Estimation of tribological performance of Al-LSP composites using grey fuzzy reasoning approach. *IOP Conf. Ser. Mater. Sci. Eng.* 1070 (1), 012120. doi:10.1088/1757-899X/1070/1/012120

Ma, J., Yang, Z., Du, W., Shen, Y., and Cheng, P. (2022). An active damping control method for direct-drive wind farm with flexible DC transmission system based on the remodeling of dynamic energy branches. *Int. J. Electr. Power & Energy Syst.* 141, 108004. doi:10.1016/j.ijepes.2022.108004

Mehdi, T., and Mehdi, N. (2020). Human reliability analysis in maintenance team of power transmission system protection. *Prot. Control Mod. Power Syst.* 5 (4), 26–282. doi:10.1186/s41601-020-00176-6

Meng, Y., Yan, S., Wu, K., Ning, L., Li, X., Wang, X., et al. (2021). Comparative economic analysis of low frequency AC transmission system for the integration of large offshore wind farms. *Renew. Energy* 179, 1955–1968. doi:10.1016/j.renene.2021.07.137

Mohamed, N., Ahmed, E., and Tamou, N. (2020). Improving low-voltage ride-through capability of a multimegawatt DFIG based wind turbine under grid faults. *Prot. Control Mod. Power Syst.* 5 (4), 33–382. doi:10.1186/s41601-020-00172-w

Nanayakkara, O., Rajapakse, A. D., and Wachal, R. (2012). Traveling-wave-based line fault location in star-connected multiterminal HVDC systems. *IEEE Trans. power Deliv.* 27 (4), 2286–2294. doi:10.1109/TPWRD.2012.2202405

Narendra, K. G., Sood, V. K., Khorasani, K., and Patel, R. (1998). Application of a radial basis function (RBF) neural network for fault diagnosis in a HVDC system. *IEEE Trans. power Syst.* 13 (1), 177–183. doi:10.1109/59.651633

Pauli, B., Mauthe, G., Ruoss, E., Ecklin, G., Porter, J., and Vithayathil, J. (1988). Development of a high current HVDC circuit breaker with fast fault clearing capability. *IEEE Trans. Power Deliv.* 3 (4), 2072–2080. doi:10.1109/61.194019

Reed, G. F., Hassan, H. A., and Kory, M. J. (2013). "Comparison of HVAC and HVDC solutions for off-shore wind farms with a procedure for system economic evaluation," in 2013 IEEE Energytech, Cleveland, USA, 21-23 May 2013, 1–7. doi:10.1109/EnergyTech.2013.6645302

Tanmay, D., Ranjit, R., and Kamal, K. M. (2020). Impact of the penetration of distributed generation on optimal reactive power dispatch. *Prot. Control Mod. Power Syst.* 5 (4), 31–357. doi:10.1186/s41601-020-00177-5

Torres-Olguin, R. E., and Garces, A. (2017). Grid integration of offshore wind farms using a hybrid HVDC composed by an MMC with an LCC-based transmission system. *Energy Procedia* 137, 391–400. doi:10.1016/j.egypro.2017.10.363

Trondoli, L., Lopes, G. N., and Vieira, J. (2022). Configurable stochastic model for high impedance faults simulations in electrical distribution systems. *Electr. Power Syst. Res.* 205, 107686. doi:10.1016/j.epsr.2021.107686

Vidal, A. R., Beltran, H., Rolan, A., Belenguer, E., Pena, R., and Blasco-Gimenez, R. (2015). Analysis of the performance of MMC under fault conditions in HVDC-based off-shore wind farms. *IEEE Trans. Power Deliv.* 31 (2), 839–847. doi:10.1109/TPWRD.2015.2468171

Vidlak, M., Gorel, L., Makys, P., and Stano, M. (2021). Sensor less speed control of brushed DC motor based at new current ripple component signal processing. *Energies* 14, 5359. doi:10.3390/en14175359

Wang, M., Xu, X., and Yan, Z. (2023). Online fault diagnosis of PV array considering label errors based on distributionally robust logistic regression. *Renew. Energy* 203, 68–80. doi:10.1016/j.renene.2022.11.126

Wang, R., Ma, D. Z., Li, M. J., Sun, Q., Zhang, H., and Wang, P. (2022). Accurate current sharing and voltage regulation in hybrid wind/solar systems: An adaptive dynamic programming approach. *IEEE Trans. Consumer Electron.* 68 (3), 261–272. doi:10.1109/TCE.2022.3181105

Wang, R., Sun, Q. Y., Hu, W., Li, Y., Ma, D., and Wang, P. (2021). SoC-based droop coefficients stability region analysis of the battery for stand-alone supply systems with constant power loads. *IEEE Trans. Power Electron.* 36 (7), 7866–7879. doi:10.1109/TPEL.2021.3049241

Wei, J. W., Lin, L., Cheng, T., and Mou, D. H. (2006). Commutation failure factors analysis in HVDC transmission system. *J. Chongqing Univ.* 29 (5), 16–18. doi:10.1016/S0379-4172(06)60085-1

Wu, J., Li, Q., Chen, Q., Peng, G., Wang, J., Fu, Q., et al. (2022). Evaluation, analysis and diagnosis for HVDC transmission system faults via knowledge graph under new energy systems construction: A critical review. *Energies* 15 (21), 8031. doi:10.3390/en15218031

Xiao, Y., Han, F., Ding, Y., and Liu, W. (2021). Research on fault diagnosis method of rapier loom based on the fusion of expert system and fault tree. *J. Intelligent Fuzzy Syst. Appl. Eng. Technol.* 41 (2), 3429–3441. doi:10.3233/JIFS-210741

Xiong, Y., Li, J., Fei, F., Liu, Z., and Luo, W. (2019). Influence of coherent vortex structures in subgrid scale motions on particle statistics in homogeneous isotropic turbulence. *Int. J. Multiph. Flow* 113, 358–370. doi:10.1016/j.ijmultiphaseflow.2018.10.021

Yang, B., Yu, T., Shu, H. C., Dong, J., and Jiang, L. (2018). Robust sliding-mode control of wind energy conversion systems for optimal power extraction via nonlinear perturbation observers. *Appl. Energy* 210, 711–723. doi:10.1016/j.apenergy.2017.08.027

Yang, B., Zhang, X., Yu, T., Shu, H., and Fang, Z. (2017). Grouped grey wolf optimizer for maximum power point tracking of doubly-fed induction generator-based wind turbine. *Energy Convers. Manag.* 133, 427–443. doi:10.1016/j.enconman.2016.10.062

Yang, B., Zhong, L. E., Yu, T., Li, H. F., Zhang, X. S., Shu, H. C., et al. (2019). Novel bio-inspired memetic salp swarm algorithm and application to MPPT for PV systems considering partial shading condition. *J. Clean. Prod.* 215, 1203–1222. doi:10.1016/j.jclepro.2019.01.150

Yao, W., Jiang, L., Wen, J. Y., Wu, Q. H., and Cheng, S. J. (2015). Wide-area damping controller for power system inter-area oscillations: A networked predictive control approach. *IEEE Trans. Control Syst. Technol.* 23 (1), 27–36. doi:10.1109/TCST.2014.2311852

Zeng, R., Xu, L., Yao, L., Finney, S. J., and Wang, Y. (2016). Hybrid HVDC for integrating wind farms with special consideration on commutation failure. *IEEE Trans. Power Deliv.* 31, 789–797. doi:10.1109/TPWRD.2015.2440354

Zeng, X., Tu, X., Liu, Y., Fu, X., and Su, Y. (2022). Toward better drug discovery with knowledge graph. *Curr. Opin. Struct. Biol.* 72, 114–126. doi:10.1016/j.sbi.2021.09.003

Zhang, H., Dou, J., and Wei, S. (2013). Study on intelligent grid-connected controller for off-shore distributed wind power system. *Lect. Notes Electr. Eng.* 216, 159–166. doi:10.1007/978-1-4471-4856-2_20

Zhang, Y., Tang, F., Qin, F., Li, Y., Gao, X., and Du, N. (2021). Research on dynamic reactive power compensation scheme for inhibiting subsequent commutation failure of MIDC. *Sustainability* 13, 7829–7918. doi:10.3390/su13147829

Zheng, R. N., Hu, Z. S., Wen, Z. X., and Wang, J. J. (2020). AC fault detection method for HVDC system. *Guangdong Electr. Power* 33 (5), 97–104. CNKI: SUN: GDDL.0.2020-05-012.

Zheng, X. X., and Peng, P. (2019). Fault diagnosis of flexible HVDC converter based on preferred wavelet packet and AdaBoost-SVM. *J. Power Syst. Automation* 31 (3), 42–49. doi:10.19635/j.cnki.csu-epsa.000024

Zhou, H. Y., Yao, W., Ai, X., Zhang, J., Wen, J., and Li, C. (2022). Coordinated power control of electrochemical energy storage for mitigating subsequent commutation failures of HVDC. *Int. J. Electr. Power Energy Syst.* 134, 107455–107514. doi:10.1016/j.ijepes.2021.107455

Frontiers in Energy Research

TYPE Technology and Code
PUBLISHED 16 March 2023
DOI 10.3389/fenrg.2023.1138446

OPEN ACCESS

EDITED BY
Xin Ning,
Institute of Semiconductors (CAS), China

REVIEWED BY
Zhang Hengmin,
University of Macau, China
Tomasz Górski,
University of Gdansk, Poland

*CORRESPONDENCE
Eric M. S. P. Veith,
eric.msp.veith@uol.de

SPECIALTY SECTION
This article was submitted to Smart Grids, a section of the journal Frontiers in Energy Research

RECEIVED 05 January 2023
ACCEPTED 16 February 2023
PUBLISHED 16 March 2023

CITATION
Veith EMSP, Wellßow A and Uslar M (2023), Learning new attack vectors from misuse cases with deep reinforcement learning.
Front. Energy Res. 11:1138446.
doi: 10.3389/fenrg.2023.1138446

Learning new attack vectors from misuse cases with deep reinforcement learning

Eric M. S. P. Veith[1]*, Arlena Wellßow[2] and Mathias Uslar[2]

[1]Adversarial Resilience Learning Resarch Group, Carl von Ossietzky University Oldenburg, Oldenburg, Germany, [2]R&D Division Energy, OFFIS—Institute for Information Technology, Oldenburg, Germany

Modern smart grids already consist of various components that interleave classical Operational Technology (OT) with Information and Communication Technology (ICT), which, in turn, have opened the power grid to advanced approaches using distributed software systems and even Artificial Intelligence (AI) applications. This IT/OT integration increases complexity, however, without argument, this advance is necessary to accommodate the rising numbers of prosumers, Distributed Energy Resources (DERs), to enable new market concepts, and to tackle world-wide CO_2 emission goals. But the increasing complexity of the Critical National Infrastructure (CNI) power grid gives way to numerous new attack vectors such that *a priori* robustness cannot be guaranteed anymore and run-time resilience, especially against the "unknown unknowns", is the focus of current research. In this article, we present a novel combination of so called misuse-case modelling and an approach based on Deep Reinforcement Learning (DRL) to analyze a power grid for new attack vectors. Our approach enables learning from domain knowledge (offline learning), while expanding on that knowledge through learning agents that eventually uncover new attack vectors.

KEYWORDS

misuse case, smart grids, smart grid cyber security, deep reinforcement learning (deep RL), offline learning, adversarial resilience learning

1 Introduction

Undoubtedly, the climate catastrophe is an unparalleled challenge for society. The urge to reduce CO_2 emissions directly leads to the imperative of reducing energy consumption, a more efficient usage of energy, and to increase the emount of renewable energy resources. This change is nowhere as apparent as in the power grid, which has undergone a rapid transformation in recent years (Bush, 2014; IEA, 2019).

Future power grids will have a much higher degree of digitalization as present ones. New approaches to balancing services management that include major prosumers (Holly et al., 2020) or multi-purpose battery storage (Tiemann et al., 2022). Multi-Agent System (MAS) are employed to facilitate real power management of DERs or solve unit-commitment problems (Roche et al., 2013; Veith, 2017; Nair et al., 2018; Frost et al., 2020; Mahela et al., 2022), while ever smaller generators are included into the grid management duties of the operator (Woltmann and Kittel, 2022). In addition, the convergence between Information Technology (IT) and OT is further emphasized by the amount of Internet of Things (IoT) technologies deployed, which have—for the better or worse—a huge impact on the power grid (Soltan et al., 2018; Huang et al., 2019; Mathas et al., 2021).

Indeed, power grids have become valuable targets for cyber attacks. The attacks on the Ukrainian power grid in 2015 and 2016 are well known (Styczynski and Beach-Westmoreland, 2016), but researchers know a multitude of attack vectors, such as message spoofing in IEC 61805 (Hong et al., 2014), false data injection (Liu et al., 2011; Hu et al., 2018), direct damage caused by nodes compromised by an attacker (Ju and Lin, 2018), or market exploitation (Wolgast et al., 2021). There are already comprehensive reviews available that consider the cyber-security of power grids; we refer the interested reader to the review article by Sun et al. (2018) for a comprehensive survey.

Researchers have not only considered each incident in isolation, but used and extended existing methodologies to document, classify, and analyze these incidents on a more general level. Structured Threat Information Expression (STIX) and Trusted Automated Exchange of Indicator Information (TAXII) are well-known documentation formats and methodologies for Cyber Threat Intelligence (CTI) (Barnum, 2012; Connolly et al., 2014; Apoorva et al., 2017; Briliyant et al., 2021). They are, of course, far from being the silver bullet; another, high-level approach is that of the Misuse-Case (MUC), introduced by Sindre and Opdahl (2005).

However, any approach in modelling cyber threats works based on already known attack vectors. They require humans to map them to actual actions—e. g, commands to be executed—on a given system, and it is also humans who devise and execute new attack vectors, which are then documented and analyzed *post hoc*.

There exists a stark contrast to more recent approaches coming from the domain of AI, specifically DRL: Learning agents that use trial-and-error approaches to probe simulated Cyber-Physical Systems (CPSs) for weaknesses (Fischer et al., 2019; Veith et al., 2019, 2020).

DRL—initially without the "Deep" prefix—introduced the notion of an agent that learns by interacting with its environment. The agent possesses sensors with which it perceives its environment, actuators to interact with it, and it receives a reward signal that indicates to the agent how well it fars with regards to its goal or utility function. Learning in the context of DRL means creating a policy such that, in any given state, the agent's actions maximize its cumulative reward. The modern breakthrough in DRL was the end-to-end learning of Atari games by Mnih et al. (2013). Since their publications of Deep Q Network (DQN), many other algorithms have followed, including the well-known modern DRL algorithms Deep Deterministic Policy Gradient (DDPG) (Lillicrap et al., 2016), Twin-Delayed DDPG (TD3) (Fujimoto et al., 2018), Proximal Policy Gradient (PPO) (Schulman et al., 2017), and Soft Actor Critic (SAC) (Haarnoja et al., 2018).

However, "vanilla" DRL is called model-free, meaning that the agents do not carry an explicit knowledge about their environment. The policy they learn includes this implicitly, because in mapping sensor readings to actions in order to maximize the (cumulative) reward, they obviously need to build a concept of their environment's inherent dynamics. But the agents learn from scratch; the interaction with their environment is the only way the have to explore it. In order to build a policy, the agents have to amass trajectories (triplets of state, action, and reward) that contain "fresh" data to learn upon. The trade-off between acting based on the current policy and exploring the environment with more-or-less random actions in order to potentially find more rewarding trajectories is expressed by the exploration-exploitation dilemma. How well an algorithm learns is often discussed in terms of its sample efficiency.

Obviously, it seems beneficial to give agents access to a repository of trajectories to learn from without the need of interacting from scratch. There are a lot of situations where data is also scarce or expensive to come by; real-world applications in the domain of robotics or medicine are such cases. Learning from preexisting data, called Offline Learning (Prudencio et al., 2022), poses a problem of its own, which stems from the fact that agents cannot interact with the environment during offline learning and, thus, might be biased to sub-optimal policies.

Still, if one can ascertain the quality of the dataset, offline learning provides a huge benefit: It introduces the agent to proven domain knowledge and reduces the training time significantly. Also, an agent initially trained from an offline learning data set can still be trained online with the usual algorithms, but it still does not start from scratch.

There exists a clear motivation in combining modelling approaches like MUCs with learning agents: A MUC is understandable by domain experts, who play an important role in drafting a MUC in the first place. MUC—along other CTI description formats—are an accessible and comprehensive way to describe *post hoc* incident knowledge. The shortcoming is, that MUCs, being a data format, contain few points (if any) to uncover variants of a known attack, or even uncover new ones that make use of existing knowledge. On the other hand, learning agents that employ, e. g, DRL, are known to develop completely new strategies—AlphaZero is a prime example for this—, but when starting with no knowledge, they require extensive training: I. e, a comprehensive simulation environment and the ability to gather enough data from a distribution resembling the real world so that the training is successful, which is computationally extensive.

The technical as well as research gap lies in the combination of the two: Learning from domain knowledge, which is offline data, would provide the learning agent with a headstart and cut the expensive initial exploration phase. But in addition, the agent would still benefit from a later online learning phase and be able to uncover new strategies. That way, agents would learn from known incidents, and then develop variants based thereof or entirely new attack vectors connected to the known ones. However, for this, the task of MUC modelling must be connected to the offline learning domain, and later than to extensive online learning, which entails careful design of experiments.

In this paper, we will combine domain knowledge from CTI with successful approaches at CPS system analysis. Namely, we present a methodology to define experiments from MUCs, paving the way towards offline learning for DRL agents for cyber-security in CNIs. Our main contribution is threefold.

- We describe a pipeline from MUC modelling to DRL-based experiments that allow to extend existing, known MUCs by having learning agents discovers new attack vectors based on a given MUC.
- We present an offline learning approach where specific agents, stemming from the MUC modelling, are imitiation learners (or adversarial imitation learners) for DRL agents.

- We outline a research direction on how to create offline learning datasets from MUCs by analyzing embedded Unified Modelling Language (UML) diagrams, based on specific anotations.

Technically, the novelty of our contribution exists in the complete software stack, from MUC to experiment definition, to Design of Experiments (DoE), to reproducible experiment execution with offline and online learning.

The remainder of this paper is structured as follows: In **Section 2**, we review related work and present the state of the art. **Section 3** outlines our approach in broad terms as a high-level overview. We then present the MUC modelling format in detail in **Section 4**. Afterwards, **Section 5** turns towards our DoE approach. **Section 6** presents our execution software stack and the data storage and analysis backend. We follow the theoretical part with an experimental validation in **Section 7**. We present initial results in **Section 8**, which we discuss in **Section 9**. We conclude in **Section 10** with an outlook towards future work.

2 Related work

2.1 Cyber Threat Intelligence

The term Cyber Threat Intelligence (CTI) describes the process of knowledge acquisition for cyber threat data and also the data itself. As there are known attack pattern and vulnerabilities in systems, sharing and maintaining this data sets becomes important.

2.1.1 Structured Threat Information eXpression (STIX™)

With Structured Threat Information eXpression (STIX™) the Organization for the Advancement of Structured Information Standards (OASIS) Cyber Threat Intelligence Technical Committee developed a standardized language. Data in form of Structured Threat Information eXpressions (short: STIX data) gives structured information about cyber attacks (Barnum, 2012). STIX data is stored in an graph based information model and OASIS defines eighteen such called *STIX* Domain Objects for entity nodes, which are connected *via* two defined *STIX* Relationship Objects (OASIS Open Cyber Threat Intelligence Committee, 2022). Some of these entity node types are referred to as TTPs, which can be traced back to the military origin of this abbreviation. The types thereby belong to the category of tactics, techniques, and procedures.

2.1.2 Trusted Automated Exchange of Intelligence Information (TAXII™)

The Trusted Automated Exchange of Intelligence Information (TAXII™), which is also developed by the OASIS Cyber Threat Intelligence Technical Committee, describes the way, STIX data is meant to be exchanged. Therefore TAXII is an application layer protocol with an RESTful API. OASIS also provides requirements for TAXII clients and servers. By development TAXII is meant to be simple and scalable to make sharing STIX data as easy as possible (Connolly et al., 2014).

2.1.3 MITRE ATT&CK® STIX data

The MITRE Adversarial Tactics, Techniques, and Common Knowledge (MITRE ATT&CK) collects and provides cyber attack data. It targets the missing communication between communities dealing with the same attacks (The MITRE Corporation, 2022).

2.2 (Mis-)Use case methodology

The misuse case methodology used in this paper is based on the use case methodology from the IEC 62559 standards family. This standard describes a systematic approach for eliciting use cases. IEC 62559-2 also provides a template for the use cases according to this standard. In this template the use case data is noted in a structured form and contains the description of the use case with its name and identifier as well as scope, objectives, conditions and narrative in natural language, further information like the relations to other use cases or its prioritization and a set of related KPIs. In the second section of the use case template, the associated diagrams of the use case are depicted. This is followed by an overview about the technical details where every acting component is listed as well as a step-by-step analysis for every scenario belonging to this use case. Linked to these steps are lists of exchanged information and requirements, which are also part of the template. Finally common terms and custom information are placed.

As shown by Gottschalk et al. (2017), the IEC 62559 is a family of standards that is used in many areas. Trefke et al. (2013) show the application of the use case methodology in a large European smart grid project, while Clausen et al. (2018) show a similar approach in the German research project enera. In the DISCERN project, Santodomingo et al. (2014) present approaches of an analysis based on the use case standard, while Schütz et al. (2021) take up these approaches as well as the related approaches from Neureiter et al. (2014), van Amelsvoort et al. (2015), and van Amelsvoort (2016) and continue them.

The here used misuse case methodology is based on the use case methodology taken from the IEC 62559. This standard is then combined with the concept of misuse cases. In general a misuse case is a description of a scenario which is known but explicitly unwanted. This contains, among others, unwanted behaviour of a system as well as cyber (-physical) attacks. The need of misuse cases was described by Sindre and Opdahl (2005) and applied to a template based on a use case template by Cockburn (2001)[1] in the work of Sindre and Opdahl (2001). Concepts and notation of misuse cases as well as textual specification and examples for the work with misuse cases are part of the paper of Sindre and Opdahl (2005). In addition to the general template according to IEC 62559-2 the misuse case template contains information about misactors, which are placed in the same section as the actors in the standard. The section containing the scenarios is adapted to failure scenarios, which need additional information like the worst case threat or the likelihood of occurrence.

This leads to a set of tables in the following structure[2].

---

[1] This template is not the same as the template from the IEC 62559-2 standard.

[2] For a detailed view on the MUC template see: https://gitlab.com/arl2/muclearner.

1. Description of the Misuse Case
2. Diagrams of the Misuse Case
3. Technical Details
4. Step-by-Step analysis of the Misuse Case
5. Requirements
6. Common Terms and Definitions
7. Custom Information (optional)

Considering the nature of a misuse case and the given information in misuse case template used here, a link to a representation of the information in the form of STIX data (cf. **Section 2.1.1**) is natural. Therefore data in STIX format shall be used in the presented approach as an expedient addition to the misuse case template.

2.3 Deep reinforcement learning and its application in smart grid cyber security

Undoubtedly, research in the domain of AI has yielded many noteworthy results in the last years. One of the most spectacular, the "superhuman" performance in the game of Go, can be largely attributed to DRL. From the resurrection of (model-free) reinforcement learning with the 2013 hallmark paper to the publicly-noted achievements of AlphaGo, AlphaGo Zero, AlphaZero, and (model-based) MuZero (Mnih et al., 2013; Lillicrap et al., 2016; Hessel et al., 2018; Silver et al., 2016a; b, 2017; Schrittwieser et al., 2019), DRL has attracted much attention outside of the AI domain. Much of the attention it has gained comes from the fact that, especially for Go, DRL has found strategies better than what any human player had been able to, and this without human teaching or domain knowledge.

DRL is based on the Markov Decision Process (MDP), which is a quintruplet (S, A, T, R, γ).

- S, the set of states, e. g, the voltage magnitudes at all buses at time t, $S_t = \{V_1(t), V_2(t), \ldots, V_n(t)\}$
- A, the set of actions, e. g, the reactive power generation (positive value) or consumption (negative value), at t, of a particular node the agent controls, $A_t = \{q_1(t), q_2(t), \ldots, q_n(t)\}$
- T, the set of conditional transition probabilities, i. e, the probability that, given an action $a_t \in A_t$ by the agent, the environment transitions to state s_{t+1}. $T\ (s_{t+1} \| s_t, a_t)$ is observed and learned by the agent
- R, the reward function of the agent $R{:}S \times A \rightarrow \mathbb{R}$
- γ, the discount factor, which is a hyperparameter designating how much future rewards will be considered in calculating the absolute Gain of an episode: $G = \Sigma_t \gamma^t r_t, \gamma \in [0;\ 1)$.

Basically, an agent observes a state s_t at time t, executes action a_t, and receives reward r_t. The transition to the following state s_{t+1} can be deterministic or probabilistic, according to T. The Markov property states that, for any state s_t, given an action a_t, only the previous state s_{t-1} is relevant in evaluating the transition. We consider many problems in CNIs to be properly modelled by a Partially-Observable Markov Decision Process (POMDP). A POMDP is a 7-tuple $(S, A, T, R, \Omega, O, \gamma)$, where, in addition to the MDP.

- Ω, the set of observations, being a subset of the total state information s_t: For each time t, the agent does observe the environment through its sensors, but this may not cover the complete state information. E. g, the agent might not obseve all buses, but only a limited number.
- O, the set of conditional observation properties determines whether an observation by the agent might be influenced by external factors, such as noise.

The goal of reinforcement learning in general is to learn a policy, such that $a_t \sim \pi_\theta(\cdot|s_t)$. Finding the optimal policy π_θ^* is the optimization problem at the heart of all reinforcement learning algorithms.

Mnih et al. (2013) introduced DRL with their DQNs. Of course, Reinforcement Learning itself is older than this particular publication (Sutton and Barto, 2018). However, Mnih et al. were able to introduce deep neural networks as estimators for Q-values, providing stable training. Their end-to-end learning approach, in which the agent is fed raw pixels from Atari 2,600 games and successfully plays the respective game, is still one of the standard benchmarks in DRL. The DQN approach has seen extensions until the Rainbow DQN (Hessel et al., 2018). DQN are only applicable for environments with discrete actions; the algorithm has been superseeded by others.

DDPG (Lillicrap et al., 2016) also builds on the policy gradient methodology: It concurrently learns a Q-function as well as a policy. It is an off-policy algorithm that uses the Q-function estimator to train the policy. DDPG allows for contiuous control; it can be seen as DQN for continuous action spaces. DDPG suffers from overestimating Q-values over time; TD3 has been introduced to fix this behavior (Fujimoto et al., 2018).

PPO (Schulman et al., 2017) is an on-policy policy gradient algorithm that can be used for both discrete and continuous action spaces. It is a development parallel to DDPG and TD3 and not an immediate successor. PPO is more robust towards hyperparamter settings than DDPG and TD3 are, but as an on-policy algorithm, it requires more interaction with the environment train, making it unsuitable for computationally expensive simulations.

SAC, having been published close to concurrently with TD3, targets the exploration-exploitation dilemma by being based on entropy regularization (Haarnoja et al., 2018). It is an off-policy algorithm that was originally focused on continuous action spaces, but has been extended to also support discrete action spaces.

PPO, TD3, and SAC are the most commonly used model-free DRL algorithms today.

With the promise of finding novel strategies, DRL has long since entered the smart grid cyber security research domain. Adawadkar and Kulkarni (2022) and Inayat et al. (2022) provide a recent survey in this regard; in the following paragraphs, we will take note of publications not listed in the survey or those which are especially interesting in the context of this article.

However, we note that the majority of publications, even recent ones, focus on a particular scenario, which is well known from the electrical engineering perspective. The authors then reproduce this scenario, using DRL algorithms to show the discoverability and feasibility of the attack, to learn a strategy of attack for changing grid models, or to provide a defense against a particular, specific type of attack, leveraging DRL to provide dynamic response. Thus, the goal is mostly to automate a specific attack with DRL, which can be deduced from the formulation of rewards. Using the versatility of DRL to discover any weakness in a power grid, regardless of a specific attack vector (i. e, letting the agent find the attack vector), is a clear research gap.

Wang et al. (2021) apply DRL to coordinated topology attacks, having the agent learn to trip transmission lines and manipulate digital circuit breaker data. Surprisingly, the authors still employ DQNs for this (rather recent) publication. Wolgast et al. (2021) have used DRL to attack local energy markets, in which the attacker aims to achieve local market dominance. Wan et al. (2021) consider a DRL agent that implements demand response as the victim, using particle swarm optimization to pertubate the DRL agent's input to cause erroneous behavior.

Roberts et al. (2020) provide a defender against attacks from malicious DERs that target the voltage band. They consider the DER inverters' P/Q plane, but disregard grid codes as well as other actions, such as line trippings. They use PPO and are explicitly agnostic to the concrete attack, but their agent also trains without prior knowledge. Roberts et al. (2021) work from a similar premise (compromised DERs), paying special attention to non-DRL controllers, but otherwise achieving similar results.

2.4 Offline reinforcement learning for deep reinforcement learning

The core of reinforcement learning is the interaction with the environment. Only when the agent explores the environment, creating trajectories and receiving rewards, can it optimize its policy. However, many of the more realistic environments, like robotics or the simulation of large power grids, are computationally expensive. Obviously, training from already existing data would be beneficial. For example, an agent could learn from an already existing simulation run for optimal voltage control before being trained to tackle more complex scenarios. Learning from existing data without interaction with an environment is called offline reinforcement learning (Prudencio et al., 2022).

The field of offline reinforcement learning can roughly be subdivided into policy constraints, importance sampling, regularization, model-based offline reinforcement learning, one-step learning, imitation learning, and trajectory optimization. For these methods, we will give only a very short overview as relevant for this article, since Levine et al. (2020)[3] and Prudencio et al. (2022) have published extensive tutorial and review papers, to which we refer the interested reader instead of providing a poor replication of their work here.

Policy constraints modify the learned policy: They modify the unconstrained objective to a constrained objective by introducing a divergence metric between the learned policy, $\pi_\theta(\cdot|\boldsymbol{s})$, and the behavioral policy created from offline data, $\pi_\beta(\cdot|\boldsymbol{s})$. Given $\hat{\pi}_\beta(\cdot|\boldsymbol{s})$ as an estimate of the behavioral policy, maximizing the objective $J(\theta)$ becomes subject to $D\left(\pi_\theta(\cdot|\boldsymbol{s}), \hat{\pi}_\beta(\cdot|\boldsymbol{s}) < \varepsilon\right)$. Peng et al. (2019) describe a different approach that eschews estimating π_β, needing only to estimate the advantage $\hat{A}^{p}i(\boldsymbol{s}, \boldsymbol{a})$. Since the advantage describes the relative improvement of an action, not the absolute one, it is easier to derive from a dataset.

Importance sampling introduces weights for the samples in the offline learning dataset. Reducing the variance of the important weights is crucial, since the produce of important weights, $w_{0:H}$, is exponential in H.

Regularization adds a regularization term, $R(\theta)$, to $J(\theta)$. It makes the estimates of the value function learned by the agent more conservative, preventing over-estimation of the value objective, thus preventing the agent to take Out-Of-Distribution (OOD) actions.

An optimization of this approach is uncertainty estimation, which allows to switch between conservative and naive off-policy DRL methods. By estimating the uncertainty of the policy or value function over their distribution, the penalty term added to the objective, $J(\theta)$, is dynamically adjusted based on this uncertainty.

Model-based methods estimate transition dynamics $T\left(\boldsymbol{s}_{t+1}|\boldsymbol{s}_t, \boldsymbol{a}_t\right)$ and the reward function $r\left(\boldsymbol{s}_t, \boldsymbol{a}_t\right)$ from a dataset D, often learned through supervised regression. E.g., a world model can be a surrogate model for a power grid, learned from a number of power flow calculations during a simulation. However, world models cannot be corrected by querying the environment as this would normally be done in online DRL. Thus, world models in offline DRL need to be combined with uncertainty estimation in order to avoid transitioning to OOD states.

One-step methods collect multiple states to estimate $Q\left(\boldsymbol{s}, \boldsymbol{a}\right)$ from offline data; afterwards, a single policy improvement step is done. This is in contrast to iterative actor-critic methods (e.g, SAC), which alternate between policy evaluation and policy improvement. Since the latter is not possible, the single-step approach ensures that the estimate for $Q\left(\boldsymbol{s}, \boldsymbol{a}\right)$ represents the distribution, i.e, evaluation is never done outside the distribution of D.

Trajectory optimization aims to learn a state-action model over trajectories, i.e, a model of the trajectory distribution introduced by the policy from the dataset. Given any initial state $\boldsymbol{s}_0$, this model can then output an optimal set of actions. Querying for whole trajectories makes selecting OOD actions less likely.

Finally, imitation learning aims to reduce the distance between the policy out of the dataset D and the agent's policy, such that the optimization goal is expressed by $J(\theta) = D\left(\pi_\beta(\cdot|\boldsymbol{s}), \pi_\theta(\cdot|\boldsymbol{s})\right)$. This so-called Behavior Cloning requires an expert behavior policy, which can be hard to come by, but is readily available in some power-grid-related use cases, such as voltage control, where a simple voltage controller could be queried as expert.

To our knowledge, there is currently no notion of employing offline learning for DRL in the context of smart grid cyber security (Adawadkar and Kulkarni, 2022; Berghout et al., 2022; Inayat et al., 2022).

---

[3] The tutorial by Levine et al. (2020) is available only as preprint. However, to our knowledge, it constitutes one of the best introductionary seminal works so far. Since it is a tutorial/survey, and not original research, we cite it despite its nature as a preprint and present it alongside the peer-reviewed publication by Prudencio et al. (2022), which cites the former, too.

2.5 Software frameworks for deep reinforcement learning in complex cyber physical system simulations

During the last years, numerous frameworks for DRL have emerged. The smallest common denominator for all these frameworks is their usage of the Application Programming Interface (API) offered by OpenAI's Gym plattform (Brockman et al., 2016), which offers standard benchmark environments, such as cartpole. Gym has been superseeded by Gymnasium,[4] which retains a comptabile API.

Several libraries exist or have existed that implement DRL algorithms, such as Stable Baselines (SB3) (Raffin et al., 2021), Tensorforce (Kuhnle et al., 2017), or Google Dopamine (Castro et al., 2018). These focus almost exclusively on a Gym-like API—SB3 enforces it by providing a code checker—, having the goal of providing well-tested implementations, but nothing beyond it. Their distinctive feature is the code style or approach on framework design. In the same vein, Facebook's ReAgent framework (formerly known has Horizon, Gauci et al. (2018)[5] provides a smaller subset of algorithms and relies on a complex preprocessing and dataflow pipeline that uses libraries from Python as well as Java. ReAgent relies on the Gym API, making inverted control flow as it is necessary for CPS simulations almost impossible. *d3rlpy* (Seno and Imai, 2022) focuses on offline learning, but shares otherwise many design decisions of the aforementioned libraries.

rllib (Liang et al., 2018), which is part of the *ray* project, has emerged as one of the most comprehensive frameworks for DRL, covering the most common algorithms (model-free and model-based), offline DRL, and supports several environment APIs, including external environments with inverted control flow (i.e, the environment queries the agent instead of the agent stepping the environment). This makes it suitable for co-simulation approaches, which are commonly applied in CPS simulations. However, rllib does not have the goal of providing a comprehensive scientific simulation platform, and as such lacks facilities for DoE, interfaces to commonly used simulators, or results data storage and analysis.

To date, there is no comprehensive framework that takes an experimentation process as a whole into account, i.e, DoE, executions, results storage, and results analysis. Furthermore, the most actively developed libraries referenced in the previous paragraphs have—with the exception of rllib—committed themselves to enforcing an Gym-style flow of execution, in which the agent "steps," i.e, controls the environment. This design decision makes them unsuitable for more complex simulation setups, such as complex co-simulation (Veith et al., 2020), in which the co-simulation framework has to synchronize all parties and, therefore, reverses control flow by querying the agent for actions instead of allowing the DRL agent to control the flow of execution.

3 High-level approach

The available CTI and descriptions from MUCs already contain domain expert knowledge that describes how a system's vulnerability is being exploited. The MUC template format contains an extended tablespace to describe actors, their behavior, and systems; it also allows for modelling of this through diagrams—mostly sequence diagrams—in the UML. UML allows to annotate diagram elements through stereotypes and parameters. UML modelling tools, such as VisualParadigm, usually allow to export diagrams as XML Metadata Interchange (XMI) (OMG Group, 2005) files. This then makes the MUC a twofold datasource, first through its table format—a specific notation can be easily enforced as well as exportet to a XML file —, second through the UML sequence diagrams.

On the other hand, DRL-based software suites allow to connect learning agents and environments so that the agents, giving the corresponding objective function, can learn to exploit a (simulated) system. However, the agent starts training with zero knowledge, effectively "wasting" iterations before the informed trail-and-error style training that DRL yields first successes. In order to converge faster to a successful policy, we describe a pipeline that connects these two domains. Its main connecting point is an experiment definition with agents that serve as experts (*via* imitation learning) to the DRL agents. It consists of five steps (cf. **Figure 1**).

1 Gathering expert knowledge
2 Formulating the MUC
3 Creating an UML diagram
4 Exporting and reading the XMI/XML file(s)
5 Generating the experiment definition from the XMI/XML file(s)

The first step of this process is knowledge gathering and, in stage 2, filling out the misuse case templates. These have to be very specific and well reviewed to be able to process the domain knowledge further. An error in this stage might lead to severe misunderstanding or wrong defined information and therefore wrong processes learned by the agent. This step is done by domain experts who are able to describe the domain knowledge in a sufficiently precise form. Since the MUC will be machine-read, enforcing certain syntactic elements is important (cf. **Section 4** for details).

Afterwards, a STIX model of the misuse case scenario can be build for later usage.

The next step (stage 3) is the generation and annotation of an UML diagram that shows the relevant information to build an experiment file. MUCs will most likely contain at least one sequence diagram in any case. UML allows to introduce archetypes and parameters, building a model repository. We define custom stereotypes, like agent and environment, along with their parameters, which are then used to derive experiments definitions. Agents are of particular interest here, since our framework does not just employ DRL algorithms, but can use any agent. We define and implement simple agents with scripted behavior that reflects actors in the MUCs. These agents with hard-coded behavior are the experts that are necessary for imitation learning[6].

---

[4] https://github.com/Farama-Foundation/Gymnasium, retrieved: 2022-01-03.

[5] The technical report for *Horizon* is available only as preprint. We treat it the same way as a website reference and provide the bibliography entry here for easier reference.

[6] At a later stage, we also plan to directly derive trajectories by parsing sequence diagrams, but this is currently future work.

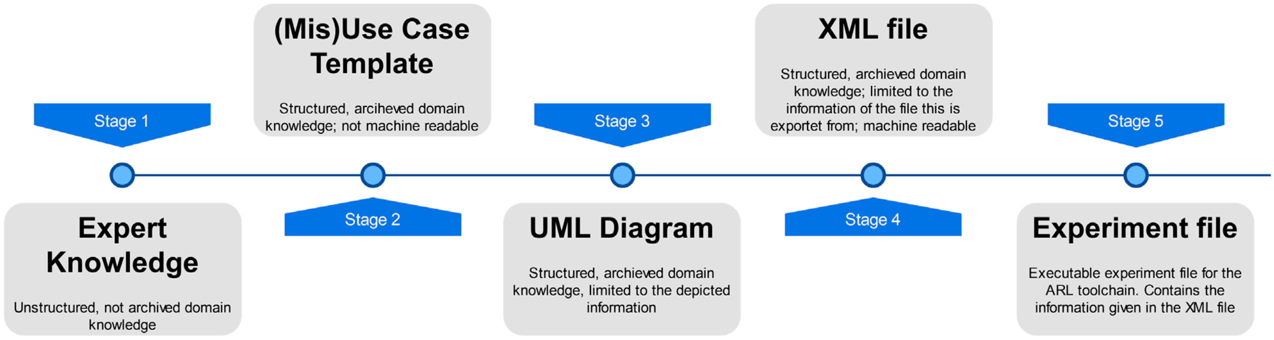

FIGURE 1
From expert knowledge to an experiment file for the ARL toolchain.

The UML diagrams are exported to XMI; along with the MUC, they serve as a data source to derive experiment definitions (stage 4).

Stage 5 entails generating the experiment defintion file. We provide details about this file in Section 5. In general, an experiment file is the basis for a sound DoE, used for experimentation and training and evaluation of DRL agents. The experiments employ several agents in different experimentation phases. DRL agents can learn from the "scripted" agents. One methodology that commonly finds application in this setup is that of Adversarial Resilience Learning (ARL). In ARL, two (or possibly more) agents work as adversaries against each other. Agents do not have knowledge of each other or their respective actions, instead, they observe a system under influence by their adversary. This adversarial condition modifies the distribution of observed sensor inputs to encourage agents to sample more extreme regions, and also to learn more robust strategies. When two learning agents compete, they push each other to learn faster than an agent alone would normally do; learning agents working against a scripted agent also adapt counterstrategies faster in comparison to training solo. Sections 7 and 8 showcase such a competition setup.

After running the experiment, the STIX data can be updated with the found vulnerabilities as well as possible mitigation or attack differentiation.

4 Misuse case modelling and data transfer method

As mentioned in Section 2.2, the misuse-case method is used to precisely describe originally unintended behavior of a system. Therefore, all information from a mostyl regular IEC 62559-based use case template is included as well as the additional knowledge, which is distinctively used to document unintended behaviour.

The overall idea of this approach is to solve an existing semantic gap between two important aspects for the topic. In order to learn form proper attack libraries with real world incidents, a large amount of information for training is needed. Usually, in knowledge management, things are structures to refrain from being anecdotal. This leads to structures documents based on meta models making sure that all important aspects and attributes are covered and, thus, the information is self-contained and useful in a different context. This often involves eliciting the knowledge and experience of domain experts and stakeholders who are not experts in modeling. Structuring this knowledge into a standardized document leads to re-useable, useful knowledge. Often, this process is done in the context of systems engineering or development. However, it is apparent that the scope and detail as well as format for a learning AI is different. There is no fixed suitable API to re-use the use cases as of now. However, the large knowlwdge base both for use cases as well as misuse cases, documenting observable behaviour which is non-intended is large. Security incidents mostly are non-intended behaviour, so re-using the knowledge gathered in a structured manner is the aim discussed in detail in this contribution.

For this paper we do not consider misbehaviour of the system in terms of a faulty implementation but respective stakeholders, e.g, people acting maliciously. Therefore, the actors (and especially the misactors, called "crooks") are in focus of the high-level modeling at first. Hence, these areas of the template must be filled out with particular care.

Two methods are conceivable for the proposed approach in this contribution: Use case supported elicitation of the templates and domain knowledge supported elicitation of the templates. In the first method, a completed use case template is examined to determine the undesired (system) behavior (or, in this case, the attacks) that could affect this use case. This can be done, e.g, by systematically checking the data within the MITRE ATT&CK data set identified to be suitable.

The second method is based on known attacks (in general terms: known undesired behavior) without an underlying use case in particular. Here, the misuse case template is filled in based on the known attack information and, thus, known mitigations.

By following one of these approaches, an domain expert is able to create a misuse case for the desired scenario. Afterwards, checking for consistency with other domain experts and by reviewing different modelling formats like the Smart Grid Architecture Model (SGAM) from the IEC SRD 63200 standard for the energy domain or the STIX data is recommended to rule out possible ambiguity and vagueness resulting from natural language usage.

For the approach presented in this paper, a nearly completed misuse case template is important as a base for the next steps since errors at this level are very likely to propagate to the next steps, thus,

```
Open XML input file ▷ MUC XML and/or diagram XML export
  name_list = empty list
  objective_list = empty list
  for actor in MUC do ▷ either from UML actor definition or by scanning the actor tables in the MUC
     Add name of agent to name_list
     Add objective to objective_list
  end for
  Close XML input file
  Open YAML output file
 Write experiment setup data to the output file ▷ This is simplified for a first presentation of this approach
 for agent_name in name_list do
  Write agent description to the output file ▷ This data is a mixture of already created experiment definitions and the agent description from the input.
  Map agent objective from objective_list
  Write mapped objective to the output file
 end for▷ The following is as well simplified for a first presentation of this approach
 Write sensor and actor information to the output file
 Define phases according to actor information in the output file
 Close YAML output file
 Output the generated YAML file
```

Algorithm 1. Pseudocode: Simplified Generation of a Experiment File from XML Data.

lowering the data quality and validity of the final conclusions to be drawn form the method.

After the MUC template is filled out, the diagrams and the tables of the MUC are exported as serialized and standardized XMI/XML files based on IEC 62559-3. Therefore, the diagrams are exported as a XMI from a tool like visual paradigm, while the MUC DOCX file is exported as a XML file *via* Microsoft Word. These files are then read into a script that generates an experiment file based on the information from the MUC and commonly known information such as the structure. The simplified version of this algorithm is presented as pseudocode in Algorithm 1. For the presentation of this approach only a limited set of information is taken from the MUC. The remaining needed information like, e.g. the environment and the mapped, distinct sensors in this environment are derived from a previous created experiment file.

For receiving the agent data the exported diagram is scanned for entities with the agent stereotype, if a MUC export is used to generate the experiment file, the XML is scanned for the actor table. From these sources the agent name and its objectives are taken. Afterwards the YAML output file is generated. Therefore the setup information from a already created experiment are taken (cf. Section 5 for a description of needed information). The information taken from the input is then merged with the additional information and put together to a complete experiment file.

5 Design of experiments with arsenAI

In order to tackle the problem outlined in Sections 1,2, namely, that currently, there exists no software stack that allows for sound, systematic, and reproducible experimentation of learning agents in CPSs (co-) simulation environments, we have created the *palaestrAI* software stack[7]. Part of the palaestrAI suite is a tool named *arsenAI*, whose focus is to read experiment definitions in YAML format. This experiment definition file contains environments, agents and their objective and defines parameters and factors to vary upon. An arsenAI run outputs a number of experiment run definitions, which contain concrete instantiations of the factors.

An experiment definition start with a unique, user-defined identifier (a unique name for the experiment), a seed value (for reproducibility), a version string to ensure software API compatibility, the number of repetitions and how many experiment runs should be generated from it. It also consists of a number of sub-definitions for agents, environments, sensor sets and actuator sets, and phase configurations.

An agent consists of a learner (nicknamed *brain*), an inference rollout worker (nicknamed *muscle*), as well as an objective. Objectives are agent-specific and based upon the *reward* definition of an environment, as well as the agent's internal state. An environment has a *reward* definition: While the reward describes the states of the environment (e.g, bus voltages), the agent's objective qualitatively describes the agent's goal with regards to the current state/reward (e.g, the deviation from 1.0 pu).

Sensor and actuator sets connect environments to agents. A sensor is a particular input to an agent (e.g, a bus voltage), an actuator is a setpoint (e.g, reactive power generation).

An experiment is subdivided into phases, each phase describing a stage of the experiment. Therefore, an experiment also contains phase configuration definitions. A phase configuration describes whether agents learn (training mode) or only exploit their policy (testing mode), and how many episodes a phase consists of.

Within phases, factors are defined. Possible factors are the combination of agents, environments, phase configurations, and sensor/actuator-set-to-agent mappings. The environments and agents factors have two levels, since agents and environments can be combined.

After computing the design of the experiment, arsenAI decides on the sampling strategy. If the computed number of runs for a full factorial design from the factors (considering all levels) is less or equal than the user-defined maximum number of runs, a full factorial design is indeed generated. Otherwise, the full factorial design is optimized (i.e, sampled) according to the maximin metric (Pronzato and Walter, 1988).

Figure 2 shows a schema of the experiment definition.

---

[7] https://gitlab.com/arl2, retrieved: 2023-01-03.

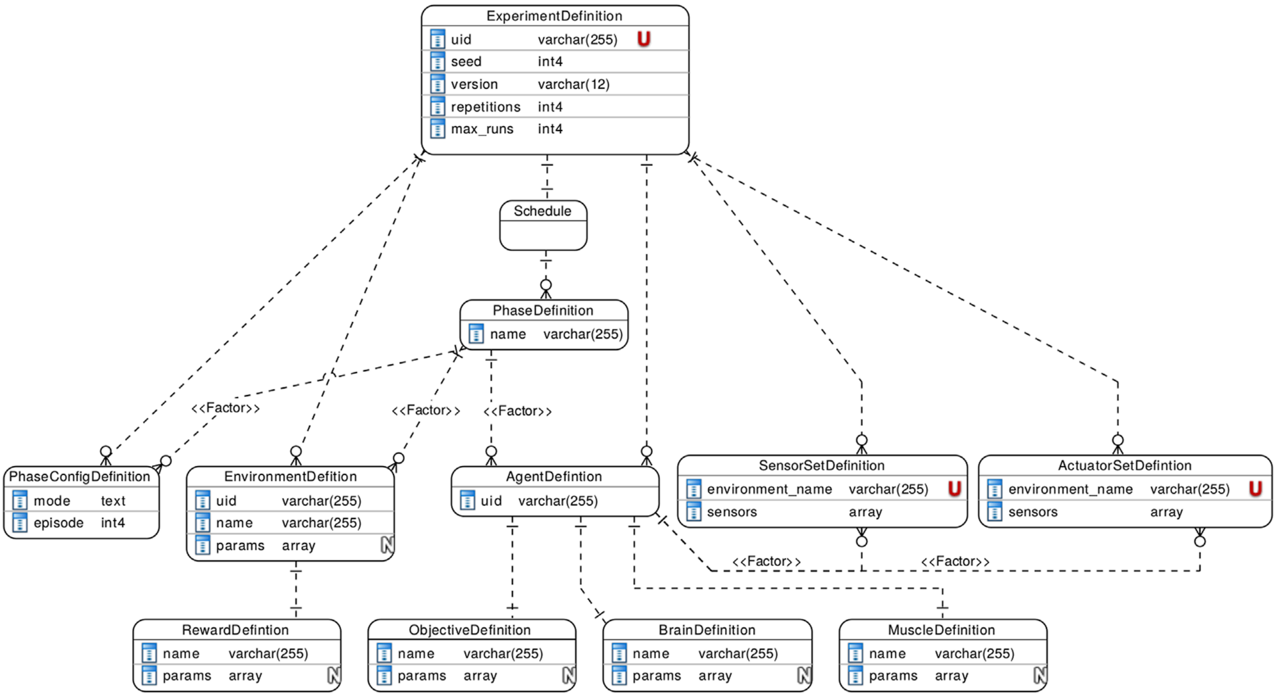

FIGURE 2
Experiment definition schema.

For each sample—and the number of desired repetitions—, arsenAI creates an experiment run definition, which is then picked up by *palaestrAI* to execute. We detail palaestrAI, along with agent designs and learning algorithms, in the next section, **Section 6**.

6 The palaestrAI execution framework

palaestrAI[8] is the execution framework. It offers packages to implement or interface to agents, environments, and simulators. The main concern of palaestrAI is the orderly and reproducible execution of experiment runs, orchestrating the different parts of the experiment run, and storing results for later analysis.

palaestrAI's Executor class acts as overseer for a series of experiment runs. Each experiment run is a definition in YAML format. Experiment run definitions are, in most cases, produced by running arsenAI on an experiment definition. An experiment defines parameters and factors; arsenAI them samples from a space filling design and outputs experiment run definitions, which are concrente instanciations of the experiment's factors.

ExperimentRun objects represent such an experiment run definition as is executed. The class acts as a factory, instanciating agents along with their objectives, environments with corresponding rewards, and the simulator. For each experiment run, the Executor creates a RunGovernor, which is responsible for governing the run. It takes care of the different stages: For each phase, setup, execution, and shutdown or reset, and error handling.

The core design decision that was made for palaestrAI is to favor loose coupling of the parts in order to allow for any control flow. Most libraries[9] enforce an OpenAI-Gym-style API, meaning that the agent controls the execution: The agent can reset() the environment, call step(actions) to advance execution, and only has to react to the step(·) method returning done. Complex simulations for CPSs are often realized as co-simulations, meaning that they couple domain specific simulators. Through co-simulation software packages like *mosaik* (Ofenloch et al., 2022), these simulators can exchange data; the co-simulation software synchronizes these simulators and takes care of proper time keeping. This, however, means that palaestrAI's agents act just like another simulator from the perspective of the co-simulation software. The flow of execution is controlled by the co-simulator.

palaestrAI's loose coupling is realized using ZeroMQ (Hintjens, 2023), which is a messaging system that allows for a reliable request-reply patterns, such as the majordomo pattern (Górski, 2022; Hintjens, 2023). palaestrAI starts a message broker (`MajorDomoBroker`) before executing any other command; the modules then either employ a majordomo client (sends a request and waits for the reply), or the corresponding worker (receives requests, executes a task, returns a reply). Clients and workers subscribe to topics, which are automatically created on first usage. This loose

---

[8] https://gitlab.com/arl2/palaestrai, retrieved: 2023-01-03.

[9] cf. **Section 2**.

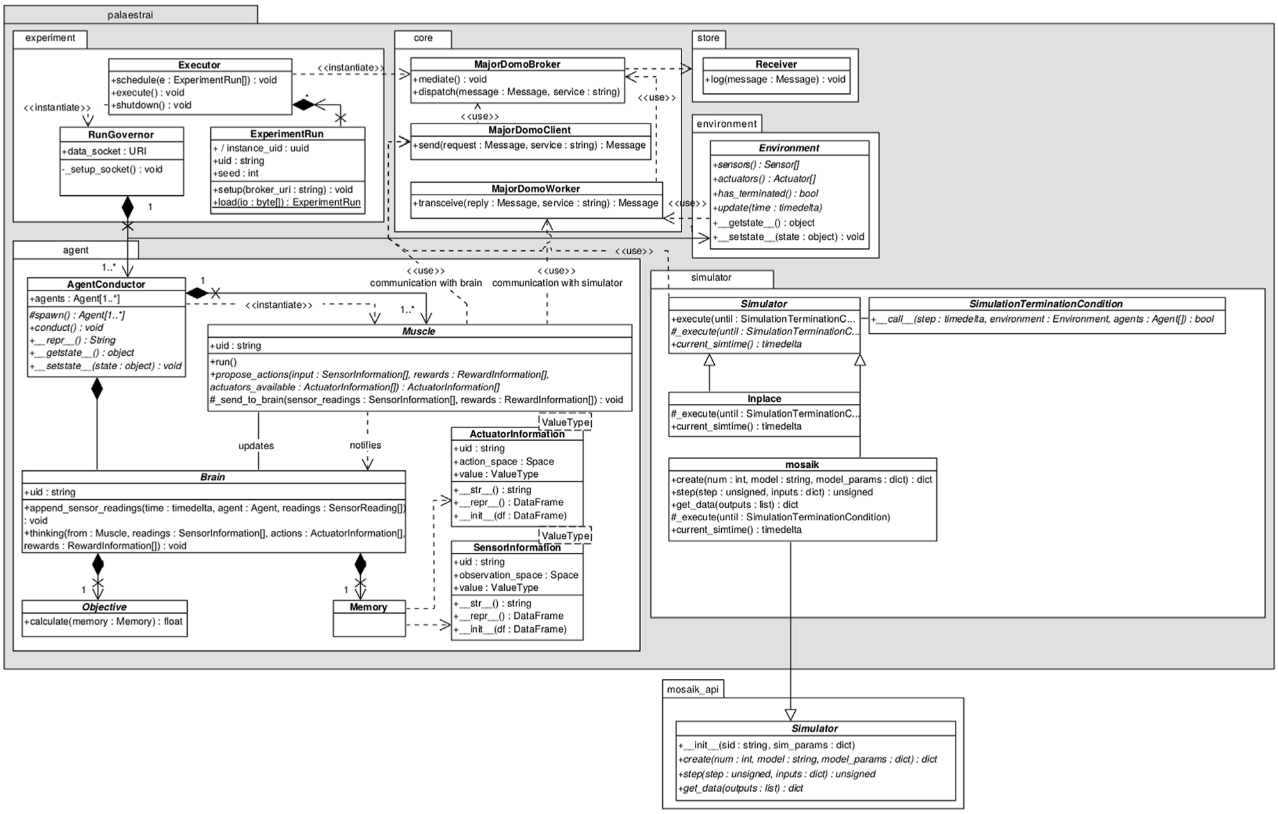

FIGURE 3
The palaestrAI core framework.

coupling through a messaging bus enables the co-simulation with any control flow.

In palaestrAI, the agent is split into a learner (`Brain`) and a rollout worker (`Muscle`). The muscle acts within the environment. It uses a worker, subscribed to the muscle's identifier as topic name. During simulation, the muscle receives requests to act with the current state and reward information. Each muscle then first contacts the corresponding brain (acting as a client), supplying state and reward, requesting an update to its policy. Only then does the muscle infer actions, which constitute the reply to the request to act. In case of DRL brains, the algorithm trains when experiences are delivered by the muscle. As many algorithms simply train based on the size of a replay buffer or a batch of experiences, there is no need for the algorithm to control the simulation.

But even for more complex agent designs, this inverse control flow works perfectly fine. The reason stems directly from the MDP: Agents act in a state, $\boldsymbol{s}_t$. Their action $\boldsymbol{a}_t$ triggers a transition to the state $\boldsymbol{s}_{t+1}$. I. e, a trajectory is always given by a state, followed by an action, which then results in the follow-up state. Thus, it is the state that triggers the agent's action; the state transition is the result of applying an agent's action to the environment. A trajectory always starts with an initial state, not an initial action, i. e, $\tau = (\boldsymbol{s}_0, \boldsymbol{a}_0, \ldots)$. Thus, the control flow as it is realized by palaestrAI is actually closer to the scientific formulation of DRL than the Gym-based control flow.

In palaestrAI, the SimulationController represents the control flow. It synchronizes data from the environment with setpoints from the agents, and different derived classes of the simulation controller implement data distribution/execution strategies (e.g, scatter-gather with all agents acting at once, or turn-taking, etc.)

Finally, palaestrAI provides results storage facilities. Currently, SQLite for smaller and PostgreSQL for larger simulation projects are supported, through SQLalchemy[10]. There is no need to provide a special interface, and agents, etc. do not need to take care of results storage. This is thanks to the messaging bus: Since all relevant data is shared *via* message passing (e.g, sensor readings, actions, rewards, objective values, etc.), the majordomo broker simply forwards a copy of each message to the results storage. This way, the database contains all relevant data, from the experiment run file through the traces of all phases to the "brain dumps," i.e, the saved agent policies.

Figure 3 shows an excerpt of the palaestrAI software stack with the packages and classes mentioned until now.

arsenAI's and palaestrAI's concept of experiment run phases allow for flexibility in offline learning or adversarial learning through autocurricula (Baker et al., 2020). Within a phase, agents

---

[10] https://www.sqlalchemy.org/, retrieved: 2023-01-04.

can be employed in any combination and any sensor/actuator mapping. Moreover, agents—specifically, brains—can load “brain dumps” from other, compatible agents. This enables both offline learning and autocurricula within an experiment run in distinct phases.

7 Experimental concept validation

7.1 (Mis-) use cases considered

For initial validation of our approach, we describe two MUCs in the power grid domain that constitute clear attacks on normal grid operation. For both scenarios, we generate experiment definitions from the MUC; we execute the experiment runs and showcase the results in **Section 8**. We believe that this validates the initial feasibility of our approach. Since we focus on the software part of the approach, we do not provide extensive analysis of agents that have learned in an autocurriculum or offline learning scenario *versus* pure (single) DRL agent learning scenarios, as we regard this as future work.

The MUCs considered in this paper are.

- Inducing of artificial congestion as a fascailly motivated attack on local energy markets
- attacking reactive power controllers by learning oscillating behavior.

While the first MUC describes an internal misbehaviour in which the participating actors have the rights to control their components, while in the second MUC, the components controlled by the attacking agent have been corrupted.

7.1.1 Market exploitation misuse case

The first scenario, which is shown in **Figure 4**, can be described as a loophole in the operation of local energy markets. Local energy markets exist to allow operation of a (sub-) grid in a more efficient manner without needing grid expansion: They incentivize load shifting or feed-in adjustment to resolve congestion situation. Whenever the grid operator forecasts a congestion, it will place an offer on the local energy market for consumption reduction. Participants can bid on this offer, and if they adjust their consumption, they will receive compensation according to their bid.

The loophole exists in market participants artificially creating the congestion. A group of participants can “game” the market by creating a bottleneck in their energy community (e.g., by charging electric vehicles). The grid operator will react by incentivizing load shifting. Since this load was created without a real need, it is easy for the crooks to place bids and, once won, follow the new load schedule in order to receive compensation. This can be repeated easily. The grid operator, however, is not able to distinguish this from legitimate demand, since consumers use the appliance they have access to in any normal case.

7.1.2 Voltage band violation attack through oscillating reactive power feed-in/consumption

The second considered scenario describes a different kind of attack. It is assumed that a attacker already claimed some components in the energy grid and is able to control them (e.g., photovoltaic panels). One of the main tasks in distribution grids is voltage control. DERs can be used for this through their inverters.

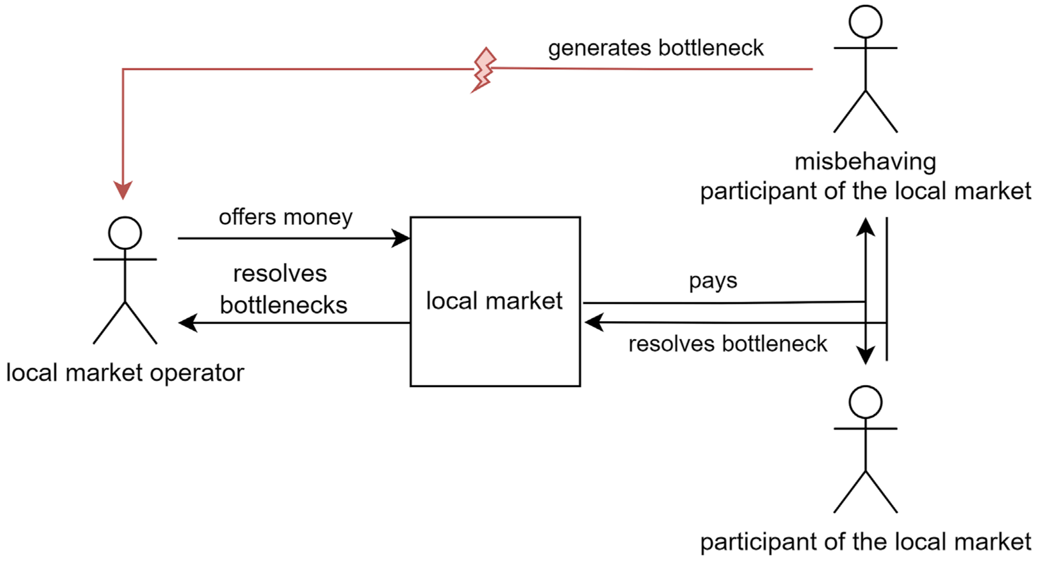

FIGURE 4
Misuse case actor diagram depicting energy market exploitation through artificially created congestions.

Since the distribution grids have been carrying most of the DER installations, incorporating these into the voltage control scheme is an obvious strategy.

DERs also turn voltage control into a distributed task. We do not propose a new voltage control scheme; instead, we employ a distributed control scheme that has also been proposed and used by other authors. Namely, Zhu and Liu (2016) proposed a distributed voltage control scheme where the reactive power injection/consumption at a time t at each node is governed by:

$$\boldsymbol{q}(t+1) = [\boldsymbol{q}(t) - \boldsymbol{D}(\boldsymbol{V}(t) - 1)]^{+}, \tag{1}$$

where the notation $[\cdot]^{+}$ denotes a projection of invalid values to the range $[\underline{\boldsymbol{q}}^{g}, \overline{\boldsymbol{q}^{g}}]$, i.e., to the feasible range of setpoints for $q\,(t+1)$ of each inverter. $\boldsymbol{D}$ is a diagonal matrix of step sizes.

We denote the attack strategy described by Ju and Lin (2018) as "hard-coded oscillating attacker behavior." It can be described by a simple Mealy automaton with the internal state t, which is a time-step counter that represents the time the agent remains in a particular state. We note two states,

$$Q = \{low, high\}. \tag{2}$$

This attacker remains in a particular state until a hold-off time T_h is reached. The hold-off time allows the benign voltage controller to adjust their reactive power feed-in/consumption, $q(t)$. The attacker then suddenly inverts its own reactive power control, i. e, switches between $\underline{\boldsymbol{q}}^{g}$ and $\overline{\boldsymbol{q}^{g}}$.

$$\delta(low, t) = \begin{cases} high & \text{if } t = T_h, \\ low & \text{else,} \end{cases} \tag{3}$$

$$\delta(high, t) = \begin{cases} low & \text{if } t = T_h, \\ high & \text{else.} \end{cases} \tag{4}$$

Thus, $q(t, low) = \underline{\boldsymbol{q}}^{g}$ and $q(t, high) = \overline{\boldsymbol{q}^{g}}$.

In this scenario, the attacker wants to exploit the behavior (= AE) of the defending agent. Therefore, the attacking agent controls the assets taken over by him in a way that the voltage level is dropped or increased. In the next step the voltage band defending agent controls its assets to compensate the changes applied by the attacking agent. The attacking agent then operates contrary to his previous action. Therefore the compensation of the defender leads to an even higher outcome for the attacker.

In the next iteration the defending agent would again compensate by an even higher value also contrary to his previous action. The attacker would repeat his behaviour. These repeated behaviours then would lead into a pendulum movement of the voltage band and eventually lead to a loss of function as the deviation becomes to high to keep the energy grid stable.

For the simulation, we define the reward as a vectorized function of all bus voltage magnitudes observable by an agent, after all agent actions are applied:

$$\boldsymbol{r}_{s,a}(t) = \left[V_1(t), V_2(t), \ldots, V_k(t), \ldots, V_n(t)\right]^{\top},\ \forall V_k(t): V_k(t) = o \in \Omega \tag{5}$$

As the agent's objective expresses the desired state (i. e, goal) of the agent, we formulate $p_{\Lambda}(\boldsymbol{r}_{s,a}(t))$ such that it induces an oscillating behavior, where the agent switches between full reactive power injection and full reactive power consumption within the boundaries of what the connected inverter is able to yield. Since we are not bound to formulate the objective in a specific way, we described this desired behavior by a function modeled after a normal distribution's probability density function:

$$g(x, A, \mu, C, \sigma) = A \cdot \exp\left(-\frac{(x-\mu)^2}{2\sigma^2} - C\right). \tag{6}$$

In order to encourage the agent to make use of the oscillating behavior, we formulate the attacker's objective by using the reward machine device (Icarte et al., 2018). That is, we introduce three states, modeled as a Mealy state machine:

$$Q = \{low, nominal, high\}. \tag{7}$$

The state machines alphabet Σ consists of the reward,

$$\Sigma = \{\tilde{r}_{s,a} = \text{median}(\boldsymbol{r}_{s,a}) \forall \boldsymbol{r}_{s,a}\}. \tag{8}$$

We transition between the three states based on the current reward as well as the time the reward machine's initial state remains the same. This holdoff time T_h is chosen deliberately to give the benign voltage controllers time to adjust, i. e, to find equilibrium in the current extreme state the attacker agent has introduced. The state transition functions are thus.

$$\delta(nominal, t) = \begin{cases} low & \text{if } \tilde{r}_{s,a} \geq 1.05 \wedge t = T_h, \\ high & \text{if } \tilde{r}_{s,a} \leq 0.95 \wedge t = T_h, \\ nominal & \text{else,} \end{cases} \tag{9}$$

$$\delta(low, t) = \begin{cases} nominal & \text{if } \tilde{r}_{s,a} \leq 0.88 \wedge t = T_h, \\ low & \text{else,} \end{cases} \tag{10}$$

$$\delta(high, t) = \begin{cases} nominal & \text{if } \tilde{r}_{s,a} \geq 1.12 \wedge t = T_h, \\ high & \text{else.} \end{cases} \tag{11}$$

For each state, we define an objective function based on Eq. 6.

$$p_{\Lambda,nominal}(\boldsymbol{r}_{s,a}) = g(\tilde{r}_{s,a}, -12, 1, -10, -0.05), \tag{12}$$

$$p_{\Lambda,low}(\boldsymbol{r}_{s,a}) = g(\tilde{r}_{s,a}, -14, 0.84, -12, -0.08), \tag{13}$$

$$p_{\Lambda,high}(\boldsymbol{r}_{s,a}) = g(\tilde{r}_{s,a}, -14, 1.16, -12, -0.08). \tag{14}$$

The values for A, μ, C, and σ are chosen by us deliberately to create the desired effect. Visual inspection of the resulting objective function, plotted over the voltage band in **Figure 5**, where the state transitions

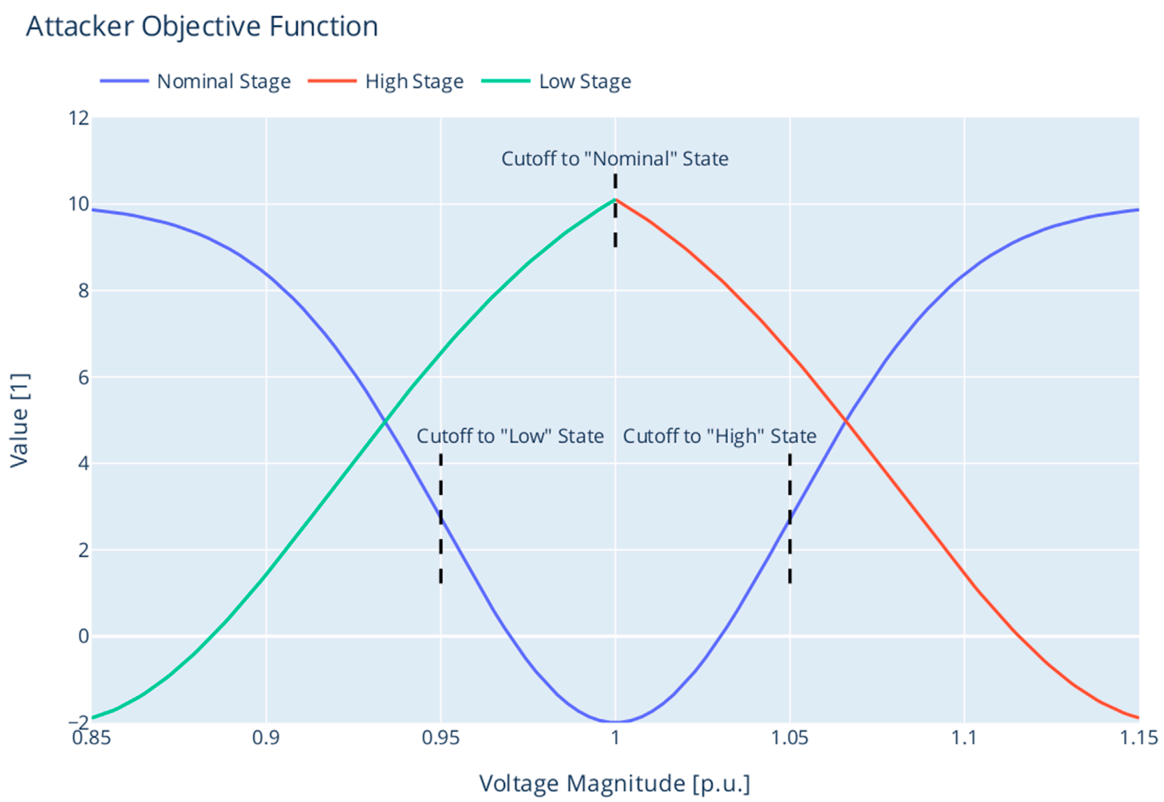

FIGURE 5
Attacker objective as a function of the voltage magnitude, with state transition boundaries.

are marked by the vertical dashed lines, shows the desired shape that urges the agent to apply an oscillating behavior to foil simple reactive power controllers. Essentially, the attacker starts in the state fitting to the current reward $r_{\widetilde{s,a}}$, which will most likely be $q = nominal$. As it then works towards over- or under-voltage. If attained, the agent remains in the state until the holdoff time is reached, all the while receiving positive objective value for keeping the extreme state. Note that the objective value will diminish due to the benign voltage controllers' actions. Then, $q \in \{low, high\}$ is chosen according to $r_{\widetilde{s,a}}$. With the changed state, the agent receives a low objective value and is subsequently forced to act towards the other extreme voltage region. The state changes back to $q = nominal$, the agent's momentum as well as the actions by the benign voltage controllers will yield the transition to the opposite extreme state. Note that $\delta(\cdot)$ implements a hysteresis with regards to $r_{\widetilde{s,a}}$.

7.2 Experiment setup

To validate the described method, an experimental setup was build. Therefore the needed information of the misuse cases described in chapter 7.1 were transferred to the misuse case template[11] described in **Section 4**. Afterwards this template (written in DOCX format) is exported to a XML-file. The next step is to then export the required information from this format and paste it into the YAML experiment description presented in chapter 5. The considered information in the experimental setup is the objective as well as the name of the agents. To achieve the correct syntax, the agents entered objectives are mapped to the syntax of the file in YAML format. In this experimental setup, the exact input is used. Therefore, a strict restriction is given.

For our experiment, we additionally employ the MIDAS[12] software suite that provides the simulation environment setup: It incorporates the PySimMods[13] software package that contains numerous models for power grid units, such as batteries, Photovoltaic (PV) or Combined Heat and Power (CHP) power plants. The grid model is a CIGRÉ Medium Voltage (MV) grid model (Rudion et al., 2006).

Each node has a constant load of $342 + j320\,\text{kVA}$ attached to; the loads are not subject to time series, but remain constant in all experiment scenarios. This constant load accounts for the real power feed-in that occurs naturally because of the inverter model. The goal is to maintain an average voltage magnitude close to 1.0 pu on every bus if no action is taken. This way, the reactive power controllers suffer no handicap in their ability to feed or consume reactive

---

[11] These templates can be found here: https://gitlab.com/arl2/muclearner.

[12] https://gitlab.com/midas-mosaik/midas, retrieved: 2023-01-04.

[13] https://gitlab.com/midas-mosaik/pysimmods, retrieved: 2023-01-04.

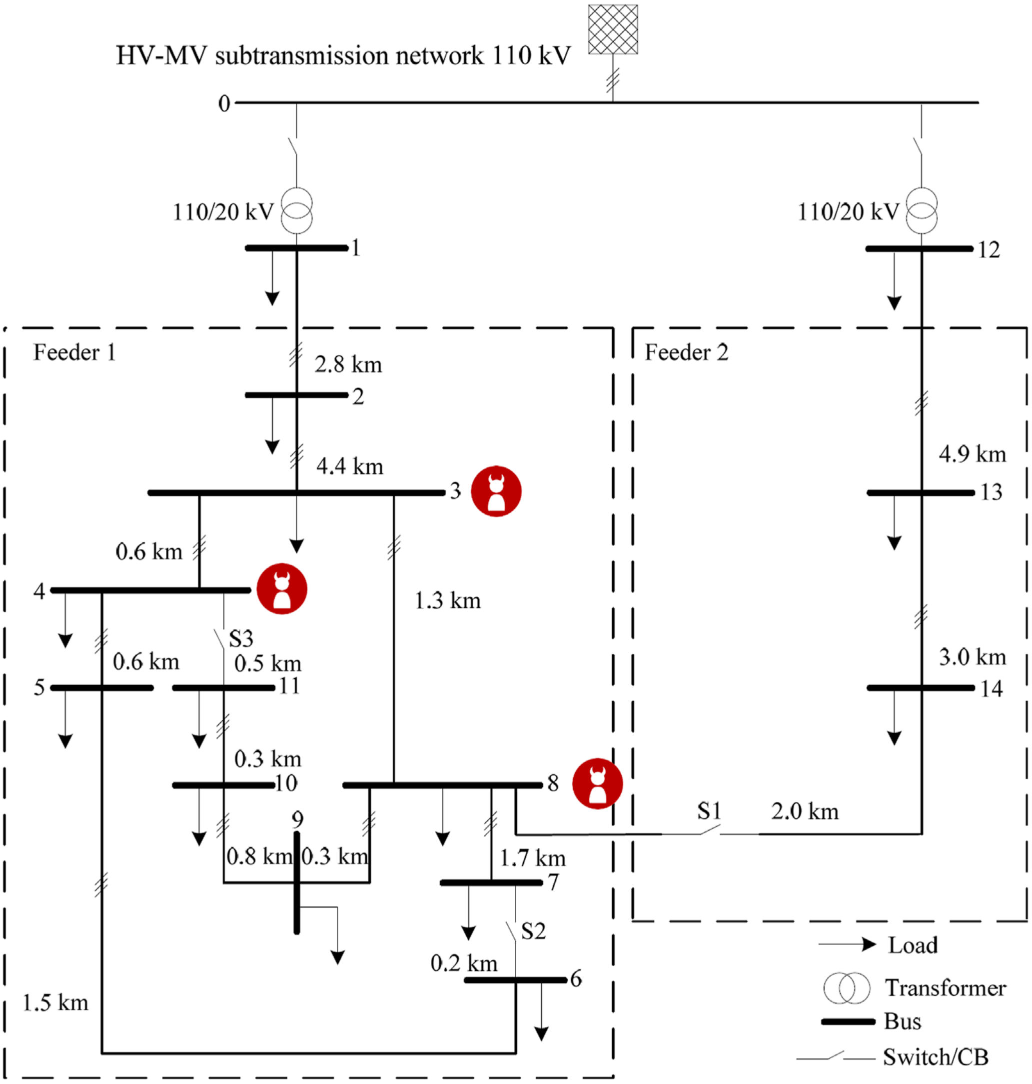

FIGURE 6
The CIGRÉ MV grid used for the simulation, with attacker nodes marked.

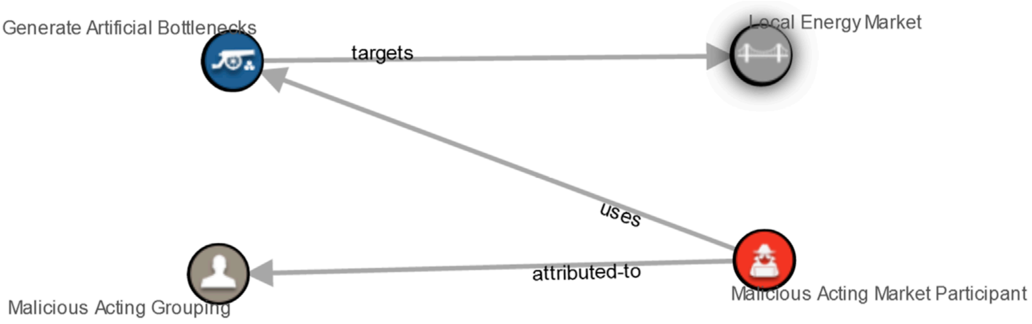

FIGURE 7
STIX visualization of the energy market exploitation through artificial congestion misuse case.

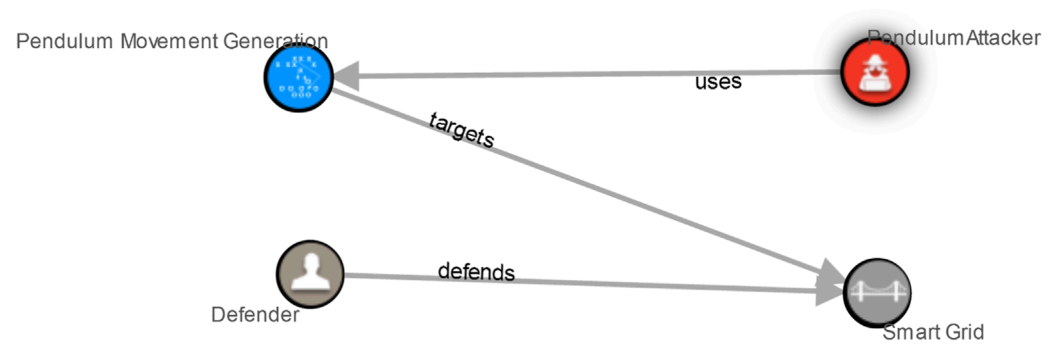

FIGURE 8
STIX visualization of the voltage band violation attack misuse case.

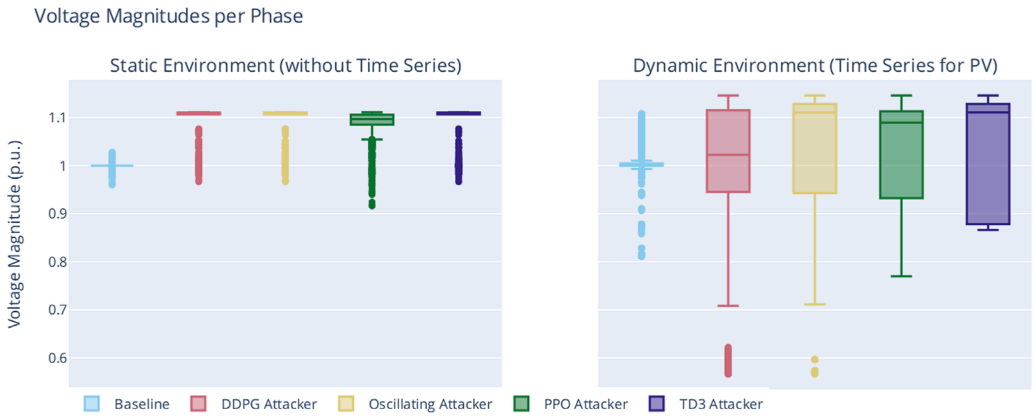

FIGURE 9
Voltage magnitudes for each experiment phase in the voltage band violation scenario.

power when the attack starts. The power grid has 9 PV power plants attached at buses 3 to 9, 11, and 13. The PV plants' output is dependent on the solar irridation, which is governed by a multi-year weather dataset from Bremen, Germany[14]. The PV installations vary between $P_{peak} = 8.2$ kW to 16.9 kW, with $\cos\varphi = 0.9$. This represents smaller PV plants in rural areas as a realistic setup. The individual values in this range have been chosen so that the reactive power control scheme can maintain 1.0 pu on all relevant buses without using the full capability range of the inverters. We have deliberately chosen not to include any consumers governed by load profiles in order to make the effect of the controlled inverters visible in isolation; we rely on the aforementioned constant load to provide a balanced grid without tap changers or other measures.

The attacker controls the buses 3, 4, and 8, as depicted in Figure 6. Buses 5, 7, 9, and 11 are governed by the distributed voltage control scheme. To each attacker and defender bus, a PV plant is connected. The other buses are not governed by any controller. Each benign voltage controller applies the distributed control law (Zhu and Liu, 2016) as described in Eq. 1. We have chosen $\boldsymbol{D} = 10\boldsymbol{J}$ for all experiments as this provides stable operation in all normal cases and allows the voltage controllers to converge at 1.0 pu quickly.

8 Initial results

After completing the MUC templates, a STIX 2.1 file was created for both scenarios. The STIX visualization for the local market MUC and the oscillating attack MUC is shown in Figures 7, 8, respectively.

From the oscillation MUC, we have derived 10 distinct simulation phases: Two baseline phases, in which only the voltage controller acted (with and without time series). Then, two reproduction phases implementing the voltage controller and the "hard-coded" oscillating attacker. Three phases then pitched learning agents as attackers against the voltage controller without time series for solar irradiation (using DDPG, PPO, and TD3). Finally, three phases with learning agents against the voltage controller with time series for PV feed-in (again, using DDPG, PPO, and TD3). For a more concise naming, we attribute all phases

---

[14] Publicly available from https://opendata.dwd.de/climate_environment/CDC/observations_germany/climate_urban/hourly/, last accessed on 2022-12-21.

TABLE 1 Bus voltage statistics per phase.

		Voltage magnitude (V)	Voltage change (ΔV)	$\|\Delta V\|$
Baseline (Dynamic Environment)	count	11516.000000	11516.000000	11516.000000
	mean	0.999872	0.057361	0.090698
	std	0.062668	0.097921	0.068207
	min	0.811263	−0.433200	0.000000
	25%	0.999930	0.010224	0.050958
	50%	1.000047	0.082429	0.092514
	75%	1.004542	0.109869	0.110435
	max	1.108212	0.299196	0.433200
Baseline (Static Environment)	count	11516.000000	11516.000000	11516.000000
	mean	0.999981	0.072921	0.110966
	std	0.001362	0.096093	0.047298
	min	0.959793	−0.433243	0.000000
	25%	1.000000	0.106728	0.106728
	50%	1.000000	0.110000	0.110459
	75%	1.000000	0.111117	0.116616
	max	1.028069	0.146148	0.433243
DDPG Attacker Test (Dynamic Environment)	count	11516.000000	11516.000000	11516.000000
	mean	0.995789	0.063267	0.101744
	std	0.152639	0.143687	0.119567
	min	0.566757	−0.353225	0.000000
	25%	0.945417	−0.029111	0.031682
	50%	1.022739	0.037074	0.056725
	75%	1.115075	0.114114	0.139078
	max	1.146148	0.543701	0.543701
DDPG Attacker Test (Static Environment)	count	11516.000000	11516.000000	11516.000000
	mean	1.107688	−0.072166	0.078247
	std	0.014004	0.104255	0.099771
	min	0.966473	−0.543701	0.000000
	25%	1.106728	−0.110459	0.010518
	50%	1.110000	−0.033108	0.034676
	75%	1.110459	−0.000402	0.110459
	max	1.111117	0.093318	0.543701
Oscillating Attacker Test (Dynamic Environment)	count	11516.000000	11516.000000	11516.000000
	mean	1.014041	0.023748	0.078241
	std	0.187259	0.148614	0.128561
	min	0.566757	−0.365138	0.000000
	25%	0.943205	−0.032850	0.000048
	50%	1.110759	0.000000	0.022270
	75%	1.128298	0.000259	0.110939
	max	1.146148	0.543701	0.543701

(Continued on the following page)

TABLE 1 (*Continued*) Bus voltage statistics per phase.

		Voltage magnitude (V)	Voltage change (ΔV)	|ΔV|
Oscillating Attacker Test (Static Environment)	count	11516.000000	11516.000000	11516.000000
	mean	1.107784	−0.061371	0.069888
	std	0.013851	0.102469	0.096860
	min	0.966473	−0.543701	0.000000
	25%	1.106728	−0.110459	0.000000
	50%	1.110000	−0.000025	0.027149
	75%	1.110459	0.000000	0.110459
	max	1.111117	0.111526	0.543701
PPO Attacker Test (Dynamic Environment)	count	11516.000000	11516.000000	11516.000000
	mean	1.040090	0.011982	0.071037
	std	0.093043	0.102387	0.074700
	min	0.769513	−0.365138	0.000000
	25%	0.932489	−0.036045	0.015108
	50%	1.089641	0.003176	0.039290
	75%	1.113058	0.044599	0.105719
	max	1.146148	0.326380	0.365138
PPO Attacker Test (Static Environment)	count	11516.000000	11516.000000	11516.000000
	mean	1.092604	−0.053452	0.074535
	std	0.019241	0.108056	0.094750
	min	0.916199	−0.543701	0.000000
	25%	1.085396	−0.101075	0.014728
	50%	1.096973	−0.004827	0.040984
	75%	1.105993	0.016971	0.101154
	max	1.111117	0.125942	0.543701
TD3 Attacker Test (Dynamic Environment)	count	11516.000000	11516.000000	11516.000000
	mean	1.043524	0.018580	0.081877
	std	0.113429	0.118515	0.087673
	min	0.865940	−0.299182	0.000000
	25%	0.878356	−0.032807	0.002785
	50%	1.110759	−0.000204	0.034394
	75%	1.128298	0.105044	0.133033
	max	1.146148	0.244519	0.299182
TD3 Attacker Test (Static Environment)	count	11516.000000	11516.000000	11516.000000
	mean	1.107784	−0.060843	0.069028
	std	0.013851	0.101105	0.095703
	min	0.966473	−0.543701	0.000000
	25%	1.106728	−0.110459	0.000000
	50%	1.110000	−0.000144	0.025354
	75%	1.110459	0.000000	0.110459
	max	1.111117	0.109631	0.543701

TABLE 2 **Number of voltage band violations.**

Phase	V < 0.96p.u.	V > 1.04p.u.	Total violations
DDPG Attacker Test (Dynamic Environment)	4554	5397	9951
DDPG Attacker Test (Static Environment)	0	11333	11333
Oscillating Attacker Test (Dynamic Environment)	3519	7780	11299
Oscillating Attacker Test (Static Environment)	0	11333	11333
PPO Attacker Test (Dynamic Environment)	3360	7263	10623
PPO Attacker Test (Static Environment)	15	11277	11292
TD3 Attacker Test (Dynamic Environment)	3248	7454	10702
TD3 Attacker Test (Static Environment)	0	11333	11333

without time series as “static” and those with time series data as “dynamic.”

Figure 9 shows a box plot of the voltage magnitudes at the victim buses for each phase. The boxplot is based on the raw data available in Table 1. Additionally, Table 2 counts the voltage band violations for each phase.

The baseline phases verify that the reactive power controller works, because apart from some outliers that are due to initial swing-in behavior of the controller (cf. also the baseline in Figure 10), voltage median is at 1.0 pu.

All “attacker” boxes in Figure 9 show deviation from 1.0 pu. The hard-coded oscillating attacker sets the Voltage Magnitude (VM) median value to ≈ 1.1 pu in the “static” as well as in the “dynamic” environment phase. From this, we infer that the attack was indeed effective. The maximum VM in terms of voltage is 1.11 pu for the static, and 1.146 pu in the dynamic case. As the only difference between the two phases the introduction of time series, we believe that, in general, the hard-coded oscillating behavior amplifies the effect of change in solar irradiation over the day. However, due to the hard-coded nature of the simple attacker, finding the “right” moment to leverage, e. g, sunrise happens most probably by coincidence, since T_h is static.

The Oscillating Attacker phases in Figures 9, 10 serve as an additional baseline in order to reproduce and ascertain the attack documented by Ju and Lin (2018). As the effects of this kind of attack have already been published, these phases serve as a validation of our simulation set-up and baseline for comparison. Thus, we believe that the effectiveness of the original attack has been reproduced, and the relationship (Ju and Lin, 2018) holds:

$$\lim_{T_h \to \infty} \left[V_b \left(T_h + 1 \right) \right] = -2 \left[\boldsymbol{X} \right] \bar{\boldsymbol{q}}, \tag{15}$$

where T_h is the hold-off time of the attacker (usually until the victim buses have reached equilibrium), $\boldsymbol{X}$ is the reactance of the subgrid with the attackers as root nodes, and $\bar{\boldsymbol{q}}$ represents the extreme reactive power value of the attacker (either feed-in or consumption).

Through Figure 9, we can compare these baselines to the phases in which the learning agents are employed. All algorithms also obtain a maximum VM of 1.1 pu and 1.146 pu (static and dynamic environment, respectively), which seems to be the maximum attainable VM for our simulation setup. Considering the VM ranges obtained by the learning agents, the high medium VM, which are on par with the hard-coded oscillating attacker (with the exception of DDPG in the dynamic environment), the simulation results indicate that the learning agents have discovered an attack.

As scenario 2 enables time series for solar irradiation, we observe that good timing of the oscillation increases the deviating effect on the voltage band, most probably owing to the real-power feed-in happens in addition to the effect of the reactive power curve on voltage levels.

Scenarios 3 and 4 replace the simple oscillating attacker with an DRL-based agent. The phases are, in accordance, labeled from the algorithm that was employed: DDPG, PPO, or TD3. Again, Figure 9 establishes that each agent was able to generate an effect that can be seen as an attack to the power grid. Each produced the same maximum voltage level, with DDPG obtaining the exact same under-voltage level and in general similar values—albeit with a lower median, close to 1.0 pu—as the simple oscillating attacker. Notably, PPO- and TD3-based attackers did not produce any outliers while maintaining a high median in the dynamic environment. The box plot of the TD3-based attacker suggests that this is the deadliest attacker, obtaining a high voltage band deviation (median VM, no outliers) throughout the simulation runs.

In order to verify our imitation learning hypothesis, we must establish whether the agents have actually learned to attack. The most commonly used method to infer whether an agent has learned to reach a certain objective is to analyze its objective function, which is the agent-specific reward for a state transition, considering its goal. We have already described the employed attacker objective in Eq. 12. Figure 11 plots the objective function (raw objective as well as moving average) for all four attacker phases for the “dynamic” grid, i. e, with time series for solar irradiation.

The objective plot of the simple oscillating attacker is straightforward, showing the oscillation clearly during the night, when the PV inverters’ capabilities directly influence the grid. During the day, the real power feed-in leads to over-voltage, no longer making the oscillating behavior effective or even visible.

DRL essentially solves the optimization problem, that each algorithm ultimately attempts to find an optimal policy π^* by maximizing the agent’s objective function. We can therefore

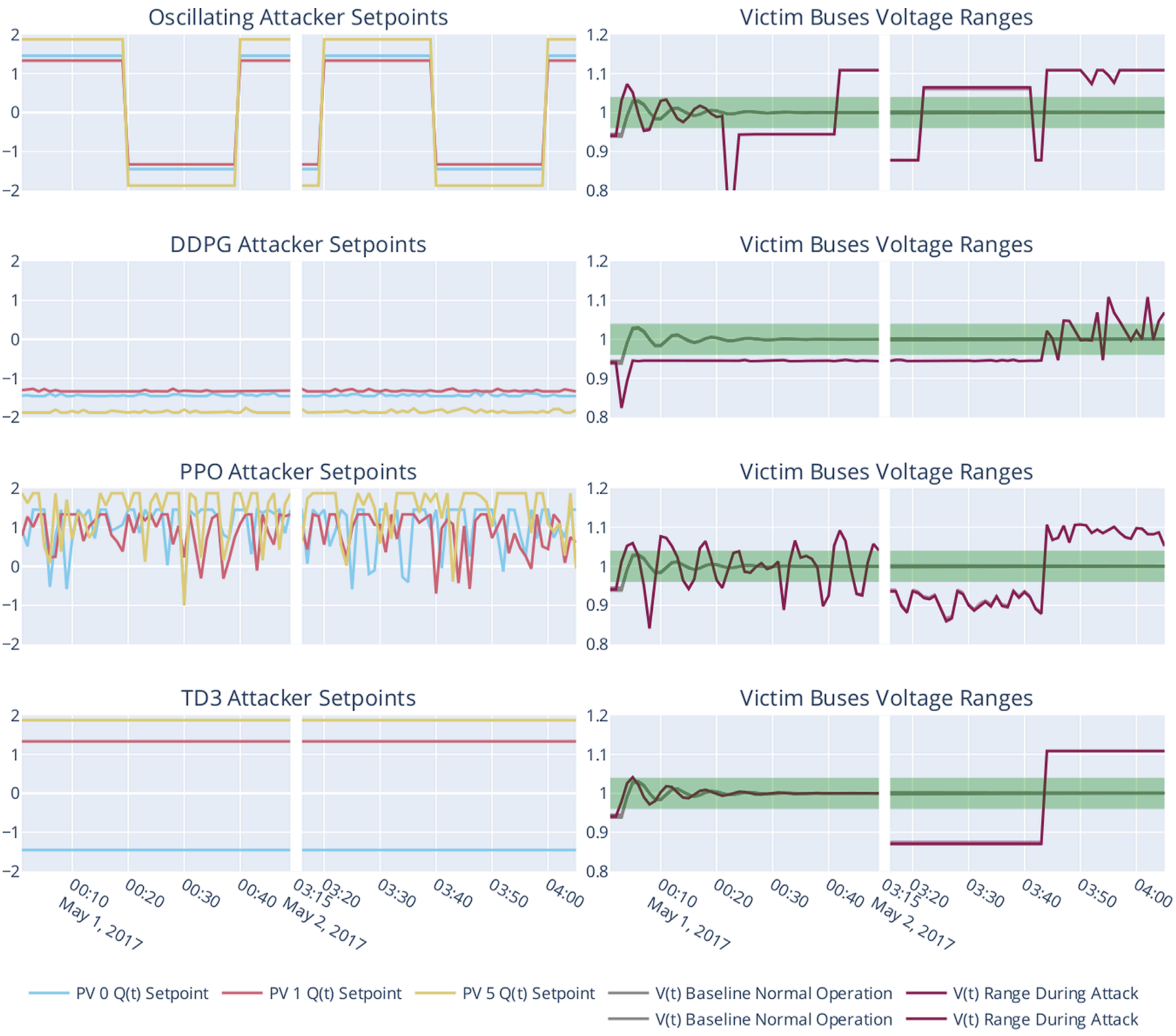

FIGURE 10
Setpoints of the attackers' actuators as well as the obtained objective value. Note that the graphs contain an intentional time gap between 00:50 and 03:15.

infer the attacker agents' policy from the objective function plots.

Both the DDPG-based as well as the PPO-based agent have derived a policy that incorporates an oscillating behavior. Although the DDPG-based agent was not able to yield behavior that came close to the original attack, with only mediocre average objective values.

The PPO-trained agent, on the other hand, obtained higher average objective values while still showing the oscillating behavior of the original attack. It obtained reliable over- and undervoltages. From the shape of the objective function (cf. Figure 5), we know that residing in extreme values is discouraged by the objective (and values close to 1.0 pu are penalized). PPO takes advantage of daytime solar irradiation but maintains the oscillating behavior even during midday.

TD3 shows to be the most interesting of all attackers. The TD3-based attacker has learned no oscillating behavior at all. However, the policy obtained by training with TD3 manages to yield consistently high objective values. By simple deduction, we can therefore infer that the oscillating behavior of malicious inverters is not necessary to yield appropriate damage to victim buses.

Investigating actual agent behavior during two timeframes in Figure 10 in combination with data displayed in Figures 9, 11 gives rise to the hypothesis that (1) damaging the power grid does not need oscillating behavior, (2) can have an equally high impact, and (3) is potentially more dangerous as it does need several oscillating steps, thus making it more surprising for benign buses and the grid operator. None of the learning agents possessed any domain knowledge or had access to sensors apart from its own, node-local ones. While the TD3-based agent has simply learned a vector of setpoints that will eventually prove to be fatal, the DDPG-based attacker's slight oscillations cause the benign reactive power controller to yield stark oscillating behavior, too.

10.3389/fenrg.2023.1138446

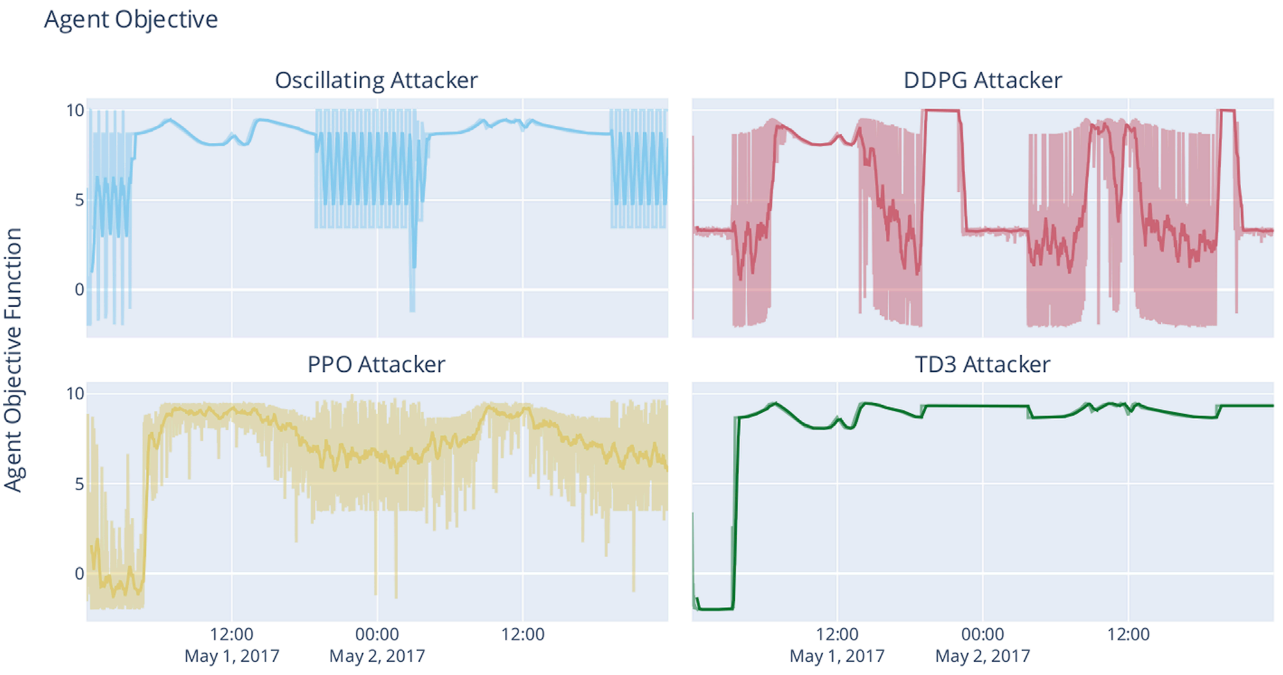

FIGURE 11
Attacker objective function, plotted over simulation time. Light colors depict absolute values, bold lines the moving avarage with a window of 100 steps.

9 Discussion

Our approach creates a bridge between informal modelling of domain expert knowledge in terms of scenarios to rigorous experimentation with learning agents. The second MUC—the one that shows the oscillation attack—is a simple, yet comprehensive scenario that allows to verify the general hypothesis, that MUCs can be part of a immediate pipeline allowing to train agents in an offline learning or autocurriculum.

Our initial approach outlined in this article uses an expert through the objective as a simple form of imitation learning, specifically, behavior cloning. The objective we presented in the experimental validation is a very focused one, based on the behavior we model in the MUC. It is based on an already known behavior, specifically created to teach the agent an exact strategy. However, the DRL agents have discovered another behavior that led to the same goal, but exhibited a different behavior, even though the objective was not changed between phases. While PPO immitated the original strategy quite well, did TD3 resort to fixed setpoints that maximized reward without oscillating. Considering a “following the goal by intention,” this makes the TD3-based agent the potentially most destructive one, as it avoids steep gradients, which would quickly alert the grid operator, because they violate grid codes. Therefore, we assume that using the agent’s objective as expert for behavior cloning is not only effective, but also does not hinder the agent in devision new attack vectors when it has the chance to interact with the environment.

Nevertheless, it is not known whether an agent would have learned a different strategy to achieve the goal without the specified behavior. Therefore, running additional experiments without predefined trajectories might be beneficial in cases where a general approach without specified behaviour is wanted. Regardless of this, the approach presented here can still be useful in such a situation because general concepts can be passed as trajectories that do not describe a direct, goal-directed action. An example is bidding on a local market, which does not yet describe misbehavior, but conveys the basic concepts for dealing with the market to the agent.

The most cumbersome part of our approach is the fact that the domain expert still needs a MUC modelling expert familiar with our approach to apply the correct stereotypes and to ensure that the correct XML/XMI file is created. Otherwise, depending on the severity of the syntax and semantic errors, our approach might lead to wrong learned behaviour or not executable experiments. Still, this technical breakthrough allows extension now that baseline scenarios have been established. For example, a direction of research could employ text recognition in the way ChatGPT was trained to arrive at properly formatted MUCs from non-precise wording.

10 Conclusion and future work

In this article, we have demonstrated a software framework that enables sound experimentation from MUC descriptions and embedded diagrams. Our approach enables domain experts to model scenarios, which are then analyzed by using learning agents. Moreover, our approach enables autocurricula and a limited form of offline learning by imitation learning with experts through the agents’ objectives. We have furthermore shown two MUCs, which have been converted into experiment definitions; one scenario has been extensively simulated and analyzed.

For future work, we will construct trajectories from sequence diagrams, extending the offline learning approach significantly. It might also be interesting to examine whether agents learn different strategies in the same environment when provided with knowledge through this approach, or whether, given sufficient training time, both procedures lead to the same behavior. As such, we plan to extend the MIDAS benchmark environment further, adding more domains, such as ICT. We will then build a repository of MUCs, and likewise, agents trained on there MUCs.

We expect to open the domain of online learning, or, more specifically, lifelong learning at this point. Agents can learn from multiple MUCs (not just one MUC per agent). However, this will surely lead the agents to encounter the plasticity-stability dilemma, where agents need to retrain learned behavior while learning new tasks. We will verify and analyze this, and propose a more complex agent that is able to incorporate knowledge from multiple MUCs.

Data availability statement

The datasets presented in this study can be found in online repositories. The names of the repository/repositories and accession number(s) can be found below: https://gitlab.com/arl-experiments.

Author contributions

EV contributed the introduction, sections on DRL, the descriptions of arsenAI and palaestrAI, as well as the execution and analysis of the oscillating voltage attack. AW contributed sections on the MUCs and the converter for MUC/XML to arsenAI experiment file. MU transferred the MUC methodology to power grid scenarios in general. He co-designed the MUCs for the scenarios described in this article.

Funding

This work has been funded by the German Federal Ministry for Education and Research (Bundesministerium für Bildung und Forschung, BMBF) under the project grant Adversarial Resilience Learning (01IS22071). The work on the Misuse Case Methodology has been funded by the German Federal Ministry for Economic Affairs and Climate Action (Bundesministerium für Wirtschaft und Klimaschutz, BMWK) under the project grant RESili8 (03EI4051A).

Conflict of interest

The authors declare that the research was conducted in the absence of any commercial or financial relationships that could be construed as a potential conflict of interest.

Publisher's note

References

Adawadkar, A. M. K., and Kulkarni, N. (2022). Cyber-security and reinforcement learning — a brief survey. *Cyber-security Reinf. Learn. — a brief Surv.* 114, 105116. doi:10.1016/j.engappai.2022.105116

Apoorva, M., Eswarawaka, R., and Reddy, P. V. B. (2017). "A latest comprehensive study on structured threat information expression (STIX) and trusted automated exchange of indicator information (TAXII)," in Proceedings of the 5th International Conference on Frontiers in Intelligent Computing: Theory and Applications. *Advances in intelligent systems and computing*. Editors S. C. Satapathy, V. Bhateja, S. K. Udgata, and P. K. Pattnaik, 477–482. doi:10.1007/978-981-10-3156-4_49

Baker, B., Kanitscheider, I., Markov, T., Wu, Y., Powell, G., McGrew, B., et al. (2020). "Emergent tool use from multi-agent autocurricula," in International Conference on Learning Representations.

Barnum, S. (2012). Standardizing cyber threat intelligence information with the structured threat information expression (STIX). *Mitre Corp.* 11, 1–22.

Berghout, T., Benbouzid, M., and Muyeen, S. M. (2022). Machine learning for cybersecurity in smart grids: A comprehensive review-based study on methods, solutions, and prospects. *prospects* 38, 100547. doi:10.1016/j.ijcip.2022.100547

Briliyant, O. C., Tirsa, N. P., and Hasditama, M. A. (2021). "Towards an automated dissemination process of cyber threat intelligence data using STIX," in 2021 6th International Workshop on Big Data and Information Security (IWBIS), 109–114. doi:10.1109/IWBIS53353.2021.9631850

Brockman, G., Cheung, V., Pettersson, L., Schneider, J., Schulman, J., Tang, J., et al. (2016). *Openai gym*.

Bush, S. F. (2014). *Smart grid: Communication-enabled intelligence for the electric power grid. IEEE*. Chichester, UL: John Wiley & Sons.

Castro, P. S., Moitra, S., Gelada, C., Kumar, S., and Bellemare, M. G. (2018). *Dopamine: A research framework for deep reinforcement learning*.

Clausen, M., Apel, R., Dorchain, M., Postina, M., and Uslar, M. (2018). Use case methodology: A progress report. *Energy Inf.* 1, 19–283. doi:10.1186/s42162-018-0036-0

Cockburn, A. (2001). *Writing effective use cases*. London, UK: Pearson Education).

Connolly, J., Davidson, M., and Schmidt, C. (2014). *The trusted automated exchange of indicator information (TAXII)* (The MITRE Corporation), 1–20.

Fischer, L., Memmen, J. M., Veith, E. M., and Tröschel, M. (2019). "Adversarial resilience learning—Towards systemic vulnerability analysis for large and complex systems," in ENERGY 2019, The Ninth International Conference on Smart Grids, Green Communications and IT Energy-aware Technologies (IARIA XPS Press), 24–32.

Frost, E., Veith, E. M., and Fischer, L. (2020). "Robust and deterministic scheduling of power grid actors," in 7th International Conference on Control, Decision and Information Technologies (CoDIT) (IEEE), 1–6.

Fujimoto, S., Hoof, H., and Meger, D. (2018). "Addressing function approximation error in actor-critic methods," in Proceedings of the 35th International Conference on Machine Learning (PMLR), 1587–1596 (Stockholm, Sweden: ISSN), 2640–3498.

Gauci, J., Conti, E., Liang, Y., Virochsiri, K., Chen, Z., He, Y., et al. (2018). *Horizon: Facebook's open source applied reinforcement learning platform. arXiv preprint arXiv:1811.00260*.

Górski, T. (2022). Uml profile for messaging patterns in service-oriented architecture, microservices, and internet of things. *Appl. Sci.* 12, 12790. doi:10.3390/app122412790

Gottschalk, M., Uslar, M., and Delfs, C. (2017). *The use case and smart grid architecture model approach: The IEC 62559-2 use case template and the SGAM applied in various domains*. Springer.

Haarnoja, T., Zhou, A., Abbeel, P., and Levine, S. (2018). *Soft actor-critic: Off-policy maximum entropy deep reinforcement learning with a stochastic actor*.

Hessel, M., Modayil, J., Van Hasselt, H., Schaul, T., Ostrovski, G., Dabney, W., et al. (2018). "Rainbow: Combining improvements in DQN," in The Thirty-Second AAAI Conference on Artificial Intelligence (AAAI-18), 3215–3222.

Hintjens, P. (2023). *0MQ — the guide*, 4. Sebastopol, CA: O'Reilly.

Holly, S., Nieße, A., Tröschel, M., Hammer, L., Franzius, C., Dmitriyev, V., et al. (2020). Flexibility management and provision of balancing services with battery-electric automated guided vehicles in the Hamburg container terminal Altenwerder (SpringerOpen). *Energy Inf.*

Hong, J., Liu, C.-C., and Govindarasu, M. (2014). "Detection of cyber intrusions using network-based multicast messages for substation automation," in *Isgt 2014*, 1–5. doi:10.1109/ISGT.2014.6816375

Hu, L., Wang, Z., Han, Q.-L., and Liu, X. (2018). State estimation under false data injection attacks: Security analysis and system protection. *Automatica* 87, 176–183. doi:10.1016/j.automatica.2017.09.028

Huang, B., Cardenas, A. A., and Baldick, R. (2019). "Not everything is dark and gloomy: Power grid protections against IoT demand attacks," in Procedings of the 28th USENIX Security Symposium, Santa Clara, CA, USA (Berkeley, CA: Usenix Association).

Icarte, R. T., Klassen, T., Valenzano, R., and McIlraith, S. (2018). "Using reward machines for high-level task specification and decomposition in reinforcement learning," in Proceedings of the 35th International Conference on Machine Learning (Stockholm, Sweden: PMLR), 2107–2116.

IEA (2019). *Status of power system transformation 2019*. Paris, France: resreport, IEA. CC-BY-SA 4.0.

Inayat, U., Zia, M. F., Mahmood, S., Berghout, T., and Benbouzid, M. (2022). Cybersecurity enhancement of smart grid: Attacks, methods, and prospects. *Attacks, methods, prospects* 11, 3854. doi:10.3390/electronics11233854

Ju, P., and Lin, X. (2018). "Adversarial attacks to distributed voltage control in power distribution networks with DERs," in Proceedings of the Ninth International Conference on Future Energy Systems, 291–302. doi:10.1145/3208903.3208912

Kuhnle, A., Schaarschmidt, M., and Fricke, K. (2017). *Tensorforce: A tensorflow library for applied reinforcement learning*.

Levine, S., Kumar, A., Tucker, G., and Fu, J. (2020). *Offline reinforcement learning: Tutorial, review, and perspectives on open problems*. arXiv. doi:10.48550/arXiv.2005.01643

Liang, E., Liaw, R., Nishihara, R., Moritz, P., Fox, R., Goldberg, K., et al. (2018). "RLlib: Abstractions for distributed reinforcement learning," in International Conference on Machine Learning (ICML).

Lillicrap, T. P., Hunt, J. J., Pritzel, A., Heess, N., Erez, T., Tassa, Y., et al. (2016). "Continuous control with deep reinforcement learning," in 4th International Conference on Learning Representations, ICLR 2016 - Conference Track Proceedings.

Liu, Y., Ning, P., and Reiter, M. K. (2011). False data injection attacks against state estimation in electric power grids. *ACM Trans. Inf. Syst. Secur. (TISSEC)* 14, 1–33. doi:10.1145/1952982.1952995

Mahela, O. P., Khosravy, M., Gupta, N., Khan, B., Alhelou, H. H., Mahla, R., et al. (2022). Comprehensive overview of multi-agent systems for controlling smart grids. *CSEE J. Power Energy Syst.* 8, 115–131. doi:10.17775/CSEEJPES.2020.03390

Mathas, C.-M., Vassilakis, C., Kolokotronis, N., Zarakovitis, C. C., and Kourtis, M.-A. (2021). On the design of IoT security: Analysis of software vulnerabilities for smart grids. *MDPI Energies* 14, 2818. doi:10.3390/en14102818

Mnih, V., Kavukcuoglu, K., Silver, D., Graves, A., Antonoglou, I., Wierstra, D., et al. (2013). *Playing atari with deep reinforcement learning*. arXiv preprint arXiv:1312.5602.

Nair, A. S., Hossen, T., Campion, M., Selvaraj, D. F., Goveas, N., Kaabouch, N., et al. (2018). Multi-agent systems for resource allocation and scheduling in a smart grid. *Technol. Econ. Smart Grids Sustain. Energy* 3, 15. doi:10.1007/s40866-018-0052-y

Neureiter, C., Engel, D., Trefke, J., Santodomingo, R., Rohjans, S., and Uslar, M. (2014). "Towards consistent smart grid architecture tool support: From use cases to visualization," in IEEE PES Innovative Smart Grid Technologies, Europe (IEEE), 1–6.

OASIS Open Cyber Threat Intelligence Committee (2022). *Introduction to STIX*. Availableat: https://oasis-open.github.io/cti-documentation/stix/intro (Accessed 02 2023, 01).

Ofenloch, A., Schwarz, J. S., Tolk, D., Brandt, T., Eilers, R., Ramirez, R., et al. (2022). "Mosaik 3.0: Combining time-stepped and discrete event simulation," in 2022 Open Source Modelling and Simulation of Energy Systems (Piscataway, NJ: OSMSES), 1–5. doi:10.1109/OSMSES54027.2022.9769116

OMG Group (2005). *Xmi*^{TM}*: Xml metadata interchange*. web page.

Peng, X. B., Kumar, A., Zhang, G., and Levine, S. (2019). *Advantage-weighted regression: Simple and scalable off-policy reinforcement learning*. arXiv. doi:10.48550/arXiv.1910.00177

Pronzato, L., and Walter, E. (1988). Robust experiment design via maximin optimization. *Math. Biosci.* 89, 161–176. doi:10.1016/0025-5564(88)90097-1

Prudencio, R. F., Maximo, M. R. O. A., and Colombini, E. L. (2022). *A survey on offline reinforcement learning: Taxonomy, review, and open problems*. arXiv. doi:10.48550/arXiv.2203.01387

Raffin, A., Hill, A., Gleave, A., Kanervisto, A., Ernestus, M., and Dormann, N. (2021). Stable-baselines3: Reliable reinforcement learning implementations. *J. Mach. Learn. Res.* 22, 1–8.

Roberts, C., Ngo, S.-T., Milesi, A., Peisert, S., Arnold, D., Saha, S., et al. (2020). "Deep reinforcement learning for DER cyber-attack mitigation," in 2020 IEEE International Conference on Communications, Control, and Computing Technologies for Smart Grids (Piscataway, NJ: SmartGridComm), 1–7. doi:10.1109/SmartGridComm47815.2020.9302997

Roberts, C., Ngo, S.-T., Milesi, A., Scaglione, A., Peisert, S., and Arnold, D. (2021). "Deep reinforcement learning for mitigating cyber-physical der voltage unbalance attacks," in 2021 American Control Conference (ACC), 2861–2867. doi:10.23919/ACC50511.2021.9482815

Roche, R., Lauri, F., Blunier, B., Miraoui, A., and Koukam, A. (2013). Multi-agent technology for power system control. *J. Abbr. Green Energy Technol.* 59, 567–609. doi:10.1007/978-1-4471-5104-3_15

Rudion, K., Orths, A., Styczynski, Z., and Strunz, K. (2006). "Design of benchmark of medium voltage distribution network for investigation of dg integration," in 2006 IEEE Power Engineering Society General Meeting, 6–14. doi:10.1109/PES.2006.1709447

Santodomingo, R., Uslar, M., Göring, A., Gottschalk, M., Nordström, L., Saleem, A., et al. (2014). "SGAM-based methodology to analyse smart grid solutions in discern European research project," in 2014 IEEE International Energy Conference (ENERGYCON IEEE), 751–758.

Schrittwieser, J., Antonoglou, I., Hubert, T., Simonyan, K., Sifre, L., Schmitt, S., et al. (2019). Mastering Atari, Go, chess and shogi by planning with a learned model. *Nature* 588, 604–609. doi:10.1038/s41586-020-03051-4

Schulman, J., Wolski, F., Dhariwal, P., Radford, A., and Klimov, O. (2017). *Proximal policy optimization algorithms*. doi:10.48550/arXiv.1707.06347

Schütz, J., Clausen, M., Uslar, M., and Gómez, J. M. (2021). "IEC 62559-2 use case template-based smart grid architecture analytics," in CIRED 2021-The 26th International Conference and Exhibition on Electricity Distribution (IET), 2935–2939.

Seno, T., and Imai, M. (2022). d3rlpy: An offline deep reinforcement learning library. *J. Mach. Learn. Res.* 23, 1–20.

Silver, D., Huang, A., Maddison, C. J., Guez, A., Sifre, L., Van Den Driessche, G., et al. (2016a). Mastering the game of Go with deep neural networks and tree search. *Nature* 529, 484–489. doi:10.1038/nature16961

Silver, D., Hubert, T., Schrittwieser, J., Antonoglou, I., Lai, M., Guez, A., et al. (2017). A general reinforcement learning algorithm that masters chess, shogi, and Go through self-play. *Science* 362, 1140–1144. doi:10.1126/science.aar6404

Silver, D., Schrittwieser, J., Simonyan, K., Nature, I. A., Huang, A., Guez, A., et al. (2016b). Mastering the game of Go without human knowledge. *Nature* 550, 354–359. doi:10.1038/nature24270

Sindre, G., and Opdahl, A. L. (2005). Eliciting security requirements with misuse cases. *Requir. Eng.* 10, 34–44. doi:10.1007/s00766-004-0194-4

Sindre, G., and Opdahl, A. L. (2001). "Templates for misuse case description," in Proceedings of the 7th International Workshop on Requirements Engineering, Switzerland (Foundation for Software Quality (REFSQ'2001).

Soltan, S., Mittal, P., and Poor, V. H. (2018). "BlackIoT: IoT botnet of high wattage devices can disrupt the power grid | USENIX," in Proceedings of the 28th Usenix Security Symposium, Baltimore, MA, USA (Berkeley, CA: Usenix Association).

Styczynski, J., and Beach-Westmoreland, N. (2016). When the lights went out: Ukraine cybersecurity threat briefing. *Booz Allen Hamilt.* 12, 20.

Sun, C.-C., Hahn, A., and Liu, C.-C. (2018). Cyber security of a power grid: State-of-the-art. *State-of-the-art* 99, 45–56. doi:10.1016/j.ijepes.2017.12.020

Sutton, R. S., and Barto, A. G. (2018). *Reinforcement learning: An introduction*. MIT press.

The MITRE Corporation (2022). *Mitre ATT&CK*®. Availableat: https://attack.mitre.org/ (Accessed 02 2023, 01).

Tiemann, P. H., Nebel-Wenner, M., Holly, S., Frost, E., Jimenez Martinez, A., and Nieße, A. (2022). Operational flexibility for multi-purpose usage of pooled battery storage systems. *Energy Inf.* 5, 14. doi:10.1186/s42162-022-00209-4

Trefke, J., Rohjans, S., Uslar, M., Lehnhoff, S., Nordström, L., and Saleem, A. (2013). "Smart grid architecture model use case management in a large European smart grid project," in IEEE PES ISGT Europe 2013 (IEEE), 1–5.

van Amelsvoort, M. A. (2016). SG-rating–putting values on smart grid architectures. *it-Information Technol.* 58, 29–36. doi:10.1515/itit-2015-0044

van Amelsvoort, M., Delfs, C., and Uslar, M. (2015). "Application of the interoperability score in the smart grid domain," in 2015 IEEE 13th International Conference on Industrial Informatics (INDIN) (IEEE), 442–447.

Veith, E., Fischer, L., Tröschel, M., and Nieße, A. (2019). "Analyzing cyber-physical systems from the perspective of artificial intelligence," in Proceedings of the 2019 International Conference on Artificial Intelligence, Robotics and Control (ACM).

Veith, E. M., Balduin, S., Wenninghoff, N., Tröschel, M., Fischer, L., Nieße, A., et al. (2020). "Analyzing power grid, ICT, and market without domain knowledge using distributed artificial intelligence," in CYBER 2020, The Fifth International Conference on Cyber-Technologies and Cyber-Systems (Red Hook, NY: IARIA XPS Press), 86–93.

Veith, E. M. (2017). *Universal smart grid agent for distributed power generation management*. Berlin, Germany: Logos Verlag Berlin GmbH.

Wan, Z., Li, H., Shuai, H., Sun, Y. L., and He, H. (2021). "Adversarial attack for deep reinforcement learning based demand response," in 2021 IEEE Power & Energy Society General Meeting (PESGM), 1–5. doi:10.1109/PESGM46819

Wang, Z., He, H., Wan, Z., and Sun, Y. (2021). "Coordinated topology attacks in smart grid using deep reinforcement learning," in Conference Name: IEEE Transactions on Industrial Informatics, 1407–1415. doi:10.1109/TII.2020.2994977

Wolgast, T., Veith, E. M., and Nieße, A. (2021). "Towards reinforcement learning for vulnerability analysis in power-economic systems," in DACH+ Energy Informatics 2021: The 10th DACH+ Conference on Energy Informatics.

Woltmann, S., and Kittel, J. (2022). Development and implementation of multi-agent systems for demand response aggregators in an industrial context. *Appl. Energy* 314, 118841. doi:10.1016/j.apenergy.2022.118841

Zhu, H., and Liu, H. J. (2016). Fast local voltage control under limited reactive power: Optimality and stability analysis. *IEEE Trans. Power Syst.* 31, 3794–3803. doi:10.1109/TPWRS.2015.2504419

frontiers | Frontiers in Energy Research

TYPE Original Research
PUBLISHED 17 March 2023
DOI 10.3389/fenrg.2023.1061779

OPEN ACCESS

EDITED BY
Xin Ning,
Institute of Semiconductors (CAS), China

REVIEWED BY
Zhekang Dong,
Hangzhou Dianzi University, China
Ghulam Hafeez,
University of Engineering and Technology, Mardan, Pakistan
Zhibin Zou,
University at Albany, United States
Hongwu Peng,
University of Connecticut, United States

*CORRESPONDENCE
Nan Zhang,
✉ znan0602@163.com

SPECIALTY SECTION
This article was submitted to Smart Grids, a section of the journal Frontiers in Energy Research

RECEIVED 05 October 2022
ACCEPTED 07 March 2023
PUBLISHED 17 March 2023

CITATION
Li W, Zhang N, Liu Z, Ma S, Ke H, Wang J and Chen T (2023), A trusted decision fusion approach for the power internet of things with federated learning. *Front. Energy Res.* 11:1061779. doi: 10.3389/fenrg.2023.1061779

A trusted decision fusion approach for the power internet of things with federated learning

Wenjing Li[1], Nan Zhang[1]*, Zhu Liu[1], Shiqian Ma[2], Huaqiang Ke[1], Jinfa Wang[1] and Ting Chen[1]

[1]State Grid Information & Telecommunication Group Co., Ltd., Beijing, China, [2]State Grid Tianjin Electric Power Company, Tianjin, China

The power Internet of Things generates a large amount of data at any time, which can be transformed into precise decisions with the help of artificial intelligence approaches. However, the owners of electricity data with boundaries are often concerned with data leakage. Therefore, when building models that feed big data into deep learning artificial intelligence approaches for precise decision-making within the power Internet of Things, it is essential to ensure the data's security. This paper proposes a framework for model training and decision making system applied to the field of power IoT, which consists of two parts: data security sharing and hierarchical decision making. The proposed framework utilizes a homomorphic encryption-based federated learning approach to protect private data from leakage. In addition, data augmentation and transfer learning are used to address the issue of insufficient local training data. Moreover, the framework attempts to incorporate the specialized nature of traditional manual decision-making in the power field by fusing expert and model values after stratifying the requirements. Experiments are conducted to simulate the decision requirements in the field of power Internet of Things (e.g., electrical material identification), using image recognition as an example. The experimental results show that the proposed models can achieve high accuracy rates and the fusion approach is feasible.

KEYWORDS

smart grid, power internet of things, data security sharing, federated learning, deep learning

Introduction

In recent years, the rapid development of science and technology has facilitated the gradual integration of Internet of Things (IoT) technology into various aspects of people's daily lives, making it an integral and closely connected part of modern life. IoT technology has an important role in public services (Wu and Xiao, 2022), smart homes (Choi et al., 2021), medical security (Wu et al., 2020), labour free farms (Ratnaparkhi et al., 2020) and smart grids (Alhariry et al., 2021), which brings a lot of convenience to people's lives. Power IoT constitutes a crucial component of IoT development, which can provide important support for the intelligence, digitalization and transparency of the electricity grid through the collection and transmission of electricity grid data to cloud platform for processing and analysis (Zhang et al., 2022a).

Modern society is highly dependent on electric energy, which is related to the people's lives and the stability of the country, and is a strategic energy source for the country (Li et al.,

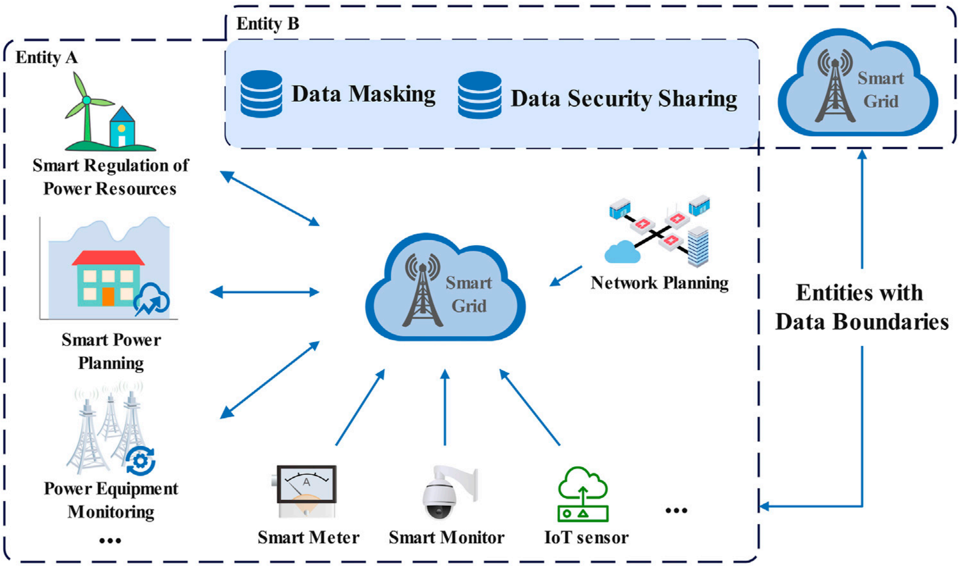

FIGURE 1
Entities with data boundaries.

2020). A smart grid is the integration of a traditional power grid with a communication system and network (Mashal, 2022), which is also one of the most important applications of IoT (Gunduz and Das, 2020). The application of IoT in the smart grid is called power IoT. Power IoT generates a large amount of data under the edge cloud architecture, and the way these data are processed is very critical (Jiang et al., 2020). Effectively utilizing such data through advanced methods like machine learning can help power companies make accurate and informed decisions, leading to a significant improvement in economic efficiency (Gilanifar et al., 2020).

However, the current power IoT still in need of effective solutions for data security sharing and decision-making. The direct collection of electricity consumption data from customers for efficient energy management is insecure from an information point of view (Wang et al., 2021). For example, users regularly report electricity consumption data to the power company through smart meters, thereby rendering their privacy exceedingly vulnerable (Xia et al., 2022). Consequently, the privacy, security and trustworthiness of data remain unconsidered in the current power IoT. The research of user information security for power data has become a hot research topic (Yan et al., 2020).

With the continued promotion of information technology in today's society, data has become increasingly valuable to humans (Corallo et al., 2022) and fine-grained security management in the IoT requires effective access control (Pal et al, 2022). However, the data collected in power IoT is often diverse and data-intensive. A large scale of data makes old supporting parsing systems and decision-making systems seem overwhelming in their presence, leading to a situation where it is challenging to tap into the total value of more data in the field.

Figure 1 shows a simple schematic of smart grids in the area of the Internet of Things for electricity. A smart grid with a well-arranged IoT path can be used to rationalize the deployment of power resources or to efficiently identify the level of wear and tear of power equipment by obtaining data from smart city devices (e.g., smart meters, smart monitors and high-performance IoT sensors). It is worth noting that most electricity data is private data, and for entities with boundaries, a secure way of sharing data is required, e.g., data masking and federated learning. However, potential security threats, such as reconstruction attacks, membership inference and model inversion, may arise in this scenario.

With the *introduction* of emerging concepts such as Industry 4.0 (Hong et al., 2021; Priya et al., 2021), the industrial and power IoT sector has put forward new requirements for mining and utilizing various electricity data. The industry is eager to obtain sufficient data from smart meters (Ahammed and Khan, 2022) or other intelligent power devices for decision-making purposes, such as using power consumption data for rational allocation of power resources, using power equipment implementation images for equipment wear and tear identification and early warning, using images data to ensure physical security of IoT devices (Yang et al., 2022) and using cross-regional electricity data to develop top-level strategies with solid generalization.

Data such as customer usage information, regional distribution lines, and internal electricity equipment is often identified as private data that needs protection. However, there exists a scarcity of credible data that can be controlled by the decision-making entities themselves on a national or even global basis. Such entities may include many electricity companies, regions, or even countries with boundaries. The difficulty in aggregating data across regions to derive practical benefits while ensuring data privacy protection poses significant challenges for these decision-making entities. Furthermore, existing machine learning methods that rely on data suffer from issues related to accuracy and reliability. With the development of the smart grid, the safety of electric power materials has attracted widespread attention, and the safety of electric power equipment is a key part of it. Since power equipment may cause some safety accidents due to overheating, effective identification and temperature detection of power equipment is extremely important, which can guarantee the safety of the energy supply (Ni, 2020).

Traditional power IoT business decision-making relies on experts' professional experience and knowledge, with layers of feedback and modifications before making decisions. This approach relies heavily on expert authoritative knowledge, and requires reconstructing the expert knowledge base if the structure of the power IoT changes. At the same time, the accuracy of the decisions made using this approach gradually decrease over time due to the accumulation of obsolete knowledge. Spending a lot of cost to update the knowledge base is often not a good choice. To address these challenges, more and more companies are building their automated decision-making solutions, hoping to fully exploit the value of power IoT data with the assistance of computers. However, these decision-making systems are typically based on traditional data analysis methods, and many aspects require manual intervention, which is time-consuming and low resource utilization. Traditional decision-making systems for the power IoT are often based on a small data level of model training, which may have problems with effectiveness and generalization. It is worth noting that traditional electricity decision-making systems have difficulty ensuring the secure sharing of data across regions. Private data cannot be secured, significantly impacting the power IoT if the data is compromised. Fortunately, research for artificial intelligence decision-making systems has also been in order at recent stages (Kaur et al., 2022). Many teams are studying the decision task of introducing artificial intelligence methods into the field of power Internet of Things, which is also the place to explore in this field. It is still a challenge to transfer the task from the traditional decision-making method to the application of artificial intelligence. For the traditional machine learning method, a large number of available features are required, while for the deep learning method, a large number of standard available data sets are required.

To address the limitations of the existing decision-making system in the field of power Internet of Things, and maximize the adaptation of new industrial equipment such as smart grid in popularity, the work of this paper integrates traditional expert decision-making and in-depth learning methods. Furthermore, in order to reduce the risk of privacy data leakage, which accounts for a large proportion of data in the field of power Internet of Things, this work also focuses on integrating a new data security sharing method. The proposed data security sharing and decision-making approach for the power IoT consist of two main parts: data security sharing and the decision-making approach. The data security sharing scheme for the power IoT is based on federated learning and homomorphic encryption, which integrates data within each region after determining the boundaries of a specific scenario. The model's performance at small data levels is further improved by using data augmentation and transfer learning. The proposed decision-making approach is a hierarchical model that integrates an expert knowledge base and machine learning (ML) decision-making. The scenario-specific requirements are hierarchically fed into the decision-making system. The machine learning model generates plausible values with expert knowledge base values to produce a decision score. The weighted fusion of models and decisions can reduce the possible effects caused by federated learning features, such as intermediate data being recovered by attackers and leading to leakage (Zhang et al., 2022b).

In summary, the main contributions of this paper are as follows.

- A security-driven decision model is proposed for the power IoT that enables deep learning-based big data analysis and decision-making for the power IoT under high security. Machine learning tools and expert knowledge bases are also integrated into the decision-making process to produce a comprehensive decision result.
- Federated learning is used to ensure the secure sharing of power IoT data by unifying different entities for collaborative training and unified management by a trusted third party without revealing sensitive data. This approach enables reasonable exploitation of data value while ensuring data security.
- Homomorphic encryption is used to prevent malicious activities, such as inference attacks, that may occur in federation learning. Homomorphic encryption processes the data without decryption, thus securing the intermediate data in the power IoT.

The remainder of this paper is organized as follows.

Section 2 provides an overview of the related work. Section 3 focuses on design details and a description of the methods for the power IoT. Section 4 shows the experimental data and analysis of an example scenario, along with a discussion of the results. Section 5 makes a summary of the paper and future perspective.

Related work

In this section, some work similar to the topic of this paper will be presented, mainly covering decision systems and privacy protection elements.

Decision-making methods

Most decision-making methods in the field of power IoT are based on traditional manual analysis or single-user machine learning. Al Metrik and Musleh (2022) proposed a medium-term prediction model that can predict electricity consumption for a given location. Predicting energy use ensures the stability of the power supply. Wang et al. (2022) have constructed a structured LSTM based on a prediction-guided autoencoder. A single model enables the accurate prediction of short-term loans for all types of users. Guang et al. (2021) proposed a decision-making approach. Power communication resource data features are analyzed and combined with data mining algorithms to design and propose intelligent application scenarios geared towards grid and communication network collaboration and assisted decision-making. Tian and Dong (2021) proposed a long-term investment decision model for transmission grid frames containing flexible transmission devices. Due to the nature of the power IoT domain, specific tasks are targeted.

Most decision-making approaches in the power IoT field are based on a single independent machine learning model or other methods. These methods may work well for specific tasks but are not highly generalizable and will be challenging to extend to other tasks. There is also a risk of privacy breaches in handling sensitive data, which is often not shared securely with the power data.

Data security sharing

Friha et al. (2022) proposed a federated learning-based intrusion detection system. They used federated learning for a specific task (i.e., intrusion detection) to protect the infrastructure of the Internet of agriculture. Their experiments demonstrate the excellence of federated learning in the Internet of agriculture. Image recognition is the main task theme in the IoT for electricity, for example, identifying wear and tear on electrical equipment. Tanwar et al. (2021) proposed a privacy-preserving image recognition model for encrypted data over the cloud. Their proposed block-based image encryption scheme can be effective in securing private images. Bhansali et al. (2022) presented a system with secure data collection and transmission for IoMT architecture integrated with federated learning and illustrated the value of this system in the medical field. The same type of federated learning is used in the medical field, Xu et al. (2021) proposed a general multi-view federated learning approach using multisource data, and it can extend the traditional machine learning model to support federated learning across different institutions or parties. To address the issue of user privacy protection in federated learning, Mugunthan et al. (2020) proposed PrivacyFL, a scalable, easily configurable and extensible simulator for federated learning environments. Miao et al. (2021) proposed a federated learning-based secure data sharing mechanism for IoT called FL2S, which improves data security and data quality. Li et al. (2021) proposed a novel privacy-preserving FL framework based on an innovative chained secure multi-party computing technology called chain-PPFL to address the leakage of participants' sensitive information due to exchanging model data in federated learning.

It is worth noting that the amount of data available for each local user may be very small after applying federal learning, resulting in a certain degree of overfitting and poor accuracy. Therefore, this paper uses federated learning, transfer learning, data augmentation methods, and model weighting fusion methods to improve the model's accuracy.

Materials and methods

In this section, the data security sharing and decision-making approach for the power IoT is introduced.

Problem formulation

This part focuses on abstract modeling of data security sharing and decision-making within the field of power IoT and illustrates the main processes and specific details of the approach proposed in this paper.

Problem description

Consider the set $ENV = \{env_1, env_2, \cdots, env_n\}$ of requirements that may need to be decided within the power IoT, and for each $env \in ENV$, determine the region boundary $LOC = \{loc_1, loc_2, \cdots, loc_m\}$ for collaborative training while dividing the env hierarchically into sub-requirements e_{ij}, where n and m are the total number of requirements and the total number of region boundaries, respectively. i and j are the j^{th} division of the i^{th} layer, respectively.

For the decision approach, the hierarchical output of the plausible decision values Sug_i of the expert knowledge base, combined with the possible values $mValue$ given by the collaboratively trained completed machine learning model $Model$, and results in the corresponding solution set $Solution = \{sol_1, sol_2, \cdots, sol_v\}$, where i is the division of the hierarchy and v is the number of solutions.

For the model to be run so that it can be trained efficiently and give credible decision recommendations, a complete description of the scenario is as follows:

- ***Input:*** i) The basic set of requirements $ENV = \{env_1, env_2, \cdots, env_n\}$ for which decision information may need to be obtained and the region boundaries $LOC = \{loc_1, loc_2, \cdots, loc_m\}$ for collaborative training. ii) A trusted central server $CServer$ for federated learning and a hierarchical algorithm for partitioning requirements. iii) Homomorphic encryption algorithms, models for migration learning, and an expert knowledge base.
- ***Output:*** A set of solutions $Solution = \{sol_1, sol_2, \cdots, sol_v\}$ corresponding to each actual requirement.
- ***Objective:*** Maximize machine learning model accuracy ACC' and complete data security sharing and decision making.

The overall flow of the proposed approach

This paper proposes a data security sharing and decision-making model to solve the problem described in the above scenario. The overall process is shown in Figure 2. The model is divided into three parts: data preparation, regional collaborative training, and output of decision making. Data preparation is mainly responsible for collecting, cleaning, and data augmentation. According to the overall training standard, these parts are mainly carried out in the local area.

The regional collaborative training component is responsible for securely sharing power IoT data. The use of federated learning and homomorphic encryption ensures private data security. The use of migration learning reduces costs and improves training effectiveness on small volumes of data. All methods are carried out under the integration of a trusted central server. The decision output part is mainly responsible for outputting credible decision values given by the decision hierarchy algorithm to give plausible suggested values by the expert knowledge base. The plausible suggested values are weighted and combined with the reasonable discounts offered by the model in the previous session to provide reference values that can be used for decision-making. The first and second of these parts are described in the following sub-section. The detailed step-by-step description is shown below:

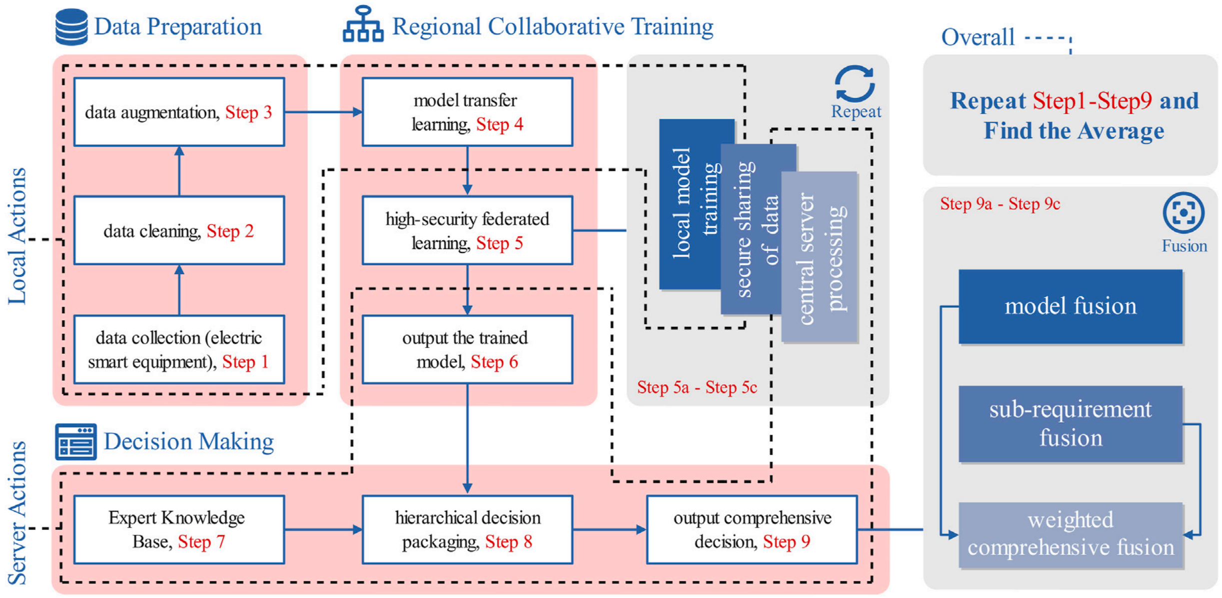

FIGURE 2
Overall flow of model.

- STAGE I: Data preparation

Step 1. Using smart electricity devices, such as smart meters, collect local data. Data collection, in this case, is a locally trusted operation;

Step 2. The regions pre-process private data. The primary check is for data consistency, followed by processing invalid and missing values;

Step 3. Due to the specific features of some of the data in the power IoT, local areas with boundaries often do not share private data with others. The methods of data augmentation vary for different tasks, e.g., for the task of identifying and warning about the wear and tear of power equipment, the main focus is on enhancing the picture data of power equipment;

- STAGE II: Collaborative training

Step 4. The model proposed in this paper evaluates the possibility of applying migration learning in actual experiments for different power IoT decision tasks;

Step 5a. Local model training. Each local model training is done by trusted operations and data;

Step 5b. Use homomorphic encryption to ensure secure sharing of data. Here the intermediate data of the local model training process is encrypted and transmitted to the central server;

Step 5c. The central server averages the local intermediate data and then distributes it to all local models;

Step 6. Output information about the completed training model. There is not necessarily only one model used for transfer in a decision process, and therefore not necessarily only one model information is output;

- STAGE III: Decision making

Step 7. The expert knowledge base is used to support the decision from the other side and is set to 0 if no matching decision information is found.

Step 8. The expert experience is packaged according to a hierarchical approach to electricity demand, all of which is provided to the subsequent decision model;

Step 9a. If multiple models are used in the co-training section, then all models are weighted and fused here;

Step 9b. If multiple sub-requirements are used in the co-training section, then all sub-requirements are weighted and fused here;

Step 9c. Weighted fusion of data from Step 9a and Step 9b.

The data security sharing approach

This part focuses on the first part of the model proposed in this paper, i.e., the data security sharing approach for the power IoT, mainly consisting of data preparation and collaborative training.

Data collection and cleaning

Data is collected by uniform standards for all smart power devices in areas with boundaries. For example, for electricity consumption data, from a uniformly deployed smart meter platform, the data is collected and stored by category number,

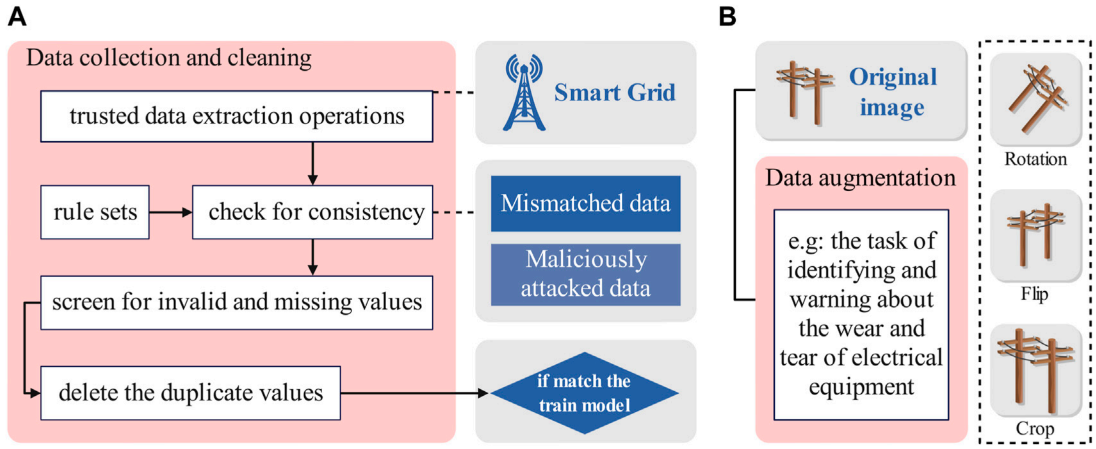

FIGURE 3
Pre-processing stage. **(A)** Data collection and data cleaning **(B)** Data augmentation.

with different regions lending themselves to a uniform standard for implementation between them.

As described in Figure 3A, the regions pre-process the privacy data. The data is first checked for consistency, starting from a prepared rule set and screens for data that does not match the characteristics of the power IoT. For example, the existing electricity theft may influence the data from smart meters (Xia et al., 2021). Then the processing of invalid and missing values is carried out, and the method used in this paper is to use sample means instead of invalid and missing values.

The third step carries out the processing of duplicate values, and the same data are deleted to reduce the model training cost.

Due to the small amount of data in this region, there may be cases where the amount of data is below the standard training threshold set after cleaning. Suppose the training requirements are still not met after data augmentation. In that case, the model proposed in this paper uniformly flags all data in this region with boundaries, and some parameters will be modified in the subsequent training process to reduce overfitting.

Local training data augmentation

Due to the unique data features in the power IoT, local areas with boundaries tend not to share private data with other regions. A possible direct result is that the dataset for local training is extremely limited, and for many machine learning models, the quality of the trained model is largely influenced by the amount of data. This paper uses data augmentation to expand the datasets in the local areas.

As described in Figure 3B, the data augmentation methods vary for different tasks. For example, for the task of identifying and warning about the wear and tear of electrical equipment, the main focus is on augmenting the picture data of electrical equipment. In this paper, the data augmentation methods for tasks involving image recognition include random cropping, image rotation, and flipping.

For random cropping, use the transformation as shown in Formula 1.

$$(l_i, w_i) \leftarrow (\alpha l_i, \beta w_i) \tag{1}$$

where l_i is the length of the i^{th} image, w_i is the width of the i^{th} image, α and β are the parameters in the transformation. Here a tuple is used to store its length and width attributes. Adjust the image to a uniform aspect ratio after cropping:

$$image_i' = resize(image_i) \tag{2}$$

Where $image_i$ and $image_i'$ are the i^{th} image before and after the random crop is completed, respectively, and $resize(\cdot)$ is a conversion function to maintain the aspect ratio.

For image rotation and flipping, use the transformations shown in Formulas 3, 4:

$$\begin{bmatrix} x' \\ y' \end{bmatrix} = \begin{bmatrix} \cos\theta & -\sin\theta \\ \sin\theta & \cos\theta \end{bmatrix} \begin{bmatrix} x \\ y \end{bmatrix} \tag{3}$$

$$\begin{bmatrix} x' \\ y' \end{bmatrix} = \begin{bmatrix} -1 & 0 & w \\ 0 & 1 & 0 \end{bmatrix} \begin{bmatrix} x \\ y \end{bmatrix} \tag{4}$$

where, y and x', y' are the position of pixel points in length and width before and after rotation and flip, respectively. θ is the rotation angle and w is the width of the image.

For other tasks within the power IoT, such as text processing, this paper uses random removal and disruption methods commonly used in the field for text data augmentation.

Transfer learning based on practical assessment

Considering a power IoT decision-making task where a local area with boundaries has only a small amount of controllable data, this paper incorporates the transfer learning method in the proposed model.

Transfer learning transposes a well-established model trained on the source domain with a large amount of data to the target domain with a small amount of local data so that the target model can also achieve excellent results. The model proposed in this paper evaluates the possibility of applying transfer learning in practical experiments for different power IoT decision-making tasks. For example, in the task of identifying and warning about the wear and tear of power equipment, this paper uses a model-based transfer learning algorithm. At the model level, the source and target domains can

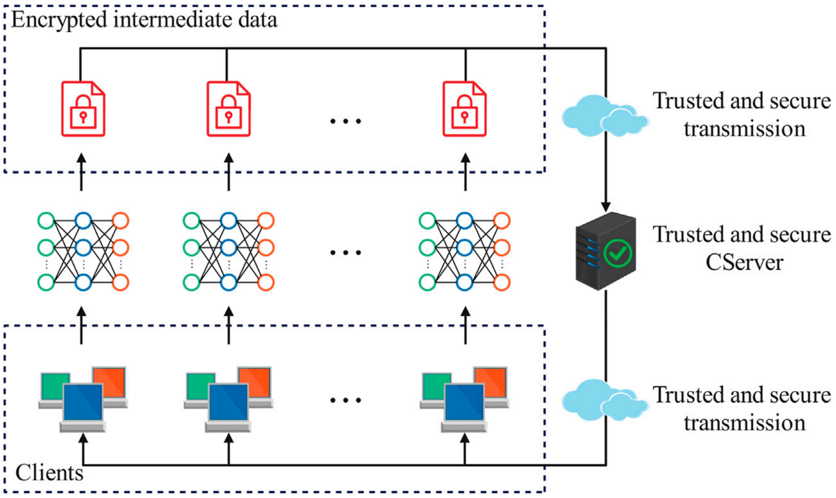

FIGURE 4
Federated learning based on homomorphic encryption.

share some of the parameters and then be trained with fine-tuning in the local domain to obtain a usable target model with stronger generalization performance.

```
Iterate through local area information to generate $LOC$;
for $rd$ in range (Round) do
    for $loc_i$ in LOC do
        if $loc_i$ meet the requirement then
            $V_c^i = doEnc(C_i, PK)$
        end if
    end for
    $V_c \leftarrow$ Transmits intermediate data and integrated into the central server
    $V_p = UD(V_p^{'}, V_c)$
    $V = doDec(V_p, SK)$
    for $loc_i$ in $LOC$ do
        $C_i^{'} = UDLoc(V, C_i)$
    end for
end for
return model
```

Algorithm 1. The model with federated learning.

The details of the experiments on the image task are described in the next section.

Federated learning based on homomorphic encryption

Federated learning is a typical example of a small data scale model training approach, where distributed learning can effectively break down the problems caused by "data silos." At the same time, much of the private data that is not expected to be shared can be securely trained in a local bounded area, which is greatly protected by the inclusion of homomorphic encryption.

Simple homomorphic encryption-based federated learning can be easily described. As in Figure 4, suppose there are n local-area data holders $L = \{l_1, l_2, \cdots, l_n\}$, each of whom has private data $D_i (i \in [1, n])$ that is not shared. A trusted central server $CServer$ is set up, and multiple local-area clients are coordinated by it for collaborative training.

It is further described that each local client freezes the parameters of the first k layers and initializes the remaining layers randomly after determining the original model. The local area client performs a training round and encrypts the intermediate data upon completion:

$$V_c^i = doEnc(C_i, PK) \tag{5}$$

where $doEnc(\cdot)$ is the encryption function, V_c^i is the information of the i^{th} local area client after encrypting the intermediate data, PK is the public key of the encryption process, and C_i is the actual intermediate data of the i^{th} local area client.

The trusted central server receives the encrypted intermediate data from the local area client and performs the parameter update:

$$V_p = UD\left(V_p^{'}, V_c\right) \tag{6}$$

where $V_p^{'}$ is the encrypted intermediate data received by the central server from local clients in the previous round, V_c is the total set of intermediate data received from all local geographical clients ($V_c = \{V_c^1, V_c^2, \cdots, V_c^3\}$), $UD(\cdot)$ is the data processing function of the central server, and in this paper, the averaging method is used, which means that the average of each intermediate data is taken, and after the calculation is completed the central server issues a new round of parameters V_p.

Each local client obtains the latest parameters from the central server, decrypts them with the private key, and receives the actual data in plaintext:

$$V = doDec\left(V_p, SK\right) \tag{7}$$

where V is the latest round's parameters from the central server after decryption, $doDec(\cdot)$ is the decryption function and SK is the private key. The local area client performs the update of the parameters in the local model based on the data obtained in this round:

$$C_i^{'} = UDLoc\left(V, C_i\right) \tag{8}$$

where $C_i^{'}$ is the actual update of the parameters of the model for the i^{th} local area client for this round, $UDLoc\left(\cdot\right)$ is the parameter update function for this local area client, V is the decrypted parameters from the central server for the latest round, and C_i is the intermediate data for the i^{th} local area client. The update here generally replaces the parameters with the new decrypted parameters, or a weighted average method can be used. For a more precise description of the algorithm, see Algorithm 1. It has a time complexity of O (rd×n).

The above homomorphic encryption-based federated learning approach for the power IoT also requires a comparison with traditional training methods, assuming that the model's accuracy obtained from the above process is ACC and considering traditional training:

$$Model = Train\left(\bigcup\nolimits_{i=1}^{n} D_i\right) \tag{9}$$

where $Model$ is the trained model, $Train\left(\cdot\right)$ is the abstract process representation of the training process, and the accuracy obtained from $Model$ is represented as ACC'. The following comparisons are generally considered:

$$\Delta \mathrm{A} = \left|ACC' - ACC\right| < \delta \tag{10}$$

where δ is a very small non-negative actual number, which has also become one of the criteria for measuring federated learning.

The hierarchical fusion decision model

This sub-section focuses on the second part of the model proposed in this paper, a hierarchical fusion decision model for the power IoT, consisting of two main parts, demand hierarchy, and decision credible value fusion.

Hierarchical power IoT demand

The delineation model is central to this subsection, considering that the actual requirements of the power IoT are often complex and diverse and usually consist of multiple sub-requirements, where individual sub-requirements can clearly unambiguously express the decisional boundaries.

Due to the complex features of the power IoT, existing segmentation methods may not reach the goal. A better solution is to cross natural language processing domain knowledge for automatic delineation or to be supported by an expert knowledge base for delineation. The hierarchical model proposed in this paper focuses on using expert knowledge base support for the delineation. The model subscribes to a single requirement (vectorized when necessary) and retrieves the expert knowledge base to delineate several linked sub-requirements. It is worth mentioning that the hierarchical results are not always optimal.

Decision credible value fusion

This paper introduces a weighted fusion strategy at the decision level, referring to various existing model fusion strategies. It can be shown in Figure 5. The weighted fusion strategy can reduce the impact of errors from the model. Considering the sources of plausible decision values: the data obtained after the completion of federated learning of multiple models and the data provided by the expert knowledge base, the weights of each fusion term should be given after lightweight testing or dynamically adjusted during the iterative training process, and the weighted fusion is given by Formula (11):

$$V = \frac{1}{2m}\sum\nolimits_{j=1}^{m}\left(\frac{Z_{ML}^{j}}{n}\sum\nolimits_{i=1}^{n} w_i^j \cdot v_i^j + \frac{Z_{KL}^{j}}{k}\sum\nolimits_{k=1}^{p} c_k^j \cdot x_k^j\right) \tag{11}$$

Where m, n, and p are the number of decisions, the number of fused models in federated learning, and the number of sub-requirements divided by the expert knowledge base, respectively. Z_{ML}^{j} is the weight on the model side at the j^{th} decision round, and Z_{KL}^{j} is the weight on the model knowledge base side at the j^{th} training round. w_i^j is the weight of the i^{th} model fused in federated learning at the j^{th} decision round, and v_i^j is the result of the i^{th} model fused in federated learning at the j^{th} decision round vector. c_k^j is the weight of the k^{th} sub-requirement divided at the expert knowledge base level at the j^{th} decision round, and x_k^j is the result vector of the k^{th} sub-requirement divided at the expert knowledge base level at the j^{th} decision round. It has a time complexity of O (m×max{n,p}).

Results and discussion

In this section, several experiments are conducted to evaluate the model proposed in this paper. In this paper, the proposed model is implemented by PyTorch code framework in Python language and tested on personal computers (PCs) such as i5-7300HQ CPU, GTX1050Ti graphics card and 8 GB RAM. There are many decision-making tasks in the field of power IoT that are worth exploring (e.g., electrical material identification). To better represent the fusion and decision-making approach proposed in this paper, the experimental part will use the power equipment wear and tear assessment task as the primary requirement. Due to the high privacy of power data, the team could not obtain sufficient data, so the experiments mainly used Caltech-256 dataset as an example and attached the data collected by our team. The approach proposed in this paper is fully extensible to specific tasks in the power domain.

Model transfer learning with (Non-) Federated learning

For the image task, this paper uses the VGG-19 and ResNet-50 models for federated learning. Using the transfer learning training dataset, the parameters used in transfer learning are shown in Table 1. For the training process, the transformation formula for the learning rate is shown in Formula (12):

$$\theta_e = \theta_{\min} + \frac{1}{2}\left(\theta_{\mathrm{init}} - \theta_{\min}\right)\left(1 + \cos\left(\frac{E_{\mathrm{cur}}}{E_{\mathrm{init}}}\right)\right) \tag{12}$$

where θ_{init} is the initial learning rate, θ_{min} is the minimum value of learning rate and is set as 0 in this paper, E_{cur} is the current train epoch.

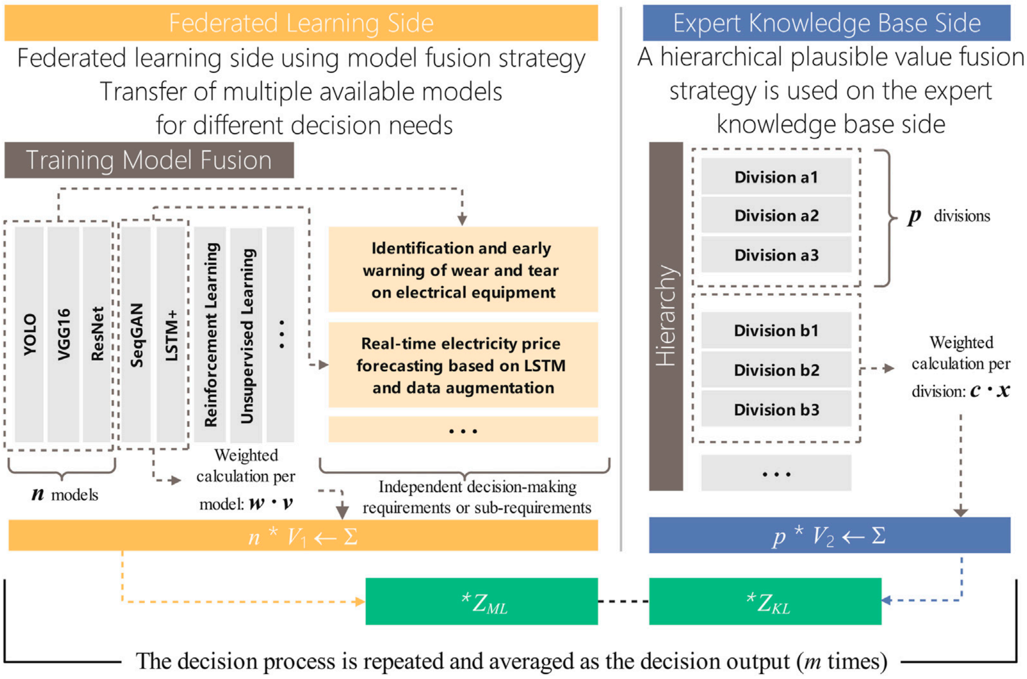

FIGURE 5
Decision confidence value fusion process.

TABLE 1 The parameters used in transfer learning.

Parameters	Value
Batch size	32
Initial learning rate	0.001
Optimizer	SGD
Loss function	Cross entropy

TABLE 2 The parameters used in federated and transfer learning.

Parameters	Value
Batch size	32
Initial learning rate	0.001
Optimizer	SGD
Loss function	Cross entropy
Number of global iterations	30
Local training rounds	2
Regularization parameter	0.5

The models after adding federated learning were evaluated on the server-side for model performance after the intermediate data had gone through FedAvg. It is worth noting that the models used in the experiments in this paper were pre-trained on ImageNet and then downloaded during the first round of training. The experiments used two clients to simulate.

The federated learning scenario, and the transfer learning used the same two models mentioned above, with some specific parameter settings in Table 2.

The effective range of the simulated federation learning used for the experiments in this paper is within a local area network, using homomorphic encryption to ensure secure data transmission. For the security of cross-domain information transmission, it is not considered in this paper for the time being. Also, due to transfer learning, most neural network layers do not need to be updated with parameters, dramatically reducing network communication's burden.

The model training results for the four combinations are shown in Table 3. Excellent accuracy can be achieved for all the mature models selected for training under transfer learning. The two models using federal learning were generally better in terms of accuracy, with the time spent on a single training session varying between models due to the fact that the VGG-19 model used had far more parameters than ResNet-50.

Model fusion

The image task selected as an example in the experiments in this paper is a simple stand-alone task, so fusing sub-requirements will not be considered for use. This part focuses on model fusion. Model fusion allows for better generalization performance of the completed training model and can compensate for possible accuracy problems associated with federated learning. This paper used the model-weighted fusion, which reduces the impact on the overall model due to errors in one

TABLE 3 Transfer learning effects of the two models with (non-)federated learning.

Model	Epoch	Training time (%)	ACC-OPT (%)	ΔA	Security strategy
non-federated transfer learning & VGG-19	30	100	93.6	0.6%	False
non-federated transfer learning & ResNet-50	30	275.07	94.4	≈0%	False
federated transfer learning & VGG-19	60	414.33	94.2	0.6%	True
federated transfer learning & ReNet-50	60	334.96	94.4	≈0%	True
Average		**281.09**	**94.15**	**0.3%**	

Bold values are highlighted for the average of the data in this column.

TABLE 4 Experimental results of model-weighted fusion.

ResNet-50: VGG-19	ACC-OPT (%)	ΔA (VGG-19) (%)	ΔA (ResNet-50) (%)	Security strategy
1.5	94.3	0.7	0.1	True
2.33	95.2	1.6	0.8	True
4	93.1	0.5	1.3	True
9	94.2	0.6	0.2	True
Average	**94.2**	**0.85**	**0.6**	

Bold values are highlighted for the average of the data in this column.

model. When there is a significant difference in structure and performance between the models to be fused, the better performing models are given more substantial weight, and the average performing models are given a lower weight, as shown in Formula (11).

As seen from the experimental results, ResNet-50 outperformed the VGG-19 model in front of the multi-classification task in both experiments with and without federated learning. Therefore, in the model-weighted fusion experiments in this subsection, greater weight was given to ResNet-50. A comparison of the experimental results is shown in Table 4. It can be seen that the best results for model fusion are obtained when the ratio is 2.33, with an optimal accuracy of 95.2%. However, it is worth noting that better than VGG-19 converges faster, and the convergence speed of the fusion model is also affected in the case of its low weights.

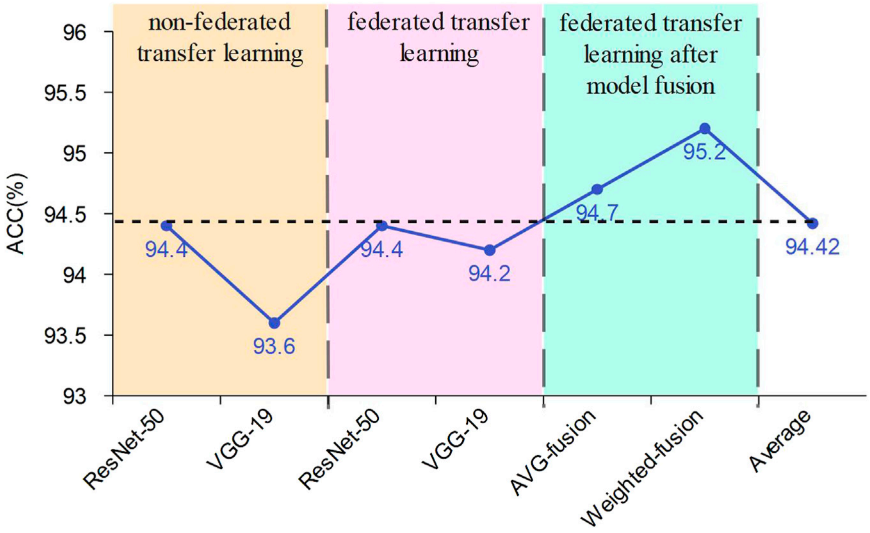

FIGURE 6
The specific experimental comparison data.

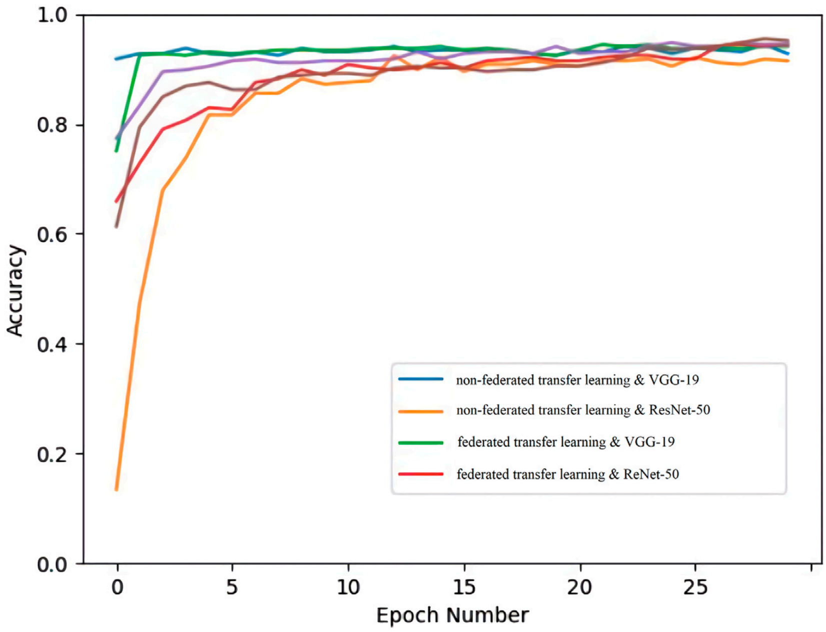

FIGURE 7
Comparison of convergence speed between different combinations.

Overall analysis

The experimental results for the two parts of the model are obtained in the first and second part. At the same time, the corresponding data are also available for the other model fusion method, as shown in Figure 6 for the specific experimental comparison data.

In comparing the best results for this task, model fusion can be optimal, with the weighted fusion method obtaining the first place at 95.2%. However, its convergence is slower in the actual training process. The fusion model is more generalizable than a single model and gives better results.

The weighted calculated result vectors are not listed in the experiments tables, as all experimental results are already expressed in accuracy. As the expert knowledge base requires a certain base reserve, the weight of this part is set to 0 in many tasks of the experiments in this paper, but this is still very scalable for tasks in the field of power IoT. In addition, the experiments in this paper focus on the security protection of electricity data, and the model is more interested in applying a secure method of secure data sharing in the power IoT domain than accuracy. From the data in Tables 3, 4, it can be seen that the experimental group considering the security strategy and the experimental group without incorporating federated learning have less than 1.7% bias in the experimental effect. The decision framework proposed in the text for federated security policies for power IoT can protect independent private data while ensuring accuracy. It improves the confidence level of decision making compared to traditional manual decision making, and it effectively and securely partitions the training data for secure sharing for privacy protection compared to the overall trained model. In addition, the use of models as well as decision-level fusion can be extended to a wide range of power decision tasks in the context of smart grid. It is worth noting that although the proposed approach in this paper is effective in the power IoT domain to ensure that the privacy data used in power tasks are shared securely, its convergence speed is slower than traditional training methods (Figure 7) and requires additional communication time. To test the extensibility of the framework in this paper, we also tested the electricity price forecasting task under smart grid, and the results were similar to this set of experiments, and the secure sharing of private data was ensured from various aspects.

Conclusion and future work

To address the complexity of traditional decision-making methods in the field of power IoT and the privacy protection of power data, this paper introduces homomorphic cryptography-based federated learning to the task of power IoT. Also, transfer learning and model fusion are used to improve the performance of the overall model. This paper also proposes a hierarchical decision model that integrates traditional expert decision making in the power IoT domain and deep learning decision making under new industrial devices, combining machine learning models and plausible values from expert knowledge bases to obtain integrated decisions with excellent results.

Future research will focus on designing new machine learning models for the data characteristics of the power IoT in order to reduce the reliance on transfer models. In addition, we hope to conduct targeted research on data types in the power IoT space to incorporate more advanced security strategies and further adapt to emerging industrial devices such as smart grids.

Data availability statement

The original contributions presented in the study are included in the article/Supplementary Material, further inquiries can be directed to the corresponding authors.

Author contributions

All authors listed have made a substantial, direct, and intellectual contribution to the work and approved it for publication.

Funding

This work is funded by the National Key R&D Program of China (2020YFB0905900); The work is funded by the Science and technology project of SGCC(State Grid Corporation of China): SGTJDK00DWJS2100223.

Conflict of interest

WL, NZ, ZL, HK, JW, and TC were employed by State Grid Information & Telecommunication Group Co., Ltd. SM is employed by State Grid Tianjin Electric Power Company.

The authors declare that this study received funding from State Grid Corporation of China. The funder had the following involvement in the study: A trusted decision fusion approach for the power internet of things with federated learning.

Publisher's note

References

Ahammed, M. T., and Khan, I. (2022). Ensuring power quality and demand-side management through iot-based smart meters in a developing country. *Energy* 250, 123747. doi:10.1016/j.energy.2022.123747

Al Metrik, M. A., and Musleh, D. A. (2022). Machine learning empowered electricity consumption prediction. *CMC-COMPUTERS Mater. CONTINUA* 72 (1), 1427–1444. doi:10.32604/cmc.2022.025722

Alhariry, A., Brown, S., Eshenbaugh, D., Whitt, N., and Browne, A. F. (2021). A survey of sensing methodologies in smart grids. *SoutheastCon* 2021, 9401840. doi:10.1109/SoutheastCon45413.2021.9401840

Bhansali, P. K., Hiran, D., and Gulati, K. (2022). Secure data collection and transmission for iomt architecture integrated with federated learning. *Int. J. Pervasive Comput. Commun.* 2022. (ahead-of-print). doi:10.1108/ijpcc-02-2022-0042

Choi, W., Kim, J., Lee, S., and Park, E. (2021). Smart home and internet of things: A bibliometric study. *J. Clean. Prod.* 301, 126908. doi:10.1016/j.jclepro.2021.126908

Corallo, A., Crespino, A. M., Lazoi, M., and Lezzi, M. (2022). Model-based big data analytics-as-a-service framework in smart manufacturing: A case study. *Robotics Computer-Integrated Manuf.* 76, 102331. doi:10.1016/j.rcim.2022.102331

Friha, O., Ferrag, M. A., Lei, S., Maglaras, L., Choo, K., and Nafaa, M. (2022). Felids: Federated learning-based intrusion detection system for agricultural internet of things. *J. Parallel Distributed Comput.* 165, 17–31. doi:10.1016/j.jpdc.2022.03.003

Gilanifar, M., Wang, H., Ozguven, E. E., Zhou, Y., and Arghandeh, R. (2020). Bayesian spatiotemporal Gaussian process for short-term load forecasting using combined transportation and electricity data. *ACM Trans. CYBER-PHYSICAL Syst.* 4 (1), 1–25. doi:10.1145/3300185

Guang, Z., Tang, J., Li, Y., Fan, X., Song, G., Zhang, N., et al. (2021). Data value mining and auxiliary decision making of power communication service. *Electr. POWER ICT* 19 (10), 5. doi:10.1109/IMCEC51613.2021.9482236

Gunduz, M. Z., and Das, R. (2020). Cyber-security on smart grid: Threats and potential solutions. *Comput. Netw.* 169, 107094. doi:10.1016/j.comnet.2019.107094

Hong, Q., Chen, Z., Dong, C., and Xiong, Q.: A dynamic demand-driven smart manufacturing for mass individualization production. In: Proceedings of the 2021 IEEE International Conference on Systems, Man, and Cybernetics (SMC), pp. 3297–3302. (2021). January 2021, Melbourne, Australia, doi:10.1109/SMC52423.2021.9659114

Jiang, G., Su, L., Liu, H., Cao, Y., Sun, R., and Diao, F. (2020). "Constructing the power knowledge graph by multi-source electricity data," in PROCEEDINGS OF THE 2020 INTERNATIONAL CONFERENCE ON COMPUTER, INFORMATION AND TELECOMMUNICATION SYSTEMS (CITS). International Conference on Computer Information and Telecommunication Systems, Hangzhou, China, October 2020. Editors M. Obaidat, K. Hsiao, P. Nicopolitidis, and D. CascadoCaballero, 111–115.

Kaur, D., Uslu, S., Rittichier, K. J., and Durresi, A. (2022). Trustworthy artificial intelligence: A review. *ACM Comput. Surv. (CSUR)* 55 (2), 1–38. doi:10.1145/3491209

Li, Y., Zhou, Y., Jolfaei, A., Yu, D., Xu, G., and Zheng, X. (2021). Privacy-preserving federated learning framework based on chained secure multiparty computing. *IEEE INTERNET THINGS J.* 8 (8), 6178–6186. doi:10.1109/JIOT.2020.3022911

Li, Z., Liu, J., and Jin, Y. (2020). Analysis of load characteristics changes in the case of large-scale electric energy substitution load connected-in. *IOP Conf. Ser. Earth Environ. Sci.* 446 (4), 042085. doi:10.1088/1755-1315/446/4/042085

Parimala, M., Priya, R. M. S., Pham, Q., Dev, K., Maddikunta, P. K. R., Gadekallu, T. R., et al. (2021). Fusion of federated learning and industrial internet of things: A survey. https://arxiv.org/abs/2101.00798.doi:10.48550/arXiv.2101.00798

Mashal, I. (2022). Smart grid reliability evaluation and assessment. *KYBERNETES.* doi:10.1108/K-12-2020-0910

Miao, Q., Lin, H., Wang, X., and Hassan, M. M. (2021). Federated deep reinforcement learning based secure data sharing for internet of things. *Comput. Netw.* 197, 108327. doi:10.1016/j.comnet.2021.108327

Mugunthan, V., Peraire-Bueno, A., and Kagal, L. (2020). "Privacyfl: A simulator for privacy-preserving and secure federated learning," in Proceeding of the CIKM '20: PROCEEDINGS OF THE 29TH ACM INTERNATIONAL CONFERENCE ON INFORMATION and KNOWLEDGE MANAGEMENT, October, 2020 (Ireland: Assoc Comp Machinery), 3085–3092. doi:10.1145/3340531.3412771

Ni, M. (2020). "Study of a quality monitoring system of electric power using internet of things technology," in Proceedings of the IOP Conference Series-Earth and Environmental Science, Bristol, UK, December, 2019. doi:10.1088/1755-1315/440/3/032005440

Pal, S., Dorri, A., and Jurdak, R. (2022). Blockchain for iot access control: Recent trends and future research directions. *J. Netw. Comput. Appl.* 203, 103371. doi:10.1016/j.jnca.2022.103371

Ratnaparkhi, S., Khan, S., Arya, C., Khapre, S., Singh, P., Diwakar, M., et al. (2020). Withdrawn: Smart agriculture sensors in iot: A review. *Mater. Today Proc.* 0. doi:10.1016/j.matpr.2020.11.138

Tanwar, V. K., Raman, B., Rajput, A. S., and Bhargava, R. (2021). SecureDL: A privacy preserving deep learning model for image recognition over cloud. *J. Vis. Commun. Image Represent.* 86, 103503. doi:10.1016/j.jvcir.2022.103503

Tian, K., and Dong, W. (2021). Investment decision-making model of transmission grids under new style power system. *Smart Power* 15, 1112. doi:10.3390/en15031112

Wang, G., Xia, X., Ji, S., and Lai, C.-F. (2021). A privacy-preserving multi-dimensional data aggregation scheme with forward security in smart grid. *J. INTERNET Technol.* 22 (1), 91–99. doi:10.3966/160792642021012201009

Wang, Z., Li, T., Wang, B., Zhang, B., and Zhao, W. (2022). Global short-term load forecasting for multi decision making units in the new power system. *China J. Econ.* 2 (1), 20. doi:10.12012/CJoE2021-0082

Wu, J., and Xiao, J. (2022). Development path based on the equalization of public services under the management mode of the internet of things. *Socio-Economic Plan. Sci.* 80, 101027. doi:10.1016/j.seps.2021.101027

Wu, X., Zhang, Y., Wang, A., Shi, M., and Liu, L. (2020). Mnssp3: Medical big data privacy protection platform based on internet of things. *Neural Comput. Appl.* 34 (4), 11491–11505. doi:10.1007/s00521-020-04873-z

Xia, X., Lin, J., Xiao, Y., Cui, J., Peng, Y., and Ma, Y. (2021). A control-chart-based detector for small-amount electricity theft (set) attack in smart grids. *IEEE Internet Things J.* 9 (9), 6745–6762. doi:10.1109/jiot.2021.3113348

Xia, Z., Zhang, Y., Gu, K., Li, X., and Jia, W. (2022). Secure multi-dimensional and multi-angle electricity data aggregation scheme for fog computing-based smart metering system. *IEEE Trans. GREEN Commun. Netw.* 6 (1), 313–328. doi:10.1109/TGCN.2021.3122793

Xu, X., Peng, H., Bhuiyan, M. Z. A., Hao, Z., Liu, L., Sun, L., et al. (2021). Privacy-preserving federated depressiondetection from multisource mobile health data. *IEEE Trans. Industrial Inf.* 18 (7), 4788–4797. doi:10.1109/tii.2021.3113708

Yan, R., Lin, C., Zhang, W.-f., Chen, L.-w., and Peng, K.-n. (2020). Research on information security of users' electricity data including electric vehicle based on elliptic curve encryption. *Int. J. DISTRIBUTED Sens. Netw.* 16 (11), 155014772096845. doi:10.1177/1550147720968458

Yang, X., Shu, L., Liu, Y., Hancke, G. P., Ferrag, M. A., and Huang, K. (2022). Physical security and safety of iot equipment: A survey of recent advances and opportunities. *IEEE Trans. Industrial Inf.* 18 (7), 4319–4330. doi:10.1109/tii.2022.3141408

Zhang, H., Zhang, H., Wang, Z., Zhou, Z., Wang, Q., Xu, G., et al. (2022). Delay-reliability-aware protocol adaption and quality of service guarantee for message queuing telemetry transport-empowered electric internet of things. *Int. J. Distributed Sens. Netw.* 18 (5), 155013292210978. doi:10.1177/15501329221097815

Zhang, K., Song, X., Zhang, C., and Yu, S. (2022). Challenges and future directions of secure federated learning: A survey. *Front. Comput. Sci.* 16 (5), 165817–165818. doi:10.1007/s11704-021-0598-z

frontiers | Frontiers in Energy Research

TYPE Review
PUBLISHED 24 March 2023
DOI 10.3389/fenrg.2023.1142243

OPEN ACCESS

EDITED BY
Xin Ning,
Institute of Semiconductors (CAS), China

REVIEWED BY
Juan Manuel Belman-Flores,
University of Guanajuato, Mexico
Achyut Shankar,
University of Warwick, United Kingdom
Zhang Hengmin,
University of Macau, China
Mohammed Shuaib,
University of Technology Malaysia,
Malaysia

*CORRESPONDENCE
Zehua Miao,
✉ ezramiao@outlook.com

SPECIALTY SECTION
This article was submitted to Smart Grids,
a section of the journal
Frontiers in Energy Research

RECEIVED 11 January 2023
ACCEPTED 03 March 2023
PUBLISHED 24 March 2023

CITATION
Miao Z (2023), Intelligent control system for the electric vehicle heat pump air conditioner based on machine learning. *Front. Energy Res.* 11:1142243.
doi: 10.3389/fenrg.2023.1142243

Intelligent control system for the electric vehicle heat pump air conditioner based on machine learning

Zehua Miao*

School of Mechanical and Automotive Engineering, South China University of Technology, Guangzhou, China

In order to break through the existing battery technology of electric vehicles, this paper proposes to use heat pump air conditioning instead of the original PTC heating system potential. First, the advantages and disadvantages of different heat pump models for new energy vehicles are analyzed and compared. Second, a fuzzy inference system is constructed based on the machine learning model to observe the temperature of the passenger compartment using the temperature sensor inside the tram and to determine the need for the air conditioning system to be turned on in the heating/cooling mode by comparing it with the set temperature. Finally, the results show that the machine learning algorithm is able to monitor and adaptively adjust the interior temperature to further enhance the adaptability of the system with low volatility and high accuracy. The proposed research study can lay the foundation for further optimizing the design of heat pump air conditioners for electric vehicles.

KEYWORDS

machine learning, electric vehicle, heat pump air conditioning, control system, defrost

1 Introduction

Automotive air conditioning technology has been developed for nearly 70 years since the 1950s, when General Motors first designed and installed the first integrated heating and cooling air conditioner in a car in the United States (Sharif et al., 2017; Bentrcia et al., 2018; Wang et al., 2020). During this period, although the components within the automotive air conditioning system have been continuously updated, its entire system based on mechanical compression for cooling and the use of waste heat from fuel vehicles for heating has remained almost unchanged (Ahn et al., 2016; Kalinichenko et al., 2018; Lee et al., 2022). With the rising awareness of environmental protection in various countries and the rapid development of technology in the new energy vehicle industry, it is the trend for vehicles to develop from traditional fuel vehicles to new energy. Therefore, the automotive air conditioning industry is facing a shift and challenge from a single indicator of comfort to comprehensive energy saving and emission reduction. Under the pressure of energy crisis and environmental pollution, new energy vehicles came into being. Among them, pure electric vehicles, with their characteristics of no pollution, low noise, and high efficiency, have received wide attention from automobile manufacturers and consumers and have gradually become an important research direction for the transformation and upgrading of the automobile industry (Wang et al., 2016; Li et al., 2019). Although electric vehicles have great potential for development, shortcomings such as short range and long charging time limit the popularity of pure electric vehicles.

Both new energy vehicles and conventional vehicles require a comfortable driving environment. Air conditioning systems can provide a comfortable interior environment for the driver and occupants under complex and changing driving conditions (Sharif et al., 2016). Pure electric vehicles have limited battery capacity and short range, so there are strict requirements for the energy consumption and efficiency of the air conditioning system. Among them, in the design of the whole vehicle thermal management system, the cooling system medium of electric drive and accessory thermal management is the coolant, and the structure is basically independent. The interior thermal management and battery thermal management are realized by the coupling of air conditioning system, and the cooling medium is an R134a refrigerant. The interior thermal management mainly includes interior cooling, interior heating, and remote control of air conditioning. The strongest coupling between the battery thermal management and air conditioning system is battery cooling, and battery heating is generally realized independently through the battery heater, which is basically not coupled with the air conditioning system.

Recently, artificial intelligence has become a socially recognized future development trend (Athey, 2018; Bi et al., 2019). By mining the implied laws from a large amount of historical data and applying them to the prediction of the system, machine learning improves the accuracy and precision of the system. With decades of research and development, automotive air conditioners have accumulated a sufficient amount of historical data and are a representative applicable object for machine learning. Most of the air conditioning systems of electric vehicles currently in circulation are used for winter heating through PTC, but according to the relevant electric vehicle regulations, if the car is to have the function of heating and defrosting, then the PTC electric heating power needs to be more than 3000 W (Park and Kim, 2017; Park and Kim, 2019). The PTC electric heating method of heating consumes a lot of power and has a large impact on the battery, and the coefficient of performance of the system is maximum 1, there is certain of energy waste. The heat cannot be propagated in the reverse direction without the interference of external forces, and heat can only be radiated from high temperature to low temperature. The working principle of the heat pump is to consume less energy and realize the propagation of heat from the low-temperature object to high-temperature object by reversing the cycle, so as to obtain a larger amount of heat. This way of consuming less energy and obtaining more heat can achieve the purpose of energy saving.

Heat pumps have a proven product history of over 20 years as a solution for home and commercial air conditioning. Although, their use of electrical energy can achieve 2–3 times of heat output. However, limited by cost and technical maturity, they have been slow to develop in the automotive air conditioning industry. However, with the imperative to address the range of electric vehicles, heat pump systems are the most promising and efficient solution available. At present, a lot of research studies have been performed by scholars in various countries on the design and application of heat pump air conditioning control systems in the context of machine learning. In this paper, we will systematically review the current research status of the electric vehicle heat pump air conditioning control system based on machine learning, summarize and conclude the technical principles of heat pump air conditioning, types of heat pumps, environmental protection work material substitution, and compressor control strategy and electric vehicle heat pump defrost system based on machine learning, and analyze the current difficulties in electric vehicle heat pump air conditioning on this basis.

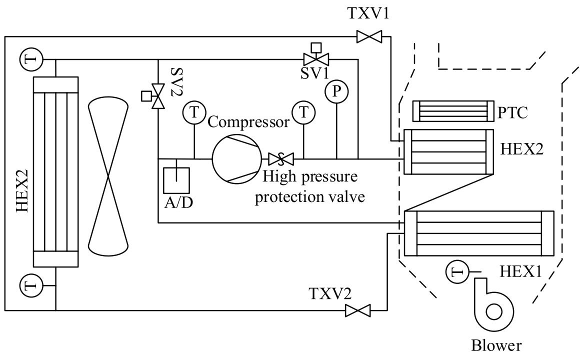

FIGURE 1
Working principle of the electric vehicle heat pump air conditioning system.

2 Principle and status of electric vehicle heat pump air conditioning

2.1 Working principle of the electric vehicle heat pump air conditioning system

The working principle of the electric vehicle heat pump air conditioning system is shown in Figure 1, which mainly consists of an electric compressor, a four-way reversing valve, an external heat exchanger, a liquid storage dryer, a capillary tube, an internal heat exchanger, and a fan (Zhou et al., 2017; Peng et al., 2021; Ning et al., 2023). The cooling cycle is similar to the heating cycle in that the direction of the mass flow can be changed simply by a four-way reversing valve.

T and P denote pressure and temperature, respectively. As can be seen from Figure 1, the electric air conditioning compressor will be a high-temperature and low-pressure gaseous refrigerant, compressed into a high-temperature and high-pressure liquid refrigerant; through the car heat exchanger condensation, heat exchanges with the air inside the car, the air temperature inside the car rises, and the refrigerant temperature drops, becoming a low-temperature and high-pressure liquid refrigerant; and then, through the electronic expansion valve, it becomes a low-temperature and low-pressure gaseous refrigerant; through the car heat exchanger, heat exchanges with the gas outside the car, the air temperature outside the car drops, and the refrigerant temperature rises, becoming a high-temperature and low-pressure gaseous refrigerant, into the next round of the refrigeration cycle. In this way, the heat exchange between the inside and outside of the car can be realized, so as to achieve the effect of heating the inside of the car.

2.2 Different types of heat pump systems

2.2.1 Direct heat pump

Automotive air conditioning systems with heat pump functions are more complex than conventional automotive air conditioning systems, and the functionality and reliability of the components are correspondingly higher. Junqi et al. (2021) pointed out that the existing four-way reversing valve design is a copper reversing valve for domestic air conditioners, and an aluminum reversing valve for automotive air conditioners has poor solderability, low reliability, and vibration resistance and, thus, has the disadvantage of being unsuitable for frequent switching and leakage between high and low pressures. Therefore, major automotive companies and system suppliers can now arrange a dual heat exchanger on the indoor side to take care of the cooling and heating needs (Han et al., 2021; Wang et al., 2022a). For the direct heat pump system, an internal condenser is arranged directly on the rear side of the evaporator inside the air conditioning box to replace the conventional warm air core. At the same time, since the outdoor heat exchanger has to take on additional heat absorption demand in winter, it is necessary to add an additional heat making valve set or throttling short pipe valve set at its inlet in the heat pump mode. The function is to realize the fine adjustment of the flow rate of outdoor heat exchanger to maintain the stable operation and heat output of the system in the heating mode. At the same time, the battery cooler and indoor evaporator also need to use solenoid valve set to cut off and bypass to the gas–liquid separator.

2.2.2 Indirect heat pump

Unlike the direct heat pump, the indirect heat pump system uses a plate heat exchanger to realize the heat exchange between the compressor high-pressure high-temperature refrigerant gas and the coolant of the cooling circuit, and the heat exchanged high-temperature coolant then flows through the warm air core in the air conditioning box *via* the secondary circuit, so as to conduct secondary heat exchange with the circulating air in the air conditioning box again. After the secondary heat exchange, the air temperature of the warm air core reaches the set target air temperature (Zhou et al., 2022). It can be seen that the arrangement inside the air conditioning box is still the same as that of the conventional air conditioning box, with the evaporator and the warm air core. The air conditioning box does not need to be redesigned again, which can reduce most of the design and verification and tooling costs and save the development cycle. Meanwhile, the indirect heat pump with secondary loop design can realize the coupling relationship between the coolant system and the heat pump system through the plate water-cooled condenser (Malinowski et al., 2017). The high-pressure water PTC of the cooling system can achieve rapid warming of the battery system in winter and can also be used as a supplementary heat source to compensate for the risk of heat deficiency of the heat pump system under severe low-temperature conditions. It also reduces the risk and cost of the high-pressure PTC in the air conditioning box. The use of electrical energy regulation not only keeps the structure design simple but also controls the current size and heat and the use of temperature models, reduces the heat loss during the operation of the air conditioning system, and increases the speed of the car's internal temperature.

2.2.3 Heat pump system with waste heat recovery

Although the heat pump system can output 2 to 3 times the electrical power of the heat and the energy efficiency is high, it relies on the external heat exchanger at low-temperature air and refrigerant heat transfer. When the external heat exchanger is in evaporating condition and the surface temperature is lower than the dew point temperature of the incoming air, the heat exchanger surface is in wet condition and the heat exchanger surface will condense or even frost. Therefore, the traditional air source heat pump, in the low-temperature and high-humidity environment will quickly frost and, thus, affect the stable output of system heat and system pressure loss. For this reason, many scholars have considered dual heat source heat pump systems that operate by using the waste heat from the coolant of electrical components such as motors.

A new heat pump system for electric vehicles is proposed in the literature (Singh and Sharif, 2019; Wang et al., 2021a), which takes the form of an additional external heat source in the system. A special device, called a bi-directional reservoir, was also designed. This device performs the filtering and drying function of the reservoir inside a conventional vehicle air conditioner and can be used in the cooling or heating mode. This replaces the original need for two expansion valves, two check valves, and two liquid storage electric compressor control tanks. The results of the improved heat pump bench test show that at an ambient temperature of −10°C, the air side absorbs 2.5 kW of heat exchange and the battery and motor recover 0.5 kW of heat. In comparison with the PTC system, the whole vehicle saves 15% of electricity consumption. It also improves the stability of the system for external heat exchanger frost.

Rajbongshi and Saikia (2018) proposed a thermal management method called the *thermal link system*, in which the waste heat recovery heat exchanger is connected in series with the outdoor heat exchanger. In the heating mode, the power consumption can be reduced to 580 W and a heating capacity of more than 2000 W can be obtained. As a result, the COP of the heat pump system exceeds 3.3.

In the study of Liu et al. (2019), a waste heat recovery heat pump system connected in parallel with an external heat exchanger was investigated. The performance of the winter EV thermal management system was enhanced by recovering the automotive waste heat, and the heating COP was improved by about 25.5% when the ambient temperature was −7°C and the waste heat was boosted from 0 W to 1000 w. At the same time, the waste heat generated by the circuit helps to increase the compressor suction pressure and outlet pressure, which in turn increases the outlet air temperature. In comparison with the PTC heating system, the remaining power of the whole vehicle is improved by about 53%.

Karnik et al (2016) noted in an SAE workshop that the I-pace heat pump system can recover 2.5 kW of heat from the motor circuit at an ambient temperature of 0°C. At the same time, only 0.3 kW of compressor power consumption is required to deliver an overall 2.8 kW of heat to the passenger compartment. Menken et al (2018) evaluated that the Audi Q7 e-tron heat pump can deliver 3.4 kW of heat with 2.5 kW of power in the waste heat recovery heat pump mode at an ambient temperature of 5°C.

TABLE 1 Overview of machine learning methods and classical applications.

Machine learning methods	Overview	Classical applications
Supervised learning	Learning to map new data to known types by a given set of manually labeled sample data. The two main types of supervised learning are classification and regression	Spam filter
Unsupervised learning	The purpose of unsupervised learning is to find correlations between data through data compression, visualization, and noise reduction, which are important skills for data analysis. There are two main types of unsupervised learning: dimensionality reduction and clustering. The use is generally combined and not limited to one	Targeted marketing programs
Intensive learning	Learning how to get reward maximization by receiving information about the environment. Reinforcement learning is primarily concerned with the performance of the system	Play games, such as Go games

2.3 Environment-friendly work substitution for heat pump air conditioners

Currently, R134a is the main working fluid in automotive air conditioning systems, while R407C, R410A, R1234yf, and CO2 are also used in a few automotive air conditioning systems.

R134a is non-toxic, non-combustible, and has good heat transfer performance, but its boiling point is relatively low (−26.5°C) and the amount of refrigerant vaporization decreases significantly when the ambient temperature decreases, resulting in a decrease in heating efficiency, insufficient low-temperature heat production, and high energy consumption, which cannot meet the load requirements of automotive air conditioners at low ambient temperatures; its GWP (1600) value is high, and it is a restricted process in the EU and the Kyoto Protocol. R407C is a ternary non-azeotropic blend of R32, R125, and R134a, with a GWP value of 1980. R134a, R407C, and R410A are three mainstream automotive air conditioning process agents whose use has been restricted due to their high GWP values. R1234yf (ODP = 0, GWP = 4) is an environment-friendly process agent for automotive air conditioners jointly introduced by Honeywell and DuPont, which can meet the requirements of EU regulations and has similar thermodynamic and heat transfer characteristics to R134a. It is one of the best alternatives to R134a for automotive air conditioners because of its low cost (Altinkaynak et al., 2019; Pabon et al., 2020; Adrian et al., 2021; Yadav et al., 2022). However, there is a 10% decrease in performance compared with R134a systems, and the performance decrease is more prominent at low-temperature heating. Meng et al. (2018) and Yang et al. (2019) applied R1234yf/R134a hybrid work gases with different mixing ratios in automotive heat pump air conditioning systems, and the COP is slightly lower than that of R134a systems, but the difference does not exceed 7%, which is feasible.

The natural work gas CO2 (ODP = 0 and GWP = 1) has the advantages of good low-temperature heating performance and high cooling capacity per unit and is considered as one of the best choices for the new generation of work gas for automotive air conditioning (Lee et al., 2014). Mercedes-Benz of Germany was the first to launch a vehicle equipped with a CO2 air conditioning system in 2017, and Toyota and others have started to apply it on a large scale. The CO2 heat pump system developed by Valeo can increase the driving range by 15% at −15°C and 30% at 20°C. The CO2 transcritical automotive heat pump air conditioning system proposed in the literature (Zheng et al., 2020; Wang et al., 2022b) can achieve an outlet air temperature of 40.4°C and a COP of 1.8 at −20°C in a fully fresh air environment, with obvious advantages of low-temperature heating effect. However, the critical temperature of CO2 work material is low (31°C), and the system must work in the transcritical cycle (pressure >7.4 MPa), and the operating pressure is much higher than that of the R134 a automotive air conditioning system, and the existing components cannot meet the requirements of system reliability and safety.

3 Machine learning-based compressor control strategy for heat pump air conditioners

A temperature sensor in the passenger compartment of the electric vehicle observes the temperature of the passenger compartment and determines that the air conditioning system needs to be turned on in the heating/cooling mode by comparing it with the set temperature. The automatically controlled air conditioning system features low volatility and high accuracy, avoiding the driving safety hazards for drivers caused by manually adjusting the air conditioning knob. Scholars at home and abroad have found that the compressor is a key part of the air conditioning control system through research on air conditioning systems. Scroll compressors can even reduce the power of the air conditioning system by avoiding the compressor to always run at very high speed.

The scroll compressor is driven by a DC motor. By adjusting the duty cycle of the voltage applied to the DC motor, the speed of the compressor can be effectively controlled to achieve effective and precise control of the occupant compartment temperature. At the same time, it can reduce the power of the air conditioning system by avoiding the compressor from running at very high speed all the time. By introducing machine learning (Agarwal et al., 2020) and combining neural networks with fuzzy control, researchers designed a fuzzy neural network compressor controller and compared it with the control effects of PID and fuzzy control to derive the best compressor control system.

In this paper, the control strategy of the heat pump air conditioning system is studied from the power of the air conditioning system by combining the heat transfer mechanism of the heat pump air conditioning system and components and relevant algorithms in machine learning with current popular control methods as the starting point. Based on the thermodynamic principle, the remaining components of the heat pump air conditioning system are modeled, and the coupling of each component is proposed to build a heat pump air conditioning system construction strategy. The deficiency of fuzzy control which relies heavily on expert experience is remedied.

3.1 Inverter compressor PID control

PID control as a linear controller is widely used in the field of mechanical control due to its excellent robustness, high reliability, simple principle, and easy implementation (Xie et al., 2022). PID achieves the control of the control target by establishing an accurate mathematical model. However, for the automotive air conditioning system, the dynamic changes of its driving state and environment make it a non-linear and time-varying strong controlled object. Therefore, it is difficult to meet the precise control of the air conditioning system by using the PID controller, a classical control algorithm that regulates by linear superposition of three items: proportional, differential, and integral. At the same time, there are also applications for the actual control object, after simplifying the PID controller, such as the PI controller.

The PID control system for the automatic air conditioning compressor was determined based on the principle of the PID control system combined with the compressor control system. The researchers found that if the set temperature of the passenger compartment is 25 °C, the compressors all run at the highest speed when the temperature difference exceeds the upper and lower limits to ensure that the set temperature is reached as soon as possible (Chunyue, 2017).

3.2 Fuzzy control of the variable-frequency compressor

Fuzzy control based on fuzzy sets, fuzzy logic, and fuzzy language is a popular research topic in the field of artificial intelligence control in recent years and has been widely used in various fields of industry. The automotive heat pump air conditioning system is easily limited by the driving status of the car and the changing heat load. Also, fuzzy control, as an important part of intelligent control, uses set fuzzy rules for effective control of the control target without the need for precise mathematical models (Nguyen et al., 2019). Yordanova et al. (2014) argued that the introduction of fuzzy control into the field of air conditioning control avoids most of the ineffective control and allows the power of the air conditioning system to be reduced.

The EV obtains the exact value of the controlled quantity by interrupt sampling and then compares this quantity with the given quantity to obtain the error signal e, error rate of change Δe, fuzzy control of the exact quantities of error signals E and Δe into fuzzy quantity E, and error rate of change Δe; then, the fuzzy decisions are made by E, ΔE, and the optimized fuzzy control rules R (fuzzy relations) based on the inferred synthetic rules. The fuzzy control quantity A is obtained as

$$U = (E \times \Delta E) \circ R. \tag{1}$$

In order to exert precise control on the controlled object, it is also necessary to convert the fuzzy quantity U into the precise quantity, i.e., non-fuzzy processing, and after getting the precise digital control quantity, it is converted into the precise analog quantity by digital-to-analog conversion and sent to the actuator for the first step control of the controlled object. The frequency of the control quantity, the rate of change of the control quantity frequency and the temperature deviation are sent back to the indoor microcontroller system for genetic evaluation and optimization, obtaining new control rules and genus functions, and then interrupting and waiting for the second sampling for the second step control. Going on in this way, the self-learning optimal control of the controlled object is achieved.

3.3 Machine learning-based inverter compressor fuzzy neural network control

Machine learning is centered on parsing data and finding patterns, learning by writing algorithms, and making decisions and predictions of relevant events based on the learned algorithms. In contrast to the traditional idea of explicitly writing programs to perform a solidified task, machine learning enables computers to perform tasks by developing learning algorithms (Durur and Yokuş, 2021). Depending on the learning method, there are three categories: supervised learning, unsupervised learning, and reinforcement learning. Different types of machine learning methods have specific advantages, disadvantages, and applications. An overview of current machine learning methods and classical applications is shown in Table 1.

Machine learning is a method of giving machines and humans the same level of intelligence (artificial intelligence). Machine learning contains a variety of algorithms that are applicable indifferent situations such as clustering and classification. Artificial neural networks are the current research hotspot and focus in machine learning. Artificial neural networks are based on the structure of biological neural networks. One or more outputs are produced by many inputs that pass through several implicit layers. These connections form specific loops that mimic the way the human brain processes information and logical connections. As the algorithm continues, the hidden layers tend to be smaller and more subtle. By using the generalized multi-feature subspace framework to learn the structural features of noisy and anomalous pixels, a unique approximate solution is computed by using the L1 sphere theory, and the complex computation of large-scale data is avoided by using the filtering technique, thus reducing the time and space complexity. Finally, machine learning provides better recognition results compared to other sparse coding methods.

Fuzzy systems and artificial neural networks belong to the same characteristic-free mathematical models and non-linear systems, and both are important tools for dealing with uncertainty problems, uncertainty, and non-linearity. Salleh et al. (2017) studied that the inference rules of fuzzy systems rely on expert experience or skilled operators to write them, and they do not have adaptive and self-learning capabilities themselves, which makes fuzzy systems have certain limitations. Moreover, the reliability of expert experience determines the reliability of fuzzy systems. Neural networks have the ability of adaptive learning, fault tolerance, parallelizable computation, and distributed information storage. However, Alashkar et al. (2017) pointed out that neural networks themselves do not make good use of empirical knowledge and are often assigned initial values and weights in the form of 0 or random

TABLE 2 Comparison of the traditional solution and the proposed solution.

Traditional solutions	The proposed program
The study mostly focuses on a single mode of cooling or heating without considering whether the same control strategy meets the demand in both heating and cooling	Meet the purpose of passenger cabin comfort and energy saving at the same time
Mainly focused on PID control, fuzzy control, and other control methods, not combined with artificial intelligence-related algorithms	Compensates for the fact that fuzzy control relies heavily on expert experience and has insufficient control accuracy due to errors in expert experience

numbers, which makes neural networks show poor performance when applied to express rule-based knowledge. Also, it makes the neural network prone to fall into local extremes and increases the training time of the neural network. In conclusion, fuzzy systems are suitable for dealing with structured knowledge, while neural networks are more effective for unstructured knowledge. Fuzzy neural network systems are modeled according to their fuzzy systems and given physical meaning to the corresponding network nodes. In contrast to neural networks, fuzzy neural networks can determine the initial values of the system. Also, compared to fuzzy systems, fuzzy neural networks have high adaptive and learning capabilities due to their neural network structure (Marín et al., 2019; Zheng et al., 2021).

Fuzzy neural networks are essentially conventional neural networks that are given fuzzy input signals and fuzzy weights, and their learning algorithms are usually neural network learning algorithms or generalization algorithms. The inference rules of Mamdani-type fuzzy neural networks conform to the normal human thinking habits and, therefore, can represent human knowledge more accurately (Yucel et al., 2017; Zhang et al., 2018a; Lucchese et al., 2021; Mohammed and Hussain, 2021). However, their computations are generally complex and are not conducive to mathematical analysis.

4 Electric vehicle heat pump air conditioning defrost research

4.1 Frost suppression structure design

The frost suppression design is mainly designed to reduce the frost rate and frost volume by changing the geometrical structure parameters and surface interface properties of the heat exchanger. The literature (Hu et al., 2020) analyzed the characteristics of frost growth in a four-process heat exchanger: the ratio of gas–liquid refrigerant differs in different processes and is influenced by gravity, the frost layer is uniformly distributed in the first process, while it is non-uniformly distributed in the second, third and fourth processes, and there is a linkage between surface frost growth and surface temperature drop. There is a lack of research on the optimization of frost suppression for this phenomenon, but in the study of improving the air inlet conditions of electric vehicle heat exchangers (Zhang et al., 2018b), the four processes were improved to six processes with more uniform air inlet, and the study provided ideas for heat exchanger frost suppression. Combining these two studies, it can be foreseen that improving the refrigerant side process has some potential in the design of heat exchanger frost suppression.

The outdoor heat exchanger of the heat pump system has two spatial arrangements, horizontal and vertical, and the conventional fuel car heat pump system mostly uses the horizontal arrangement with the reservoir function, while the electric car microchannel heat exchanger mostly uses the vertical arrangement that helps drainage. Gillet et al. (2018) studied the heat production and air outlet temperature variation of horizontal and vertical arrangement methods under evaporator conditions in high cold, high humidity, and cold and wet conditions. The performance of the horizontal arrangement is better than that of the vertical arrangement under frost conditions, mainly because the vertical arrangement leads to uneven refrigerant distribution and severe frosting at local locations, while defrosting will not be complete. This shows that the vertical arrangement of the heat exchanger, although conducive to frost water drainage, but not conducive to frost suppression. In the work of Mahvi et al. (2021), a superhydrophobic heat exchanger was studied, which was able to significantly reduce the amount of frost and keep the thermal conductivity above 50% of the maximum value and reduce the time and energy required for defrosting.

Surface treatment can reduce the amount and speed of frosting, but the high cost of the surface treatment and the complexity of the process make it difficult to spread, so reducing costs and simplifying the process are the key points of whether this type of technology can be applied. Considering the long-time operation of the electric vehicle heat exchanger, surface treatment cannot fundamentally solve the frosting problem, and we still need to rely on the defrosting equipment and system, but surface treatment has a positive effect in extending the defrosting cycle and reducing defrosting energy consumption, as shown in Table 2.

In order to reduce the energy consumption, the air conditioning system works at the optimal working condition and achieves the economic performance index; the machine learns and makes calculations based on the input command and operation status and adjusts the action of relevant actuators, especially the speed of electric compressor, in time. To achieve the aforementioned control objectives, the air conditioning controller needs to collect information on the operating status of the air conditioning system and the environment, including the temperature inside and outside the vehicle, sunlight intensity, cooling water temperature, and compressor speed, and then output the corresponding control signals through the microprocessor to adjust the corresponding actuators to meet the requirements of the occupants. Based on the aforementioned conditions, unnecessary calculations are reduced.

4.2 Electric vehicle heat pump defrost technology

The common defrosting methods of heat pump systems include manual defrosting, water flushing, compressed air defrosting,

TABLE 3 Four defrost modes and performance parameters.

Defrost modes	Defrost time/min	Compressor energy consumption/kJ	Advantages and disadvantages
High-pressure hot gas	2.1	86.79	Short time, high energy consumption, and high comfort level
Reverse cycle	3.1	140.61	Large temperature fluctuations in the car and low comfort
Low-pressure hot gas-S	11.9	457.68	Long time and high energy consumption
Low-pressure hot gas-M	12.6	505.86	

electric defrosting, and hot air defrosting. For electric vehicles, hot air defrosts is valued because it does not require auxiliary equipment and has high energy efficiency. The following is the main introduction of hot air defrost technology; there are two forms of hot air defrost: the hot air bypass method and reverse cycle method:

1) The hot gas bypass method refers to the direct introduction of high-pressure high-temperature exhaust from the compressor into the heat exchanger to melt the frost, which has the advantages of short bypass piping, low resistance, and small temperature fluctuations inside the vehicle during defrosting (Xi et al., 2021). The defrosting time and energy consumption of the four defrosting modes are shown in Table 3. Among them, the thawing performance of the high-pressure hot gas bypass is the most satisfactory.

Hu et al. (2014) systematically studied the hot gas bypass method and obtained the optimal opening of the bypass valve and the optimal defrost cycle for the studied heat pump system. The optimal defrost cycle is based on the basic complete defrost, while the residual frost at the edges where the heat exchange is small can be neglected. In addition, Wang et al. (2018) introduced the method of refrigerant subcooling defrosting, which is similar to the hot gas bypass method and uses the refrigerant liquid just coming out from the condenser to the evaporator for defrosting; the characteristics of this method are similar to those of the hot gas bypass method, which does not affect the heating, but requires a long operation time and is suitable for defrosting out the frost in the case of microfrost to prevent further frost generation. The condenser has the following advantages over conventional hot air corps: First, it has low system operating costs. Condensing temperatures within 8.3°C of the wet bulb design temperature are very practical and economical, with the result that compressor power saves at least 10% of the power consumption of other cooling tower/condenser systems and saves 30% of the power consumed by the fan, which is comparable to the power consumed by the fan of a cooling tower/condenser system and is approximately 1/3 of the power of an air-cooled condenser fan of the same size. Second, the condenser requires only approximately 50% of the windward area of the same size.

2) Circular method

The advantage of reverse cycle defrosting is fast defrosting and low energy consumption, but the disadvantage is that the heating stops when defrosting, which has a greater impact on the vehicle temperature. Minglu et al (2020) pointed out the mechanism by which reverse cycle reduces the circulation efficiency of the system. In the work of Wang et al. (2021b), a reverse cycle defrost system with CO2 as the working fluid was investigated, the parameters in the defrost process were optimized, and a reverse cycle defrost model with CO2 working fluid was established, and the optimal time point and duration of defrost were studied on this basis. Zhou Guanghui et al. proposed a combined reverse cycle defrost-based defrost technology, the core of which is to enhance the temperature and enthalpy of airflow during defrosting, to achieve rapid defrosting by controlling the external air speed, controlling the compressor speed, and enhancing the interior temperature, and to reduce the impact on the interior temperature during reverse cycle defrosting. Li et al. (2022) built a platform for frost defrosting the heat exchanger outside the real vehicle and concluded that the degree of heat exchanger frosting can be indirectly characterized by the change of suction temperature or suction pressure relative to the frost-free state, and the large-diameter electronic expansion valve combined with intelligent control can achieve effective defrosting. The continuous frosting–defrosting experiment was studied by frost time recording and real-time shooting of the frost layer, and the results showed that after continuous operation of frosting for 150 min, the heating capacity decreased by 22.6% and 15.6% respectively, and the second frosting time was only 28.5% of the first frosting time, and the reverse cycle defrosting effect was obvious.

4.3 Electric vehicle heat pump defrost system control

In the defrost system control, the timing control method only needs to confirm the defrost cycle and defrost duration based on experience or experiment, but this defrost method is more suitable for areas with relatively high ambient humidity, while in areas with low ambient humidity, there will be no frost and defrost phenomenon. When the timing module in the air conditioner controller detects that the heat pump air conditioning system is running continuously for a certain value, the heat pump air conditioning system automatically enters defrost mode, which outputs the speed of the compressor and the time for the defrost function to run. In the actual experimental process, the control strategy is verified, when the ambient humidity is above 50%, the air conditioning system continuous heating for a certain period of time, the outdoor heat exchanger will appear frost phenomenon, and the control strategy can complete the defrost function. However, when the ambient humidity is lower than 50%, the heat pump air conditioning system does not have frost in the continuous heating for a certain period of time, but the control strategy will still perform defrosting action, so there will be an unnecessary defrosting process, thus increasing the energy consumption.

The time–temperature control method is a common method in which the air conditioning system defrosts for a certain period of time when the ambient temperature and ambient humidity are relatively high (Liang et al., 2019). When the air conditioning controller detects that the ambient temperature reaches the ambient temperature value set in the defrost control strategy, the CCM will control the air conditioning system to automatically enter the defrost function and then control the corresponding components to complete the corresponding action, i.e., output the speed of the electric compressor and the time for which the defrost function runs. In the actual experimental process, when the ambient temperature reaches below 3°C and the ambient humidity is above 50%, the outdoor heat exchanger will frost for a certain period of time when the air conditioning system is heating continuously, and the control strategy can achieve the defrost function. However, when the ambient temperature is higher than 3°C and the ambient humidity is lower than 50%, the outdoor heat exchanger will be frosted when the air conditioning system heats up continuously for a certain period of time, and at this time, the air conditioning controller will not defrost by judging that the ambient temperature has not reached the condition, so there will be no defrosting action when defrosting is needed.

The air and heat exchanger surface temperature difference control method uses the difference between the heat exchanger outlet temperature and the ambient temperature for defrost control (Nilpueng et al., 2019; Su et al., 2021; Yi, 2021). It can be said that assuming that the ambient temperature remains unchanged and the heat exchanger surface does not reach the condition of frost, the heat exchanger surface temperature is basically unchanged at this time, so the difference with the ambient temperature is unchanged, but when the heat exchanger surface reaches the condition of frost, that is, when it starts to frost, the difference between the two will show significant changes (Juárez et al., 2021; Singh and y Sora, 2021). So, you only need to determine the appropriate temperature difference value; it is good to determine whether the outdoor heat exchanger surface has been frosted and a certain defrost time can be, but the defrost method is only suitable for specific situations because different systems need to determine other temperature difference values and different defrost time, and the heat pump air conditioning system is more sensitive to changes in load, such as changes in ambient temperature will cause excess defrost action. When the air conditioner controller detects the ambient temperature and the heat exchanger surface temperature and determines that the difference between the two changes, the air conditioner controller will control the heat pump air conditioning system to automatically enter the defrost function and output the corresponding electric compressor speed and defrost function running time. In the actual experimental verification process, because the ambient temperature will be affected by the speed of the vehicle and other factors, when using this control strategy at this time, due to changes in ambient temperature, there will be defrost action when the defrost should be carried out, or when there is no need to carry out defrost, there is a redundant defrost action (Mohammed et al., 2022).

5 Outlook

In a comprehensive view, researchers in various countries have explored a lot in compressor control strategy optimization and heat pump defrost technology, but the combination with emerging technologies such as machine learning is not close enough. As the application of new energy technology, some basic work and key technologies of heat pump air conditioning for electric vehicles still need to be broken through.

1) Development of heat pump air conditioners toward environmental protection, full-scene energy saving, and extreme environmental applicability: Research and development of new alternative masses, high-efficiency heat pump air conditioning systems and their components, such as supercritical CO2 heat pump air conditioners, new high-efficiency make-up gas compressors, and high-efficiency microchannel heat exchangers should be carried out to solve the problems of high energy consumption and insufficient capacity for heat production. Research and development of new heat pump air conditioners for extreme environments (extreme cold, extreme heat, high humidity, and high salt) and other areas should be carried out to improve the applicability of the whole vehicle.
2) The heat pump system has great potential and advantages in solving the heat and cold management of the passenger compartment, and further research on the enthalpy charge technology, new defrosting method, multiple heat sources for heating at low temperature, and new alternative refrigerants can allow the heat pump system to be applied and promoted in a low-temperature environment.
3) In the optimization of the compressor control strategy, the existing algorithm can be further improved to accelerate the global convergence rate by combining techniques such as small habitats under machine learning models (classifying individuals of each generation and selecting individuals with high fitness from the classification to form a population and re-hybridize).
4) Most of the studies on the defrosting of EV heat pumps only consider that the frosting of the heat exchanger affects its effective area for heat exchange. At present, further research is needed on the actual frost area of the heat exchanger and the extent of the effect of heat exchange.
5) Based on machine learning models, the heat pump air conditioner monitors and adaptively adjusts ambient temperature and humidity, indoor temperature and humidity, air outlet temperature, battery temperature, water temperature, mass temperature and pressure, indoor CO2 concentration, and PM2.5 to further enhance the system's adaptability.

6 Conclusion

Good progress has been made in the research of the heat pump air conditioning control system for electric vehicles in the context of machine learning. Although the heat pump air conditioning system has many advantages and is one of the ideal solutions for electric vehicle air conditioning systems, the system also has defects such as low heating efficiency under low-temperature conditions, slow heating speed, and frosting of the heat exchanger outside the vehicle. In this paper, the advantages and disadvantages of various new energy vehicle heat pump systems are first described separately, and the system performance under different heat pumps is compared and analyzed. Second, in terms of electric vehicle design, the focus of attention is elaborated on the system cooling and heating under the charge volume, compressor oil return, winter frosting, and different electronic expansion valve control. In the future, a commercial CO2 vehicle heat pump air conditioning system can be used to make the performance of the new energy vehicle heat pump system more superior, thus solving the problem of electric vehicle range.

Author contributions

ZM carried out all the work on the article independently.

Conflict of interest

The author declares that the research was conducted in the absence of any commercial or financial relationships that could be construed as a potential conflict of interest.

Publisher's note

References

Adrian, Ł., Szufa, S., Piersa, P., Kuryło, P., Mikołajczyk, F., Kurowski, K., et al. (2021). Analysis and evaluation of heat pipe efficiency to reduce low emission with the use of working agents R134A, R404A and R407C, R410A. *Energies* 14 (7), 1926. doi:10.3390/en14071926

Agarwal, P., Rakshit, M., and Chand, M. (2020). Fractional calculus involving (p, q)-mathieu type series. *Appl. Math. Nonlinear Sci.* 5 (2), 15–34. doi:10.2478/amns.2020.2.00011

Ahn, J. H., Lee, J. S., Baek, C., and Kim, Y. (2016). Performance improvement of a dehumidifying heat pump using an additional waste heat source in electric vehicles with low occupancy. *Energy* 115, 67–75. doi:10.1016/j.energy.2016.08.104

Alashkar, T., Jiang, S., Wang, S., and Fu, Y. (2017). "Examples-rules guided deep neural network for makeup recommendation," in Thirty-First AAAI Conference on Artificial Intelligence (AAAI-17), San Francisco, California, USA, February 2017. doi:10.1609/aaai.v31i1.10626

Altinkaynak, M., Olgun, E., and Şahi̇n, A. Ş. (2019). Comparative evaluation of energy and exergy performances of R22 and its alternative R407C, R410A and R448A refrigerants in vapor compression refrigeration systems. *El-Cezeri* 6 (3), 659–667.

Athey, S. (2018). "The impact of machine learning on economics," in *The economics of artificial intelligence: An agenda* (University of Chicago Press), 507–547.

Bentrcia, M., Alshitawi, M., and Omar, H. (2018). Developmens of alternative systems for automotive air conditioning-A review. *J. Mech. Sci. Technol.* 32 (4), 1857–1867. doi:10.1007/s12206-018-0342-2

Bi, Q., Goodman, K. E., Kaminsky, J., and Lessler, J. (2019). What is machine learning? A primer for the epidemiologist. *Am. J. Epidemiol.* 188 (12), 2222–2239. doi:10.1093/aje/kwz189

Chunyue, P. A. N. (2017). "Air compressor pressure control system based on gearshift integral PID controller," in MATEC Web of Conferences (EDP Sciences), 00199.

Durur, H., and Yokuş, A. (2021). Exact solutions of (2 + 1)-Ablowitz-Kaup-Newell-Segur equation. *Appl. Math. Nonlinear Sci.* 6 (2), 381–386. doi:10.2478/amns.2020.2.00074

Gillet, T., Andres, E., El-Bakkali, A., Lemort, V., Rulliere, R., and Haberschill, P. (2018). Sleeping evaporator and refrigerant maldistribution: An experimental investigation in an automotive multi-evaporator air-conditioning and battery cooling system. *Int. J. Refrig.* 90, 119–131. doi:10.1016/j.ijrefrig.2018.04.004

Han, Z., Guo, J., Zhang, H., Chen, J., Huai, X., and Cui, X. (2021). Experimental and numerical studies on novel airfoil fins heat exchanger in flue gas heat recovery system. *Appl. Therm. Eng.* 192, 116939. doi:10.1016/j.applthermaleng.2021.116939

Hu, B., Wang, X., Cao, F., He, Z., and Xing, Z. (2014). Experimental analysis of an air-source transcritical CO2 heat pump water heater using the hot gas bypass defrosting method. *Appl. Therm. Eng.* 71 (1), 528–535. doi:10.1016/j.applthermaleng.2014.07.017

Hu, Y., Yuill, D. P., and Ebrahimifakhar, A. (2020). The effects of outdoor air-side fouling on frost growth and heat transfer characteristics of a microchannel heat exchanger: An experimental study. *Int. J. heat mass Transf.* 151, 119423. doi:10.1016/j.ijheatmasstransfer.2020.119423

Juárez, F. F., Esenarro, D., Díaz, M., and y Frayssinet, M. (2021). Model based on balanced scorecard applied to the strategic plan of a peruvian public entity. *Investig. Pensam. crítico* 10 (4), 127–147. doi:10.17993/3cemp.2021.100448.127-147

Junqi, D., Yibiao, W., Shiwei, J., Xianhui, Z., and Linjie, H. (2021). Experimental study of R744 heat pump system for electric vehicle application. *Appl. Therm. Eng.* 183, 116191. doi:10.1016/j.applthermaleng.2020.116191

Kalinichenko, A., Havrysh, V., and Hruban, V. (2018). Heat recovery systems for agricultural vehicles: Utilization ways and their efficiency. *Agriculture* 8 (12), 199. doi:10.3390/agriculture8120199

Karnik, A. Y., Fuxman, A., Bonkoski, P., Jankovic, M., and Pekar, J. (2016). Vehicle powertrain thermal management system using model predictive control. *SAE Int. J. Mater. Manuf.* 9 (3), 525–533. doi:10.4271/2016-01-0215

Lee, H., Lee, D., and Kim, Y. (2022). Heating performance of a coolant-source heat pump using waste heat from stack and electric devices in fuel cell electric vehicles under cold conditions. *Energy Convers. Manag.* 252, 115092. doi:10.1016/j.enconman.2021.115092

Lee, J. S., Kim, M. S., and Kim, M. S. (2014). Studies on the performance of a CO2 air conditioning system using an ejector as an expansion device. *Int. J. Refrig.* 38, 140–152. doi:10.1016/j.ijrefrig.2013.08.019

Li, K., Xia, D., Luo, S., Zhao, Y., Tu, R., Zhou, X., et al. (2022). An experimental investigation on the frosting and defrosting process of an outdoor heat exchanger in an air conditioning heat pump system for electric vehicles. *Appl. Therm. Eng.* 201, 117766. doi:10.1016/j.applthermaleng.2021.117766

Li, Z., Khajepour, A., and Song, J. (2019). A comprehensive review of the key technologies for pure electric vehicles. *Energy* 182, 824–839. doi:10.1016/j.energy.2019.06.077

Liang, L., Guo, L., Wang, Y., and Li, X. (2019). Towards an intelligent FE simulation for real-time temperature-controlled radial-axial ring rolling process. *J. Manuf. Process.* 48, 1–11. doi:10.1016/j.jmapro.2019.09.032

Liu, Y., Wang, X., Meng, X., and Wang, D. (2019). A review on tube external heat transfer for passive residual heat removal heat exchanger in nuclear power plant. *Appl. Therm. Eng.* 149, 1476–1491. doi:10.1016/j.applthermaleng.2018.11.114

Lucchese, L. V., de Oliveira, G. G., and Pedrollo, O. C. (2021). Mamdani fuzzy inference systems and artificial neural networks for landslide susceptibility mapping. *Nat. Hazards* 106 (3), 2381–2405. doi:10.1007/s11069-021-04547-6

Mahvi, A. J., Boyina, K., Musser, A., Elbel, S., and Miljkovic, N. (2021). Superhydrophobic heat exchangers delay frost formation and enhance efficency of electric vehicle heat pumps. *Int. J. Heat Mass Transf.* 172, 121162. doi:10.1016/j.ijheatmasstransfer.2021.121162

Malinowski, L., Lewandowska, M., and Giannetti, F. (2017). Analysis of the secondary circuit of the DEMO fusion power plant using GateCycle. *Fusion Eng. Des.* 124, 1237–1240. doi:10.1016/j.fusengdes.2017.03.026

Marín, L. G., Cruz, N., Sáez, D., Sumner, M., and Núñez, A. (2019). Prediction interval methodology based on fuzzy numbers and its extension to fuzzy systems and neural networks. *Expert Syst. Appl.* 119, 128–141. doi:10.1016/j.eswa.2018.10.043

Meng, Z., Zhang, H., Lei, M., Qin, Y., and Qiu, J. (2018). Performance of low GWP R1234yf/R134a mixture as a replacement for R134a in automotive air conditioning systems. *Int. J. Heat Mass Transf.* 116, 362–370. doi:10.1016/j.ijheatmasstransfer.2017.09.049

Menken, J. C., Strasser, K., Anzenberger, T., and Rebinger, C. (2018). Evaluation of the energy consumption of a thermal management system of a plug-in hybrid electric vehicle using the example of the Audi Q7 e-tron. *SAE Int. J. Passeng. Cars-Mechanical Syst.* 11 (3), 203–212. doi:10.4271/06-11-03-0017

Minglu, Q., Rao, Z., Jianbo, C., Yuanda, C., Xudong, Z., Tongyao, Z., et al. (2020). Experimental analysis of heat coupling during TES based reverse cycle defrosting method for cascade air source heat pumps. *Renew. Energy* 147, 35–42. doi:10.1016/j.renene.2019.08.120

Mohammed, H. R., and Hussain, Z. M. (2021). Hybrid mamdani fuzzy rules and convolutional neural networks for analysis and identification of animal images. *Computation* 9 (3), 35. doi:10.3390/computation9030035

Mohammed, S., Hafizah, H. N., Sahnius, U., Shadab, A., Surbhi, B., Arwa, M., et al. (2022). Self-sovereign identity solution for blockchain-based land registry system: A comparison. *Mob. Inf. Syst.* 2022, 1–17. doi:10.1155/2022/8930472

Nguyen, A. T., Taniguchi, T., Eciolaza, L., Campos, V., Palhares, R., and Sugeno, M. (2019). Fuzzy control systems: Past, present and future. *IEEE Comput. Intell. Mag.* 14 (1), 56–68. doi:10.1109/mci.2018.2881644

Nilpueng, K., Ahn, H. S., Jerng, D. W., and Wongwises, S. (2019). Heat transfer and flow characteristics of sinusoidal wavy plate fin heat sink with and without crosscut flow control. *Int. J. Heat Mass Transf.* 137, 565–572. doi:10.1016/j.ijheatmasstransfer.2019.03.114

Ning, X., Tian, W., He, F., Bai, X., Sun, L., and Li, W. (2023). Hyper-sausage coverage function neuron model and learning algorithm for image classification. *Pattern Recognit.* 136, 109216. doi:10.1016/j.patcog.2022.109216

Pabon, J. J., Khosravi, A., Belman-Flores, J. M., Machado, L., and Revellin, R. (2020). Applications of refrigerant R1234yf in heating, air conditioning and refrigeration systems: A decade of researches. *Int. J. Refrig.* 118, 104–113. doi:10.1016/j.ijrefrig.2020.06.014

Park, M. H., and Kim, S. C. (2017). Heating performance characteristics of high-voltage PTC heater for an electric vehicle. *Energies* 10 (10), 1494. doi:10.3390/en10101494

Park, M. H., and Kim, S. C. (2019). Heating performance enhancement of high capacity PTC heater with modified louver fin for electric vehicles. *Energies* 12 (15), 2900. doi:10.3390/en12152900

Peng, B., Zhang, Y., Zhang, P., and Ullah, H. (2021). Recent advances on the electric vehicle heat pump air conditioning system. *Recent Pat. Mech. Eng.* 14 (3), 354–365. doi:10.2174/2212797614666210125142854

Rajbongshi, R., and Saikia, L. C. (2018). Combined voltage and frequency control of a multi-area multisource system incorporating dish-Stirling solar thermal and HVDC link. *IET Renew. Power Gener.* 12 (3), 323–334. doi:10.1049/iet-rpg.2017.0121

Salleh, M. N. M., Talpur, N., and Hussain, K. (2017). "Adaptive neuro-fuzzy inference system: Overview, strengths, limitations, and solutions," in International conference on data mining and big data (Cham: Springer), 527–535.

Sharif, M. Z., Azmi, W. H., Redhwan, A. A. M., and Mamat, R. (2016). Investigation of thermal conductivity and viscosity of Al2O3/PAG nanolubricant for application in automotive air conditioning system. *Int. J. Refrig.* 70, 93–102. doi:10.1016/j.ijrefrig.2016.06.025

Sharif, M. Z., Azmi, W. H., Redhwan, A. A. M., Mamat, R., and Yusof, T. M. (2017). Performance analysis of SiO2/PAG nanolubricant in automotive air conditioning system. *Int. J. Refrig.* 75, 204–216. doi:10.1016/j.ijrefrig.2017.01.004

Singh, A. D., and Sharif, M. (2019). Bi-Directional storage capacity and elevation level calculator for reservoir operation management. *Am. J. Water Resour.* 7 (3), 121–127.

Singh, A. K., and y Sora, M. (2021). An optimized deep neural network-based financial statement fraud detection in text mining. *Investig. Pensam. crítico* 10 (4), 77–105. doi:10.17993/3cemp.2021.100448.77-105

Su, J., Yuan, S., and Rita, J. N. (2021). Mathematical simulation experiment based on optimisation of heat treatment process of aluminium alloy materials. *Appl. Math. Nonlinear Sci.* 7, 609–616. doi:10.2478/AMNS.2021.1.00083

Wang, A., Cao, F., Fang, J., Jia, F., Yin, X., and Wang, X. (2022). Research on efficient defrosting control logic for transcritical CO2 electric vehicle heat pump air-conditioning system. *Int. J. Refrig.* 138, 13–22. doi:10.1016/j.ijrefrig.2022.03.028

Wang, C., Ning, X., Sun, L., Zhang, L., Li, W., and Bai, X. (2022). Learning discriminative features by covering local geometric space for point cloud analysis. *IEEE Trans. Geoscience Remote Sens.* 60, 1–15. doi:10.1109/TGRS.2022.3170493

Wang, H., Amini, M. R., Hu, Q., Kolmanovsky, I., and Sun, J. (2020). Eco-cooling control strategy for automotive air-conditioning system: Design and experimental validation. *IEEE Trans. Control Syst. Technol.* 29 (6), 2339–2350. doi:10.1109/tcst.2020.3038746

Wang, J., Cao, J., and Yuan, S. (2021). Deep learning reservoir porosity prediction method based on a spatiotemporal convolution bi-directional long short-term memory neural network model. *Geomechanics Energy Environ.* 32, 100282. doi:10.1016/j.gete.2021.100282

Wang, M., Zang, R., Hu, E., and Ezzat, A. W. (2018). Investigation of air cooler fan start-up delay in liquid refrigerant defrosting system. *Appl. Therm. Eng.* 143, 302–307. doi:10.1016/j.applthermaleng.2018.07.066

Wang, Q., Jiang, B., Li, B., and Yan, Y. (2016). A critical review of thermal management models and solutions of lithium-ion batteries for the development of pure electric vehicles. *Renew. Sustain. Energy Rev.* 64, 106–128. doi:10.1016/j.rser.2016.05.033

Wang, Y., Ye, Z., Song, Y., Yin, X., and Cao, F. (2021). Experimental analysis of reverse cycle defrosting and control strategy optimization for transcritical carbon dioxide heat pump water heater. *Appl. Therm. Eng.* 183, 116213. doi:10.1016/j.applthermaleng.2020.116213

Xi, Z., Yao, R., Li, J., Du, C., Yu, Z., and Li, B. (2021). Experimental studies on hot gas bypass defrosting control strategies for air source heat pumps. *J. Build. Eng.* 43, 103165. doi:10.1016/j.jobe.2021.103165

Xie, Y., Yang, P., Qian, Y., Zhang, Y., Li, K., and Zhou, Y. (2022). A two-layered eco-cooling control strategy for electric car air conditioning systems with integration of dynamic programming and fuzzy PID. *Appl. Therm. Eng.* 211, 118488. doi:10.1016/j.applthermaleng.2022.118488

Yadav, S., Liu, J., and Kim, S. C. (2022). A comprehensive study on 21st-century refrigerants-r290 and R1234yf: A review. *Int. J. Heat Mass Transf.* 182, 121947. doi:10.1016/j.ijheatmasstransfer.2021.121947

Yang, M., Zhang, H., Meng, Z., and Qin, Y. (2019). Experimental study on R1234yf/R134a mixture (R513A) as R134a replacement in a domestic refrigerator. *Appl. Therm. Eng.* 146, 540–547. doi:10.1016/j.applthermaleng.2018.09.122

Yi, Q. (2021). Radar system simulation and non-Gaussian mathematical model under virtual reality technology. *Appl. Math. Nonlinear Sci.* 7, 573–580. doi:10.2478/AMNS.2021.1.00079

Yordanova, S., Merazchiev, D., and Jain, L. (2014). A two-variable fuzzy control design with application to an air-conditioning system. *IEEE Trans. fuzzy Syst.* 23 (2), 474–481. doi:10.1109/tfuzz.2014.2312979

Yucel, E., Ali, M. S., Gunasekaran, N., and Arik, S. (2017). Sampled-data filtering of Takagi–Sugeno fuzzy neural networks with interval time-varying delays. *Fuzzy sets Syst.* 316, 69–81. doi:10.1016/j.fss.2016.04.014

Zhang, S., Jiang, H., Yin, Y., Xiao, W., and Zhao, B. (2018). The prediction of the gas utilization ratio based on TS fuzzy neural network and particle swarm optimization. *Sensors* 18 (2), 625. doi:10.3390/s18020625

Zhang, Z., Wang, D., Zhang, C., and Chen, J. (2018). Electric vehicle range extension strategies based on improved AC system in cold climate–A review. *Int. J. Refrig.* 88, 141–150. doi:10.1016/j.ijrefrig.2017.12.018

Zheng, K., Zhang, Q., Hu, Y., and Wu, B. (2021). Design of fuzzy system-fuzzy neural network-backstepping control for complex robot system. *Inf. Sci.* 546, 1230–1255. doi:10.1016/j.ins.2020.08.110

Zheng, S., Wei, M., Song, P., Hu, C., and Tian, R. (2020). Thermodynamics and flow unsteadiness analysis of trans-critical CO2 in a scroll compressor for mobile heat pump air-conditioning system. *Appl. Therm. Eng.* 175, 115368. doi:10.1016/j.applthermaleng.2020.115368

Zhou, G., Li, H., Liu, E., Li, B., Yan, Y., Chen, T., et al. (2017). Experimental study on combined defrosting performance of heat pump air conditioning system for pure electric vehicle in low temperature. *Appl. Therm. Eng.* 116, 677–684. doi:10.1016/j.applthermaleng.2017.01.088

Zhou, J., Zeng, C., Wang, Z., Lyu, W., Tang, Y., Wu, D., et al. (2022). Indirect expansion solar assisted heat pump system: A review. *Sustain. Energy Technol. Assessments* 53, 102409. doi:10.1016/j.seta.2022.102409

frontiers | Frontiers in Energy Research

TYPE Original Research
PUBLISHED 03 April 2023
DOI 10.3389/fenrg.2023.1170138

Multi-interval settlement system of rolling-horizon scheduling for electricity spot market

Qian Feng[1], Xu Dong[2] and Wang Jinghua[3]*

[1]State Grid Shanghai Electric Power Company, Shanghai, China, [2]State Grid Shanghai PuDong Electric Power Company, Shanghai, China, [3]Shanghai Jiao Tong University, Shanghai, China

OPEN ACCESS

EDITED BY
Praveen Kumar Donta,
Vienna University of Technology, Austria

REVIEWED BY
Banoth Ravi,
Indian Institute of Information Technology Tiruchirappalli, India
Luyang Hou,
Beijing University of Posts and Telecommunications (BUPT), China
Gabriel Gomes,
State University of Campinas, Brazil
Achyut Shankar,
University of Warwick, United Kingdom

*CORRESPONDENCE
Wang Jinghua,
✉ jane950110@sjtu.edu.cn

SPECIALTY SECTION
This article was submitted to Smart Grids, a section of the journal Frontiers in Energy Research

RECEIVED 20 February 2023
ACCEPTED 14 March 2023
PUBLISHED 03 April 2023

CITATION
Feng Q, Dong X and Jinghua W (2023), Multi-interval settlement system of rolling-horizon scheduling for electricity spot market.
Front. Energy Res. 11:1170138.
doi: 10.3389/fenrg.2023.1170138

Multi-interval settlement is conducive to meeting the needs of growing renewable energy resources with great intermittency and volatility and managing the effective operation in the electricity spot market. However, the insufficient incentive of market price inaccurately reflecting the total cost of the electricity spot market caused by the inaccuracy of generation and load prediction in the current multi-interval settlement will lead to inefficient market scheduling, causing the market participants to deviate from dispatch instructions. Based on the problem above, a new multi-interval settlement system of rolling-horizon scheduling including the period selection of look-ahead schedules and enhanced settlement mechanism is proposed to improve the price incentive for the electricity spot market. The proposed multi-interval settlement system can produce a better look-ahead period and a more economically efficient dispatch solution inducing dispatch-following incentives. A numerical example shows that the proposed multi-interval settlement system outperforms the traditional settlement mechanism regarding economic efficiency.

KEYWORDS

multi-interval settlement, rolling-horizon scheduling, period selection, electricity spot market, settlement priority

1 Introduction

1.1 Background and motivation

According to the plan vision of carbon peak and carbon neutrality, Chinese renewable energy will enter a new stage of high-quality leapfrog development, and a high proportion of renewable energy grid connection will become the basic new feature of the power system in the future. In order to adapt to the development of renewable energy, the demand for power system flexibility has increased significantly, the role of cross-time constraints of spot market optimization has been significantly strengthened, and the coupling between optimization periods has become closer. How to design a real-time prospective and optimized settlement mechanism with universal practicality for the spot market of electricity to meet the construction and development needs of the electricity market adapting to the characteristics of the new power system is a practical problem that needs to be solved urgently in the construction of Chinese electricity market. On the basis of the current operation mechanism, this paper improves and designs a set of new real-time prospective optimization settlement mechanism for the spot market of electricity, which can provide reference for the construction of the spot market of electricity in China.

1.2 Literature survey

According to the plan vision of "30 carbon peak, 60 carbon neutral," Chinese renewable energy will enter a new stage of high-quality leapfrog development, and a high proportion of renewable energy grid connection will become the basic new feature of the power system in the future (Jiang et al., 2020; Chen et al., 2021). In order to adapt to the development of renewable energy, the demand for flexibility of the power system has increased significantly, and the role of cross-time constraints in the optimization of the spot market has been significantly strengthened, and the coupling between the optimization periods has become closer (CAISO, 2014; Massachusetts gov, 2016). Therefore, in order to better adapt to the characteristics of flexible resources operating across time periods, the mature spot power markets at home and abroad have adopted the look-ahead optimization method (CAISO, 2019; NYISO, 2020).

Compared with single-period optimization, look-ahead optimization can more effectively improve the success rate of solving the mathematical model by expanding the time range, reduce inefficient scheduling by pre-regulating resources (Xie and Ilic, 2009), avoid peak electricity prices due to insufficient power supply capacity, and give the clearing price cross-period economic significance (Ela and O'Malley, 2016).

However, there is still a problem of insufficient price incentives in forward-looking optimization. In typical practice, look-ahead optimization is based on short-term load forecasting to optimize the scheduling of resources in future multi-periods, but only the optimization results of the current period are settled (single settlement mechanism) (Bakirtzis et al., 2014; CAISO, 2019; NYISO, 2020). When the current outlook optimization is applied to the real-time market rolling clearing scenario, the supporting single settlement mechanism will regard the historical clearing results as "sunk costs," directly ignoring the components that affect the current or future optimization results, and implicitly "burying" the economic value of cross-time constraints. Even if the day-ahead market has made a perfect load forecast, the forward order settlement mechanism will still lead to the lack of market price incentives, and the power generation companies cannot recover costs through the market price, but choose to deviate from the dispatching order (Wilson, 2002). Literature (Peng et al., 2013) pointed out the motivation of market members to deviate from scheduling in look-ahead optimization, but only gave qualitative solutions.

The academic solutions can be divided into two categories: one is to improve the mathematical optimization model, and introduce the time series correlation quantity of historical real-time optimization into the model (Schiro, 2017; Zhou et al., 2017). However, how to select the appropriate time series correlation quantity has become the problem faced by this method. Selecting the inappropriate correlation quantity may cause new incentive problems. There is no definite result of this research idea at present. The second is to increase the number of settlement rounds, bridge the gap between the clearing results before and after the settlement rounds, eliminate the motivation of market users to speculate, reduce compensation costs, and improve the incentive of market participants to follow the schedule. This article adopts the second train of thought. Based on this idea, the literature (Yao et al., 2020) proposed a real-time multi-settlement mechanism based on look-ahead optimization. The prices of all periods in the optimization cycle need to be settled. This settlement method alleviates the problem of market incentives, but will increase the complexity of settlement. Therefore, it is necessary to redesign the look-ahead and optimized settlement mechanism to alleviate the problem of insufficient settlement price. The overviews of the literature survey can be seen in Figure 1.

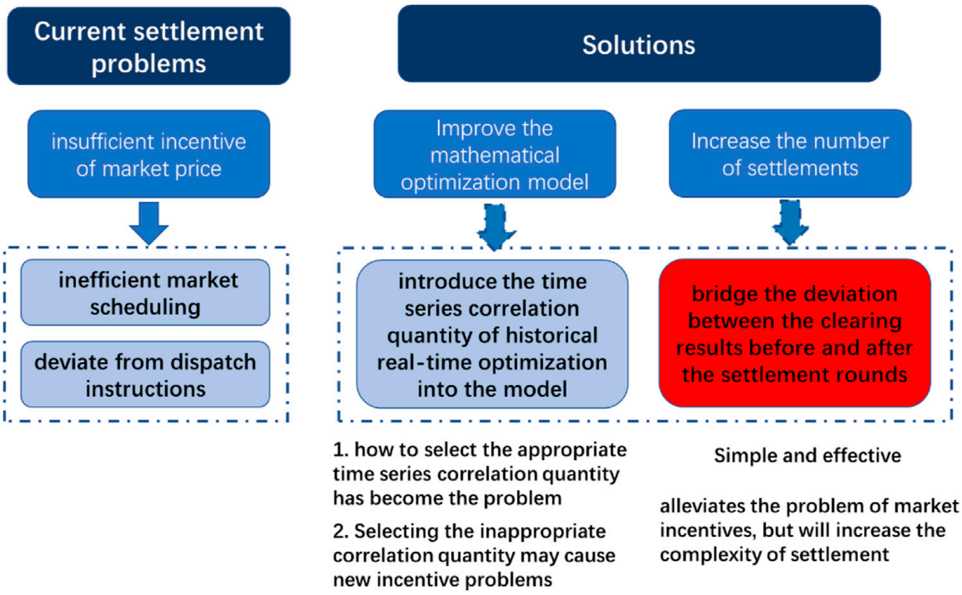

FIGURE 1
Overview of the survey.

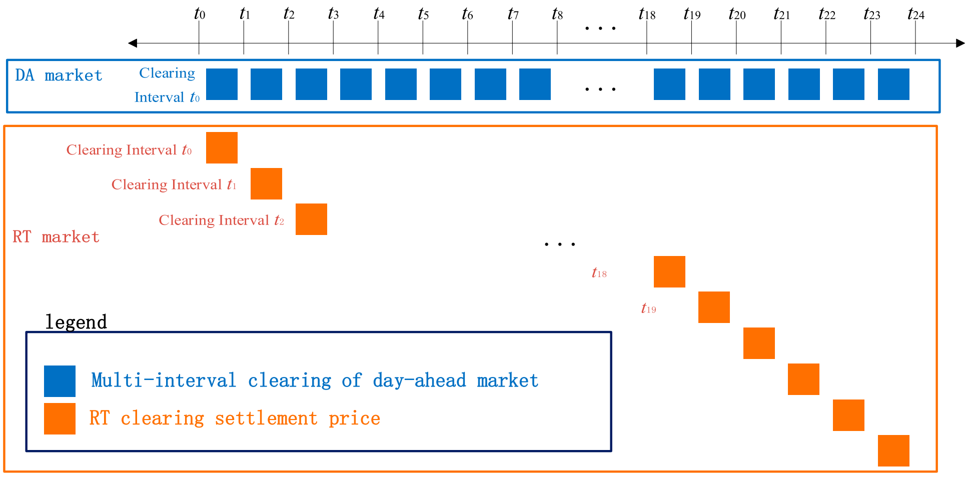

FIGURE 2
Single-interval settlement.

The fairness and rationality of the electricity spot market settlement mechanism plays an important role in the sound operation of the entire power system and the optimal allocation of power market resources (Huang et al., 2019). Due to the particularity of electricity commodities, electricity trading needs to establish a centralized electricity spot market, and support the corresponding deviation electricity settlement mechanism. At present, most mature electricity spot markets adopt a double settlement mechanism.

On the basis of the current double settlement mechanism in the spot electricity market, this paper focuses on the analysis of the factors that affect the prospective optimization incentive, and selects a quantifiable priority standard for this purpose, and innovatively designs a new real-time prospective optimization settlement mechanism in the spot electricity market. This mechanism can effectively improve the incentive of the settlement price, and will not cause excessive settlement burden, It can better meet the demand of real-time prospective optimization of power in the new era.

2 Prior work

Unlike ordinary commodities, electric power commodities have obvious particularity: 1) Physical electric power commodities are almost conducted at the same time in the four links of power generation, transmission, distribution and utilization. The electricity market transactions need to be consistent with the actual operation of the power system as much as possible, and the execution of the electricity trading contract needs to simulate the real-time balance scenario of the power generation and consumption of the power system as much as possible; 2) With the access of centralized and distributed renewable energy to the grid, there will inevitably be prediction errors on both sides of the power system's power generation and consumption, which will cause the actual power generation and consumption curve to deviate from the market transaction curve, which is inconsistent with the real-time balance of the power system, and the market subject is required to bear the costs of real-time power balance according to the transaction agreement; 3) There is a strong homogeneity of power commodities, and the power commodities delivered by each market transaction cannot be measured separately. It is necessary to formulate unified measurement and settlement rules to deal with the deviation between the actual electricity generated and the electricity traded in the market, so as to realize the decoupling of the power transaction contract and the actual electricity consumption at the level of settlement time sequence, so that the two can be settled separately (Xiao et al., 2021). Therefore, it is necessary to establish a centralized electricity spot market and set up a corresponding offset electricity settlement mechanism.

Most of the world's centralized electricity spot markets use the double settlement system to settle between the day-ahead market and the real-time market. Some scholars also call it multi-settlement systems. In the field of electric power, the double settlement mechanism refers to the power transaction settlement mechanism that divides the power transaction settlement into pre-settlement and post-settlement according to the contract behavior and default deviation behavior. Among them, prior settlement refers to the prior settlement of the signed contract according to the contract agreement before the physical delivery of electric power to ensure the full implementation of the electric power contract; After the physical delivery of electricity, the settlement refers to the settlement according to the agreed deviation price according to whether there is any deviation between the behavior of the market subject and the agreement and the extent of the deviation, and the negative incentive for breach of contract is given economically. The double-settlement mechanism in the spot electricity market means that the day-ahead market is based on the day-ahead price to settle the bid-winning electricity quantity in the day-ahead market, while the real-time market is based on the real-time price to settle the deviation between the real-time bid-winning electricity quantity and the day-ahead bid-winning electricity quantity.

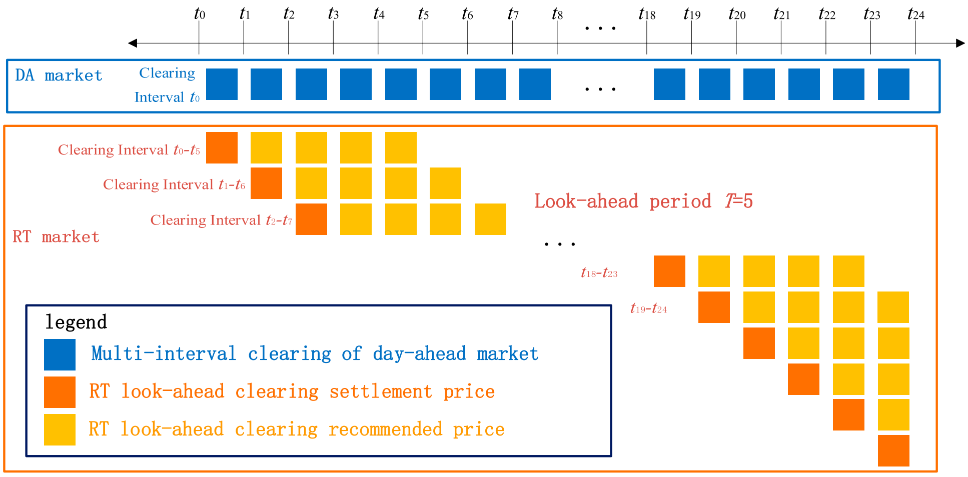

FIGURE 3
Look-ahead single-interval settlement.

The spot market of PJM and ERCOT in the United States adopts the double settlement system to realize the settlement of the day-ahead market and the real-time market. The real-time price of PJM is calculated every 5 min, but the weighted average price within 1 h of each node is taken as the settlement price of the real-time market; The time granularity of ERCOT's day-ahead market clearing is 1 h, while that of real-time market is 5 min. The real-time market is settled according to the weighted average price within 15 min, and the settlement price does not include the network loss component.

The centralized power real-time market model can be divided into single-period optimization model and look-ahead optimization model according to the optimization cycle, and the corresponding real-time settlement mechanism can be divided into real-time single settlement and real-time multi-settlement.

2.1 The myopic approach

This optimization model does not take into account the future predicted power grid operation, and only optimizes the current period in each round when the real-time market rolls out. Each round of clearing only generates the market price and clearing electricity quantity of the current period, and the market will use the price and electricity quantity as the basis for single period settlement.

Real-time single settlement mechanism is a real-time single settlement mechanism connected with single-period optimization. It is applicable to single-period optimization. The operation mode is shown in Figure 2.

The mathematical model corresponding to single-period optimization has a small solution scale, is easy to search for optimization in a short time, and is easy to meet the calculation

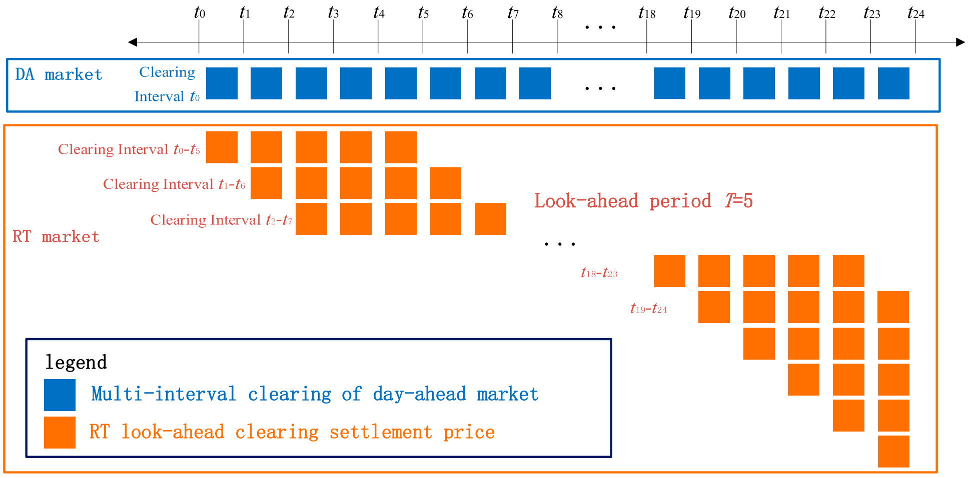

FIGURE 4
Look-ahead multi-interval settlement.

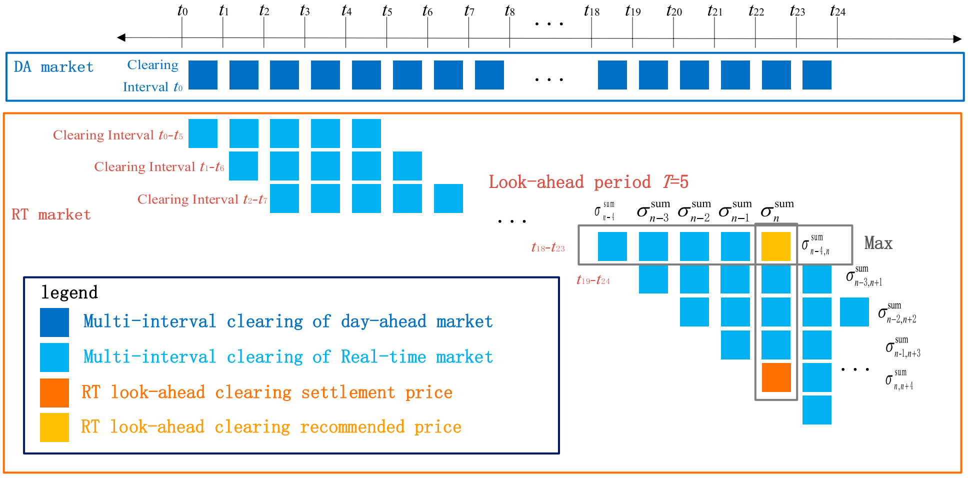

FIGURE 5
New settlement mechanism.

speed requirements of the real-time market; In addition, real-time single settlement is relatively simple and intuitive, easy for market participants to understand, and the workload of settlement is also less. Therefore, the single-period price model has been adopted by many market operators in the United States, such as ISO New England, MISO, PJM and SPP. However, the single-period optimization model has obvious defects in the economy and reliability of market clearing. In terms of economy, compared with multi-period optimization, if the current single period is successfully cleared, because it only considers the load situation of the current period for optimization, and ignores the economic value of the cross-period constraints before and after, the result is not necessarily the global optimal solution, but only the sub-optimal solution, and there is still large optimization space in general; In terms of reliability, if the clearing of the current period fails, the market members will not be able to actively respond to the regulation instructions because they cannot obtain real-time market information, and the system stability will be affected. The market operating agencies may need to take measures outside the market to regulate resources.

2.2 The multi-period approach

The look-ahead optimization model takes into account the forecast situation of the future power grid. When the real-time market is rolling out, each round will carry out look-ahead optimization for the current and future periods, and obtain the market price and clearing electricity of all periods in the look-ahead period.

2.2.1 Single-period settlement

Look-ahead single settlement mechanism is a real-time single settlement mechanism connected with look-ahead optimization. It is applicable to forward-looking optimization. See Figure 3 for its operation mode.

Under normal circumstances, only the price and energy of the current period have the basis for settlement; The market information in the other look-ahead periods is only instructive, which can provide the basis for market members to make future decisions, and can also be used as the "backup" basis for the settlement of subsequent clearing rounds. When the clearing fails in the current period, the market cannot form the current settlement scheme. The "standby" basis of the previous round of settlement corresponding to the current period can be used to ensure the reliability of settlement. Therefore, the power market operators in New York (NYISO) and California (CAISO) have adopted the look-ahead single settlement mechanism. However, the current look-ahead optimization still has some defects, because the look-ahead order settlement mechanism needs to introduce real-time look-ahead optimization, and taking the clearing result as the basis for settlement may lead to inefficient scheduling, insufficient system compensation, incentive incompatibility and increased price volatility.

2.2.2 Multi-period settlement

Look-ahead multi-settlement mechanism is also a real-time multi-settlement mechanism connected with look-ahead optimization. It is also applicable to forward-looking optimization. See Figure 4 for its operation mode.

Similar to the nature of the look-ahead single settlement mechanism, the look-ahead multiple settlement mechanism also needs to carry out real-time rolling look-ahead optimization to obtain the clearing information of all periods in the look-ahead period. However, the look-ahead multi-settlement mechanism will take the clearing information of the whole period as the settlement basis, without distinguishing between the current period or the look-ahead period.

Due to the increase of settlement frequency, look-ahead multi-settlement can better adapt to the problem of increased real-time volatility of the power system, promote the price response of flexible resources, and to some extent alleviate the problems of insufficient compensation and incentive incompatibility caused by forward-

TABLE 1 **Technical parameters and cost quotation.**

unit	Minimum output/MW	Maximum output/MW	Ramping rate/MW	Cost quotation/$
1	0	800	80	10
2	0	500	75	50
3	0	500	200	100

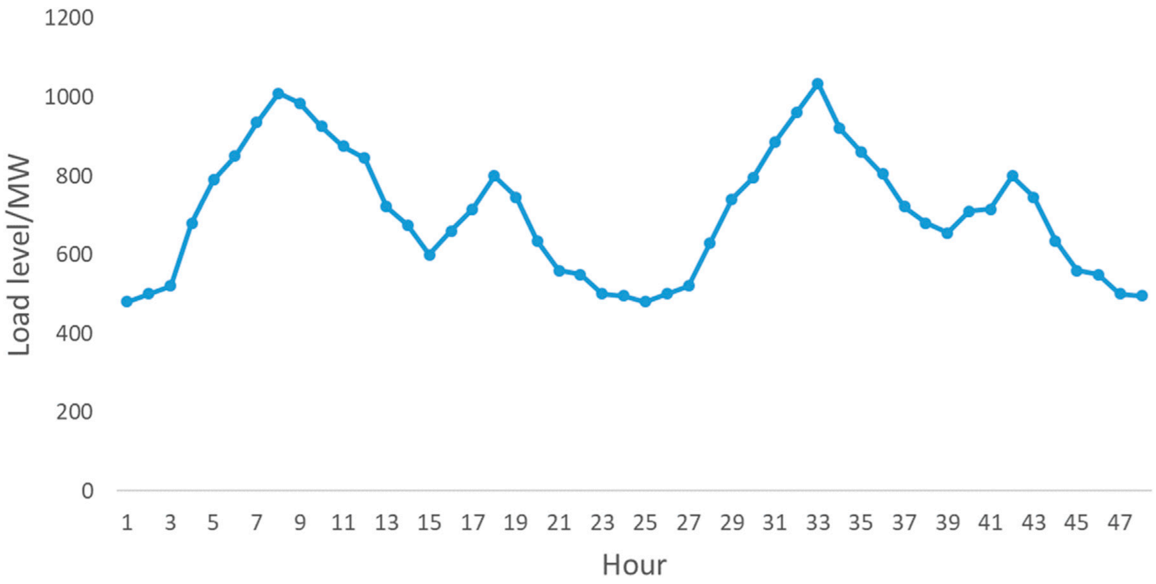

FIGURE 6
Load parameters.

looking optimization. Compared with the forward single settlement mechanism, forward multiple settlement relies more on the reliability of market solution. Once the market clearing fails, it will lead to the loss of settlement data, which is not conducive to the settlement work. In addition, look-ahead multi-settlement requires several times of real-time clearing data, which greatly increases the settlement complexity of the real-time market, and also puts forward higher requirements for the storage space, accuracy and security of market data. At present, the settlement mechanism is still only the proposed scheme (Schiro, 2017), and has not been applied in the actual market.

3 The proposed multi-interval settlement system

Cross-period constraint is an important factor affecting the incentive of forward-looking optimization settlement. Cross-period constraints couple the optimization results of different periods in the electricity spot market, and the clearing prices of each period are intertwined. Therefore, look-ahead optimization is not suitable for the optimization and pricing of resources by simply cutting the period. However, due to the lack of incentives for the price of the look-ahead single settlement mechanism, power generation companies may not be able to recover costs through the market price and choose to deviate from the dispatching order. Therefore, when necessary, they should appropriately and flexibly increase the number of settlement rounds to make the settlement price highlight the real value of the actual resources as much as possible, thus increasing the incentive of the settlement price. In general, the longer the optimization period is considered, the more the clearing results can reflect the real economic signals, and the more incentive. Therefore, in the case of perfect forecast or low forecast deviation, compared with real-time look-ahead optimization, the day-ahead market takes into account the 24-h load situation, and the economic signals expressed by the clearing result are more comprehensive and more incentive, which can be regarded as the best clearing result. The problem to be solved by the new settlement mechanism is to minimize the deviation of clearing results between day-ahead and real-time settlement rounds, and improve the incentive of market participants to follow the schedule.

The look-ahead optimization cycle is 3–5 h, and the day-ahead optimization cycle is 24 h. Under the same load, the essential difference between the two is the optimization cycle. Therefore, it is necessary to analyze the influencing factors closely related to the look-ahead cycle. The constraint of ramp rate has a cross-time

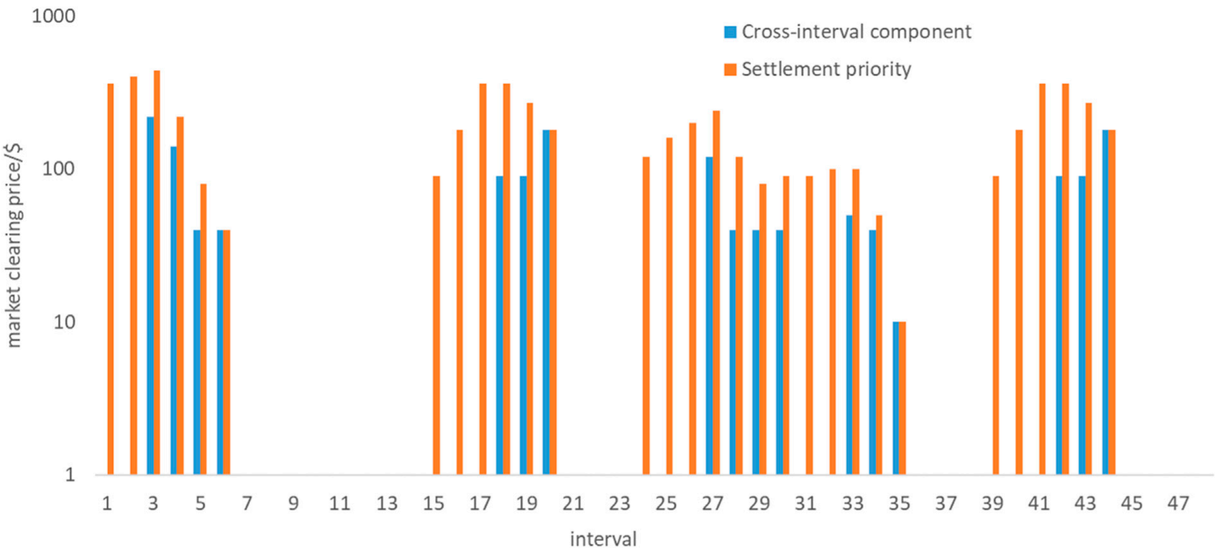

FIGURE 7
Settlement priority.

TABLE 2 The selection result of first-settlement in the first 18 intervals.

Interval	Selection period of first real-time settlement	Interval	Selection period of first real-time settlement	Interval	Selection period of first real-time settlement
1	1–4	7	4–7	13	10–13
2	2–5	8	5–8	14	11–14
3	3–6	9	6–9	15	15–18
4	3–6	10	7–10	16	16–19
5	3–6	11	8–11	17	17–20
6	3–6	12	9–12	18	17–20

nature, and its shadow price reflects the economic value of the cross-time component, which has a great relationship with the look-ahead cycle.

3.1 Settlement design

When the real-time market adopts the forward optimization with a forward period of T, T electricity prices will be calculated for each period. The forward single settlement only selects the electricity prices of the current period as the basis for settlement, while the forward multiple settlement will include all electricity prices in the settlement system. The former is too mechanical and lacks motivation; The latter is too complex and lacks flexibility. Therefore, it is necessary to choose a balance between them, which can not only increase the incentive of settlement, but also limit the settlement complexity to a reasonable range.

For this reason, this paper designs a new mechanism of two settlements in the real-time market, and adds another settlement process on the basis of prospective single settlement, in order to increase the incentive of settlement without excessively increasing the complexity of settlement. In connection with the day-ahead market settlement, real-time one-time settlement can form the original double settlement mechanism with the day-ahead settlement combination. This content is the same as the existing double settlement mechanism, which will not be repeated in this article.

Real-time secondary settlement is based on the current target period's settlement electricity price and clearing electricity quantity, and the deviation electricity quantity between secondary settlement and primary settlement is settled according to the target period's settlement electricity price. The new settlement mechanism design can be seen in Figure 5.

3.2 Settlement priority

It is known that when the real-time market adopts the forward optimization with a forward period of T, T electricity prices will be calculated in each time period, and

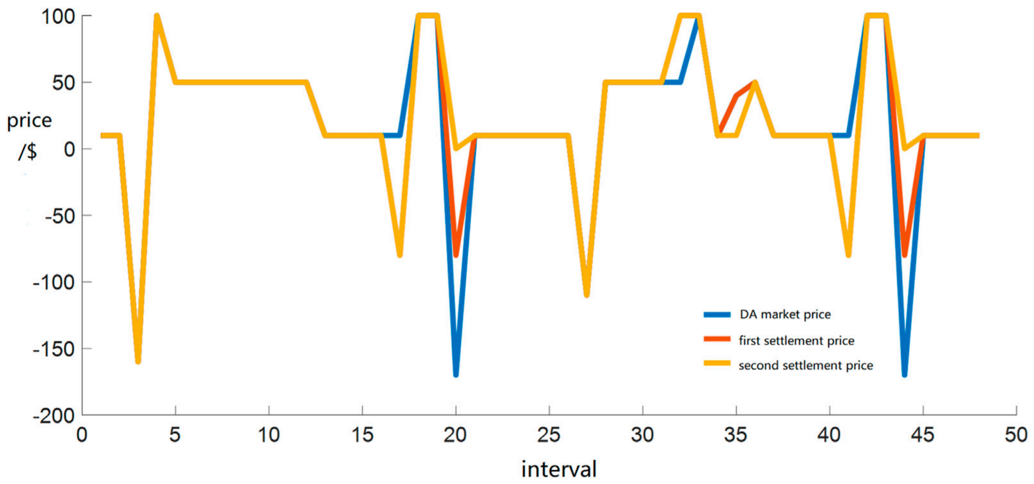

FIGURE 8
Settlement price.

the calculated electricity prices need to be prioritized. Therefore, it is necessary to explore the economic value of the cross-time components in the look-ahead optimization of electricity prices. See Eq. 1 for the mathematical model of real-time prospective optimization.

$$\begin{aligned} \min \sum_i \sum_t c_i\left(p_{i,t}\right) \\ \beta_t\colon \sum_i p_{i,t} = \sum_j d_{j,t} \\ \xi_{i,t}{}^{\max}\colon p_{i,t} \le p_i{}^{\max} \\ \xi_{i,t}{}^{\min}\colon p_{i,t} \ge p_i{}^{\min} \\ \sigma_{i,t}^{\mathrm{up}}\colon p_{i,t} - p_{i,t-1} \le \Delta p_i \\ \sigma_{i,t}^{\mathrm{down}}\colon p_{i,t-1} - p_{i,t} \le \Delta p_i \\ \mu_l{}^{\max}\colon p_{l,t}^{\mathrm{c}} \le p_l^{\max,\mathrm{c}} \\ \mu_l{}^{\min}\colon p_{l,t}^{\mathrm{c}} \ge p_l^{\min,\mathrm{c}} \end{aligned} \tag{1}$$

Where: $c_i(\cdot)$ is the operation cost function of generator i; $p_{i,t}$ is the active output of generator set i in time period t; $d_{j,t}$ is the load of load j period t; $p_i{}^{\min}$ and $p_i{}^{\max}$ are the minimum and maximum output limits of unit i; Δp_i is the ramping constraint for unit i in each period. $p_{l,t}^{\mathrm{c}}$, $p_l^{\min,\mathrm{c}}$ and $p_l^{\max,\mathrm{c}}$ are the power flow power, power lower limit and power upper limit of line l respectively; β_t is the shadow price of the reference node; $\xi_{i,t}{}^{\max}$ and $\xi_{i,t}{}^{\min}$ is the shadow price constrained by the upper limit and lower limit of unit power respectively; $\sigma_{i,t}^{\mathrm{up}}$ and $\sigma_{i,t}^{\mathrm{down}}$ the shadow price of the unit ramping constraint and the landslide constraint respectively; $\mu_l{}^{\max}$ and $\mu_l{}^{\min}$ the shadow price constrained by the upper power limit and lower power limit of line l.

By constructing the Lagrange function and according to the Karush-Kuhn-Tucker (KKT) condition, it can be concluded that:

$$\begin{aligned} \frac{\partial L}{\partial p_{i,t}} = \frac{\partial c_i\left(p_{i,t}\right)}{\partial p_{i,t}} + \beta_t + \left(\xi_{i,t}{}^{\max} - \xi_{i,t}{}^{\min}\right) + \left(\sigma_{i,t}^{\mathrm{up}} - \sigma_{i,t+1}^{\mathrm{up}}\right) + \\ \left(\sigma_{i,t+1}^{\mathrm{down}} - \sigma_{i,t}^{\mathrm{down}}\right) + \sum_l \left(\mu_l{}^{\max} - \mu_l{}^{\min}\right) \frac{\partial p_{l,t}^{\mathrm{c}}}{\partial p_{i,t}} = 0 \end{aligned} \tag{2}$$

Where: L is the Lagrange function of optimization problem Eq. 1.

According to the definition of locational marginal price, spot market electricity price has two expressions:

$$\begin{aligned} \lambda_{n,t} &= -\beta_t + \sum_l \left(\mu_l{}^{\max} - \mu_l{}^{\min}\right) \frac{\partial p_{l,t}^{\mathrm{c}}}{\partial d_{j,t}} \\ &= \frac{\partial c_i\left(p_{i,t}\right)}{\partial p_{i,t}} + \left(\xi_{i,t}{}^{\max} - \xi_{i,t}{}^{\min}\right) \\ &\quad + \left(\sigma_{i,t}^{\mathrm{up}} - \sigma_{i,t+1}^{\mathrm{up}}\right) + \left(\sigma_{i,t+1}^{\mathrm{down}} - \sigma_{i,t}^{\mathrm{down}}\right) \end{aligned} \tag{3}$$

Where: $\lambda_{n,t}$ is spot market electricity price.

Eq. 3 explains the connotation of spot market electricity price from the perspective of system and generator respectively (Shi et al., 2019). It can be seen from Formula 3 that the economic value of the cross-time component in the electricity price is mainly reflected in the Lagrangian multiplier constrained by the ramp rate, which is also a key factor affecting the incentive of look-ahead optimization (Hua et al., 2019; Zhao et al., 2020). There is a significant price deviation from the day-ahead optimization model using the traditional forward optimization rolling clearing electricity price, because it cannot reflect the value of cross-time constraints. All clearing results in history are regarded as "sunk costs" without distinction, which will make the unit have the impulse to deviate from scheduling (Schiro et al., 2016).

Among them, the willingness of the unit to deviate from the dispatching can be measured by the opportunity cost (LOC) compensation cost. The LOC compensation cost of units in the real-time market is defined as the difference between the maximum revenue of unit self-dispatch under the determined market clearing price and the actual revenue of units following the dispatching order. The calculation formula is shown in Formula 4:

$$R_{\mathrm{LOC}} = \max \sum_t \sum_i \left(\left(\lambda_{i,t} - c_{i,t}\right) p_{i,t} - \left(\lambda_{i,t} - c_{i,t}\right) p_{i,t}^{*} \right) \tag{4}$$

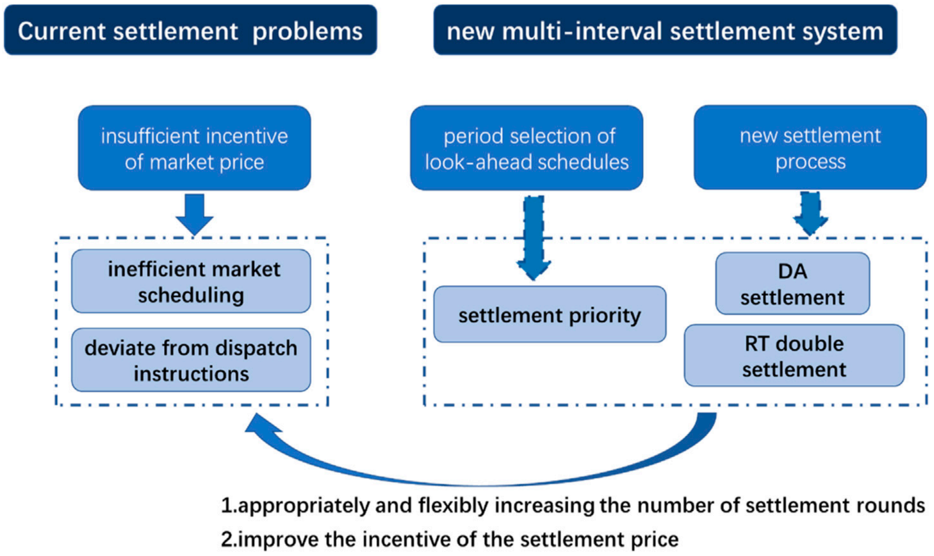

FIGURE 9
Proposed multi-interval settlement system.

TABLE 3 The incentive of first-settlement price.

Item	New settlement mechanism	Current settlement mechanism
Average value of electricity price deviation rate/%	41.8	45.3
Change amplitude/%	−7.8	0
Opportunity cost compensation fee/$	25,750	36,650
Change amplitude/%	−29.7	0
Calculation complexity/s	5.82	5.43
Change amplitude/%	+7.2	0

Where: $R^{\mathrm{RT}}_{i,t}$ is the total opportunity cost of the unit; $p_{i,t}$ is the output of unit self-dispatch; $p^{*}_{i,t}$is the output of the unit following the dispatching instructions; $\lambda_{i,t}$ is the market electricity price.

At the real-time one-time settlement meeting, the settlement electricity price with the highest priority of prospective optimization and the clearing electricity quantity will be selected as the basis for settlement. Among them, the determination of settlement priority needs to select quantifiable criteria. The standard needs to reflect the deviation of clearing results between the day-ahead and real-time settlement rounds, and highlight the incentive of following the schedule. There are two types of quantifiable criteria that meet the requirements, namely, the Lagrange multiplier that reflects the economic value of cross-time components, or the LOC compensation that reflects the incentive to follow the scheduling.

Because the calculation of LOC compensation cost is relatively complex, it does not meet the time requirement of real-time rolling calculation. The Lagrange multiplier of the ramping constraint is the companion variable of the real-time prospective optimization result, which can be directly extracted, greatly simplifying the calculation process of settlement priority. Therefore, this paper selects the Lagrangian multiplier with ramping constraints as the key factor to quantify the deviation between the real-time prospective optimization results and the day-ahead optimization results, in order to maximize the incentive of cross-cycle prospective optimization. In this paper, LOC compensation cost of real-time one-time settlement price is taken as one of the incentive evaluation indicators.

3.3 Settlement process

1) Calculation of settlement priority. The look-ahead period has a periodicity, and the factors affected by the optimization period in the optimization model are mainly cross-time components. According to Formula 3, the cross-time component in the electricity price is mainly the ramping constraint, and the formula is expressed as $(\sigma^{\mathrm{up}}_{i,t} - \sigma^{\mathrm{up}}_{i,t+1}) + (\sigma^{\mathrm{down}}_{i,t+1} - \sigma^{\mathrm{down}}_{i,t})$. It is necessary to extract the cross-time component value of a

single time period, that is, the cross-time components of each unit are superimposed, as shown in Formula 5. Because the deviation of day-ahead load forecasting is low and the number of time periods considered in day-ahead optimization is more comprehensive, the Lagrange multiplier with cross-time constraints can be taken from the day-ahead clearing results.

$$\sigma_t^{\mathrm{sum}} = \sum_i \left| \left(\sigma_{i,t}^{\mathrm{up}} - \sigma_{i,t+1}^{\mathrm{up}}\right) + \left(\sigma_{i,t+1}^{\mathrm{down}} - \sigma_{i,t}^{\mathrm{down}}\right) \right| \tag{5}$$

Where: σ_t^{sum} is the cross-time component value of interval t in the day-ahead clearing result.

Summarize the cross-time component values of all time periods in the look-ahead optimization cycle to form a qualitative settlement priority. The formula is shown in Formula 6. By summing the Lagrange multipliers with cross-time constraints in the T cycle, the economic value of the cross-time components in the T cycle can be comprehensively obtained. The larger the sum, the more real the economic value can be reflected by selecting this cycle. Taking this as the basis for settlement can better reduce the deviation from the day-ahead settlement, more truly reflect the scarce value of the system's cross-era resources, and improve the incentive of the settlement price.

$$\sigma_{t,t+T_L}^{\mathrm{sum}} = \sum_{t}^{t+T_L} \sigma_t^{\mathrm{sum}} \tag{6}$$

Where: T_L is the number of intervals extended by the forward looking optimization. The forward looking period described above is $T=(T_L+1)$; $\sigma_{t,t+T_L}^{\mathrm{sum}}$ is the settlement priority of the optimized round when the corresponding current interval is t.

To make a settlement selection for time period t, it is necessary to compare the settlement priority of each optimization cycle including time period t. Select the clearing result of the optimized round with the highest priority as the basis for real-time one-time settlement.

$$\sigma_t^{\mathrm{settle}} = \max\left(\sigma_{t-T_L,t}^{\mathrm{sum}}, \sigma_{t-T_L+1,t+1}^{\mathrm{sum}}, \ldots, \sigma_{t,t+T_L}^{\mathrm{sum}}\right) \tag{7}$$

Assuming that the result of Formula 7 is $\sigma_t^{\mathrm{settle}} = \sigma_{t-T_L,t}^{\mathrm{sum}}$, the electricity price and electricity quantity of the optimized round with the optimization period from interval (t-T_L) to interval t are selected as the clearing basis.

2) Day-ahead settlement. The day-ahead settlement is consistent with the current market model, and the day-ahead electricity price and the day-ahead clearing electricity quantity are used for settlement. The formula can be seen in Formula 8.

$$R_{i,t}^{\mathrm{DA}} = \lambda_{i,t}^{\mathrm{DA}} p_{i,t}^{\mathrm{DA}} \tag{8}$$

Where: $R_{i,t}^{\mathrm{DA}}$ is the day-ahead settlement fund of unit i in time period t; $\lambda_{i,t}^{\mathrm{DA}}$ and $p_{i,t}^{\mathrm{DA}}$ are the day-ahead settlement electricity price and settlement electricity quantity of the corresponding period t of unit i.

3) Real-time settlement. Real-time settlement adopts the mode of deviation power settlement. The real-time first settlement will select the settlement electricity price with the highest priority of prospective optimization and the settled electricity as the settlement basis. Real-time secondary settlement is based on the settlement electricity price and clearing electricity quantity of the current target period. The deviation electricity quantity between secondary settlement and primary settlement is settled according to the settlement electricity price of the target period. The formula can be seen in Formula 9.

$$R_{i,t}^{\mathrm{RT}} = \lambda_{i,t}^{\mathrm{fst}}\left(p_{i,t}^{\mathrm{fst}} - p_{i,t}^{\mathrm{DA}}\right) + \lambda_{i,t}^{\mathrm{sec}}\left(p_{i,t}^{\mathrm{sec}} - p_{i,t}^{\mathrm{fst}}\right) \tag{9}$$

Where: $R_{i,t}^{\mathrm{RT}}$ is the real-time settlement fund of unit i in interval t; $\lambda_{i,t}^{\mathrm{fst}}$ and $p_{i,t}^{\mathrm{fst}}$ are the real-time first settlement electricity price and settlement electricity quantity of the corresponding interval t of unit i; $\lambda_{i,t}^{\mathrm{sec}}$ and $p_{i,t}^{\mathrm{sec}}$ are the real-time secondary settlement electricity price and settlement electricity quantity of unit i corresponding to time period t.

4 Numerical experiments

4.1 Case data

The calculation example uses IEEE 9- node-3-units system to demonstrate the incentive of the new mechanism of prospective optimization settlement. The example sets 48 time periods, and the period of real-time prospective optimization is 4. See Table 1 for the technical parameters and cost quotation of the unit and Figure 6 for the load parameters. It can be seen from the price characteristics that unit 1 has the lowest cost and the largest capacity, and is suitable for serving as the base load unit. Unit 3 has the highest climbing speed and is suitable for being a flexible unit. In period 3, period 20, period 27 and period 44, the electricity price drops sharply, which proves that the economic effect of cross-period constraints in the model is more obvious and can better verify the incentive of the new settlement mechanism in this paper.

4.2 Case analysis

The settlement priority is shown in Figure 7. See Table 1 for the selection results of partial time periods for real-time one-time settlement. When the settlement priority of all optimization rounds is completely consistent, the earliest optimization round is generally selected as the basis for a settlement.

According to Figure 7; Table 2, the time period with high settlement limit is easier to be selected as the optimal time period for first real-time settlement.

The situation of real-time one-time settlement electricity price is shown in Figure 8. It can be seen that compared with the secondary settlement electricity price (the real-time settlement electricity price of the original mode), the one-time settlement electricity price is closer to the day-ahead electricity price.

According to Table 2, the shadow price of cross-time constraints corresponding to optimization periods 3–6 and 17–20 is higher, and the settlement priority is also higher. Corresponding to the change rule of the settlement electricity price in Figure 8, periods 3–6 and 17–20 are periods of violent fluctuations in electricity price. The system needs more flexible resources for cross-time scheduling, and the flexible resources have cross-time economic value in this situation.

Assuming zero error in real-time load forecasting, that is, there is no deviation between day-ahead load and real-time load, it can be seen from Table 3 that the electricity price selected for one-time settlement can better connect the results of day-ahead market, and the deviation is relatively low, and the average deviation rate of electricity price is reduced by 7.8%. In addition, through calculation, the opportunity cost (LOC) compensation cost of the real-time one-time settlement electricity price is reduced by about 30% compared with the original look-ahead settlement and only increased 7.2% of the calculation burden. If the updated research (Changshuo et al., 2022; Liping et al., 2022; Ning et al., 2022) methods are applied, the computational burden can be further reduced.

It should be noted that the biggest difference between the new settlement mechanism and the original settlement mechanism is to add real-time primary settlement. The real-time secondary settlement in the new settlement mechanism is the real-time settlement in the original settlement mechanism. The example deeply analyzes the most direct difference, that is, the incentive of one-time settlement electricity price, which can eliminate unnecessary interference, and is more conducive to directly and objectively highlight the differences between different mechanisms, reflecting the incentive effect of the new mechanism.

The calculation example shows that the new mechanism of look-ahead optimization settlement designed in this paper and the introduction of real-time one-time settlement electricity price can effectively reduce the deviation rate of real-time market electricity price, and can significantly reduce the opportunity cost compensation costs of power generation companies, and greatly improve the incentive of market members to follow the dispatching instructions. Figure 9 summarizes the effect of the calculation example.

5 Conclusion

Prospective optimization plays an important role in adapting to the development needs of renewable energy and ensuring the good operation of the electricity spot market. However, the current look-ahead optimization model has the problem of insufficient electricity price incentives, which brings challenges to market construction. For this reason, this paper introduces the settlement priority. By appropriately and flexibly increasing the settlement rounds, it will not cause excessive settlement burden, but also enable the settlement price to highlight the real value of actual resources as much as possible, effectively improve the incentive of the settlement price, better adapt to the demand of real-time prospective optimization of the new era, and provide reference for the construction of Chinese electricity spot market. (Peng and Chatterjee, 2013).

In view of the above conclusions, the following conclusions are drawn:

1. Increase the incentive of real-time optimization. Under the current look-ahead optimization model, the value of cross-time constraints is only reflected in the day-ahead market clearing results, but not in the real-time market rolling optimization. Therefore, the price factor of cross-time constraints in the spot market can be introduced into the objective function of the mathematical optimization model, so that the price of real-time optimization covers the value of cross-time constraints and increases the incentive of real-time optimization.
2. Select an appropriate look-ahead settlement period. The current look-ahead optimization model always has differences between the day-ahead and real-time settlement due to the forecast deviation, and the selection of different look-ahead settlement periods will affect this deviation. Therefore, on the premise of not reducing the real-time incentive, select the most efficient look-ahead settlement cycle, try to reduce the settlement difference between the day-ahead market and the real-time market, and ensure the stability of the market.
3. Flexibly increase the number of settlement rounds and improve the settlement mechanism. Under the current look-ahead settlement mode, the settlement basis is relatively mechanical, and the market entities may deliver at the settlement price with insufficient incentive. Therefore, the incentive of settlement price can be increased by flexibly increasing the number of settlement rounds at the cost of increasing the amount of calculation, or the most efficient settlement price can be selected by the priority of settlement incentive, and the incentive of real-time optimization can be increased at the cost of increasing the complexity of settlement process, so as to improve the settlement mechanism.
4. Improve the calculation efficiency of settlement and increase the adaptability of practical engineering applications. Under the current forward-looking settlement mode, there is an obvious lack of incentive, and increasing the number of settlement rounds is a relatively feasible solution. Increasing the number of settlement rounds will inevitably increase the computational burden, so applying the latest research results to improve the computational efficiency of the actual settlement operation is the future development direction.

Data availability statement

The raw data supporting the conclusion of this article will be made available by the authors, without undue reservation.

Author contributions

FQ: Supervision, review and editing; DX: Validation and experimentation; WJ: Methodology, validation and software.

Conflict of interest

Author QF was employed by State Grid Shanghai Electric Power Company. XD was employed by State Grid Shanghai PuDong Electric Power Company.

The remaining authors declare that the research was conducted in the absence of any commercial or financial relationships that could be construed as a potential conflict of interest.

Publisher's note

References

Bakirtzis, E. A., Biskas, P. N., Labridis, D. P., and Bakirtzis, A. G. (2014). Multiple time resolution unit commitment for short-term operations scheduling under high renewable penetration. *IEEE Trans. Power Syst.* 29 (1), 149–159. doi:10.1109/tpwrs.2013.2278215

CAISO (2014). Advancing and maximizing the value of energy storage technology: A California road map. https://www.caiso.com/Documents/AdvancingMaximizingValueofEnergyStorageTechnology_CaliforniaRoadmap.pdf.

CAISO (2019). Business practice manual for market operations. https://bpmcm.caiso.com/BPM%20Document%20Library/Market%20Operations/BPM_for_Market%20Operations_V71_redline.pdf.

Changshuo, W., Ning, X., Linjun, S., Zhang, L., Li, W., and Bai, X. (2022). Learning discriminative features by covering local geometric space for point cloud analysis. *IEEE Trans. Geoscience Remote Sens.* 60, 1–15. doi:10.1109/tgrs.2022.3170493

Chen, Y., Zhuo, Y., Liu, Y., Guan, L., Lu, C., Xiao, L., et al. (2021). Development and recommendation of fast frequency response market for power system with high proportion of renewable energy. *Automation Electr. Power Syst.* 45 (10), 174–183. doi:10.7500/AEPS20200726004

Ela, E., and O'Malley, M. (2016). Scheduling and pricing for expected ramp capability in real-time power markets. *IEEE Trans. Power Syst.* 31 (3), 1681–1691. doi:10.1109/tpwrs.2015.2461535

Hua, B., Schiro, D., Zheng, T., Baldick, R., and Litvinov, E. (2019). Pricing in multi-interval real-time markets. *IEEE Trans. Power Syst.* 34 (4), 2696–2705. doi:10.1109/tpwrs.2019.2891541

Huang, X., Zhang, T., and Xu, Z. (2019). Analysis on characteristics of Singapore′s power market settlement and risk management. *South. Energy Constr.* 6 (4), 29–34. doi:10.16516/j.gedi.issn2095-8676.2019.04.004

Jiang, H., Du, E., Zhu, G., Huang, J., Qian, M., Zhang, N., et al. (2020). Review and prospect of seasonal energy storage for power system with high proportion of renewable energy. *Automation Electr. Power Syst.* 44 (19), 194–207. doi:10.7500/AEPS20200204003

Liping, Z., Linjun, S., Weijun, L., Zhang, J., Cai, W., Cheng, C., et al. (2022). A joint bayesian framework based on partial least squares discriminant analysis for finger vein recognition. *IEEE Sensors J.* 22, 785–794. doi:10.1109/jsen.2021.3130951

Massachusetts gov (2016). State of charge, Massachusetts energy storage initiative study https://www.mass.gov/files/2017-07/state-ofcharge-report.pdf.

Ning, X., Weijun, L., Feng, H., Bai, X., Sun, L., and Li, W. (2022). Hyper-sausage coverage function neuron model and learning algorithm for image classification. *Pattern Recognit.* 136 (2023), 109216–109313. doi:10.1016/j.patcog.2022.109216

NYISO (2020). New York independent system operator services tariff. https://nyisoviewer.etariff.biz/ViewerDocLibrary/MasterTariffs/9FullTariffNYISOOATT.pdf.

Peng, T., and Chatterjee, D. (2013). Pricing mechanism for time coupled multi-interval real-time dispatch. https://cms.ferc.gov/sites/default/files/2020-05/20140411125224-M2%2520-%2520Peng.pdf.

Schiro, D. A. (2017). Flexibility procurement and reimbursement: A multi-period pricing approach. https://www.ne-rto.net/static-assets/documents/2017/09/20170920-procurement-pricing-of-ramping-capability.pdf.

Schiro, D. A., Zheng, T., Zhao, F., and Litvinov, E. (2016). Convex hull pricing in electricity markets: Formulation, analysis, and implementation challenges. *IEEE Trans. Power Syst.* 31 (5), 4068–4075. doi:10.1109/tpwrs.2015.2486380

Shi, X., Zheng, Y., Xue, B., and Feng, S. (2019). Effect analysis of unit operation constraints on locational marginal price of unit nodes. *Power Syst. Technol.* 43 (8), 2658–2664. doi:10.13335/j.1000-3673.pst.2019.0540

Wilson, R. (2002). Architecture of power markets. *Econometrica* 70 (4), 1299–1340. doi:10.1111/1468-0262.00334

Xiao, Y., Guan, Y., Zhang, L., Cai, Q., Liu, S., and Lin, S. (2021). Analysis and construction path of risk hedging mechanism in centralized LMP-based electricity spot market. *Power Syst. Technol.* 45 (10), 3981–3991. doi:10.13335/j.1000-3673.pst.2020.1975

Xie, L., and Ilic, M. D. (2009). Model predictive economic/environmental dispatch of power systems with intermittent resources. Proceedings of the 2009 IEEE Power Energy Society General Meeting, Calgary, AB, Canada, July 2009 1–6.

Yao, X., Zeng, Z., Yang, W., Wu, J., Yang, L., and Zhong, H. (2020). Electricity market settlement mechanism design and practice in Guangdong. *Power Syst. Prot. Control* 48 (2), 76–85. doi:10.19783/j.cnki.pspc.190253

Zhao, J., Zheng, T., and Litvinov, E. (2020). A multi-period market design for markets with intertemporal constraints. *IEEE Trans. Power Syst.* 35 (4), 3015–3025. doi:10.1109/tpwrs.2019.2963022

Zhou, M., Yan, Y., Ding, Q., Wu, Z., He, Y., Long, S., et al. (2017). Transaction and settlement mechanism for foreign representative power markets and its enlightenment for Chinese power market. *Automation Electr. Power Syst.* 41 (20), 1–8. doi:10.7500/AEPS20170223001

frontiers | Frontiers in Energy Research

TYPE Original Research
PUBLISHED 13 April 2023
DOI 10.3389/fenrg.2023.1156007

EDITED BY
Xin Ning,
Chinese Academy of Sciences (CAS),
China

REVIEWED BY
Luyang Hou,
Beijing University of Posts and
Telecommunications (BUPT), China
Zijun Zhang,
City University of Hong Kong, Hong Kong
SAR, China

*CORRESPONDENCE
Dianwei Chi,
✉ dianwei.chi@163.com

RECEIVED 01 February 2023
ACCEPTED 03 April 2023
PUBLISHED 13 April 2023

CITATION
Chi D and Yang C (2023), Wind power
prediction based on WT-BiGRU-
attention-TCN model.
Front. Energy Res. 11:1156007.
doi: 10.3389/fenrg.2023.1156007

Wind power prediction based on WT-BiGRU-attention-TCN model

Dianwei Chi[1]* and Chaozhi Yang[2]

[1]School of Artificial Intelligence, Yantai Institute of Technology, Yantai, China, [2]College of Computer Science and Technology, China University of Petroleum (East China), Qingdao, China

Accurate wind power prediction is crucial for the safe and stable operation of the power grid. However, wind power generation has large random volatility and intermittency, which increases the difficulty of prediction. In order to construct an effective prediction model based on wind power generation power and achieve stable grid dispatch after wind power is connected to the grid, a wind power generation prediction model based on WT-BiGRU-Attention-TCN is proposed. First, wavelet transform (WT) is used to reduce noises of the sample data. Then, the temporal attention mechanism is incorporated into the bi-directional gated recurrent unit (BiGRU) model to highlight the impact of key time steps on the prediction results while fully extracting the temporal features of the context. Finally, the model performance is enhanced by further extracting more high-level temporal features through a temporal convolutional neural network (TCN). The results show that our proposed model outperforms other baseline models, achieving a root mean square error of 0.066 MW, a mean absolute percentage error of 18.876%, and the coefficient of determination (R^2) reaches 0.976. It indicates that the noise-reduction WT technique can significantly improve the model performance, and also shows that using the temporal attention mechanism and TCN can further improve the prediction accuracy.

KEYWORDS

power grid, wind power, wavelet transform, gated recurrent unit, attention mechanism, temporal convolutional neural network, prediction

1 Introduction

Wind power is a form of clean and renewable energy. Wind power generation alleviates environmental pollution and the dependence of power generation on traditional energies (Han et al., 2019a; Ma et al., 2019a). At present, there are many large-capacity wind farms in the world, which have accumulated a large amount of wind power operation data. Wind power prediction data, as one of the functional data modules of wind power big data, can be used to make wind power prediction. However, the instability of wind power generation affects the performance of the power grid, so it is necessary to accurately predict the wind power. Therefore, an effective model needs to be developed to accurately forecast the wind power (Wang et al., 2018; Ma et al., 2019b). Non-etheless, accurate prediction of wind power generation is hardly attainable because of the randomness and non-linearity of wind energy. In this study, a new wind power prediction model is proposed to solve this problem, improve the accuracy and generalization ability of the model, and thereby ensure safe and reliable operation of the microgrid.

Recent works on wind power prediction principally employ statistical analysis approaches or deep learning methods. Statistical analysis approaches include single-model prediction and combined-model prediction. Typical single-model prediction methods are support vector machine (SVM) (Dang et al., 2019), autoregressive moving average (ARMA), autoregressive integrated moving average (ARIMA), autoregression model (Shao et al., 2015), fuzzy model (Zhao and Guo, 2016), wavelet-based model (Liu et al., 2015a), and artificial neural network (ANN) (Wu et al., 2018). Among them, ARIMA is suitable for scenarios where the volume of training samples is small. The ARMA is suitable for the occasions where the wind power forecast is short and the fluctuation is large (Torres et al., 2005; Li and Ye, 2010; Liu et al., 2015b; Haigesa et al., 2017; Korprasertsak and Leephakpreeda, 2019; Lu et al., 2020; Sun et al., 2020; Lu et al., 2021). Given the unsatisfactory prediction of single-model methods, combined-model prediction, therefore, is proposed as a solution to wind power prediction. Wang et al. (Wang et al., 2021) put forward a wind power signal forecasting method based on the improved empirical mode decomposition (EMD) and SVM, which was proved to have high accuracy and strong stability of the model in experiments. Zhao and Ding (Zhao and Ding, 2020) proposed a wind power forecasting model termed MEEMD-KELM and found that their model has good forecasting performance. Huang et al. (Huang et al., 2020) optimized the SVM model by the particle swarm optimization-genetic algorithm (PSO-GA), and achieved good performance in forecasting. However, statistical methods have limited ability in extracting time-series features and cannot adapt well to the non-linear and unstable characteristics of wind power. Deep learning methods, especially recurrent neural networks (RNN) and their variants, are increasingly used in wind power prediction. LSTM and GRU, as RNN variants, can solve the long-term dependence problem of RNN itself, and are suitable for applications such as wind power forecasting and power grid dispatching (Liu and Zhang, 2022; Liu et al., 2022a; Niu et al., 2018; Liu et al., 2021; Yu et al., 2018; Shahid et al., 2021; Han et al., 2019b; Duan et al., 2021; Ding et al., 2019; Zn et al., 1016). Liu et al. (Liu and Zhang, 2022) proposed a novel bilateral branch learning-based WPP modeling framework, and through a comprehensive computational study, they verified that their proposed framework achieves the state-of-the art performance as it beats a large set of classical data-driven and recent deep learning-based WPP methods considered in their study. Liu et al. 2(2022a) proposed a novel LSTM-AODEN network architecture combining a long short-term memory (LSTM) network with an attention-assisted ordinary differential equation network (AODEN), and showed by experiments the superior ability of their proposed method in generating higher resolution probabilistic wind power prediction results. Niu et al. (2018) put forward a model that combines CNN and GRU, where the CNN reduces the dimension of features, and the GRU captures relations between data in the time sequence, and the model was found to have a high accuracy in forecasting. Li and Li, 2021 proposed a short-term wind power forecasting model based on deep learning and error correction, which uses the BiGRU model for forecasting, the random forest algorithm for construction of the error model, and continuously corrects the error; their model was proved to be effective and applicable by experiments. Liu et al. (2022b) proposed a hybrid deep learning model based on wavelet transform, temporal convolutional neural network and LSTM, and experiments proved that their model has good prediction performance. Liao et al. (2022) proposed a short-term wind power prediction model based on a two-stage attention mechanism and an encoding-decoding LSTM model; in their model, the two-stage attention mechanism can select key information, where the first stage focuses on important feature dimensions, and the second stage focuses on important time steps in the time series; the model was proved to have good prediction performance.

In summary, the single-model method has poor sensitivity to the sample data, so it cannot achieve high accuracy in predicting wind power which comes with large fluctuations. In contrast, the combined-model method has better performance in this regard. However, the combined-model method has poor capacity in grasping the dependence of time series, and it cannot adapt well to the characteristics of non-linearity and instability of wind power. With the extensive use of deep neural networks (Dong et al., 2023; Ning et al., 2023), deep learning methods, especially models such as LSTM and GRU, can effectively grasp the non-linear relationship between wind power, wind speed and other features while effectively mining the time-dimensional features of the data and dealing with complex time series. Its combination with techniques such as dimensionality reduction, feature extraction, and attention mechanism can improve the prediction effect of the models to varied degrees.

Given analyses above, deep learning provides a better solution to short-term wind power forecasting than other methods because wind power is characterized by fluctuations and uncertainties. Some studies (Han et al., 2019b; Liu et al., 2022a; Liu et al., 2022b; Liao et al., 2022; Liu and Zhang, 2022) used LSTM as the basic prediction model with complex model parameters and high expressiveness, but did not show high operational efficiency. Although some others (Niu et al., 2018; Li and Li, 2021) used GRU as the basic model, which simplified the model parameters, but the time-series data features were not sufficiently extracted, which affected the accuracy of prediction. Therefore, to obtain better operational efficiency and prediction results, this study integrates three aspects: data denoising and smoothing, simplification of the base model parameters, and adequate extraction of data features, which is innovative in construction of prediction models. The wavelet transform is used for data denoising, and suitable wavelet functions are selected for different sample features to reduce the impact of abnormal data on the accuracy of prediction. Meanwhile, the GRU model, which has a simpler structure than the LSTM model, is chosen as the base model, which is conducive to improving the operational efficiency, and the GRU model can be applied to larger-scale wind power data forecasting. Moreover, a bi-directional GRU is used for more adequate extraction of timing features, while an attention mechanism is introduced to enhance the weights of key time steps in order to highlight the degree of influence of different time-series nodes on wind power, and further extracts more high-level temporal features by a temporal convolutional network (TCN) layer. Based on the combination of several aspects, the operational efficiency, stability, and accuracy of the model are significantly improved. The model is expected to help control the performance of wind turbines and provide statistical support for safe operation of wind power stations (Yang and Zhou, 2019).

The remainder of the paper is organized as follows. First, Section 2 introduces the concepts and theories related to the WT-BiGRU-Attention-TCN model, and then discusses the structure and workflow of the model. Then, Section 3 elaborates on the experiments we have made and the discussions, detailing the source of the data sample set and various descriptive statistical metrics, data denoising and model evaluation; four models (LSTM, GRU, WT-GRU,WT-BiGRU-Attention) are compared with our model to illustrate the effectiveness of our model, and the performance of each model is discussed through the experimental results. Finally, in Section 4, conclusions are made based on the experiment result.

2 Model construction

2.1 Data denoising based on wavelet transform

There are noises in the sample data of wind power, which need to be cleansed before model training.

In the denoising process, effective signals and noises are separated. The wavelet transform (WT) technique, which can achieve the separation based on the difference between signals and noises in their time domain and frequency domain, provides a good solution to data denoising. In the present work, the WT method is employed to reduce the noises in the wind power sample data while maintaining effective data (Li, 2007) to ensure the complete time sequence and reliability of the sample data. WT can decompose the time sequence, decomposing the original signals into child signals, so that the time sequence and other details can be observed. There are two types of WT methods: continuous wavelet transform (CWT) and discrete wavelet transform (DWT). The latter can discretize the scale and time, keep the construction error at a low level, and reduce the time cost and computing overheads. Therefore, DWT is employed in our work to decompose the time sequences.

The specific steps to reduce noise by using wavelet transform method are as follows.

(1) Selection of wavelet functions: proper wavelet functions are selected as per the features of the samples to decompose the signals. In the present work, three common discrete wavelets are used: Daubechies wavelet (db), Coiflet wavelet (coif) and Symlet wavelet (sym).
(2) Thresholding: one threshold is selected for each layer to perform soft-thresholding of high-frequency coefficients to smoothen the reconstructed signals. The soft threshold is to solve the local jitter and wavelet domain mutation of the denoising results brought by the unified threshold of the hard threshold function. The significance of the threshold is not only for signal denoising, but also for data compression to improve data transmission efficiency.
(3) Wavelet reconstruction: the wavelet reconstruction of the signal is calculated from the high frequency coefficients of each layer and the low frequency coefficients of the last layer.
(4) Identification of the best wavelet function: two indicators, root mean square error (RMSE) and signal-to-noise ratio (SNR), are used to evaluate the noise reduction effect of each wavelet transform function so as to determine the wavelet function with the best noise reduction effect for each feature of the sample.

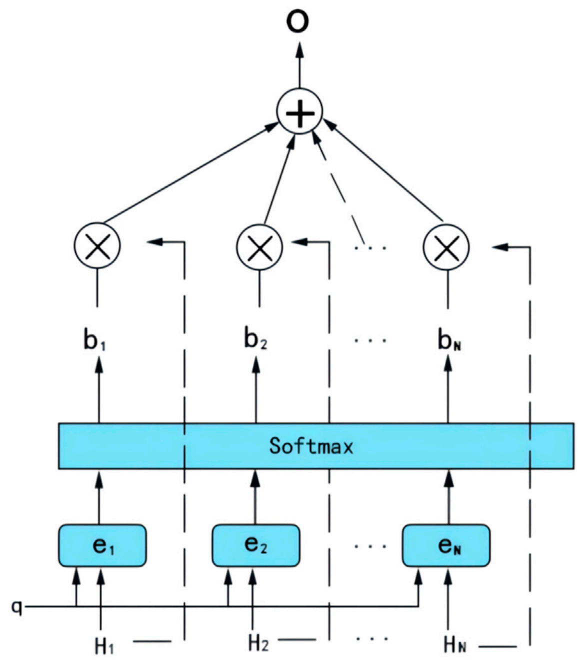

FIGURE 1
Attention mechanism based on the time sequence.

2.2 Attention mechanism

Despite the good performance of GRU in processing long time series, it does not discriminate the information of different time steps of long time series, and hence it can possibly overlook information in some key nodes of the time sequence that may affect the forecasting result. Therefore, the time sequence-based attention mechanism can highlight the impact of different nodes on the wind power and hence improve the model's performance.

The attention mechanism in the time sequence is the summation of weights of hidden-layer vectors output from the GRU network, where the weight reflects the impact of each time node on the forecast result. Figure 1 shows the attention mechanism, where there are N time steps, $H_1, H_2, \ldots, H_N$ represent the hidden state value of each time step, and q is assumed to be the output of the last hidden layer H_N.

The similarity score e_i between H_N and the output of hidden layer of each time step H_i is calculated:

$$e_i = Dot\,(H_i, H_N]). \tag{1}$$

The importance of each time series node to the prediction result is different. Therefore, the state value of the hidden layer at the i-th time step and the state value of the final N-th time step are used to perform the dot product operation. A larger the result of the dot product operation indicates a stronger association between the time series node and the final predicted value.

Then, the Softmax function is employed for normalization to calculate the focus probability b_i of the input sequence at the i-th time step:

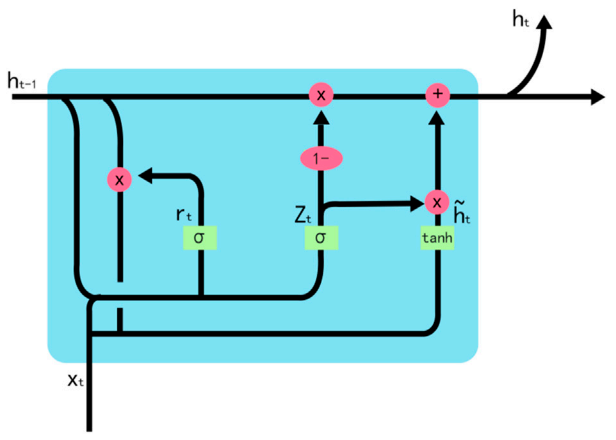

FIGURE 2
GRU neuron structure model.

$$b_i = e_i \Big/ \left(\sum_{j=1}^{N} e_j\right). \tag{2}$$

Last, the attention weight b_i is multiplied by the corresponding hidden state value to obtain the output vector O of the attention layer:

$$C = \sum_{j=1}^{N} b_j * H_j. \tag{3}$$

The vector O is transferred to the fully-connected layer of the model to reach the final forecasting result.

2.3 BiGRU model

2.3.1 GRU model

The recurrent neural network (RNN) can create connections, i.e., short-term memories, between adjacent samples in a time sequence. When the input sequence is long, however, the problem of the vanishing gradient emerges, the long-distance dependence relations cannot be learned.

As a variant of RNN, the long short-term memory (LSTM) model improves the RNN by introducing selective memory and unit gates. LSTM solves the problem of the vanishing gradient that haunts RNNs and can learn long-term dependence relations in the sample data. Non-etheless, the LSTM network has complex structures and lots of parameters.

The GRU model is an improved variant of LSTM, with update gates and reset gates. Compared with LSTM, the GRU has less parameters and a more simplistic structure, which allows the parameters to converge quicklier and reduces the risks of overfitting. Figure 2 shows the GRU neuron structure model.

The update gate in the GRU is defined as follows:

$$z_t = \sigma\left(W_z * [x_t, h_{t-1}]\right), \tag{4}$$

where x_t is the input vector of the t-th time step; W_z is the weight matrix of the update gate; and h_{t-1} is the output of the previous time step. The gated signal of the update gate is within 0 and 1, and a value closer to 1 indicates more past information being memorized.

The reset gate is defined as follows:

$$r_t = \sigma\left(W_r * [x_t, h_{t-1}]\right), \tag{5}$$

where W_r is the reset weight matrix. The reset gate is used to control the neglect of information in the previous time point. The obtained information after resetting is h'_{t-1}:

$$h'_{t-1} = h_{t-1} \otimes r_t. \tag{6}$$

Then, the current cell state $\tilde{h}_t$ is calculated. The current cell state means selective memorization of the screened information and the current input, where ⊗ means multiplying the corresponding positions in two matrices or vectors, tanh is the activation function, and W is the weight:

$$\tilde{h}_t = \tanh\ \left(W * [x_t, h'_{t-1}\right]. \tag{7}$$

The current output is h_t, and the vector will retain the current cell information and transfer it to the next cell:

$$h_t = (1 - z_t) \otimes h_{t-1} + z_t \otimes \tilde{h}_t. \tag{8}$$

The final output of the current cell is:

$$y_t = \sigma\left(W_0 * h_t\right), \tag{9}$$

where W_0 is the weight matrix.

2.3.2 BiGRU model

In a conventional GRU, information in the time sequence is transferred in a forward direction, the information far away from the current sequence suffers substantial attenuation, and the time-series information in the context is not considered. In a BiGRU model, two GRU running in opposite directions are trained (Lu and Duan, 2017). A BiGRU model combines two single-directional GRU, and the model output is determined by these two GRU. If the output of the forward GRU is $\overrightarrow{h_t}$, and the output of the backward GRU is $\overleftarrow{h_t}$, then the output of the BiGRU is as follows:

$$h_t = \overrightarrow{h_t} \oplus \overleftarrow{h_t} \tag{10}$$

Figure 3 shows the structure of a BiGRU model, in which $\{h_1 \rightarrow h_2 \rightarrow \ldots \rightarrow h_n\}$ represents the hidden state sequence produced by the forward GRU, whereas $\{h_n \rightarrow \ldots h_2 \rightarrow\rightarrow h_1\}$ is the hidden state sequence generated by the backward GRU.

2.4 Temporal convolutional neural networks

Bai et al. (Bai et al., 2018) proposed the temporal convolutional network (TCN) adding causal convolution and dilated convolution and using residual connections between each network layer to extract sequence features while avoiding gradient disappearance or explosion. A temporal convolutional network is essentially a deformation of one-dimensional convolution, which can be used for prediction of both temporal and textual data, and can achieve better results than recurrent neural networks for some tasks. Its layered structure of TCN is shown in Figure 4.

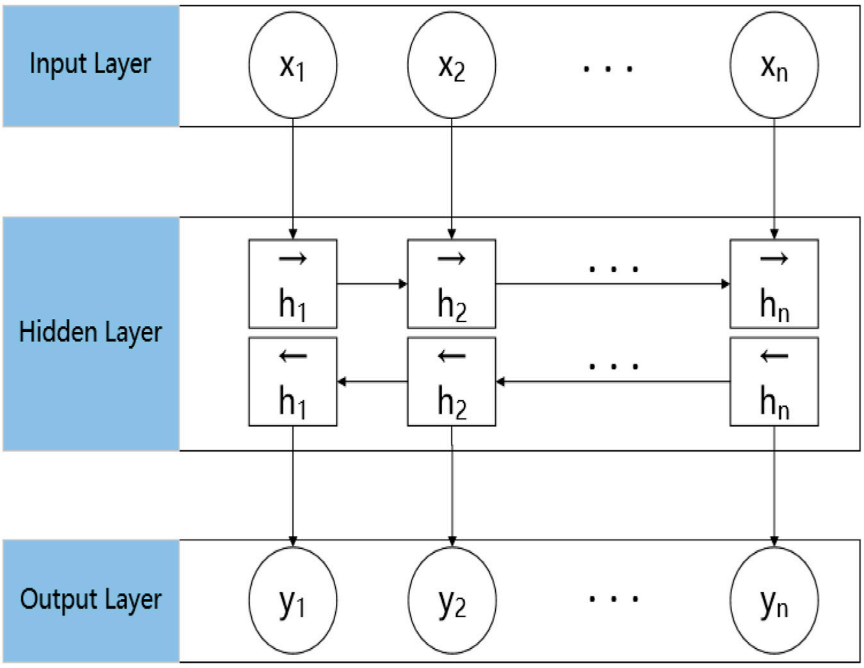

FIGURE 3
Structure of a BiGRU model.

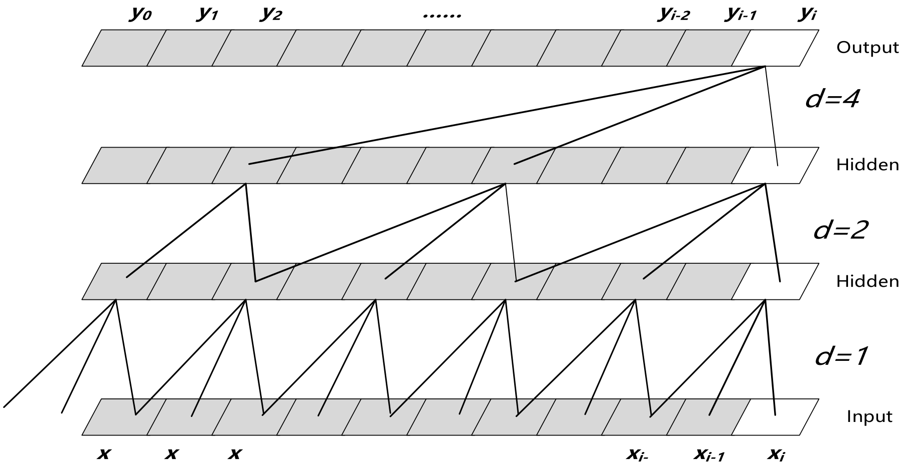

FIGURE 4
TCN network structure.

In Figure 4, x_t indicates the input temporal data, y_t indicates the predicted values, and d indicates the size of the voids for the dilated convolution of each layer. The temporal convolutional network has two new operations compared with the ordinary 1-D convolutional network.

2.4.1 Causal convolution

The causal convolution strictly requires that only the information before the current moment to be predicted can be used to predict the current value, i.e., the information of the current moment is calculated based on $x_1 \ldots x_{t-1}$ and the current moment input x_t, which is calculated as follows.

$$P(x) = \prod_{t=1}^{T} p(x_t|x_1, x_2, \ldots x_{t-1}). \tag{11}$$

This ensures that information after the current moment is not involved in the calculation, and the historical information is not missed as in traditional CNN networks. Thus, the prediction of the temporal data is improved.

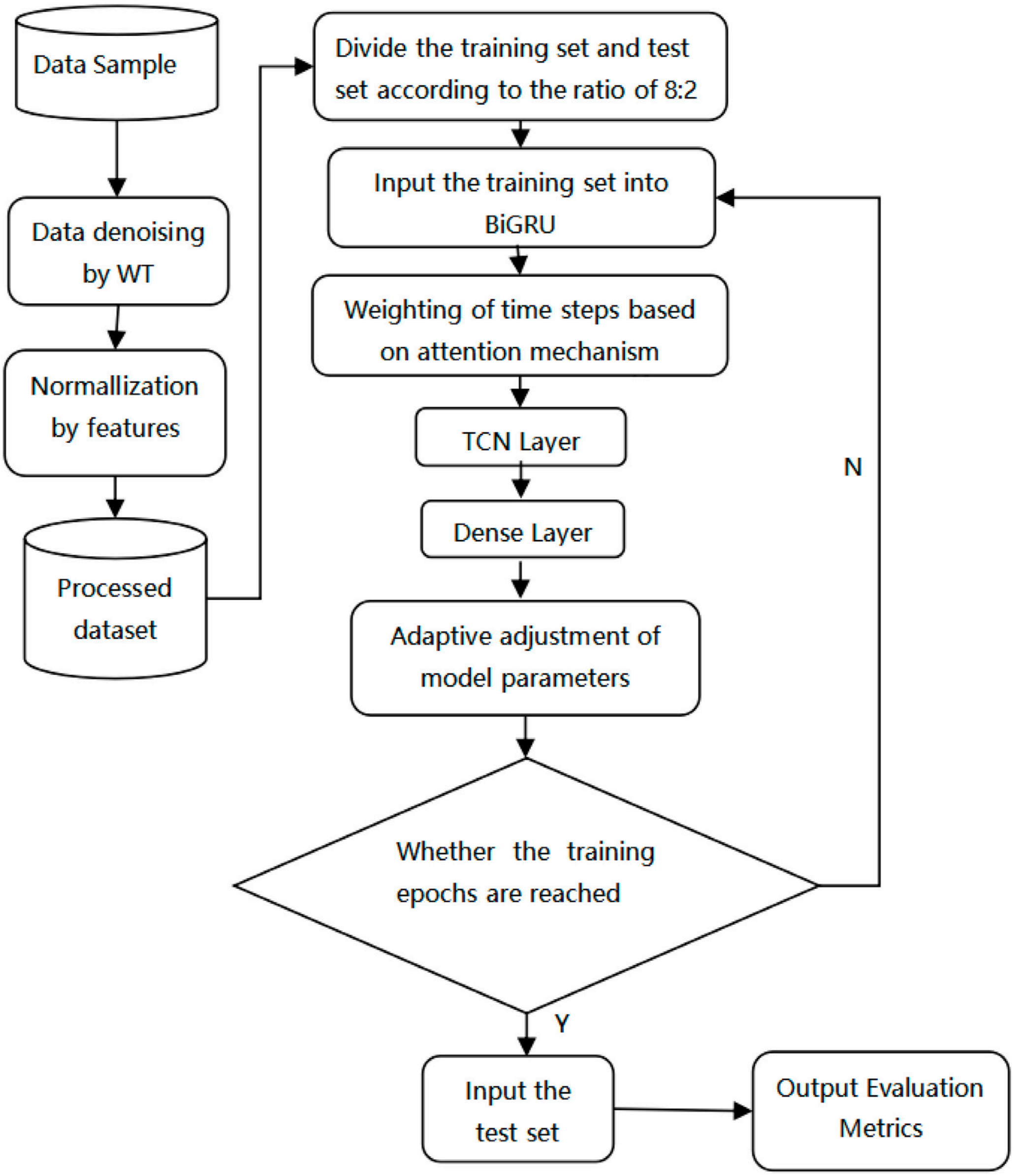

FIGURE 5
Workflow of our WT-BiGRU-Attention-TCN model.

2.4.2 Dilated convolution

Dilated convolution is also called null convolution. In order to increase the perceptual field of convolution, it is necessary to increase the number of layers or the size of a very large filter, which is also a problem of causal convolution. Dilated convolution, on the other hand, expands the field of perception by skipping some of the inputs, which is equivalent to adding d zeros (d is the number of holes) between the elements of the convolution kernel, disguisedly expanding the size of the convolution kernel. The size of the convolution kernel after adding the dilation convolution is:

$$f_{k\_d} = (d-l) * (f_k - l) + f_k, \tag{12}$$

where f_k denotes the convolutional kernel size of the current layer. Since it can be computed in parallel, the computational efficiency of the model is lower than that of an ordinary convolutional network.

In addition, in order to make the sensory field increase and learn text features of larger lengths, the number of network layers is increased by expanding the convolution. However, an excessive increase in the number of network layers may incur the problem of gradient disappearance, and to solve this problem, residual links are introduced in the network structure.

2.5 WT-BiGRU-Attention-TCN model

Figure 5 shows the workflow of the WT-BiGRU-Attention-TCN model proposed in the present work.

TABLE 1 The hierarchical structure and parameter information of our proposed model.

Layer (type)		Output shape	Param	Connected to
input_1 (InputLayer)		[(None, 8, 3)]	0	
bidirectional(Bidirectional)		(None, 8, 128)	26,496	input_1[0][0]
Attention Layer	permute (Permute)	(None, 128, 8)	0	bidirectional[0][0]
	dense (Dense)	(None, 128, 8)	72	permute[0][0]
	permute_1 (Permute)	(None, 8, 128)	0	dense[0][0]
	multiply (Multiply)	(None, 8, 128)	0	bidirectional[0][0],permute_1[0][0]
tcn (TCN)		(None, 8, 32)	35,232	multiply[0][0]
flatten (Flatten)		(None, 256)	0	tcn[0][0]
dense_1 (Dense)		(None, 1)	257	flatten[0][0]

TABLE 2 Descriptive indicators for sample data.

	DIR (degree)	WS (m/s)	POWER (MW)
Mean	169.13	7.02	0.46
Maximum	360.00	31.88	17.23
Minimum	0.00	0.35	0.00
Standard deviation	99.87	3.12	0.59
Coefficient of variation	44.51%	59.05%	128.26%

The proposed model is applied to wind power forecasting. The four methods (WT, BiGRU, Attention, TCN) in the model are used to solve problems at different stages of prediction: the wavelet transform is mainly used for data denoising at the data cleaning stage, while the other three methods are related to temporal feature extraction, including contextual feature extraction, feature weight calculation, and higher-level feature capturing. The methods are related by the data flow to form the framework of our model. The specific working process of the model is described below. First, the WT method is employed to denoise the dataset, and all sample features are normalized. Second, the BiGRU model is used to extract forward and backward features of the time-sequence data. Third, the weight of output information at each historical time sequence node is calculated by the time-sequence attention layer. Then, the hidden state output of the current state after adjustment is calculated based on the weight. Then, the TCN is used to obtain higher-level temporal features through causal and dilation convolution. Finally, the hidden state outputs by the TCN layer are input to the fully connected layer to obtain the forecasting result. The hierarchical structure and parameters of the model are shown in Table 1.

The input layer of the proposed model has a data dimension of (8,3) for each batch, i.e., the time step is 8 and the number of sample features is 3. The input data are combined by the GRU in both forward and backward propagation directions of the bidirectional layer, and the features learned by the two one-way GRU are stitched together to generate the set of vectors as the input of the attention layer. The attention layer calculates the generated weight vector for each time step and obtains the output of the attention layer by multiplying the weight vector with the output vector of the BiGRU layer. The vector generated by the attention layer is input to the TCN layer, and the field-of-perception size of the convolution is expanded to extract higher-level features by setting multiple expansion and causal convolution layers. The TCN output vector is subjected to the flatten operation to obtain the vector C. The vector C is then passed through the fully connected layer to obtain the value of the predicted wind power.

3 Experiment and analysis

3.1 Sample data

The wind power data used here are from the Galicia Wind Power Plant in northwestern Spain. A total of 52,123 pieces of valid data (from 1 January 2016 to 31 December 2016) were collected, with a sampling interval of 10 min. The features include meteorological indicators like wind speed and wind direction. Table 2 shows the specifics of the collected data, where WS represents the wind speed, DIR represents the wind direction, POWER represents the wind power, which is the target forecasting feature (the same applies to other tables and figures throughout this article).

As Table 2 shows, the sample data consists of three features. As these features have different dimensions and are substantially different from each other, normalization is required in the data preprocessing stage. The coefficient of variation of the feature "POWER" reaches 128.26%, which means large fluctuations of the wind power with time.

3.2 Data preprocessing

Data preprocessing mainly includes normalization of sample data and data denoising based on wavelet transform.

3.2.1 Data normalization

As the features of the data, including wind speed, wind direction and power, have different dimensions and show considerable

TABLE 3 Denoising effects of the three feature variables by different wavelet functions.

Feature variables	Evaluation indicators	coif5	sym10	db8
WS	SNR/db	27.085	27.304	25.126
	RMSE	0.15	0.146	0.187
DIR	SNR/db	24.852	23.573	23.344
	RMSE	4.466	5.162	5.285
POWER	SNR/db	27.215	29.263	26.976
	RMSE	28.345	22.419	28.982

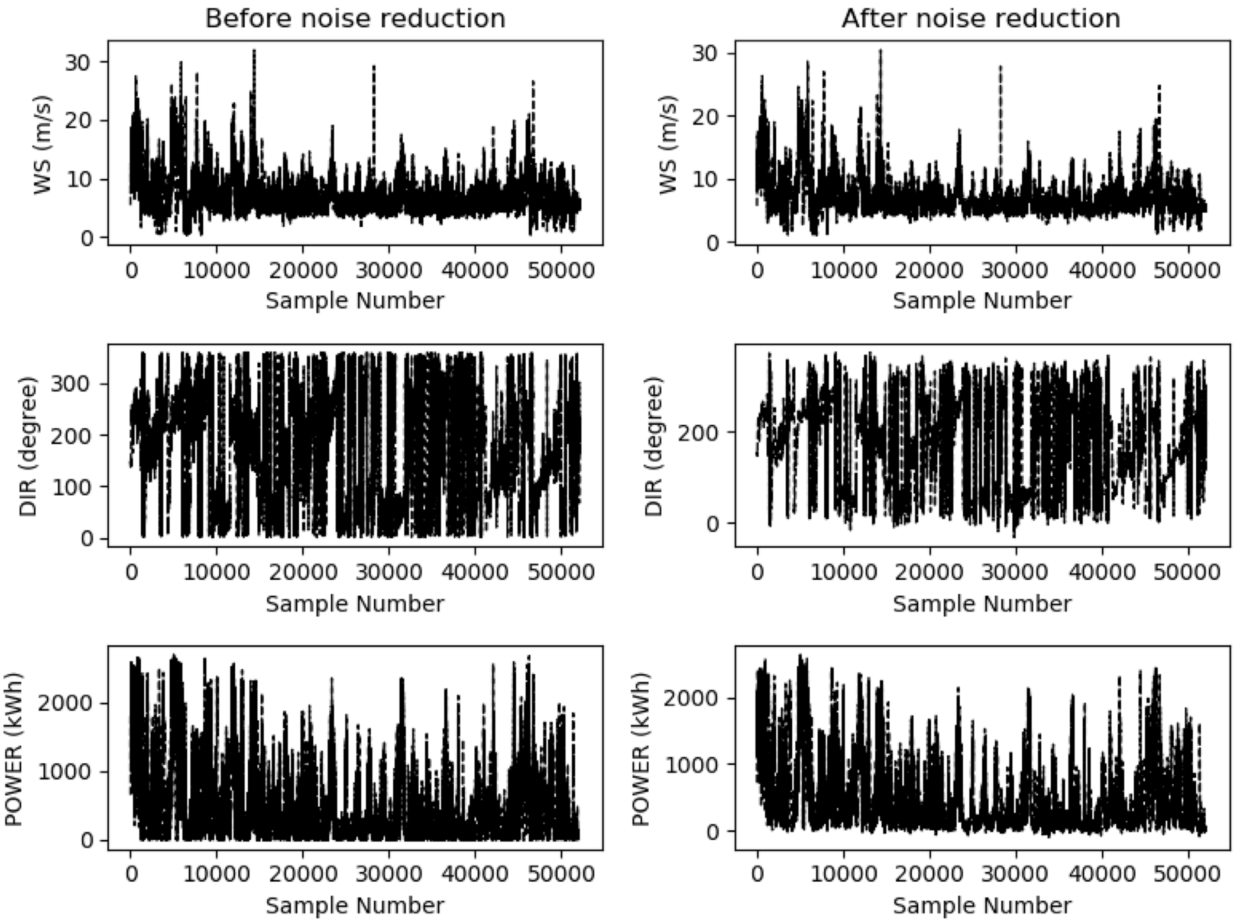

FIGURE 6
Comparison of the three feature variables before and after denoising.

differences in their range of value, normalization was performed to preclude the impact of the differences on the forecast result. Specifically, the values of the features were adjusted to a given range by min-max normalization, and the feature values were converted into a range of [0, 1]. The equation for min-max normalization is as follows:

$$x_t' = \frac{(x_t - x_{min})}{(x_{max} - x_{min})}, \tag{13}$$

where x_{max} and x_{min} represent the maximum and the minimum of the same feature; x_t represents the sample input data and x_t' represents the data after normalization.

3.2.2 Data denoising

There are inevitably noises in the sample data of wind power because of system error, random error, or human error, making it is imperative to perform data denoising. In the present work, the wavelet soft-thresholding method was employed. Specifically, with the valid information in the sample maintained, the wavelet decomposition was performed on the sample dataset, and thresholding was used to process the decomposed wavelet coefficient; then, wavelet reconstruction of the signals was performed to reduce the noise. The layers of the wavelet decomposition were set at 3, the global soft-thresholding was adopted, with a threshold set at 0.004. Three wavelet functions were employed to denoise the sample data. Table 3 shows denoising effects of the three feature variables by different wavelet functions.

By the two evaluation indicators—SNR and RMSE, the most suitable denoising wavelet function for each feature variable was identified. Specifically, the function that reaches a higher SNR and a smaller RMSE would be selected. Finally, the appropriate wavelet function was selected for each feature: the sym10 function for WS and POWER, and the coif5 function for DIR.

Each feature variable was denoised by the selected wavelet functions. Figure 6 compares the curves of the three features before and after denoising.

As Figure 6 shows, the curves of denoised features have a high fitting precision with the curves of the original signals, which manifests the good smoothing effect of WT-based denoising. The denoising worked particularly well on the two features, “wind speed” and “power, which showed substantial fluctuations before denoising. Denoising has improved the SNR and reduced the noises of these two features, achieving a good smoothing effect on their curves, which alleviated the impact of abnormal values on the forecasting accuracy.

3.3 Model evaluation indicators

The sample data after data processing were transferred to the attention-based BiGRU network for model training. The GRU model was optimized based on the Adam algorithm (Kingma and Ba, 2014) by using an adaptive learning rate to effectively update the network weights. The Adam algorithm combines the advantages of Adagrad in dealing with sparse gradients and RMSProp in dealing with non-stationary targets, and calculates different adaptive learning rates for different parameters.

To measure the deviation between the predicted value and the actual value, we used root mean square error (RMSE) as the performance evaluation index of wind power forecasting. The root mean square error is the arithmetic square root of the mean square error (MSE). The calculation formula of the RMSE is shown in Eq. 14, where y_i is the true value, and p_i is the predicted value.

$$\mathrm{RMSE} = \sqrt{\frac{1}{N}\sum\nolimits_{i=1}^{N}\left(y_i - p_i\right)^2}. \tag{14}$$

Two evaluation indicators, the mean absolute percentage error (MAPE) and R^2, were employed to assess the model’s forecast precision and fitting effect. MAPE indicates the absolute percentage errors of forecasts, and the closer the MAPE is to 0, the more accurate the model is. MAPE can be obtained by Eq. 15:

$$\mathrm{MAPE} = \frac{1}{N}\sum\nolimits_{i=1}^{N}\frac{\left|y_i - \hat{y}_i\right|}{\left|y_i\right|}, \tag{15}$$

where $\hat{y}_i$ is the predicted value, and y_i is the actual value.

TABLE 4 Comparative experimental results of each model.

Models	RMSE	MAPE (%)	R^2	Time (s)
LSTM	0.111	41.299	0.938	1.57
GRU	0.115	40.374	0.935	1.37
WT-GRU	0.096	28.469	0.949	1.33
WT-BiGRU-Attention	0.069	20.838	0.973	2.38
WT-BiGRU-Attention-TCN	0.066	18.876	0.976	2.56

R^2, which is known as the goodness of fit, indicates the percentage of variations in the dependent variables caused by the changes in the independent variable. It describes the fitting effect of the model, and is within a range of [0, 1]. A larger R^2 indicates a better fitting effect. The coefficient of determination can be calculated by Eq. 16:

$$R^2 = 1 - \frac{\sum\nolimits_{i=1}^{N}\left(y_i - \hat{y}_i\right)^2}{\sum\nolimits_{i=1}^{N}\left(y_i - \bar{y}_i\right)^2}, \tag{16}$$

where $\hat{y}_i$ is the predicted value, and y_i is the actual value.

3.4 Comparative experiments and discussions

Our proposed model was compared with LSTM, GRU, WT-GRU, WT-BiGRU-Attention models to verify its superiority. The settings of the experiment are as follows: the time step of GRU and LSTM was set to 8 and the number of hidden units was 64. The convolutional kernel size of the TCN network was 3, the number of convolutional layers was 6, the list of expansion coefficients was (Liu et al., 2015a; Liu et al., 2015b; Wang et al., 2018; Han et al., 2019a; Ma et al., 2019a; Liu et al., 2022b), the number of filters used in the convolutional layers was 32, and relu was used as the activation function. The batch size of the prediction model was set to 100 and the epoch time was set to 50. Eighty percent of the total sample data was used as the training set and the remaining 20% was used as the test set. Table 3 shows the experiment result.

As Table 4 shows, the difference between the GRU model and the LSTM model in the two evaluation metrics of RMSE and R^2 is very small, which indicates that the prediction accuracy and the fitting effect of both are comparable. The prediction time used for the two models in the test set in the experiments is 1.37 s and 1.57 s, respectively, which means that the GRU operation efficiency is improved by 12.74% compared to LSTM. The reason is that the GRU model is more simplified and has fewer parameters than the LSTM model, and the model runs more efficiently. Therefore, the GRU model is considered as the base model in the combined model of our work, which can be applied to larger-scale data prediction.

The comparison between WT-GRU and the conventional GRU model clearly shows that the model with a denoising module (WT-GRU) achieves a higher precision and accuracy than the one without. Specifically, WT-GRU reduces the RMSE by 0.019, which means it improves the forecasting precision by 16.52%; it achieves a significantly lower MAPE (29.49% lower than that

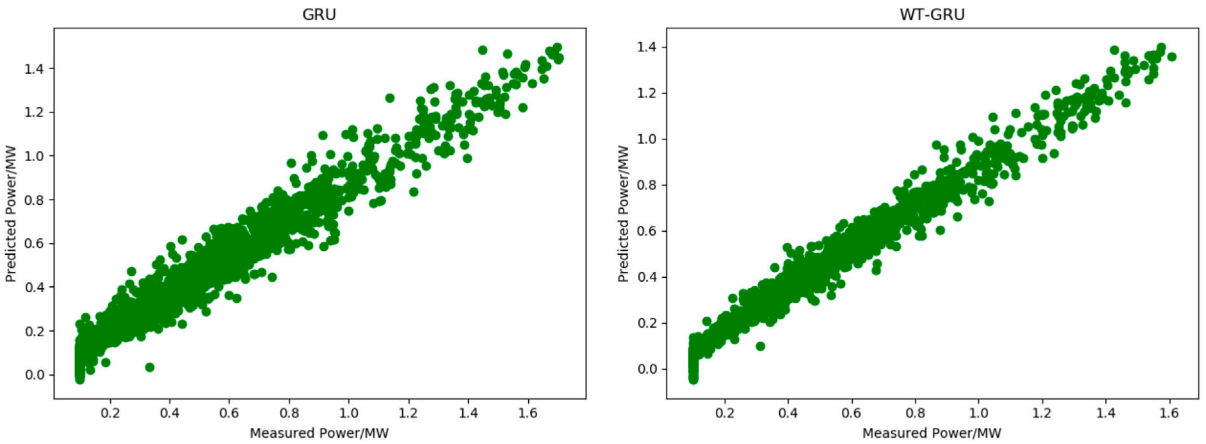

FIGURE 7
Fitting curves of true and predicted values of WT-GRU model and conventional GRU model.

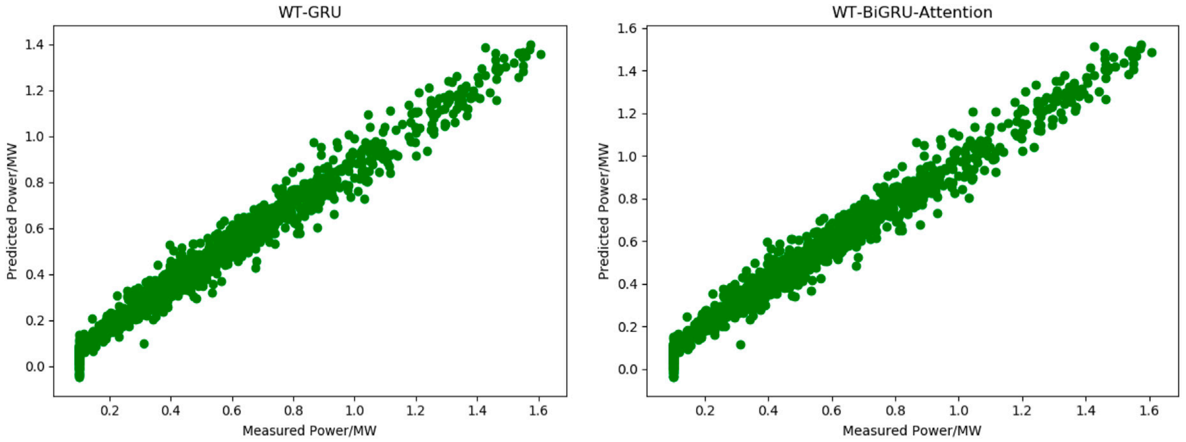

FIGURE 8
Fitting curves of measured and predicted power by WT-GRU model and WT-BiGRU-Attention model.

achieved by the conventional GRU), which suggests the WT-GRU model has substantially improved the forecasting accuracy. The WT-GRU model has also increased the R^2 from 0.935 to 0.949, suggesting that it has improved the fitting effect by 1.5%. Figure 7 displays the fitting effect of the two models.

As Figure 7 shows, after denoising, the curve of predicted power has a better fitting effect with the measured power curve, indicating that denoising can significantly improve the model's forecasting performance. Experiments show that there is a certain amount of noise data in the wind power generation data samples, which will affect the effect of the prediction model. It is necessary to de-noise the data through wavelet transform.

Compared with WT-GRU, the WT-BiGRU-Attention model achieves an RMSE that is 0.027 lower, which means a 28.13% increase in the precision of prediction. Moreover, it achieves an MAPE that is 7.63% smaller and reaches an R^2 of 0.973, which means it has also improved the fitting effect. Although the WT-BiGRU-Attention model takes 1.01 s more prediction time than the GRU model on the full test set, its overall performance and efficiency is better. Figure 8 shows the fitting effect of the curve of predicted power achieved by WT-GRU and WT-BiGRU-Attention with the curve of the measured power.

As shown in Figure 8, the WT-BiGRU-Attention achieves a better fitting effect than the WT-GRU. And according to the indicators in Table 4, we can find that the use of bi-directional GRU combined with temporal attention can improve the prediction accuracy of the traditional GRU model because bi-directional GRU is able to extract the forward and backward features of the sample data, and the attention mechanism enables the model to capture the features of key nodes in the time series and assign higher weights to these nodes, thus improving the prediction accuracy and the fitting effect of the model.

Figure 9 shows the fitting effect of forecasting power curves achieved by WT-BiGRU-Attention and our model with the measured power curve.

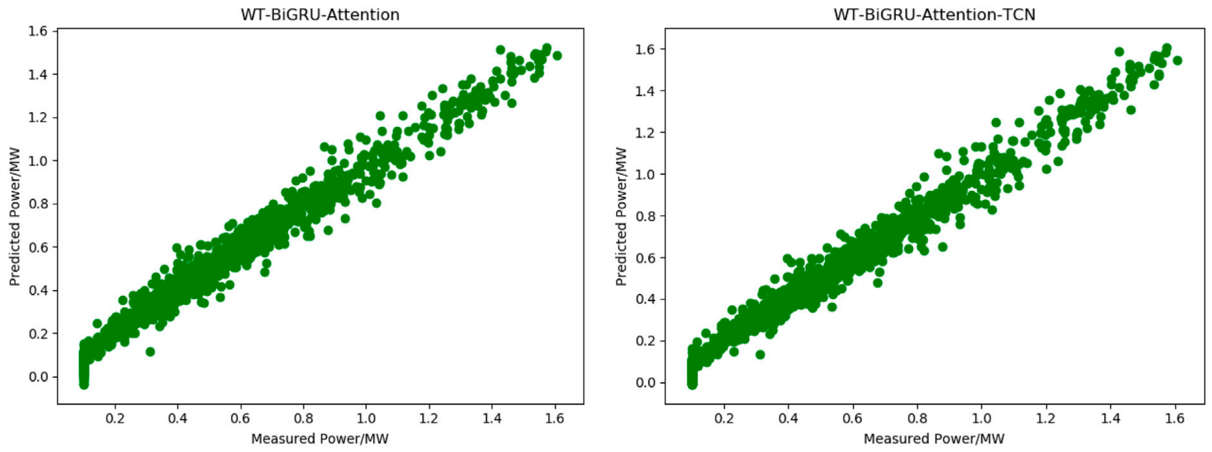

FIGURE 9
Fitting curves of measured and predicted power by WT-BiGRU-Attention and our model.

Figure 9 shows our model has further improved the fitting effect of the WT-BiGRU-Attention model. According to Table 4, though our model shares similar time for prediction to the WT-BiGRU-Attention model, it has reduced the RMSE by 4.35% and the MAPE by 9.42%, and improves the R^2 from 0.973 to 0.976. These statistics indicate that the TCN layer has further improved the accuracy of prediction. The TCN can make fullest of causal convolution and dilation convolution to obtain more higher-level temporal features, thus improving the model's performance. As Table 4 shows, our model has the best performance overall.

4 Conclusion

Wind power is characterized by random fluctuations and is susceptible to impacts from various factors. Based on these characteristics, a new method termed WT-BiGRU-Attention-TCN model is proposed in the present work for wind power prediction. Experiments were made to compare its performance with other models, and the following conclusions were reached.

(1) The GRU model shows little difference from the LSTM model in terms of the fitting effect and forecasting precision, and the prediction performance of LSTM is slightly higher. However, they are considerably different in the model training and forecasting efficiency: the GRU model reduces the running time by 15.45%, suggesting that the GRU model is more suitable to forecasting tasks with large quantities of data. Thus, the GRU model is used as the fundamental model in the combination of models in our proposed method.
(2) The model that incorporates the wavelet transform-based denoising technique (WT-GRU) achieves higher forecasting accuracy than the traditional GRU model. WT-GRU also reaches a higher coefficient of determination (R^2), indicating that introduction of the denoising module can significantly improve the model's forecasting performance.
(3) The bidirectional GRU can extract both forward and backward features in the time sequence, thus outperforming the conventional GRU model. Moreover, by incorporating the attention mechanism, the model can capture the information of key nodes in the historical time steps and hence achieve higher precision.
(4) The temporal convolutional network (TCN) is used to obtain more higher-level temporal features through causal and dilation convolution. At the same time, its residual link structure is used to avoid the problem of gradient disappearance that may be caused by the excessive increase in the number of network layers. Thus, the TCN network can further improve the accuracy of the model.

In conclusion, with all evaluation indicators considered, our WT-BiGRU-Attention-TCN model performs best among all models compared in the present work. The model provides a new solution to high-precision forecasting of wind power generation.

Data availability statement

The original contributions presented in the study are included in the article/Supplementary Material, further inquiries can be directed to the corresponding author.

Author contributions

Conceptualization, DC; Methodology, DC; Software, DC; Validation, DC; Investigation, DC; Writing—original draft preparation, DC; Writing—review and editing, DC; Visualization, CY; Supervision, DC. All authors have read and agreed to the published version of the manuscript.

Conflict of interest

The authors declare that the research was conducted in the absence of any commercial or financial relationships that could be construed as a potential conflict of interest.

Publisher's note

References

Bai, S., Kolter, J. Z., and Koltun, V. (2018). An empirical evaluation of generic convolutional and recurrent networks for sequence modeling. https://arxiv.org/abs/1803.01271, arXiv preprint arXiv: 1803. 01271.

Dang, D., Zhang, S., Ge, P., and Tian, X. (2019). Transformer fault diagnosis method based on improved quantum particle swarm optimization support vector machine. *J. Electr. Power Sci. Technol.* 34 (3), 6. CNKI:SUN:CSDL.0.2019-03-012.

Ding, M., Zhou, H., Xie, H., Wu, M., Nakanishi, Y., and Yokoyama, R. (2019). A gated recurrent unit neural networks based wind speed error correction model for short-term wind power forecasting. *Neurocomputing* 365 (Nov.6), 54–61. doi:10.1016/j.neucom.2019.07.058

Dong, X., Ning, X., Xu, J., Yu, L., Li, W., and Zhang, L. (2023). PFAS contamination: Pathway from communication to behavioral outcomes. *IEEE Trans. Comput. Soc. Syst.*, 1–13. doi:10.1080/10810730.2023.2193144

Duan, J., Wang, P., Ma, W., Tian, X., Liu, H., Cheng, Y., et al. (2021). Short-term wind power forecasting using the hybrid model of improved variational mode decomposition and correntropy long short -term memory neural network. *Energy* 214, 118980. doi:10.1016/j.energy.2020.118980

Haigesa, R., Wanga, Y. D., Ghoshrayb, A., and Roskillya, A. P. (2017). Forecasting electricity generation capacity in Malaysia: An auto regressive integrated moving average approach. *Energy Procedia* 105, 3471–3478. doi:10.1016/j.egypro.2017.03.795

Han, L., Jing, H., Zhang, R., and Gao, Z. (2019). Wind power forecast based on improved long short term memory network. *Energy* 189, 116300. doi:10.1016/j.energy.2019.116300

Han, Z., Jing, G., Zhang, Y., Bai, R., Guo, K., and Zhang, Y. (2019). A review of wind power forecasting methods and new trends. *Power Syst. Prot. Control* 47 (24), 10. CNKI:SUN:JDQW.0.2019-24-023.

Huang, X., Yu, H., Gong, X., and Liu, A. (2020). Wind power short-term prediction based on pso-ga-svm. *Electr. Eng.* 2020 (6), 4. CNKI:SUN:DGJY.0.2020-06-014.

Kingma, D., and Ba, J. (2014). Adam: a method for stochastic optimization. *Comput. Sci.* [Preprint]. doi:10.48550/arXiv.1412.6980

Korprasertsak, N., and Leephakpreeda, T. (2019). Robust short-term prediction of wind power generation under uncertainty via statistical interpretation of multiple forecasting models. *Energy* 180 (AUG.1), 387–397. doi:10.1016/j.energy.2019.05.101

Li, D., and Li, Y. (2021). Ultra short term wind power prediction based on Deep learning and error correction. *J. Sol. Energy* 42 (12), 200–205. doi:10.19912/j.0254-0096.tynxb.2019-1464

Li, L. (2007). The generation, development and application of wavelet analysis. *China Water Transp. Theor. Ed.* 5 (3), 96–98. CNKI:SUN:ZYUN.0.2007-03-044.

Li, L., and Ye, L. (2010). Short-term wind power prediction based on improved persistence method. *Trans. Chin. Soc. Agric. Eng.* 26 (012), 182–187. doi:10.3969/j.issn.1002-6819.2010.12.031

Liao, X., Wu, J., and Chen, C. (2022). Short-term wind power prediction model combining attention mechanism and lstm. *Comput. Eng.* 9, 048. doi:10.19678/j.issn.1000-3428.0062059

Liu, D., Wang, J., and Wang, H. (2015). Short-term wind speed forecasting based on spectral clustering and optimised echo state networks. *Renew. Energy* 78, 599–608. doi:10.1016/j.renene.2015.01.022

Liu, H., Tian, H. Q., and Li, Y. F. (2015). An emd-recursive arima method to predict wind speed for railway strong wind warning system. *J. Wind Eng. Industrial Aerodynamics* 141, 27–38. doi:10.1016/j.jweia.2015.02.004

Liu, H., and Zhang, Z. (2022). A bilateral branch learning paradigm for short term wind power prediction with data of multiple sampling resolutions. *J. Clean. Prod.* 380 (1). 134977. doi:10.1016/j.jclepro.2022.134977

Liu, X., Mo, Y., Wu, Z., and Yan, K. (2022). Hybrid deep learning model for ultra - short - term wind power prediction. *J. Overseas Chin. Univ. Nat. Sci. Ed.* 43 (5), 043.

Liu, X., Yang, L., and Zhang, Z. (2022). The attention-assisted ordinary differential equation networks for short-term probabilistic wind power predictions. *Appl. Energy* 324, 119794. doi:10.1016/j.apenergy.2022.119794

Liu, X., Zhou, J., and Qian, H. (2021). Short-term wind power forecasting by stacked recurrent neural networks with parametric sine activation function. *Electr. Power Syst. Res.* 192 (4), 107011. doi:10.1016/j.epsr.2020.107011

Lu, P., Ye, L., Pei, M., He, B., Tang, Y., Zhai, B., et al. (2021). Optimization of GRACE risk stratification by N-terminal pro-B-type natriuretic peptide combined with D-dimer in patients with non-ST-elevation myocardial infarction. *Proc. CSEE* 41 (17), 13–19. doi:10.1016/j.amjcard.2020.10.050

Lu, P., Ye, L., Zhong, W., Qu, Y., Zhai, B., Tang, Y., et al. (2020). A novel spatio-temporal wind power forecasting framework based on multi-output support vector machine and optimization strategy. *J. Clean. Prod.* 254, 119993. doi:10.1016/j.jclepro.2020.119993

Lu, R., and Duan, Z. (2017). "Bidirectional GRU for sound event detection," in *Detection and Classification of Acoustic Scenes and Events (DCASE)*, 1–3.

Ma, T., Wang, C., Peng, L., Guo, X., and Fu, Ming. (2019). Short term load forecasting of power system including demand response and deep structure multitasking learning. *Electr. Meas. Instrum.* 56 (16), 11. doi:10.19753/j.issn1001-1390.2019.016.009

Ma, W., Cheng, R., Shi, J., Hua, Dong., Sun, G., and Zhang, C. (2019). Affine interval power flow calculation considering wind farm model. *Guangdong Electr. Power* 32 (11), 10. doi:10.3969/j.issn.1007-290X.2019.011.004

Ning, X., Tian, W., He, F., Bai, X., Sun, L., and Li, W. (2023). Hyper-sausage coverage function neuron model and learning algorithm for image classification. *Pattern Recognit.* 136, 109216. doi:10.1016/j.patcog.2022.109216

Niu, Z., Yu, Z., Li, B., and Tang, W. (2018). Short-term wind power prediction model based on depth-gated circulation unit neural network. *Electr. Power Autom. Equip.* 38 (5), 7. doi:10.16081/j.issn.1006-6047.2018.05.005

Shahid, F., Zameer, A., and Muneeb, M. (2021). A novel genetic lstm model for wind power forecast. *Energy* 1, 120069. doi:10.1016/j.energy.2021.120069

Shao, Z., Gao, F., Zhang, Q., and Yang, S. (2015). Multivariate statistical and similarity measure based semiparametric modeling of the probability distribution: A novel approach to the case study of mid-long term electricity consumption forecasting in China. *Appl. Energy* 156 (OCT.15), 502–518. doi:10.1016/j.apenergy.2015.07.037

Sun, Y., Li, Z., Yu, X., Li, B., and Yang, M. (2020). Research on ultra-short-term wind power prediction considering source relevance. *IEEE Access* 8 (99), 147703–147710. doi:10.1109/ACCESS.2020.3012306

Torres, J. L., Garcia, A., Blas, M. D., and Francisco, A. D. (2005). Forecast of hourly average wind speed with arma models in navarre (Spain). *Sol. Energy* 79 (1), 65–77. doi:10.1016/j.solener.2004.09.013

Wang, T., Gao, J., Wang, Y., Shi, Z., Liu, T., Yang, B., et al. (2021). Research on wind power prediction based on improved empirical mode decomposition and support vector machine. *Electr. Meas. Instrum.* 58 (6), 6. doi:10.19753/j.issn1001-1390.2021.06.007

Wang, Y., Wang, Y., Wang, L., and Chang, Q. (2018). Optimization of short-term load prediction model of neural network based on improved Drosophila algorithm. *Electr. Meas. Instrum.* 55 (22), 7. doi:10.3969/j.issn.1001-1390.2018.22.003

Wu, J., Ding, M., and Zhang, J. (2018). Optimal allocation of wind farm energy storage capacity based on cloud model and k-means clustering. *Automation Electr. Power Syst.* 42 (24), 7. doi:10.7500/AEPS20180725007

Yang, M., and Zhou, Y. (2019). Ultra-short-term prediction of wind power accounting for wind farm states. *Chin. J. Electr. Eng.* 39 (5), 10. CNKI:SUN:ZGDC.0.2019-05-001.

Yu, R., Gao, J., Yu, M., Lu, W., Xu, T., Zhao, M., et al. (2018). Lstm-efg for wind power forecasting based on sequential correlation features. *Future Gener. Comput. Syst.* 93, 33–42. doi:10.1016/j.future.2018.09.054

Zhao, H., and Guo, S. (2016). An optimized grey model for annual power load forecasting. *Energy* 107 (jul.15), 272–286. doi:10.1016/j.energy.2016.04.009

Zhao, R., and Ding, Y. (2020). Short-term wind power prediction based on meemd-kelm. *Electr. Meas. Instrum* 57 (21), 7. doi:10.19753/j.issn1001-1390.2020.21.013

Zn, A., Zy, A., Wt, A., Qw, A., and Mrb, C. Wind power forecasting using attention-based gated recurrent unit network. *Energy* 196. 117081. doi:10.1016/j.energy.2020.117081

Frontiers in Energy Research
TYPE Original Research
PUBLISHED 25 April 2023
DOI 10.3389/fenrg.2023.1187620

OPEN ACCESS

EDITED BY
Xin Ning,
Chinese Academy of Sciences, China

REVIEWED BY
Gabriel Gomes,
State University of Campinas, Brazil
Yao Liang,
City University of Hong Kong, Hong Kong, SAR China
Yassine Himeur,
Qatar University, Qatar

*CORRESPONDENCE
Shanshan Wang,
✉ ryh513121837@outlook.com

RECEIVED 16 March 2023
ACCEPTED 13 April 2023
PUBLISHED 25 April 2023

CITATION
Ren Y, Sun H, Wang S, Zhao B, Xu S, Liu M and Lian P (2023), Study on the characteristic of the grounding fault on the cascaded midpoint side of the hybrid cascaded HVDC system.
Front. Energy Res. 11:1187620.
doi: 10.3389/fenrg.2023.1187620

Study on the characteristic of the grounding fault on the cascaded midpoint side of the hybrid cascaded HVDC system

Yonghao Ren[1], Huadong Sun[2], Shanshan Wang[1]*, Bing Zhao[1], Shiyun Xu[1], Min Liu[1] and Panjie Lian[1]

[1]China Electric Power Research Institute Co. Ltd, Beijing, China, [2]State Key Laboratory of Power Grid Safety and Energy Conservation, Beijing, China

The hybrid cascaded high-voltage direct current (HVDC) system combines the system support capabilities of the modular multilevel converter (MMC) with the capacity of the line-mutated converter's (LCC's) advantage of high-power transmission. The HVDC system is among the key elements of a smart grid where artificial intelligence is applied extensively. However, the characteristics of a grounding fault on the cascaded midpoint side of a hybrid cascaded HVDC system remain unclear. This study analyzes fault characteristics and the impact of faults using analytical methods. First, the topology and basic control strategy are presented. The fault response process is then analyzed by dividing systems into the MMC and LCC parts at the inverter side. A separate theoretical analysis is also conducted. In addition, the impacts of faults on HVDC and alternating current (AC) networks are analyzed. Therefore, even after the HVDC system is disabled, the AC network can supply fault currents using an antiparallel diode. The simulation results show that the proposed analysis method is feasible, and the theoretical analysis is correct. The proposed method can provide a theoretical basis for the selection of equipment for HVDC systems and smart grid construction.

KEYWORDS

smart grid, artificial intelligence, hybrid cascaded HVDC system, cascaded midpoint fault, fault characteristics, Ac low voltage, fault response

1 Introduction

By examining and interpreting power grid data, artificial intelligence (AI) technology can enhance the intelligent management of power grids, thus reducing energy consumption and environmental pollution (Cai et al., 2022; Tang et al., 2022; Wu et al., 2023). The hybrid-cascaded high-voltage direct current (HVDC) transmission technique can effectively reduce power transmission losses, and a combination of the two can boost further the energy utilization efficiency and intelligence of the power grid (Tang et al., 2021; Dong et al., 2023; Liang et al., 2023). In China, the energy distribution is opposite with respect to the center, with bounteous renewable energy sources in the west and developed economies and high-energy demand in the east, and HVDC has numerous potential applications as an important means of large-scale energy transfer. Using the Yangtze Delta area in eastern China as an example, 12-circuit line-mutated converter-based HVDC (LCC-HVDC) landings are located in this area (Zhang et al., 2007). With the commissioning of multiple new LCC-HVDCs, the power grid strength in the Yangtze Delta area of China will be reduced further, thus leading to an increased risk of commutation failure in LCC-HVDC and a gradual reduction in grid voltage stability, which in turn limits the scale of LCC-HVDC development (Shao and Tang, 2017). Following the rapid development of modular multilevel converter-based HVDC (MMC-HVDC) in recent years, the requirements for the recipient grid strength are low, and they have a certain fault ride-through capability; however, its rated voltage and transmission power are not as good as LCC-HVDC, and MMC-HVDC construction costs are higher compared with LCC-HVDC, thus limiting its application scale (Zhu et al., 2021; Saeedifard and Iravani, 2010; Swedesford et al., 2010). Therefore, hybrid HVDC technology, which considers the scale of the AC network as well as the system characteristics and combines the respective benefits of LCC-HVDC and MMC-HVDC, has become a novel technology used to solve the aforementioned problems and a major research focus in the field of HVDC.

The hybrid cascaded HVDC system forms a hybrid transport unit by the series–parallel connection of the LCC and MMCs. The various series–parallel connections of LCCs and MMCs and the location of the hybrid transport unit constitute different topologies of hybrid cascaded HVDC systems, which can be adapted for different applications (Zhao and Iravani, 1994; Torres-Olguin et al., 2012; Haleem et al., 2018). An HVDC system (with an LCC at the rectifier side) and multiple MMCs in parallel (with the LCC in series topology at the inverter side, which has superior DC fault ride-through capability), has been proposed, while the MMCs at the inverter side can provide a certain voltage support capability (Liu et al., 2018; Meng et al., 2021; Qahraman and Gole, 2005). The topology proposed above was used in the ±800 kV Baihetan–Jiangsu HVDC project in China, and the hybrid cascaded HVDC system based on this topology was also evaluated in this study. Related scholars have studied hybrid cascaded HVDC systems using this topology. A coordinated control strategy based on the dynamic limiter, diodes and LCC-MMC active orders is proposed was suggested to improve the AC side voltage stability (Zhao and Tao, 2021). A supplementary coupling mitigation control strategy was suggested to enhance the stability of a hybrid cascaded HVDC system connected to a weak grid (He et al., 2021). A suppression strategy based on fuzzy clustering and an identification method were proposed to repress the DC overcurrent caused by LCC commutation failure at the inverter side (Guo et al., 2021). When an alternating current (AC) short-line fault occurs in the MMC of the hybrid cascaded HVDC system, the imbalanced power between the AC and DC sides of the MMCs will cause capacitor charging of the submodule, which may lead to the blocking of the MMCs. To address the above problems, (Niu et al., 2020), analyzed the mechanism of the MMC submodule's overvoltage caused by an AC fault and proposed a fault-ride-through strategy based on the fast response of the DC current on the rectifier side. In addition, (Kang et al., 2022), presented a novel method to control the decrease of the adaptive DC voltage that can fully absorb imbalanced power. In the Baihetan–Jiangsu HVDC project in China, a controllable and adaptive energy absorption device was used to absorb surplus power from the DC side to increase the system transient stability (Liu et al., 2021). In addition, considering the MMC overcurrent in DC fault conditions, (Yang et al., 2019), proposed a recovery control strategy for the power regulation of a fixed-active-power MMC. Related studies that have been conducted for hybrid cascaded HVDC systems focused on the solution of the operational characteristics and fault ride-through problems when AC short-line faults occur.

Most previous studies on internal HVDC system faults were conducted on MMC-HVDC: when a short-circuit fault occurs in its DC line, the submodule capacitor discharge and other circumstances will cause a rapid fault-surge current; thus, a reasonable solution for the fault current is needed to provide a basis for the electric design of submodule components in MMC-HVDC (Wang et al., 2011; Wang et al., 2011). When a fault occurs in the DC line of a hybrid cascaded HVDC system, the inverter-side LCC uses its back-blocking characteristics to isolate the fault current fed from the inverter side to the fault point, thus greatly reducing the impact on the HVDC system (Li et al., 2022; Xu et al., 2022). The Comparison of existing contributions and this paper is shown in Table 1. Related studies that have been conducted for hybrid cascaded HVDC systems focused on the solution of the operational characteristics and fault ride-through problems when AC and DC line faults occur.

The topology of the hybrid cascaded HVDC system shows that the high- and low-end connection line parts of the cascaded side include an area with a negative outlet for the DC filter, a negative outlet for the bypass switch of the high-voltage valve, and a positive outlet for the parallel bus and bypass switch of the low-voltage valve. This area is unique to hybrid cascaded HVDC system by its topology and does not exist in LCC-HVDC and MMC-HVDC. Although the length of the line in this area is shorter than that of the DC line, there are numerous connection parts and the structure is more complex. The lines in this area are mostly arranged in the valve hall, and a general fault occurs, which is a permanent grounding fault. Therefore, it is necessary to carry out a detailed theoretical analysis of fault in this area. Based on the fault section and mode mentioned above, this study proposes a detailed theoretical analysis of the fault responses of the cascaded-side MMC and LCC, divides the fault current evolution process into two steps before and after blocking, and proposes a mathematical calculation method for the fault current. Using an advanced digital power system simulator (ADPSS) as a base, an electromechanical–electromagnetic transient hybrid simulation with a hybrid cascaded HVDC system model was constructed (Tian et al., 2016), and the precision of the theoretical calculation was confirmed based on simulation experiments. Based on the simulation results, the dynamic characteristics of the receiving-end system in fault conditions were analyzed to provide a theoretical basis for equipment selection and power system planning of the hybrid cascaded HVDC system. The conclusions of this study provide important support for the construction of smart grids.

2 Hybrid cascaded HVDC system topology and steady-state control strategy

2.1 System topology

The hybrid cascaded HVDC system adopts a symmetrical wiring form for the positive and negative poles with symmetrical positive and negative structures and consistent parameters; the monopole topology is shown in Figure 1. In Figure 1, U_{dr} and U_{di} are the rectifier- and inverter-side DC voltages, U_{diL} and U_{diM} are the high- and low-end DC voltages of the high- and low-end voltages at the inverter side,

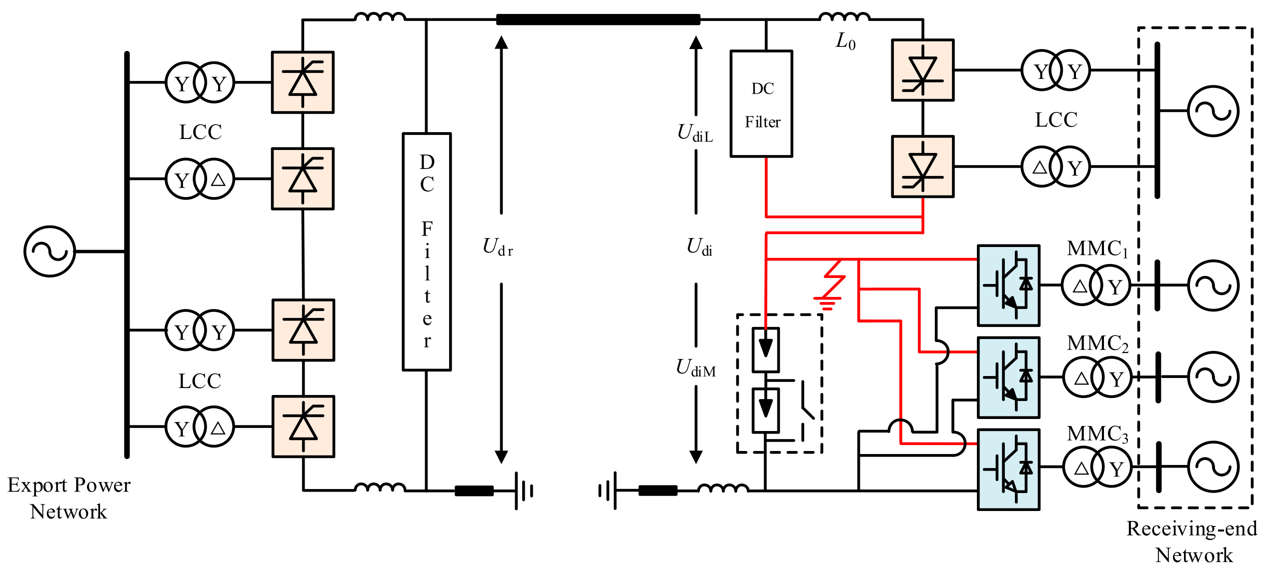

FIGURE 1
Single-pole structure of the hybrid-cascaded high-voltage direct current (HVDC) system.

TABLE 1 Comparison of existing contributions.

Object	AC fault	DC line fault	Cascaded side fault
Guo et al. (2021)	√		
Zhao and Tao (2021)	√		
Kang et al. (2022)	√		
Yang et al. (2019)	√		
Xu et al. (2022)		√	
Li et al. (2021)		√	
This paper			√

respectively; and L_0 is the smoothing reactor. The rectifier side is composed of two groups of 12-pulse LCCs in series, and the inverter side is composed of LCC and MMCs in series, where the high-voltage valve comprises one group of 12-pulse LCC and the low-voltage valve three parallel MMCs; these three parallel MMCs all adopt half-bridge structures, and the inverter side LCC and each parallel MMCs are associated with different buses of the equal AC network.

Meanwhile, to reduce the discharge current induced by a DC line short-circuit defect and to reduce the system's harmonic current, the HVDC system adopts the symmetrical arrangement principle of the pole and neutral lines and sets L_0 on the rectifier and inverter sides, respectively. Table 2 lists the primary parameters of the HVDC system.

2.2 System control strategy

The methods for both the positive and negative controls were the same in the hybrid cascaded HVDC system. A voltage-dependent current-order limiter (VDCOL), minimum trigger angle control, and constant DC current control were configured on the LCC at the rectifier side (Mao et al., 2021). Based on constant DC voltage control, the LCC on the inverter side is configured with a VDCOL, and it uses constant extinction angle and constant current control as standby controls. The corresponding control structure and switching principle are illustrated in Figure 2A. In Figure 2A, UdiLref and UdiL are the reference and instruction values of the DC voltage at the inverter side, respectively, Idcref and Idcf are the reference and instruction values of the DC current of the HVDC system, respectively, and γmin and γ are the reference and instruction values of the extinction angle at the inverter side, respectively.

The parallel MMCs on the inverter side use a DQ axis-based DC vector control approach, which has two control dimensions: one for active control, similar to controlling the active power or DC voltage, and the other for reactive control, similar to controlling the AC bus voltage or reactive power (Saeedifard and Iravani, 2010; Debnath et al., 2014). To guarantee the system's voltage stability, one of the three parallel MMCs which cooperates with the MMC at the inverter side is selected to adopt constant DC voltage control mode, the other MMCs adopt the control mode of constant active power, and Figure 2B displays the equivalent control block diagram. After determining the control strategies for the rectifier and inverter sides of the hybrid cascaded HVDC system, the static I–V characteristic curve can be obtained, as illustrated in Figure 3. The characteristics of the rectifier side consist of 1, 2, and 3 segments; among these, segment 1 is the minimum trigger angle control characteristic; usually, the minimum value of trigger angle α is taken as 5°; segment 2 is the constant DC current control characteristic, which is also the normal operational characteristic; and segment 3 is the control characteristic of the VDCOL because the low end of the inverter side is the MMC converter, its DC voltage retention

TABLE 2 Main parameters of the hybrid-cascaded high-voltage direct current (HVDC) system.

Object	Parameters	Values
HVDC system	DC voltage	800 kV
	DC Current	5 kA
	DC power (bipolar)	8000 MW
	Flat wave reactor	150 mH
	Grounding pole line resistance	2.17 Ω
	Grounding pole line inductance	68.5 mH
Line-mutated converter (LCC) converter transformer at rectifier side	Variable ratio	525 kV/172.3 kV
	Rated capacity	1218 MVA
	Short circuit voltage percentage	23%
LCC converter transformer at the inverter side	Variable ratio	510 kV/161.4 kV
	Rated capacity	1141 MVA
	Short circuit voltage percentage	18%
Modular multilevel converter (MMCs) at the inverter side	Rated DC power	1000 MW
	Number of sub-modules	200 + 24
	Bridge Arm Inductors	50 mH
	Sub-module capacitance	18 mF
MMCs converter transformer at the inverter side	Variable ratio	510 kV/182.6 kV
	Rated capacity	1125 MVA
	Short circuit voltage percentage	15%

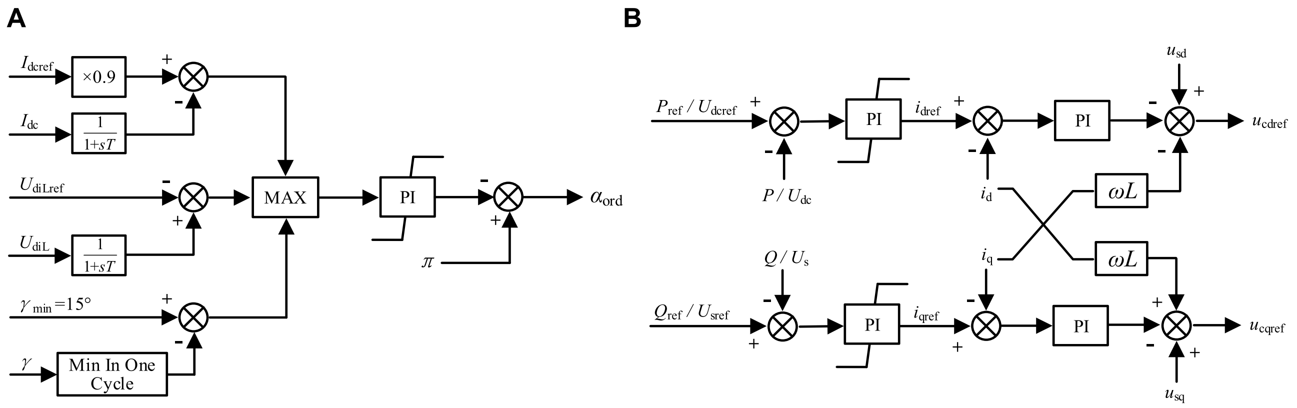

FIGURE 2
Control block diagram. **(A)** Line-mutated converter (LCC) at the inverter side; **(B)** modular multilevel converter (MMC) at the inverter side.

characteristics are better, which limits the reduction of the rectifier side voltage. The characteristics of the inverter side are composed of four, five, six, and seven segments; among these, four segments are constant extinction angle control characteristics, with γ set to 15°; five segments are constant DC voltage control characteristics, which are also normal operating characteristics; and six segments are constant DC current control characteristics. To ensure that the DC current control on the inverter side is inoperative during steady-state operation, its current setting value should be lower than the rectifier-side control setting value. Segment 7 is the control characteristic of the VDCOL. In normal conditions, the HVDC system operates at the black point as shown in Figure 3.

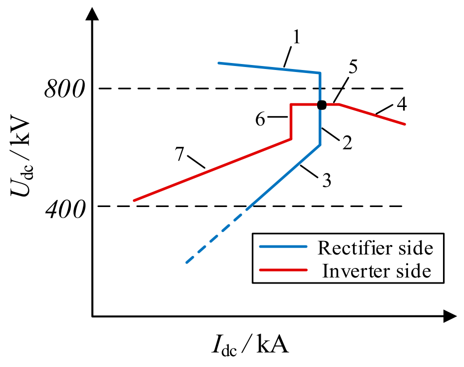

FIGURE 3
Static I–V characteristic of HVDC system.

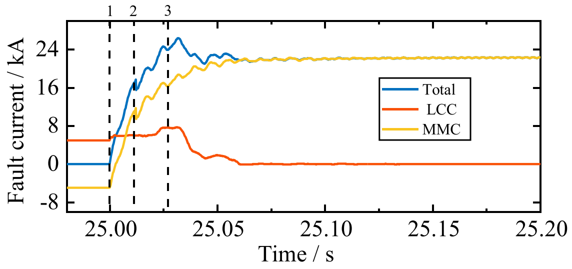

FIGURE 4
Fault current of HVDC system.

3 Failure mechanism

The fault area in the fault conditions described above is shown in Figure 1, and is mostly arranged in the valve hall; therefore, the general occurrence tends to be a permanent ground fault.

In this study, we built a hybrid simulation model containing a hybrid cascaded HVDC system, including an actual control protection program of the HVDC system. The fault current was obtained, as illustrated in Figure 4, and was based on the model used to simulate the fault in this area.

Among them, the actions that play a major role in the transformation of the fault current evolution process include the following.

- Occurrence of failure
- Approximately 10 ms after the failure occurs, MMCs at the inverter side are blocked
- Approximately 40 ms after the failure occurs, the LCC at the rectifier side is forced to undergo a phase shift

From the topology of the hybrid cascaded HVDC system, it is known that after a permanent ground fault occurs in this area, the fault currents originate from the LCC and each parallel MMCs on the inverter side, and are defined as I_{dcL} and I_{dcM}, respectively. When the system operates in the steady state, I_{dcL} and I_{dcM} are equal. Owing to the manufacturing level, the insulated-gate bipolar transistor (IGBT) and capacitor, which are important components of the MMC submodule, have high costs and weak overcurrent capabilities. Before the MMC is blocked, the IGBT and capacitor have to withstand overcurrents at specific levels; once the IGBT or capacitor are damaged by the overcurrent problem, it will affect the equipment's life and may endanger the system's ability to run securely and consistently (Ni et al., 2020). Meanwhile, although the thyristor used in LCC has enhanced overvoltage and overcurrent capabilities, the contact between the HVDC system and the receiving-end system changes significantly during the transient process after a failure occurs (Aik and Andersson, 2018). A theoretical examination of the fault current and system impact in this fault situation is necessary because the power flow of the receiving-end system after a failure differs significantly from that before the failure.

4 Fault current theory analysis of MMCs side

Each parallel MMCs on the inverter side is in normal operation, and there are 2N submodules in the upper and lower bridge arms among which a total of N submodules are in the bypass state, whereas N more submodules are in the input state. It is essentially a time-varying circuit, but during the transient process after a failure occurs, the DC voltage of the MMCs does not increase suddenly; therefore, it can be assumed that each phase's input of the submodules will always have the same number, that is, the equivalent capacitance of any phase is constant. MMCs can be considered linear circuits during this time and can be analyzed using the superposition theorem.

4.1 State before MMCs are blocked

During fault response analysis, the fault current is the sum of three parallel MMC fault currents. The MMCs have the same primary parameters on both sides and are connected to different nodes in the same AC network. The voltage amplitude and phase angle of each MMC are approximately the same. To facilitate the calculations, we assumed that the voltage amplitudes and phase angles of the three parallel MMCs were identical. Taking MMC1 as an example to begin the analysis, the time-domain model is shown in Figure 5.

The complicated frequency-domain model of MMC1, shown in Figure 5, transforms the time-domain model into an arithmetic circuit model, as shown in Figure 6A, where the impedances of the grounding electrode line and smoothing reactor L0 were unified and combined as Rg + jwLg. The excitation sources are shown in Figure 6A were separated as follows.

- DC side excitation source
- AC side excitation source

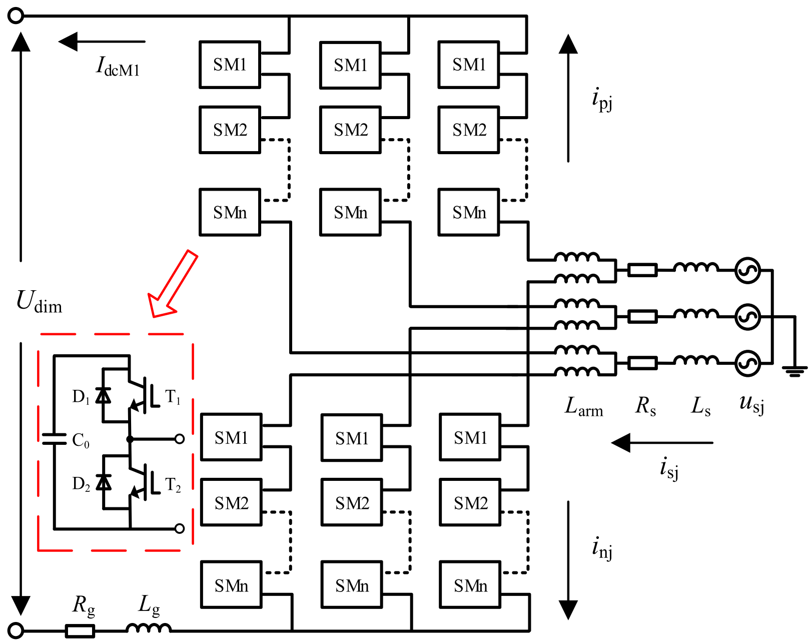

FIGURE 5
Time domain model of MMC1.

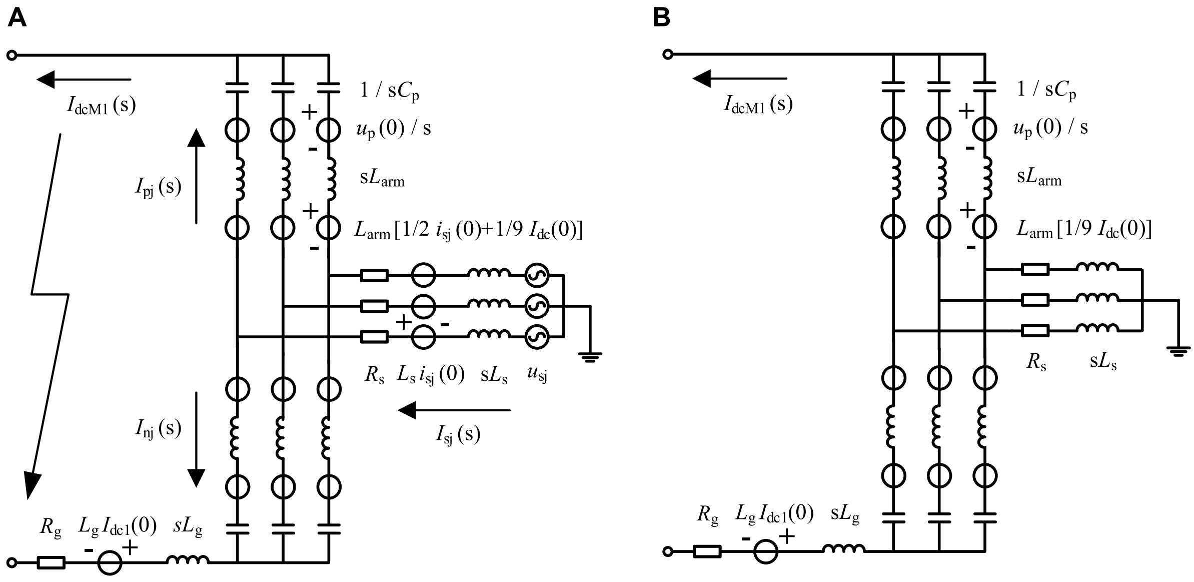

FIGURE 6
(A) Complex frequency domain model of MMC1; **(B)** response circuit of DC excitation source.

The fault current on the MMC_1 side is the outcome of the synergistic work of the two types of excitation sources described above. Therefore, the two types of excitation sources above were decomposed, the response of each group of excitation sources (acting separately) was calculated according to the principle of the superposition theorem, and the total response of the MMC_1 circuit was obtained by summing them.

4.1.1 Response of DC side excitation source

The excitation source for this part of the response circuit consists of three parts: all-submodule capacitors, the excitation source matching the initial value of I_{dc} in the bridge arm reactor, and the source of excitation for the starting value of the current in the smoothing reactor. The DC-side excitation-source response circuit is shown in Figure 6B.

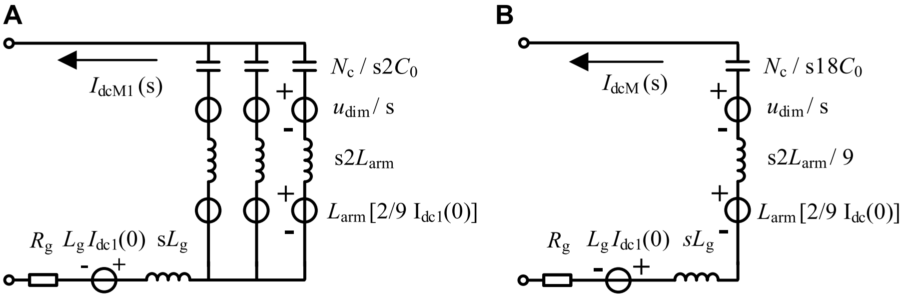

FIGURE 7
Simplified circuit of the DC side excitation source. **(A)** MMC1; **(B)** three parallel MMCs.

To solve this part of the excitation source response, the following simplifications were made.

- In this part of the response, there is no excitation source in the three-phase symmetric AC network. Therefore, the role of the AC network can be disregarded when analyzing the DC line's current
- Each submodule can be considered to have the same capacitance voltage Uc based on the principle of constant-capacitance storage in each submodule. The equivalent capacitance of each phase bridge arm Ceq is expressed as follows,

$$\frac{1}{2}C_{\text{eq}}U_{\text{dim}}^2 = 2N_c\frac{1}{2}C_0U_c^2 \tag{1}$$

Additionally, considering that $U_{\text{diM}} = N_c U_c$, it is obtained that

$$C_{\text{eq}} = \frac{2}{N_c}C_0 \tag{2}$$

Based on the simplification principle above, the DC-side excitation source circuit of MMC_1 can be simplified as follows,

As the major part of the circuit is a parallel connection of nine phase units and the lower end of the inverter side is linked in parallel with three groups of MMCs, the circuit of this part may be simplified, as shown in Figure 7B. By solving this simplified circuit, the fault current of the MMCs subject to the response of the excitation source in the complex frequency domain is obtained as follows,

$$I_{\text{dcM}}(\text{s}) = \frac{\text{s}\left(L_g + 2L_{\text{arm}}\big/9\right)I_{\text{dc}}(0) + U_{\text{dim}}}{\text{s}^2\left(L_g + 2L_{\text{arm}}\big/9\right) + \text{s}R_g + N_c\big/18C_0} \tag{3}$$

The fault current $I_{\text{dcm}}(\text{t})$ is obtained by substituting the specific parameters of the HVDC system and the system state quantities into the $I_{\text{dcM}}(s)$ expression and performing the inverse Laplace transform. In addition, because of the symmetry of each phase unit, $I_{\text{dcm}}(t)$ is spread equally throughout the phase units, and the current flowing in each bridge arm is $I_{\text{dcm}}(t)/9$.

$$I_{\text{dcM}}(t) = -\frac{1}{\sin\theta_1}i_{\text{dc}}(0)\text{e}^{-\frac{t}{\tau 1}}\sin(\omega_1 t - \theta_1) + \frac{U_{\text{dc}}}{R_1}\text{e}^{-\frac{t}{\tau 1}}\sin(\omega_1 t) \tag{4}$$

where τ_1 is the time constant of the current decay, ω_1 is the resonant frequency, and θ_1 is the initial phase angle. These parameters are determined by the system parameters.

$$\tau_1 = \frac{4L_{\text{arm}} + 18L_g}{9R_g}, \omega_1 = \sqrt{\frac{2N\left(2L_{\text{arm}} + 9L_g\right) - 81C_0R_g^2}{C_0\left(4L_{\text{arm}} + 18L_g\right)^2}} \tag{5}$$

$$R_1 = \sqrt{\frac{2N\left(2L_{\text{arm}} + 9L_g\right) - 81C_0R_g^2}{324C_0}}, \theta_1 = \arctan(\tau_1\omega_1) \tag{6}$$

4.1.2 Response of AC side excitation source

The excitation source for this section of the response circuit consisted of an AC network equivalent power supply, an excitation source allied with the initial value of the inductor current, and an excitation source allied with the initial value of the AC current in the bridge arm reactor. The response circuit is shown in Figure 8A.

Because the equivalent power supply of the AC network and the entire circuit configuration are three-phase symmetric, no current enters the DC line from the AC side. The response circuit was simplified according to this principle, as shown in Figure 8B.

Each bridge arm in each phase carries half of the current on the AC side. When phase A of the upper bridge arm of MMC_1 is used for analysis, the expression of the equivalent source of phase A is assumed to be $u_{\text{sa}}(t) = E\sin(\omega_0 t)$. The upper bridge arm's response expression is,

$$i_{\text{pa2}}(t) = \frac{1}{2}I_{\text{m2}}\sin(\omega_0 t - \varphi_2) + \frac{1}{2}i_{\text{sa}}(0)\text{e}^{-\frac{t}{\tau_2}} \tag{7}$$

Among them

$$I_{\text{m2}} = \frac{E}{\sqrt{{R_s}^2 + \omega^2\left(L_s + L_{\text{arm}}/2\right)^2}}, \varphi_2 = \arctan\frac{\omega\left(L_s + L_{\text{arm}}/2\right)}{R_s},$$
$$\tau_2 = \frac{L_s + L_{\text{arm}}/2}{R_s} \tag{8}$$

In summary, the total response process of the MMCs before blockage can be obtained. It is evident from the above study that the fault current on the MMCs side is related only to the DC-side excitation source response. The response process is described in (4), (5), (6). From the calculation of ω_1, it is evident that the fault current

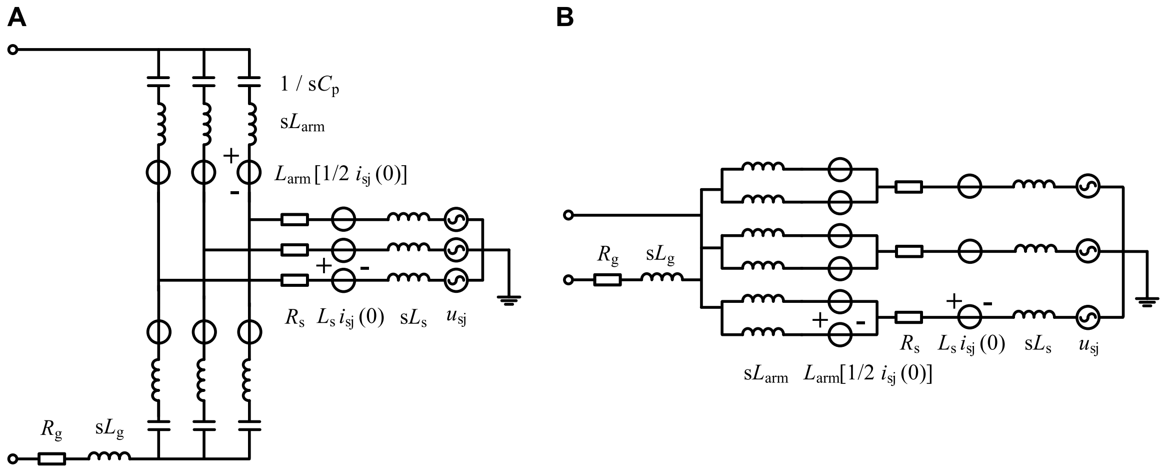

FIGURE 8
Circuit of the AC excitation source. **(A)** Response circuit and **(B)** simplified circuit.

reaches a peak approximately 17 ms after a failure occurs. However, the MMCs were prompted to block approximately 10 ms after failure; therefore, the fault current before blocking increased monotonically. The fault current calculated by (4) was 11.7 kA at 10 ms after failure occurred and matches the simulation results in Figure 4.

4.2 State after MMCs are blocked

In a hybrid cascaded HVDC system, three parallel MMCs transmit power to the DC side. Using the present direction of Figure 5 as an illustration, there exists a DC bias with a value of 1/9 I_{dcM} for each phase of the upper bridge arm current i_{pj} and a DC bias with a value of $-1/9$ I_{dcM} for each phase of the lower bridge arm current i_{nj}. Before the MMC is triggered to block, the fault current at the MMCs and the bridge arm current of each phase mainly originate from the DC-side excitation source response. The rate of change of this current is extremely fast, which makes the I_{dcM} change from negative to positive within milliseconds, while the reversal process of I_{dcM} also delays the time for the fault current to reach its peak to a certain extent. After the MMCs were blocked, the flow path and pattern of the fault current changed. It is also an important part of the complete response of the HVDC system after the failure occurs. The following is an example of MMC_1 for fault current change characteristic analysis after blocking.

As shown from the topology, each submodule of MMC_1 uses the half-bridge topology. After the blocking command is issued, each submodule is in a blocking state, and there are two operation modes in this state due to the renewal of the antiparallel diodes D_1 and D_2 in each submodule. In the first operation mode, D_1 is on and current passes through D_1 to charge the capacitor. In the second mode of operation, D_2 is turned on, and the current passes through D_2 to bypass the capacitor.

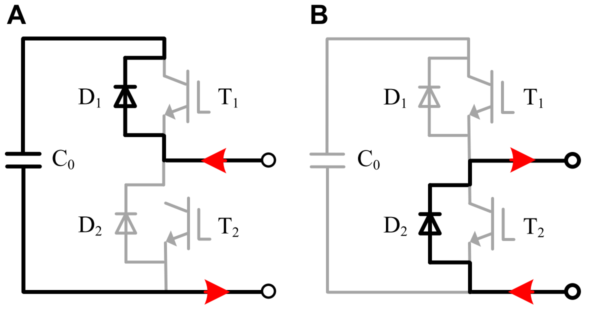

FIGURE 9
Operation mode of MMCs in the blocking state. **(A)** Charging and **(B)** bypassing the capacitor.

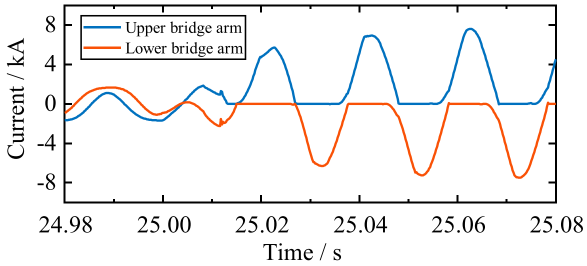

FIGURE 10
Bridge arm current of MMC1.

Because the sum voltage of the capacitors on each bridge arm in MMC_1 is greater than the AC voltage amplitude, each submodule operates as illustrated in Figure 9B. Before the bridge-arm current reaches zero, the antiparallel diodes of the upper and lower bridge arms operate in the conducting state, and the single-phase conductivity of the antiparallel diodes is not considered.

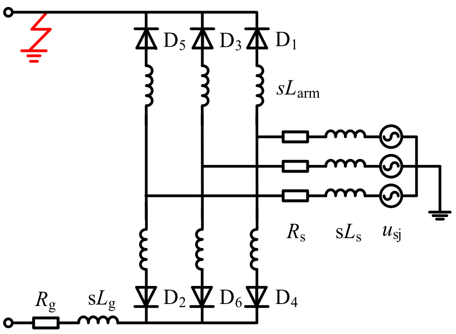

FIGURE 11
Response circuit after MMC1 is blocked.

Compared with MMC$_1$ before blocking, the DC-side excitation source response changed into a persistent current circuit in the bridge arm reactor. The remaining two excitation source circuits remained unchanged, and the three excitation source responses were superimposed to produce the bridge arm current. Figure 10.

After this part of the current decays to zero for the first time, the antiparallel diode cannot operate. The upper and lower bridge arm currents are switched from a two-way flow to a one-way flow limited by the antiparallel diode; at this time, the three-phase uncontrolled rectifier circuit begins its steady-state operation phase.

In a three-phase uncontrolled rectifier circuit, the conduction instant of the antiparallel diode on each phase bridge arm is the intersection of the phase voltage of that phase with that of the adjacent phase (i.e., the natural phase-change point). In the steady-state operation phase after MMC$_1$ is blocked, any phase bridge arm midpoint voltage is greater than zero because of the MMC$_1$ fault ground at the high-tension side, and the phase on the bridge arm's antiparallel diode meets the conduction conditions; thus, the upper bridge arm conducts. In addition, if the midway voltage of the bridge arm of the phase changes from positive to negative, the antiparallel diode will not immediately arc out owing to the current-continuing bridge arm reactor but will continue to conduct for a while and then turn off.

Define θ_{arm} as the angle of continuous conduction of each bridge arm. Based on the above analysis, $\theta_{\mathrm{arm}} > \pi$; additionally, define the sum of the inductance of each phase bridge arm in the uncontrolled rectifier as L_{sum}. It is known from Figure 11 that $L_{\mathrm{sum}} = L_{\mathrm{arm}} + L_{\mathrm{s}}$. Owing to the different ratios of R_{g} to L_{arm}, the θ_{arm} values are different (Li et al., 2016); this leads to different operating response characteristics. When $R_{\mathrm{g}}/L_{\mathrm{sum}} > 100$, $\pi \le \theta_{\mathrm{arm}} < 4\pi/3$, and the operating response is alternating between three and four bridge arm conduction. When $R_{\mathrm{g}}/L_{\mathrm{sum}} \le 100$, $\theta_{arm} \ge 4\pi/3$, and the operating response is alternating between four and five bridge arms conduction. According to the calculation of the parameters of the HVDC system, $R_{\mathrm{g}}/L_{\mathrm{sum}}$ is much less than 100; therefore, the steady-state operating response characteristics of MMC$_1$ after blocking are based on alternate switch-on operations of four and five bridge arms, and the angle of continuous conduction of each bridge arm can be found as follows,

$$\theta_{\mathrm{arm}} = \arcsin\left[\frac{3\omega_0 L_{\mathrm{sum}}}{\sqrt{\left(5.2\omega_0 L_{\mathrm{sum}} + 27.3R_{\mathrm{g}}\right)^2 + 3\omega_0 L_{\mathrm{sum}} + 28.2R_{\mathrm{g}}}}\right] - \arctan\left(\frac{3\omega_0 L_{\mathrm{sum}} + 28.2R_{\mathrm{g}}}{5.2\omega_0 L_{\mathrm{sum}} + 27.3R_{\mathrm{g}}}\right) + \frac{5\pi}{3} \tag{9}$$

Utilizing the antiparallel diode D$_1$'s conduction as the starting point, the analytic expression for the current in one power frequency period was analyzed. The steady-state circuit after the MMC is blocked, as shown in the figure, and always conducts and opens according to the conduction sequence D$_1$-D$_2$-D$_3$-D$_4$-D$_5$-D$_6$-D$_1$. Before D$_1$ was set, D$_3$, D$_4$, D$_5$ and D$_6$ were tested. According to the circuit analysis, this period satisfies the following expression,

$$\begin{aligned} u_{\mathrm{dc}}(t) &= u_{\mathrm{sa}} - L_{\mathrm{sum}}\frac{\mathrm{d}i_{\mathrm{pa}}}{\mathrm{d}t} - u_{\mathrm{sb}} + L_{\mathrm{sum}}\frac{\mathrm{d}i_{\mathrm{nb}}}{\mathrm{d}t} = L_{\mathrm{sum}}\frac{\mathrm{d}i_{\mathrm{pa}}}{\mathrm{d}t} + L_{\mathrm{sum}}\frac{\mathrm{d}i_{\mathrm{na}}}{\mathrm{d}t} = u_{\mathrm{sb}} - L_{\mathrm{sum}}\frac{\mathrm{d}i_{\mathrm{pb}}}{\mathrm{d}t} - u_{\mathrm{sa}} + L_{\mathrm{sum}}\frac{\mathrm{d}i_{\mathrm{na}}}{\mathrm{d}t} \\ &= L_{\mathrm{sum}}\frac{\mathrm{d}i_{\mathrm{pb}}}{\mathrm{d}t} + L_{\mathrm{sum}}\frac{\mathrm{d}i_{nb}}{\mathrm{d}t} = u_{\mathrm{sc}} - L_0\frac{\mathrm{d}i_{pc}}{\mathrm{d}t} - u_{\mathrm{sa}} + L_0\frac{\mathrm{d}i_{\mathrm{na}}}{\mathrm{d}t} = u_{\mathrm{sc}} - L_0\frac{\mathrm{d}i_{\mathrm{pc}}}{\mathrm{d}t} - u_{\mathrm{sb}} + L_0\frac{\mathrm{d}i_{\mathrm{nb}}}{\mathrm{d}t} \end{aligned} \tag{10}$$

Meanwhile, according to Kirchhoff's current law, it is obtained that

$$\frac{\mathrm{d}\left(i_{\mathrm{pa}} + i_{\mathrm{pb}} + i_{\mathrm{pc}}\right)}{\mathrm{d}t} = -\frac{\mathrm{d}\left(i_{\mathrm{na}} + i_{\mathrm{nb}}\right)}{\mathrm{d}t} = \frac{\mathrm{d}i_{\mathrm{dc}}}{\mathrm{d}t} = 0 \tag{11}$$

Substitution of (11) into (10) yields,

$$\begin{cases} L_{\mathrm{sum}}\dfrac{\mathrm{d}i_{\mathrm{pa}}}{\mathrm{d}t} = u_{\mathrm{sb}} - u_{\mathrm{sc}} \\ L_{\mathrm{sum}}\dfrac{\mathrm{d}i_{\mathrm{pb}}}{\mathrm{d}t} = u_{\mathrm{sc}} - u_{\mathrm{sa}} \\ L_{\mathrm{sum}}\dfrac{\mathrm{d}i_{\mathrm{pc}}}{\mathrm{d}t} = u_{\mathrm{sa}} - u_{\mathrm{sb}} \end{cases} \tag{12}$$

LLet the phase A equivalent source expression be $u_{\mathrm{sa}}(t) = E\sin(\omega_0 t)$. Then, when $\omega_0 t = 0$, it satisfies $i_{\mathrm{pa}} = 0$. By substituting this initial condition, the phase-A upper bridge arm current under this conduction condition can be obtained as follows,

$$i_{\mathrm{pa}}(t) = \frac{E}{\omega_0 L_{\mathrm{sum}}} - \frac{E}{\omega_0 L_{\mathrm{sum}}}\cos(\omega_0 t) \tag{13}$$

Thereafter, the operating response of the bridge arm current is defined by the alternative operation of the four- and five-bridge arm conductions; thus, the above analysis method can be used to solve all conduction conditions to obtain an analytical expression for the current in one power frequency period as follows,

$$i_{\mathrm{pa}}(t) = \begin{cases} -\dfrac{E}{\omega_0 L_{\mathrm{sum}}}\cos(\omega_0 t) + \dfrac{E}{\omega_0 L_{\mathrm{sum}}} & 0 \le \omega_0 t \le \theta - \dfrac{4\pi}{3} \\ -\dfrac{0.866E}{\omega_0 L_{\mathrm{sum}}}\cos\left(\omega_0 t - \dfrac{\pi}{6}\right) + \dfrac{E}{\omega_0 L_{\mathrm{sum}}} - \dfrac{E}{2\omega_0 L_{\mathrm{sum}}}\sin\left(\theta - \dfrac{\pi}{2}\right) & \theta - \dfrac{4\pi}{3} \le \omega_0 t \le \theta - \pi \\ -\dfrac{1.732E}{2\omega_0 L_{\mathrm{sum}}}\sin(\omega_0 t) + \dfrac{E}{\omega_0 L_{\mathrm{sum}}} + \dfrac{\sqrt{7}\,E}{2\omega_0 L_{\mathrm{sum}}}\sin\left(\theta - \dfrac{25\pi}{18}\right) & \theta - \pi \le \omega_0 t \le \dfrac{2\pi}{3} \\ -\dfrac{E}{\omega_0 L_{\mathrm{sum}}}\cos(\omega_0 t) - \dfrac{E}{4\omega_0 L_{\mathrm{sum}}} + \dfrac{\sqrt{7}\,E}{2\omega_0 L_{\mathrm{sum}}}\sin\left(\theta - \dfrac{25\pi}{18}\right) & \dfrac{2\pi}{3} \le \omega_0 t \le \theta - \dfrac{2\pi}{3} \\ -\dfrac{\sqrt{3}\,E}{2\omega_0 L_{\mathrm{sum}}}\cos\left(\omega_0 t + \dfrac{\pi}{6}\right) - \dfrac{E}{4\omega_0 L_{\mathrm{sum}}} + \dfrac{1.803E}{\omega_0 L_{\mathrm{sum}}}\sin(\theta - 4.468) & \theta - \dfrac{2\pi}{3} \le \omega_0 t \le \dfrac{4\pi}{3} \\ -\dfrac{E}{\omega_0 L_{\mathrm{sum}}}\cos(\omega_0 t) - \dfrac{3E}{4\omega_0 L_{\mathrm{sum}}} + \dfrac{1.803E}{\omega_0 L_{\mathrm{sum}}}\sin(\theta - 4.468) & \dfrac{4\pi}{3} \le \omega_0 t \le \theta \\ 0 & \theta \le \omega_0 t \le 2\pi \end{cases} \tag{14}$$

Based on the operating response characteristics of the different stages after MMC_1 is blocked and the conduction of each bridge arm, the fault current of MMC_1 can be determined as follows,

$$I_{\text{dcMMC1}} = \frac{3.12E}{\omega_0 L_{\text{sum}}} \sin(\theta - 4.64) \tag{15}$$

In conclusion, it was possible to determine MMC_1's steady-state operational response properties. The angle of continuous conduction of each bridge arm was calculated to be equal to 280° by (9), MMC_1 fault current was calculated to be 7.87 kA using (15), and the fault current I_{dcM} provided by each parallel MMCs was 23.6 kA, which coincides with the simulation results in Figure 5.

5 Fault current theory analysis of LCC side

From the topology of the HVDC system, the LCC fault current I_{dcL} is equal to I_{dc} and is expressed as

$$R_{\text{line}} I_{\text{dc}} + L_{\text{line}} \frac{\text{d}I_{\text{dc}}}{\text{dt}} = U_{\text{dr}} - U_{\text{di}} = \Delta U_{\text{d}}(t) \tag{16}$$

where U_{dr} and U_{di} are the DC voltages within L_0 on the rectifier and inverter sides, and R_{line} and L_{line} are the DC line impedances, respectively. The differential term in (16) is zero during the steady-state operation; therefore, I_{dc} is related only to the difference between U_{dr} and U_{di}. The differential term is not zero after a failure occurs, and its solution is obtained as follows,

$$I_{\text{dc}} = \text{e}^{-\frac{t}{\tau_{\text{L}}}} \left[\int \frac{\Delta U_{\text{d}}(t)}{L} \text{e}^{\frac{t}{\tau_{\text{L}}}} \text{dt} + C \right] \tag{17}$$

where $\tau_{\text{L}} = L_{\text{dc}}/R_{\text{dc}}$. Expanding for U_{di}, we obtain

$$\begin{aligned} U_{\text{di}} &= L_0 \frac{\text{d}I_{\text{dc}}}{\text{dt}} + U_{\text{diL}} + U_{\text{diM}} \\ &= L_0 \frac{\text{d}I_{\text{dc}}}{\text{dt}} + N_{\text{i}} \left(1.35 \frac{U_{\text{sL}}}{k_{\text{L}}} \cos\beta + \frac{3}{\pi} X_{\text{sL}} I_{\text{dc}} \right) + U_{\text{diM}} \end{aligned} \tag{18}$$

where N_{i} is the number of 6-pulse LCC converters in each pole, U_{sL} is the LCC bus line voltage at the inverter side, k_{rL} and X_{sL} are the LCC converter transformer ratio and leakage resistance at the inverter side, respectively, and β is the advanced LCC trigger angle of the inverter side.

After a failure occurs, the system's triggers a blocking fault-pole strategy. Meanwhile, the pole control system sends a blocking command to each valve control system running the LCC after receiving the pole-blocking command from the station or the opposite station. During this process, the LCC on the rectifier side is forced to shift the phase to accelerate the fault current decay. Therefore, the LCC-side fault response is also discussed in two phases: before and after the forced phase shift of the LCC on the rectifier side.

5.1 State before forced phase shift

When the AC voltage at the inverter side is lowered, a constant extinction angle control is utilized to lower the possibility of commutation failure. Constant current control is employed to keep the I_{dc} flowing when the rectifier side experiences a defect and to speed up power recovery after a failure has occurred. During steady-state operation, U_{diL} and U_{diM} were both 400 kV, U_{di} was approximately 800 kV, and γ_{iL} was greater than 15°. The output signal of the constant extinction angle control was negative, and the output signal of the constant DC voltage control was zero; therefore, the constant extinction angle control did not operate.

After the fault occurred, U_{di} decreased to ~400 kV. Eq. 17 shows that a significant decrease in U_{di} after a failure leads to an increase in I_{dc}. From the commutation principle of the LCC, it is known that there is a relationship between μ_{iL}, γ_{iL}, and β_{iL},

$$\begin{aligned} \mu_{\text{iL}} &= \arccos\left[\cos\gamma_{\text{iL}} - \frac{6X_{\text{sL}} I_{\text{dc}}}{1.35\pi U_{\text{sL}}/k_{\text{L}}} \right] - \gamma_{\text{iL}}, \gamma_{\text{iL}} \\ &= \arccos\left[\frac{U_{\text{diL}} + 3X_{\text{sL}} I_{\text{dc}}/\pi}{1.35 U_{\text{sL}}} \right], \beta_{\text{iL}} = \gamma_{\text{iL}} + \mu_{\text{iL}} \end{aligned} \tag{19}$$

The increase in I_{dc} causes μ_{iL} to increase and γ_{iL} to decrease, thus resulting in a) the output <0 in the constant DC voltage control side, b) an output signal of the constant extinction angle control side <0, and c) the LCC at the inverter side moving to constant extinction angle control. Simultaneously, when $\gamma_{\text{iL}} < \gamma_{\text{min}}$, the LCC on the inverter side induces a commutation failure. The LCC extinction angle on the inverter side during a fault is shown in Figure 12A.

Unlike general AC system faults at the inverter side, which cause commutation failure induced by voltage dips at the commutation bus, the same problem of commutation failure is induced at the internal fault conditions of the HVDC system. However, the essence is that the increase of I_{dc} causes the increase of the μ_{iL} and the decrease of t γ_{iL}, thus resulting in γ_{iL} values $< \gamma_{\text{min}}$.

5.2 State after the forced phase shift

After receiving the pole blocking command, the LCC system adopts the forced phase shift strategy to reduce U_{dr} to a negative value so that the HVDC system's energy can be promptly transferred back to the AC system. This helps I_{dcL} decay to zero quickly. During the initial stage, after the forced phase shift of the LCC at the rectifier side, the trigger angle increased to 120° instead of 165° to avoid commutation failure induced by small phase-change angles after entering the inverted state. When I_{dc} was detected to be lower than 0.05 p. u., after a time delay, the LCC triggered phase-shift locking.

6 Characterization of the AC network at the receiving end

After failure occurs, it is clear from the above analysis that U_{dr} reduces to a negative value during the blocking process through a forced phase-shift strategy, which helps I_{dcL} decay to zero quickly, thus ensuring that the LCCs on the rectifier and inverter sides are reliably blocked and have no power interaction with the AC side after blocking. Figure 13.

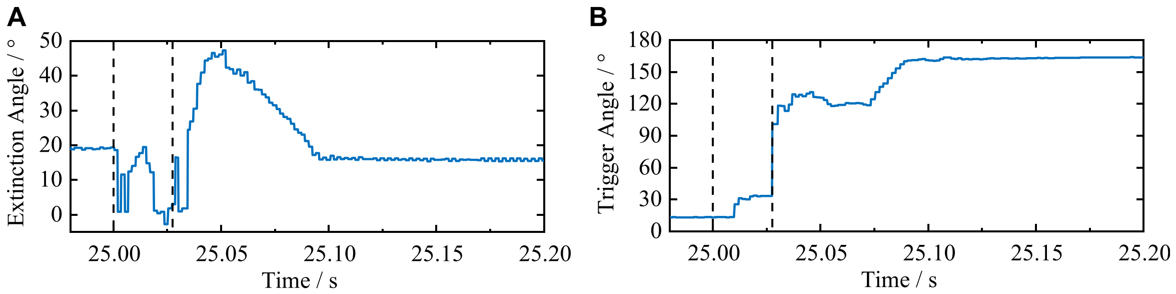

FIGURE 12
(A) LCC extinction angle at the inverter side; **(B)** LCC trigger angle at the rectifier side.

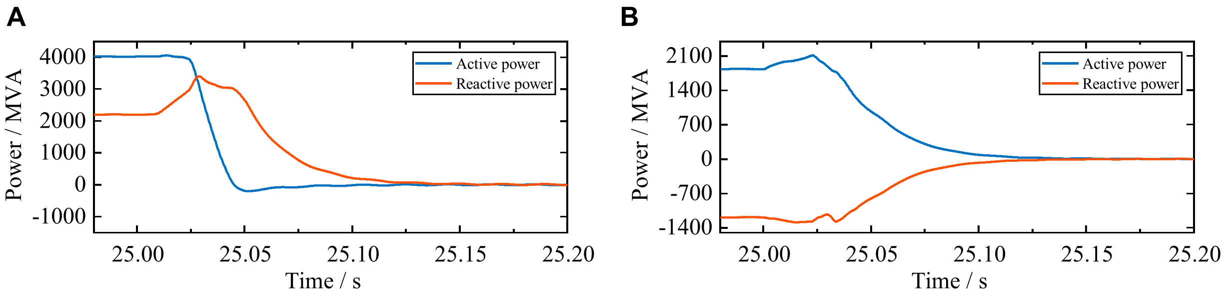

FIGURE 13
(A) Total power and **(B)** LCC power responses.

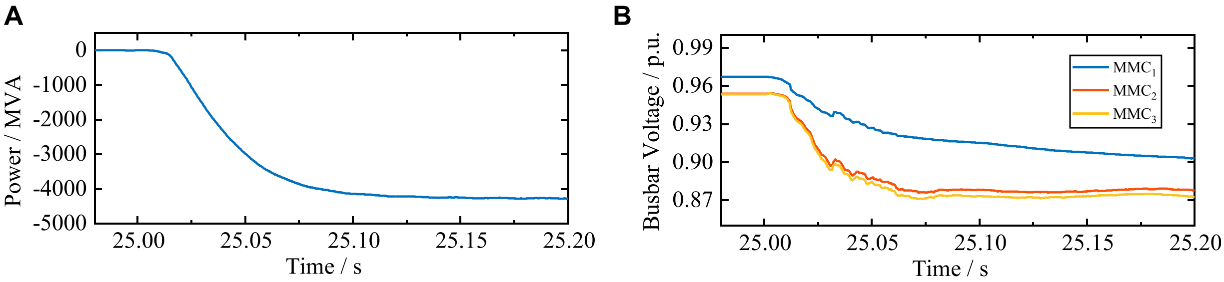

FIGURE 14
(A) Reactive power response of MMCs; **(B)** busbar voltage responses of MMCs.

On the inverter side, each parallel MMC uses a constant reactive power regulation method, and the reactive power interaction between the MMCs and the AC network is nearly zero before failure occurs. After the MMCs are blocked, the submodule capacitor no longer provides fault currents to the fault point. However, the AC network can still provide fault currents, and the converter leakage resistance and bridge arm reactance of the MMC consume a significant amount of reactive power.

From the receiving-end grid VQ curve of the reactive power supply and load, the load reactive power suddenly increases significantly, and the load VQ curve shifts upward (Liu et al., 2016). If the reactive power supply capacity is insufficient, the voltage at the new intersection of the VQ curves of the reactive power supply and the load decreases, thus forcing the reactive power supplier to increase the output of Q and the load side to decrease consumption. Thus, the receiving-end grid reaches a new stable balance state at a low-voltage level, and the AC bus voltage of each parallel MMC side is shown in Figure 14B.

Therefore, because of the slow opening and shutting times of the AC switch, the MMC approximates a three-phase uncontrolled rectifier, and its converter leakage resistance and bridge arm reactance must consume a large amount of Q. If the reactive power capacity is insufficient, the voltage at each node is reduced. The simulation results show that if the responses of the long-term dynamic components and parts are not considered, the AC network does not meet the relevant long-term voltage stability evaluation criteria.

7 Conclusion

This study used a hybrid cascaded HVDC system as the research object and simulated a permanent ground fault in high- and low-end connecting lines on the cascaded side. It then conducted a thorough theoretical analysis of the fault responses of MMCs and LCCs as well as the impact of the AC network. The relevant conclusions are as follows:

The fault current on the MMC_1 side was the result of the combined action of the aforementioned two types of excitation sources. Therefore, the two types of excitation sources were decomposed, the response of each group of excitation sources acting separately was calculated according to the principle of the superposition theorem, and the total response of the MMC_1 circuit was obtained by adding them together.

- Because of the reliable blocking of the MMCs and the reverse process of I_{dcm}, there was no need to consider the IGBT overcurrent of each submodule before the MMCs were blocked
- The LCC on the inverter side may lead to commutation failure owing to the increase in I_{dc} in the fault conditions described above
- During the steady-state process, after the MMCs were blocked, the HVDC system consumed a significant amount of reactive power; this resulted in a reduction in the AC voltage at the receiving grid. This does not satisfy the relevant long-term voltage stability evaluation criteria.

From the calculation and simulation results, the theoretical analysis presented above yielded results that were consistent with the actual response, thus providing a theoretical basis and calculation method for the design, testing, and performance evaluation of HVDC systems. In addition, the HVDC system is a significant part of smart grids in the broad range of applications of AI and there is a close connection between the two. The theoretical analysis presented above can also realize intelligent management and control of power systems, improve the energy utilization efficiency and stability of the power grid, and provide strong support for energy transformation. In the future, further research will be conducted in terms of reducing the overcurrent peak of the bridge arm after the failure occurs.

Data availability statement

The original contributions presented in the study are included in the article/supplementary material, further inquiries can be directed to the corresponding author.

Author contributions

YR, HS, SW, BZ, and SX was responsible for contributing conception and design of the study and writing sections of the manuscript. YR wrote the first draft of the manuscript. ML and PL was responsible for model building, simulation. All authors participated in the reading and approved the submitted version.

Funding

This research was funded by the National Natural Science Foundation of China under integration project (U216660003).

Conflict of interest

YB, SW, BZ, SX, ML, and PL were employed by China Electric Power Research Institute Co. Ltd.

The remaining author declares that the research was conducted in the absence of any commercial or financial relationships that could be construed as a potential conflict of interest.

Publisher's note

References

Aik, D., and Andersson, G. (2018). Fundamental analysis of voltage and power stability of single-infeed voltage-source converter HVDC systems. *IEEE Trans. Power Deliv.* 34 (1), 365–375. doi:10.1109/TPWRD.2018.2874335

Cai, W., Ning, X., Zhou, G., Bai, X., Jiang, Y., Li, W., et al. (2022). A novel hyperspectral image classification model using bole convolution with three-direction attention mechanism: Small sample and unbalanced learning. *IEEE Trans. Geosci. Remote Sens.* 61, 1–17. doi:10.1109/TGRS.2022.3201056

Debnath, S., Qin, J., Bahrani, B., Saeedifard, M., and Barbosa, P. (2014). Operation, control, and applications of the modular multilevel converter: A review. *IEEE Trans. Power Electron.* 30 (1), 37–53. doi:10.1109/TPEL.2014.2309937

Dong, X., Ning, X., Xu, J., Yu, L., Li, W., and Zhang, L. (2023). PFAS contamination: Pathway from communication to behavioral outcomes. *IEEE Trans. Comput. Soc. Syst. Early Access* 28, 1–13. doi:10.1080/10810730.2023.2193144

Guo, C., Wu, Z., Yang, S., and Hu, J. (2021). Overcurrent suppression control for hybrid LCC/VSC cascaded HVDC system based on fuzzy clustering and identification approach. *IEEE Trans. Power Deliv.* 37 (3), 1745–1753. doi:10.1109/TPWRD.2021.3096954

Haleem, N., Rajapakse, A., Gole, A., and Fernando, I. (2018). Investigation of fault ride-through capability of hybrid VSC-LCC multi-terminal HVDC transmission systems. *IEEE Trans. Power Deliv.* 34 (1), 241–250. doi:10.1109/TPWRD.2018.2868467

He, Y., Xiang, W., Ni, B., Lu, X., and Wen, J. (2021). Impact of strength and proximity of receiving AC systems on cascaded LCC-MMC hybrid HVDC system. *IEEE Trans. Power Deliv.* 37 (2), 880–892. doi:10.1109/TPWRD.2021.3073896

Kang, Z., Zhang, Z., Wang, S., and Yin, R. (2022). "A new adaptive DC voltage droop control for hybrid cascaded HVDC transmission system," in 2022 4th Asia Energy and Electrical Engineering Symposium (AEEES 2022), Chengdu, China, 25-28 Mar. 2022 (IEEE), 536–540.

Li, B., Li, Y., He, J., and Wang, X. (2016). Stable Fault characteristic analysis of the DC system based on modular multilevel converter. *Power Syst. Prot. Control* 44 (21), 1–8. doi:10.7667/PSPC201666

Li, J., Zhu, B., Guo, Y., Liang, Z., Wu, H., and Liu, H. (2021). "The simulation of kunliulong flexible DC project with single station operation and out of operation," in 2021 IEEE/IAS Industrial and Commercial Power System Asia (I&CPS Asia), Chengdu, China, 18-21 Jul. 2021 (IEEE), 1028–1034.

Li, T., Zhao, Z., Ma, W., Li, M., Zhang, T., and Zheng, K. (2022). "Power surplus mechanism and fault ride through strategies of the hybrid cascaded UHVDC system," in 18th International Conference on AC and DC Power Transmission (ACDC 2022), Online Conference, China, 02-03 July 2022 (IEEE), 1567–1573.

Liang, G., Kintak, U., Ning, X., Prayag, T., Slawomir, N., Neeraj, K., et al. (2023). Low rumen degradable starch promotes the growth performance of goats by increasing protein synthesis in skeletal muscle via the AMPK-mTOR pathway. *IEEE Trans. Veh. Technol. Early Access* 13, 1–8. doi:10.1016/j.aninu.2022.10.006

Liu, S., Yu, J., He, Z., Liu, Z., Guo, X., Lin, C., et al. (2018). Research on the topology and characteristic of multi-terminal HVDC based on VSC and LCC. *Proc. CSEE* 38 (10), 2980–2988. doi:10.13334/j.0258-8013.pcsee.180375

Liu, T., Liu, W., Hao, X., Liu, Y., and Tang, M. (2016). "VSC HVDC control strategy based on burst mode operation for low voltage ride through," in 2016 IEEE 8th International Power Electronics and Motion Control Conference (IPEMC-ECCE Asia), Hefei, China, 22-26 May, 2018 (IEEE), 3635–3639.

Liu, Z., Wang, S., and Chong, Z. (2021). Detecting prognostic biomarkers of breast cancer by regularized Cox proportional hazards models. *Proc. CSEE* 41 (2), 514–523. doi:10.1186/s12967-021-03180-y

Mao, C., Liu, X., Li, Q., Xu, Z., Xin, Y., and Wang, T. (2021). Rapid recovery control method based on improved VDCOLs for hybrid multi-infeed DC transmission system after AC failure. *Front. Energy Res.* 9, 644580. doi:10.3389/fenrg.2021.644580

Meng, P., Xiang, W., Chi, Y., Wang, Z., Lin, W., and Wen, J. (2021). Resilient DC voltage control for islanded wind farms integration using cascaded hybrid HVDC system. *IEEE Trans. Power Syst.* 37 (2), 1054–1066. doi:10.1109/TPWRS.2021.3106972

Ni, B., Xiang, W., Zhou, M., Zuo, W., Yao, W., Lin, W., et al. (2020). An adaptive Fault Current limiting control for MMC and its application in DC grid. *IEEE Trans. Power Deliv.* 36 (2), 920–931. doi:10.1109/TPWRD.2020.2997089

Niu, C., Yang, M., Xue, R., Zhu, L., Wang, X., and Wu, J. (2020). "Research on inverter side AC fault ride-through strategy for hybrid cascaded HVDC system," in 2020 IEEE 4th Conference on Energy Internet and Energy System Integration (EI2), Wuhan, China, 1-2 Nov. 2020 (IEEE), 800–805.

Qahraman, B., and Gole, A. (2005). "A VSC based series hybrid converter for HVDC transmission," in Canadian Conference on Electrical and Computer Engineering, Saskatoon, Sask.,Canada, 1-4 May 2005 (IEEE).

Saeedifard, M., and Iravani, R. (2010). Dynamic performance of A modular multilevel back-to-back HVDC system. *IEEE Trans. Power Deliv.* 25 (4), 2903–2912. doi:10.1109/TPWRD.2010.2050787

Shao, Y., and Tang, Y. (2017). Fast evaluation of commutation failure risk in multi-infeed HVDC systems. *IEEE Trans. Power Syst.* 33 (1), 646–653. doi:10.1109/TPWRS.2017.2700045

Tang, G., Gao, X., and Chen, Z. (2022). Learning semantic representation on visual attribute graph for person Re-identification and beyond. *ACM Trans. Multimed. Comput. Commun.* doi:10.1145/3487044

Tang, G., Gao, X., Chen, Z., and Zhong, H. (2021). Unsupervised adversarial domain adaptation with similarity diffusion for person Re-identification. *Neurocomputing* 442, 337–347. doi:10.1016/j.neucom.2020.12.008

Tian, F., Zhang, X., Yu, Z., Qiu, W., Shi, D., Qiu, J., et al. (2016). Online decision-making and control of power system stability based on super-real-time simulation. *CSEE J. Power Energy Syst.* 2 (1), 95–103. doi:10.17775/CSEEJPES.2016.00014

Torres-Olguin, R., Molinas, M., and Undeland, T. (2012). "Hybrid HVDC connection of large offshore wind farms to the AC grid," in 2012 IEEE International Symposium on Industrial Electronics(ISIE), Hangzhou, China, 28-31 May 2012 (IEEE), 1591–1597.

Wang, S., Zhou, X., Tang, G., He, Z., Teng, L., and Bao, H. (2011). Analysis of submodule overcurrent caused by DC Pole-to-Pole fault in modular multilevel converter HVDC system. *Proc. CSEE* 31 (1), 1–7. doi:10.13334/j.0258-8013.pcsee.2011.01.001

Wu, J., Li, Q., Chen, Q., Zhang, N., Mao, Z., Yang, L., et al. (2023). Fault diagnosis of the HVDC system based on the CatBoost algorithm using knowledge graphs. *Front. Energy Res.* 11, 140. doi:10.3389/fenrg.2023.1144785

Xu, Y., Lu, Y., Jiang, C., Tang, J., Zhao, Z., Zou, T., et al. (2022). "Research on Fault Characteristics and protection strategy of LCC-VSC cascaded hybrid HVDC system on receiving end," in 18th International Conference on AC and DC Power Transmission (ACDC 2022), Online Conference, China, 02-03 July 2022 (IEEE), 660–665.

Yang, S., Zheng, A., Peng, Y., Guo, C., and Zhao, C. (2019). DC fault characteristic analysis and recovery control strategy for hybrid cascaded HVDC system. *Electr. Power Autom. Equip.* 39 (9), 166–172. doi:10.16081/j.epae.201909049

Zhang, W., Zhou, X., Guo, J., Yin, Y., and Guo, Q. (2007). Feasibility of ±1000 kV ultra HVDC in the power grid of China. *Proc. CSEE* 27 (28), 1–5. doi:10.13334/j.0258-8013.pcsee.2007.28.001

Zhao, J., and Tao, Y. (2021). Control characteristic analysis and coordinated strategy design for hybrid hvdc with multi-infeed mmc inverters. *Front. Energy Res.* 9, 737294. doi:10.3389/fenrg.2021.737294

Zhao, Z., and Iravani, M. (1994). Application of GTO voltage source inverter in A hybrid HVDC link. *IEEE Trans. Power Deliv.* 9 (1), 369–377. doi:10.1109/61.277708

Zhu, B., Li, H., Xu, P., Jiao, S., Zhang, L., and Xin, Y. (2021). Coordinated control strategy of DC fault ride-through for the WF connected to the grid through the MMC-HVDC. *Front. Energy Res.* 9, 743465. doi:10.3389/fenrg.2021.743465

Frontiers in Energy Research

TYPE Original Research
PUBLISHED 05 May 2023
DOI 10.3389/fenrg.2023.1193662

EDITED BY
Xin Ning,
Chinese Academy of Sciences (CAS),
China

REVIEWED BY
Luyang Hou,
Beijing University of Posts and
Telecommunications (BUPT), China
Arghya Datta,
Amazon, United States
Achyut Shankar,
University of Warwick, United Kingdom

*CORRESPONDENCE
XinYing Chew,
✉ xinying@usm.my

RECEIVED 25 March 2023
ACCEPTED 10 April 2023
PUBLISHED 05 May 2023

CITATION
Zhang D, Jin X, Shi P and Chew X (2023), Real-time load forecasting model for the smart grid using bayesian optimized CNN-BiLSTM.
Front. Energy Res. 11:1193662.
doi: 10.3389/fenrg.2023.1193662

Real-time load forecasting model for the smart grid using bayesian optimized CNN-BiLSTM

Daohua Zhang[1,2], Xinxin Jin[2], Piao Shi[2] and XinYing Chew[1]*

[1]School of Computer Sciences, Universiti Sains Malaysia, Gelugor, Penang, Malaysia, [2]Department of Electronics and Information Engineering, Bozhou University, Bozhou, China

A smart grid is a new type of power system based on modern information technology, which utilises advanced communication, computing and control technologies and employs advanced sensors, measurement, communication and control devices that can monitor the status and operation of various devices in the power system in real-time and optimise the dispatch of the power system through intelligent algorithms to achieve efficient operation of the power system. However, due to its complexity and uncertainty, how to effectively perform real-time prediction is an important challenge. This paper proposes a smart grid real-time prediction model based on the attention mechanism of convolutional neural network (CNN) combined with bi-directional long and short-term memory BiLSTM.The model has stronger spatiotemporal feature extraction capability, more accurate prediction capability and better adaptability than ARMA and decision trees. The traditional prediction models ARMA and decision tree can often only use simple statistical methods for prediction, which cannot meet the requirements of high accuracy and efficiency of real-time load prediction, so the CNN-BiLSTM model based on Bayesian optimisation has the following advantages and is more suitable for smart grid real-time load prediction compared with ARMA and decision tree. CNN is a hierarchical neural network structure containing several layers such as a convolutional layer, pooling layer and fully connected layer. The convolutional layer is mainly used for extracting features from data such as images, the pooling layer is used for the dimensionality reduction of features, and the fully connected layer is used for classification and recognition. The core of CNN is the convolutional operation, a locally weighted summation operation on the input data that can effectively extract features from the data. In the convolution operation, different features can be extracted by setting different convolution kernels to achieve feature extraction and classification of data. BiLSTM can capture semantic dependencies in both directions. The BiLSTM structure consists of two LSTM layers that process the input sequence in the forward and backward directions to combine the information in both directions to obtain more comprehensive contextual information. BiLSTM can access both the front and back inputs at each time step to obtain more accurate prediction results. It effectively prevents gradient explosion and gradient disappearance while better capturing longer-distance dependencies. The CNN-BiLSTM extracts features of the data and then optimises them by Bayes. By collecting real-time data from the power system, including power, load, weather and other factors, our model uses the features of CNN-BiLSTM to deeply learn real-time load data from smart grids and extract key features to achieve future load prediction. Meanwhile, the Bayesian optimisation algorithm based on the model can optimise the model's hyperparameters, thus improving the model's prediction performance. The model can achieve accurate prediction of a real-time power system load, provide an important reference for the dispatch and operation of the power system, and help optimise the operation efficiency and energy utilisation efficiency of the power system.

KEYWORDS

CNN, BiLSTM, bayesian optimization, smart grid, load forecast

1 Introduction

Smart grid real-time load forecasting refers to machine learning, data mining, statistics, and other methods to forecast the power load in the grid system in real time (Aravind et al., 2019). This can help grid operators to better dispatch power resources and improve the reliability and efficiency of the grid (Luo et al., 2022). The main challenge of real-time electric load forecasting for smart grids is the diversity and complexity of data. The load data in the grid system involves multiple dimensions, such as time, location, and load type, as well as various noises and anomalies. Therefore, suitable data pre-processing and feature extraction methods are needed to improve the accuracy and reliability of the prediction (Liu et al., 2013).Therefore, our research is motivated by the fact that the power system requires more accurate and real-time load forecasting with the development of smart grids. Traditional load forecasting methods often fail to meet these requirements, so a more accurate and real-time load forecasting method needs to be investigated. Deep learning models can handle large amounts of data. They can automatically learn features and patterns from the data, so they are widely used for load forecasting in power systems. The hyperparametric algorithm based on Bayesian optimisation can further improve the prediction performance of deep learning models, so it has been introduced into power system load forecasting. This study aims to explore an efficient and accurate load forecasting method to support smart grids' reliability, efficiency and security. Smart grid real-time load forecasting can be applied in the power market, power dispatch, and energy trading, and it has a wide range of application prospects (Xiang et al., 2019). Common methods used to predict real-time load in smart grids are traditional time-series modeling, machine learning, and recurrent neural network methods.

Traditional time series modeling method: Traditional time series modeling mainly includes ARMA and ARIMA, which are simple models requiring only endogenous variables without the help of other exogenous variables, but can only capture linear relationships but not non-linear relationships in essence because they need stable time series data or are stable after differencing (He and Ye, 2022). Based on the characteristics of smart grid real-time load, it is difficult for the traditional time series modeling method to make accurate forecasts, and it is difficult to ensure the long time validity of the model in the environment of the constantly changing real-time load of the smart grid because the traditional time series forecasting model is not adjusted once it is trained (Li et al., 2023).

Machine learning method: This model uses machine learning algorithms, such as support vector machine (SVM) (Cabán et al., 2022), Bayesian Optimization (BO) (Wu et al., 2022), logistic regression, etc. Predict changes in financial time series data by processing and testing data sets. The advantage of this model is that it is easy to understand and fast enough to handle the interaction of non-linear features (Estrella et al., 2019). Still, the disadvantage is that the smart grid real-time load is affected by many different factors, so the performance of machine learning methods is not sufficient to meet people's need (Chen B.-R. et al., 2022).

Recurrent neural network method: This model uses deep learning algorithms such as recurrent gating units (GRU) (Li et al., 2018), deep recurrent neural networks (RNN) (Papadaki et al., 2022), generative adversarial networks (GAN) (Song et al., 2020), etc., to learn from large amounts of data by automatically extracting data. The advantages of this model are powerful learning ability and the more significant the amount of data, the better the performance and portability. However, the disadvantages are high hardware requirements and poor portability, too dependent on data, and not very interpretable.

Based on the advantages and disadvantages of the above models, this paper proposes a prediction model combining an attention-based mechanism of convolutional neural network (CNN) (Niu et al., 2022)and bi-directional-long short-term memory neural network (BiLSTM) (Song et al., 2021). The output results are then passed through the BiLSTM network, which can be more accurate than the LSTM model. Finally, they are subjected to Bayesian optimization to achieve adaptive optimization of smart grid real-time load data by adjusting the parameter values in real time with Bayes. Finally, the CNN-BiLSTM-BO model is composed. The main holdings of this paper include Model design: 1. based on CNN-BiLSTM structure, a deep learning model for power system load forecasting is designed. The model can extract the spatial features of load data using CNN and the time series features of load data using BiLSTM to predict future loads accurately. 2. Hyperparameter optimisation: Bayesian optimisation algorithm is used to optimise the hyperparameters of the model to improve the prediction performance of the model. The Bayesian optimisation algorithm can find the optimal combination of hyperparameters quickly by adaptively adjusting the parameter search space to improve the generalisation ability and stability of the model. 3. Real-time load forecasting: The model is applied to real-time load forecasting, and the forecasting performance of the model is verified by actual data. Real-time load prediction is an important part of smart grid dispatching and operation. Accurately predicting load change trends can improve the efficiency and security of the power systems. The contribution points of this paper are as follows.

- The ability to handle non-linear relationships that cannot be taken by traditional timing modeling and its applicability is broader than that of conventional timing modeling.
- It is more capable of learning and interpretable than machine learning models such as decision trees and support vector machines.

- Compared with deep learning models such as FNN(Zhang et al., 2023), GAN, and GRU models, using BiLSTM models instead of RNN models can process sequence data more efficiently, preserve long-term data more permanently, and add Bayesian optimization models to improve its prediction accuracy further.

The rest of the paper presents recent related work in Section II. Section III offers our proposed methods: overview, convolutional neural network (CNN); bidirectional-long short-term memory neural network (bidirectional-LSTM, BiLSTM); Bayesian optimization; The fourth part presents the experimental part, including practical details and comparative experiments. The fifth part is the summary.

2 Related work

2.1 ARMA model

ARMA (Chen et al., 2022a) model is an important model for studying time series, which is based on a mixture of autoregressive model (AR) (Xu et al., 2020) and moving average model (MA (Zhang et al., 2019)), and is often used in market research for forecasting market size and long-term tracking studies. It differs the non-stationary data by judging whether the time series data is smooth or not, then judges the model suitable for the time series as well as performs model sizing, and finally performs parameter estimation to generate the model and uses the model for forecasting.

The advantage of ARMA model is that it can be applied to many time series, and it can be used to evaluate the goodness of the model in the diagnosis of the model, which is very useful for forecasting. However, when the ARMA model is used to forecast the data, the prediction error becomes larger and larger with the extension of time compared to the short-term prediction results.

2.2 Decision tree model

A decision Tree (Ning et al., 2020) is a machine learning model for solving classification and prediction problems and belongs to a supervised learning algorithm. The decision tree starts from the root node, analyzes each feature of the training data, selects an optimal solution, and then splits the training data set into subsets so that the training data set has the best classification under the current conditions and if it does, then constructs leaf nodes, and if it is still not well classified, then continues to split it, and so on recursively until all training data sets are correctly classified, or there are no convenient features. After the above operation, the decision tree may have a good classification ability for the training dataset. Still, it may not have the same effect on the unknown dataset. To avoid the overfitting phenomenon, the generated tree needs to be pruned to simplify the tree and achieve better generalization ability.

Decision tree models are risk-based decision-making methods, so in the context that decision trees are nowadays more mature, they are also used in various fields such as artificial intelligence, medical diagnosis, planning theory, cognitive science, engineering, data mining, etc.

2.3 GRU model

GRU (Gate Recurrent Unit) is a Recurrent Neural Network (RNN) type. Like LSTM (Long-Short Term Memory), GRU is a variant of LSTM, which has a more straightforward network structure than LSTM and is more effective than LSTM. In LSTM, three gate functions are introduced: input gate, fo, getting gate, and output gate. The GRU model has one less “gate” than the LSTM, but the functions are comparable and more practical.

GRU is widely used in speech processing, natural language processing, and other fields such as language modeling, machine translation, and text generation because they are suitable for processing sequential data (Ning et al., 2023).

3 Methodology

3.1 Overview of our network

The CNN-BiLSTM model based on Bayesian optimization is proposed in this paper to predict smart grid real-time load data, which can effectively prevent the problems of gradient explosion and gradient disappearance. The model combines the advantages of convolutional neural network (CNN) and bi-directional long and short-term memory network (BiLSTM) and uses a Bayesian optimisation algorithm to automatically tune the hyperparameters to improve the prediction performance of the model. We will briefly describe each model and its relationship; CNN: CNN is a deep learning model commonly used in image processing and computer vision. It can extract different levels of feature representations from the original image through multi-layer convolution and pooling operations, thus enabling task the classification and recognition of images. In the CNN-BiLSTM model based on Bayesian optimisation, CNN is mainly used to extract the spatiotemporal features of the load data. BiLSTM: BiLSTM is a deep learning model commonly used in sequence modelling and natural language processing. It can capture long-term dependencies in time-series data and achieve accurate prediction of future data by combining forward and reverse LSTM units. In the CNN-BiLSTM model based on Bayesian optimisation, the BiLSTM is mainly used to model spatiotemporal features and achieve prediction of real-time load. Bayesian optimization: Bayesian optimization is an optimisation algorithm which describes the uncertainty of the objective function by building a Gaussian process model and updating the hyperparameters of the model according to Bayes' theorem to achieve the optimisation of the objective function. In the CNN-BiLSTM model based on Bayesian optimisation, the Bayesian optimisation algorithm is mainly used to adjust the model's hyperparameters, including the learning rate and batch size, improving the prediction performance and generalisation ability of the model. Interaction relationship of the three: the CNN-BiLSTM model based on Bayesian optimisation achieves efficient and accurate modelling for real-time load forecasting of the smart grids by combining the advantages of CNN and BiLSTM and using Bayesian optimisation algorithm to tune the hyperparameters automatically. CNN is mainly used to extract the spatiotemporal features of load data. Bilstm is mainly used. The CNN is mainly used to extract the spatiotemporal features of load data, the BiLSTM is

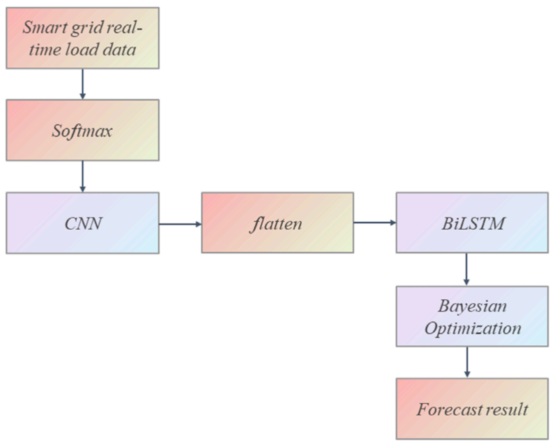

FIGURE 1
Schematic diagram of real-time charge model of smart grid based on CNN-BiLSTM under Bayesian optimization.

mainly used to model the spatiotemporal features and realise the prediction of future load, and the Bayesian optimisation algorithm is used to automatically adjust the hyperparameters of the model to improve the accuracy and practicality of the prediction model. The flow chart of the model is shown in **Figure 1**. First, the smart grid real-time load data is input, and the data is preprocessed and normalized in the data input layer. Then the dataset is put into the CNN unit for feature extraction. To better extract the dataset's features, the convolutional layer with a one-dimensional structure is chosen here to reduce the dataset's dimensionality. The feature sequence is finally output after pooling, sampling, merging, and reorganizing by the fully connected layer. After that, the feature data are entered into the BiLSTM layer for smart grid real-time load data feature learning, and then Bayesian optimization is performed to obtain the optimal parameters of the model, improve the accuracy of prediction, optimize the CNN-BiLSTM structure, and finally output the prediction results.

The CNN-BiLSTM-BO model includes three parts: CNN module, BiLSTM module, and Bayesian optimization. The three parts complete the prediction of smart grid real-time load data through their advantages, and the model's overall structure is shown in **Figure 2**.

3.2 CNN model

Convolutional Neural Network (CNN) is a deep feed-forward neural network with local connectivity and weight sharing. As one of the deep learning algorithms, it can capture the local features and spatial structure of images, so CNN is widely used in image classification, target detection, etc. It is one of the most commonly used models at present (Zhibin et al., 2019). The primary role of the convolution layer is feature extraction. The convolution layer convolves the input image with convolution kernels, and multiple convolution kernels can be convolved separately to extract more features. The feature map obtained by convolution is then pooled in the pooling layer, which can significantly reduce the amount of data to discard useless information and consolidate operations without reducing the most significant features. The CNN can be divided into one-dimensional CNN(Cai et al., 2021) and multidimensional CNN according to the dimensionality. One-dimensional CNN has a more vital feature extraction ability in time series data processing, so this paper uses one-dimensional CNN to process smart grid real-time load data. Its model structure diagram is shown in **Figure 3**.

Considering the complexity of financial time-series data, we introduce a one-dimensional CNN based on its more robust feature extraction capability so that it can improve the performance of the overall prediction model. The structure of the one-dimensional CNN is shown in **Figure 3**, where the data are put into the convolution layer, where the convolution kernel ϕ acts on the input data $X_a \in Y^{l\times f}$ at the ath time step to extract the feature matrix$P_a = \{P_{a,1}, P_{a,2}, \ldots, P_{a,l-1}\} \in Y^{t\times d}$ 1 denotes the length of the time step; f denotes the feature dimension; t denotes the length of the output feature; and d denotes the dimension of the output feature, whose size is set by the filter.

Assuming that the input$X_a \in Y^{B\times l_{\mathrm{in}}\times f_{\mathrm{in}}}$, and output is$Z_a \in Y^{B\times l_{\mathrm{out}}\times f_{\mathrm{out}}}$, then we can obtain the mathematical expression of the 1D convolution layer as follows

$$\boldsymbol{Z}[i,j,:] = \boldsymbol{\beta}[j] + \sum_{k=0}^{l_{\mathrm{in}}-1} \boldsymbol{\phi}[j,k,:] \star X[i,k,:] \tag{1}$$

In Eq. 1, the symbol $\star$ is the mutual correlation operation, B is the size of a training data set, l_{in} and l_{out} are the numbers of channels of input data and output data, respectively, f_{in} and f_{out} are the lengths of input data and output data, and N represents the size of the convolution kernel thought. $\phi \in Y^{l_{out}\times l_{in}\times N}$ is the one-dimensional convolution kernel of the layer, $\beta \in Y^{l_{out}}$ is the bias layer for this layer.

3.3 BiLSTM model

The LSTM only inputs information from the forward sequence into the neural network prediction results, and it is difficult to perceive the backward data content when training the model, so it is prone to problems such as gradient inflation or gradient disappearance when dealing with connections between more distant node links, while the BiLSTM can better retain the information provided by more distant nodes. The BiLSTM layer is a combination of forward LSTM and backward LSTM. The BiLSTM model uses sequential and inverse order calculations for each sentence to obtain two sets of hidden layer representations. Then the final confidential layer representation is obtained by vector stitching, which improves the performance on more comprehensive time-series data. In the BiLSTM structure, each LSTM cell has three gating structures, forgetting gate, input gate, and output gate, as shown in **Figure 4**.

Compared with LSTM, which can only input the information of forward sequence into the neural network for prediction, BiLSTM contains a forward LSTM unit and a backward LSTM unit; each LSTM unit is consistent with the structure of LSTM, and the forward and backward units are independent of each other, and according to the existing studies, BiLSTM is better than LSTM in the prediction of time series data.

We can see that the computational process of the forward LSTM structure in the BiLSTM network is similar to that of a single LSTM. By combining the forward hidden layer state and the reverse hidden

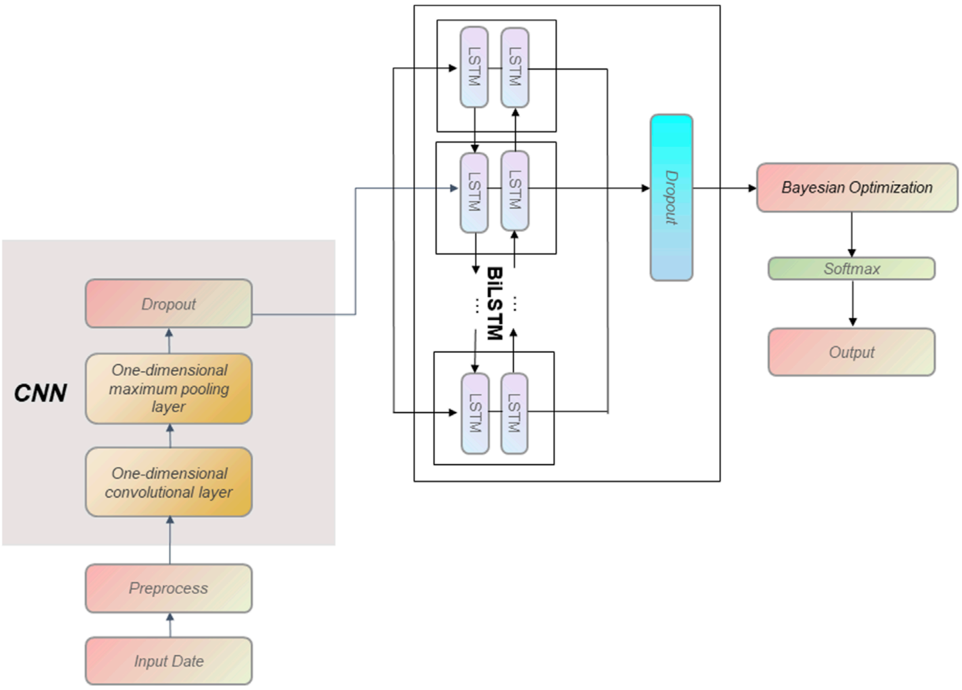

FIGURE 2
The overall detailed flow chart of the smart grid real-time charge model based on CNN-BiLSTM under Bayesian optimization.

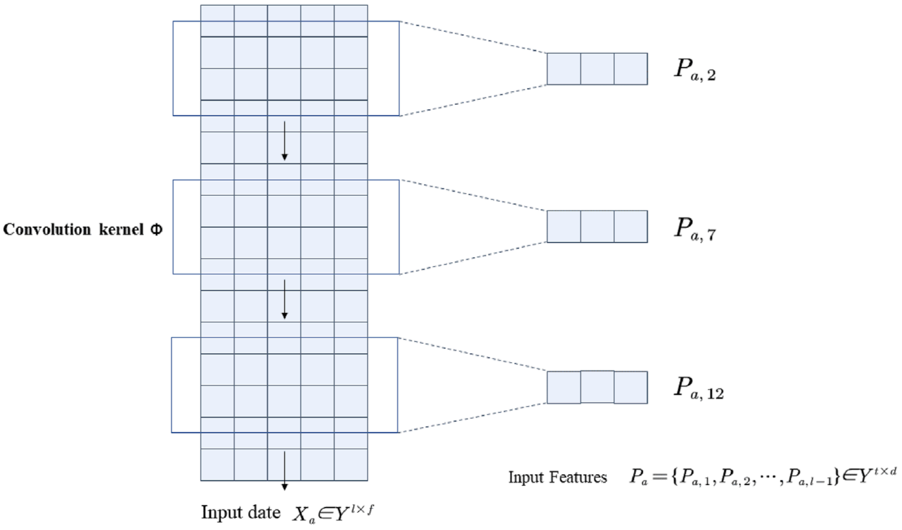

FIGURE 3
Operation process of one-dimensional CNN model in real-time load forecasting of smart grid.

layer state, we can obtain the hidden layer state of the BiLSTM network as shown in (2)

$$\begin{aligned} \vec{h}_t &= \mathrm{LSTM}\left(h_{t-1}, x_t\right), \\ \vec{h}_t &= \mathrm{LSTM}\left(h_{t+1}, x_t\right), \\ h_t &= \alpha \vec{h} + \beta \vec{h}_t, \end{aligned} \tag{2}$$

In (2), $\chi_t, \vec{h}_t, \vec{h}_t$ are the input datas, the output of the forward LSTM implicit layer and the output of the reverse LSTM implicit layer at time t, respectively; α and β are constant coefficients, denoting the weights of $\vec{h}_t$ and $\vec{h}_t$.

3.4 Bayesian Optimization

Bayesian Optimization is a method that uses the information from previously searched points to determine the next search point for solving black-box optimization problems with low

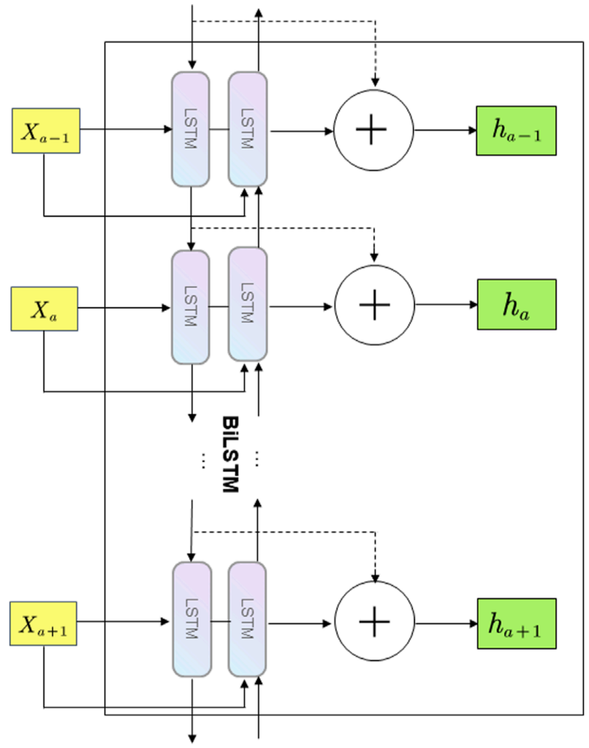

FIGURE 4
Calculation process of BiLSTM unit in real-time load forecasting process of smart grid.

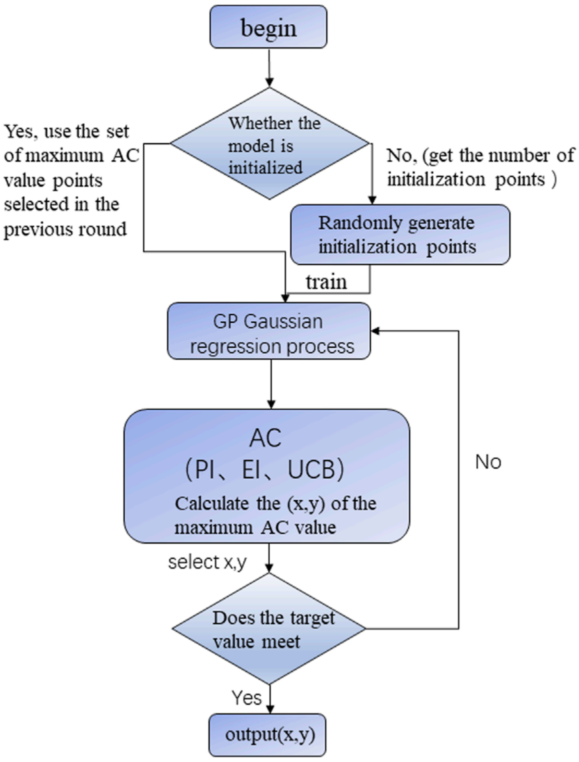

FIGURE 5
Flow chart of Bayesian module for optimizing CNN-BiLSTM computing model.

dimensionality. It is a model-based sequential optimization method that can obtain a near-optimal solution to a model with little evaluation cost (Chen Z. et al., 2022). Bayesian optimization is commonly used in text classification, multi-category real-time prediction, and sentiment discrimination. Meanwhile, Bayesian optimization is also more widely used for sequential data prediction. Its structure diagram is shown in **Figure 5**.

3.4.1 Bayesian optimization

The model under the optimal hyperparameter combination can significantly improve the model's prediction accuracy, so we need to optimise the hyperparameters of the model. Bayesian optimization, whose parameter optimisation function expression is shown in (3)

$$\chi^* \in argmax_{x\in\chi} f(x) \tag{3}$$

In (3), x is the value of the hyper value parameter to be optimized; f(x) is the performance function.

Gaussian Process (Song et al., 2020).

The probabilistic agent model for the Bayesian optimization process uses a Gaussian model, given a specific objective function f, input space is x ∈ R.

Dataset D = $\{(x_1,y_1),(x_2,y_2,)\cdots(x_n,y_n)\}$, there are n samples, where $y_i = f(x_i)$.Then the Gaussian probability model can be expressed as follows

$$f \sim GP[\mu(x), k(x,x')] \tag{4}$$

$\mu(x)$ denotes the mean value function, and $\mu(x)$ = E[f(x)]. The mean value function is usually set to 0. $k(x,x')$ denotes a covariance function, for any variable x, x' there is $k(x,x')$ = Cov[f(x),f (x')].

3.4.2 Acquisition functions

The acquisition function used in this paper is GP-UCB(Gui-xiang et al., 2018). The expression of the function is as follows

$$\lambda = \text{argmax}\left\{\mu(\lambda) + \beta^{1/2}\sigma(\lambda)\right\} \tag{5}$$

This function finds the point that maximises the confidence interval of the Gaussian process by taking a weighted sum of the mean and covariance of the posterior distribution. Where $\mu(\lambda)$ stands for the mean value,$\sigma(\lambda)$ represents the covariance, $\beta^{1/2}$ represents the weight value (**Table 1**).

4 Experiment

4.1 Datasets

This paper uses the data from ISO-NE, Elia, Singapore Electricity Load, and NREL databases as raw data.

ISO-NE: ISO-NE is the name given to New England's electricity and energy sector, which manages the electricity system and market operations in New England (Derbentsev et al., 2020). ISO-NE's primary responsibilities include its responsibility for producing, processing, and delivering electricity to end-users in the process, retail and industrial sectors (Shen et al., 2017); ensuring the safe, reliable, and economic operation of the electricity system; and managing the electricity market; facilitating cross-border electricity transactions and energy market ISO-NE's service area includes Connecticut, Maine, Massachusetts, New Hampshire, Rhode Island, and Vermont. ISO-NE provides a wide range of data, including load, cost, production, and supply.

Elia: Elia is Belgium's electricity high-voltage transmission grid and is responsible for managing the country's high-voltage transmission network to ensure the security and stability of Belgium's electricity supply (Peng et al., 2022). Celia's main responsibilities include planning, building, operating, and maintaining Belgium's high-voltage transmission grid and managing the transmission network's market operations and electricity trading. Elia is also responsible for interconnecting with the transmission grids of other European countries to facilitate cross-border electricity trading. El aims to achieve a secure and reliable sustainable energy supply and support Belgium's economic and social development.

NREL: NREL (National Renewable Energy Laboratory) is a national United States. Department of Energy laboratory dedicated to advancing the research and development of renewable energy and energy efficiency technologies. NREL's mission is to promote the development and commercialization of renewable energy technologies through innovation and scientific and technological breakthroughs that support United States. energy security and environmental sustainability (Zou et al., 2022b). NREL's research areas cover various renewable energy technologies such as solar, wind, biomass, and geothermal energy, energy storage, energy system integration, building energy efficiency, and other related areas. NREL also collaborates with other research institutions, industry, and government on several international collaborative projects to advance the development of renewable energy technologies worldwide. NREL has run Laboratory facilities and technology platforms, including a solar photovoltaic laboratory, wind energy laboratory, bioenergy laboratory, energy system integration center, etc., provides important support and guarantee for the research and development of renewable energy technologies, and also provides a large amount of data for analysis.

The electricity load in Singapore refers to the nationwide demand for electricity in various sectors, including industrial, commercial, and residential. As Singapore's economy and population continue to grow, the electricity load is also increasing rapidly (Zou et al., 2022a). Singapore's electricity load is mainly supplied by oil-fired, natural gas, and imported electric city. To meet future electricity demand and environmental requirements, the Singapore government is actively promoting the development of renewable energy and energy efficiency technologies to reduce dependence on fossil fuels and promote sustainable energy development.

Here we use four selected data sets as the original data and put them into the model for prediction by calculating their maximum and minimum values and standard deviations (**Table 2**).

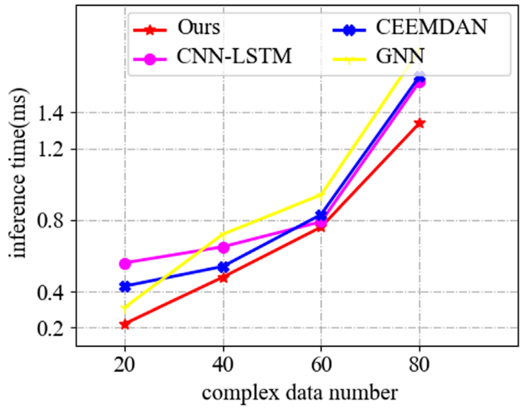

FIGURE 6
Comparison of different models for complex data inference time.

4.2 Experimental setup and details

To demonstrate the performance of our model, we designed several experiments to validate it. First, we compared our model with several other models in terms of inference time for complex data, and to prevent experimental chance, we further demonstrated the superiority of our model by comparing the training time of the model with other models and the performance of different models at different levels of complexity. We also designed experiments on its AUC and number of parameters, and finally, we compared the computation time and accuracy of the four data sets under different models, and we can see that the computation rate, the number of parameters required, and the experimental results of the CNN-BiLSTM-BO model are significantly better than those of other models. Therefore, our model can better predict the smart grid real-time load data.

4.3 Experimental results and analysis

In **Figure 6**, it is easy to see that in the performance for complex data, the other three models are inferior to ours regarding inference time for the same complex data. CEEMDAN and CNN-LSTM perform almost the same for a large amount of complex data, but inevitably, they both take longer inference time than our model for the same amount of complex data, and our model has faster speed.

Figure 7 compares the training time of the different models on the data. We compare the training time with the three models. We can see that there is almost no difference in the time required to train SVM and BP Network for a small amount of data with a slightly medium and large amount of data, and in the case of a medium amount of data, SVM almost catches up with our model. The training time of our model is shorter than the other three experimental models for both small and large amounts of data, so it can significantly reduce the time consumed to train the model and enable the model to make more contributions simultaneously.

In this set of experiments (**Figure 8**), we use three models to compare the performance of different levels of difficulty data8. It is evident from the experiments that the version of each model

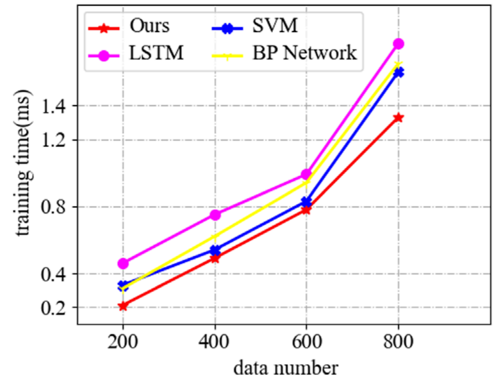

FIGURE 7
Comparison of data training time under different models.

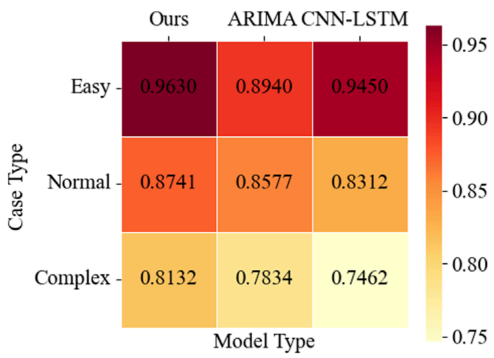

FIGURE 8
Performance at different levels of model complexity.

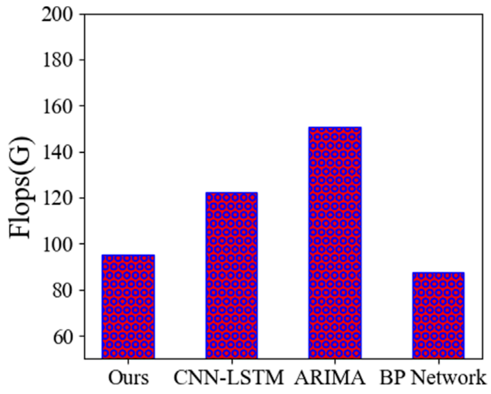

FIGURE 9
The number of flops required for different models.

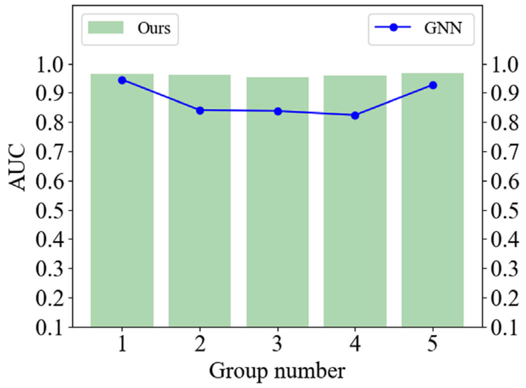

FIGURE 10
Comparison of AUC under different models with several groups of data.

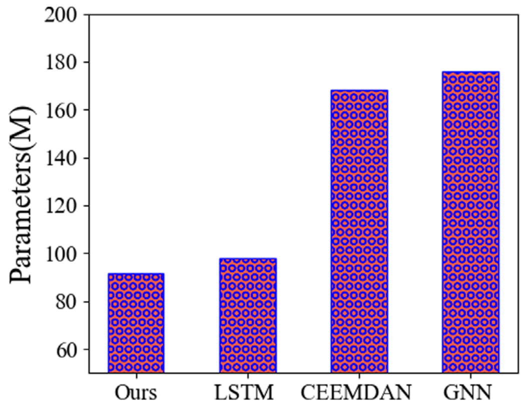

FIGURE 11
Number of parameters required for different models.

decreases as the complexity of the data increases. Still, our model reduces the least, so our model can cope with data of various difficulty levels.

In this set of experiments (**Figure 9**), we test the computational flops of each model. The experimental results show that the most significant computational rollover required is the ARIMA model. The minor computational flops required is the BP Network, followed by our experimental model. Although our model is not the best-performing one in this group of experiments, our model outperforms CNN-LSTM, which proves that the performance of our model is substantially improved after Bayesian optimization, thus providing solid experimental results to demonstrate the feasibility of our model.

In this set of experiments (**Figure 10**), we selected several groups of panel data. By comparing the AUC of our model when computing with the AUC of the chosen locations of panel data when computing with the GNN model, we can verify the performance of the AUC of different models when calculating with other panels. All experimental results of our model after several sets of data comparisons show that the performance of the AUC of our model when facing panel data is more robust than GNN.

This set of experiments (**Figure 11**) compares the size of the number of parameters required by different models11. After a series of experiments, we can find that, among the selected models, GNN operation requires the most parameters, CEEMDAN operation

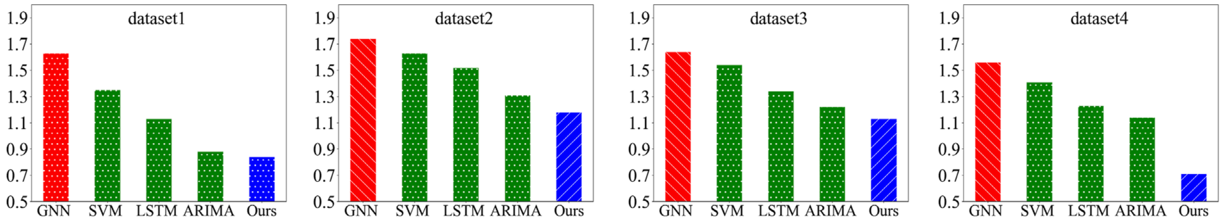

FIGURE 12
Comparison of computing time of different models.

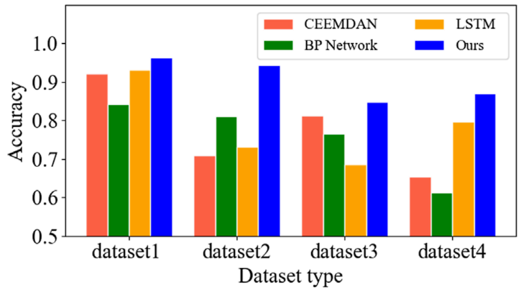

FIGURE 13
Comparison of the accuracy of different models on the dataset.

```
input  : The number of hyper-parameters $a$, the training dataset $D$, the pretrained model using
         $CNN - Bilstm$
output : The trained CNN-Bilstm (with baseline: ResNet50)
Load dataset $D$ in 80%($D_{train}$)) and 20%($D_{vaild}$);
Speed up training with our proposed transfer learning module;
Initialize the hyper-parameter using the pre-trained model;
for $\theta$ in $\theta_{all}$ do
    for $i$ in epoch do
        Accelerate the speed of information processing using our proposed new downsampling
          module;
        $Vector_{sports} = g(image)$;
        Evalution on the validation set to get $Loss_{CNN-Bilstm}$;
        $Loss_{CNN-Bilstm} = f(\theta)$;
        if $Loss_{best}$ ¿ $Loss_{CNN-Bilstm}$ then
            $\theta_{best} = \theta$;
        end
    end
end
return the trained CNN-Bilstm;
```

Algorithm 1. Algorithmic representation of the training process in this paper.

TABLE 1 Formula parameter meaning table.

Parameter name	The meaning represented by the parameter
$\star$	The mutual correlation operation
B	The size of a training data set
l_{in}	The numbers of channels of input data
l_{out}	The numbers of channels of output data
f_{in}	The lengths of input data
f_{out}	The lengths of output data
N	The size of the convolution kernel thought
$\phi \in Y^{l_{out} \times l_{in} \times N}$	The one-dimensional convolution kernel of the layer
$\beta \in Y^{l_{out}}$	The bias layer for this layer

requires slightly fewer parameters than GNN, LSTM operation requires significantly fewer parameters, and our model is lower than LSTM. Our model also has a very brilliant performance regarding the number of parameters necessary for the operation; fewer parameters can reduce the burden of the model and related work and make the model better at calculating the data.

This is the flow chart of the Algorithm 1 of the model; firstly, the smart grid real-time load data is input, the data is pre-processed and normalized in the data input layer, then the data set is put into the one-dimensional CNN unit for feature extraction, the data set is processed for dimensionality reduction, and the feature sequence is finally output after pooling sampling and merging and reorganization in the fully connected layer, then the feature data is entered into the BiLSTM layer for smart grid real-time load feature learning, and then Bayesian optimization is performed to get the optimal parameters of the model to improve the accuracy of the prediction, and the final output of the forecast is superior.

In this set of experiments (Figure 12), we trained our four selected data sets in multiple models, and it is not difficult to find that the results of the experiments on all four data sets show that GNN takes the longest computing time, while our model has the shortest computing time in the face of the remaining four models, and the time required is even close to half of that of GNN. This set of experiments powerfully demonstrates the superiority of our model's computing speed and significantly reduces the time required for our work, but also provides experimental data to prove the feasibility of choosing our model.

In the last group of experiments (Figure 13), we used four models to conduct experiments on the four data sets we selected to compare the accuracy of the experiments. From the experimental results, we can find that SEEMDAN, LSTM, and BPNetwork have different performances in dealing with other data sets, i.e., the accuracy of the three models selected in this group, except our model, varies significantly in the face of different data. This is fatal to the accuracy and precision of the experiments. If the models do not have stable experimental stability in the face of other data, the testing results are not convincing. Then our model, in the f of the performance of the four data sets we have selected, accuracy does not vary significantly and can be said to be the same, so it can guarantee the accuracy of the experimental results, which can make our testing results have better accuracy and persuasive power.

Table 3 compares the accuracy, computation, and parameter size of the models mentioned in the paper with our model. The table shows that our model has significant advantages in these aspects.

TABLE 2 Data sets from different databases.

Database	Count	Mean	Max	Min	Standard deviation
ISO-NE Ayub et al. (2020)	2580	1781.42	2760.59	655.36	486.35
Elia Jia et al. (2020)	2466	21,135.44	31,371.25	13,127.29	3141.62
Singapore electricity	2535	3200.64	5628.43	1834.41	563.01
NREL Mohamed et al. (2020)	2632	1813.41	2804.92	731.52	501.43

TABLE 3 A comparison of different models.

Model	Accuracy ↑	Flops(G) ↓	Parameters(M) ↓	AUC ↑
CEEMDAN Cao et al. (2019)	0.921	126.53	168.13	0.831
GNN Cheng et al. (2022)	0.880	175.67	159.99	0.835
SVM Khalid et al. (2019)	0.823	112.50	113.43	0.838
BP Network Qian and Gao (2017)	0.8432	87.34	127.15	0.841
ARIMA Siami-Namini and Namin (2018)	0.894	150.66	168.27	0.846
LSTM Yan and Ouyang (2018)	0.931	112.43	97.86	0.848
CNN-LSTM Livieris et al. (2020)	0.945	122.23	98.21	0.852
Albogamy et al. (2021)	0.885	121.36	98.73	0.862
Aslam et al. (2021)	0.895	102.33	98.61	0.878
Yao et al. (2021)	0.945	110.13	94.61	0.893
Ours	0.963	95.32	91.45	0.951

5 Conclusion and discussion

In this paper, a smart grid real-time load prediction model based on Bayesian optimization of CNN-BiLSTM is proposed, which effectively solves the problem of gradient disappearance and gradient explosion while improving the accuracy and practicality of the model, the more vital feature extraction ability of the one-dimensional CNN, first, the smart grid real-time load data is first input into the one-dimensional CNN network, and after convolution for feature extraction into the pooling Simplify the feature data. Then the simplified feature data is input into the BiLSTM network; BiLSTM is based on a kind of LSTM extension, which can better retain the information provided by the nodes at a longer distance; BiLSTM memory network has two directions of transmission layer compared to the LSTM network can handle more data volume at the same time. It has a more efficient exploration efficiency for predicting smart grid real-time load.

Nevertheless, our model still has some shortcomings, as the BiLSTM network is used instead of the LSTM network. Hence, the operation speed is more complicated, which may impact the operation rate, and the number of parameters required will increase year-on-year because of the complexity of deep learning and the degree of model combination.

Smart grid real-time load forecasting is an important technology that has many functions (Aslam et al., 2020).The following are the roles of conducting smart grid real-time load forecasting: 1. Optimize power system operation: Smart grid real-time load forecasting can help power system managers to rationally deploy power resources according to load demand to ensure stable and reliable power system operation. 2. Improve the efficiency of the power system: Through smart grid real-time load forecasting, power system managers can better understand the demand of power loads, thus optimizing the operation efficiency of the power system and reducing energy waste and cost. 3. Promote the application of renewable energy: Smart grid real-time load forecasting can help power system managers more accurately predict the production and supply of renewable energy, thus better planning and managing the application of renewable energy and promoting the development and utilization of renewable energy. 4. Improve the operation of energy markets: Smart grid real-time load forecasting can provide energy market participants with more accurate electricity load forecasts and market information, facilitating the efficient process and development of energy markets.

Therefore, smart grid real-time load forecasting is indispensable for both power system managers and the whole grid system. Our smart grid real-time load forecasting model can help power system managers to forecast the demand of power load more accurately for better planning and management of power system operation.

Data availability statement

The original contributions presented in the study are included in the article/supplementary material, further inquiries can be directed to the corresponding author.

Author contributions

DZ, XJ, and XC contributed to conception and design of the study. PS organized the database. DZ performed the statistical analysis and wrote the first draft of the manuscript. XC reviewed and edited sections of the manuscript. All authors have read and agreed to the published version of the manuscript.

Funding

The research is funded partially by Excellent Young Talents Support Program of Anhui Universities (gxyq2021233), Key Science Research Project of Industry-University Research (BYC2021Z01), Teaching Quality Engineering of Anhui Province (2021xsxxkc181,2019sxzx24), and Teaching Demonstration Course Project of Anhui Province (2020jxsfk002), Key Science Research Project of Anhui Universities (2022AH052413), Scientific and technological innovation team project (BKJCX202202).

Conflict of interest

The authors declare that the research was conducted in the absence of any commercial or financial relationships that could be construed as a potential conflict of interest.

Publisher's note

References

Albogamy, F. R., Hafeez, G., Khan, I., Khan, S., Alkhammash, H. I., Ali, F., et al. (2021). Efficient energy optimization day-ahead energy forecasting in smart grid considering demand response and microgrids. *Sustainability* 13, 11429. doi:10.3390/su132011429

Aravind, V. S., Anbarasi, M., Maragathavalli, P., and Suresh, M. (2019). "Smart electricity meter on real time price forecasting and monitoring system," in 2019 IEEE international conference on system, computation, automation and networking (ICSCAN), Pondicherry, India, 29-30 March 2019 (IEEE), 1–5.

Aslam, S., Ayub, N., Farooq, U., Alvi, M. J., Albogamy, F. R., Rukh, G., et al. (2021). Towards electric price and load forecasting using cnn-based ensembler in smart grid. *Sustainability* 13, 12653. doi:10.3390/su132212653

Aslam, S., Khalid, A., and Javaid, N. (2020). Towards efficient energy management in smart grids considering microgrids with day-ahead energy forecasting. *Electr. Power Syst. Res.* 182, 106232. doi:10.1016/j.epsr.2020.106232

Ayub, N., Javaid, N., Mujeeb, S., Zahid, M., Khan, W. Z., and Khattak, M. U. (2020). "Electricity load forecasting in smart grids using support vector machine," in *Advanced information networking and applications: Proceedings of the 33rd international conference on advanced information networking and applications (AINA-2019) 33* (Cham: Springer), 1–13.

Cabán, C. C. T., Yang, M., Lai, C., Yang, L., Subach, F. V., Smith, B. O., et al. (2022). Tuning the sensitivity of genetically encoded fluorescent potassium indicators through structure-guided and genome mining strategies. *ACS sensors* 7, 1336–1346. doi:10.1021/acssensors.1c02201

Cai, W., Liu, D., Ning, X., Wang, C., and Xie, G. (2021). Voxel-based three-view hybrid parallel network for 3d object classification. *Displays* 69, 102076. doi:10.1016/j.displa.2021.102076

Cao, J., Li, Z., and Li, J. (2019). Financial time series forecasting model based on ceemdan and lstm. *Phys. A Stat. Mech. its Appl.* 519, 127–139. doi:10.1016/j.physa.2018.11.061

Chen, B.-R., Liu, Z., Song, J., Zeng, F., Zhu, Z., Bachu, S. P. K., et al. (2022a). "Flowtele: Remotely shaping traffic on internet-scale networks," in Proceedings of the 18th International Conference on emerging Networking EXperiments and Technologies, Roma Italy, December 6 - 9, 2022, 349–368.

Chen, Z., Silvestri, F., Tolomei, G., Wang, J., Zhu, H., and Ahn, H. (2022b). Explain the explainer: Interpreting model-agnostic counterfactual explanations of a deep reinforcement learning agent. *IEEE Trans. Artif. Intell.*, 1–15. doi:10.1109/tai.2022.3223892

Cheng, D., Yang, F., Xiang, S., and Liu, J. (2022). Financial time series forecasting with multi-modality graph neural network. *Pattern Recognit.* 121, 108218. doi:10.1016/j.patcog.2021.108218

Derbentsev, V., Matviychuk, A., Datsenko, N., Bezkorovainyi, V., and Azaryan, A. (2020). *Machine learning approaches for financial time series forecasting (CEUR Workshop Proceedings).*

Estrella, R., Belgioioso, G., and Grammatico, S. (2019). A shrinking-horizon, game-theoretic algorithm for distributed energy generation and storage in the smart grid with wind forecasting. *IFAC-PapersOnLine* 52, 126–131. doi:10.1016/j.ifacol.2019.06.022

Gui-xiang, S., Xian-zhuo, Z., Zhang, Y.-z., and Chen-yu, H. (2018). Research on criticality analysis method of cnc machine tools components under fault rate correlation. *IOP Conf. Ser. Mater. Sci. Eng.* 307, 012023. doi:10.1088/1757-899X/307/1/012023

He, F., and Ye, Q. (2022). A bearing fault diagnosis method based on wavelet packet transform and convolutional neural network optimized by simulated annealing algorithm. *Sensors* 22, 1410. doi:10.3390/s22041410

Jia, Y., Lyu, X., Xie, P., Xu, Z., and Chen, M. (2020). A novel retrospect-inspired regime for microgrid real-time energy scheduling with heterogeneous sources. *IEEE Trans. Smart Grid* 11, 4614–4625. doi:10.1109/tsg.2020.2999383

Khalid, R., Javaid, N., Al-Zahrani, F. A., Aurangzeb, K., Qazi, E.-u.-H., and Ashfaq, T. (2019). Electricity load and price forecasting using jaya-long short term memory (jlstm) in smart grids. *Entropy* 22, 10. doi:10.3390/e22010010

Li, C., Chen, Z., and Jiao, Y. (2023). Vibration and bandgap behavior of sandwich pyramid lattice core plate with resonant rings. *Materials* 16, 2730. doi:10.3390/ma16072730

Li, Y., Wei, D., Chen, X., Song, Z., Wu, R., Li, Y., et al. (2018). "Dumbnet: A smart data center network fabric with dumb switches," in Proceedings of the Thirteenth EuroSys Conference, Porto, Portugal, April 23-26, 2018, 1–13.

Liu, Z., Chen, S., and Luo, X. (2013). "Judgment and adjustment of tipping instability for hexapod robots," in 2013 IEEE International Conference on Robotics and Biomimetics (ROBIO), Shenzhen, China, 12-14 December 2013 (IEEE), 1941–1946.

Livieris, I. E., Pintelas, E., and Pintelas, P. (2020). A cnn–lstm model for gold price time-series forecasting. *Neural Comput. Appl.* 32, 17351–17360. doi:10.1007/s00521-020-04867-x

Luo, X., Jiang, Y., and Xiao, X. (2022). "Feature inference attack on shapley values," in Proceedings of the 2022 ACM SIGSAC Conference on Computer and Communications Security, Los Angeles CA USA, November 7 - 11, 2022, 2233–2247.

Mohamed, A. A., Day, D., Meintz, A., and Jun, M. (2020). Real-time implementation of smart wireless charging of on-demand shuttle service for demand charge mitigation. *IEEE Trans. Veh. Technol.* 70, 59–68. doi:10.1109/tvt.2020.3045833

Ning, X., Duan, P., Li, W., and Zhang, S. (2020). Real-time 3d face alignment using an encoder-decoder network with an efficient deconvolution layer. *IEEE Signal Process. Lett.* 27, 1944–1948. doi:10.1109/lsp.2020.3032277

Ning, X., Tian, W., He, F., Bai, X., Sun, L., and Li, W. (2023). Hyper-sausage coverage function neuron model and learning algorithm for image classification. *Pattern Recognit.* 136, 109216. doi:10.1016/j.patcog.2022.109216

Niu, H., Lin, Z., Zhang, X., and Jia, T. (2022). "Image segmentation for pneumothorax disease based on based on nested unet model," in 2022 3rd International Conference on Computer Vision, Image and Deep Learning and International Conference on Computer Engineering and Applications (CVIDL and ICCEA), Changchun, China, 20-22 May 2022 (IEEE), 756–759.

Papadaki, S., Wang, X., Wang, Y., Zhang, H., Jia, S., Liu, S., et al. (2022). Dual-expression system for blue fluorescent protein optimization. *Sci. Rep.* 12, 10190. doi:10.1038/s41598-022-13214-0

Peng, H., Huang, S., Chen, S., Li, B., Geng, T., Li, A., et al. (2022). "A length adaptive algorithm-hardware co-design of transformer on fpga through sparse attention and dynamic pipelining," in Proceedings of the 59th ACM/IEEE Design Automation Conference, San Francisco California, July 10 - 14, 2022, 1135–1140.

Qian, X.-Y., and Gao, S. (2017). Financial series prediction: Comparison between precision of time series models and machine learning methods. arXiv preprint arXiv:1706.00948, 1–9.

Shen, G., Zeng, W., Han, C., Liu, P., and Zhang, Y. (2017). Determination of the average maintenance time of cnc machine tools based on type ii failure correlation. *Eksploatacja i Niezawodnosc - Maintenance Reliab.* 19, 604–614. doi:10.17531/ein.2017.4.15

Siami-Namini, S., and Namin, A. S. (2018). Forecasting economics and financial time series: Arima vs. lstm. arXiv preprint arXiv:1803.06386.

Song, Z., Johnston, R. M., and Ng, C. P. (2021). Equitable healthcare access during the pandemic: The impact of digital divide and other sociodemographic and systemic factors. *Appl. Res. Artif. Intell. Cloud Comput.* 4, 19–33.

Song, Z., Mellon, G., and Shen, Z. (2020). Relationship between racial bias exposure, financial literacy, and entrepreneurial intention: An empirical investigation. *J. Artif. Intell. Mach. Learn. Manag.* 4, 42–55.

Wu, S., Wang, J., Ping, Y., and Zhang, X. (2022). "Research on individual recognition and matching of whale and dolphin based on efficientnet model," in 2022 3rd International Conference on Big Data, Artificial Intelligence and Internet of Things Engineering (ICBAIE), Xi'an, China, 15-17 July 2022 (IEEE), 635–638.

Xiang, C., Wu, Y., Shen, B., Shen, M., Huang, H., Xu, T., et al. (2019). "Towards continuous access control validation and forensics," in Proceedings of the 2019 ACM SIGSAC conference on computer and communications security, London United Kingdom, November 11 - 15, 2019, 113–129.

Xu, F., Zheng, Y., and Hu, X. (2020). "Real-time finger force prediction via parallel convolutional neural networks: A preliminary study," in 2020 42nd Annual International Conference of the IEEE Engineering in Medicine and Biology Society (EMBC), Montreal, QC, Canada, 20-24 July 2020 (IEEE), 3126–3129.

Yan, H., and Ouyang, H. (2018). Financial time series prediction based on deep learning. *Wirel. Personal. Commun.* 102, 683–700. doi:10.1007/s11277-017-5086-2

Yao, R., Li, J., Zuo, B., and Hu, J. (2021). Machine learning-based energy efficient technologies for smart grid. *Int. Trans. Electr. Energy Syst.* 31, e12744. doi:10.1002/2050-7038.12744

Zhang, H., Zhang, F., Gong, B., Zhang, X., and Zhu, Y. (2023). The optimization of supply chain financing for bank green credit using stackelberg game theory in digital economy under internet of things. *J. Organ. End User Comput.* 35, 1–16. doi:10.4018/joeuc.318474

Zhang, R., Zeng, F., Cheng, X., and Yang, L. (2019). "Uav-aided data dissemination protocol with dynamic trajectory scheduling in vanets," in ICC 2019-2019 IEEE International Conference on Communications (ICC), Shanghai, China, 20-24 May 2019 (IEEE), 1–6.

Zhibin, Z., Liping, S., and Xuan, C. (2019). Labeled box-particle cphd filter for multiple extended targets tracking. *J. Syst. Eng. Electron.* 30, 57–67. doi:10.21629/JSEE.2019.01.06

Zou, Z., Careem, M., Dutta, A., and Thawdar, N. (2022a). Joint spatio-temporal precoding for practical non-stationary wireless channels. arXiv preprint arXiv:2211.06017.

Zou, Z., Wei, X., Saha, D., Dutta, A., and Hellbourg, G. (2022b). "Scisrs: Signal cancellation using intelligent surfaces for radio astronomy services," in GLOBECOM 2022-2022 IEEE Global Communications Conference, Rio de Janeiro, Brazil, 04-08 December 2022 (IEEE), 4238–4243.

frontiers | Frontiers in Energy Research

TYPE Original Research
PUBLISHED 09 May 2023
DOI 10.3389/fenrg.2023.1194415

OPEN ACCESS

EDITED BY
Xin Ning,
Chinese Academy of Sciences (CAS),
China

REVIEWED BY
Arghya Datta,
Amazon, United States
Aditya Kumar Sahu,
Amrita Vishwa Vidyapeetham University,
India
Yao Liang,
City University of Hong Kong, Hong Kong
SAR, China
Lia Elena Aciu,
Transilvania University of Brașov,
Romania
Xiyun Yang,
North China Electric Power University,
China

*CORRESPONDENCE
Wei Ding,
✉ dingw@sdas.org

RECEIVED 27 March 2023
ACCEPTED 13 April 2023
PUBLISHED 09 May 2023

CITATION
Feng R, Yu H, Wu X, Huang C, Du T and
Ding W (2023), Steady-state deduction
methods of a power system based on the
prediction of large-scale wind
power clusters.
Front. Energy Res. 11:1194415.
doi: 10.3389/fenrg.2023.1194415

Steady-state deduction methods of a power system based on the prediction of large-scale wind power clusters

Rongqiang Feng[1,2], Haiping Yu[1,2], Xueqiong Wu[1,2],
Chenxi Huang[1,2], Tianchi Du[3] and Wei Ding[4]*

[1]NARI Group (State Grid Electric Power Research Institute) Co., Ltd., Nanjing, China, [2]NARI-TECH Nanjing Control Systems Co., Ltd., Nanjing, China, [3]College of Energy and Electrical Engineering, Hohai University, Nanjing, China, [4]Shandong Computer Science Center (National Supercomputer Center in Jinan), Qilu University of Technology (Shandong Academy of Sciences), Jinan, China

The integration of a high proportion of wind power has brought disorderly impacts on the stability of the power system. Accurate wind power forecasting technology is the foundation for achieving wind power dispatchability. To improve the stability of the power system after the high proportion of wind power integration, this paper proposes a steady-state deduction method for the power system based on large-scale wind power cluster power forecasting. First, a wind power cluster reorganization method based on an improved DBSCAN algorithm is designed to fully use the spatial correlation of wind resources in small-scale wind power groups. Second, to extract the temporal evolution characteristics of wind power data, the traditional GRU network is improved based on the Huber loss function, and a wind power cluster power prediction model based on the improved GRU network is constructed to output ultra-short-term power prediction results for each wind sub-cluster. Finally, the wind power integration stability index is defined to evaluate the reliability of the prediction results and further realize the steady-state deduction of the power system after wind power integration. Experimental analysis is conducted on 18 wind power farms in a province of China, and the simulation results show that the RMSE of the proposed method is only 0.0869 and the probability of extreme error events is low, which has an important reference value for the stability evaluation of large-scale wind power cluster integration.

KEYWORDS

large-scale wind power cluster, stability assessment, steady deduction, cluster division, ultra-short-term power cluster forecasting, improved GRU

1 Introduction

With the proposal of the "carbon peaking and carbon neutrality" goal, the utilization of new energy for power generation has been elevated to a crucial strategic position (Wang et al., 2021). Wind power utilization has a dual nature: on the one hand, its lack of pollution and renewable nature make it more economically efficient from the perspective of generation cost. On the other hand, the inherent intermittency, randomness, and uncertainty of wind power make it difficult for power systems to schedule and affect the stable operation of the power system (Kazari et al., 2018; Mostafaeipour et al., 2022). The high penetration of wind power, in particular, significantly increases the uncertainty of power grid operation. If wind power is not accurately grasped and reasonably used, it will reduce the economy and safety of power grid operation. Wind power forecasting technology is one of the key technologies for realizing wind power utilization. The ultra-short-term wind power cluster forecasting method provides wind power forecasting results for the subsequent 4 h, which provide technical reference for dispatchers to arrange unit combinations and formulate power generation plans. For large-scale wind power clusters, accurate wind power forecasting technology can improve the absorption of wind power, increase the power system's grasping ability for wind power, and thereby enhance the stability of the power system after wind power is connected to the grid (Ju et al., 2019).

The current main ultra-short-term wind power cluster forecasting methods are divided into two categories: physical model and data-driven (Wu et al., 2020). The physical model method is highly dependent on atmospheric physical characteristics and requires support from a large amount of meteorological observation data. If the mathematical description of the wind power farm is accurate enough, the prediction accuracy is often high. However, the performance of the prediction will be seriously affected when the wind power farm is expanded or the mechanical characteristics change (Dolatabadi et al., 2021). Data-driven methods include support vector machines (Li et al., 2020), extreme learning machines (ELMs) (Wan et al., 2020), and neural networks (Nazir et al., 2020; Tang et al., 2022), which have made significant breakthroughs in prediction accuracy compared with physical prediction methods.

With the application of new generations of artificial intelligence algorithms and the proposals of improvement methods such as combined models and switching mechanisms, the prediction accuracy of a single power prediction algorithm has gradually improved (Carneiro et al., 2022). However, China's wind power development is transitioning from decentralized to centralized and large-scale, and wind power farms are mostly connected to the grid in a centralized manner. It is beneficial to improve wind power prediction accuracy by using the smoothing effect presented by the aggregation of wind power farms and promoting wind power consumption. Therefore, wind power cluster prediction has become extremely important (Mu et al., 2022).

For wind power cluster prediction methods, the principle of superposition is relatively simple, which obtains the cluster power prediction result by adding single-site power predictions and is suitable for sparsely distributed and small-scale wind power farms (Zong and Porté-Agel, 2020). The time-series extrapolation method analyzes historical power data to predict future trends in time series. As meteorological data are not sufficiently introduced, they are significantly affected by the quality of power data. The statistical upscaling method only needs to linearly upscale the predicted output of the reference wind power farm to obtain the cluster prediction result. This method can offset potential correlation factors between different wind power farms' data and has good dynamic adaptability, but the selection criteria for the reference wind power farms are difficult to determine (Yang et al., 2022). The cluster division method divides the wind power farms in the region into several wind sub-clusters according to the fluctuation patterns of power and meteorological data and establishes a separate prediction model for each sub-cluster.

The division of wind power clusters is generally based on the spatio-temporal characteristics of meteorological and power data as inputs, which are partitioned into finite cluster units through clustering or other similarity measures. Predictive models are established for each cluster unit separately. Wang et al. (2022) used wind power as the input for a fuzzy clustering algorithm to achieve cluster division. Zhao et al. (2021) clustered the fluctuations of wind power and considered numerical weather prediction (NWP) meteorological features for short-term wind power forecasting. Abedinia et al. (2020) divided clusters by determining the correlation of output features through empirical orthogonal functions. Fan et al. (2020) proposed using NWP information of the predicted period as input for cluster division. These references used wind power, wind speed, and their constructed attributes as features for clustering, but a single feature's input may not guarantee the rationality of cluster division when there are quality issues in the data.

The current research on power prediction for large-scale wind power clusters lacks consideration for the stability of wind power integration. Under the condition of a high frequency of extreme errors and inflated overall prediction accuracy, the rationality of the application of prediction results cannot be guaranteed. Additionally, the rationality of cluster division also has a major impact on prediction accuracy. Based on the previously mentioned analysis, a wind power cluster ultra-short-term power prediction method is proposed to consider the stability of wind power integration. Based on the stability evaluation results, further implementation of the power system steady-state deduction is recommended after the wind power grid connection is achieved. A multi-dimensional input feature construction and an improved DBSCAN (density-based spatial clustering of applications with noise) algorithm-based wind power cluster division scheme are proposed, which divide the wind power farms in the region into several subsets. Then, the gated neural unit is improved to extract the temporal features of the wind power cluster and provide the cluster power prediction results. Finally, a stability evaluation index is constructed to assess the reliability of the wind power prediction model, and the effectiveness of the proposed method is verified in 18 wind farms in a province in northeast China.

This paper is organized as follows: Section 2 improves the DBSCAN algorithm and its clustering of wind farm groups. The wind power cluster forecasting model based on the improved GRU network is introduced in detail in Section 3. Section 4 describes the framework for steady-state power system analysis based on large-scale wind power clusters. The effectiveness of the proposed method is verified in Section 5 based on actual wind farm data. Finally, conclusions and future recommendations are presented in Section 6.

2 Wind power subset cluster division based on the improved DBSCAN algorithm

2.1 Improved DBSCAN algorithm

DBSCAN is one of the most typical density-based spatial clustering algorithms, which clusters samples with high similarity in the form of partitioning clusters, and clusters are defined as the largest set of density-connected points (Mao et al., 2021). Therefore, the DBSCAN algorithm can divide regions with sufficient data

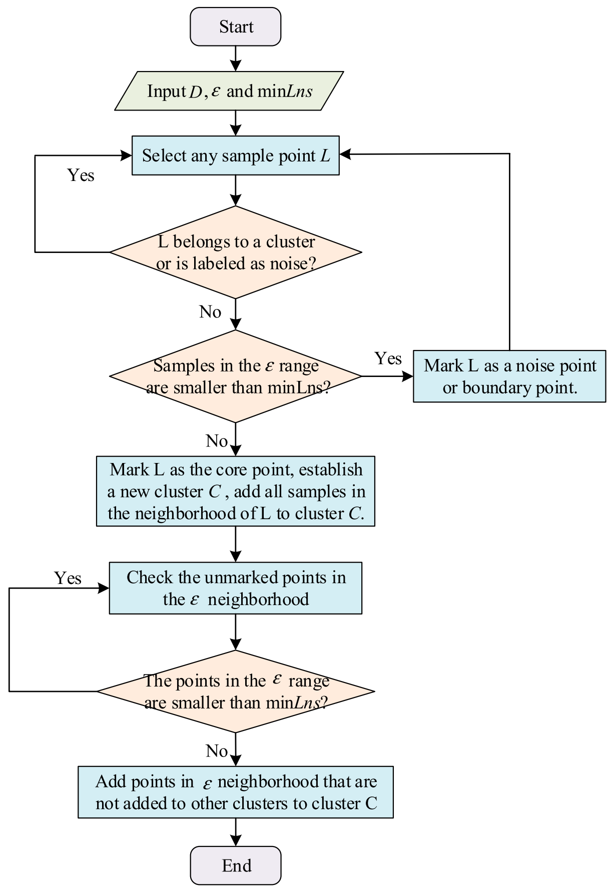

FIGURE 1
Flowchart of the improved DBSCAN algorithm.

density into clusters and is less sensitive to noisy data. The partitioning idea of wind power clusters based on the DBSCAN algorithm is as follows. Input indicates that the status of all input samples is marked as unclustered, an input sample is read, and then the sample is judged as a core sample point according to the neighborhood ε and threshold min Lns. If yes, a new cluster is formed in the neighborhood of the sample, and then all points in the neighborhood ε are added to the cluster. The cluster C is judged by the black core sample in the neighborhood ε extending outward continuously until the cluster C is no longer growing. The DBSCAN algorithm is defined as follows:

Definition 1: The neighborhood L_i is defined as shown in Eq. 1:

$$N_{\varepsilon}(L_i) = \left\{L_j \in D \middle| D_{dist}\left(L_i, L_j\right) \le \varepsilon\right\}, \tag{1}$$

where ε represents the density radius of the sample point, D represents the data space of L_i and L_j, and L_i, $L_j \in D$. All sample points whose spatial distance from L_i does not exceed ε constitute the neighborhood L_i.

Definition 2: For $L_i \in D$, the condition that L_i is the core sample is as follows: the neighborhood L_i must meet the following conditions:

$$|N_{\varepsilon}(L_i)| \ge \min Lns. \tag{2}$$

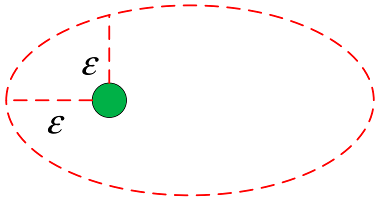

FIGURE 2
Diagram of the core sample search area.

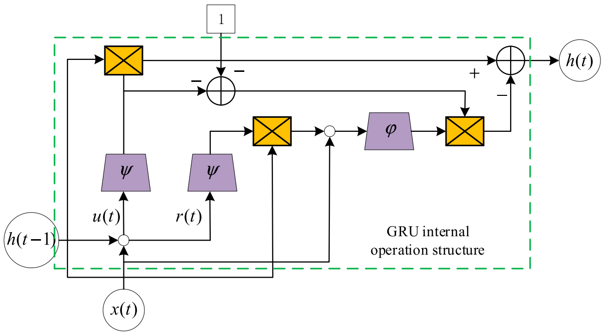

FIGURE 3
GRU neural network structure.

Definition 3: Given data space $D\,(L_i \in D)$, the conditions of direct density reachability of L_i and L_j are as follows:

$$L_i \in N_{\varepsilon}\left(L_j\right), \tag{3}$$

$$\left|N_{\varepsilon}\left(L_j\right)\right| \ge \min Lns, \tag{4}$$

where, Eq. 3 presents that L_i is within the ε neighborhood of L_j and Eq. 4 presents that L_j is the core sample point.

Definition 4: Given data space $D\,(L_i \in D)$, the reachable densities of L_n and L_1 are as follows: existing L_1, L_2, L_3, . . ., L_i, . . ., L_n $(1 \le i \le n)$, L_{i+1} starts from L_1, there is a direct density accessibility relation for ε and min Lns.

Definition 5: Given data space $D\,(L_i, L_j \in D)$, L_i and L_j are density-related condition as follows: any sample point $L_k\,(L_k \in D)$ exists, such that L_i and L_j are both starting from L_k, and there is a direct density accessibility relation for ε and min Lns.

Figure 1 shows the flow based on the improved DBSCAN algorithm.

Through the aforementioned algorithm process, we can see that all sample points must be traversed in order to finally determine the cluster C. Figure 2 is a schematic diagram of the core sample point segment search area. As can be seen from the figure, the region for searching the core track segment is an outsourcing ellipse with radius ε and density threshold min Lns, and all samples in the ellipse region form the final cluster.

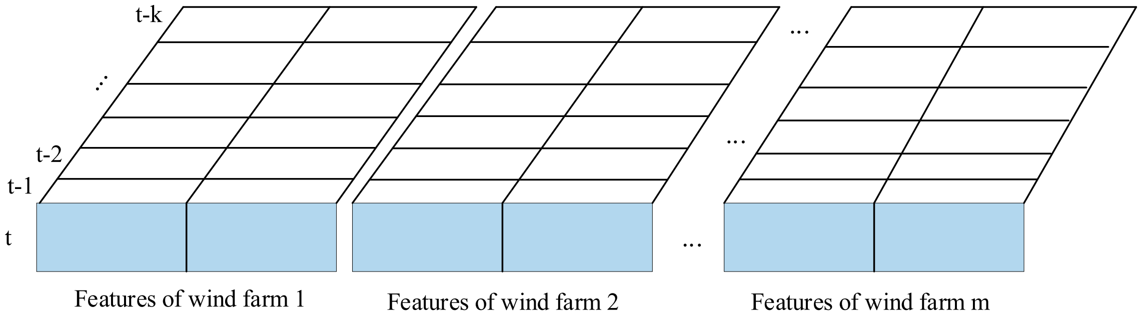

FIGURE 4
Spatio-temporal feature data structure.

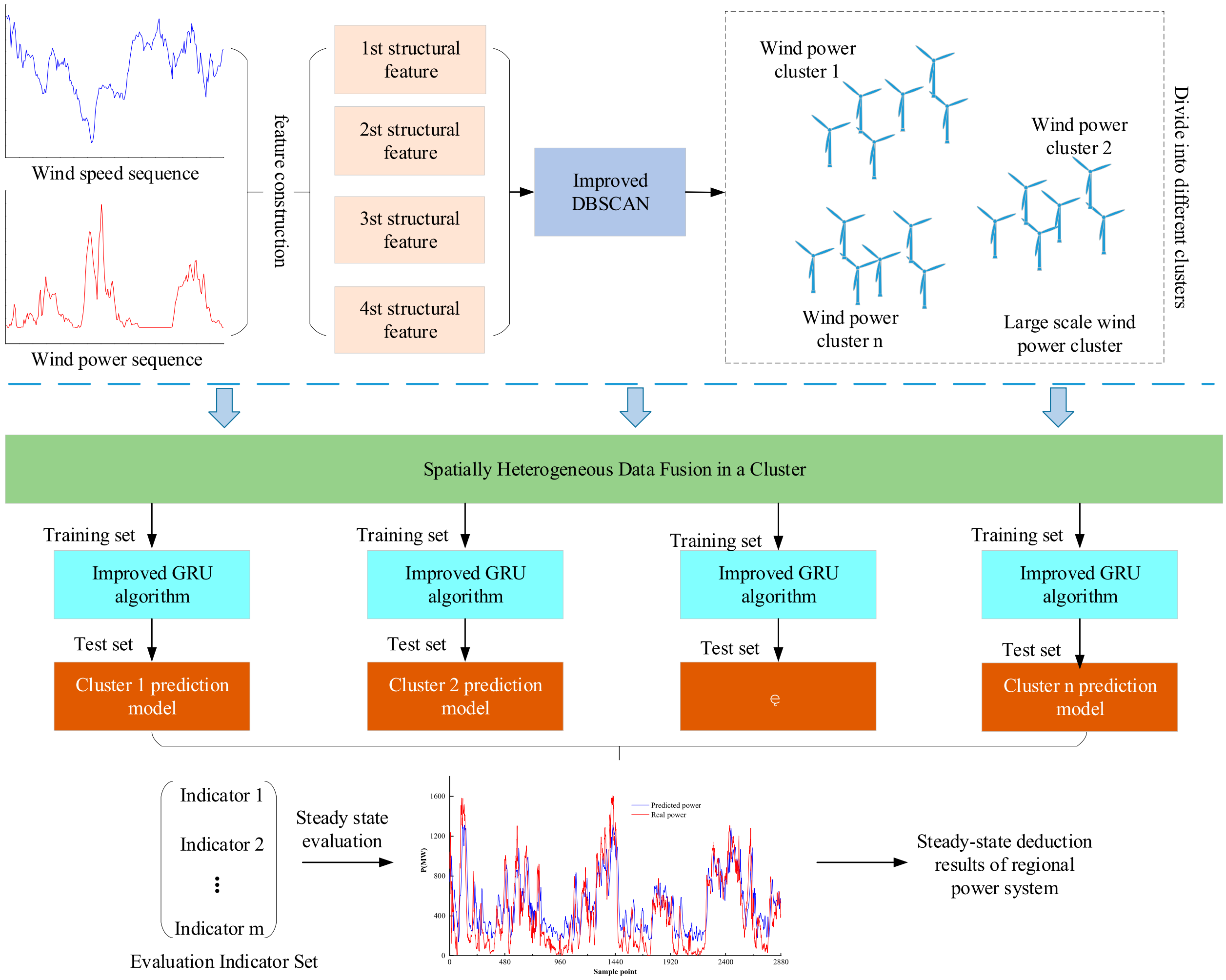

FIGURE 5
Power system stability assessment framework.

2.2 Clustering of wind power cluster sub-regions based on the DBSCAN algorithm

The input features are a key factor affecting the output of cluster algorithms. Since cluster algorithms generally perform feature engineering separately, the paper characterizes the meteorological and power fluctuation characteristics of each wind power farm by manually constructing features. Salazar et al. (2022) pointed out that hub-height wind speed and power fluctuations in NWP are far more correlated than other meteorological attributes; so, wind speed is one

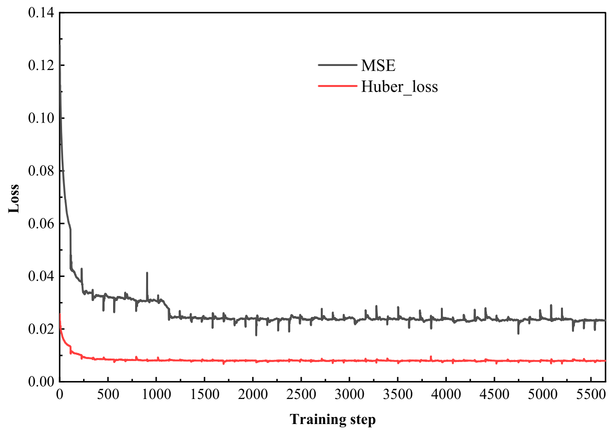

FIGURE 6
Loss curve.

of the key constructed features. Using a 1-h observation window, the variance between the wind speed and the average wind speed in the observation window is extracted to describe the wind speed fluctuations, as shown in Eq. 5.

$$F_1 = \frac{1}{4}\left[(WS_1 - \overline{WS})^2 + (WS_2 - \overline{WS})^2 + (WS_3 - \overline{WS})^2 + (WS_4 - \overline{WS})^2\right], \tag{5}$$

where $WS_1, WS_2, WS_3,$ and WS_4, respectively, represent the wind speed at 15 min, 30 min, 45 min, and 1 h within the observation window, . F_1 represents the scatter of each wind speed point from the mean wind speed in the observation window, which is the first constructed feature.

Similarly, the power variability within the 1-h observation window is calculated using Eq. 5 as the second constructed feature. The trend of wind speed quantification within the 1-h observation window is shown in Eq. 6.

$$\begin{aligned} F_3 = \operatorname{sign}(WS_2 - WS_1) + \operatorname{sign}(WS_3 - WS_2) + \operatorname{sign}(WS_4 - WS_3) \\ + \operatorname{sign}(WS_5 - WS_4), \end{aligned} \tag{6}$$

where sign represents the sign function; $P_1, P_2, P_3,$ and P_4, respectively, represent the change trends of wind speed at 15 min, 30 min, 45 min and 1 h; WS_5 represents the 15-min wind speed in the next observation window; and F_3 represents the change trend of wind speed in the observation window, which is the third structural feature.

Similarly, the power change trend within the 1-h observation window is obtained by Eq. 5 as the fourth structural feature. Finally, a structural feature set is formed by $F_1, F_2, F_3,$ and F_4, which are used as the input of the improved DBSCAN algorithm to realize the division of wind electronic clusters.

3 Wind power cluster prediction model based on the improved GRU network

GRU is a simplified variation of the LSTM network, which is a kind of gate recurrent unit network and is widely used in extracting time-series features of time series. The update gate in the GRU is a combination of the forget gate and the input gate in the LSTM network, but the GRU model structure is simpler, which effectively reduces the training time while ensuring the model prediction accuracy (Qu et al., 2021; Xiao et al., 2023). The internal structure of the GRU is shown in Figure 3.

Each GRU includes an $u(t)$ and an $r(t)$. At the time of t, the GRU accepts the current $x(t)$, the hidden state of the previous $h(t-1)$, and the update gate performs two steps of forgetting and remembering at the same time. The calculation determines how much information to choose to input into the network and how much to remember from past information; the reset gate determines the amount of past forgotten information; the output $h(t)$ of the GRU network is finally formed by the dynamic control of the update gate and the reset gate. The calculation method for each variable is as follows:

$$u(t) = \psi(\boldsymbol{W}_{\mathrm{u}} h(t-1) + \boldsymbol{U}_{\mathrm{u}} x(t)), \tag{7}$$

$$r(t) = \psi(\boldsymbol{W}_{\mathrm{u}} h(t-1) + \boldsymbol{U}_{\mathrm{r}} x(t)), \tag{8}$$

$$\bar{h}(t) = \varphi(\boldsymbol{W}_{\mathrm{c}}(r(t) \otimes h(t-1)) + \boldsymbol{U}_{\mathrm{c}} x(t)), \tag{9}$$

$$h(t) = u(t) \otimes h(t-1) + (1 - u(t)) \otimes \bar{h}(t), \tag{10}$$

where $W_u, W_r,$ and W_c are the parameter matrices connecting the output signal of the hidden layer; $U_u, U_r,$ and U_c are the parameter matrices connecting the input signal; $\psi(.)$ is a non-linear function; and $\bar{h}(t)$ is the intermediate memory state that mixes the cell state and the hidden state. $\otimes$ is a logical operator that multiplies corresponding elements in a matrix.

During the training stage, in order to reduce the sensitivity of the model to abnormal data, the gradient update of the deep neural network decreases with the decrease of the error, which is conducive to speeding up the convergence speed, and the Huber loss function is used as the measurement rule of the GRU network training loss (Tang et al., 2021). The principle is as follows:

$$L(y, f(x)) = \begin{cases} \frac{1}{2}(y - f(x))^2 & \text{for } |y - f(x)| \le \delta \\ \delta|y - f(x)| - \frac{1}{2}\delta^2 & \text{otherwise} \end{cases} \tag{11}$$

where y represents the actual value and $f(x)$ represents the predicted value. δ is a hyperparameter, which is introduced by the loss function, and it determines how to treat outliers. If the residual is greater than δ, we can use L1 to minimize the loss. If the residual is less than δ, then we can use L2 to minimize the loss. In this paper, the setting of δ is 0.1. The GRU model improved by the loss function is less sensitive to the outliers of meteorological and power input data, increasing the convergence speed, and it can improve the accuracy of wind power prediction to some extent.

According to the wind power cluster division results, the wind power farm data in each sub-cluster are fused with spatial data. Taking a cluster containing m wind power as an example, the model data structure with characteristic k steps as input is shown in Figure 4. The characteristics of each wind power cluster are combined and then processed into a 3-dimensional tensor whose time series lags behind one time-point in turn. The first dimension of the data is the current moment t, which represents the forecast time. The second dimension is the characteristics of each wind farm, which represent the spatial characteristics. The third dimension is the temporal characteristics with sequential lags in time series. The improved GRU network is used as the predictor to extract temporal features from the fused data of spatial features to realize the power prediction of sub-clusters. Finally, the ultra-short-term power prediction of large-scale wind power clusters is realized by superimposing the prediction results of each sub-cluster.

4 Framework for steady-state power system analysis based on large-scale wind power cluster forecasting

The traditional modeling approach for wind power cluster forecasting is to first predict the power of each individual wind power farm and then add up the predicted results to obtain the forecasted power of the entire wind power cluster (Wu et al., 2021; Ning et al., 2023). The rationale for this approach is that the prediction units for individual wind power farms are relatively small, and each wind power farm has relatively complete historical data. Achieving high prediction accuracy for each wind power farm will lead to higher accuracy for the regional wind power cluster forecast. Based on this advantage, all the current provincial-level wind power cluster power forecasts use this modeling method.

However, historical power analysis of individual wind power farms shows that the high-frequency components of wind power fluctuate more violently, reducing the predictability of wind power. The randomness and volatility caused by such local effects are difficult to reflect in NWP, making it difficult for prediction models to extract such fluctuation characteristics. However, within a certain spatial range, wind power farms with similar output can smooth out this random fluctuation to some extent, resulting in a smoother aggregated power curve and improved predictability.

Based on the aforementioned analysis, dividing wind power farms in a region into several clusters and modeling them separately can improve the prediction accuracy for each cluster, thereby improving wind power forecasting accuracy and enhancing the stability of power system operation after wind power integration. The steady-state extrapolation framework for power systems based on the forecast results of large-scale wind power clusters is shown in Figure 5.

The establishment of this framework involves the following three steps:

i) Partitioning wind power sub-clusters: the DBSCAN algorithm was improved based on Eqs 1–4, features were constructed representing the fluctuation characteristics of wind power speed and wind power according to Eqs 5, 6, they were used as inputs for the improved DBSCAN algorithm, and the wind power farms in the region were partitioned into several clusters.
ii) Ultra-short-term power prediction for wind power clusters: the data were merged within the same wind power cluster, spatial data tensors were constructed, the improved GRU neural network was used to extract the temporal characteristics of the wind power cluster, and the wind power cluster forecast was output.
iii) Steady-state deduction of power systems: stability evaluation indicators for wind power prediction were constructed, the stability and accuracy of the wind power prediction model were evaluated comprehensively based on traditional wind power error indicators, and the steady-state deduction of power systems was further realized.

5 Experimental analysis

5.1 Dataset and prediction metrics

The data used in this study consist of 6 months (January to July) of actual power generation data and corresponding NWP data with 15-min resolutions from 18 wind power farms located in northeast China with a total installed capacity of 2,564.81 MW. The meteorological variables included in the NWP dataset are wind speed, temperature, humidity, and pressure. Wind direction was not included as a feature in this study. The first 6 months of data were used as the training set, and the last month data were used as the testing set. To ensure fairness in evaluating the correlation between each feature variable and power, both the NWP features and power were normalized to the [0, 1] range using the normalization algorithm shown in Eq. 12.

$$x' = \frac{x - x_{\min}}{x_{\max} - x_{\min}}, \tag{12}$$

where x and x', respectively, represent the normalized and original feature or power values; $x_{\min}$ and $x_{\max}$, respectively, represent the minimum and maximum values of the feature or power. After prediction, the resulting values are denormalized to zero, the maximum output range, to restore their physical meaning. The denormalization principle is shown in Eq. 13.

$$x = x' (x_{\max} - x_{\min}) + x_{\min}. \tag{13}$$

To reduce the impact of abnormal data on prediction accuracy (Dong et al., 2023), the following pre-processing steps were taken:

1) Power values exceeding the installed capacity were reassigned to the installed capacity;
2) Negative power values were set to zero;
3) For time points where the power is zero, the corresponding wind speed value was set to zero.

The deep learning network designed in this paper consists of three GRU network layers with 16, 32, and 16 neurons, respectively. The last GRU layer is connected with a fully connected layer, and the 16-step wind power prediction results are directly output. The training parameters are as follows: {epoch:50, batch_size: 128, droup_out:0.2}. This paper uses a CPU for training, and the parameters of the computer are as follows: {CPU: Intel(R) Core(TM) i5-7300HQ CPU @ 2.50 GHz 2.50 GHz, RAM: 16.0 GB}.

The loss curve modeled by Cluster 1 is shown in Figure 6. MSE loss declines slowly, with oscillations occurring in the middle of the process, while Huber loss declines faster and has a more stable downward trend.

In the past, the index for ultra-short-term wind power prediction often selected the average forecast value within 4 h. However, in the “Technical Regulation for Wind Power Prediction,” the assessment has been modified to the fourth hour,

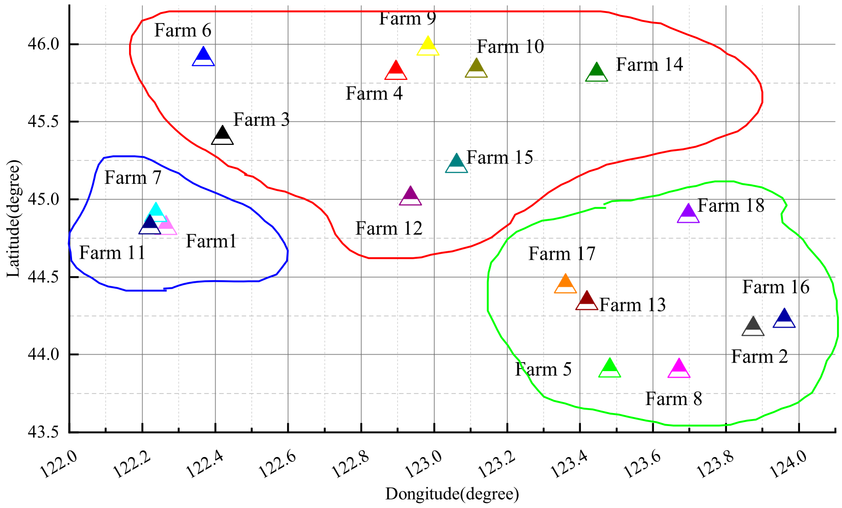

FIGURE 7
Cluster partitioning results.

namely, the results of the 16th step of the prediction (Demolli et al., 2019). Therefore, in this study, the normalized root mean square error (RMSE) and normalized maximum absolute error (MAE) were used as the final evaluation criteria to evaluate the performance of the 16th-step prediction (Zhao et al., 2022).

The calculation of normalized RMSE is shown in Eq. 14:

$$RMSE = \frac{1}{Cap}\sqrt{\frac{1}{N}\sum_{i=1}^{n}(x_i - y_i)^2}, \tag{14}$$

where Cap represents the rated capacity of the wind power cluster, x_i represents the actual wind power generation, y_i represents the predicted wind power generation, and n is the number of samples in the testing set.

The calculation of normalized MAE is shown in Eq. 15:

$$MAE = \frac{1}{nCap}\sum_{i=1}^{n}|x_i - y_i|. \tag{15}$$

In addition, the extreme error frequency (SA) index was established to evaluate the stability of the wind power prediction model, using 40% of the installed capacity as the threshold for extreme errors. The calculation is shown in Eq. 16:

$$ID_i = \begin{cases} 1, & |y_i - \hat{y}_i|/Cap \le 0.4 \\ 0, & |y_i - \hat{y}_i|/Cap > 0.4 \end{cases}$$
$$SA = \frac{num(ID_i = 0)}{n} \tag{16}$$

where ID_i is the criterion for determining whether a sample is an extreme error. If the absolute error value is greater than 40% of the installed capacity, it is considered an extreme error.

The calculation of the extreme error bandwidth ratio (EWR) of wind power prediction results is shown in Eq. 17:

$$EWR = \frac{|\max(y_i - \hat{y}_i)| + |\min(y_i - \hat{y}_i)|}{2^*\mathrm{Cap}}. \tag{17}$$

During the assessment period, if the extreme error frequency is less than 4% and the normalized RMSE is less than 15% of the installed capacity, it is considered that the power system meets the static stability requirements during long-term operation. If the extreme error bandwidth gradually increases in the 1–16 step prediction results for the next 1–4 h and remains below 40% of the error bandwidth, then it is considered that the power system is in dynamic stability within the next 4 h from the forecast time. It should be noted that the perspective of the power system steady-state deduction in this study starts from the perspective of the power grid and evaluates its impact on the power system after being connected to the grid based on the comprehensive indicators of wind power prediction. High prediction accuracy and stable model performance are required to ensure the stable operation of the power system after connection. If the model performance is unstable, regardless of the overall accuracy during the assessment period, stable operation of the power system cannot be guaranteed.

5.2 Analysis of cluster results

The iteration number of the clustering algorithm was set to 50 times, with a cluster quantity of 3. The final clustering results of each cluster and the relative positions of each wind power farm are shown in Figure 7:

Cluster 1: including 7 wind power farms, namely, Wind Power Farms 2, 5, 8, 13, 16, 17, and 18.

Cluster 2: including 8 wind power farms, namely, Wind Power Farms 3, 4, 6, 9, 10, 12, 14, and 15.

Cluster 3: including 3 wind power farms, namely, Wind Power Farms 1, 7, and 11.

The cluster results show that the improved DBSCAN algorithm can effectively identify spatially adjacent wind power farm and group them into the same cluster. This indicates the rationality of using the improved DBSCAN algorithm for cluster analysis.

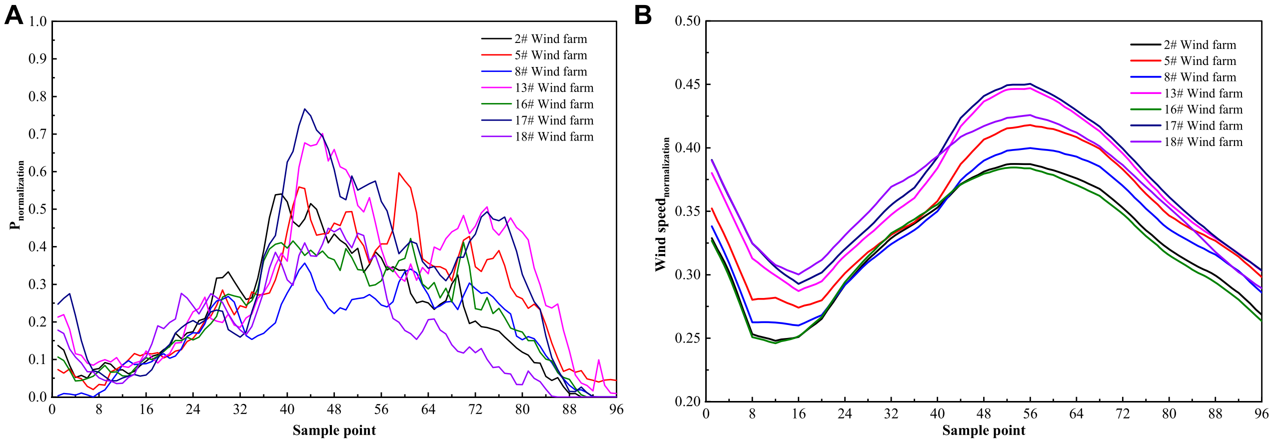

Power output curve of Cluster 1

Wind speed curve of Cluster 1

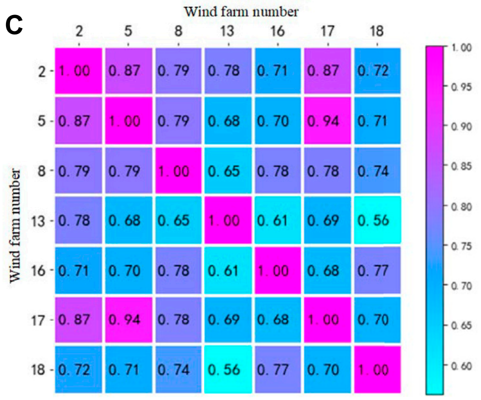

	2	5	8	13	16	17	18
2	1.00	0.87	0.79	0.78	0.71	0.87	0.72
5	0.87	1.00	0.79	0.68	0.70	0.94	0.71
8	0.79	0.79	1.00	0.65	0.78	0.78	0.74
13	0.78	0.68	0.65	1.00	0.61	0.69	0.56
16	0.71	0.70	0.78	0.61	1.00	0.68	0.77
17	0.87	0.94	0.78	0.69	0.68	1.00	0.70
18	0.72	0.71	0.74	0.56	0.77	0.70	1.00

Correlation coefficient matrix of power output for each wind farm

FIGURE 8
Visualization of Cluster 1 partitioning results. **(A)** Power output curve of Cluster 1. **(B)** Wind speed curve of Cluster 1. **(C)** Correlation coefficient matrix of power output for each wind farm.

To further verify the rationality of the clusters' division, a visualization analysis was conducted on the normalized power and wind speed of the wind power farms in Cluster 1. The correlation coefficient matrix of the power output of each wind power farm is also provided, as shown in Figure 8. (Note: Wind Power Farms 1, 7, and 11 are close to each other and share the same NWP data). The correlation coefficient (I) is calculated as shown in Eq. 18.

$$I = \frac{\operatorname{cov}(x_1, x_2)}{\sqrt{D(x_1) \times D(x_2)}}. \tag{18}$$

Based on the analysis of the previous figure, after cluster division, the power outputs of various wind power farms within the same cluster have certain similarities. Strictly speaking, wind power farms' output values that are close in distance should exhibit highly similar states. However, during the wind turbine climbing phase between sampling points 192 and 384, there are also differences in power output curves between different wind power farms. Due to factors such as unit maintenance, malfunctions, and power limitations, the relationship between wind power farms' output and single-unit output is not strictly linearly proportional. Therefore, from the correlation coefficient matrix perspective, the correlation coefficients among the power outputs of various wind power farms within the same wind power cluster do not uniformly maintain high values. For example, the power correlation coefficient between wind power farm 13 and wind power farm 18 is only 0.56. From the analysis of wind speed curves, wind speed trends among the various clusters of wind power farms are relatively similar. Thus, introducing wind speed fluctuation characteristics in clustering features can reduce errors caused by using pure power features.

The normalized power and wind speed, and the correlation coefficient matrix of the normalized power output, for each wind power farm in Clusters 2 and 3 are presented in Figure 9.

5.3 Analysis of wind power cluster prediction results

The normalized RMSE and MAE indicators of the three clusters' power predictions are shown in Figure 10. The normalized RMSE

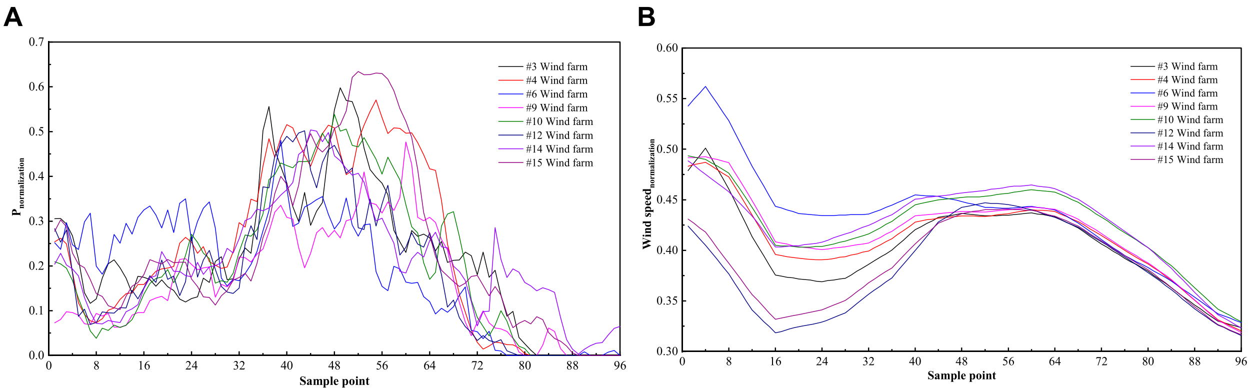

Power output curve of Cluster 2

Wind speed curve of Cluster 2

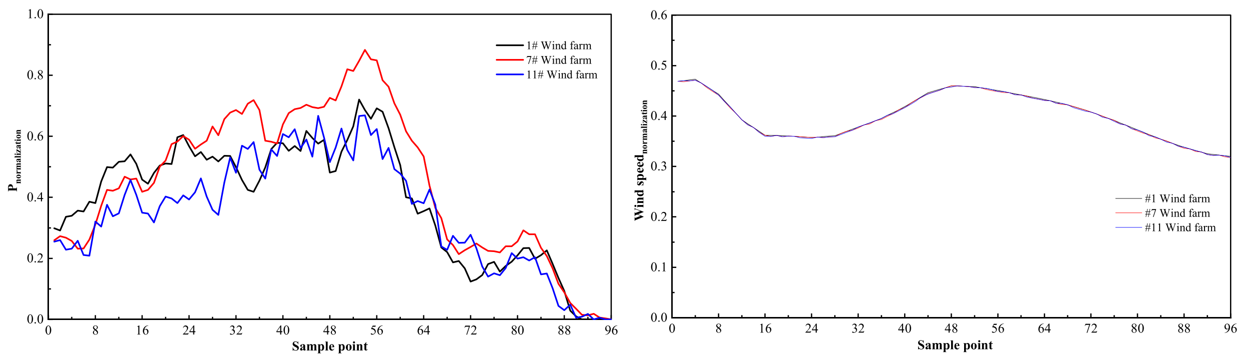

Power output curve of Cluster 3

Wind speed curve of Cluster 3

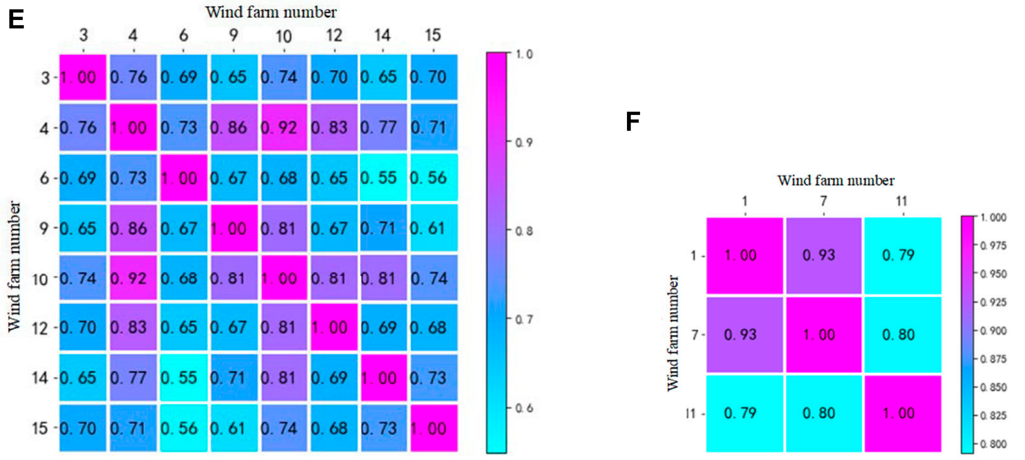

	3	4	6	9	10	12	14	15
3	1.00	0.76	0.69	0.65	0.74	0.70	0.65	0.70
4	0.76	1.00	0.73	0.86	0.92	0.83	0.77	0.71
6	0.69	0.73	1.00	0.67	0.68	0.65	0.55	0.56
9	0.65	0.86	0.67	1.00	0.81	0.67	0.71	0.61
10	0.74	0.92	0.68	0.81	1.00	0.81	0.81	0.74
12	0.70	0.83	0.65	0.67	0.81	1.00	0.69	0.68
14	0.65	0.77	0.55	0.71	0.81	0.69	1.00	0.73
15	0.70	0.71	0.56	0.61	0.74	0.68	0.73	1.00

	1	7	11
1	1.00	0.93	0.79
7	0.93	1.00	0.80
11	0.79	0.80	1.00

Correlation coefficient matrix of Cluster 2

Correlation coefficient matrix of Cluster 3

FIGURE 9
Visualization of division results of Clusters 2 and 3. **(A)** Power output curve of Cluster 2. **(B)** Wind speed curve of Cluster 2. **(C)** Power output curve of Cluster 3. **(D)** Wind speed curve of Cluster 3. **(E)** Correlation coefficient matrix of Cluster 2. **(F)** Correlation coefficient matrix of Cluster 3.

and MAE indicators for Cluster 1 are 0.1018 and 0.0796, respectively; for Cluster 2, they are 0.0602 and 0.1050, respectively; and for Cluster 3, they are 0.0272 and 0.0914, respectively. The prediction RMSE and MAE indicators for all three clusters do not exceed 10% of the installed capacity, indicating that the wind power cluster prediction model proposed in this paper has high prediction accuracy.

To further verify the performance of wind power cluster power prediction, the test set prediction results for each of the three clusters were visualized. Figure 11 shows the results of the 16th step of ultra-

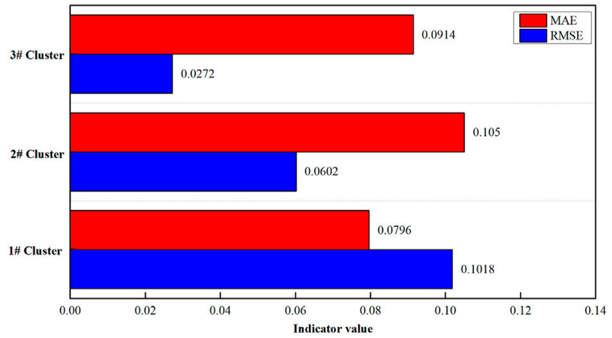

FIGURE 10
Prediction indicators of Clusters 1, 2, and 3.

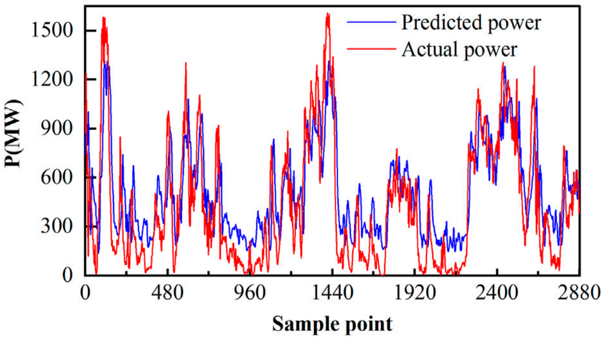

FIGURE 12
Visualization of regional prediction results.

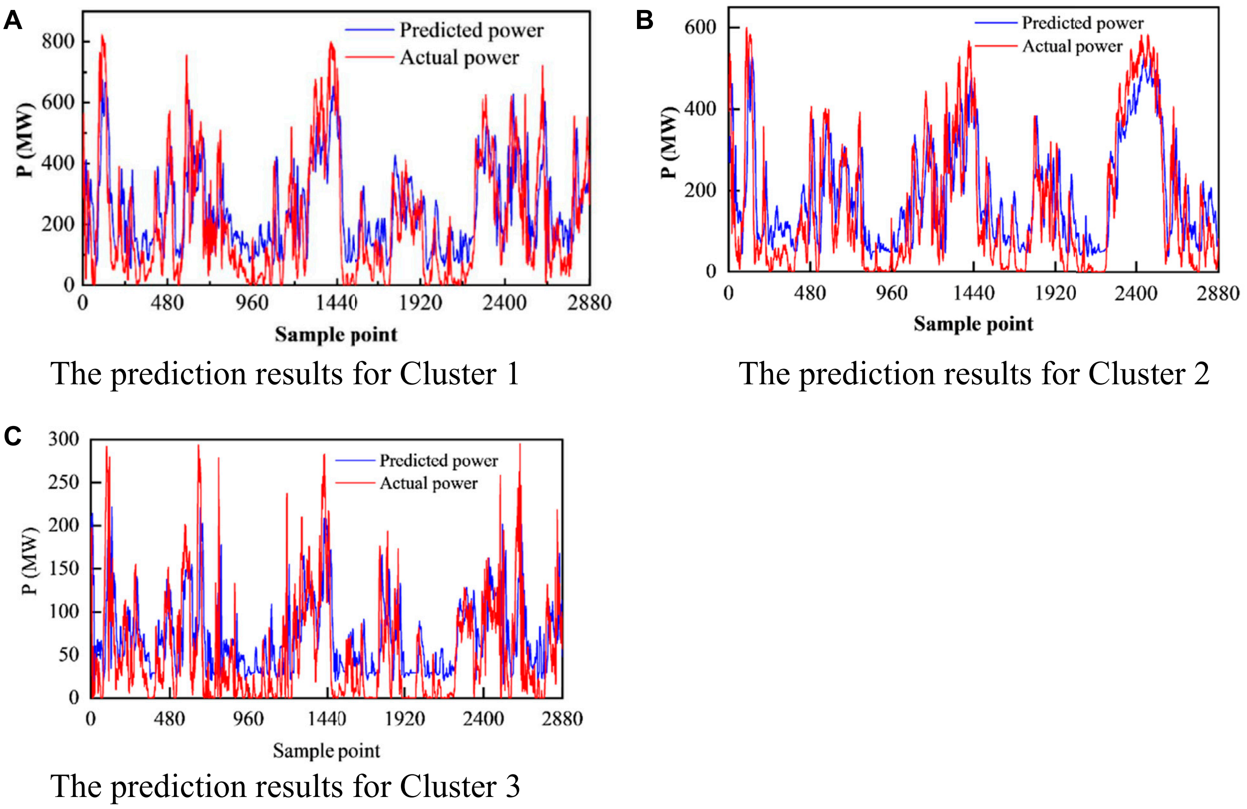

The prediction results for Cluster 1

The prediction results for Cluster 2

The prediction results for Cluster 3

FIGURE 11
Visualization of cluster prediction results. **(A)** Prediction results for Cluster 1. **(B)** Prediction results for Cluster 2. **(C)** Prediction results for Cluster 3.

short-term prediction, where the predicted curve is still able to track the actual power curve very well. It should be noted that predicting wind power at the cluster level cannot overcome the time delay problem that exists in single-farm prediction. That is, there is a notable time delay between the predicted power sequence and the actual power sequence on the waveform. By shifting the predicted sequence forward according to the prediction step, its fluctuation trend almost coincides with the actual power. Due to the presence of the time delay problem, the prediction results for high-power points tend to be lower, while those for low-power points tend to be higher in the overall prediction results. Cluster 1 has a lower installed capacity and thus more high-frequency noise signals in its power, making it difficult to weaken fluctuations through convergence effects. In contrast, Clusters 2 and 3 have higher installed capacities, resulting in better tracking of the actual power curves and higher prediction accuracy than Cluster 1.

The prediction results for the entire region are shown in Figure 12, where the prediction results for the three wind power

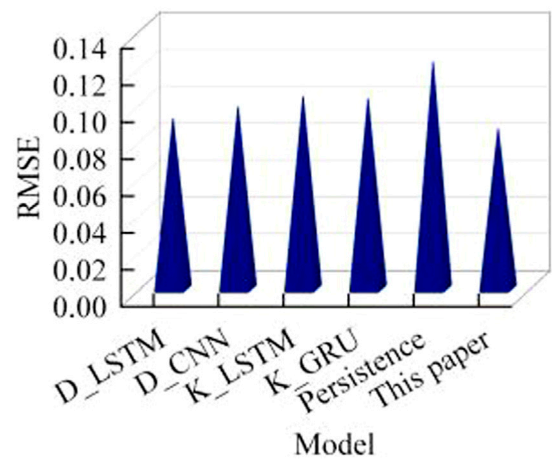

FIGURE 13
Performance comparison of different algorithms.

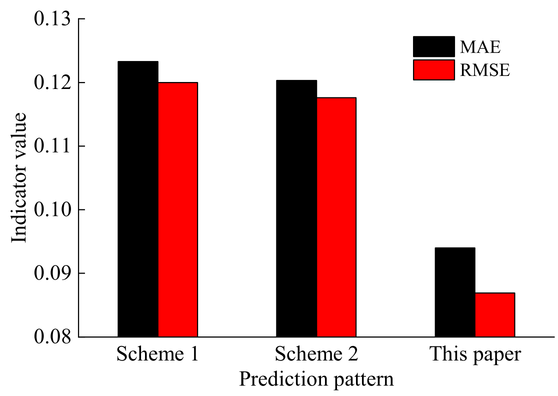

FIGURE 14
Performance comparison of different prediction patterns.

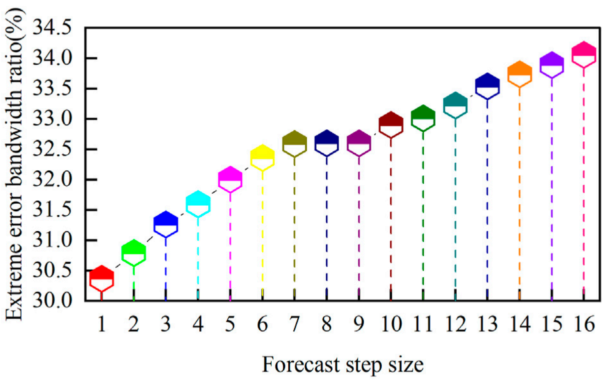

FIGURE 15
Extreme error bandwidth ratio for 16-step prediction.

clusters are combined to obtain the prediction results for the entire region's wind power farms. The RMSE is 0.0869, and the MAE is 0.094. The mean absolute error is approximately equal to 10% of the installed capacity, indicating that the model's performance accuracy can be guaranteed.

We offer a comparison of several different prediction models, including DBSCAN_LSTM(D_LSTM), DBSCAN_CNN(D_CNN), KMeans_LSTM(K_LSTM), KMeans_GRU(K_GRU), and the persistence method. The comparison index is the normalized RMSE of wind power forecast in the future 4 h. The comparison results are shown in Figure 13. For the prediction of the future 4 h, the error of the model proposed in this paper is the lowest. Among them, the KMeans algorithm has a poor effect on cluster division, and LSTM has poor performance in predicting cluster wind power compared with GRUs; baseline persistence method of time series prediction has the worst predictive performance.

In addition, we compared the other two prediction patterns. Pattern 1: power prediction is carried out separately for all wind farms, and the final results are added to get the regional power forecast sum. Pattern 2: the total power of the region is taken as the prediction target, and the power prediction results of 4 h are directly output. The performance of the comparison is RMSE in the 4 h; the comparison results are shown in Figure 14. Compared with the other two patterns, the prediction model proposed in this paper has the lowest prediction error.

5.4 Analysis of steady-state power system analysis results for a regional grid

During the 1-month assessment period, a total of 59 extreme errors occurred in the wind power clusters in the region, with a frequency of 2.048%, which is not higher than the required 4%. Thus, the large-scale wind power cluster ultra-short-term wind power prediction method proposed in this paper can satisfy the static stability requirements of the power system.

The extreme error bandwidth ratio and the percentage of extreme errors at each prediction step to the extreme error bandwidth for 16-step wind power prediction during the assessment period are shown in Figure 15. The extreme error bandwidth for 16-step prediction gradually increases, but the upward trend is not significant for future steps 7, 8, and 9, indicating that the model proposed in this paper can suppress extreme errors as the prediction step increases. At the 16th prediction step, the proportion of extreme errors is 34.0546%. This result suggests that, under the stable evaluation system proposed in this paper, the wind power prediction accuracy of the wind power cluster in the region can meet the requirements, ensuring stable operation of the power system after grid connection.

6 Conclusion

The proposed power system steady-state deduction method, based on the reliability of large-scale wind power cluster power prediction, has improved the stability of power system operation after mass wind power grid connection. The conclusions are as follows:

(1) The improved DBSCAN algorithm can effectively divide wind power clusters based on the constructed wind speed and wind power fluctuation characteristics. The divided wind power clusters have relatively similar actual distances and similar actual power outputs.
(2) The ultra-short-term wind power cluster power prediction method based on the improved GRU algorithm can achieve high prediction accuracy with an RMSE for the fourth hour prediction below 10% of the installed capacity and stable model performance.
(3) Under the power system stability evaluation system constructed in this paper, the proposed ultra-short-term wind power prediction model can effectively improve the operation stability of the power system after a wind power grid connection, with a narrow extreme error bandwidth and a low frequency of extreme errors during the assessment period occurring below 4%.

The next step of this work will further improve the power system stability evaluation indicators and comprehensively evaluate the performance of wind power prediction models from both the grid and generation sides, analyzing their impact on the stable operation of power systems after the wind power grid connection.

Data availability statement

The original contributions presented in the study are included in the article/Supplementary Material; further inquiries can be directed to the corresponding author.

Author contributions

RF designed this study. HY contributed to the improved DBSCAN algorithm. XW contributed to the wind power cluster sub-region clustering method based on DBSCAN. CH contributed to the wind power cluster prediction model based on the improved GRU network. WD performed the framework for steady-state power system analysis based on large-scale wind power cluster forecasting. TD collected and cleansed the data. All authors contributed to the writing of the article, and all agreed to the submitted version of the article.

Funding

This paper was supported by the NARI group science and technology project (grant number: 524609220149).

Conflict of interest

Authors RF, HY, XW, and CH were employed by NARI Group (State Grid Electric Power Research Institute) Co., Ltd. and NARI-TECH Nanjing Control Systems Co., Ltd.

The remaining authors declare that the research was conducted in the absence of any commercial or financial relationships that could be construed as a potential conflict of interest.

The authors declare that this study received funding from the NARI group. The funder had the following involvement in the study: collection, analysis, interpretation of data.

Publisher's note

References

Abedinia, O., Lotfi, M., Bagheri, M., Sobhani, B., Shafie-Khah, M., and Catalão, J. P. (2020). Improved EMD-based complex prediction model for wind power forecasting. *IEEE Trans. Sustain. Energy* 11 (4), 2790–2802. doi:10.1109/TSTE.2020.2976038

Carneiro, T. C., de Carvalho, P. C. M., Alves dos Santos, H., Lima, M. A. F. B., and Braga, A. P. D. S. (2022). Review on photovoltaic power and solar resource forecasting: Current status and trends. *J. Sol. Energy Eng.* 144 (1). doi:10.1115/1.4051652

Demolli, H., Dokuz, A. S., Ecemis, A., and Gokcek, M. (2019). Wind power forecasting based on daily wind speed data using machine learning algorithms. *Energy Convers. Manag.* 198, 111823. doi:10.1016/j.enconman.2019.111823

Dolatabadi, A., Abdeltawab, H., and Mohamed, Y. A. R. I. (2021). Deep spatial-temporal 2-D CNN-blstm model for ultrashort-term LiDAR-assisted wind turbine's power and fatigue load forecasting. *IEEE Trans. Industrial Inf.* 18 (4), 2342–2353. doi:10.1109/TII.2021.3097716

Dong, X., Ning, X., Xu, J., Yu, L., Li, W., and Zhang, L. (2023). PFAS contamination: Pathway from communication to behavioral outcomes. *IEEE Trans. Comput. Soc. Syst.* 2023, 1–13. doi:10.1080/10810730.2023.2193144

Fan, H., Zhang, X., Mei, S., Chen, K., and Chen, X. (2020). M2gsnet: Multi-modal multi-task graph spatiotemporal network for ultra-short-term wind farm cluster power prediction. *Appl. Sci.* 10 (21), 7915. doi:10.3390/app10217915

Ju, Y., Sun, G., Chen, Q., Zhang, M., Zhu, H., and Rehman, M. U. (2019). A model combining convolutional neural network and LightGBM algorithm for ultra-short-term wind power forecasting. *Ieee Access* 7, 28309–28318. doi:10.1109/ACCESS.2019.2901920

Kazari, H., Oraee, H., and Pal, B. C. (2018). Assessing the effect of wind farm layout on energy storage requirement for power fluctuation mitigation. *IEEE Trans. Sustain. Energy* 10 (2), 558–568. doi:10.1109/TSTE.2018.2837060

Li, L. L., Zhao, X., Tseng, M. L., and Tan, R. R. (2020). Short-term wind power forecasting based on support vector machine with improved dragonfly algorithm. *J. Clean. Prod.* 242, 118447. doi:10.1016/j.jclepro.2019.118447

Mao, Y., Mwakapesa, D. S., Xu, K., Lei, C., Liu, Y., and Zhang, M. (2021). Comparison of wave-cluster and DBSCAN algorithms for landslide susceptibility assessment. *Environ. Earth Sci.* 80, 734–814. doi:10.1007/s12665-021-09896-w

Mostafaeipour, A., Bidokhti, A., Fakhrzad, M. B., Sadegheih, A., and Mehrjerdi, Y. Z. (2022). A new model for the use of renewable electricity to reduce carbon dioxide emissions. *Energy* 238, 121602. doi:10.1016/j.energy.2021.121602

Mu, G., Wu, F., Zhang, X., Fu, Z., and Xiao, B. (2022). Analytic mechanism for the cumulative effect of wind power fluctuations from single wind farm to wind farm cluster. *CSEE J. Power Energy Syst.* 8 (5), 1290–1301. doi:10.17775/CSEEJPES.2022.00300

Nazir, M. S., Alturise, F., Alshmrany, S., Nazir, H. M. J., Bilal, M., Abdalla, A. N., et al. (2020). Wind generation forecasting methods and proliferation of artificial neural network: A review of five years research trend. *Sustainability* 12 (9), 3778. doi:10.3390/su12093778

Ning, X., Tian, W., He, F., Bai, X., Sun, L., and Li, W. (2023). Hyper-sausage coverage function neuron model and learning algorithm for image classification. *Pattern Recognit.* 136, 109216. doi:10.1016/j.patcog.2022.109216

Qu, Z., Li, M., Zhang, Z., Cui, M., and Zhou, Y. (2021). Dynamic optimization method of transmission line parameters based on grey support vector regression. *Front. Energy Res.* 9, 634207. doi:10.3389/fenrg.2021.634207

Salazar, A. A., Che, Y., Zheng, J., and Xiao, F. (2022). Multivariable neural network to postprocess short-term, hub-height wind forecasts. *Energy Sci. Eng.* 10 (7), 2561–2575. doi:10.1002/ese3.928

Tang, G., Gao, X., and Chen, Z. (2022). Learning semantic representation on visual attribute graph for person re-identification and beyond. *ACM Trans. Multimedia Comput. Commun. Appl.* 2022, 3487044. doi:10.1145/3487044

Tang, G., Gao, X., Chen, Z., and Zhong, H. (2021). Unsupervised adversarial domain adaptation with similarity diffusion for person re-identification. *Neurocomputing* 442, 337–347. doi:10.1016/j.neucom.2020.12.008

Wan, C., Zhao, C., and Song, Y. (2020). Chance constrained extreme learning machine for nonparametric prediction intervals of wind power generation. *IEEE Trans. Power Syst.* 35 (5), 3869–3884. doi:10.1109/TPWRS.2020.2986282

Wang, Y., Guo, C. H., Chen, X. J., Jia, L. Q., Guo, X. N., Chen, R. S., et al. (2021). Carbon peak and carbon neutrality in China: Goals, implementation path and prospects. *China Geol.* 4 (4), 720–746. doi:10.31035/cg2021083

Wang, Y., Wang, J., Cao, M., Li, W., Yuan, L., and Wang, N. (2022). Prediction method of wind farm power generation capacity based on feature clustering and correlation analysis. *Electr. Power Syst. Res.* 212, 108634. doi:10.1016/j.epsr.2022.108634

Wu, X., Shen, X., Zhang, J., and Zhang, Y. (2021). A wind energy prediction scheme combining cauchy variation and reverse learning strategy. *Adv. Electr. Comput. Eng.* 21 (4), 3–10. doi:10.4316/AECE.2021.04001

Wu, Z., Xia, X., Xiao, L., and Liu, Y. (2020). Combined model with secondary decomposition-model selection and sample selection for multi-step wind power forecasting. *Appl. Energy* 261, 114345. doi:10.1016/j.apenergy.2019.114345

Xiao, Y., Zou, C., Chi, H., and Fang, R. (2023). Boosted GRU model for short-term forecasting of wind power with feature-weighted principal component analysis. *Energy* 267, 126503. doi:10.1016/j.energy.2022.126503

Yang, M., Yan, Q., Dai, B., Chen, X., Ma, M., and Su, X. (2022). An improved spatial upscaling method for producing day-ahead power forecasts for wind farm clusters. *IET Generation, Transm. Distribution* 16 (19), 3860–3873. doi:10.1049/gtd2.12569

Zhao, J., Guo, Z., Guo, Y., Lin, W., and Zhu, W. (2021). A self-organizing forecast of day-ahead wind speed: Selective ensemble strategy based on numerical weather predictions. *Energy* 218, 119509. doi:10.1016/j.energy.2020.119509

Zhao, M., Wang, Y., Wang, X., Chang, J., Zhou, Y., and Liu, T. (2022). Modeling and simulation of large-scale wind power base output considering the clustering characteristics and correlation of wind farms. *Front. Energy Res.* 10, 237–243. doi:10.19746/j.cnki.issn.1009-2137.2022.01.040

Zong, H., and Porté-Agel, F. (2020). A momentum-conserving wake superposition method for wind farm power prediction. *J. Fluid Mech.* 889, A8. doi:10.1017/jfm.2020.77

frontiers | Frontiers in Energy Research

TYPE Original Research
PUBLISHED 11 May 2023
DOI 10.3389/fenrg.2023.1178631

OPEN ACCESS

EDITED BY
Imr Fattah,
University of Technology Sydney,
Australia

REVIEWED BY
Miguel A. Sanz-Bobi,
Comillas Pontifical University, Spain
Adriano Chaves Lisboa,
Gaia, solutions on demand, Brazil
Fei Mei,
Hohai University, China

*CORRESPONDENCE
Lin Zhu,
✉ zhul@scut.edu.cn

RECEIVED 03 March 2023
ACCEPTED 28 April 2023
PUBLISHED 11 May 2023

CITATION
Zhu L, Wu Z and Huang S (2023),
Assessment method of distribution
network health level based on
multivariate information.
Front. Energy Res. 11:1178631.
doi: 10.3389/fenrg.2023.1178631

Assessment method of distribution network health level based on multivariate information

Lin Zhu*, Zilong Wu and Shiyu Huang

School of Electric Power Engineering, South China University of Technology, Guangzhou, China

In order to enhance self-monitoring and self-diagnosis capabilities in smart distribution networks, this paper proposes a method for assessing the health level of the network based on multivariate information. First, we construct an evaluation indicator system for the health of the smart distribution network by integrating the smart distribution network information system. Next, we utilize the improved back propagation (BP) neural network and multivariate indicator information to calculate the health indexes of both the grid layer and equipment. We then solve the health index of the equipment layer based on network topology and goal-oriented methodology. Furthermore, by utilizing the health information of both the equipment and grid layer, we apply fuzzy evaluation and Dempster-Shafer (D-S) evidence theory to obtain the health level of the distribution network. We provide a comprehensive evaluation of the overall health status of the smart distribution network. Finally, the proposed method is validated using data from a regional distribution network. The results demonstrate its effectiveness in improving the smart distribution networks' overall health and stability by enabling more effective self-monitoring and self-diagnosis.

KEYWORDS

smart distribution network, health index, neural network, GO methodology, fuzzy evaluation, D-S evidence theory

1 Introduction

The distribution network plays a crucial role in modern power systems, as it ensures that customers receive a reliable and high-quality power supply. With the integration of distributed energy, new requirements have emerged for the operation level of equipment, grid economy, and environmental sustainability (Trentini et al., 2021). This has also increased the demands on network planning, management, and maintenance (Gumpu et al., 2019). However, the distribution network operates in a complex environment, with many pieces of equipment and a complex grid, leading to a high frequency of failures. According to historical data, more than 85% of failures occur on the distribution network (Li et al., 2015). Therefore, a comprehensive and accurate evaluation of the distribution network's health is essential to optimize its operation and enhance maintenance efficiency.

Most existing operational risk assessment methods for distribution networks are based on reliability theory, which uses equipment failure rate and outage time as indicators (Su et al., 2014; Chen et al., 2020). While useful, these approaches have certain limitations and more comprehensive and refined methods are required to evaluate the conditions of the distribution network. One such approach that has gained prominence is the concept of a power equipment health index. It was first proposed by British scholar D. Hughes in 2003 Hughes et al. (2008) and has been expanded to various fields, such as power supply reliability. It can characterize the equipment's health status and overall performance (Ashkezari et al., 2013; Zhao et al., 2016).

The determination of the equipment health index relies on an indicator system. Researchers have considered real-time monitoring data such as the current, voltage, winding temperature, gas content of distribution transformers, and contact temperature of breakers (Khoddam et al., 2016; Yong-Xiang, 2019; Zhang et al., 2022). The equipment health index can be calculated with these data. However, it is essential to consider not only the current state of equipment but also its lifetime in general, as the health condition of transformers degrades over time (Sibuea and Suwarno, 2022). Moreover, different equipment may exhibit varying susceptibility to failure under similar conditions. Therefore, integrating data from various information systems, facilitated by advancements in smart grid and artificial intelligence technology, can lead to a more comprehensive indicator system. Establishing such a system makes it possible to develop a rational assessment method that quantitatively calculates the equipment health index.

In the field of smart distribution networks, assessing the health level of equipment and the overall network is essential for ensuring a reliable power supply to customers. A critical tool for this is the equipment health index, which can reflect the performance of individual components and the network. While much research has been done to determine the relationship between equipment health index and distribution network operation risk, some studies have not considered the equipment's location (Zhao et al., 2016). To address this issue, researchers utilize Goal-Oriented (GO) methodology to analyze the outages caused by equipment failures at different locations in a distribution network containing distributed generators (DGs) (Gong et al., 2012). This allows for a more comprehensive understanding of the network's performance and the potential impact of equipment failures on customers. In addition, fuzzy evaluation has been introduced to assess the health status of the equipment layer and grid layer (Sun et al., 2016). This approach recognizes health level assessment's uncertain and imprecise nature and can provide a more nuanced understanding. By integrating these methods and approaches, it is possible to develop a more comprehensive and accurate assessment of smart distribution network health.

Furthermore, with the increasing emphasis on the economy and environmental sustainability of distribution networks, traditional methods that only consider reliability are no longer sufficient. To address this, researchers have attempted to integrate smart grid information technology into assessing distribution network health. For instance (Sun et al., 2022), integrated the grid and equipment health indexes to evaluate the health level of distribution networks. However, this approach may lose some key information that is critical to accurately reflecting changes in the health status of equipment or grid.

Therefore, to achieve a more accurate assessment of the health status of a smart distribution network, a comprehensive approach is needed that integrates both short-term and long-term equipment indicators, as well as the overall reliability, economy, and environmental sustainability of the grid. However, directly combining the equipment and grid health indexes may not be appropriate. Meanwhile, the location of the equipment in the network topology affects the outage range, and there are significant differences in the indicators' meaning and the optimal values range. Thus, a novel method is required to effectively integrate the above multiple sources of heterogeneous information and accurately reflect changes in the health conditions of equipment and the grid.

The main contributions of this paper are as follows:

1. The paper proposes a more comprehensive health assessment indicator system for smart distribution networks, which considers multiple aspects such as real-time equipment monitoring data, equipment ledger data, and grid economics level. By integrating these different sources of information, a more accurate and comprehensive picture of the health of the distribution network can be obtained.
2. To integrate multiple indicator information with different meanings and optimal ranges, an improved BP neural network is proposed to calculate the health index of the grid layer and individual equipment. It provides a more nuanced understanding of the health status of the distribution network.
3. The paper analyzes the impact of equipment failure on load outage by combining network topology with the goal-oriented methodology. The relationship between the health of individual equipment and the power supply probability of the overall load in a distribution network containing distributed generations is also analyzed, providing essential insights into the network's overall performance.
4. Fuzzy evaluation is introduced to evaluate the health level of the equipment and grid layers. The information from both layers is fused by D-S evidence theory to assess the distribution network health level based on multiple information. This approach considers the uncertainty and imprecision of health level assessment and provides a more accurate and comprehensive assessment of the health status of the distribution network.

The rest of the paper is structured as follows: Section 2 presents the proposed indicator system for the health assessment of smart distribution networks. Section 3 constructs a comprehensive health index calculation method for the equipment and grid layers. Section 4 assesses the distribution network health level by combining the equipment layer health index and grid layer health index. Section 5 validates the proposed assessment method through case study, demonstrating its effectiveness in accurately reflecting the changes in equipment and grid health conditions. Finally, in Section 6, we draw conclusions and suggest potential areas for future research.

2 Indicator system for smart distribution network health assessment

In order to ensure an accurate assessment of a smart distribution network's health, it is crucial to gather and combine information at both the equipment and grid levels. In this paper, a hierarchical indicator system for health assessment is constructed. The indicator system divides the health indicators of a smart distribution network in terms of power equipment and grid, respectively.

The determination of power equipment health indexes is considered from two different points. It is necessary to consider the condition of the equipment from both a short-term and long-

TABLE 1 Equipment health assessment indicators.

Equipment category	Indicator	Indicator implications
Circuit Breaker	Temperature	Switch temperature can reflect poor contact and mismatch of drop-out currents
	Coil Current	Coil Current exceeding the limit may result in equipment damage
	Mechanical switching on time	A long switch-on time is likely to cause arcing and contact ablation
	Contact travel	A short contact travel is not conducive to breaking, while a long one is not conducive to closing
	Operating years	To measure equipment aging
	Unreliable action times	To assess the status of the equipment by the number of historical equipment failures
Distribution Transformer	Total hydrocarbon content	To reflect faults such as transformer overheating or partial discharge
	Tank temperature difference	To reflect transformer insulation damage and other faults
	Historical failures times	To assess the status of the equipment by the number of historical equipment failures
	Operating years	To measure equipment aging
	Maximum load rate	A low load rate is uneconomical, while high load rates can easily lead to insulation damage to the equipment

TABLE 2 Grid health evaluation indicators.

Category	Indicator	Indicator implications
Grid operation level	Maximum line loading rate	Maximum load rate among all distribution network lines
	Maximum transformer loading rate	Maximum load rate among all distribution transformers
Grid economic efficiency level	Capacity load ratio of network	Ratio of total capacity of main transformer to maximum load in substation
	Rate of high loss distribution transformer	The proportion of high loss distribution transformers to all distribution transformers
Grid security level	Line insulation rate	The proportion of the insulation length to the total length of the line
	Automation Coverage	Coverage ratio of automation intelligent equipment
Grid environmental sustainability level	Distributed power penetration	The proportion of distributed energy output to total power output

term perspective. In terms of equipment operation status, the real-time monitoring data can reflect the short-term health condition of the power equipment. In contrast, information such as equipment ledger can reflect the health condition from a long-term perspective. According to the above two perspectives, 11 indicators are selected as the indicator system to calculate the health indexes for power equipment, as shown in Table 1 below.

It is not easy to fully reflect the overall health level of the smart distribution network by only assessing the health of the equipment. There is also a demand to take the grid health status into the assessment system to evaluate whether non-faulty grid need to be upgraded and renovated. By considering the indicators closely related to the health level of the smart distribution network, the health assessment indicator system of the network is constructed from 4 dimensions: grid operation level, grid economic efficiency level, grid security level, and grid environmental sustainability level, as shown in Table 2. It is worth mentioning that as a business, economic efficiency is of great importance to power companies. If the distribution network does not meet economic requirements, it may lead to a decline in profits, then it is necessary to upgrade and renovate the distribution network to ensure that it is in a better state. Therefore, this article comprehensively selects economic efficiency indicators to calculate the health index of the distribution network.

3 The health indexes calculation of the equipment layer and grid layer

Since the indicators are functionally related to the health index, this paper proposes the BP neural network. BP neural network, well-suited for approximating complex nonlinear relationships, has strong robustness and fault tolerance. Additionally, it can provide fast output results without requiring human involvement after model training. Thus, it can be utilized to calculate the health index of power equipment and the grid.

The above equipment and grid information is mainly stored in the smart distribution network information system, such as the ledger management system, equipment status online monitoring system, voltage monitoring system, operation monitoring system, and grid planning assistance system. Moreover, due to differences in the meaning and optimal intervals of indicators, it is not appropriate to preprocess the data directly using traditional data normalization methods. Therefore, the BP neural network is

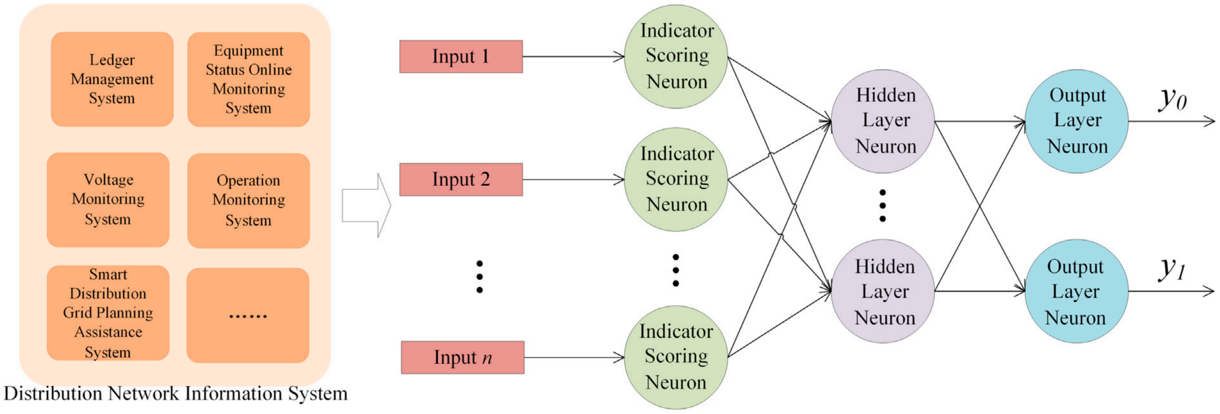

FIGURE 1
Improved BP neural network and its input diagram.

improved in this paper to extract multivariate heterogeneous indicators effectively.

3.1 Health indexes calculation of grid layer and single power equipment based on improved BP neural network

Grid indicators have their respective optimal value ranges. In addition, the indicator values of the equipment will gradually deteriorate from the ideal value to the warning value of the fault state when the health status decreases. Therefore, the problem of heterogeneity of multivariate information can be solved by uniformly evaluating indicators accordingly. For this purpose, in this paper, the input layer neurons of the traditional BP neural network are replaced by indicator-scoring neurons. The improved BP neural network is constructed for the circuit breaker, distribution transformer, and grid, respectively, as shown in Figure 1 below.

Based on the relationship between indicator values and health status, the following three types of indicator-scoring neurons are proposed: 1) Higher indicator values indicate better health status using inverse type indicator-scoring neuron, whose output function is $E_1(x)$; 2) intermediate-range indicator values indicate better health status uses an intermediate type indicator-scoring neuron with the output function $E_2(x)$; 3) lower indicator values indicate better health status using positive type indicator-scoring neuron, whose output function is $E_3(x)$. The specific output functions of each indicator-scoring neuron type are shown below.

$$E_1(x) = \begin{cases} 1, x \le x_1 \\ \dfrac{x - x_2}{x_1 - x_2}, x_1 < x < x_2 \\ 0, x_2 \le x \end{cases} \tag{1}$$

$$E_2(x) = \begin{cases} 1, x \le x_1 \\ \dfrac{x - x_2}{x_1 - x_2}, x_1 < x < x_2 \\ 0, x_2 \le x \le x_2' \\ \dfrac{x - x_2'}{x_1' - x_2'}, x_2' < x < x_1' \\ 1, x_1' \le x \end{cases} \tag{2}$$

$$E_3(x) = \begin{cases} 0, x \le x_2' \\ \dfrac{x - x_2'}{x_1' - x_2'}, x_2' < x < x_1' \\ 1, x_1' \le x \end{cases} \tag{3}$$

where $E_i(x)\,(i = 1, 2, 3)$ is the output of the indicator-scoring neuron, x is the input indicator value, x_1, $x_1{}'$ are the preset alert values for this indicator, and x_2, $x_2{}'$ are the preset ideal values of this indicator.

The indicator-scoring neuron types, preset ideal, and alarm values for each indicator can be determined using equipment manuals, existing planning standards, and expert opinions. Tables 3, 4 showcase the indicator-scoring neuron types and corresponding thresholds employed in this paper for the power equipment and grid indicators, respectively.

In addition, the output fnctions of the neurons in the hidden layer and the output layer, respectively, are

$$\begin{cases} h_j = f\left(\sum_{i=0}^{n} w_{ij} e_i - \theta_j\right), j = 0, 1, \ldots, m \\ y_k = f\left(\sum_{j=0}^{m} w_{jk}' e_j - \theta_k'\right), k = 0, 1 \\ H = \dfrac{y_1}{y_0 + y_1} \end{cases} \tag{4}$$

TABLE 3 Equipment health indicator-scoring neuron type, preset ideal value, and alarm value.

Equipment category	Indicator	Indicator-scoring neuron type	x_1	x_2	x_2'	x_1'
Circuit breaker	Temperature	Positive type	-	-	35°C	80°C
	Coil current	Intermediate type	0.8 A	1.15 A	1.25 A	1.6 A
	Mechanical switching on time	Intermediate type	190 ms	195 ms	208 ms	213 ms
	Contact travel	Intermediate type	19 mm	21 mm	23 mm	25 mm
	Operating years	Positive type	-	-	0	30
	Unreliable action times	Positive type	-	-	0	10
Distribution transformer	Total hydrocarbon content	Positive type	-	-	0	150 μL/L
	Tank temperature difference	Positive type	-	-	85°C	105°C
	Historical failures times	Positive type	-	-	0	10
	Operating years	Positive type	-	-	0	30
	Maximum load rate	Intermediate type	0	20	80	100

TABLE 4 Grid health indicator-scoring neuron type, preset ideal value, and alarm value.

Category	Indicator	Indicator-scoring neuron type	x_1	x_2	x_2'	x_1'
Grid operation level	Maximum line loading rate	Intermediate type	0	20	80	100
	Maximum transformer loading rate	Intermediate type	0	20	80	100
Grid economic efficiency level	Capacity load ratio of network	Positive type	-	-	1.8	2.2
	Rate of high loss distribution transformer	Positive type	-	-	0	5
Grid security level	Line insulation rate	Inverse type	0	100	-	-
	Automation Coverage	Inverse type	0	100	-	-
Grid environmental sustainability level	Distributed power penetration	Positive type	-	-	10	20

where h_j is the output of the jth neuron of the hidden layer, y_k is the output of the kth neuron of the output layer neuron, H is the health index; e_i is the output of the ith indicator-scoring neuron, w_{ij} and w'_{jk} are the weights from the indicator-scoring neurons to the hidden layer neuron and the hidden layer neuron to the output layer neuron, respectively; θ_j and θ_k' are the threshold values; and activation function $f(x)$ is:

$$f(x) = \frac{1}{1+e^{-x}} \tag{5}$$

The loss function employed in this study is cross-entropy. It is defined mathematically as follows:

$$loss = \sum_{i=0}^{1} y_i{*}log(y_i) + (1-y_i{*})log(1-y_i) \tag{6}$$

In order to effectively balance the step size and momentum to optimize the weight vector of the neural network, here we adopt the adaptive moment estimation (Adam) algorithm. It dynamically adjusts the learning rate in the training process and accelerates convergence toward the optimal solution in the early stage while preventing oscillations caused by high learning rates later.

The training set input for the neural network model includes historical data of circuit breakers, distribution transformers, etc., comprising normal and failure data samples. The sample labels $[y_0,y_1]$ with outage faults are set to [0,1], and the sample labels for normal operation are set to [1,0]. The neural network model is trained using this dataset. The model training is completed when the output error meets the requirement, or the number of iterations is reached.

3.2 Equipment layer health index calculation based on GO methodology

The range of equipment outages depends on the equipment's location in the network topology. Therefore, it is not appropriate to add up the health of individual equipment to evaluate the overall health index of the power equipment layer. It is necessary to consider the network topology information comprehensively. At present, GO methodology is able to find the relationship between equipment failure and load outage based on the network topology. Thus, this paper seeks the relationship between single power equipment health index and equipment layer health index based on GO methodology.

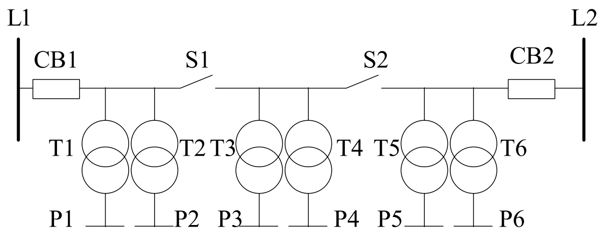

FIGURE 2
The network topology with dual power sources.

The following distribution network in Figure 2 is used to illustrate the methodological steps for obtaining the health index of the equipment layer using the Goal-Oriented (GO) methodology. This approach involves analyzing the impact of equipment failure on load outage by combining network topology with goal-oriented techniques. It provides a more nuanced understanding of the health status of the distribution network, allowing for a more comprehensive and accurate assessment.

(1) Referring to (Shi et al., 2018), the relationship between the level of equipment health and the probability of successful operation of the equipment is

$$P_i = 1 - e^{-\left(\frac{H_i-1}{H_i}\right)^2} \tag{7}$$

(2) When only a single-side power supply exists at L1, the normal power supply of P3 is equivalent to the successful operation of CB1, S1 and T3, which is shown in the following equation:

$$P_{\mathrm{P3}} = P_{\mathrm{L1\text{-}P3}} = P_{\mathrm{CB1}} \cdot P_{\mathrm{S1}} \cdot P_{\mathrm{T3}} \tag{8}$$

where P_{P3} is the probability that P3 load is supplied normally, $P_{\mathrm{L1\text{-}P3}}$ is the probability that P3 load is successfully supplied by L1, P_{CB1}, P_{S1}, P_{T3} are the probability of successful operation of CB1, S1, and T3, respectively.

(3) When feeder 1 and feeder 2 are available, the power supply of P3 is equivalent to the successful operation of CB1, S1 and T3 or CB2, S2 and T3, which is shown in the following equation:

$$P_{\mathrm{P3}} = 1 - (1 - P_{\mathrm{L1\text{-}P3}})(1 - P_{\mathrm{L2\text{-}P3}}) \tag{9}$$

where $P_{\mathrm{L2\text{-}P3}}$ is the probability that P3 load is successfully supplied by L2.

(4) To calculate the probability of successful operation of other loads, we can obtain the probability of successful operation of all loads by using the proportion of each load and its corresponding probability of successful operation, as shown in the following equation:

$$\begin{cases} P = \sum_{i=1}^{n} (a_i \times P_i) \\ \sum_{i=1}^{n} a_i = 1 \end{cases} \tag{10}$$

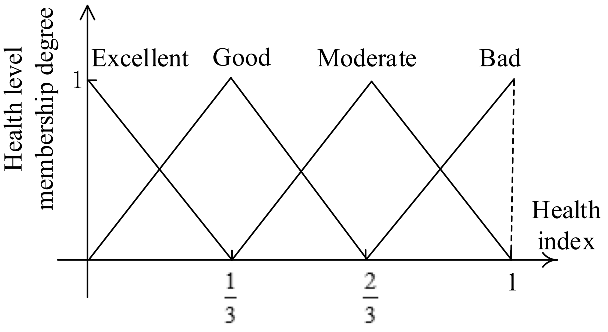

FIGURE 3
Membership function of health level.

where P is the probability of successful operation of all loads, P_i is the probability of successful operation of the ith load, a_i is the ratio of the corresponding load to the total load.

(5) Subsequently, based on the overall probability of successful load operation, the inverse function of Eq. 7 is applied to determine the health index of the power equipment layer, which can be expressed as the following equation:

$$H_{equip} = \frac{1}{1 + \sqrt{-\ln(1 - P)}} \tag{11}$$

4 Distribution network health level assessment

The assessment of health status levels is commonly accomplished through the use of health index. However, the transition process between different health levels is often unclear, making the concept of fuzzy sets from fuzzy mathematics particularly relevant. Consequently, applying fuzzy mathematical theory and membership functions to assess health levels is appropriate. The core concept of the fuzzy theory is the fuzzy set, which allows for the inclusion of elements with different degrees of belonging. The membership function is the key tool used to describe the degree to which an object belongs to a fuzzy set. It maps each object to a real number between 0 and 1, representing the object's degree of membership in the set. When the value is closer to 1, the object belongs more strongly to the set, while a value closer to 0 indicates a weaker membership. Referring to the literature (Sun et al., 2016), health status can be classified into four levels: "Excellent," "good," "moderate," and "bad." Eqs 12–15; Figure 3 depict the membership function of the health level.

$$M(L_1) = \begin{cases} 1 - 3H, 0 \le H \le \frac{1}{3} \\ 0, \frac{1}{3} < H \end{cases} \tag{12}$$

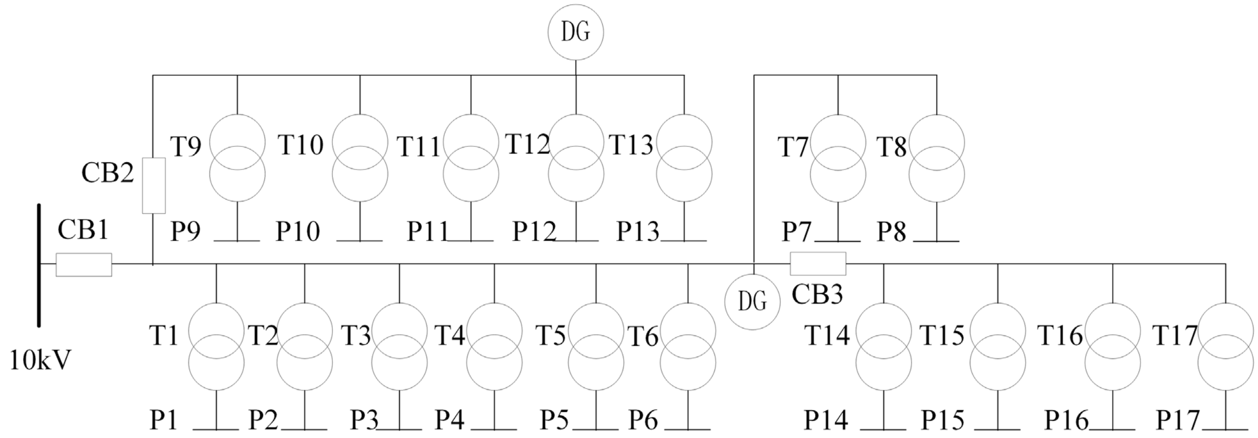

FIGURE 4
Topology diagram of 10 kV distribution network.

TABLE 5 Neural network parameter setting.

Parameter	Distribution transformer neural network	Circuit breaker neural network	Grid neural network
Learning rate	0.05	0.05	0.05
Number of iterations	200,000	200,000	200,000
Minimum error threshold	0.0001	0.0001	0.0001
Number of neurons in the input layer	5	6	9
Number of neurons in the first hidden layer	10	12	20
Number of neurons in the second hidden layer	15	15	20
Number of neurons in the output layer	2	2	2

$$M(L_2) = \begin{cases} 3H, \ H < \frac{1}{3} \\ -3H + 2, \ \frac{1}{3} \le H \le \frac{2}{3} \\ 0, \ \frac{2}{3} < H \end{cases} \tag{13}$$

$$M(L_3) = \begin{cases} 0, \ H < \frac{1}{3} \\ 3H - 1, \ \frac{1}{3} \le H < \frac{2}{3} \\ -3H + 3, \ \frac{2}{3} \le H \le 1 \end{cases} \tag{14}$$

$$M(L_4) = \begin{cases} 0, \ H < \frac{2}{3} \\ 3H - 2, \ \frac{2}{3} \le H \le 1 \end{cases} \tag{15}$$

Where H is the health index, $M(L_1), M(L_2), M(L_3), M(L_4)$ are the membership degree of “Excellent”, “Good”, “Moderate” and “Bad” of health level.

The vector representing health levels is defined as:

$$V = [M(L_1), M(L_2), M(L_3), M(L_4)] \tag{16}$$

When the health index changes gradually within the range of [0,1], the corresponding health level vector also changes gradually, reflecting a more nuanced and accurate evaluation of the health status. The vector ranges from “excellent” to “bad”, allowing for a more accurate assessment of the health level.

The health levels of equipment and the grid layers obtained through the methods above can provide a valuable perspective on distribution network health by integrating various indicator information and network topology. However, relying on either of these levels alone may not provide a complete and accurate assessment of the overall distribution network’s health. Instead, they provide fuzzy criteria and independent sources of uncertainty evidence for distribution network health status. In order to obtain a more comprehensive and accurate distribution network health level, uncertainty inference and information fusion techniques can be applied based on the information provided by both the equipment and grid layer health levels.

D-S evidence theory can handle uncertain information, enabling the fusion of information among multiple bodies of evidence, which has also been used in information fusion in the electrical field (Shafer, 1978; Li et al., 2015). In this paper, we introduce an improved D-S evidence theory to establish an information fusion model for the health level of the equipment layer and the grid layer to assess the overall health level of the distribution network comprehensively.

In this paper, an enhanced D-S evidence theory is proposed to develop an information fusion model for the health level of both equipment and grid layers, thereby achieving a comprehensive evaluation of the overall health level of the distribution network. The implementation process of the improved D-S evidence theory is outlined below.

Assume that Θ is a hypothetical space containing all health levels of the distribution network, in which $M(L_1), M(L_2), M(L_3), M(L_4)$ are the levels of “excellent,” “good,” “moderate,” and “bad” of the distribution network health level according to the equipment layer health index. According to the definition of D-S evidence theory, M_{equip} satisfies the following two equations.

$$M_{equip}(\phi) = 0 \tag{17}$$

$$\sum_{L\subseteq\Theta} M_{equip}(L) = 1 \tag{18}$$

Then the function M_{equip} is a mass function on this hypothesis space. Similarly, another mass function M_{grid} can be obtained based on the construction of the grid layer health index.

In Θ, the mass functions M_{equip} and M_{grid} are independent of each other. According to the definition of D-S evidence theory, they can be informationally fused to obtain the new mass function $M_{net} = M_{equip} \oplus M_{grid}$. The improved synthesis rule is as follows.

$$\begin{gathered} M_{\text{net}}(L_k) = M_{\text{equip}}(L_k) \times M_{\text{grid}}(L_k) + K \times \frac{M_{\text{equip}}(L_k) + M_{\text{grid}}(L_k)}{2} \\ where\ k = 1, 2, 3, 4;\ K = \sum_{i\neq j} M_{\text{equip}}(L_i) M_{\text{grid}}(L_j) \end{gathered} \tag{19}$$

The function M_{net} can effectively integrate the health assessment information contained in both the equipment and the power grid mass functions to obtain the assessment result of distribution network health levels, presented as a vector V_{net}:

$$V_{net} = [M_{net}(L_1), M_{net}(L_2), M_{net}(L_3), M_{net}(L_4)] \tag{20}$$

This vector reflects the level of the distribution network in terms of “Excellent,” “Good,” “Moderate,” and “Bad” by integrating multiple information such as equipment indicators, grid indicators, and network topology through D-S theory. It realizes a comprehensive assessment of the smart distribution network’s health level, which enables self-monitoring and self-diagnosis of the smart distribution network.

5 Study cases

A 10 kV distribution network is selected for calculation example analysis, with its network topology shown in Figure 4. The network comprises 3 circuit breakers and 17 distribution transformers and is connected to two distributed power sources.

The historical data of this distribution network is exported from the network information system to train the improved BP neural network model. 562 sets of transformer historical data, 378 sets of circuit breaker data, and 124 sets of grid data are divided into training sets, and testing sets at a ratio of 8:2, respectively. The parameters of the model are set, as shown in Table 5.

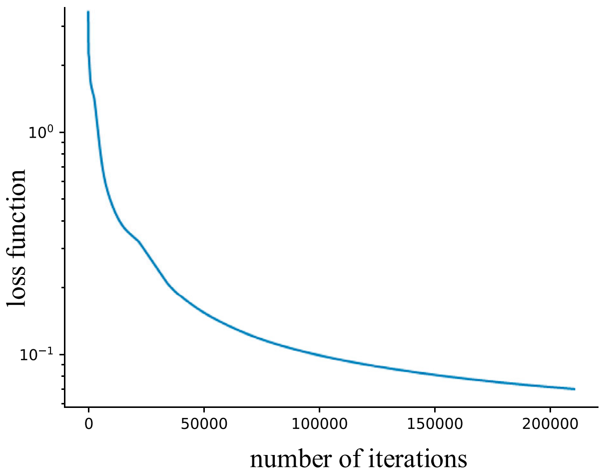

FIGURE 5
Training loss curve.

TABLE 6 Confusion matrix.

	Judgment as fault	Judged as normal
Actually normal	46	4
Actual fault	5	57

Take the distribution transformer neural network model as an example to illustrate the model training process. The change between the loss function and the number of iterations in the model training process is shown in Figure 5.

It can be seen that the model has good stability and convergence in the training process, and the training loss tends to be stable when the iteration reaches 200,000 times.

The higher the health level of the device, the more likely it is to have equipment failure. When a health index threshold is set, any equipment with a health index surpassing this threshold is considered at risk for failure. On the contrary, those below the threshold are deemed to be functioning normally. In this paper, the threshold is trained as 0.75. Comparing this criterion with the actual failure status of the equipment in the test set, we obtain a confusion matrix, as shown in Table 6.

As seen from Table 6, the accuracy of this judgment method reaches 91.96%, which means that the health index of the equipment evaluated by the model can accurately and effectively reflect the failure potential of the equipment.

Afterward, the real-time values of the grid indicators are obtained from the operation and information system, as shown in Table 7.

The grid health neural network model calculates the grid health index as 0.235647.

Taking the T5 transformer as an example, the corresponding indicator values of the indicators are extracted from the smart grid information system, as shown in Table 8.

The health index of this distribution transformer is 0.506836 obtained by the distribution transformer health neural network model. The equipments models and equipments health indexes are shown in Table 9 and Figure 6.

TABLE 7 Real-time value of grid indicators.

Category	Indicator	Real-time value
Grid operation level	Maximum line loading rate	63
	Maximum transformer loading rate	98
Grid economic efficiency level	Capacity load ratio of network	1.9
	Rate of high loss distribution transformer	0.03
Grid security level	Line insulation rate	25
	Automation coverage	86
Grid environmental sustainability level	Distributed power penetration	11.2

TABLE 8 Real-time value of distribution transformer indicators.

Indicator	Real-time value
Total hydrocarbon content	98 μL/L
Tank temperature difference	92°C
Historical failures times	4
Operating years	13
Maximum load rate	95

It can be observed from Figure 6 that T13, T5, and CB3 have a higher health index, indicating that they do not have any abnormalities, but in poor health. This enables the smart grid to perform self-diagnosis based on equipment self-monitoring. The health index of the device layer obtained by the method in this paper is 0.363,152. According to the membership function, the mass functions of the equipment and grid layers are obtained, as shown in the following table.

Table 10 presents the classification of equipment layer health level, which predominantly falls under the "Good" category. Meanwhile, the grid layer health level ranges from "Good" to "Moderate", with a majority being classified as "Good". This highlights the efficacy of utilizing fuzzy evaluation in accurately reflecting the differences in health level, in contrast to employing health index interval segmentation. By integrating the fuzzy criteria derived from both the equipment and grid layers' health index, the health level of the distribution network can be determined using an improved D-S evidence theory model for uncertainty inference and information fusion, as demonstrated in Table 11.

The distribution network health level vector V_{net} is [0.052208, 0.931855, 0.015937, 0]. This vector is a self-diagnosis of the current health status of the distribution network, reflecting that the overall health level of the distribution network is mainly at the "Good" level. Therefore, a maintenance plan could be proposed to enhance the health level.

The distribution network's health level can be enhanced by implementing various improvement options, such as repairing or replacing equipment and improving the grid condition. For example, this paper considers three options: repairing CB3, replacing CB3, and increasing the distributed power penetration rate from 11.2% to 13.2%. After implementing the first two schemes, the equipment layer's health index decreases from 0.363152 to 0.303145 and 0.301278, respectively, while the grid health index remains unchanged. After implementing the third scheme, the grid health index decreases from 0.235647 to 0.187692, and the equipment layer's health index remains unchanged. Using the method proposed in this paper, the distribution network's health level is calculated after the implementation of each scheme and presented in Table 12.

TABLE 9 Equipments models.

Equipment no.	Equipment model	Equipment no.	Equipment model
T1	S13-M.RL-315/10	T11	S11-M-50/10
T2	S11-M-250/10	T12	S11-M-30/10
T3	S13-M-200/10	T13	SBH10-100/10
T4	S11-M.RL-200/10	T14	S11-M-160/10
T5	S11-M-200/10	T15	S13-M-200/10
T6	S13-M.RL-315/10	T16	S13-M-100/10
T7	SH15-M-100/10	T17	S11-M.R-250/10
T8	S11-M-80/10	CB1	ZW32-12
T9	S11-M.R-500/10	CB2	ZW8-12
T10	S11-M-250/10	CB3	ZW8-12

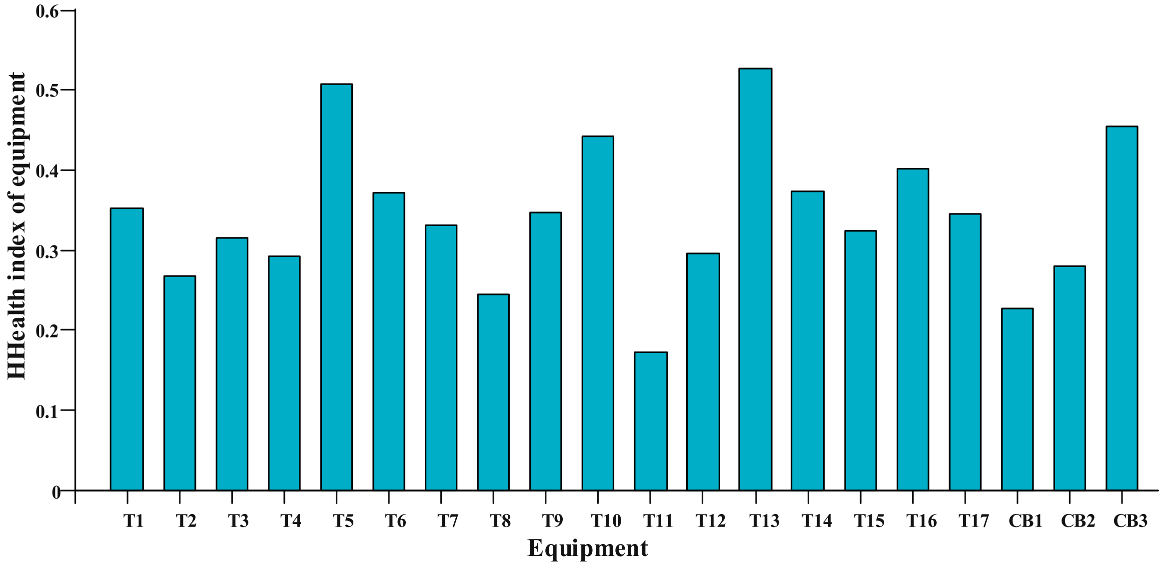

FIGURE 6
Health index of each equipment.

TABLE 10 Mass functions of equipment layer and grid layer.

Health level	Excellent	Good	Moderate	Bad
M_{equip}	0	0.910 544	0.089 456	0
M_{grid}	0.293 059	0.706 941	0	0

As shown in Table 12, after the implementation of the three options, the degree of the distribution network health belonging to the "Excellent" level has increased, and the abnormal state of the network can be eliminated when CB3 is repaired. Increasing the penetration rate of distributed power can improve the health level of the network through the grid layer but cannot eliminate the abnormalities caused by the equipment layer. It can be seen that an accurate evaluation of the health level of the distribution network has been achieved through the proposed method.

From a long and short-term perspective, the indicator system constructed in this paper can better reflect the impact of different schemes on the health of the distribution network. If the indicators related to long-term statistical information of equipment are not considered, repairing or replacing CB3 can result in the monitoring data returning to an optimal state. In this case, after implementing both schemes, the neural network inputs are completely identical, leading to the same health index, thus failing to reflect the differences between the two schemes.

In contrast to the interval partitioning method, our proposed approach in this paper offers a more precise and comprehensive evaluation of the health status of the distribution network. For instance, a previous study (Sun et al., 2022) uses four equally sized intervals to represent four distinct health levels. In cases where the health levels of the equipment and the grid layers do not match, the lower of the two levels is deemed as the health level of the distribution

TABLE 11 Assessment of distribution network health level.

Distribution network health level	Excellent	Good	Moderate	Bad
M_{net}	0.052 208	0.931 855	0.015 937	0

TABLE 12 Comparison of the effects of different schemes.

Schemes	Distribution network health level			
	Excellent	Good	Moderate	Bad
Primary health level of the distribution network	0.052208	0.931855	0.015937	0
Repairing CB3	0.058231	0.941769	0	0
Replacing CB3	0.092961	0.907039	0	0
Increasing the distributed power penetration rate from 11.2% to 13.2%	0.106455	0.871749	0.021796	0

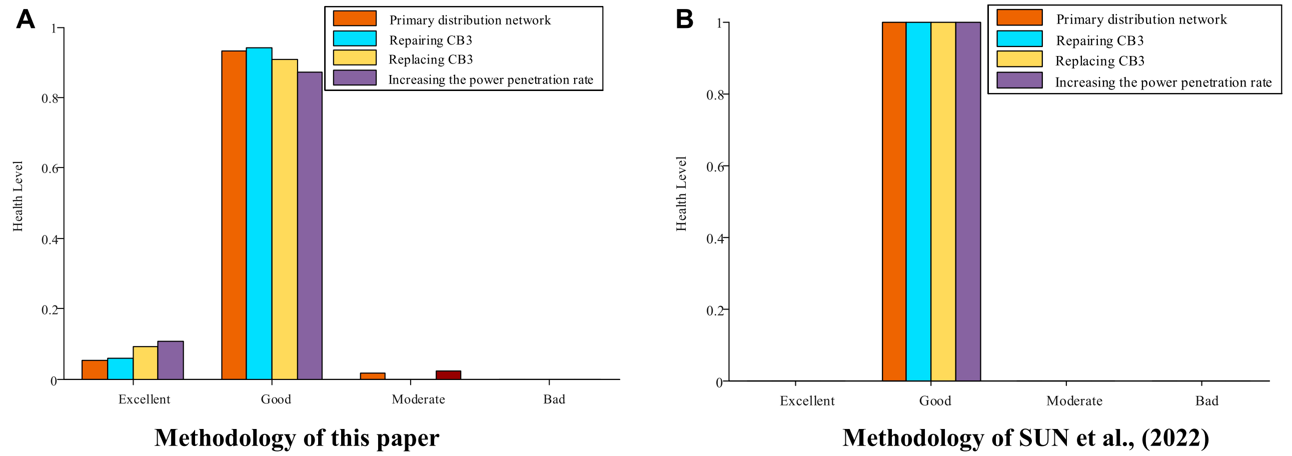

FIGURE 7
Comparison of different schemes. **(A)** Methodology of this paper **(B)** Methodology of SUN et al. (2022).

network. However, this method fails to reflect the effectiveness of different improvement schemes, particularly when the health levels of the two layers are inconsistent. When applied to our health index results, this approach fails to differentiate the benefits of our three proposed schemes. Interestingly, we found that the health levels of the equipment layer were all classified as “Good” and the health levels of the grid layer were rated as “Excellent” before and after implementing the three schemes. The health levels of the distribution network after the original state, repairing CB3, replacing CB3, and increasing the distributed power penetration rate from 11.2% to 13.2% are 0.363152, 0.303145, 0.301,278, and 0.363152, respectively, and the health levels are all “Good”. It can be seen that the ratings method used by SUN et al. (2022) fails to accurately capture the differences in the effectiveness of the schemes. To better illustrate the changes in the risk level of the distribution network after implementing different schemes, we provide a comparative analysis in Figure 7.

The method presented in this paper allows smart grids to achieve more accurate self-diagnosis than other methods. This method provides practical guidance for further self-healing of the smart grid, helping staff propose and evaluate maintenance and planning plans. In this way, the method effectively reduces the fault risk of the smart distribution network and improves the reliability of the power supply.

6 Conclusion

This paper proposes a novel approach to evaluate the health level of smart distribution networks based on multivariate information. Specifically, we construct a comprehensive indicator system to assess the health of both equipment and grid layers. We adopt an improved neural network model to achieve a precise and comprehensive quantitative evaluation of the individual health status of equipment and grid based on multiple indicators. Furthermore, we utilize the GO methodology to determine the likelihood of all loads operating normally by integrating the single equipment health index with the network topology, which allows us to obtain the health index of the equipment layer. Based on the health index of both equipment and grid layers, we employ fuzzy theory and D-S evidence theory to present a method for self-diagnosing the health status of smart distribution networks by evaluating the health level.

The findings of this study can provide valuable theoretical guidance for the self-healing, operation, and planning of smart distribution networks. Our proposed approach can be of great practical significance for maintaining the reliability and stability of power systems.

Data availability statement

The raw data supporting the conclusion of this article will be made available by the authors, without undue reservation.

Author contributions

LZ: Formulation of overarching research goals and design of methodology ZW: performing the data analysis SH: Creation of the published work. All authors contributed to the article and approved the submitted version.

Funding

This work is supported by Guangdong Provincial Key Laboratory of Intelligent Operation and Control for New Energy Power System (No. GPKLIOCNEPS-2021-KF-01).

Conflict of interest

The authors declare that the research was conducted in the absence of any commercial or financial relationships that could be construed as a potential conflict of interest.

Publisher's note

References

Ashkezari, A. D., Ma, H., Saha, T. K., and Ekanayake, C. (2013). Application of fuzzy support vector machine for determining the health index of the insulation system of in-service power transformers. *IEEE Trans. Dielectr. Electr. insulation* 20 (3), 965–973. doi:10.1109/tdei.2013.6518966

Chen, L., Liu, L., Peng, Y., Chen, W., Huang, H., Wu, T., et al. (2020). Distribution network operational risk assessment and early warning considering multi-risk factors. *IET Generation, Transm. Distribution* 14 (16), 3139–3149. doi:10.1049/iet-gtd.2019.1198

Gong, J., Huang, M., and Sun, F. (2012). Reliability assessment based on GO methodology for the distribution system including distributed generation. *Power Syst. Prot. Control* 40, 90–100. doi:10.3969/j.issn.1674-3415.2012.16.015

Gumpu, S., Pamulaparthy, B., and Sharma, A. (2019). Review of congestion management methods from conventional to smart grid scenario. *Int. J. Emerg. Electr. Power Syst.* 20. doi:10.1515/ijeeps-2018-0265

Hughes, D., Pears, T., and Tian, Y. (2008). "Linking engineering knowledge and practical experience to investment planning by means of condition based risk management," in 2008 International Conference on Condition Monitoring and Diagnosis, Beijing, 21-24 April 2008, 539–542.

Khoddam, M., Sadeh, J., and Pourmohamadiyan, P. (2016). Performance evaluation of circuit breaker electrical contact based on dynamic resistance signature and using health index. *IEEE Trans. Components, Packag. Manuf. Technol.* 6 (10), 1505–1512. doi:10.1109/tcpmt.2016.2601316

Li, L., Liu, J., Ling, Y., Zhou, X., and Zhang, Y. (2015). Power quality comprehensive evaluation based on matter-element theory and evidence theory. *Trans. China Electrotech. Soc.* 30, 383–391. doi:10.3969/j.issn.1000-6753.2015.12.048

Shafer, G. A. (1978). *A mathematical theory of evidence*. Princeton, NJ: Princeton University Press.

Shi, C., Ning, X., Sun, Z., Kang, C., Du, Y., and Guoming, M. (2018). Quantitative risk ssessment of distribution network based on real-time health index of equipment. *High. Volt. Eng.* 44 (2), 534–540. doi:10.13336/j.1003-6520.hve.20171107001

Sibuea, E. B., and Suwarno (2022). "Correlation of oil dielectric characteristics, dissolved gases, and operating life to insulation paper degradation of 150 kV power transformers," in 2022 International Seminar on Intelligent Technology and Its Applications (ISITIA), Surabaya, July 20-21, 2022 (IEEE), 360–364.

Su, H., Jiang, X., and Liang, Z. (2014). Distribution network operation risk assessment considering various influencing factors. *Electr. Meas. Instrum.* 51 (6), 38–42. doi:10.3969/j.issn.1001-1390.2014.06.008

Sun, L., Ma, Z., Shang, Y., Liu, Y., Yuan, H., and Wu, G. (2016). Research on multi-attribute decision-making in condition evaluation for power transformer using fuzzy AHP and modified weighted averaging combination. *IET Generation, Transm. Distribution* 10 (15), 3855–3864. doi:10.1049/iet-gtd.2016.0381

Sun, L., Wang, Z., Dai, H., Tian, Y., and Chen, X. (2022). Long-term manure amendment sustains black soil biodiversity by mitigating acidification induced by chemical N fertilization. *Power Syst. Prot. Control* 50 (4), 64–74. doi:10.3390/microorganisms11010064

Trentini, C., de Oliveira Guedes, W., de Oliveira, L. W., Dias, B. H., and Ferreira, V. H. (2021). Maintenance planning of electric distribution systems—a review. *J. Control, Automation Electr. Syst.* 32 (1), 186–202. doi:10.1007/s40313-020-00663-z

Yong-Xiang, Y. (2019). Time-varying failure model of multi-factor driven distribution transformer and its application. *Smart Grid* 9 (6), 253–262. doi:10.12677/sg.2019.96028

Zhang, Y., Tang, Y., Liu, Y., and Liang, Z. (2022). Research on variable weight synthesizing model for transformer condition assessment. *Front. Energy Res.* 10. doi:10.3389/fenrg.2022.941985

Zhao, H., Feng, W., Yanghong, T., Xuzhu, D., Zhengrong, W., Chun, C., et al. (2016). Pristimerin triggers AIF-dependent programmed necrosis in glioma cells via activation of JNK. *Electr. Power Autom. Equip.* 36 (06), 136–148. doi:10.1016/j.canlet.2016.01.055

Frontiers in Energy Research

TYPE Original Research
PUBLISHED 16 May 2023
DOI 10.3389/fenrg.2023.1198855

OPEN ACCESS

EDITED BY
Praveen Kumar Donta,
Vienna University of Technology, Austria

REVIEWED BY
Lia Elena Aciu,
Transilvania University of Brașov,
Romania
Baoli Lu,
University of Portsmouth, United
Kingdom

*CORRESPONDENCE
Guofeng Ni,
✉ 080260@sdyu.edu.cn

RECEIVED 02 April 2023
ACCEPTED 04 May 2023
PUBLISHED 16 May 2023

CITATION
Ni G, Zhang X, Ni X, Cheng X and Meng X (2023), A WOA-CNN-BiLSTM-based multi-feature classification prediction model for smart grid financial markets.
Front. Energy Res. 11:1198855.
doi: 10.3389/fenrg.2023.1198855

A WOA-CNN-BiLSTM-based multi-feature classification prediction model for smart grid financial markets

Guofeng Ni[1]*, Xiaoyuan Zhang[1], Xiang Ni[2], Xiaomei Cheng[1] and Xiangdong Meng[3]

[1]School of Accounting, Shandong Youth University of Political Science, Jinan, China, [2]School of Economics and Management, Tiangong University, Tianjin, China, [3]School of Information Engineering, Shandong Youth University of Political Science, Jinan, China

Introduction: Smart grid financial market forecasting is an important topic in deep learning. The traditional LSTM network is widely used in time series forecasting because of its ability to model and forecast time series data. However, in long-term time series forecasting, the lack of historical data may lead to a decline in forecasting performance. This is a difficult problem for traditional LSTM networks to overcome.

Methods: In this paper, we propose a new deep-learning model to address this problem. This WOA-CNN-BiLSTM model combines bidirectional long short-term memory network BiLSTM and convolution Advantages of Neural Network CNN. We replace the traditional LSTM network with a bidirectional long short-term memory network, BiLSTM, to exploit its ability in capturing long-term dependencies. It can capture long-term dependencies in time series and is bidirectional modelling. At the same time, we use a convolutional neural network (CNN) to extract features of time series data to better represent and capture patterns and regularity in the data. This method combining BiLSTM and CNN can learn the characteristics of time series data more comprehensively, thus improving the accuracy of prediction. Then,to further improve the performance of the CNN-BiLSTM model, we optimize the model using the whale algorithm WOA. This algorithm is a new optimization algorithm, which has good global search ability and convergence speed, and can complete the optimization of the model in a short time.

Results: Optimizing the CNN-BiLSTM model through the WOA algorithm can reduce its calculation and training speed, improve the prediction accuracy of the smart grid financial market, and improve the prediction ability of the smart grid financial market. Experimental results show that our proposed CNN-BiLSTM model has better prediction accuracy than other models and can effectively deal with the problem of missing historical data in long-term sequence forecasting.

Discussion: This provides necessary help for the development of smart grid financial markets and risk management services, and can promote the development and growth of the smart grid industry. Our research results are of great significance in deep learning, and provide an effective method and idea for solving the financial market forecasting problem of smart grid.

KEYWORDS

WOA, CNN, BiLSTM, smart grid, financial market forecasting

1 Introduction

Smart grid financial market refers to the market that provides financial support and risk management services for smart grid construction and operation through financial means and financial tools, with smart grid construction and function as the core and the financial market as the support (Ning et al., 2020). The main participants of the smart grid financial market include financial institutions, smart grid enterprises, investors, and government departments (Ning et al., 2023). The development of a smart grid financial market can promote the diversification of funding sources for smart grid construction and operation, reduce the financing cost of smart grid construction and operation, improve the operational efficiency and safety of smart grid, promote the deep integration of smart grid and financial market, and promote the development and growth of smart grid industry (Xiang et al., 2019). The main business of the smart grid financial market includes: Smart grid project financing. Smart grid asset securitization. Smart grid risk management. Smart grid investment. Smart grid financial innovation. Among them, smart grid asset securitization is one of the important businesses of the smart grid financial market. Packaging smart grid assets into securitized products attracts more investors to participate in smart grid construction and operation to improve the smart grid's financing and capital utilization efficiency. In short, developing a smart grid financial market will provide more comprehensive and diversified funding sources and risk management services for smart grid construction and operation and promote the development and growth of the smart grid industry. There is a wide variety of smart grid financial market forecasting models, mainly using this model for time series forecasting (Li et al., 2017). The following is a brief overview of some of the models commonly used for smart grid financial market forecasting:

Time series models: ARIMA (Huang et al., 2023), SARIMA (Song et al., 2020), VAR model Cai et al. (2021), etc. These traditional time series models are better for modelling linear relationships, but for modelling nonlinear relationships These traditional time series models are better for modelling linear relations but weaker for modelling nonlinear relations. They need to rely on the assumptions of smoothness and periodicity of time series data, and if these assumptions do not hold, the prediction effect of the models may be affected.

Next, there are neural network models Song et al. (2021): BP neural network Zahid et al. (2019), RBF neural network Hammami et al. (2020) and CNN neural network Zhang et al. (2019), etc.; neural network models can model nonlinear relationships but require a large amount of data for training, and the model is poorly interpretable, making it difficult to explain the decision-making process of the model, while neural network models are prone to the problem of overfitting and require hyperparameter adjustment and regularization, etc.;

Models of machine learning: decision trees Fan et al. (2023), random forests Lin et al. (2020), support vector machines Dai and Zhao (2020), etc. Machine learning models can model nonlinear relationships but require feature engineering to extract useful features. Also, require processing such as hyperparameter adjustment and regularization, and the models are poorly interpretable, making it difficult to explain the decision-making process of the models;

Deep learning-based models: recurrent neural networks Lu and Hong (2019) and long and short-term memory networks Wu et al. (2022), etc. Deep learning-based models can model nonlinear relationships while automatically extracting features, but they require a large amount of data for training, and the models are poorly interpretable, making it difficult to explain the decision process of the model and also prone to overfitting problems;

Bayesian network model Bessani et al. (2020):Bayesian network model can model nonlinear relationships and simultaneously deal with uncertainty. Still, it requires learning Bayesian network structure and estimating parameters, which is more difficult. At the same time, the interpretability of the model could be better, and it is difficult to explain the model's decision-making process.

At this stage, the widely used and effective temporal prediction model is the long short-term memory network LSTM Chen et al. (2022). Long short-term memory network (LSTM) is a commonly used time-series forecasting model, which can capture important features and trends in a sequence by modelling the long-term dependence of sequence data. However, LSTM models have problems, such as poor processing for long series and poor interpretability. This paper proposes a temporal sequence prediction model based on a bi-directional long and short-term memory network (BiLSTM) to solve these problems. The BiLSTM model adds a reverse layer to the LSTM model, which can better handle contextual information. The bi-directional model can consider past and future information when processing sequence data, making the model capture features and trends in the sequence more accurately. At the same time, the BiLSTM model also has better interpretability, which can help users better understand the model's decision process. To further improve the model prediction accuracy and reduce the training time and computation, this paper adopts the Whale Algorithm (WOA) to optimize the CNN-BiLSTM network. The WOA algorithm is an emerging optimization algorithm that finds the optimal solution by simulating whales' foraging behaviour. The WOA algorithm has a faster convergence speed and stronger global search capability than traditional optimization algorithms. In this paper, the WOA algorithm is applied to the optimization of the CNN-BiLSTM network to optimize the model's prediction effect by adjusting the network's weights and biases. The experimental results show that the CNN-BiLSTM model optimized with the BiLSTM model and WOA algorithm achieves better performance in temporal sequence prediction. The model can accurately capture the features and trends in the sequences and has better interpretability and higher prediction accuracy. At the same time, the training time and computational effort of the optimized model using the WOA algorithm are effectively reduced, which helps to improve the practicality and application value of the model.

In the rest of this paper, we present recent related work in **Section 2**. **Section 1** offers our proposed methods: overview, convolutional neural network, bi-directional long and short-term memory network BiLSTM, and WOA whale algorithm. **Section 4** presents the experimental part, including practical details and comparative experiments. **Section 5** concludes.

2 Related work

2.1 VAR model

The VAR model is a Vector Autoregression Model (VAR). It is a widely used method for time series analysis to explore the dynamics between a set of correlated variables. The VAR model assumes that the current value of each variable is correlated with the past matters and the current values of the other variables He and Ye (2022). In the VAR model, each variable is modeled as a linear combination of the other variables. The core idea of the model is to predict the values of multiple variables at the current point in time from the importance of various variables at the past point in time. Zhang et al. (2023) proposed an enterprise supply chain management system based on deep learning and game theory, and achieved good results, further reducing the financial risk and carbon emissions of enterprises. Thus, the VAR model can be used to predict future values of one variable and multiple variables. VAR models can be applied in various fields, such as economics, finance, meteorology, etc., to analyze the relationship between variables and future trends.

2.2 BP neural network

BP neural network is a common artificial neural network called back propagation neural network, which is usually used to solve classification and regression problems. BP neural network is a directed graph that consists of an input layer, an output layer, and at least one hidden layer. In the network, each neuron is connected to all neurons in the previous layer, and each connection has a weight. The BP algorithm adjusts the weights by backpropagation error to make the network output results closer to the actual results Li et al. (2023).

The training process of the BP neural network is usually divided into two stages: forward propagation and backward propagation. In the forward propagation process, the input signal reaches the output layer from the input layer through the hidden layer and generates the network output result. The error between the network output result and the actual result is calculated in the backpropagation process. The error is propagated backward from the output layer to the input layer. Finally, the weight of each connection is adjusted to reduce the error. BP neural networks have many applications, such as image recognition, natural language processing, speech recognition, financial prediction, and other fields. However, the training process of BP neural networks usually requires a lot of computational resources and time and is prone to overfitting problems. In recent years, significant breakthroughs have been made in developing deep learning technology, and deep neural networks have become important tools for various application areas.

2.3 Bayesian Network

Bayesian Network (BN) is a probabilistic graphical model for representing probabilistic dependencies between variables. It usually uses directed acyclic graphs (DAGs) to define conditional dependencies between variables. Each node represents a variable, and each edge represents a conditional probability. The combination of nodes and edges forms a directed acyclic graph Bessani et al. (2020). Bayesian network models have two types of nodes: random variable nodes and parameter nodes. The random variable nodes represent the variables in the model, and the parameter nodes represent the parameters in the model, such as the mean and variance. Each random variable node has a conditional probability distribution that represents the probability distribution of that node given its parent node. In Bayesian networks, we can use Bayes' theorem to compute the posterior probabilities. Suppose we want to calculate the probability distribution of a variable given certain conditions of evidence; we can use Bayes' formula to do so.

Bayesian networks can be used in various applications such as risk assessment, medical diagnosis, financial analysis, natural language processing, etc. It has the advantages of simple modeling, good interpretability, and good generalization ability.

3 Methodology

In this paper, we use the WOA-CNN-BiLSTM model to predict changes in the financial market of smart grids, first combining the advantages of the CNN and BiLSTM models to incorporate into the CNN-BiLSTM model. Using the WOA whale algorithm to optimize the model and finally integrating it into the WOA-CNN-BiLSTM model, after training, the model is used to predict the financial market of the smart grid; the overall flow of the model is shown in **Figure 1**:

After the data input in **Figure 1** enters the CNN module, extracting the text's key features with the help of the CNN network elements, then passes through the Dropout layer to avoid overfitting the neural network. The obtained characteristics are fed into the bidirectional long and short-term memory network to get the temporal information of the text for the prediction of the smart grid financial market. Then it is processed by the fully connected layer and normalization, optimized by the WOA layer, and finally, the prediction results are output.

3.1 CNN model

Convolutional Neural Network (CNN) is a deep learning algorithm commonly used in image recognition, computer vision, natural language processing, etc Yang et al. (2023). The main features of CNN are its ability to automatically extract features from data and its parameter sharing and sparse connectivity. It consists of several convolutional, pooling, and fully connected layers (Cheng et al., 2023). In the convolutional layer, CNN extracts the features of an image by convolving the input data using a convolutional kernel. In the pooling layer, the CNN improves the features' robustness by reducing the feature map's size. Finally, in the fully connected layer, CNN classifies the pooled feature maps by feeding them into a

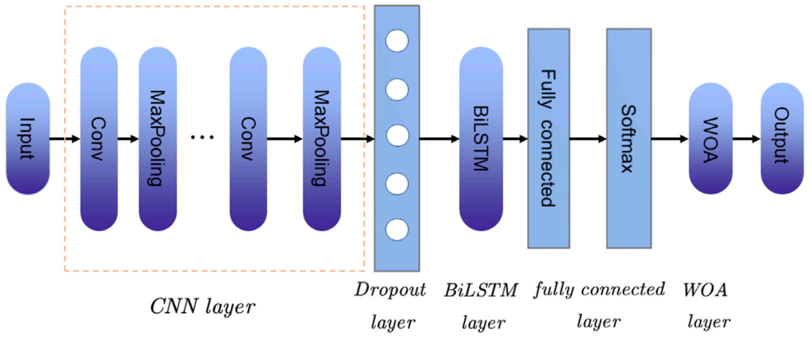

FIGURE 1
Overall flow chart of WOA-CNN-BiLSTM network.

fully connected neural network. A flowchart of the CNN network is shown in **Figure 2**:

CNN can effectively reduce the number of parameters in a neural network and avoid the phenomenon of overfitting, thus improving the model's generalization ability. In addition, CNNs can also quickly build models with powerful recognition capabilities through pre-training techniques and migration learning. One-dimensional CNN has the same structure and processing method as multidimensional CNN. Still, the difference lies in the number of dimensions of the input data and the way the convolution kernel slides over the data.

$$Y(i) = \sum_{n=1}^{m} \left(x_n \times \omega_n^i\right) + c^i \tag{1}$$

where: i is the serial number of the convolution kernel, c is the bias of the convolution kernel, $Y(i)$ is the result of the ith convolution operation, x is the input data, ω is the corresponding weight, n is the dimension of the input data.

3.2 BiLSTM model

BiLSTM (Bidirectional Long Short-Term Memory) is a bi-directional recurrent neural network model that combines the advantages of LSTM (Long Short-Term Memory) and a bi-directional recurrent neural network. BiLSTM model can consider both forward and backward contextual information, thus better capturing the long-term dependencies in the sequence. The flow chart of the BiLSTM model is shown in **Figure 3**:

The input to the BiLSTM model is a sequence, and each element is a vector. Each piece is fed into an LSTM cell for processing in the model. The LSTM cell can remember the previous state and update the state and output based on the current and last input. In the BiLSTM model, each element is fed into two LSTM units: a forward LSTM unit and a backward LSTM unit. The bold LSTM cell starts processing from the first element of the sequence Munawar et al. (2022), and the back LSTM cell starts processing from the last part. Ultimately, the output of the BiLSTM model is a stitching of the results of the forward and backward LSTM units. The BiLSTM model performs well in natural language processing tasks like sentiment analysis, named entity recognition, machine translation, etc.

BiLSTM is used to extract periodic features from the load data, and the BiLSTM network is used to calculate the forward and backward propagation states, respectively, as follows:

$$\vec{h}_f = \mathrm{LSTM}\left(x_t, \vec{h}_{f-1}\right) \tag{2}$$

$$\overleftarrow{h}_b = \mathrm{LSTM}\left(x_t, \overleftarrow{h}_{b-1}\right) \tag{3}$$

$$h_t = \boldsymbol{W}_f \vec{h}_t + \boldsymbol{W}_b \overleftarrow{h}_t + C_t \tag{4}$$

Where: $\vec{h}_f$ is the hidden layer state of the tth cell of forward propagation; X_t is the input at the current moment; $\vec{h}_{f-1}$ is the hidden layer state of the last cell of forward propagation; $\overleftarrow{h}_b$ is the hidden layer state of the t th cell of backward propagation; $\overleftarrow{h}_{b-1}$ is the hidden layer state of the previous cell of back propagation; W_f is the hidden layer output weight matrix of the forward propagation cell; W_b is the hidden layer output weight matrix of the backward propagation cell; C_t is the current moment hidden layer bias optimization parameter.

3.3 WOA whale algorithm

The WOA (Whale Optimization Algorithm) whale algorithm is an optimization algorithm based on the behavior of whale populations, proposed by Mirjalili et al., in 2016. The algorithm simulates the food-seeking behavior of a whale population and searches for the optimal solution through continuous search and iteration Adetunji et al. (2020). The basic idea of the WOA algorithm is to divide the whale population into three categories: leader whales, follower whales, and peripheral whales. The leader whales are the individuals with the optimal solution in the whole group, and their positions and fitness values play a decisive role in the search direction of the entire group. The follower whales update their posts by imitating the behavior of the leader whales, while the peripheral whales search for a better solution by random search (Zhu et al., 2020).

First, for the whale to surround the prey before spitting bubbles, swimming in a straight line, the individual whale tends to the optimal personal position, a certain range of space for the roundup; the formula is as follows:

$$\vec{D} = \left\|\boldsymbol{C}\cdot\boldsymbol{X}_P(t) - \boldsymbol{X}(t)\right\|, \tag{5}$$

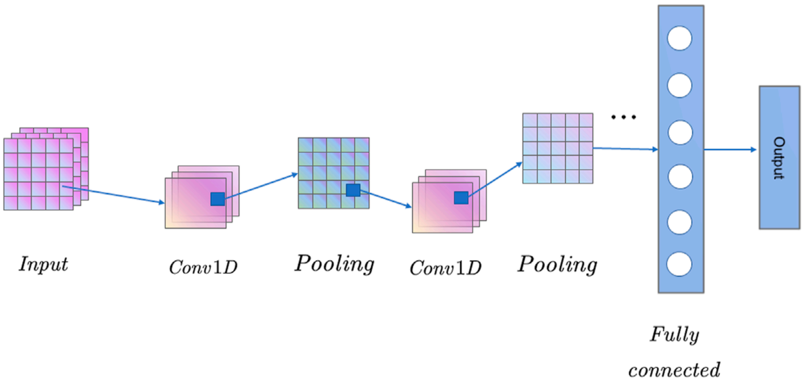

FIGURE 2
CNN network operation flow chart (This article uses one-dimensional convolution, after two convolutions and pooling, and finally output through the fully connected layer).

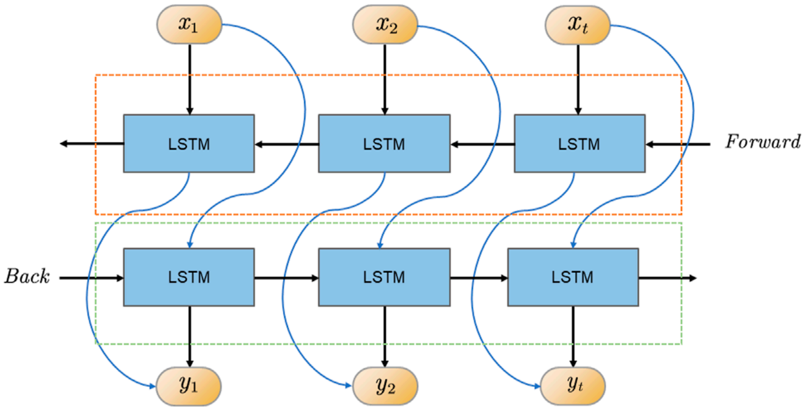

FIGURE 3
Flow chart of two-way long and short-term memory network (This article uses a two-way structure, which can better identify past and future texts and improve prediction accuracy).

$$\boldsymbol{X}(t+1) = \boldsymbol{X}_P(t) - \boldsymbol{A} \cdot \vec{D}, \tag{6}$$

$$\boldsymbol{A} = a(2r) - 1, \tag{7}$$

$$a = 2 - 2\left(t/t_{\max}\right), \tag{8}$$

$$\boldsymbol{C} = 2r, r \in (0,1), \tag{9}$$

Where: $\vec{D}$ is the distance between the individual $\boldsymbol{X}$(t) and the optimal individual $\boldsymbol{X}_p(t)$ within the population at time t; A, C is a vector of random coefficients, showing the difference in perceived distance between whale individuals within the population, and this search $A \in [-1,1]$, which limits the search space; a is the iteration factor of the algorithm as a whole, through the algorithm global.

Another whale predation model is bubble spitting predation, an optimization algorithm based on the behavior of whale populations. First, the distance between each individual within the people and the optimal individual is calculated and then constrained according to the mathematical modeling formula of spitting bubbles. Then, the search space is restricted to the helix according to the idea of local search to find the optimal solution. The bubble helix modeling is shown in **Figure 4**:

The search formula for this mechanism is as follows:

$$\vec{D}' = |\boldsymbol{X}_P(t) - \boldsymbol{X}(t)|, \tag{10}$$

$$\boldsymbol{X}(t+1) = \vec{D}^{r} e^{bl} \cos(2\pi l) + \boldsymbol{X}_P(t) \tag{11}$$

$\vec{D}'$ determines the shape of the spiral curve, where I is a random number in the range of [-1, 1]. The above two predation and foraging strategies occur asynchronously among individual whales, each with a probability of 0.5. When the perceived distance control parameter $|A|$ is greater than 1, the whales will randomly search for each other based on their positions using the same formulation used for bubble net hunting. The WOA algorithm has the advantage of high convergence speed and global search capability and is suitable for solving various optimization problems. However, the algorithm also has some disadvantages, such as the tendency to fall into local optimal solutions and high parameter sensitivity (Nazari et al., 2020).

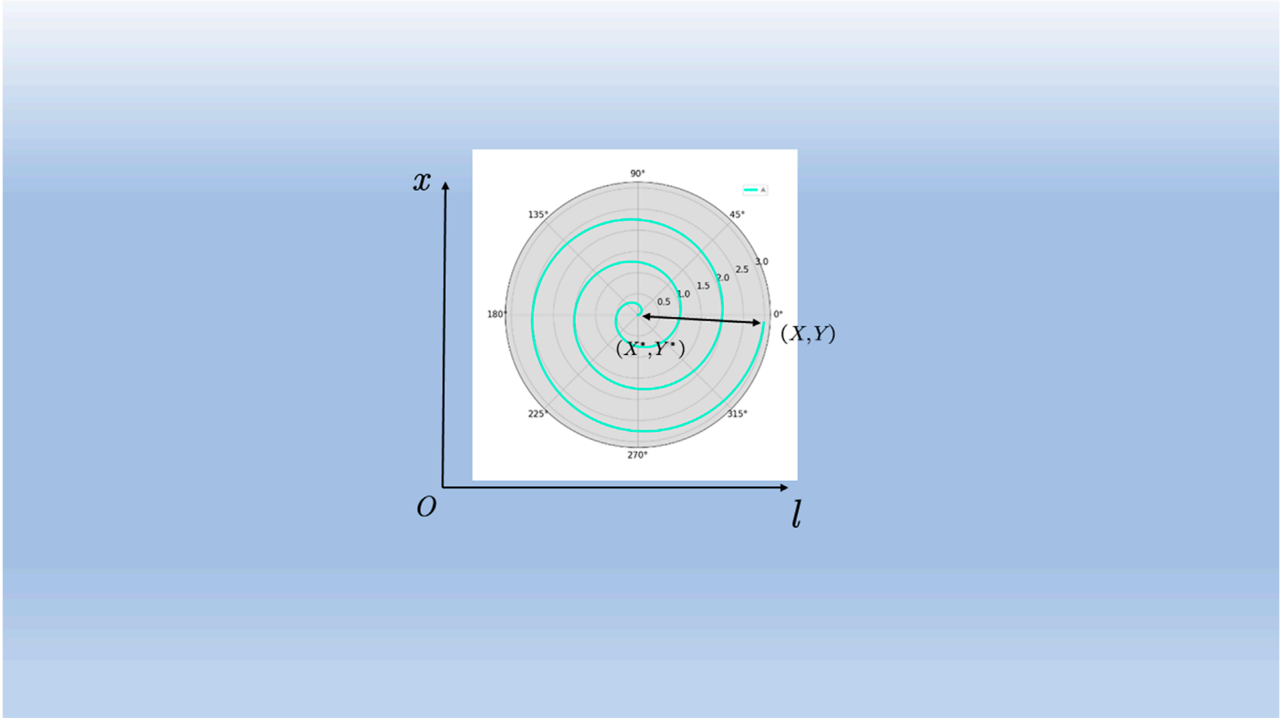

FIGURE 4
WOA helix position search range.

4 Experiment

4.1 Datasets

Based on the characteristics of the smart grid financial market, this paper selected four datasets Smart grid control systems (SGCSs) datasets, National Renewable Energy Laboratory (NREL), Dow Jones and S&P 500, one directly from the smart grid financial market, one from the energy market and two from the financial market.

Smart Grid Control Systems (SGCS) are advanced computer-based systems that help manage and control the grid more efficiently Ben Youssef (2022). They use modern communication technologies and advanced analytics to monitor the grid's performance and make real-time adjustments to optimize energy delivery. SGCSs are designed to provide a range of features, including: Monitoring and controlling tides: SGCSs are equipped with sensors and smart meters that allow them to monitor energy flows in real-time. They can detect interruptions or anomalies and adjust the power flow to minimize consumer impact. Demand Response: SGCS can help manage peak demand by encouraging consumers to shift their usage to off-peak hours. They can also prioritize certain areas of the grid to prevent outages or power drops. Renewable energy grid integration: SGCS can manage renewable energy grid integration. This allows for more efficient use of renewable energy sources and reduces reliance on traditional power sources. Fault detection and isolation: SGCS can detect faults in the grid and isolate affected areas to prevent cascading faults and widespread outages. Asset Management: SGCS monitors the health of grid assets and predicts maintenance needs to reduce downtime and improve reliability.

Overall, SGCSs play a key role in ensuring the reliability and efficiency of the modern grid. They are important for managing the transition to a more sustainable renewable energy future.

The National Renewable Energy Laboratory (NREL) is a research laboratory in Golden, Colorado, United States, dedicated to developing and disseminating renewable energy and energy efficiency technologies Singh and Mahajan (2021). It is part of the U.S. Department of Energy's (DOE) National Laboratory Network. NREL's research activities cover a wide range of renewable energy and energy efficiency areas, including solar, wind, geothermal, hydrogen, fuel cells, energy storage, bioenergy, and advanced manufacturing. The laboratory conducts research in materials science, engineering, and technology development, as well as analysis and modeling of renewable energy systems and markets. NREL also operates several test and evaluation facilities, including the National Wind Energy Technology Center, the National Bioenergy Center, and the Energy Systems Integration Facility. These facilities enable researchers and industry partners to test and validate new renewable energy technologies under realistic conditions. In addition to its research activities, NREL provides technical assistance and information to help individuals, businesses, and government agencies adopt renewable energy and energy efficiency technologies. This includes training and workshops, developing tools and resources, and providing technical support for renewable energy projects.

TABLE 1 Key indicators of smart grid investment.

Index	Code	Variable	Categories
Index 1	X_1	Smart Grid Market Scale Growth Trend	Financial Indicators
Index 2	X_2	Smart Grid Company Revenue	Financial Indicators
Index 3	X_3	Smart Grid Company Profit	Financial Indicators
Index 4	X_4	Policy Changes	Policy Environment
Index 5	X_5	Technology Innovation Progress	Competitive Landscape
Index 6	X_6	Competitive Landscape	Competitive Landscape
Index 7	X_7	Consumer Demand	Consumer Demand
Index 8	X_8	Market Share	Consumer Demand
Index 9	X_9	User Feedback	Consumer Demand
Index 10	X_{10}	Energy Price Volatility	Energy Prices
Index 11	X_{11}	Global Economic Situation	International Market
Index 12	X_{12}	International Trade Policy	International Market

Overall, NREL is a key player in developing and diffusing renewable energy and energy efficiency technologies in the United States and worldwide.

The Dow Jones Index, also known as the Dow Jones Industrial Average (Dow Jones), is a stock market index created by Dow Jones & Company in 1896 Metlek (2022). It is one of the indices used to reflect the overall situation of the U.S. stock market and is one of the world's most famous stock market indices. The Dow Jones Index consists of 30 stocks of publicly traded companies representing the major sectors of the U.S. economy. These companies cover various industries, such as finance, retail, manufacturing, and energy, and include large, well-known U.S. companies such as Apple, Microsoft, and Coca-Cola. At the end of each trading day, the gains and losses of the Dow Jones are widely reported and become one of the key indicators of market conditions. It is important to note that the Dow Jones does not represent the entire U.S. stock market, as it only selects 30 stocks and is based on a price-weighted index, meaning that companies with higher stock prices have a greater impact on the index. Therefore, some believe that the S&P 500 is a better reflection of the overall U.S. stock market.

The S&P 500 Index (S&P 500 Index) is a stock market index compiled by Standard & Poor's, which selects a sample of 500 large U.S. companies, including companies in various industries from NASDAQ to NYSE, to reflect the overall U.S Bera et al. (2020). stock market. The S&P 500 is a market capitalization-weighted index calculated by adding up the market capitalization of each company and then assigning index weights proportionally. This calculation method allows companies with larger market capitalizations to have a greater impact on the index, while companies with smaller market capitalizations have a smaller effect on the index. The S&P 500 is one of the most representative indices of the U.S. stock market and one of the world's most famous stock market indices. It is widely used in investment management, stock market analysis, and asset allocation. The S&P 500 is also the reference index for many funds, exchange-traded funds (ETFs), and financial derivatives, and investors can track the index's performance by purchasing funds or ETFs.

Smart grid financial market forecast indicators can involve several aspects: such as smart grid market size, policy environment, technological innovation, competitive landscape, consumer demand, energy prices, global economic situation, and seven categories of primary indicators, which can be divided into several secondary hands, in **Table 1**, this paper selects the indicators of which, as the input variables of the model.

4.2 Experimental setup and details

To test the running effectiveness of our models, we choose three baseline models, LSTM, CNN-LSTM, CNN-BiLSTM, and five innovative models Bit et al., Dia et al. Then we also test the accuracy and recall (Precision & Recall) of different models; the model's prediction accuracy is one of the important indicators of the model, which can be a good measure of the model's performance. Secondly, we will also compare the lift value and the amount of operations Flops (G) of different models; the larger the lift (lift index), the better the model. The smaller the value of Flops(G), the less the number of text processed by the model, and the faster the training and computing speed. Finally, we compare different models' stability index (population stability index), PSI, on other datasets.

4.3 Experimental results and analysis

In **Figure 5**, we compare the inference speed of different models in two simple datasets, Dow Jones for dataset 1 and S&P 500 for dataset 2. In **Figure 5**, we compare the inference speed of LSTM Stryczek and Natkaniec (2023) and CNN-LSTM Kuyumani et al. (2023): CNN-BiLSTM Yanmei et al. (2023) and our model for different amounts of historical data. Similarly, in Fig. b, we compare the inference speed of Bitirgen and Filik (2023), Diaba and Elmusrati (2023), BiLSTM, CNN-LSTM, Bit et al., and our model for a total of six models, and the results show that our model outperforms the other models in terms of inference speed, both in dataset 1 and in dataset 2.

Figure 6 compares the inference speed of different models in more complex datasets. The ability to handle complex datasets is one of the important metrics of time series forecasting models, where **Figure 6A** compares the number of inferences of four models, LSTM, CNN-LSTM, Bit et al., and our model in dataset 3, **Figure 6B** compares the number of assumptions of three models, LSTM, CNN-LSTM, CNN-BiLSTM and our model in dataset 3, **Figure 6C** compares the number of inferences of three models, Bit et al. CNN-BiLSTM and our model for different historical data on dataset 3. **Figure 6C** reaches the inference speed of Bit et al., Dia et al., and Dairi et al. (2023). The results show that the inference speed of our model is still faster than other models in complex datasets, showing good generalization.

In **Figure 7**, we compare the accuracy and Recall of different models for different data, where accuracy is the ratio of the number of relevant documents retrieved to the total number of records retrieved, which measures the accuracy of the retrieval system. The Recall is the ratio of the number of relevant documents retrieved to the total number of relevant documents in the document library, which measures the completeness of the retrieval system. Both

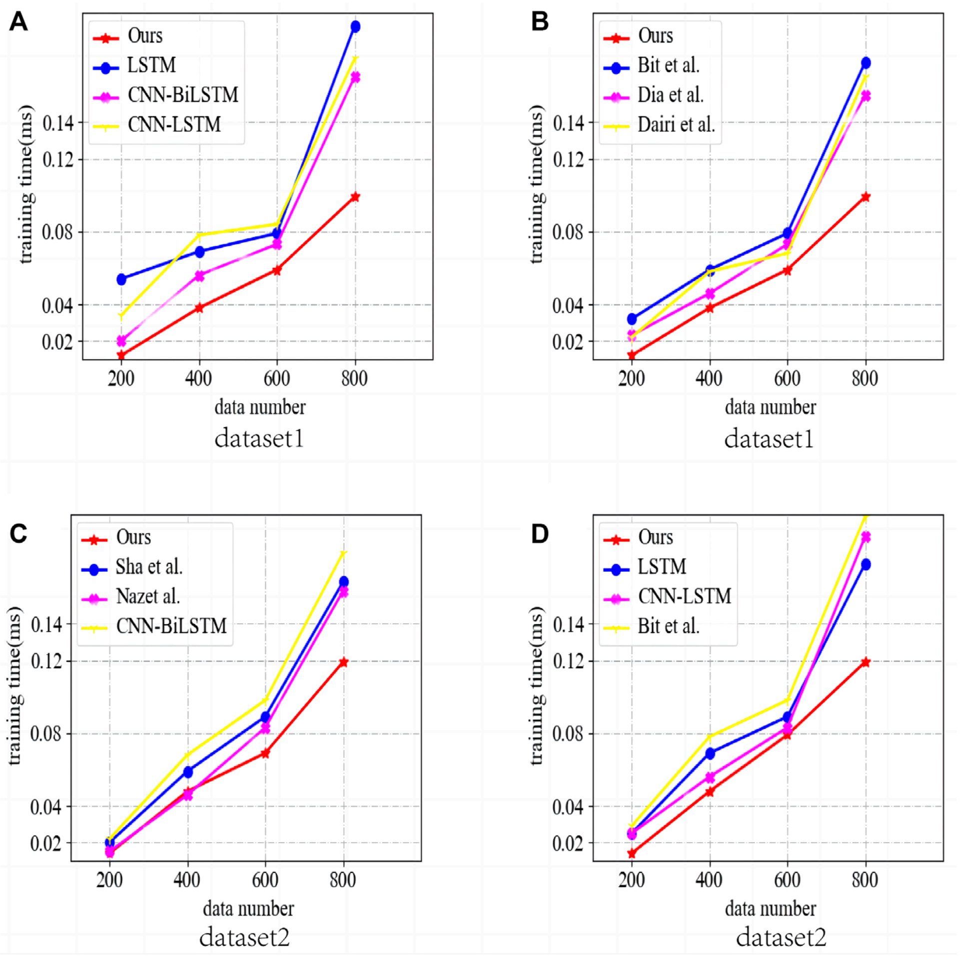

FIGURE 5
Comparison of inference speed of different models in different datasets (Dataset 1 is the Dow Jones index (Dow Jones), and dataset 2 is the S & P 500 index (S & P 500), both of which are simpler datasets because they have only financial variables, **(A,B)** are from data set 1, **(C,D)** from Dataset 2).

values are between 0 and 1; the closer the matter is to 1, the higher the accuracy or completeness rate. In **Figure 7A**, we compare the Precision and Recall (Precision & Recall) of LSTM, CNN-LSTM, CNN-BiLSTM, Bit et al., and in **Figure 7B**, we compare the Precision and Recall (Precision & Recall) of LSTM, CNN-LSTM, CNN-BiLSTM, Bit et al., Dia et al., Dairi et al., Shanmugapriya and Baskaran (2023), Nazir et al. (2023) and our models on Dataset 3 and Dataset 4. Recall). The results show that the Precision and Recall (Precision & Recall) of our model, in all four datasets, are better than the other models, showing strong generalization and accuracy.

In **Figure 8**, we compare the amount of operations Flops (G) of different models; the size of the functions of a model is one of the important indicators of model performance. Therefore, we compare the LSTM, CNN-LSTM, CNN-BiLSTM, Bit et al., and Dia et al. The results show that after the feature extraction of CNN and the optimization of the WOA whale algorithm, our model's operations are significantly reduced compared with other models, which means that our model's training time and prediction time can be shorter. The performance of our model is This means that our model's training time and forecast time can be faster, and the version of our model is better than other models.

In **Figure 9**, we compare the Lift values of different models, and the lift metric is more intuitive and easy to understand in practical applications. It can be used to measure the effectiveness of a model for a specific group of a certain size based on business requirements. In a given scenario, the binary classification model has a random rate, representing the probability of an unexpectedly positive response or the proportion of actual positive samples to the entire piece (equivalent to empirical data). With a classification model, the population can be effectively targeted. ”Valid” means that the proportion of positive observations in the top ranking (e.g., top 0.1) is higher than the random rate when all words are ranked in descending order of predicted probability. Boosting can be calculated as the proportion of positive observations among the top comments to the random rate. The numerator is the capture rate. The higher the lift value, the better the performance of the model. *X*-axis numbers 1 to 9 represent this model LSTM, CNN-LSTM, CNN-BiLSTM, Bit et al., Dia et al., Dairi et al., Sha et al., Nazet al., and our model, respectively. The results show that the lift value of our model

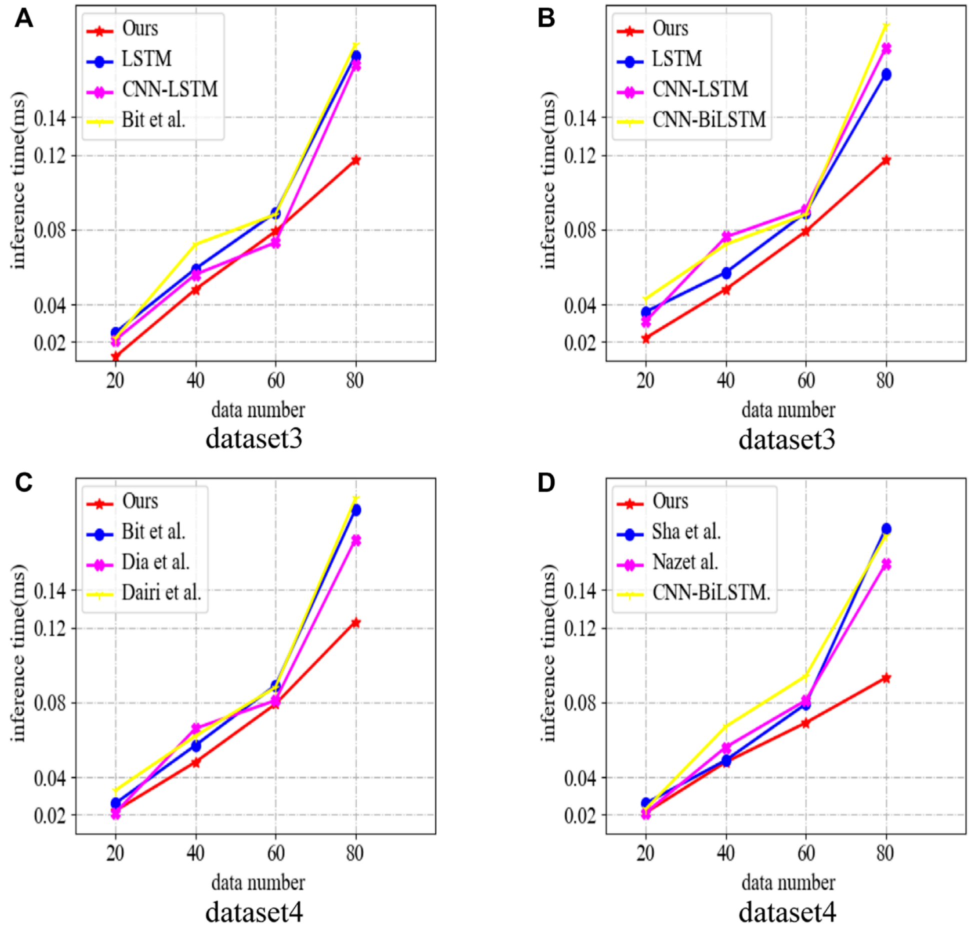

FIGURE 6
Comparison of inference speed of different models in different datasets (dataset 3 is Smart grid control systems (SGCSs) datasets, and dataset 4 is National Renewable Energy Laboratory (NREL) datasets, because these two datasets contain indicators of the policy environment, technological innovation, competitive landscape, consumer demand, energy prices, etc., and are therefore more complex datasets, **(A,B)** are from data set 3, **(C,D)** from Dataset 4).

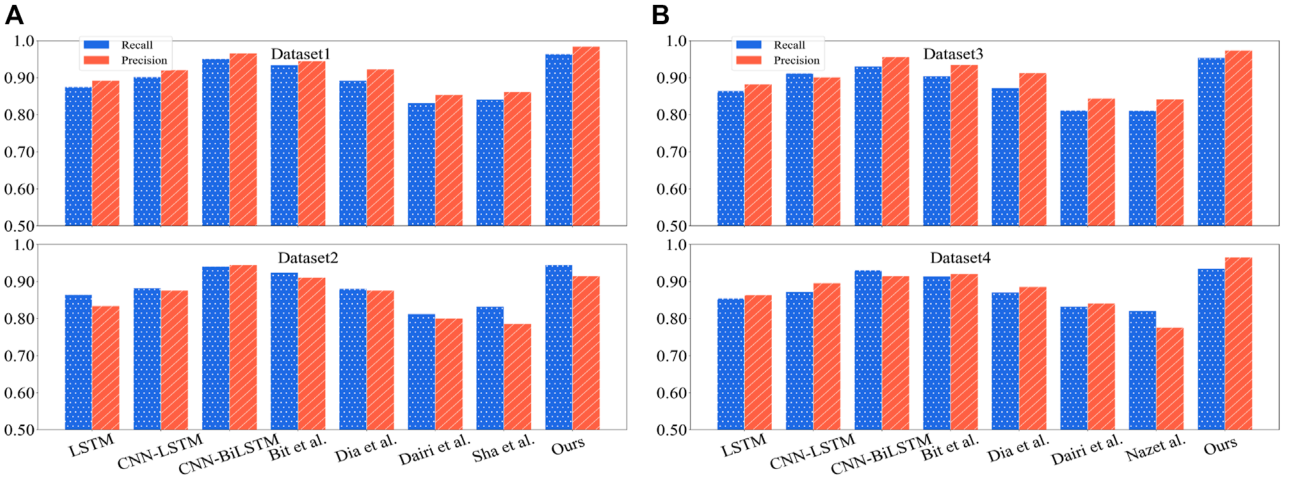

FIGURE 7
Comparison of Recall Precision values for different models in different datasets (Dataset 1 is Dow Jones, Dataset 2 is S & P 500, Dataset 3 is Smart grid control systems (SGCSs) datasets, Dataset 4 is National Renewable Energy Laboratory (NREL) datasets, **(A)** are from data set 1 and 2, **(B)** from Dataset 3 and 4).

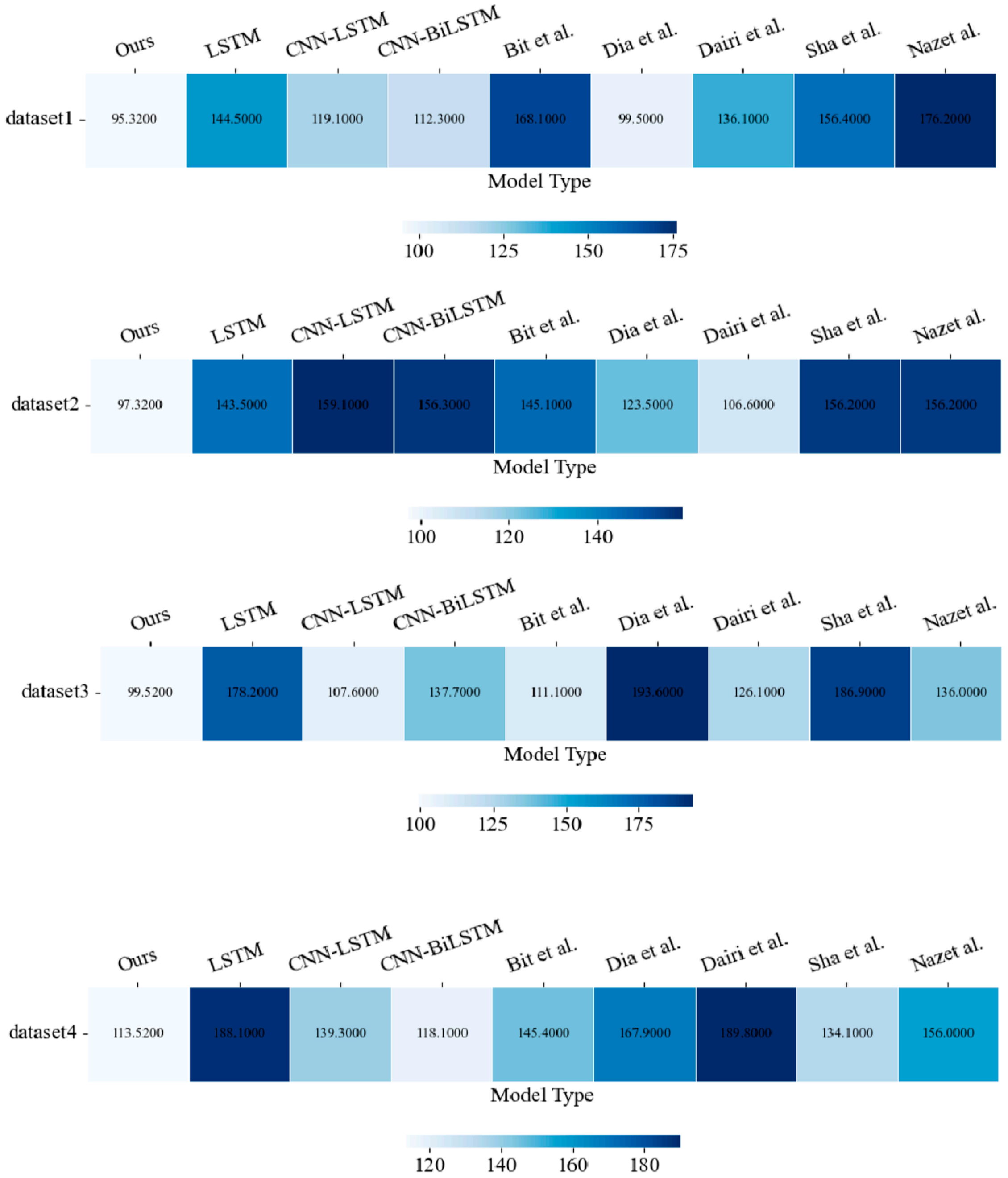

FIGURE 8
Comparison of different models in different datasets (Dataset 1 is Dow Jones, Dataset 2 is S&P 500, Dataset 3 is Smart grid control systems (SGCSs) datasets, Dataset 4 is National Renewable Energy Laboratory (NREL) datasets).

is significantly higher in four different data sets. The results show that our model has substantially higher Lift values in four different data sets than the other models, which means that our model has the ”better” predictive power and the model best runs.

This is the flow chart of the model **Algorithm 1**; first input the historical data of the smart grid financial market, preprocess and normalize the data at the data input layer, and then put the data set into a one-dimensional CNN unit for feature Extract and process the data set to reduce the dimensionality, and then input the feature data into the BiLSTM layer to learn the historical data of the smart grid financial market, and then optimize the WOA whale algorithm to obtain the optimal parameters of the model, improve the accuracy of prediction, and increase the reasoning time, and finally output the predicted value.

In **Figure 10**, we use a scatter plot to more visually compare the PSI values of our model when the number of inferences varies. The sample stability index (PSI) is commonly used to measure the stability of a sample. For example, if the model is stable between

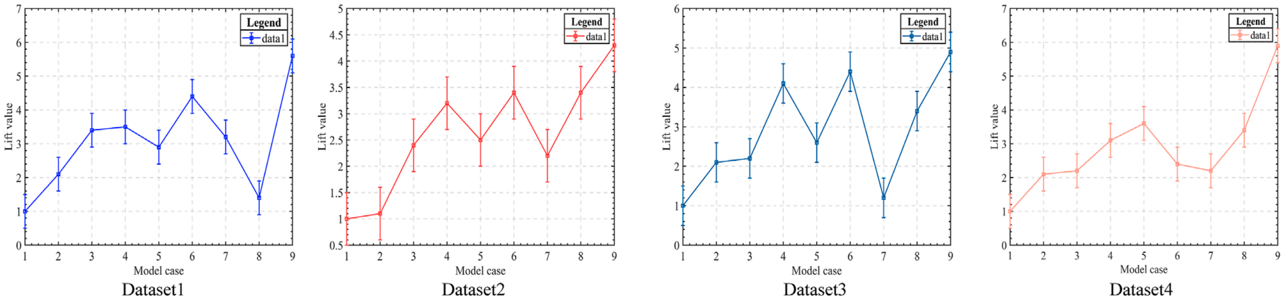

FIGURE 9
Comparison of Lift values for different models (The lift curve measures how much "better" the model is at predicting compared to not using the model; the larger the lift, the better the model runs.

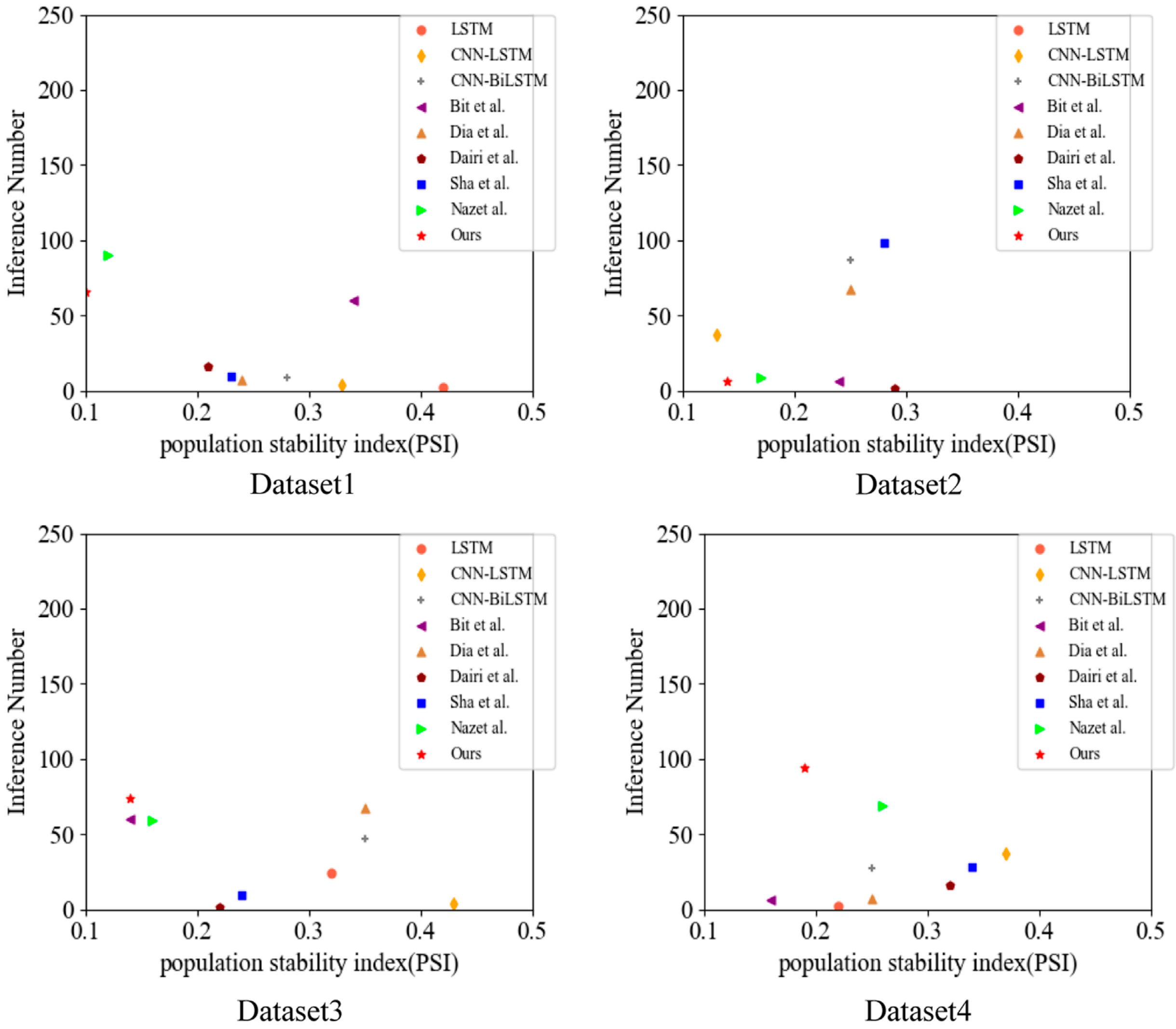

FIGURE 10
Comparison of population stability index, PSI for different models on different datasets (dataset 1 is Dow Jones, dataset 2 is S&P 500, dataset 3 is Smart grid control systems (SGCSs) datasets, and National Renewable Energy Laboratory (NREL) datasets for dataset 4).

TABLE 2 **A comparison of different models.**

Model	Time (Second) ↓	Flops(G) ↑	Recal ↑	Precision ↑	Lift ↑	PSI ↓
LSTM Stryczek and Natkaniec (2023)	0.31	144.5	0.875	0.892	1	0.42
CNN-LSTM Kuyumani et al. (2023)	0.24	119.1	0.902	0.921	2.1	0.33
CNN-BiLSTM Yanmei et al. (2023)	0.14	112.3	0.951	0.966	3.4	0.28
Bitirgen and Filik (2023)	0.32	168.1	0.934	0.945	3.5	0.34
Diaba and Elmusrati (2023)	0.23	99.5	0.892	0.923	2.9	0.24
Dairi et al. (2023)	0.22	136.1	0.832	0.854	4.4	0.21
Shanmugapriya and Baskaran (2023)	0.20	156.4	0.841	0.862	3.2	0.23
Nazet al. Nazir et al. (2023)	0.15	176.2	0.881	0.911	1.4	0.12
Ours	**0.12**	**95.32**	**0.964**	**0.984**	**5.6**	**0.10**

```
input  : The train $D$, the dataset for transfer learning $D_{TL}$, the parameters $\theta_{best}$, the best loss
         $Loss_{best}$
output : The trained CNN-LSTM $Model_{Ours}$
Random initialization W,b ;
while The error rate of the neurat network model on the vatidation set v no longer decreases do
    for epoch in iterations do
        $Loss_{now} = f(\theta_{now})$ ;
        if $Loss_{now}$ ¡ $Loss_{best}$ then
            $\theta_{best} = \theta_{now}$ ;
            $Loss_{best} = Loss_{now}$;
        end
    end
    $\theta_{now} = Adam(\theta_{now}, D_{TL})$ ;
end
Load the best model with $\theta_{best}$ ;
for epoch in iterations do
    $\theta_{now} = Adam(\theta_{now}, D)$ ;
    if $Loss_{now}$ ¡ $Loss_{best}$ then
        $\theta_{best} = \theta_{now}$ ;
        $Loss_{best} = Loss_{now}$;
    end
end
Return the trained model $Model_{Ours}$
```

Algorithm 1. Algorithmic representation of the training process in this paper.

2 months, a PSI value of less than 0.1 for a variable indicates that the change is less significant. If the PSI value is between 0.1 and 0.25, it means a more substantial change. If the PSI value is greater than 0.25, the variable changes more dramatically and requires special attention. As can be seen from the figure, even with a higher number of inferences, the stability of our model's operation still has a better performance compared to other models, and the strength of our model has a good performance in different data sets, which is due to the high convergence speed and global search capability of the Whale Algorithm (WOA), and after optimization using the Whale Algorithm (WOA), the operation of our model's stability is significantly better than other models.

Table 2 compares the accuracy, computation, and parameter size of the models mentioned in the paper with our model. The table shows that our model has significant advantages in these aspects.

5 Conclusion and discussion

This paper uses a WOA-based CNN-BiLSTM model to predict the smart grid financial market. Firstly, it is determined that the long short-term memory network model (LSTM), which performs better in long-term prediction, is used. Then, the bi-directional long short-term memory network model (BiLSTM) to consider both forward and backward contextual information is more applicable for the smart grid financial market, and then the one-dimensional CNN network is selected by combining the feature selection characteristics of convolutional neural network (CNN) for historical data filtering, optimizing the input data of BiLSTM for shorter training time, faster prediction, and higher accuracy of prophecy, and finally the Whale Algorithm (WOA) with higher convergence speed and global search capability, which is suitable for solving a variety of optimization problems. Combining it with the CNN- BiLSTM model, the advantages of WOA can effectively solve the problem of missing historical data that may occur in the BiLSTM network in the prediction of long time series, which leads to the reduction of prediction accuracy, and also has the advantages of speeding up the model operation, improving the AUC value and reducing the operation volume.

The contribution points of this paper are as follows.

- Compared with traditional time series models, our model has improved the prediction accuracy of the smart grid financial market due to the inherent advantages of deep learning models and the optimization of other models.
- Compared with neural network models such as BP neural network, RBF neural network, and CNN neural network, our model is much more interpretable. With the dimensionality reduction of the CNN network, our model is much less computationally intensive than neural network models.
- Compared with deep learning models, including recurrent neural networks and long and short-term memory networks, etc., our model can avoid the problem of missing historical data when dealing with a large amount of historical data, thus improving the model's prediction accuracy.

At the same time, the method in this paper still has some limitations; compared with other deep learning algorithms, its training speed is greatly accelerated, but the reduction of computing is not very obvious at the same time because this paper combines three models, the overall structure of the model framework has some complex, for the above problems, our sub-module test comparison, continue to optimize each module, compared with other deep learning algorithms. Based on the LSTM model, we look for modules that are more suitable for solving the smart grid financial market prediction.

Smart grid financial market prediction also helps to promote the rapid development of smart grid-related industries. With the rapid changes in the energy industry, smart grid technologies and solutions have become the focus of many companies Li et al. (2020); ? The rapid development of this technology has brought a lot of investment opportunities and business opportunities, but there are also certain investment risks. By forecasting the smart grid financial market, investors can better understand the risks and opportunities of the market and develop investment strategies accordingly. For example, predicting future market demand and supply conditions can help investors decide which areas are more promising and which should be avoided. Policymakers can use financial market forecasts to facilitate the rapid development of smart grids. Policy-making requires understanding market demand and conditions and forecasting future market trends to develop appropriate policies and measures. By predicting the direction of the smart grid financial market, policymakers can better plan future policies to promote industry development. Entrepreneurs can use financial market forecasts to adjust their strategies and investments to adapt to future market changes. For example, based on market forecasts, companies can decide whether to enter a new market, adopt a new marketing strategy, or adjust their product lines.

In summary, smart grid financial market forecasting is important for promoting the sustainable development of smart grids. Our work can help investors, policymakers, and entrepreneurs better understand market trends and future directions to make more informed decisions and promote the rapid development of the smart grid industry.

Data availability statement

The original contributions presented in the study are included in the article/supplementary material, further inquiries can be directed to the corresponding author.

Author contributions

GN, XZ, and XN contributed to conception and design of the study. XC organized the database. XM performed the statistical analysis. GN wrote the first draft of the manuscript. XZ, GN, XC, and XN wrote sections of the manuscript. All authors contributed to manuscript revision, read, and approved the submitted version. All authors listed have made a substantial, direct, and intellectual contribution to the work and approved it for publication.

Conflict of interest

The authors declare that the research was conducted in the absence of any commercial or financial relationships that could be construed as a potential conflict of interest.

Publisher's note

References

Adetunji, K., Hofsajer, I., and Cheng, L. (2020). "A coordinated charging model for electric vehicles in a smart grid using whale optimization algorithm," in Proceeding of the 2020 IEEE 23rd International Conference on Information Fusion (FUSION), Rustenburg, South Africa, July 2020 (IEEE), 1–7.

Ben Youssef, N. E. H. (2022). Analytical analysis of information-centric networking in smart grids. *Int. J. Wirel. Inf. Netw.* 29, 354–364. doi:10.1007/s10776-022-00565-8

Bera, B., Saha, S., Das, A. K., and Vasilakos, A. V. (2020). Designing blockchain-based access control protocol in iot-enabled smart-grid system. *IEEE Internet Things J.* 8, 5744–5761. doi:10.1109/jiot.2020.3030308

Bessani, M., Massignan, J. A., Santos, T. M., London, J. B., Jr, and Maciel, C. D. (2020). Multiple households very short-term load forecasting using bayesian networks. *Electr. Power Syst. Res.* 189, 106733. doi:10.1016/j.epsr.2020.106733

Bitirgen, K., and Filik, Ü. B. (2023). A hybrid deep learning model for discrimination of physical disturbance and cyber-attack detection in smart grid. *Int. J. Crit. Infrastructure Prot.* 40, 100582. doi:10.1016/j.ijcip.2022.100582

Cai, W., Liu, D., Ning, X., Wang, C., and Xie, G. (2021). Voxel-based three-view hybrid parallel network for 3d object classification. *Displays* 69, 102076. doi:10.1016/j.displa.2021.102076

Chen, B.-R., Liu, Z., Song, J., Zeng, F., Zhu, Z., Bachu, S. P. K., et al. (2022). "Flowtele: Remotely shaping traffic on internet-scale networks," in Proceedings of the 18th International Conference on emerging Networking EXperiments and Technologies, November 2022 (ACM), 349–368.

Cheng, K., Huang, Z., Wang, P., Sun, L., Ghasemi, H., Ardebili, H., et al. (2023). Antibacterial flexible triboelectric nanogenerator via capillary force lithography. *J. Colloid Interface Sci.* 630, 611–622. doi:10.1016/j.jcis.2022.10.129

Dai, Y., and Zhao, P. (2020). A hybrid load forecasting model based on support vector machine with intelligent methods for feature selection and parameter optimization. *Appl. energy* 279, 115332. doi:10.1016/j.apenergy.2020.115332

Dairi, A., Harrou, F., Bouyeddou, B., Senouci, S.-M., and Sun, Y. (2023). "Semi-supervised deep learning-driven anomaly detection schemes for cyber-attack detection in smart grids," in *Power systems cybersecurity: Methods, concepts, and best practices* (Springer), 265–295.

Diaba, S. Y., and Elmusrati, M. (2023). Proposed algorithm for smart grid ddos detection based on deep learning. *Neural Netw.* 159, 175–184. doi:10.1016/j.neunet.2022.12.011

Fan, X., Zhao, S., Zhang, X., and Meng, L. (2023). The impact of improving employee psychological empowerment and job performance based on deep learning and artificial intelligence. *J. Organ. End User Comput. (JOEUC)* 35, 1–14. doi:10.4018/joeuc.321639

Hammami, Z., Sayed-Mouchaweh, M., Mouelhi, W., and Ben Said, L. (2020). Neural networks for online learning of non-stationary data streams: A review and application for smart grids flexibility improvement. *Artif. Intell. Rev.* 53, 6111–6154. doi:10.1007/s10462-020-09844-3

He, F., and Ye, Q. (2022). A bearing fault diagnosis method based on wavelet packet transform and convolutional neural network optimized by simulated annealing algorithm. *Sensors* 22, 1410. doi:10.3390/s22041410

Huang, H., Shen, B., Zhong, L., and Zhou, Y. (2023). "Protecting data integrity of web applications with database constraints inferred from application code," in Proceedings of the 28th ACM International Conference on Architectural Support for Programming Languages and Operating Systems, Volume 2, January 2023 (ACM), 632–645.

Kuyumani, E., Hasan, A. N., and Shongwe, T. (2023). A hybrid model based on cnn-lstm to detect and forecast harmonics: A case study of an eskom substation in South Africa. *Electr. Power Components Syst.* 1–15, 746–760. doi:10.1080/15325008.2023.2181883

Li, Y., Shen, B., Zhang, J., Gan, X., Wang, J., and Wang, X. (2017). Offloading in hcns: Congestion-aware network selection and user incentive design. *IEEE Trans. Wirel. Commun.* 16, 6479–6492. doi:10.1109/twc.2017.2724027

Li, Y., Wang, C., and Li, G. (2020). A mini-review on high-penetration renewable integration into a smarter grid. *Front. Energy Res.* 8, 84. doi:10.3389/fenrg.2020.00084

Li, C., Chen, Z., and Jiao, Y. (2023). Vibration and bandgap behavior of sandwich pyramid lattice core plate with resonant rings. *Materials* 16, 2730. doi:10.3390/ma16072730

Lin, R., Pei, Z., Ye, Z., Wu, B., and Yang, G. (2020). A voted based random forests algorithm for smart grid distribution network faults prediction. *Enterp. Inf. Syst.* 14, 496–514. doi:10.1080/17517575.2019.1600724

Lu, R., and Hong, S. H. (2019). Incentive-based demand response for smart grid with reinforcement learning and deep neural network. *Appl. energy* 236, 937–949. doi:10.1016/j.apenergy.2018.12.061

Metlek, S. (2022). Forecasting of dow jones sukuk index prices using artificial intelligence systems. *Economic computation & economic cybernetics studies & research* 56.

Munawar, S., Javaid, N., Khan, Z. A., Chaudhary, N. I., Raja, M. A. Z., Milyani, A. H., et al. (2022). Electricity theft detection in smart grids using a hybrid bigru–bilstm model with feature engineering-based preprocessing. *Sensors* 22, 7818. doi:10.3390/s22207818

Nazari, M., Nazifi, S., Huang, Z., Tong, T., Ouro-Koura, H., Bao, J., et al. (2020). Surface tension nanogates for controlled ion transport. *ACS Appl. Nano Mater.* 3, 6979–6986. doi:10.1021/acsanm.0c01304

Nazir, A., Shaikh, A. K., Shah, A. S., and Khalil, A. (2023). Forecasting energy consumption demand of customers in smart grid using temporal fusion transformer (tft). *Results Eng.* 17, 100888. doi:10.1016/j.rineng.2023.100888

Ning, X., Duan, P., Li, W., and Zhang, S. (2020). Real-time 3d face alignment using an encoder-decoder network with an efficient deconvolution layer. *IEEE Signal Process. Lett.* 27, 1944–1948. doi:10.1109/lsp.2020.3032277

Ning, X., Tian, W., He, F., Bai, X., Sun, L., and Li, W. (2023). Hyper-sausage coverage function neuron model and learning algorithm for image classification. *Pattern Recognit.* 136, 109216. doi:10.1016/j.patcog.2022.109216

Shanmugapriya, J., and Baskaran, K. (2023). Rapid fault analysis by deep learning-based pmu for smart grid system. *Intelligent Automation Soft Comput.* 35, 1581–1594. doi:10.32604/iasc.2023.024514

Singh, N. K., and Mahajan, V. (2021). End-user privacy protection scheme from cyber intrusion in smart grid advanced metering infrastructure. *Int. J. Crit. Infrastructure Prot.* 34, 100410. doi:10.1016/j.ijcip.2021.100410

Song, Z., Mellon, G., and Shen, Z. (2020). Relationship between racial bias exposure, financial literacy, and entrepreneurial intention: An empirical investigation. *J. Artif. Intell. Mach. Learn. Manag.* 4, 42–55.

Song, Z., Johnston, R. M., and Ng, C. P. (2021). Equitable healthcare access during the pandemic: The impact of digital divide and other sociodemographic and systemic factors. *Appl. Res. Artif. Intell. Cloud Comput.* 4, 19–33.

Stryczek, S., and Natkaniec, M. (2023). Internet threat detection in smart grids based on network traffic analysis using lstm, if, and svm. *Energies* 16, 329. doi:10.3390/en16010329

Wu, S., Wang, J., Ping, Y., and Zhang, X. (2022). "Research on individual recognition and matching of whale and dolphin based on efficientnet model," in Proceeding of the 2022 3rd International Conference on Big Data, Artificial Intelligence and Internet of Things Engineering (ICBAIE), Xi'an, China, July 2022 (IEEE), 635–638.

Xiang, C., Wu, Y., Shen, B., Shen, M., Huang, H., Xu, T., et al. (2019). "Towards continuous access control validation and forensics," in Proceedings of the 2019 ACM SIGSAC conference on computer and communications security, November 2019 (ACM), 113–129. doi:10.1145/3319535.3363191

Yang, Z., Sun, L., Sun, Y., Dong, Y., and Wang, A. (2023). A conceptual model of home-based cardiac rehabilitation exercise adherence in patients with chronic heart failure: A constructivist grounded theory study. *Patient Prefer. adherence* 17, 851–860. doi:10.2147/ppa.s404287

Yanmei, J., Mingsheng, L., Yangyang, L., Yaping, L., Jingyun, Z., Yifeng, L., et al. (2023). "Enhanced neighborhood node graph neural networks for load forecasting in smart grid," in *International journal of machine learning and cybernetics* (Springer), 1–20. doi:10.1007/s13042-023-01796-8

Zahid, M., Ahmed, F., Javaid, N., Abbasi, R. A., Zainab Kazmi, H. S., Javaid, A., et al. (2019). Electricity price and load forecasting using enhanced convolutional neural network and enhanced support vector regression in smart grids. *Electronics* 8, 122. doi:10.3390/electronics8020122

Zhang, R., Zeng, F., Cheng, X., and Yang, L. (2019). "Uav-aided data dissemination protocol with dynamic trajectory scheduling in vanets," in Proceeding of the ICC 2019-2019 IEEE International Conference on Communications (ICC), Shanghai, China, May 2019 (IEEE), 1–6.

Zhang, H., Zhang, F., Gong, B., Zhang, X., and Zhu, Y. (2023). The optimization of supply chain financing for bank green credit using stackelberg game theory in digital economy under internet of things. *J. Organ. End User Comput. (JOEUC)* 35, 1–16. doi:10.4018/joeuc.318474

Zhu, T., Yang, Y., Yao, X., Huang, Z., Liu, L., Hu, W., et al. (2020). Solution-processed polymeric thin film as the transparent electrode for flexible perovskite solar cells. *ACS Appl. Mater. interfaces* 12, 15456–15463. doi:10.1021/acsami.9b22891

Frontiers in Energy Research

TYPE Methods
PUBLISHED 05 June 2023
DOI 10.3389/fenrg.2023.1180555

OPEN ACCESS

EDITED BY
Peng Li,
Tianjin University, China

REVIEWED BY
Wenjie Zhang,
National University of Singapore,
Singapore
Mou-Fa Guo,
Fuzhou University, China

*CORRESPONDENCE
Zhaobin Du,
✉ epduzb@scut.edu.cn

RECEIVED 06 March 2023
ACCEPTED 16 May 2023
PUBLISHED 05 June 2023

CITATION
Bai H, Jiang W, Du Z, Zhou W, Li X and Li H (2023), An evolution strategy of GAN for the generation of high impedance fault samples based on Reptile algorithm. *Front. Energy Res.* 11:1180555.
doi: 10.3389/fenrg.2023.1180555

An evolution strategy of GAN for the generation of high impedance fault samples based on Reptile algorithm

Hao Bai[1], Wenxin Jiang[2], Zhaobin Du[2]*, Weixian Zhou[2], Xu Li[3] and Hongwen Li[4]

[1]Electric Power Research Institute, China Southern Power Grid, Guangzhou, China, [2]Engineering School of Electric Power, South China University of Technology, Guangzhou, China, [3]Zunyi Power Supply Company of Guizhou Power Grid, Zunyi, China, [4]Electric Power Research Institute of Yunnan Power Grid, Kunming, China

In a distribution system, sparse reliable samples and inconsistent fault characteristics always appear in the dataset of neural network fault detection models because of high impedance fault (HIF) and system structural changes. In this paper, we present an algorithm called Generative Adversarial Networks (GAN) based on the Reptile Algorithm (GANRA) for generating fault data and propose an evolution strategy based on GANRA to assist the fault detection of neural networks. First, the GANRA generates enough high-quality analogous fault data to solve a shortage of realistic fault data for the fault detection model's training. Second, an evolution strategy is proposed to help the GANRA improve the fault detection neural network's accuracy and generalization by searching for GAN's initial parameters. Finally, Convolutional Neural Network (CNN) is considered as the identification fault model in simulation experiments to verify the validity of the evolution strategy and the GANRA under the HIF environment. The results show that the GANRA can optimize the initial parameters of GAN and effectively reduce the calculation time, the sample size, and the number of learning iterations needed for dataset generation in the new grid structures.

KEYWORDS

generative adversarial networks, few sample, Reptile algorithm, meta learning, high impedance fault, evolution strategy

1 Introduction

The pole-to-ground faults are the most likely short-circuit faults in distribution systems, which are mainly caused by insulation degradation. The pole-to-ground faults can be either low impedance faults or high impedance faults (HIFs) depending on the grounding impedance (Xi et al., 2021). The pole-to-pole faults are generally low impedance faults and more easily to be found (Salomonsson et al., 2007). Under the HIFs, the fault current is not sufficient to trip the overcurrent relays due to high grounding impedance. The typical zero-sequence voltage waveforms of high impedance fault and low impedance fault is shown in **Figure 1A**. Therefore, a better way to prompt HIFs should be proposed. Recently, the applications of neural networks in a HIF detection model, especially in the distribution system, are widely reported. Flauzino et al. (2006) propose a model for discriminating HIF by combining artificial neural networks (ANN) with several statistical techniques. But it mainly focuses on designing practical applications, and the details of ANN are ignored. Ye et al. (2016) discuss a distribution system faults' classification by combining a traditional BP neural network with wavelet packet technology. However, this conventional neural network is used less due to the low training speed and complex connection. Considering these shortcomings of traditional BP neural networks; Zhang (2018) uses Convolutional Neural Network (CNN) as the HIF detection model and exploits the hidden characteristics from the decomposition of the HIF waveform to develop CNN's classification capability. CNN is considered to be promising as the identification fault model because of its good performance in reducing training time and connection complexity.

Applying neural networks in distribution system fault detection provides new possibilities for improving fault detection accuracy and even detecting faults with obscure characteristics (such as minor current faults). However, the particularity of small probability faults and frequent changes in the distribution system grid structure (Geng et al., 2013) directly lead to a shortage of reliable training data, which limits the practical application scope of neural networks. In recent literature, some solutions have been proposed for the above defects. In emphasizing hidden fault features, Wan and Zhao (2018) use Hilbert-Huang transform with wavelet packet transform preprocessing (WPT-HHT) to process the transient zero-sequence current. In solving the problem of rare realistic data, Xie (2019) restores a relatively accurate PSCAD customized model based on the summer real grid operation mode to increase the number of reliable samples. Nevertheless, the simulation samples cannot always fit a frequently changed system. Usually, the regular updating of the simulation model is hard to keep up with the positive changes in the natural system; Wang (2020) proposes a virtual fault sample generation method based on a multiple up-down sampling procedure to expand the dataset and avoid the above problems. However, this method can analyze a few types of faults, and its generalizability remains to be verified. It is uncertain whether a fault with unprecedented characteristics can be generated. In addition; Wang (2020) ignores that such generation methods require a large amount of data for data feature extraction, which is contrary to practical engineering situations. Hence; Zhang and Su (2022) propose an algorithm that applies Knowledge Graph Variational Auto-encoders (KG-VAE) to create samples from unknown data tags. And (Goodfellow et al., 2014) propose Generative Adversarial Networks (GAN) to extract data features from a small dataset. The generative model is pitted against an adversary in the proposed adversarial nets framework.

The above solutions try to expand the training dataset's size and improve the generated data's quality. But these solutions consider less in terms of generalization, and lots of their neural networks choose initial parameters randomly instead of finding how to optimize the initial parameters of the neural networks. Admittedly, randomizing the initial parameters has advantages, for it ensures that the model under various initial parameter settings is considered. However, optimizing the initial parameters of the neural networks can improve the speed and quality of sample generation.

Optimizing the initial parameters of GAN is similar to determining a valuable search space before the gradient descent search. It means that when the application scenario changes, the model can quickly learn a new task based on the "knowledge" it already has. These methods of optimizing the initial parameters are often called meta-learning (ML). The meta-learning methods that have been mentioned in the studies so far mainly involve Model-Agnostic Meta-Learning (MAML) (Finn et al., 2017), First-order MAML (FOMAML) (Wang et al., 2021) and Reptile (Amir and Gandomi, 2022). Many applications in this direction appear. Like Li et al. (2020) use ML to determine voting weights for load forecasting, Wang et al. (2022) combine misjudged samples with ML to find initial parameters of detection models and Xu et al. (2022) retrofit a model-free ML with Bayesian function. These applications of ML bring us inspiration. When it comes to the efficiency of ML, compared with MAML, FOMAML, and other ML methods, the algorithm of Reptile is faster. This is because, as a population-based and gradient-free method, Reptile can address complicated or straightforward optimization problems subject to specific constraints (Amir and Gandomi, 2022). Its weight update of the meta-network does not directly use gradient or Hesse matrix (Nichol et al., 2018). It makes the Reptile algorithm more suitable for an online power system with multi parameters.

In this paper, our research discusses the influence of a shortage of HIF training samples and the grid structure changes on the neural network fault detection model. Then, regarding unsatisfactory fault data samples in terms of quantity and quality, we present an algorithm structure called Generative Adversarial Networks (Goodfellow et al., 2014) based on Reptile Algorithm (GANRA), which generates samples with few-shot HIF samples. At the same time, we propose an evolution strategy to make the optimized initialization parameters better serve the practical application of neural networks in power systems. The evolution strategy considers information about various parameters in the distribution systems. It is empowered by integrating GANRA, the neural network's parameter transfer learning, and the solution to distribution system configurations' alternation. This composite method can make the fault detection model more robust in recognition accuracy and generalization ability, and reduce the influence of grid structure changes on the fault detection model. And we choose CNN as the identification fault model to complete verification experiments.

2 Related principle

2.1 Reptile algorithm

The Reptile algorithm is an efficient ML algorithm. It is designed to find an appropriate initialization parameter for a neural network to quickly become a target network with a small number of samples and perform well in future task training (Nichol et al., 2018). The schematic diagram of parameter update direction in the Reptile algorithm is shown in **Figure 1B**. In **Figure 1B**, the iteration of the training task network is set to 4 in this section.

The Reptile algorithm is nested by a meta-network and a training task network. The parameters ϕ of the meta-network are updated by the parameters θ finding from several stochastic gradient descents (SGD). SGD is also called the iteration of the training task network in this paper. The definition of the meta-network updating formula's

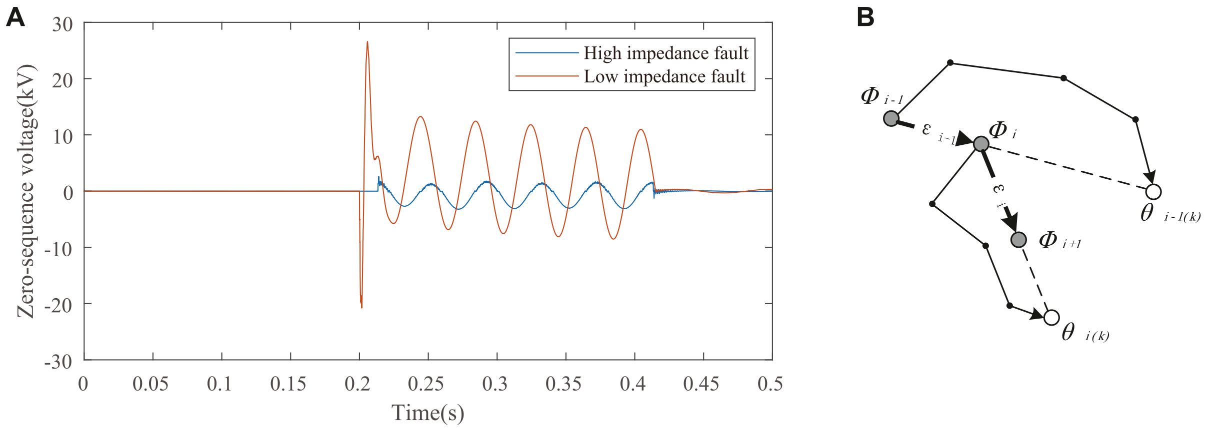

FIGURE 1
(A). The typical zero-sequence voltage waveforms of high impedance fault and low impedance fault. **(B)** Schematic diagram of parameter update direction.

parameter is shown in Eq. 1.

$$\phi_{i+1} \leftarrow \phi_i + \varepsilon_i\left(\theta_{i(k)} - \phi_i\right) \tag{1}$$

Where ϕ_i is obtained from the ith meta-network update, $\theta_{(k)}$ is obtained after several network training task iterations with iteration number K, and ε is the meta-network learning rate, i.e., iterative step.

The algorithm requires a consistent structure of the meta-network, training task network, and target network to ensure that the parameters obtained by the Reptile algorithm can be used as initialization parameters of the target network.

2.2 Adversarial generative network

GAN and its derived models have many applications in generating samples for data enhancement and data preprocessing in deep learning (Wang and Zhang, 2021). The critical point is to train the generator (G) to generate samples. The generator is supposed to cheat the discriminator (D), which means the samples generated by the generator will be incorrectly identified as the actual samples. At the same time, the discriminator constantly recognizes these generated samples to create more new samples that are infinitely close to the actual situation. Then, the GAN model composed of G and D conforms to Nash equilibrium (Mo et al., 2020). The objective function of GAN:

$$\min_{\mathrm{G}}\left(\max_{\mathrm{D}} V(\mathrm{G},\mathrm{D})\right) \tag{2}$$

Where the function $V(\cdot)$ describing the cognitive differences between G and D for the same kind of things can be expressed as:

$$V(\mathrm{G},\mathrm{D}) = E_{x\sim P_{data}}[\log \mathrm{D}(x)] + E_{x\sim P_{\mathrm{G}}}[\log(1-\mathrm{D}(x))] \tag{3}$$

Where $E_{x\sim P_{data}}$ is the mathematical expectation that the generated sample is recognized as the actual sample and x is the set of actual samples. P_{data} is the characteristic distribution of the training samples, P_{G} is the characteristic distribution of generated samples, and $\mathrm{D}(x)$ is the recognition degree of the discriminator to the actual sample.

The objective function V can finally be solved through gradient updating. The gradient update formula is shown in Eq. 4.

$$\begin{cases} \theta_{\mathrm{G}} \leftarrow \theta_{\mathrm{G}} - \eta_{\mathrm{G}} \dfrac{\partial V(G,D)}{\partial \theta_{\mathrm{G}}} \\ \theta_{\mathrm{D}} \leftarrow \theta_{\mathrm{D}} + \eta_{\mathrm{D}} \dfrac{\partial V(G,D)}{\partial \theta_{\mathrm{D}}} \end{cases} \tag{4}$$

Where θ is defined as the set of parameters used by the specific function expression in G and D in the design process, and $\theta_{\mathrm{G}}(\theta_{\mathrm{D}})$ is the parameter of G (D), $\eta_{\mathrm{G}}(\eta_{\mathrm{D}})$ is the search step of G(D).

3 Generative adversarial network based on Reptile algorithm

The structures of the meta-network, training task network and target network are required to be consistent. These networks' structures refer to the neural network's layer of the classical GAN (Geng et al., 2013). The training task network provides the layer weights and bias in the neural networks G and D. We get these parameters by several gradient descent iterations with fewer rounds. The relationship between meta-network, training network, target network and GAN is shown in **Figure 2A**.

3.1 Meta-network

According to the updated parameters in the training task network, the search direction of initialization parameters with more potential for employment in the future training task is determined. Furthermore, meta-networks directly determine the specific value of the initialization parameters.

The meta-network learning rate ε (iteration step) is an adaptive value that changes with the iterations, as shown in Eq. 5.

$$\varepsilon = a\frac{i}{I_{meta}} + b\left(1 - \frac{i}{I_{meta}}\right) \tag{5}$$

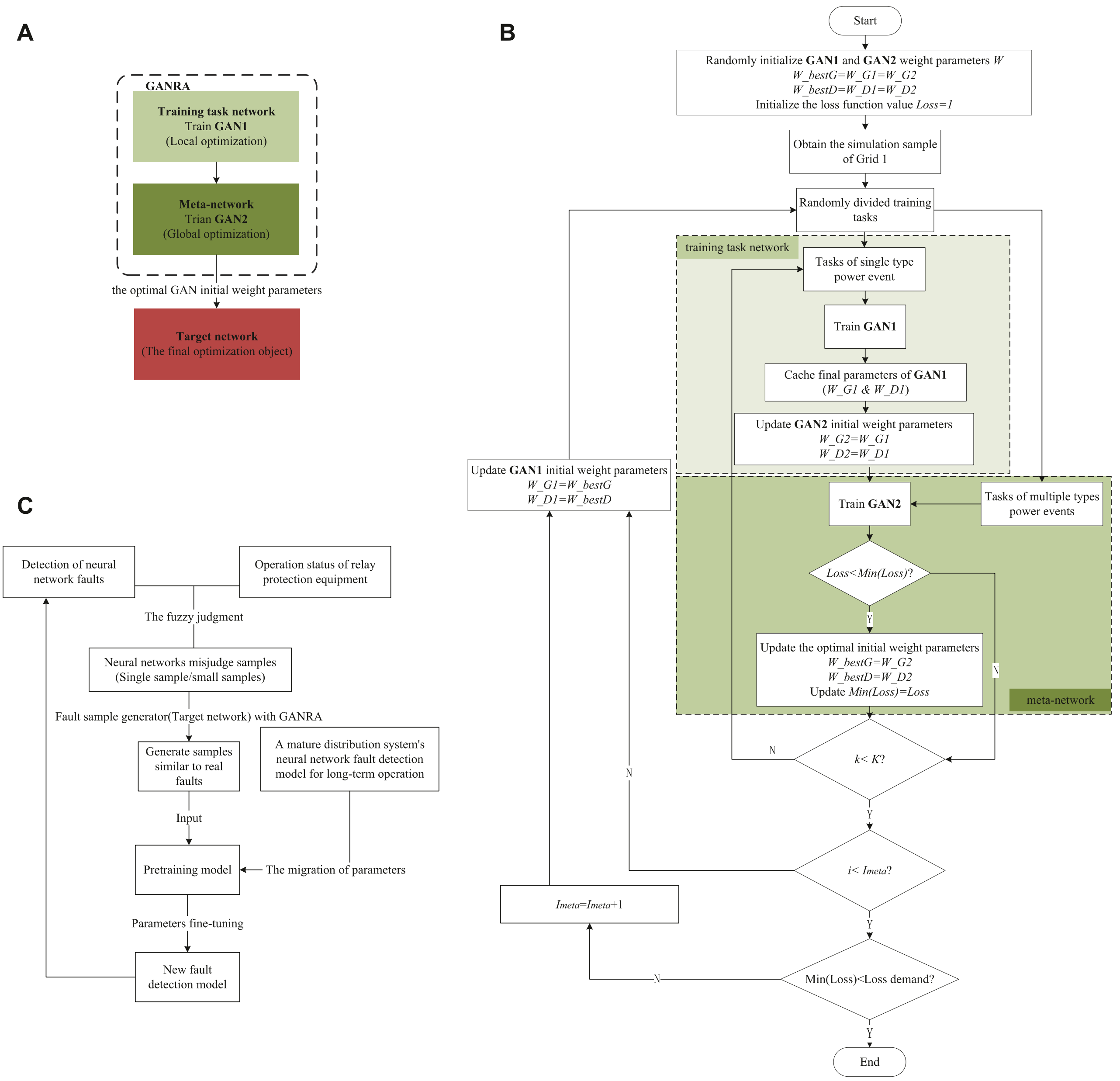

FIGURE 2
(A). The relationship between meta-network, training network, target network and GAN. **(B)**. The algorithm process of GANRA to optimize the initial parameters of the target network. **(C)**. The diagram of practical evolution strategy.

Where I_{meta} is the meta-network loop iteration, i is the current meta-network iteration, a and b are adjustable learning rate parameters. a and b decide the parameter update vector of the meta-network. Nichol et al. (2018) shows the learning curves for various loop gradient combinations. The improvement is more significant when using a sum of all gradients in Reptile rather than using just the final gradient in FOMAML. When a=b=1, the parameter update vector of the meta-network is the sum of all iterations' gradients from the training task network. These two reasons suggest that a=b=1 can benefit from taking many meta-network loop steps.

When multiple training tasks are running in parallel, the weight updating formula of the meta-network layer is shown in Eq. 6.

$$\phi \leftarrow \phi + \varepsilon \frac{1}{N} \sum_{j=1}^{N} \left(\tilde{\phi}_j - \phi \right) \tag{6}$$

Where ϕ are all layer weight parameters of the meta-network, $\tilde{\phi}_j$ are all layer weight parameters obtained by network training of the jth training task in the current meta-network iteration round, N is the number of parallel training tasks used in a meta-network iteration, j is the task network's number undergoing training in the current meta-network iteration.

Compared with MAML (Wang et al., 2021), First-order MAML (FOMAML), and other meta-learning optimization algorithms, without using gradient or Hesse matrix in the weight update of the meta-network, the Reptile algorithm is faster.

3.2 Training task network

In essence, the training task network is a GAN. And the parameters' optimization reference direction of the meta-network is obtained through two aspects. One is randomly setting sample tasks with a specified number and categories, i.e., *shot* and *ways*, and the other is using the parameters obtained during the training task network after several iterations, i.e., *k*. Moreover, to ensure the generalization of the meta-network, the training task network uses multi-task parallel training. Finally, the parameters obtained by the training task network are averaged. The above steps are shown in Eq. 6 in section 3.1.

Since GAN is selected as the grid structure of the meta-network, training task network, and target network, the loss function L in the GANRA is defined as the approximate expression $\widetilde{V}$ of Eq. 3, as shown in Eq. 7. It can obtain parameter updates and estimate loss values more concretely.

$$L = -\widetilde{V} = -\left(\frac{1}{m}\sum_{i=1}^{m}\log \mathrm{D}\left(x_i\right) + \frac{1}{m}\sum_{i=1}^{m}\log\left(1 - -\mathrm{D}\left(\widetilde{x}_i\right)\right)\right) \tag{7}$$

Where x_i is the ith point sampled in function $P_{data}(x)$, $\widetilde{x}_i$ is the ith point sampled in function $P_{\mathrm{G}}(x)$, m is the total number of sampling points in the feature distribution of x.

3.3 Generalization and rapidity of initial parameter search

The study takes two rounds of SGD training task network iteration, i.e., K=2, in a meta-network training as an example of the parameter updating process. The initialization parameters of the training task network are shown in Eq. 8.

$$\theta_0 = \phi = \{\theta_{\mathrm{G}}, \theta_{\mathrm{D}}\} \tag{8}$$

Parameters obtained in the next two training rounds are shown in Eqs 9, 10.

$$\theta_1 = \theta_0 - \alpha L_0'\left(\theta_0\right) \tag{9}$$

$$\theta_2 = \theta_0 - \alpha L_0'\left(\theta_0\right) - \alpha L_1'\left(\theta_1\right) \tag{10}$$

Where α is the learning rate of the training task network, $L'(\theta)$ is the derivative of the training task network's loss function when the parameter is θ.

The simplified expressions of each function are shown in Eqs 11–14.

$$g_k = L_k'\left(\theta_k\right) \tag{11}$$

$$\theta_{k+1} = \theta_i - \alpha g_k \tag{12}$$

$$\bar{g}_k = L_k'\left(\theta_0\right) \tag{13}$$

$$\bar{H}_k = L_k''\left(\theta_0\right) \tag{14}$$

According to Figure 1 in Section 2.1 and the Reptile principle, the parameter descent gradient of the meta-network can be obtained in Eq 15.

$$g_{meta} = g_1 + g_2 = \bar{g}_1 + \bar{g}_2 - \alpha \bar{H}_2 \bar{g}_1 + o\left(\alpha^2\right) \tag{15}$$

According to the derivation of g_{meta} in Eq. 15, when θ_0 is the initialization parameter of the training task network, the overall average expectation (*AvgGrad*) of the loss function L's gradient $\bar{g}$ from a training task network is defined in Eq 16.

$$AvgGrad = \mathrm{E}_{\tau,i}\left[\bar{g}\right] \tag{16}$$

The current training sequence of data leads to different training results in the training tasks. Still, due to the random selection of data, the average expectation of θ_0 on the gradient in L is consistent in Eq 17.

$$AvgGrad = \mathrm{E}_{\tau,1}\left[\bar{g}_1\right] = \mathrm{E}_{\tau,2}\left[\bar{g}_2\right] \tag{17}$$

Similarly, the expected value of the other part of g_{meta} is shown in Eq 18.

$$AvgGradInner = \mathrm{E}_{\tau,1,2}\left[\bar{H}_2\bar{g}_1\right] = \mathrm{E}_{\tau,1,2}\left[\bar{H}_1\bar{g}_2\right] \tag{18}$$

Then we obtain

$$\begin{aligned} AvgGradInner &= \frac{1}{2}\mathrm{E}_{\tau,1,2}\left[\bar{H}_2\bar{g}_1 + \bar{H}_1\bar{g}_2\right] \\ &= \frac{1}{2}\mathrm{E}_{\tau,1,2}\left[\frac{\partial}{\partial\phi_1}\left(\bar{g}_1 \cdot \bar{g}_2\right)\right] \end{aligned} \tag{19}$$

The expected value of g_{meta} can be obtained as shown in Eq 20.

$$\begin{aligned} \mathrm{E}\left[g_{meta}\right] &= 2 \times AvgGrad \\ &\quad - \alpha \times AvgGradInner + o\left(\alpha^2\right) \end{aligned} \tag{20}$$

It shows that the meta-network wants to obtain the same gradient in each training task network's iteration. This target requires that the initial parameters have generalization. At the same time, the smaller the gradient difference in each iteration of the training task network, the more consistent the search direction of the meta-network to seek the optimal initial parameters and the shortest search path.

3.4 Algorithm implementation

The algorithm process of GANRA to optimize the initial parameters of the target network is shown in **Algorithm 1**; **Figure 2B**.

The hyper-parameters set in the algorithm include the meta-network iterations I_{meta}, the number of parallel training tasks N, the training task network iteration rounds K, single task size *shot*, and task type (or fault type) *ways*.

```
Initialize the weights of the meta-network $\phi_0$,
Set each hyper-parameter in GANRA,
for meta-network iteration rounds $i=1,2,\ldots,I_{meta}$ do:
    $N$ tasks of $T$ are sampled,
    for $j=1,2,\ldots,N$ do:%Train $N$ parallel tasks in the training task network
        Initialize the network weights of training tasks $\theta_j=\phi_{i-1}$,
        for train task network iteration rounds $k=1,2,\ldots,K$ do:
            Perform GAN training on task $T_j$,
            Obtain the training task network weight $\theta_j$ of task $T_j$,
        end for
    end for
    Update the weights of the meta-network $\phi_i \leftarrow \phi_{i-1} + 1/K*\varepsilon\Sigma_{j=1}^{N}(\theta_j - \phi_i)$
end for
```

Algorithm 1. GANRA

4 A practical evolution strategy for neural networks applied to distribution system

4.1 Existing problems

When investigating the fault detection application of neural network in the distribution system, it is found that the transmission lines of the distribution system usually have the following characteristics not conducive to the fault detection application of neural network.

1. The distribution system grid structure is complex and frequently changes, so the training model without continual and timely updating is not applicable.
2. The number of lines in the distribution system is huge, and it is impossible to record fault samples for each branch by installing recording devices. And the types of fault samples recorded are few, mostly single-phase grounding faults. The above reasons result in a small number of recorded waves. In addition, because of low fault current and obscure waveform characteristics, the recorded waves of HIF identified and recorded by subsequent protection devices are rare.
3. The fault characteristics of the distribution system cannot be learned entirely by using samples generated by the simulation model. First, due to the randomness and time-varying nature of the weather and the terrain, it is difficult to determine the fault current and fault types on the line or completely restore the complex factors through modeling. These lead to a truncation error. Second, the neural network is a "black box". It is unclear if the neural network misses the characteristics of the faults, making it challenging to generate new samples with corresponding tags.

Since the neural network directly learns fault features instead of grid operation rules, the mature fault detection model in the actual grid structure cannot be immediately used in the alternative or changed grid structure. The judgment accuracy of the changed grid structure would be significantly reduced.

4.2 Practical evolution strategy

For applying the neural network fault detection model to practical engineering, the evolution strategy armed with GANRA is designed as the following three stages.

1. Use the GANRA to generate optimal initialization parameters of the misjudgment sample generator.
2. The misclassification sample generator constructs samples with hidden features not learned by the neural network fault detection model. The hidden features are from a few actual misclassification fault samples.
3. The fault detection model trained with a large number of simulation samples or the model in the long-term operation of the distribution system is used as the pre-training model. Deep transfer learning (Bousmalis et al., 2016) is used to transfer the pre-training model to the training model. Then input the generated samples from Step (2) for the parameter fine-tuning training of the training model. A detailed description of the migration strategy is shown in Section 5.5.

The flow of the practical evolution strategy is roughly shown in Figure 2C.

5 Simulation experiment and result analysis

This section analyzes the effect of GANRA on generating HIF samples based on simulation data. Section 5.2 proves the effectiveness of GANRA in the study of initial training parameters with generalization. Moreover, this section observes the learning speed of sample generation and the quality of generated samples. The generated samples are made with the initial parameters obtained by GANRA and tested in the target network. Section 5.3 compares several sample generation algorithms to get their effect on the fault discrimination model generated by CNN under different sample mixing ratios. The algorithms include the conventional GAN with random initial parameters, the conventional GAN with GANRA initial parameters, and Variational Auto-encoders (VAE) (Zhai et al., 2019). It is worth noting that the GANRA in this section optimizes initial parameters from the CNN. Section 5.4 conducts experiments under the influence of different proportions of generated samples on the training accuracy of neural networks. Section 5.5 uses GANRA to find a group of initial parameters based on grid structure 1, then generates samples of grid structure 2 with these parameters and random initial parameters. Finally, Section 5.5 tests the effect of the fault detection model with these training samples. The specific structure composition of the grids can be found in Section 5.1, and the hyper-parameter values used by the GANRA to generate the initial parameters are given in Section 5.3.

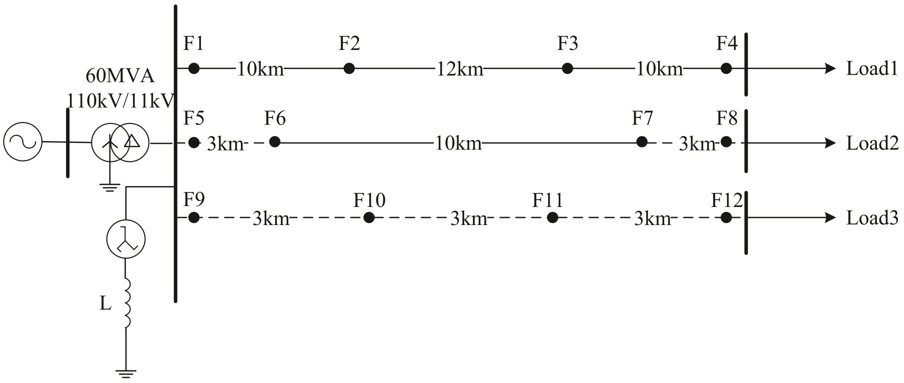

FIGURE 3
Schematic diagram of distribution system grid structure 1.

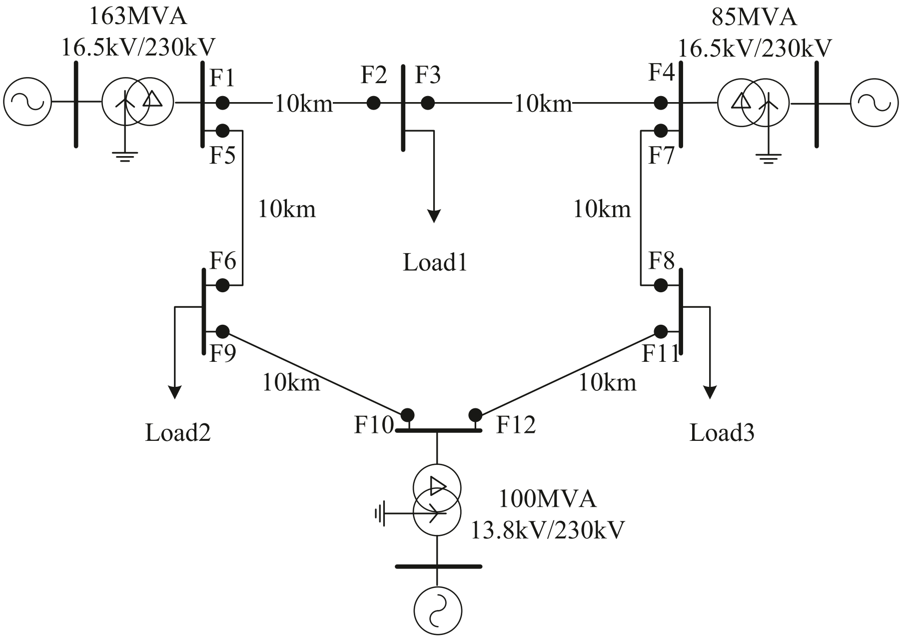

FIGURE 4
Schematic diagram of ring network grid structure 2.

5.1 Simulation grid structure and sample composition

A distribution system simulation model is constructed for flexibility in data acquisition, processing and analysis. The simulation sample is taken as the actual sample.

The grid structure of the 10 kV distribution system is shown in Figure 3. The simulation diagram can refer to Supplementary Figure S1. In Figure 3; Figure 4, the symbol "F (·)" represents the location of the failure point, the solid line means the overhead line, the dotted line represents the cable line, and every "Load" can be adjusted.

The actual samples used for neural network training and verification, including waveform samples of various faults and normal distribution system conditions, are collected from the fault occurrence point F1. Fifteen thousand nine hundred ninety three fault data are generated for training task extraction and neural network training and testing. This paper mainly studies the situations of HIF. Most of the fault data are HIF data, with a total of 13,438 items. The account of each fault type is shown in Table 1.

TABLE 1 Proportion of each failure type in grid structure 1.

Fault Type	HIF	LL	LLG	LLLG	Normal State	SLG	Single Phase Open
Data Rate(%)	84.02	2.70	2.70	0.67	6.27	3.37	0.27

TABLE 2 Proportion of each failure type in grid structure 2.

Fault Type	HIF	LL	LLG	LLLG	Normal Station	SLG	Single Phase Open
Data Rate(%)	34.29	17.14	17.14	5.71	6.43	17.14	2.14

Where LL represents line-to-line fault (or phase fault), LLG represents line-to-line ground fault (or two-phase ground fault), LLLG represents three lines ground fault (or three-phase ground fault), and SLG represents single-line ground fault (or Normal Single Phase). The common working conditions include load switching, line reclosing, and capacitor switching at the load terminal.

Grid structure 2 is used to verify the generality of the initial parameters generated in Section 5.4. And it is shown in Figure 4, where the classical IEEE 9 node structure model is adopted. The simulation diagram can refer to Supplementary Figure S2. In the experiment, grid structure 2 runs in a way of open loop. Similarly, the collection point of waveform samples for various faults is F1. To simulate the lack of fault detection experience in a new grid structure or system operation mode, it is designed to generate and collect only 4,200 fault data for training task extraction, neural network training, and neural network testing. And among these 4,200 fault data, only 1,440 are high impedance fault data. The account of each fault type is shown in Table 2.

The use of such a large difference between the ring network and the radial network as a control experiment is mainly to emphasize that even in the case of huge changes in the grid structure, the initial parameters generated by GANRA under the original grid structure still have the ability to assist the new grid structure to generate accurate samples.

The study collects the waveforms of three-phase voltage, three-phase current, zero-sequence voltage, and zero-sequence current in the above simulations and decomposes the signals, respectively. The wavelet decomposition method with a 6 dB parent wavelet extracts the relevant characteristic quantities of wavelet coefficients. Four wavelet coefficients are obtained by three wavelet decomposition. It consists of a three-layer complex wavelet coefficient and one-layer neighboring wavelet coefficient, and thirty-two lines of information can be obtained. Then, by summarizing the high-resolution waveform data in detail and getting the sum of the multiple sampling points, it receives waveform information with thirty-two columns. The formula (Pan, 2019) for the energy relationship between the time domain and frequency domain is shown in Eq 21.

$$e_m^n = \sum_{x=1}^{X} |a_m^2(x) \cdot \Delta t| \tag{21}$$

Where e_m^n represents the nth pixel block containing time-frequency information of the wavelet coefficient of the corresponding waveform in the mth line of the actual input image sample, $a_m(x)$ represents the sampling amplitude of the xth sampling point of the wavelet coefficient of the corresponding waveform in the mth row, $\triangle t$ is the sampling step, X means that the pixel block contains X sampling points, and each row of 32-pixel blocks contains 32*X amount of sampling point (waveform) information. Figure 5 shows

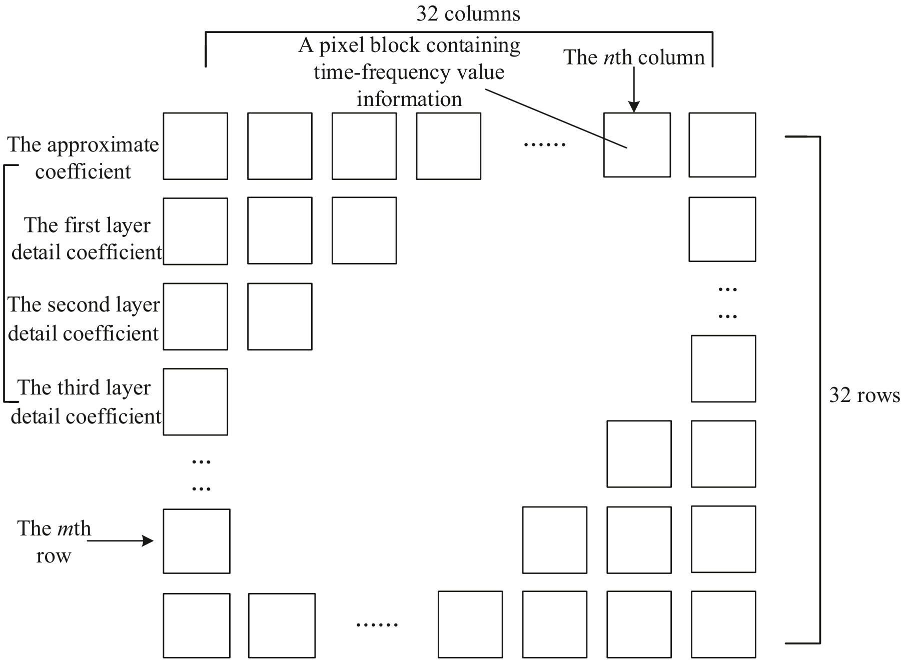

FIGURE 5
Image sample composition schematic diagram.

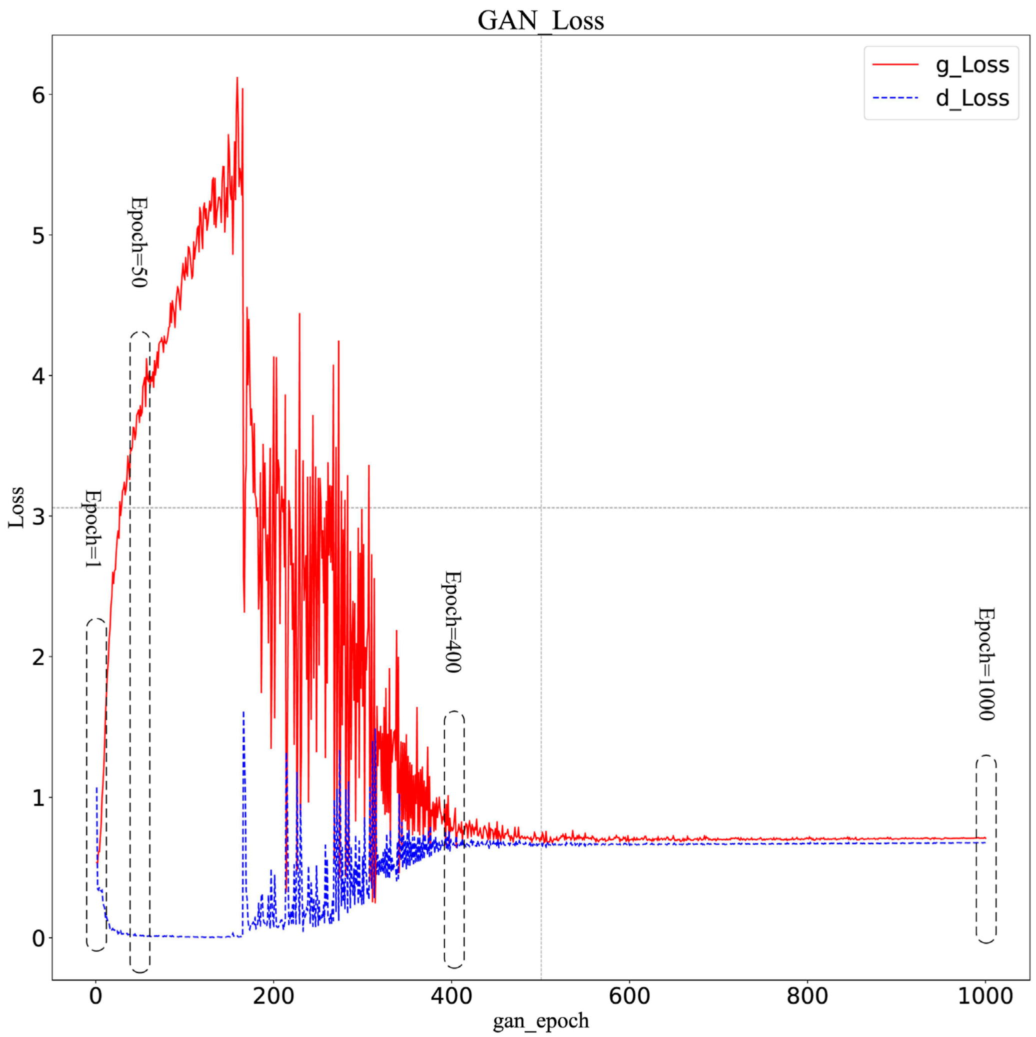

FIGURE 6
Loss chart for a single training mission.

the sample composition of the simulated waveform data obtained by sample processing.

5.2 Sample generation experiment

A single training task is extracted to conduct GAN training with 1,000 iteration rounds *gan_epoch*, and the loss values of G and D are obtained respectively, as shown in **Figure 6**.

Compare the lines of **Figure 6** with the broken line graphs of G and D loss values from the GAN training tasks (Task1, Task2, Task3, and Task4). These tasks use initialization parameters obtained from four different I_{meta} training of GANRA (as shown in **Figure 7**). In **Figure 7**, the training task network's iteration limit K of the four tasks is 10, and the learning rate of G and D is 0.002. It is found that the G and D loss (g_Loss and d_Loss) of each training task roughly corresponds to the loss trend within the corresponding interval of GAN training rounds in a single training task. Wherein the meta-network iterations I_{meta}= 1, 50, 400, 1,000.

The hyper-parameter settings of GANRA to the four training tasks in **Figure 7** are shown as follows: the number of parallel training tasks N=4, iterations of training task network K=10, adjustable parameters of learning rate of meta-network a =1, b=1, single task size *shot* =5, and task type *ways*=7.

The actual samples, the samples generated by the conventional GAN with random initial parameters and the samples generated by the conventional GAN with the optimized initial parameters are compared to study the influence of the initial parameters, the GANRA's meta-network iterations, and the GAN's iterations on specific GAN's generated samples. GANRA generates all the defined initial parameters. The comparison between the actual sample image and the generated sample image is shown in **Figure 8**. **Figures 8A,B** compare the sample pictures of HIF generated by the GAN network with and without the optimized initialization parameters. Both are trained for 400 rounds. It can be found

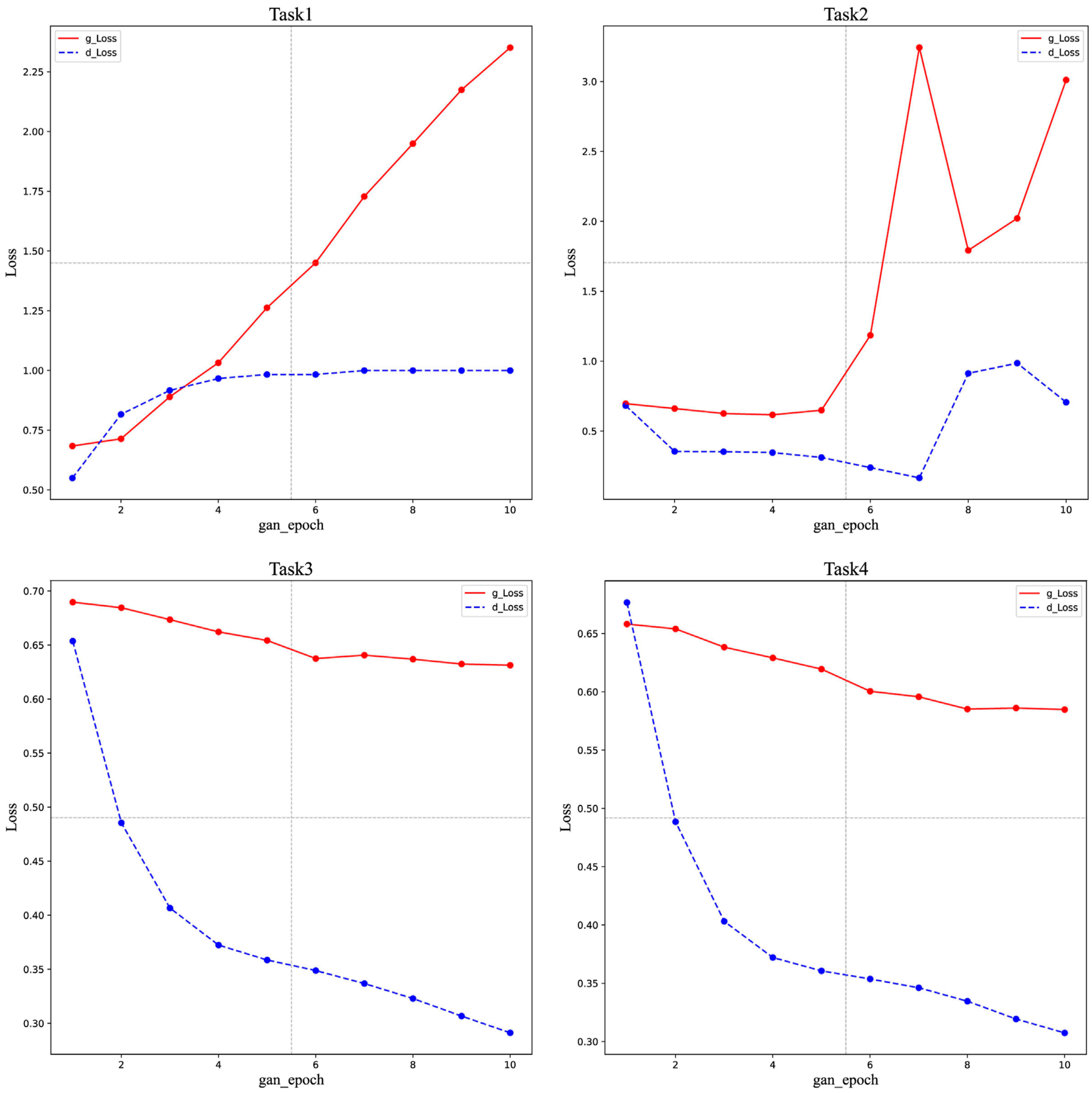

FIGURE 7
Diagram of training task loss under different I_{meta}.

that the GAN with the optimized initialization parameters can preliminarily generate images with actual image sample features. This result is obtained with the GAN iterations *epoch*=400 and 50 rounds of meta-network training. And it reflects that GANRA can accelerate GAN's collection of image features. **Figures 8C, D** compare the results of more rounds of GAN training based on **Figures 8A, B**. In this case, the GAN assisted by GANRA can generate a noiseless image sample, while some of the image samples generated by general GAN still have high noise. This phenomenon indicates that GANRA can reduce the noise of the generated samples. **Figures 8E, F** provide a comparison diagram between 950 GAN epochs generation sample with 1000 GANRA meta-network iterations and the original sample. The generated sample is almost consistent with the actual one, and the research results show this method is promising. However, contrasting the GANRA-assisted sample generation in **Figures 8C, D** with **Figures 8E, F**, the initialization parameters generated by multiple iterations of the meta-network have a specific "saturation value". In other words, the GAN's iterations for a particular task will not be further reduced. The quality of the generated samples and the GAN's iterations to generate

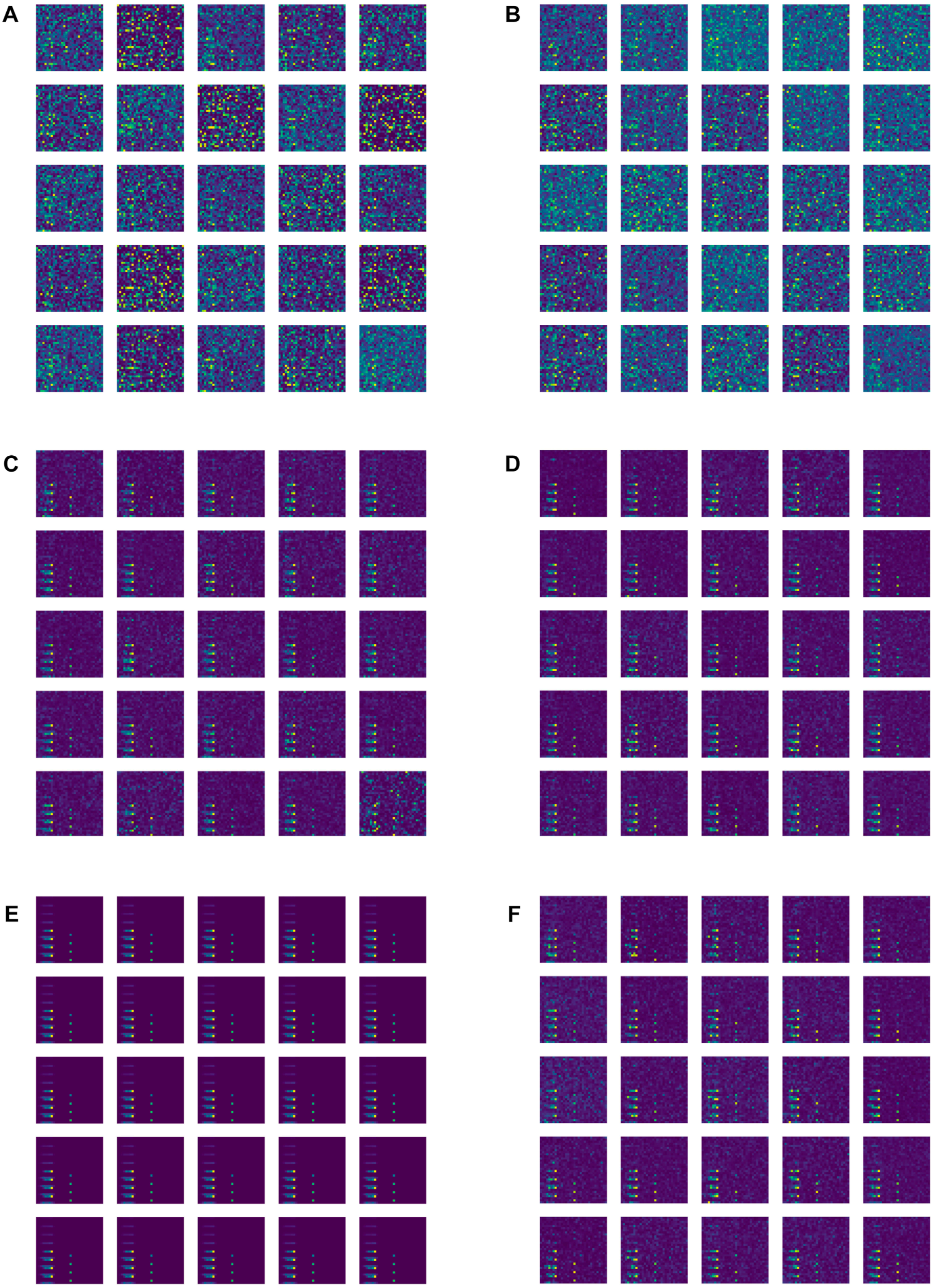

FIGURE 8
The actual sample of high resistance ground fault and the generated sample diagram under different experimental conditions. **(A)** GAN, *epoch*=400 **(B)** GANRA, l_{meta}=50, *epoch*=400. **(C)** GAN, *epoch*=960. **(D)** GANRA, l_{meta}=50, *epoch*=950. **(E)** Original samples. **(F)** GANRA, l_{meta}=1,000, *epoch*=950.

TABLE 3 The similarity between the samples generated by different methods and the actual samples of grid 1.

Proportion of training samples (Actual sample: Generated sample)	Sample generation algorithm		
	GANRA	VAE	GAN
HIF recognition accuracy (%)	99.85	68.66	98.66

quality-compliant samples will not change significantly in the case of a sharp increase in I_{meta}. The above experimental results are limited by the expectation of GANRA parameters' generalizability. The detail of Figure 8 can refer to the Supplementary Material S1

5.3 Experiments on the similarity between samples generated by several generation methods and the actual samples

The settings of GANRA's hyper-parameters and the base model used in fault detection in Sections 4.3, 4.4, and 4.5 are the same. The hyper-parameters of GANRA are set as follows: the meta-network iteration rounds I_{meta}=1,000, the number of parallel training tasks N=4, the training task network iteration rounds K=10, the meta-network learning rates a =1, b=1, the single task size *shot*=35, and the task type *ways*=1. Only the binary classification of the HIF and non-HIF faults is performed in this study. And the HIF recognition accuracy in this study is used to reflect the similarity between the generated HIF samples and the actual samples. The training set comprises the generated samples from different generation methods of grid structure 1, and the testing set contains the simulated samples (called actual samples) of grid structure 1.

A CNN consisted of three convolutional layers and two fully connected layers is selected for the basic model settings used in fault detection. The Relu function is used as the activation function. The learning rate α=0.001, iteration *epoch*=20, and single training scale *batch_size*=66. In this section, the iterations of GAN with initial parameters generated by the GANRA and with random initial parameters are 500 rounds. The VAE sample generation model in the study refers to the classical model (Pan, 2019).

It can be seen from Table 3 that the samples generated by GANRA and the samples generated by conventional GAN both have a high degree of similarity with the actual sample. And several experimental phenomena show that the recognition accuracy does not fluctuate much with different GAN initial parameters. At the same time, the recognition accuracy of VAE-generated samples jumps between 55% and 100% during the experiment. The study indicates that VAE learns some features of actual samples accurately but lacks robustness in other areas. By contrast, GANRA knows these features of samples in a stable and satisfactorily precise way. However, compared with the network that only uses GAN to learn and generate HIF samples, the generated HIF samples are slightly less reductive than the actual samples because it emphasizes the generalization of all fault initialization parameters instead of the optimum of current parameters.

TABLE 4 Influence of different sample composition on fault detection accuracy of grid 2.

Proportion of training samples (Actual sample: Generated sample)	HIF recognition accuracy (%)
1:0	97.73
7:3	99.36
1:1	88.03
3:7	92.39
0:1	66.56

5.4 Influence experiment of sample proportion on training accuracy

The testing set includes 2,100 actual samples from grid structure 2, and the training set includes both the actual and the samples generated by GANRA. The proportions of mixed samples are shown in Table 4. In addition, the data from the training set and testing set are not coincidental, and the proportions between the training set and testing set are always kept at a 1:1 ratio. The effect of different sample structures on the fault detection accuracy of grid structure 2 is shown in Table 4.

As seen from Table 4, the generated samples supported by GANRA achieve optimal performance in the experiments. Its HIF recognition accuracy is 99.36% when the proportion of training samples (actual sample: generated sample) is 7:3.

5.5 Fault detection experiments under changing conditions of the grid structure

According to the practical evolution strategy proposed in Section 4.2, relevant simulation experiments are carried out on the grid structure 2 with several samples. In the simulation experiment setting, the initial GAN parameters generated by GANRA through grid structure 1 are applied to the generation of small samples of grid structure 2 to show whether the GANRA focuses on predicting initialized parameters on future tasks.

The fault pre-training model adopted is the basic CNN model mentioned in Section 5.2. The migration parameters used in the new neural network are obtained after training the actual sample from grid 1. On this basis, a mixture of samples is used to prepare the fine-tuned parameters of the new fault detection model. The mixed samples include generated samples and a small number of actual samples. The specific transfer learning strategies are as follows: first, the top-level 1 of the actual model is turned into the top-level 2 of the new model, and this new model is more suitable for the current training data; second, freeze the parameter training of the bottom and middle layers of the new model, and train only the top layer 2; third, the parameter training of the bottom layer and middle layer 1 of the new model is frozen, and then the top layer 2 and middle layer 2 are trained simultaneously. The corresponding transfer learning strategy is shown in Figure 9. The box is filled with grey layers for the parameters to be trained in the specified step.

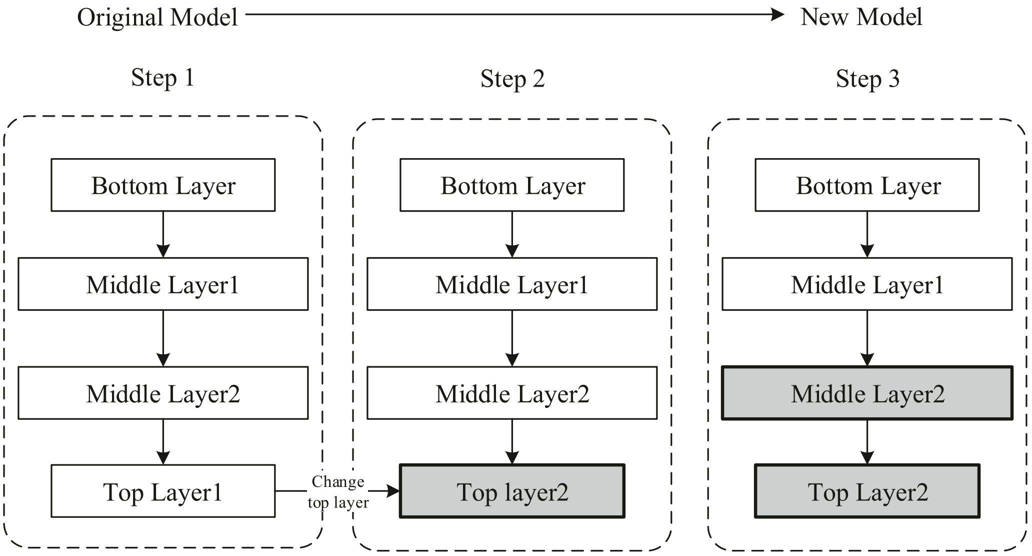

FIGURE 9
Transfer learning strategy.

TABLE 5 HIF recognition accuracy in grid structure 2 under different training conditions.

Situation	Whether to perform model fine-tuning	Proportion of training samples (Actual sample: Generated sample)	HIF recognition accuracy (%)
(1)*	No	1:0	97.73
(2)	Yes	1:0	100
(3)	Yes	7:3	100
(4)	Yes	0:1	89.70
(5)	Yes	-	34.32

[a]The situation (1) is consistent with the mixed sample experiment with a training samples ratio of 1:0 in Table 4, and the experiment will not be repeated.

The proportion of mixed training samples is 7:3 based on Section 5.4, which can make the recognition of HIF relatively more accurate. The specific experimental control group is set as follows.

1. Train the new neural network with the actual sample of grid 2.
2. The actual sample of grid 2 is used to fine-tune the parameters from the neural network of grid 1.
3. The generated sample are mixed with fine-tuning the parameters from the neural network of grid 1 and the actual sample of grid 2.
4. The generated samples of grid 2 are used to fine-tune the parameters from the neural network of grid 1.
5. The neural network of grid 1 detects test samples of grid 2.

The influence of the different proportions of models' fine-tuning and training samples on HIF recognition accuracy of grid structure 2 is shown in Table 5.

The comparison between situations (1) and (2) shows that neural network transfer learning can effectively improve the identification accuracy of HIF. By the comparison of (2), 3, and 4, it is easy to find that using appropriate mixed samples to increase the training sample size is feasible when there are few fault samples in the new grid structure. This method will not decrease the fault identification accuracy. However, a large proportion of generated samples will decrease the identification accuracy. The comparison between cases (2) and (5) shows that the parameter fine-tuning in the new grid structure is feasible. It can significantly improve fault identification accuracy. Therefore, the practical evolution strategy of neural networks for distribution systems is effective. It can optimize the utilization of neural networks in power system fault detection.

6 Conclusion

This paper proposes a GAN evolution strategy based on the Reptile algorithm to solve practical problems such as small HIF samples and network structure changes in distribution systems. The validity, generalization, and speed of GANRA are verified by mathematics and simulation. The sample generated by the neural network evolution strategy helps solve some problems (like a shortage of reliable training data and faults with obscure characteristics) existing in practical applications through the auxiliary neural network fault detection model. Furthermore, GANRA generates the initial parameters of GAN through indirect gradient calculation and completes a general optimization of initial parameters. GANRA can generate samples with better quality faster than GAN, but when the number of iterations tends to a certain upper limit, the quality of samples generated by GAN is better than that of GANRA because of GANRA parameters' generalizability. And the quality of samples generated by GANRA is usually better than that of VAE. This algorithm effectively reduces the computing time, sample size and the number of learning iterations required to generate samples in different tasks and grid structures in the future.

For the electrical field, considering the requirements of timeliness and stability of fault judgment in engineering practice, such a study can be done by presenting the process of GANRA optimization of initial parameters in a dynamic and online way. In addition, the influence of other GAN algorithm variants on parameter iteration can be explored. For example, a tagged grid structure emphasizing classification ability can be considered. That is for enhancing the training ability in the category of samples with significant differences. Then, the research can extend this ability to other categories of fault identification.

Data availability statement

The raw data supporting the conclusion of this article will be made available by the authors, without undue reservation.

Author contributions

HB and WJ were responsible for providing the study idea, experiment design, experiment execution, result analyses, and manuscript draft. ZD were responsible for supervision, review, and funding acquisition. WZ, XL, and HL were responsible for providing part of experiment execution. All authors contributed to the article and approved the submitted version.

Funding

This work was supported by the Science and Technology Project of the China Southern Power Grid (GDKJXM20198281). The funder was not involved in the study design, collection, analysis, interpretation of data, the writing of this article, or the decision to submit it for publication.

Conflict of interest

Author HB was employed by China Southern Power Grid. XL was employed by the Zunyi Power Supply Company of Guizhou Power Grid.

The remaining authors declare that the research was conducted in the absence of any commercial or financial relationships that could be construed as a potential conflict of interest.

Publisher's note

Supplementary material

The Supplementary Material for this article can be found online at: https://www.frontiersin.org/articles/10.3389/fenrg.2023.1180555/full#supplementary-material

References

Amir, H., and Gandomi, L. M. P. Z. (2022). Reptile search algorithm (rsa): A nature-inspired meta-heuristic optimizer. *Expert Syst. Appl.* 191, 116158. doi:10.1016/j.eswa.2021.116158

Bousmalis, K., Trigeorgis, G., Silberman, N., Krishnan, D., and Erhan, D. (2016). "Domain separation networks," in Annual Conference on Neural Information Processing Systems 2016, Barcelona, Spain, December 5-10, 2016, 343–351.

Finn, C., Abbeel, P., and Levine, S. (2017). "Model-agnostic meta-learning for fast adaptation of deep networks," in Proceedings of the 34th International Conference on Machine Learning, Sydney, August 6 - 11, 2017, 1126–1135.

Flauzino, R. A., Ziolkowski, V., and Silva, I. N. D. (2006). "Using neural network techniques for identification of high-impedance faults in distribution systems," in 2006 IEEE/PES Transmission and Distribution Conference and Exposition: Latin America, Caracas, August, 15-18, 2006, 1–5.

Geng, J., Wang, B., Dong, X., and Dominik, B. (2013). Analysis and detection of high resistance grounding fault in neutral effective grounding distribution network. *Power Syst. autom.* 37, 85–91.

Goodfellow, I. J., Pouget-Abadie, J., Mirza, M., Xu, B., Warde-Farley, D., Ozair, S., et al. (2014). "Generative adversarial nets," in Advances in Neural Information Processing Systems 27: Annual Conference on Neural Information Processing Systems 2014, Montreal, Quebec, Canada, December 8-13 2014, 2672–2680.

Li, Y., Zhang, S., Hu, R., and Lu, N. (2020). A meta-learning based distribution system load forecasting model selection framework. *Appl. Energy* 294, 116991. doi:10.1016/j.apenergy.2021.116991

Mo, S., Cho, M., and Shin, J. (2020). Freeze discriminator: A simple baseline for fine-tuning gans. Available at: https://arxiv.org/abs/2002.10964 (Accessed February 25, 2020).

Nichol, A., Achiam, J., and Schulman, J. (2018). On first-order meta-learning algorithms. Available at: https://arxiv.org/abs/1803.02999 (Accessed March 8, 2018).

Pan, X. (2019). "Research on high resistance grounding fault detection of distribution lines,". Thesis (Changsha: Hunan university).

Salomonsson, D., Söder, L., and Sannino, A. (2007). "An adaptive control system for a dc microgrid for data centers," in Conference Record of the 2007 IEEE Industry Applications Conference Forty-Second IAS Annual Meeting, New Orleans, LA, USA, September 23-27, 2007 (IEEE), 2414–2421. doi:10.1109/07IAS.2007.364

Wan, Q., and Zhao, L. (2018). "A novel fault section location method for small current grounding fault based on hilbert-huang transform with wavelet packet transform preprocessing," in 2018 11th International Conference on Intelligent Computation Technology and Automation (ICICTA), Changsha, September 22-23, 2018, 365–370. doi:10.1109/ICICTA.2018.00089

Wang, F., Chai, G., Li, Q., and Wang, C. (2022). Small sample malware classification method based on parameter optimization meta-learning and difficulty sample mining. *J. Wuhan Univ. Nat. Sci.* 68, 17–25. doi:10.14188/j.1671-8836.2021.2008

Wang, J. (2020). “Research on cloud fault diagnosis method of Service robot based on mixed samples,”. Thesis (Jinan: Shandong university).

Wang, X., Yu, Z., Shi, B., Bao, Z., Qian, H., and Zhao, Y. (2021). Small sample data generation algorithm based on meta-learning. *Comput. Syst. Appl.* 30, 161–170. doi:10.15888/j.cnki.csa.008063

Wang, Z., and Zhang, B. (2021). A review of generative adversarial networks. *J. Netw. Inf. Secur.* 7, 68–85.

Xi, J., Pei, X., Song, W., Xiang, B., Liu, Z., and Zeng, X. (2021). Experimental tests of dc sfcl under low impedance and high impedance fault conditions. *IEEE Trans. Appl. Supercond.* 31, 1–5. doi:10.1109/TASC.2021.3065886

Xie, J. (2019). “Modeling and debugging of PSCAD for the main grid of power transmission from west to East of China Southern Power Grid,”. Thesis. Guangzhou, China: (South China University of Technology).

Xu, R., Liu, B., Zhang, K., and Liu, W. (2022). Model independent element learning algorithm based on bayesian weight function. *Comput. Appl.*, 1–5. doi:10.11772/j.issn.1001-9081.2021040758

Ye, J., Chu, F., and Wu, Y. (2016). Fault type identification of distribution network based on wavelet packet and improved neural network. *Sci. Technol. innovation Appl.* 1, 18–19.

Zhai, Z., Liang, Z., Zhou, W., and Sun, X. (2019). A review of variational autoencoder models. *Comput. Eng. Appl.* 55, 1–9.

Zhang, H., and Su, L. (2022). Zero-sample image recognition for variational autoencoder combined with knowledge graph. *Comput. Eng. Appl.*, 1–10. doi:10.3778/j.issn.1002-8331.2106-0430

Zhang, J. (2018). “Research on intelligent identification method of high resistance grounding fault in distribution network,”. Thesis (Fuzhou: Fuzhou university).

Frontiers in Energy Research

TYPE Original Research
PUBLISHED 09 June 2023
DOI 10.3389/fenrg.2023.1202090

EDITED BY
Imr Fattah,
University of Technology Sydney,
Australia

REVIEWED BY
Lia Elena Aciu,
Transilvania University of Brașov,
Romania
Jianchu Lin,
Huaiyin Institute of Technology, China
Ziheng Chen,
Walmart Labs, United States

*CORRESPONDENCE
Yingrui Wang,
✉ wyr191123@njrts.edu.cn
Shengjie Huang,
✉ huangshengjie1@sgepri.sgcc.com.cn

RECEIVED 07 April 2023
ACCEPTED 15 May 2023
PUBLISHED 09 June 2023

CITATION
Wang Y, Huang S and Guo C (2023), Application of smart grid and non-dominated sorting genetic algorithm in adaptive energy-saving control of building lighting.
Front. Energy Res. 11:1202090.
doi: 10.3389/fenrg.2023.1202090

Application of smart grid and non-dominated sorting genetic algorithm in adaptive energy-saving control of building lighting

Yingrui Wang[1]*, Shengjie Huang[2]* and Chong Guo[2]

[1]Nanjing Vocational Institute of Railway Technology, Institute of Architecture and Art Design, Nanjing, China, [2]Nari Technology Co., Ltd., Nanjing Electric Control Branch, Nanjing, China

Introduction: In the wave of urbanization, the increase of public lighting equipment in buildings has brought about more prominent problems of energy saving and consumption reduction.

Methods: In order to solve the above problems, this paper designs a set of intelligent lighting solutions for digital buildings by combining the smart grid and non-dominant sorting genetic algorithms. Firstly, an intelligent lighting monitoring solution is constructed through ZigBee *ad hoc* network and sensor technology to monitor the relevant environment and lighting control of the laboratory building. Secondly, this paper uses the DIALux software network to build a public lighting light distributiona public lighting light distribution model in the building, and deeply studies the dimming control strategy of the system under the principle of making full use of sunlight and natural light.

Results: The purpose ofself-adaptive intelligent control of desktop illuminance, finally using this scheme to achieve the optimal balance of desktop lighting.

Discussion: The simulation experiment counts the power data of the intelligent lighting system under different weather conditions. The experimental results verify that the intelligent lighting control scheme can effectively reduce the output luminous flux of the lamps, thereby reducing power consumption.

KEYWORDS

smart lighting, digital buildings, non-dominating sorting genetic algorithms, augmented reality, smart grid

1 Introduction

Building a resource-saving and environment-friendly society is an inevitable requirement for maintaining sustained and healthy economic development and promoting social harmony and stability (Özçelik, 2018). With the anti-war of science and technology and the gradual improvement of human living standards (Zhang et al., 2021), the people's requirements for modern intelligent buildings, smart homes, and intelligent lighting are not only limited to ordinary lighting needs, but also need modern intelligent lighting systems to meet the different comfort and energy-saving requirements of different groups of people. Improving the efficiency and use time of electric light sources and developing energy-efficient lamps are the main methods of energy-saving technology in early lighting (Ning et al., 2023). Lee et al. first proposed to control shutters and lights to reduce energyconsumption (Cai et al., 2022), and then many scholars conducted a lot of research on the blade angle control method of shutters He and Ye (2022), such as pure fuzzy control methods (Zhang et al., 2023), genetic algorithms (Long et al., 2023) and BP neural networks Zhong et al. (2023). David et al. used the light sensor calibration prior information to control daylight adaptive lighting, in order to reasonably introduce natural light to achieve energy saving, and corresponding scholars have also studied natural lighting. They also started from the intelligent control method of shutters, and adopted fuzzy neural networks (Fei and Yang, 2023), adaptive fuzzy control (Chen et al., 2022) and other methods. Xiao Hui of Tongji University and others combined artificial lighting and natural lighting, proposed a joint control model, and formulated a joint control strategy. In addition, starting from the principle of illuminance, reduce the indoor light reduction coefficient, improve the illuminance of the working area, and also improve the light distribution effect to achieve the purpose of energy saving. With the improvement of people's light distribution design level in light environment, the benefits of energy saving will become higher and higher. Alice et al. used wireless integrated dimming ballast technology to develop wireless command reception from the central control server and convert it into ballast control signal for lighting adjustment, realizing the personalized dynamic design of energy-saving network lighting in open office (Antoine et al., 2021).

In the adaptive energy-saving control of architectural lighting, the smart grid can provide more energy information and management capabilities, making the lighting system more intelligent and efficient. For example, real-time monitoring and control of lighting equipment can be achieved through smart grids to adjust according to energy prices and load demand. Non-dominated sorting genetic algorithms can optimize multiple objective functions of lighting equipment, such as the balance between energy saving and comfort. Using this algorithm, a set of optimal solutions can be found that do not have a dominance relationship, resulting in more efficient lighting control.

In this paper, we will mainly use smart grid based and non-dominated ranking genetic algorithm, which has developed from the original univariate theory to multivariate theory, from continuous-time system to discrete-time system, and has been applied in many fields (Rehman et al., 2023). And we combine it with the smart grid to apply it to the control of lighting energy efficiency, we can design a new cognitive lighting control system, that is, a type of PID controller for stable setting of the appropriate illumination, while using a genetically optimized controller to minimize power consumption. We also compared our model with other models, and the results show that our model performs better than other models and can effectively control energy savings.

The contribution points of this paper are as follows.

- Compared with pure fuzzy control methods, and genetic algorithms, this paper uses the smart grid as the basis for a higher degree of automation. Good flexibility can effectively improve energy utilization efficiency and economic benefits;
- Compared with the BP neural network model, our model has a simpler structure, less computation, and can provide adaptive solutions faster. It adopts a modular design, convenient for flexible combination and expansion, and can be customized according to different needs. The application needs in various complex environments;
- Compared with adopted fuzzy neural networks, and adaptive fuzzy control methods, our method can effectively solve complex optimization problems with multiple objective functions; by effectively preserving the diversity and convergence speed in the population, we can obtain a The optimal solution of the group is more applicable to the problem.

In the rest of this paper, we present recent related work in **Section 2**. **Section 3** offers our proposed methods: overview, convolutional neural networks; long and short-term memory networks; transfer learning. **Section 4** presents the experimental part, details, and comparative experiments. **Section 5** concludes.

2 Related work

2.1 BP neural networks

BP neural network is a widely used feed-forward artificial neural network known as multilayer perceptron (Multilayer Perceptron, MLP). The BP neural network implements tasks such as pattern recognition, classification, and regression by passing input data from the input layer to the hidden layer and output layer and then adjusting the weight and bias of each layer according to the error signal (Han et al., 2021).

BP neural network usually has three or more layers: an input layer, a hidden layer (there may be more than one) and an output layer. Each neuron is connected to other neurons in the upper and lower adjacent layers, and the corresponding weight value determines the connection strength between them. The input data enters from the input layer and passes through the nonlinear transformation of the hidden layer to the output layer to calculate the final result. The BP neural network training usually uses a backpropagation algorithm (Backpropagation, BP). The algorithm uses the gradient descent method to minimize the error function (usually the mean square error function). It updates the weights of all connections by calculating the error between the output layer and the target value to reduce the error. This process iterates until the error reaches a preset threshold or other stopping conditions are met (Wu et al., 2022).

BP neural network has the following advantages: It has a strong nonlinear fitting ability and can handle complex pattern recognition problems; It has good generalization ability and can accurately predict unknown data; It can further improve the network performance by increasing the number of hidden layers. Flexibility and performance (Niu et al., 2022). However, the BP neural network also has the following disadvantages: the training process requires a large amount of data and calculations, and it is easy to fall into a local minimum; for different types of data, different preprocessing and feature selection processes are required; the number of hidden layers, the number of neurons, etc. The parameters need to be adjusted manually, affecting the network's learning efficiency and performance (Li et al., 2023).

2.2 The fuzzy logic model

The fuzzy logic model is an artificial intelligence model based on fuzzy set theory and fuzzy reasoning method, mainly used to deal with complex, uncertain information and fuzzy information. Compared with the traditional binary logic model, the fuzzy logic model can better deal with fuzzy, uncertain and contradictory problems in real life (Ge et al., 2019).

2.2.1 Fuzzy logic models typically include the following components

Fuzzy set: A fuzzy concept that describes a variable or object, which can be a real number interval, a function, or a formalized mathematical structure; Fuzzy relationship:used to describe the relationship between two or more fuzzy sets, such as fuzzy equality, fuzzy inclusion, fuzzy intersection, fuzzy union, etc.; Fuzzy rule: The law used to map fuzzy input to fuzzy output, usually expressed as a statement in the form of ”IF-THEN”, where the IF part represents the condition of the input variable, and the THEN part represents the value of the output variable; Fuzzy reasoning: Carry out fuzzy reasoning on the input according to the fuzzy rules and obtain the corresponding output results, usually using fuzzy logic operators (such as fuzzy AND, fuzzy OR, fuzzy NOT, etc.) for calculation (Yang et al., 2023).

In practical applications, fuzzy logic models can be used for decision-making and control problems in various fields, such as intelligent transportation, industrial control, financial forecasting, medical diagnosis, etc. Its main advantage is that it can deal with fuzzy and uncertain information and has good adaptability and flexibility; the disadvantage is that it needs to model the input variables and output results mathematically, and the model structure is complex and difficult to explain and understand Cheng et al. (2023).

2.3 SVM model

Support Vector Machine (SVM) is a supervised learning algorithm widely used in classification, regression and anomaly detection, which divides data into different categories by finding the optimal hyperplane. The basic idea of SVM is to map low-dimensional input data to high-dimensional space so that the data can be more easily divided linearly or nonlinearly (Wei et al., 2022).

The core of SVM is to select the appropriate kernel function, commonly used kernel functions include linear kernel, polynomial kernel, radial basis kernel (RBF) and so on. For linearly separable datasets, SVM uses a linear kernel function; for nonlinearly separable datasets, SVM uses a nonlinear kernel function to map the original data space to a high-dimensional space for segmentation. During training, SVM tries to find an optimal hyperplane to split the data. This hyperplane has the largest margin and the furthest distance from the support vectors. Support vectors refer to some points closest to the hyperplane, which determine the position and direction of the hyperplane. Since SVM focuses on the points closest to the hyperplane, it is less susceptible to noise. The advantages of SVM include: its the number of support vectors is small, the memory usage is small, and it suitable for high-dimensional data Zhu et al. (2020); It can handle nonlinear data sets and adapt to various complex problems flexibly through the selection of kernel functions; it has strong generalization ability and good prediction performance for new data. The disadvantages of SVM include: for large-scale data sets, the training time is long, and the calculation complexity is high; selecting an appropriate kernel function and performing parameter tuning is necessary, and it is not easy to deal with the noise brought by the input data (Nazari et al., 2020).

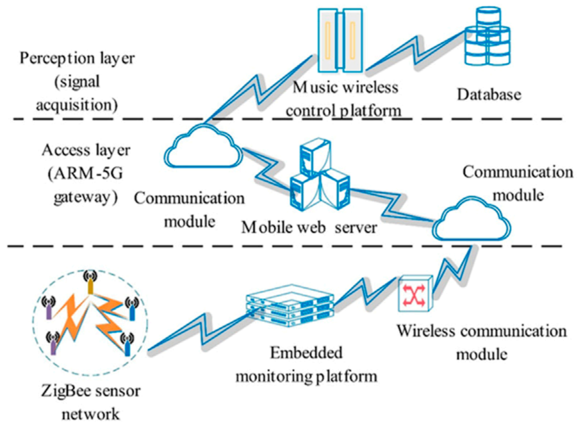

FIGURE 1
Schematic diagram of intelligent lighting monitoring scheme based on smart grid.

In conclusion, SVM is a powerful, flexible, supervised learning algorithm with wide application.

3 Intelligent lighting monitoring solution based on smart grid

3.1 Indoor light distribution model

The system adopts a 3-layer network structure, in which the perception layer uses low-power ZigBee *ad hoc* network and sensor technology to achieve state data acquisition. The transport layer forms an ARM-5G gateway through ARM embedded technology and 5G mobile communication technology to realize the remote transmission of sensing and control data (Xiang et al., 2019). The application-layer client monitors the experimental building-related environment and lighting control through the PC or mobile phone. In order to achieve the purpose of environmental monitoring and lighting control, the system should have the capabilities of data acquisition, data transmission, storage management and analysis decision-making (Song et al., 2020). Thus, the system designs the overall scheme of intelligent experimental building environment monitoring system, as shown in **Figure 1**. As can be seen from the figure, the system adopts three levels of network structure, which are the perception layer, the transport layer and the application layer. Schematic diagram of intelligent lighting monitoring scheme based on smart grid is shown in **Figure 1**.

Among them, the perception layer consists of a ZigBee network, various sensor modules, alarm modules and relay modules to build a wireless sensor network. This layer mainly solves the problem

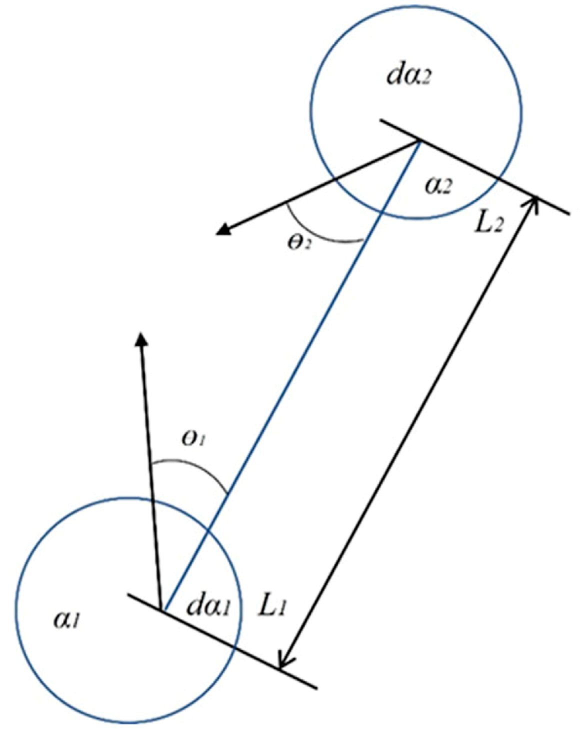

FIGURE 2
Luminous flux transfer schematic.

of interconnec-tion of the underlying wireless sensor network, which is responsible for collecting data on ambient temperature, humidity, and smoke concentration and monitoring lighting facilities Song et al. (2021). Among them, the sensor module and the ZigBee module form an endpoint node, ZigBee routes and forwards data, and the coordina-tor collects and manages data, and sends the data to the ARM-5G gateway at the transport layer (Yang et al., 2023).

4 Smart lighting overall control strategy

This topic discusses the intelligent control of indoor lighting, so we need to consider the direct illumination of the lighting source and the reflected illuminance generated by the mutual reflection between the various surfaces, so as to obtain the closest calculation results. Suppose there are two diffuse surfaces with an area of a1 and a2 with average luminous intensities of L1 and L2, respectively. According to the corresponding photometric calculation method in electrical lighting technology, the Lambert's cosine law and the inverse theorem of luminous flux transfer are followed when diffuse reflection surfaces are followed. Based on the illumination flux transfer function matrix, that is, the illuminance of each point in the room is calculated when the direct illumination of each light source and the mutual reflection illuminance of each surface in the room are considered at the same time. Luminous flux transfer schematic is shown in **Figure 2**.

Assuming that there are two points a and b in the room, it can be seen from the linear correlation between the illuminance of the indoor point and the luminous flux of each light source, and the illuminance of point a and point b are respectively:

$$E_a = g_{a1}\xi_1 + g_{a2}\xi_2 + \cdots + g_{an}\xi_m \tag{1}$$

$$E_b = g_{b1}\xi_1 + g_{b2}\xi_2 + \cdots + g_{bm}\xi_m \tag{2}$$

The ratio of illuminance is:

$$f_{ab}(E_a, E_b) = \frac{E_a}{E_b} = \frac{g_{a1}\xi_1 + g_{a2}\xi_2 + \cdots + g_{am}\xi_m}{g_{b1}\xi_1 + g_{b2}\xi_2 + \cdots + g_{bm}\xi_m} = \frac{G_a\xi^T}{G_b\xi^T} \tag{3}$$

Since the luminous flux matrix of two points a and b is fixed, the ratio of the illuminance value of any two points in the room depends on the luminous flux value output by each light source in the determined multi-light source indoor environment. In a spatial environment such as a room, when multiple light sources are known (Tran et al., 2021), the proportional relationship between the specific values of the illumination degree of any two locations in the room is related to the energy value of the light output by each light source. Therefore, when the illuminance of a point in the room (sensor detection point) is known, we can find the illuminance value of each point in the room through the luminous flux transfer function matrix.

In the design process of this project, it is necessary to place a illuminance sensor at a certain point in the room to collect light data. The selection of sensor position is related to the complexity of the intelligent control algorithm, and the better the position selection, the simpler the algorithm. In this paper, DIALux lighting design software is used to calculate and measure laboratory lighting data, which we will use to determine the optimal position of the indoor illuminance sensor and the luminous flux transfer function matrix of the indoor working surface and sensor points.

4.1 Intelligent light distribution control based on genetic algorithm

In the process of intelligent lighting control design, the luminous flux output of each light source determines the illuminance of each desktop surface, which is a one-way irreversible process. In the previous article, the luminous flux transfer function matrix model was mentioned, and here we use it to determine the effect of natural light on the illuminance of the desktop surface in the room, so as to obtain the illuminance of outdoor natural light projected onto each desktop in the room, and then compare this illumination with the given standard illuminance to determine the surface illumination required by each desktop from artificial lighting fixtures (Soheilian et al., 2021). Although the luminous flux output by each light source is a fixed value, it is not easy to determine it. Therefore, in the research process of this topic, the genetic algorithm of no dominated ranking (NSGA) was used to study the desktop equilibrium illumination optimization distribution model Tavares et al. (2021).

The main difference between NSGA and simple genetic algorithms is that the algorithm is layered according to the dominance relationship between individuals before the

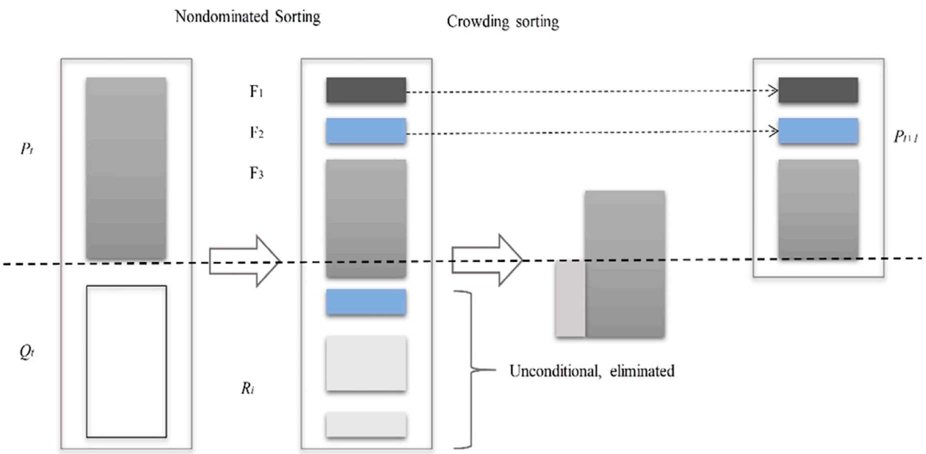

FIGURE 3
Schematic diagram of the NSGA-II algorithm flow.

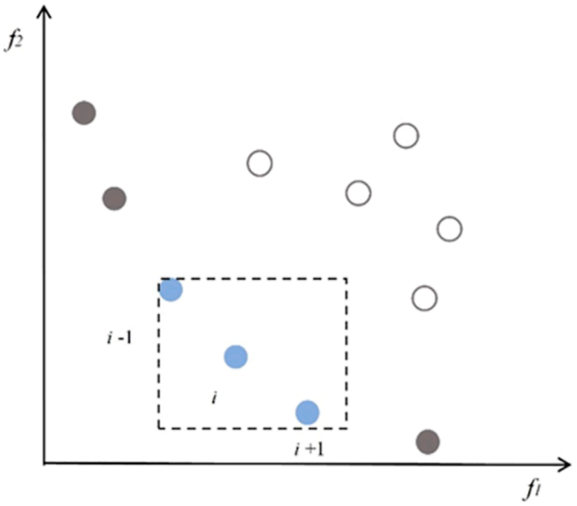

FIGURE 4
Crowding of individual i.

selection operator is executed. The following is added: Non-Dominated Sorting Genetic Algorithm (NSGA) is a multi-objective optimization algorithm for finding the Pareto optimal solution set among multiple objective functions. The core idea of NSGA algorithm is to stratify each individual in the population according to the number of times other individuals dominate it The core idea of NSGA algorithm is to stratify each individual in the population according to the number of times it is dominated by other individuals, i.e., to rank the individuals in the population non-dominantly. By grouping individuals and calculating the crowding degree of individuals in each group, the NSGA algorithm can converge the solution set to the Pareto optimal solution set while maintaining the diversity of solution sets.

The optimization process of the NSGA algorithm can be divided into the following steps:

1. Initialize the population: Randomly generate the initial population of individuals.
2. Calculate fitness: Calculate the fitness value of each individual under each objective function.
3. Non-dominance ranking: Each individual in the population is stratified according to the number of times other individuals, i.e., dominate it, non-dominance ranking is performed.
4. Calculate crowding degree: For each individual in the hierarchy, calculate its crowding degree under a specific objective function.
5. Selection operation: Selecting the next-generation of individuals. When selecting the next-generation of individuals, the individuals with higher non-dominance levels and higher crowding degrees are preferred.
6. Crossover and mutation operations: Crossover and mutation operations are performed on the selected individuals to generate the next-generation of individuals.
7. Repeat steps 2-6 until the stopping condition (e.g., the maximum number of iterations or the Pareto optimal solution set is found).

In adaptive energy-saving control of building lighting, the NSGA algorithm can optimize multiple objective functions, such as illuminance, colour temperature, and colour reproduction, to obtain the best lighting solution. With the NSGA algorithm, energy consumption can be minimized while maintaining lighting quality within acceptable limits. In practical applications, NSGA algorithms can be used with sensor networks and intelligent control systems to achieve adaptive lighting control.

To optimize the NSGA algorithm to save energy, the following measures can be taken:

1. Optimize parameter settings: Select appropriate genetic algorithms parameters, such as population size, crossover and variation probability, to improve the convergence speed and efficiency of the algorithm.
2. Improving the selection strategy: choosing suitable selection strategies, such as tournament selection, roulette wheel selection, etc., to improve the selection efficiency of the algorithm.

3. Variable constraints for multi-objective optimization problems: Set appropriate variable constraints for multi-objective optimization problems to improve the stability and reliability of the algorithm and avoid unreasonable solutions.

4. Improvement of crossover and variational operations: Improve the crossover and variational operations to improve the convergence speed and efficiency of the algorithm.

NSGA algorithm can find the multi-objective optimization algorithm of the Pareto optimal solution set among multiple objective functions. In adaptive energy-saving control of building lighting, the NSGA algorithm can optimize multiple objective functions to obtain the best lighting solution and further improve the algorithm efficiency and energy saving by optimizing algorithm parameters, selection strategies, variable constraints and crossover and variation operations.

$$s(d(x,y)) = \begin{cases} 1 - \left(\dfrac{d(x,y)}{\sigma_{\text{share}}} \right) \\ 0 \end{cases} \tag{4}$$

The sharing mode can be divided into fitness sharing in the coding space, fitness sharing in the decision variable space, and fitness sharing in the objective function space. First, a parent population is randomly initialized, and all individuals are sorted by monodominance and a fitness value can be specified, which can be specified that the fitness value is equal to its monodominant order, then 1 is the best fitness value. Then, selective, cross, and mutation operators are used to produce the next-generation of population, with a size of N. Schematic diagram of the NSGA-II algorithm flow is shown in Figure 3.

As shown in Figure 3, the new population generated by the *t* generation is first merged with the parent generation to form, and the population size is 2N. Then a no dominated sort is performed, resulting in a series of disdominated sets and calculating crowding. New offspring populations are then generated by genetic operators (selection, crossover, mutation). When the number of individuals in the disdominated set produced by the sorting is sufficient to fill, it is not necessary to continue sorting the remaining parts. The diversity of no dominated solutions is guaranteed by crowding comparison operators and does not require additional shared parameters. By hierarchical storage of all individuals in the current solution and population, the best individuals are not lost.

In the original NSGA, we used a sharing function to ensure the diversity of the population, but this required the decision maker to specify the value of the shared radius. To solve this problem, we propose the concept of crowding: the density of surrounding individuals at a given point in the population, which indicates the smallest rectangle around individual i that contains individual *i* itself but no other individuals, as shown in Figure 4.

From Figure 4, we can see that a small value indicates that the surrounding area of the individual is crowded. In order to maintain population diversity, we need a relatively crowded operator to ensure that the algorithm converges to a uniformly distributed Pareto surface.

As shown in the Algorithm 1 is the flow chart of the Non-dominated sorting genetic algorithm.

```
Input: Population size $N$; number of generations $G$; crossover probability $P_c$;
    mutation probability $P_m$; number of objectives $M$
Output: Pareto-optimal solutions
Initialize population $P_0$ of size $N$;
for $g \leftarrow 1$ to $G$ do
    Calculate fitness of each individual in $P_g$;
    Divide $P_g$ into fronts $F_1, F_2, ..., F_n$ based on non-domination;
    $Q \leftarrow \emptyset$;
    $i \leftarrow 1$;
    while $|Q| + |F_i| \leq N$ do
        Perform binary tournament selection within $F_i$ to select parents;
        Perform crossover and mutation to create offspring;
        Add offspring to $Q$;
    end
    Sort $F_i$ based on crowding distance;
    Select remaining individuals for next generation based on crowding distance;
    $P_{g+1} \leftarrow Q$;
end
```

Algorithm 1. Non-dominated Sorting Genetic Algorithm.

5 Experiment

5.1 Datasets

The experimental environment has four windows facing south, and a window facing west, the building dimensions in the room are 12 m, 5 m and 3 m in length, width and height, the reflection ratio of the ceiling, wall and ground is 0.6, 0.4, 0.2, respectively, a total of 8 sets of dimmable fluorescent lamps are installed in the room, each set is two 18W fluorescent lamps and an LED lamp installed in the middle of the two fluorescent lamps. The paper is simulated based on software designed by DIALux, replacing the intensity of the outdoor sensor based on changes in the light intensity of the table outside the window. If we assume that there are two planes in the room that can be diffuse reflection, 01 (placed in the plane of the external sensor) and A2 (placed in the plane of the sensor inside the room), then the general energy of the illumination of 01 irradiating Q2 and the brightness of 01 are directly proportional and have a certain relationship with the inclination angle. At the same time, because the light flux of the sensor position placed indoors and the light degree of the sensor placed outdoors are in a linear proportional relationship, plus the irradiation range is known, the light intensity between the two is also linear to a certain extent. Based on the above theory, this paper is based on the software designed by DIALux to simulate the natural lighting situation that occurs at every moment of life (and the light energy emitted by the lamp does not count), and calculate the corresponding indoor sensor illuminance and outdoor sensor approximate illumination at each time point, and obtain data from 6 a.m. to 6 p.m., as shown in Table 1.

In this project, sunny and cloudy weather were selected for experiments, and relevant weather data were obtained, and then this data was brought into the above moderate function formula for calculation, and the power change of each lamp and the illuminance change of each desktop surface were measured. By bringing the collected data into the matrix moderation function formula mentioned above, the influence of natural light on the illumination can be obtained. Finally, through the distribution model of illumination and the distribution model of the neural network to calculate the lighting data of these two different weathers, the consumption of room lamps will be obtained by comparing the two sets of data, and the power of the lamps at this time and

TABLE 1 Working surface luminous flux transfer function matrix.

Luminous flux function	Luminous flux transfer function matrix artificial light source function								Natural light transfer function
G1	1.0200	0.0000	0.3164	10.571	0.0371	0.3008	10.571	0.0716	4.4731
G2	0.9059	0.0000	0.4456	7.3139	0.0000	0.4668	7.3139	0.0874	3.7009
G3	0.6978	0.0476	0.8299	2.2541	0.0849	0.3518	2.2541	0.1914	3.7738
G4	0.5208	0.1435	2.3142	0.6357	0.1533	0.6566	0.6357	0.3947	4.6848.
G5	0.3736	0.8348	10.232	0.1554	0.2878	0.3468	0.1554	0.7042	4.8257
…	…	…	…	…	…	…	…	…	…
G14	0.2404	0.6681	0.7299	0.5817	6.6614	0.3740	0.5817	3.5706	1.0163
G15	0.3285	2.4157	0.7201	0.7299	1.9951	3.5706	0.7299	9.3448	0.8784
G16	0.6581	7.5688	0.5531	0.7201	0.4541	9.3448	0.7201	8.7557	0.7971

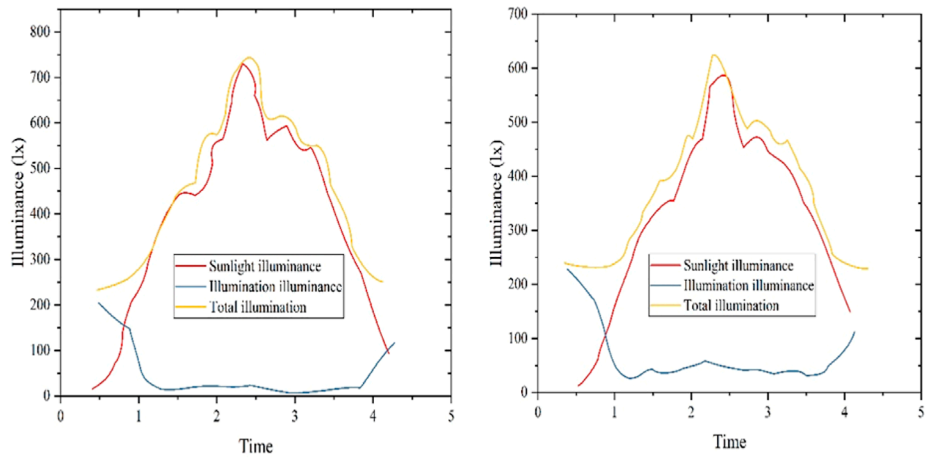

FIGURE 5
Daylight illuminance variation chart in cloudy weather.

the illuminance of the artificial light source on the desktop can be further calculated, and the total illumination of the desktop can be obtained by adding the two. **Figure 5** shows lighting in cloudy conditions and **Figure 6** shows lighting on sunny days. As can be seen from the figure, the illuminance of the room varies greatly in these two weathers.

Without using any lighting control system, simply turn on all the lighting fixtures, the total power of the luminaire is 450W. When we only use the window to introduce natural light, the row of lamps closest to natural light will generally turn off, and the natural luminosity will change over time due to the operation of the earth, and the average total power for 8 h is 220W. The average power of enabling intelligent lighting control for 8 h in a multi-cloud environment is 210W, while the average power of enabling intelligent lighting control for 8 h in a clear sky environment is 115W, because the use of intelligent lighting control can reduce the output luminous flux of the luminaire and reduce the power used by the luminaire. Of course, if we want to achieve overall lighting comfort, adaptive intelligent lighting control will highlight its advantages.

5.2 Experimental results and analysis

In the third chapter, we introduce the adaptive intelligent control based on the non-dominated ranking genetic algorithm to achieve the illumination of indoor desktop surface, and finally use the program to achieve the optimal balance of desktop lighting. The test of system energy consumption verifies the practicality of the scheme in energy consumption optimization. In order to further compare the efficiency of the scheme, we compare the scheme with the existing extreme value search algorithm based on gradient method. According to the experimental results, we make the change plot of the illumination of the two algorithms over time as shown in **Figure 7**, and the relationship between the two algorithms of E-T is shown in **Figure 8**, and we put the illumination and output of the two algorithms on a graph respectively in order to visually compare. In **Figure 8**, we made two error bars, one with an error bar of 5{%}E, which is the solid red line in the figure, and the other with an error bar of 27{%} E, which is the green line in the figure. The purpose of marking these two lines is to give a visual comparison between the results of the search experiment and the results of the traversal

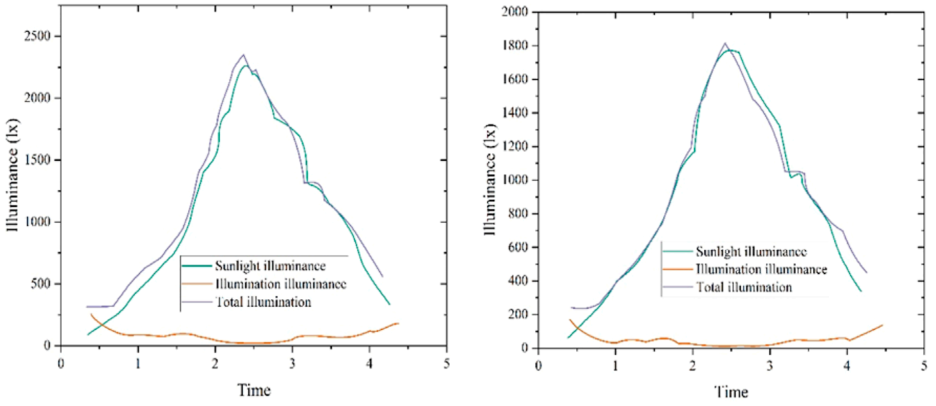

FIGURE 6
Illuminance change curve of each desktop during daylight on a sunny day.

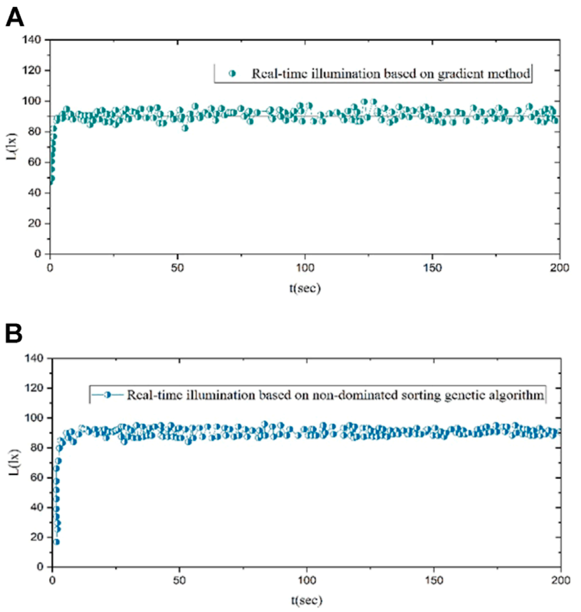

FIGURE 7
Schematic diagram of light variation curve with time. (**(A)** The gradient method is used to search the illumination variation diagram with time; **(B)** Time-dependent graph of illumination for genetic search based on non-dominated sequencing).

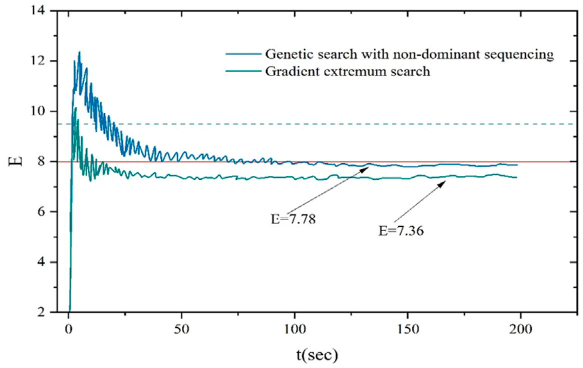

FIGURE 8
Schematic diagram of E-t relationship change.

experiment. Schematic diagram of light variation curve with time is shown in **Figure 7**. Schematic diagram of E-t relationship change is shown in **Figure 8**.

As can be seen from **Figure 7**, the real-time illumination value change under the two algorithms is basically stable near the set value. It can be seen from **Figure 8** that the energy consumption of the gradient-based extreme value search algorithm is basically stable at about 7.78 after 80 s, and the energy consumption of the no dominated ranking genetic algorithm is basically stable at about 7.36 after 30 s. In the energy-saving control of intelligent lighting system, the time required to search for the relative minimum energy consumption based on the no dominated ranking genetic algorithm is significantly less than that based on the gradient method extreme value search algorithm. This shows that the search rate based on the no dominated ranking genetic algorithm is faster than that based on the gradient method extremum search algorithm. Compared with the relative minimum energy consumption value searched, the relative minimum energy consumption value searched based on the no dominated ranking genetic algorithm is smaller than that based on the gradient method extreme value search algorithm, indicating that the no dominated ranking genetic algorithm is better in terms of energy saving effect. In the traversal experiment, we obtain a relative minimum energy consumption value of 7.4658, and the calculation results by the error show that the search results based on the no dominated sorting genetic algorithm are closer to the results of the traversal experiment.

In **Figure 9**, we compare "pure fuzzy control" (Diethorn, 2021), "genetic algorithms" (Luo and Oyedele, 2021), "BP neural networks" (Liu et al., 2019), "adaptive fuzzy control" (Wei et al., 2021), "Mou et al. (Moudgil et al., 2023)", "Rou et al." (Roumi et al., 2023), and "Yaz et al. (Yazdanpanah, 2023)" There are a total of 8 models with

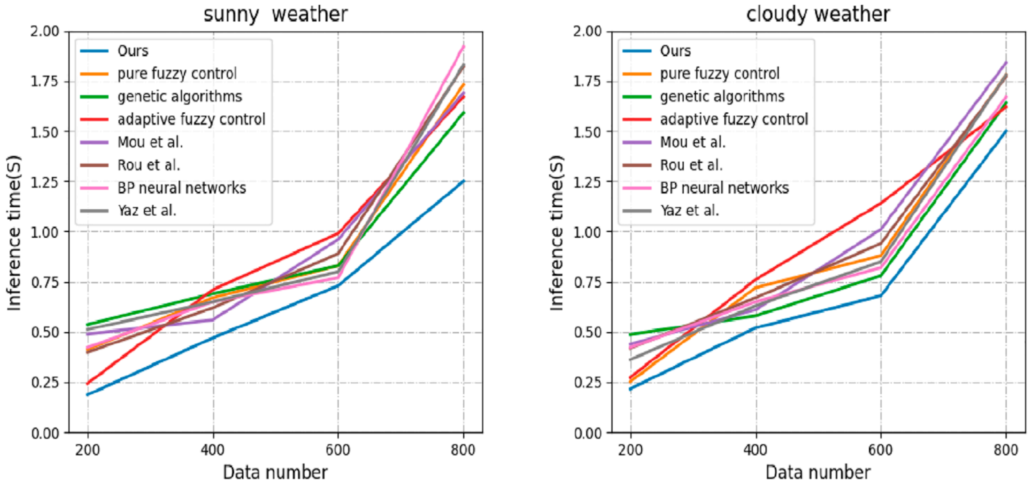

FIGURE 9
Comparison of inference speed of different models under different conditions (the left picture is the data obtained under sunny weather, and the right picture is the data obtained under cloudy sky).

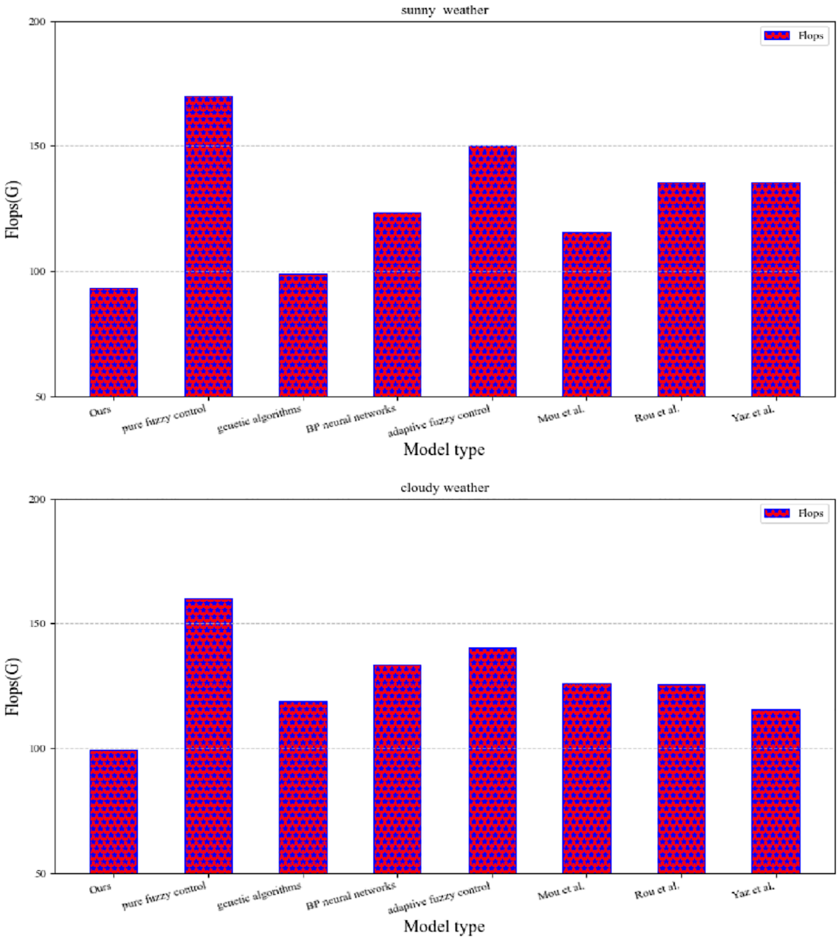

FIGURE 10
Comparison of calculation amount of different models (the picture above shows the data under a sunny day, and the picture below shows the data under a cloudy day).

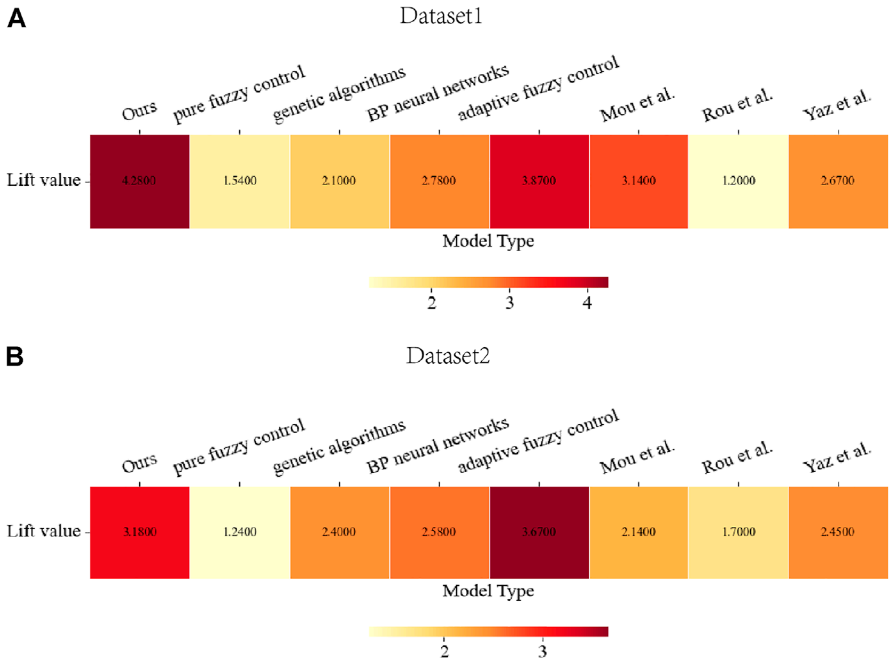

FIGURE 11
Comparison of Lift values of different models on different datasets [Picture **(A)** is the data obtained from Dataset 1 on sunny days, and Picture **(B)** is the data obtained from Dataset 2 on cloudy days. The larger the Lift value (lift index), the better the model. better].

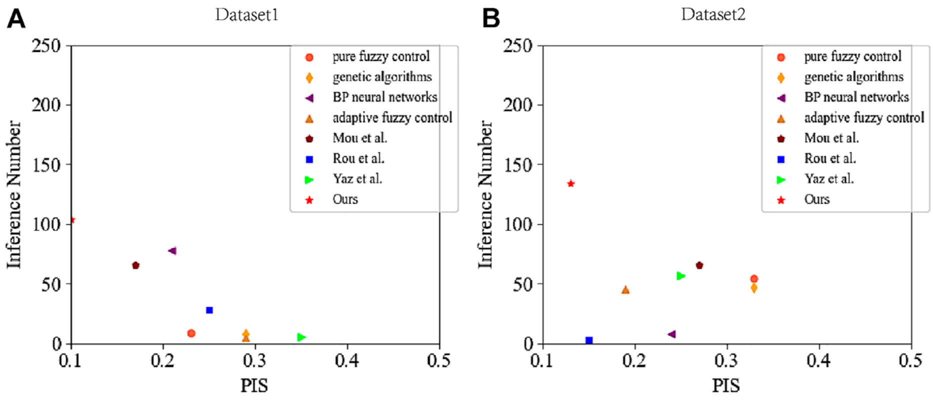

FIGURE 12
Changes in the stability index (PIS) of different models when the number of inferences is different [Picture **(A)** is from the data collected on sunny days in Dataset 1, It is a relatively simple data set, and picture **(B)** is from the data collected on cloudy days in data set 2, which is a relatively complex data set].

our model. With the increase in the number of inferences, the change of inference time needs to consider the characteristics of real-time response and adjustment of architectural lighting adaptive energy-saving control. Our model is compared with other models on different data sets. , have better performance in terms of inference speed. The reasoning speed is faster, indicating that the data processing capability of the model is stronger. The adaptive energy-saving control of architectural lighting needs to monitor and analyze various factors (such as the light intensity inside and outside the building, temperature, humidity, etc.), and the artificial intelligence model needs to have strong Data processing capabilities to obtain accurate and effective data information. Therefore, our model has a strong fit for this study.

In Figure 10, we compared the calculation amount of data obtained by different models under different weather conditions. The smaller the calculation amount of a model, the less data it processes, the simpler the model structure and the corresponding model, and The better the performance; it can be seen from the figure that no matter the data set, our model has the smallest amount of calculation, which can provide conditions for faster reasoning and training speed.

In Figure 11, we compare “Ours”, “pure fuzzy control”, “genetic algorithms”, “BP neural networks”, “adaptive fuzzy control”, “Mou

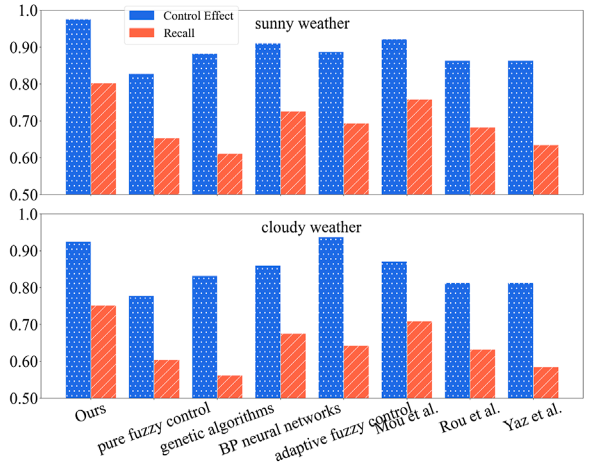

FIGURE 13
Comparison of the control effect and recall rate of different models (dataset 1 is the data collected on sunny days, which is a relatively simple data set, and data set 2 is the data collected on cloudy days, which is a relatively complex data set).

et al.", "Rou et al.", "Yaz et al." The Lift values of a total of 8 models. The Lift value measures the performance of a classification model, which describes how well the model's predictions compare to random guessing. A Lift value greater than 1 indicates that the model performs better than random guessing, while a Lift value less than 1 indicates that the model does not perform as well as random guessing. Lift values are often used to evaluate classification models in scenarios such as marketing or recommender systems, such as advertisement click-through rate prediction and product purchase probability prediction, etc. In these scenarios, the goal of the model is to identify those users who are interested or have purchase intentions as much as possible to improve recommendations' accuracy and transaction rate. Therefore, the Lift value is also an important indicator to measure the running effect of a model. It can be seen from the figure that the Lift value (lift index) of our model is higher than that of other models in both dataset 1 and dataset 2., showing good performance.

For example, process 2 is the running process of our model. First input the data set Dataset "sunny weather", "cloudy weather", then perform Feature extraction and Pre-training, then input the data into the NSGA network and smart grid for training, and finally repeat the training process through a series of calculations to complete the network train.

In Figure 12, we compare the stability indicators of different models in different data sets. The Population Stability Index (PSI) is an indicator used to measure the stability between two groups, usually in evaluating risk models or other predictive model performance. It can help us determine whether a model has consistent predictive power over different periods or across different sample populations. The smaller the PSI value, the smaller the distribution difference between the new data set and the historical data set, and the better the stability of the model. A PSI value less than 0.10 indicates good model stability, while a value greater than 0.25 indicates poor model stability. It can be seen from the figure that when our model has a large number of inferences, its stability index is still within a good index, and it is suitable for simple and complex data sets and has strong generalization.

```
Input: Dataset "sunny weather", "cloudy weather"
Output: Trained network "NSGA"
Step 1: Feature extraction
    Extract features from the input images using a pre-trained convolutional neural network (CNN).
Step 2: Pre-training
    Train the feature extractor using unsupervised pre-training, such as autoencoder, to learn better representations of the input data.
Step 3: Transfer learning
    Fine-tune the pre-trained feature extractor on the "sunny weather" dataset to adapt it to the specific domain.
Step 4: Non-dominated sorting genetic algorithm (NSGA)
    Use NSGA to optimize the network's architecture and hyperparameters for multi-objective performance, such as accuracy and efficiency.
Step 5: Smart grid
    Use a smart grid to search for the optimal hyperparameters of the network, such as learning rate and batch size.
Step 6: Loss calculation
    Calculate the loss of the network using a specific loss function, such as cross-entropy or mean squared error.
Step 7: Parameter update
    Update the parameters of the network using an optimization algorithm, such as stochastic gradient descent (SGD).
Step 8: Warm start
    Use a warm start strategy to initialize the network's parameters for faster convergence.
Step 9: Adversarial training
    Train the network with adversarial examples to improve its robustness to input perturbations.
Step 10: Repeat
    Repeat Steps 4-9 until the network achieves satisfactory performance on the "cloudy weather" dataset.
```

Algorithm 2. Training process of network "NSGA".

Figure 13 compares different models' control effects and recall rates on different data sets. The control effect of the model is one of the most important indicators to evaluate the adaptive energy-saving control model of architectural lighting, that is, the brightness and

TABLE 2 Performance evaluation of different methods.

Method	Inference Time(s) ↓	Flops(G) ↑	Lift ↑	PIS ↓	Control Effect (%) ↑	Recall (%) ↑
pure fuzzy control (Diethorn, 2021)	0.412 ± 0.05	170.02 ± 0.04	1.54 ± 0.01	0.23 ± 0.06	82.78 ± 0.11	65.39 ± 0.09
genetic algorithms (Luo and Oyedele, 2021)	0.537 ± 0.07	98.76 ± 0.08	2.10 ± 0.03	0.29 ± 0.09	88.23 ± 0.08	61.17 ± 0.04
BP neural networks (Liu et al., 2019)	0.243 ± 0.08	123.45 ± 0.07	2.78 ± 0.02	0.21 ± 0.07	79.34 ± 0.02	72.56 ± 0.03
adaptive fuzzy control (Wei et al., 2021)	0.489 ± 0.03	150.10 ± 0.03	3.87 ± 0.01	0.29 ± 0.05	91.04 ± 0.09	69.32 ± 0.06
Mou et al. (Moudgil et al., 2023)	0.398 ± 0.04	115.67 ± 0.09	3.14 ± 0.01	0.17 ± 0.02	88.76 ± 0.05	75.89 ± 0.08
Rou et al. (Roumi et al., 2023)	0.422 ± 0.06	135.31 ± 0.06	1.20 ± 0.02	0.25 ± 0.03	92.13 ± 0.07	68.23 ± 0.04
Yaz et al. (Yazdanpanah, 2023)	0.512 ± 0.09	135.31 ± 0.04	2.67 ± 0.03	0.35 ± 0.08	86.34 ± 0.06	63.45 ± 0.03
Ours	**0.187** ± 0.02	**93.21** ± 0.05	**4.28** ± 0.03	**0.1** ± 0.01	97.56 ± 0.04	**80.21** ± 0.07

The values marked in black in the table represent the best performance.

switch of the light controlled by the model. The degree to which the status matches the actual needs. The recall rate of the model is used to measure the ability of the model to identify positive samples, that is, how many real positive examples the model can correctly find. It is also one of the important indicators to measure the model. As can be seen from **Figure 13**, whether our model is in data set 1 or data set 2, its control effect and recall rate are greater than other models, showing a good performance. The effect can effectively deal with this problem.

In **Table 2**, we summarize the previous comparisons, mainly composed of accuracy, calculation amount, and parameter amount, and mark the literature we refer to in different models. Our model is superior to other models in terms of accuracy, computation, and parameters, and we can have a more comprehensive and intuitive understanding of our model.

6 Conclusion and discussion

This paper proposes applying a smart grid and non-dominated sorting genetic algorithm in adaptive energy-saving control of architectural lighting, which can solve the energy-saving problem of architectural lighting. Data, combined with a non-dominated sorting genetic algorithm, which supports unconstrained and constrained problems; can effectively deal with multi-objective problems; effectively maintain diversity; high search efficiency and good accuracy. It is used to solve the problem of optimizing multiple objective functions simultaneously, which can effectively help solve the power system scheduling problem. In the experiment, we compared our model with other models. The results show that our model has the advantages of faster reasoning speed, lower calculation load, and the highest control rate and recall rate. It has a good operating effect and can Effectively solve the problem of adaptive energy-saving control of architectural lighting.

However, our method also has some limitations, such as parameter adjustment difficulties: non-dominated sorting genetic algorithm needs to set a series of parameters, such as population size, crossover probability, mutation probability, etc., and the adjustment of these parameters may have an important impact on the performance of the algorithm. Influence, but it is difficult to determine the optimal value intuitively. The optimization process of the non-dominated sorting genetic algorithm is relatively complicated, and its results are difficult to explain intuitively, which may cause difficulties for users to understand. To solve these problems, consider optimizing the model, using the form of a combined model, combining the advantages of each model to make the model work better.

Presently, lighting energy saving has been paid attention to by countries worldwide, and some developed countries have formulated green lighting plans. Relevant departments of the United Nations have also proposed developing intelligent lighting buildings with scientific and advanced lighting technology, which shows the significance of lighting energy-saving research. This paper counts the power data of the intelligent lighting system under different weather conditions through simulation experiments. By comparing the power data of other different lighting control methods, it is found that the intelligent lighting system maximizes the utilization of natural light and achieves the purpose of maximum energy saving without affecting normal lighting, which provides a theoretical basis for the intelligent lighting system. Promote the lighting control system based on the DALI protocol. The system designed in this paper is an intelligent lighting system, but there still needs to be a big gap from real intelligence. In this paper, grouping control of lamps is carried out, but grouping is only artificial grouping, which is not allowed in practical applications, and many factors need to be considered. For example, indoor facilities, the main activity area of personnel, etc. These are the difficulties that need to be solved in the later stage.

Data availability statement

The raw data supporting the conclusions of this article will be made available by the authors, without undue reservation.

Author contributions

Contributions YW, SH, and CG contributed to the conception and design of the study. YW organized the database. SH performed the statistical analysis. CG wrote the first draft of the manuscript. YW, SH, and CG wrote sections of the manuscript.

All authors contributed to the article and approved the submitted version.

Funding

2021 Jiangsu University Blue Project excellent young backbone teacher training project funded (RCQL202102); 2020 Nanjing Vocational Institute of Railway Technology "Blue Project" excellent young backbone teacher training project (RCQL20205).

Conflict of interest

SH and CG were empolyed by Nari Technology Co., Ltd.

The remaining author declares that the research was conducted in the absence of any commercial or financial relationships that could be construed as a potential conflict of interest.

Publisher's note

References

Antoine, G., Mikeka, C., Bajpai, G., and Jayavel, K. (2021). Speed management strategy: Designing an iot-based electric vehicle speed control monitoring system. *Sensors* 21, 6670. doi:10.3390/s21196670

Cai, W., Ning, X., Zhou, G., Bai, X., Jiang, Y., Li, W., et al. (2022). A novel hyperspectral image classification model using bole convolution with three-direction attention mechanism: Small sample and unbalanced learning. *IEEE Trans. Geoscience Remote Sens.*, 61, 1, 17. doi:10.1109/tgrs.2022.3201056

Chen, B.-R., Liu, Z., Song, J., Zeng, F., Zhu, Z., Bachu, S. P. K., et al. (2022). Flowtele: Remotely shaping traffic on internet-scale networks. In Proceedings of the 18th International Conference on emerging Networking EXperiments and Technologies. 349–368.

Cheng, K., Huang, Z., Wang, P., Sun, L., Ghasemi, H., Ardebili, H., et al. (2023). Antibacterial flexible triboelectric nanogenerator via capillary force lithography. *J. Colloid Interface Sci.* 630, 611–622. doi:10.1016/j.jcis.2022.10.129

Diethorn, J. A. (2021). *Implementation of fuzzy logic control into an equivalent minimization strategy for adaptive energy management of A parallel hybrid electric vehicle* (West Virginia University)

Fei, J., Yang, J., Liang, L., Meng, C., and Mei, S. (2023). Exploring the impact of emotional and cognitive factors on anxiety symptoms of Chinese adolescents: A serial mediation study. *IEEE Internet Things J.*, 1, 15. doi:10.1007/s11469-022-01004-8

Ge, Y., Song, B., Pei, Y., Mollet, Y., and Gyselinck, J. (2019). A fuzzy logic based method for fault tolerant hierarchical load management of more electric aircraft. *Proc. Institution Mech. Eng. Part G J. Aerosp. Eng.* 233, 3846–3856. doi:10.1177/0954410018807598

Han, J.-X., Ma, M.-Y., and Wang, K. (2021). Retracted article: Product modeling design based on genetic algorithm and BP neural network. *Neural Comput. Appl.* 33, 4111–4117. doi:10.1007/s00521-020-05604-0

He, F., and Ye, Q. (2022). A bearing fault diagnosis method based on wavelet packet transform and convolutional neural network optimized by simulated annealing algorithm. *Sensors* 22, 1410, doi:10.3390/s22041410

Li, C., Chen, Z., and Jiao, Y. (2023). Vibration and bandgap behavior of sandwich pyramid lattice core plate with resonant rings. *Materials* 16, 2730, doi:10.3390/ma16072730

Liu, B., Zhang, L., Wang, F., Liu, M., Mao, Y., Zhao, L., et al. (2019). Adaptive dynamic wavelength and bandwidth allocation algorithm based on error-back-propagation neural network prediction. *Opt. Commun.* 437, 276–284. doi:10.1016/j.optcom.2018.12.064

Long, J., Wu, S., Han, X., Wang, Y., and Liu, L. (2023). Autonomous task planning method for multi-satellite system based on a hybrid genetic algorithm. *Aerospace* 10, 70, doi:10.3390/aerospace10010070

Luo, X., and Oyedele, L. O. (2021). Forecasting building energy consumption: Adaptive long-short term memory neural networks driven by genetic algorithm. *Adv. Eng. Inf.* 50, 101357, doi:10.1016/j.aei.2021.101357

Moudgil, V., Hewage, K., Hussain, S. A., and Sadiq, R. (2023). Integration of iot in building energy infrastructure: A critical review on challenges and solutions. *Renew. Sustain. Energy Rev.* 174, 113121, doi:10.1016/j.rser.2022.113121

Nazari, M., Nazifi, S., Huang, Z., Tong, T., Ouro-Koura, H., Bao, J., et al. (2020). Surface tension nanogates for controlled ion transport. *ACS Appl. Nano Mater.* 3, 6979–6986. doi:10.1021/acsanm.0c01304

Ning, X., Tian, W., He, F., Bai, X., Sun, L., and Li, W. (2023). Hyper-sausage coverage function neuron model and learning algorithm for image classification. *Pattern Recognit.* 136, 109216, doi:10.1016/j.patcog.2022.109216

Niu, H., Lin, Z., Zhang, X., and Jia, T. (2022). Image segmentation for pneumothorax disease based on based on nested unet model. In *2022 3rd international conference on computer vision, image and deep learning & international conference on computer engineering and applications* (CVIDL & ICCEA) (IEEE) 756–759.

Özçelik, M. A. (2018). The design and comparison of central and distributed light sensored smart led lighting systems. *Int. J. Photoenergy* 2018, 1–14. doi:10.1155/2018/4589085

Rehman, G. U., Zubair, M., Qasim, I., Badshah, A., Mahmood, Z., Aslam, M., et al. (2023). Ems: Efficient monitoring system to detect non-cooperative nodes in iot-based vehicular delay tolerant networks (vdtns). *Sensors* 23, 99, doi:10.3390/s23010099

Roumi, S., Zhang, F., Stewart, R. A., and Santamouris, M. (2023). Weighting of indoor environment quality parameters for occupant satisfaction and energy efficiency. *Build. Environ.* 228, 109898, doi:10.1016/j.buildenv.2022.109898

Soheilian, M., Fischl, G., and Aries, M. (2021). Smart lighting application for energy saving and user well-being in the residential environment. *Sustainability* 13, 6198, doi:10.3390/su13116198

Song, Z., Johnston, R. M., and Ng, C. P. (2021). Equitable healthcare access during the pandemic: The impact of digital divide and other sociodemographic and systemic factors. *Appl. Res. Artif. Intell. Cloud Comput.* 4, 19–33.

Song, Z., Mellon, G., and Shen, Z. (2020). Relationship between racial bias exposure, financial literacy, and entrepreneurial intention: An empirical investigation. *J. Artif. Intell. Mach. Learn. Manag.* 4, 42–55.

Tavares, P., Ingi, D., Araújo, L., Pinho, P., and Bhusal, P. (2021). Reviewing the role of outdoor lighting in achieving sustainable development goals. *Sustainability* 13, 12657, doi:10.3390/su132212657

Tran, T., Baroutaji, A., Estrada, Q., Arjunan, A., Le, H., and Thien, N. (2021). Crashworthiness analysis and optimization of standard and windowed multi-cell hexagonal tubes. *Struct. Multidiscip. Optim.* 63, 2191–2209. doi:10.1007/s00158-020-02794-y

Wei, C., Chen, Y., Li, X., and Lin, X. (2022). Integrating intelligent driving pattern recognition with adaptive energy management strategy for extender range electric logistics vehicle. *Energy* 247, 123478. doi:10.1016/j.energy.2022.123478

Wei, C., Sun, X., Chen, Y., Zang, L., and Bai, S. (2021). Comparison of architecture and adaptive energy management strategy for plug-in hybrid electric logistics vehicle. *Energy* 230, 120858. doi:10.1016/j.energy.2021.120858

Wu, S., Wang, J., Ping, Y., and Zhang, X. (2022). Research on individual recognition and matching of whale and dolphin based on efficientnet model. In *2022 3rd international conference on big data, artificial intelligence and internet of things engineering* (ICBAIE) (IEEE) 635–638.

Xiang, C., Wu, Y., Shen, B., Shen, M., Huang, H., Xu, T., et al. (2019). Towards continuous access control validation and forensics. In *Proc. 2019 ACM SIGSAC Conf. Comput. Commun. Secur.* 113–129. doi:10.1145/3319535.3363191

Yang, Z., Sun, L., Sun, Y., Dong, Y., and Wang, A. (2023). A conceptual model of home-based cardiac rehabilitation exercise adherence in patients with chronic heart failure: A constructivist grounded theory study. *Patient Prefer. adherence* 17, 851, 860. doi:10.2147/ppa.s404287

Yazdanpanah, F. (2023). A low-power wnoc transceiver with a novel energy consumption management scheme for dependable iot systems. *J. Parallel Distributed Comput.* 172, 144–158. doi:10.1016/j.jpdc.2022.10.010

Zhang, H., Zhang, F., Gong, B., Zhang, X., and Zhu, Y. (2023). The optimization of supply chain financing for bank green credit using stackelberg game theory in digital economy under internet of things. *J. Organ. End User Comput. (JOEUC)* 35, 1–16. doi:10.4018/joeuc.318474

Zhang, L., Sun, L., Li, W., Zhang, J., Cai, W., Cheng, C., et al. (2021). A joint bayesian framework based on partial least squares discriminant analysis for finger vein recognition. *IEEE Sensors J.* 22, 785–794. doi:10.1109/jsen.2021.3130951

Zhong, J., Hu, S., Wang, Z., and Han, Z. (2023). A cascade bp neural network tuned pid controller for a high-voltage cable-stripping robot. *Micromachines* 14, 689, doi:10.3390/mi14030689

Zhu, T., Yang, Y., Yao, X., Huang, Z., Liu, L., Hu, W., et al. (2020). Solution-processed polymeric thin film as the transparent electrode for flexible perovskite solar cells. *ACS Appl. Mater. interfaces* 12, 15456–15463. doi:10.1021/acsami.9b22891

frontiers | Frontiers in Energy Research

TYPE Original Research
PUBLISHED 31 July 2023
DOI 10.3389/fenrg.2023.1182287

OPEN ACCESS

EDITED BY
Aneela Jaffery,
Pakistan Institute of Engineering and Applied Sciences, Pakistan

REVIEWED BY
Farah Shahid,
University of Agriculture, Faisalabad, Pakistan
Muhammad Asif Zahoor Raja,
National Yunlin University of Science and Technology, Taiwan

*CORRESPONDENCE
Haibo Li,
✉ lihb@sie.edu.cn

RECEIVED 08 March 2023
ACCEPTED 11 July 2023
PUBLISHED 31 July 2023

CITATION
Pang X, Sun W, Li H, Ma Y, Meng X and Liu W (2023), Ultra-short-term power load forecasting method based on stochastic configuration networks and empirical mode decomposition.
Front. Energy Res. 11:1182287.
doi: 10.3389/fenrg.2023.1182287

Ultra-short-term power load forecasting method based on stochastic configuration networks and empirical mode decomposition

Xinfu Pang[1,2], Wei Sun[1,3], Haibo Li[1]*, Yihua Ma[1], Xiangbin Meng[1] and Wei Liu[1]

[1]Key Laboratory of Energy Saving and Controlling in Power System of Liaoning Province, Shenyang Institute of Engineering, Shenyang, China, [2]School of Computer Science and Informatics, De Montfort University, Leicester, United Kingdom, [3]Fuxin Power Supply Company, State Grid Liaoning Electric Power Co., Ltd., Fuxin, China

Ultra-short-term power load forecasting (USTPLF) can provide strong support and guarantee the decisions on unit start-up, shutdown, and power adjustment. The ultra-short-term power load (USTPL) has strong non-smoothness and nonlinearity, and the time-series characteristics of the load data themselves are difficult to explore. Therefore, to fully exploit the intrinsic features of the USTPL, a stochastic configuration networks (SCNs) USTPLF method based on *K*-means clustering (*K*-means) and empirical mode decomposition (EMD) is proposed. First, the load data are decomposed into several intrinsic mode functions (i.e., IMFs) and residuals (i.e., Res) by EMD. Second, the IMFs are classified by *K*-means, and the IMF components of the same class are summed. Third, the SCNs is used to forecast the electric load on the basis of the classified data. Lastly, on the basis of the real load of Shenzhen City, the proposed method is applied for emulation authentication. The result verifies the efficiency of the proposed measure.

KEYWORDS

ultra-short-term power load forecasting, feature extraction, stochastic configuration networks, empirical mode decomposition, *K*-means clustering

1 Introduction

1.1 Literature review

Ultra-short-term power load forecasting (USTPLF) is an essential reference for real-time dispatching orders and a fundamental basis for determining real-time tariffs, grid peaking, and valley filling (Lin et al., 2022; Lin et al., 2022). In recent years, the increase in distributed energy sources and the grid connection of new energy generation has led to the strong nonlinearity, non-smoothness, and randomness of ultra-short-term power load (USTPL), which brings challenges to USTPLF. Accurate USTPLF can realize the advanced control of automatic generation, reduce the adjustment pressure on automatic generation control, guarantee the stable operation of the power system, and enhance the efficiency of grid dispatch (Yan et al., 2021; Pham et al., 2022; Sun and Cai, 2022).

Research on power load forecasting methods. USTPLF is mainly divided into traditional statistical methods and machine learning methods. The traditional statistical methods mainly include the linear regression model (Liang and Tang, 2022), the Kalman filter method (Guo et al., 2022), and the time series model (He et al., 2022). Literature (Kim et al., 2022) used the curve extrapolation method for USTPLF based on short-term load forecasting results, eliminating the influence of holidays and load inflection points on the forecasting results. Literature (Guan et al., 2013) used the Kalman filter to generate prediction intervals and perform USTPLF automatically. Traditional statistical methods have high data requirements and cannot obtain accurately predicted load values when dealing with large amounts of nonlinear load data. Machine learning methods mainly include BP neural networks (Chen et al., 2023; da Silva and de Andrade, 2016), support vector machines (SVM) (Jiang et al., 2020), and deep learning (Tan et al., 2020). In Literature (Huang et al., 2022), a two-way weighted LS-SVM was used for USTPLF, which proved the characteristic of "large near and small far" for USTPLF. It did not rely on long-range data and considered near-term load data more. However, the fast leave-one-out method could not find the optimal parameters of the LS-SVM, which affected the prediction accuracy. Literature (Madhukumar et al., 2022) first used phase space reconstruction to find the intrinsic pattern between load data, established an SVM load prediction model after determining the import and output data, and optimized the SVM parameters by using an improved particle swarm algorithm to enhance the model prediction capability. Literature (Mir et al., 2021) adopted an enhanced firework algorithm to find the optimal weights and thresholds of the extreme learning machine to overcome the problem of model instability caused by randomly generated weights and thresholds of the extreme learning machine in USTPLF. Literature (Gunawan and Huang, 2021) used a stochastic distributed embedding framework and a BP neural network to solve the problem of low accuracy of USTPLF caused by a small amount of data. However, the BP is prone to overfitting when the import data are significant. In Literature (Xuan et al., 2021), the tree model in the lightweight gradient boosting machine (Light-BM) was used to evaluate the importance of each import feature quantitatively. At the same time, an attention mechanism was introduced to give different weights to different time series information, which overcomes the problem of easy loss of crucial information in gated recurrent neural networks when the import time series is longer. Additionally, in the field of wind power forecasting, several studies have proposed novel models to enhance the accuracy of wind power prediction. For instance, the study by (Shahid et al., 2021) presented a novel genetic LSTM model for wind power forecast, which leverages the genetic algorithm to optimize the LSTM network parameters and improve the forecasting accuracy. Furthermore, in financial market forecasting, the study conducted by (Bukhari et al., 2020) proposed a Fractional Neuro-Sequential ARFIMA-LSTM model, which integrates the ARFIMA model with LSTM to forecast financial market dynamics more accurately In Literature (Ageng et al., 2022), a method of USTPLF based on an extreme gradient enhancement algorithm (XGBOOST) combined with a long- and short-term memory neural network (LSTM) was proposed to enhance the accuracy of USTPLF by using XGBOOST for point prediction and then using LSTM for probabilistic prediction. The machine learning method is good at handling a large amount of nonlinear data. It has a good generalization ability to anonymous data, but it often affects the USTPLF accuracy due to improper human-set parameters.

A study on the Import feature of USTPLF. USTPLF is usually influenced by the load data in the hours before the moment to be predicted and external factors, e.g., wind force and wind direction do not change much during this period; hence, the external factors, such as wind force and wind direction, are not considered in USTPLF (Bouktif S et al., 2018). Tapping the laws of the electric load data themselves is the key to improving the accuracy of USTPLF. Literature (Zhao et al., 2019) used the attention mechanism to assign different weights to the import data so that the gated recurrent unit (GRU) focuses on learning important information, which overcomes the disadvantage that the GRU tends to lose sequence information in the learning process and improves the prediction efficiency. However, the attention mechanism only exploits the shallow features of the load data and does not perform deep mining of the data themselves. Literature (Li et al., 2017) utilized wavelet decomposition to decompose the load and a second-order gray neural network to predict and sum the components. Another study by (Shahid et al., 2020) introduced a novel Wave nets long short-term memory paradigm for wind power prediction, which combines the Wave nets model with LSTM to capture the long-term dependencies in wind power time series data. Literature (Kong et al., 2020) used multiple clustering analysis to filter the import features, wavelet decomposition to classify the load into high- and low-frequency components, a convolutional neural network (CNN) to predict the high-frequency components, and a multiplexed CNN (MCNN) to predict low-frequency components. Cluster analysis and wavelet decomposition can fully exploit the inherent features and patterns of load data and enhance the accuracy of USTPLF. Although the wavelet decomposition method can decompose load sequences, the selection of wavelet basis functions and decomposition layers has a significant impact on the decomposition effect for sequences with poor stability, which increases the prediction difficulty. Literature (Tang et al., 2019) decomposed the load sequence into different modal components via empirical mode decomposition (EMD) and predicted the modal components through deep belief networks and bi-directional recurrent neural networks. In Literature (Li et al., 2020), the EMD with adaptive noise was used to decompose the load sequence into different components, and the SVM with optimized parameters using the whale algorithm was employed to predict the different components with enhanced prediction accuracy. The EMD method is adaptive and can decompose the load on the basis of its time-series characteristics without artificially setting parameters, simplifying the prediction difficulty. Therefore, the decomposition of the prediction model's import load data can explore the data's laws. However, it also increases the prediction time and reduces the prediction efficiency because of the excessive decomposed components. A brief summary of the studied literature is presented in Table 1. In the research of power load forecasting, machine learning methods such as neural networks, support vector machines, and deep learning have shown excellent performance in handling large amounts of nonlinear data. Researchers have employed techniques such as attention mechanisms, wavelet decomposition, and clustering analysis to uncover the intrinsic patterns and features

TABLE 1 Literature review summary.

Ref	Method	Forecasted variable	Augmentation strategies
Huang et al. (2022)	LS-SVM	The load values for a future time period	—
Madhukumar et al. (2022)	SVM	Ultra-Short-Term Power	Particle swarm algorithm
Mir et al. (2021)	ELM	Ultra-Short-Term Power	Enhanced firework algorithm
Gunawan and Huang, (2021)	BP	Ultra-Short-Term Power	The stochastic distributed embedding framework and the backpropagation (BP) neural network
Xuan et al. (2021)	Light-BM	The load values	Attention Mechanism
Shahid et al. (2021)	LSTM	Wind power	GA
Bukhari et al. (2020)	LSTM	Financial market	ARFIMA-LSTM
Ageng et al. (2022)	LSTM	Ultra-Short-Term Power	Combining XGBOOST and LSTM
Zhao et al. (2019)	GRU	Ultra-Short-Term Power	Attention Mechanism
Li et al. (2017)	Second-order Gray Neural Network	The load values for a future time period	Wavelet Decomposition
Shahid et al. (2020)	LSTM	Wind power	WN-LSTM.
Kong et al. (2020)	MCNN	Ultra-Short-Term Power	Multiple clustering analysis and Wavelet decomposition
Tang et al. (2019)	BRNN	Ultra-Short-Term Power	EMD
Li et al. (2020)	SVM	Ultra-Short-Term Power	EMD whale algorithm

of load data, aiming to improve prediction accuracy. However, the decomposition methods may increase prediction time and reduce efficiency. Therefore, when selecting a forecasting method, it is necessary to consider the characteristics of load data and the requirements for prediction accuracy.

1.2 Motivation

Despite the widespread application of data-driven methods in feature construction and model training, they are not without limitations. One notable drawback is their excessive reliance on parameter optimization algorithms, such as particle swarm optimization or the whale optimization algorithm, which necessitates parameter tuning and manual intervention. This reliance adds complexity and subjectivity to the methods. Another significant limitation is the substantial impact of parameter selection on the results. In certain methods, such as selecting wavelet basis functions and determining decomposition levels, the choice of parameters heavily influences the prediction outcomes. Determining the appropriate parameters often requires expertise and rigorous experimental investigation, further complicating the methods and introducing uncertainty. Additionally, the need for different parameter settings across diverse datasets and problems can impede the methods' generalizability.

These limitations pose challenges and constraints in the practical application of data-driven methods. To overcome these issues, a novel approach that integrates Empirical Mode Decomposition (EMD), K-means clustering, and stochastic configuration networks (SCNs) has been proposed. This approach offers a unique and innovative solution that effectively addresses the aforementioned limitations, thereby enhancing the accuracy and robustness of load forecasting. Finally, the ultra short term power load (USTPL) has strong non smoothness and nonlinearity, making it difficult to explore the time series characteristics of the load data itself.

1.3 Contributions

This approach makes the following contributions:

(1) It introduces a combined method based on Empirical Mode Decomposition (EMD), K-means clustering, and stochastic configuration networks (SCNs) for ultra-short-term load forecasting. By decomposing the load data into Intrinsic Mode Functions (IMFs) and residuals using EMD, and then classifying the IMFs with K-means clustering, the method effectively explores the intrinsic features of the load data.
(2) The utilization of stochastic configuration networks as the training model is a significant contribution. SCNs possess adaptive characteristics and require minimal manual parameter settings. They are capable of leveraging the key information in the load sequence and achieving accurate predictions.
(3) By using the classified components as input features for training SCNs, the method reduces the dependence on parameters, thus enhancing the reliability and efficiency of ultra-short-term load forecasting.

In summary, the proposed approach based on EMD, K-means, and SCNs effectively tackles the limitations of data-driven methods while enhancing the accuracy and robustness of load forecasting. By effectively extracting the intrinsic features of historical load

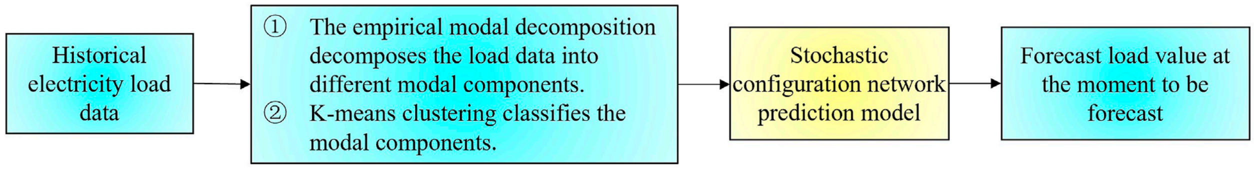

FIGURE 1
Description of the USTPLF problem.

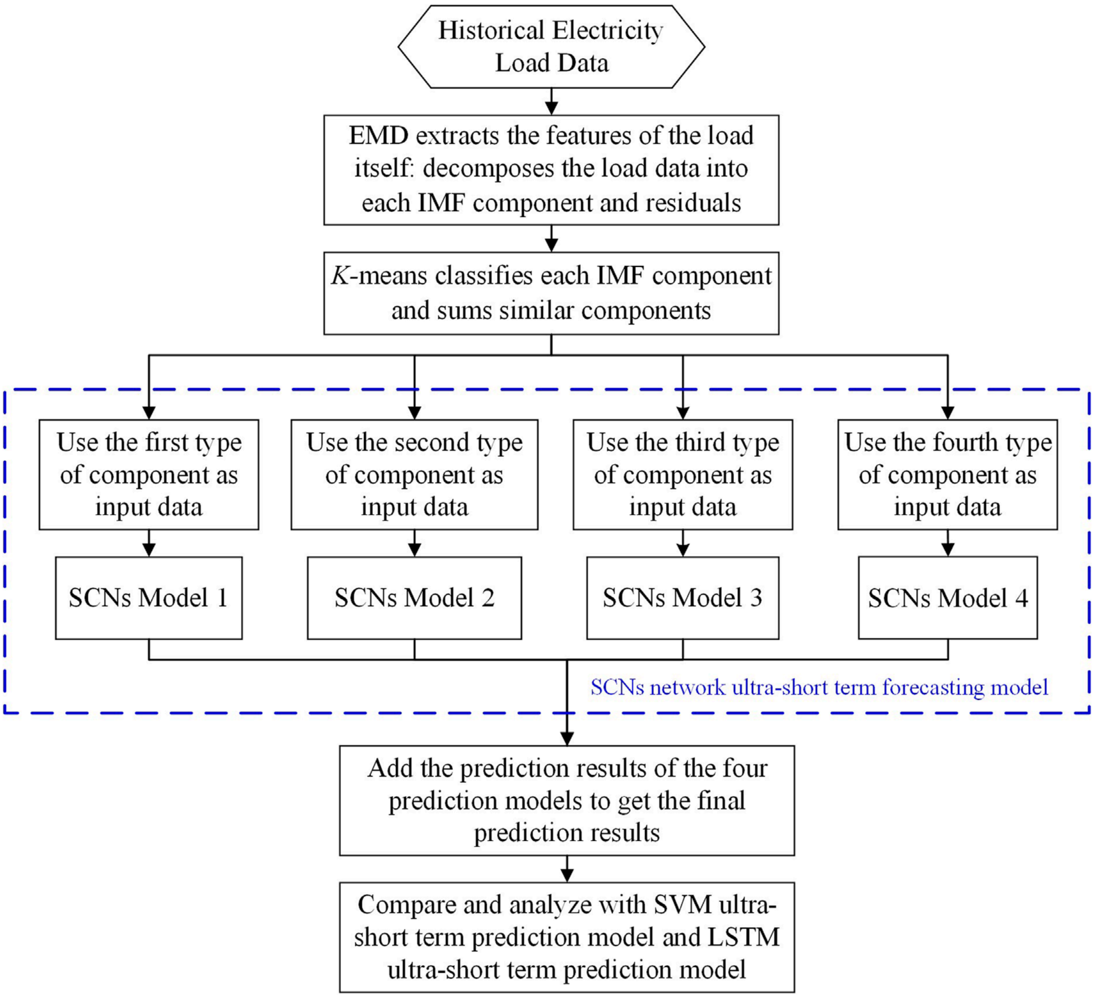

FIGURE 2
Strategy diagram of the USTPLF method.

data and reducing dependence on parameters, this approach offers a more efficient and accurate solution for ultra-short-term load forecasting, surpassing the performance of LSTM and SVM models.

The study is organized as follows: Section 2 provides the background and objectives of the research, highlighting the existing challenges in the field and clarifying the research purpose and questions. Section 3 introduces the methodology or strategy employed to address the research problem. Section 4 presents the approach used for feature extraction from the load data. Section 5 describes the application of the K-means clustering algorithm to group the load sequences. Section 6 outlines the load forecasting model based on stochastic configuration networks. Section 7 provides a description of the dataset used in the study.

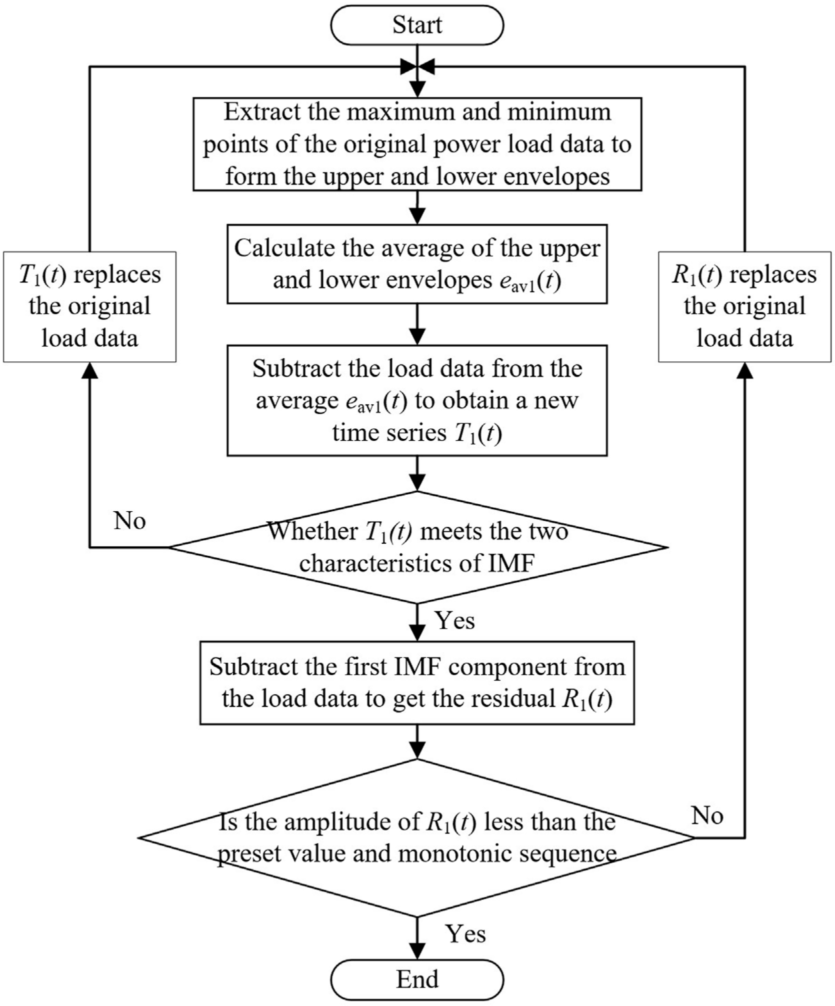

FIGURE 3
Flowchart of EMD breakdown load data.

2 Problem description

The difference between the USTPLF and the short-term power load forecast is that it follows the principle of large near and small far, i.e., the first n hours of the time to be forecasted are crucial for the USTPLF. Short-term power load forecasting is to forecast a load of a day on the day to be forecasted simultaneously. It cannot take into account the interactions between the loads at each moment on the day to be forecasted, whereas USTPLF is hourly granular. The accuracy rate is higher, and the moment to be forecasted is very close to the first n hours. External influencing factors, such as wind force, wind direction, and humidity, do not change much. Therefore, in USTPLF, external influences on the load are usually not considered. The key to improving the accuracy of USTPLF is digging deeper into the laws in the load data themselves. Traditional forecasting methods have limited ability to map nonlinear data, and the LSTM has excessive artificially set parameters, which is prone to the problem of time series information loss and affects its forecasting accuracy. SCNs are suitable for USTPLF given the advantages of less artificially set parameters, high intelligence, and shorter time required for forecasting. The application of our research lies in Ultra-Short-Term Power Load Forecasting (USTPLF). USTPLF aims to accurately predict power load variations in the near future. This application is crucial for the operation and scheduling of power systems, enabling power companies to plan generation capacity, optimize grid operations, and enhance energy utilization efficiency. The problem description of USTPLF is shown in Figure 1.

3 Strategy structure

Suppose only the extrinsic features of load data are observed without digging deeper into the intrinsic features of the load data themselves. In this case, the prediction accuracy will decrease, and the prediction time will increase. EMD can decompose

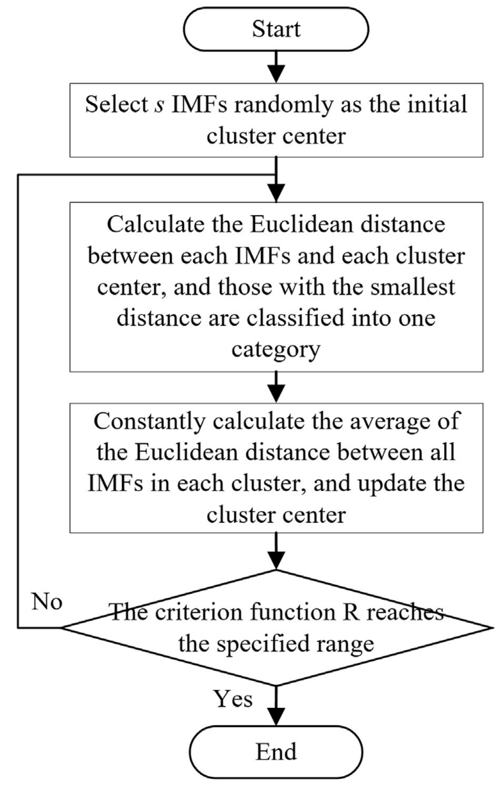

FIGURE 4
Flowchart of *K*-means cluster with IMFs.

the original load data into several load sequence components to explore the original load data's intrinsic features deeply. *K*-means can integrate the components to reduce the prediction time. Therefore, this study proposes an SCNs ultra-short-term load forecasting method based on *K*-means and EMD. First, missing load data are filled. Second, EMD is used to decompose the load data into several IMFs and residuals to reduce the randomness and volatility of the load data. Third, *K*-means is used to classify several components, and the components contained at the center of each cluster are summed. Lastly, the summed components are imported to stochastic configuration networks for training. The mean absolute error (MAE), mean absolute percentage error (MAPE), and root-mean-square error (RMSE) are chosen to measure the performance of the prediction method. The specific implementation strategy of the method is shown in Figure 2.

4 Load data feature extraction

USTPLF predicts the load changes in the next few hours. During this period, the weather, temperature, humidity, and other external factors have minimal changes, so the influence of external factors on the load is not considered. When forecasting, only observing the external characteristics of the load data and not digging into the internal laws of the load data themselves will reduce the forecasting accuracy. Therefore, determining how to mine the inherent characteristics of load data is important. The load series is decomposed into IMFs and residuals by EMD (Gloersen and Huang, 2003) in accordance with the time scale of the load data themselves. Each IMFs represents the characteristic components of the load series on this time scale. The characteristic law of each IMF is the characteristic law of the load data themselves. The composition of the IMF must meet two characteristics: ① The difference between the number of extreme points and the number of zero points of the intrinsic mode component cannot be greater than 1. ② The average value of the upper and lower envelopes of the eigenmode components at any time is zero (Yang et al., 2018).

Algorithm 1 is a method used for Empirical Mode Decomposition (EMD) of historical power load data. The algorithm takes historical power load data and a preset value R as input, and it outputs the power load sequence components and the residual error of the power load series, R(t). The algorithm begins by extracting all maximum points (e max(t)) and minimum points (e min(t)) from the load data (P(t)). It then calculates the average of the load data and generates a new load series based on this average. Next, the algorithm checks if the difference between the number of extreme points and the number of zero points is not greater than 1 and if specific conditions are met. If these conditions are satisfied, the algorithm selects the first Intrinsic Mode Function (IMF), which represents a characteristic component of the load series on a particular time scale. It also calculates the residual of the load series. The algorithm further evaluates if the residual is less than the preset value R and if it represents a monotonic load sequence. If both conditions are met, the algorithm retains the residual as part of the decomposition process. Otherwise, it returns to step 1 and repeats the process with the historical power load data. The specific steps of EMD decomposition of power load data are shown in Figure 3; **Algorithm 1**.

5 *K*-means of load series

After load feature extraction, the load data are decomposed into several IMFs and residuals. If all the IMFs and residuals are imported into the SCNs as import data for training, it will lead to a large amount of data and increase the prediction time. Given its real-time characteristics (Ding et al., 2020), USTPLF requires high forecasting speed. *K*-means is used to integrate IMFs and residuals to reduce the import data of the SCNs and enhance the forecasting speed. First, *K*-means centers are built, and the coordinates of the clustering centers are determined. Then, the Euclidean distances of each IMF, each residual, and the cluster center are calculated. The calculation formula is shown in Formula (1), and each IMF and each residual are classified in accordance with the Euclidean distance. Lastly, the IMFs of the same category are added, and the added components are used as the import data of the SCNs ultra-short-term load forecasting model. The process is shown in Figure 4.

$$d_j = \sqrt{\sum_{s=1}^{n} \left(x_s - p_{fs}\right)^2} \tag{1}$$

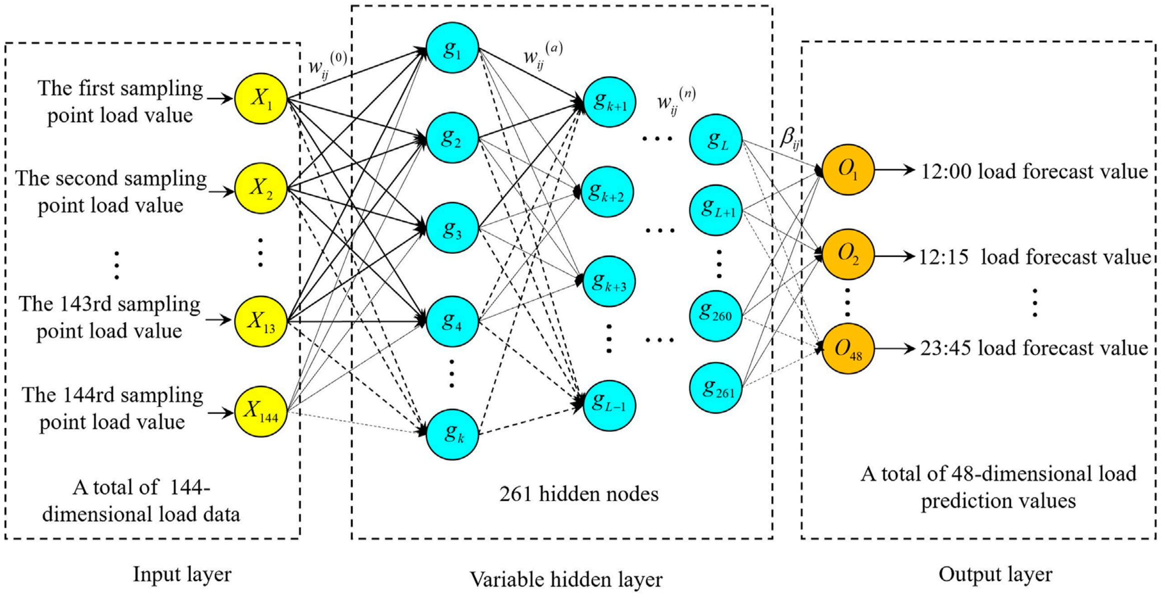

FIGURE 5
SCNs ultra-short-term load forecasting model.

```
    Input: Historical power load data
    $P(t), t = 1,2,\cdots,4032$; Preset value $R$
    Output: Power load sequence component
    $f_{\mathrm{IMF}k}(t), k = 1,2,\cdots,9$, Residual error of power load
    series $R(t)$
1:  Extract all maximum points $e_{\max}(t)$ and minimum
    points $e_{\min}(t)$ in load data $P(t)$
2:  Calculate the average: $e_{av1}(t) = \frac{e_{\max}(t)+e_{\min}(t)}{2}$
3:  Calculate new load series $T_1(t) = P(t) - e_{av1}(t)$;
4:  If the difference between the number of
    extreme points of $T_1(t)$ and the number of zero
    points is not greater than 1 and $e_{av}(t) = 0$
5:    The first IMF $f_{\mathrm{IMF1}}(t) := T_1(t)$
6:    Calculate the residual of load series
    $R_1(t) = P(t) - f_{\mathrm{IMF1}}(t)$
7:     If$R_1(t)$ is less than the preset value $R$ and
    is a monotonic load sequence
8:       The residual $R(t) := R_1(t)$
9:     Else
10:      The historical power load data $P(t) := R_1(t)$
    go to step 1
11:    End if
12: Else
13:   The historical power load data $P(t) := T_1(t)$ go
    to step 1
14: End if
```

Algorithm 1. EMD decomposes historical power load data

where $x_s(s = 1,2,\cdots,n)$ is the load value of the IMF component, and $p_{fs}(f = 1,2,\cdots,z; s = 1,2,\cdots,n)$ is the coordinate value of the fth cluster center.

6 Load forecasting model based on stochastic configuration networks

SCNs have the advantages of fewer parameters set manually, automatically adjusting the weight of each unit in accordance with the prediction error, avoiding the problem of affecting the accuracy of load forecasting caused by improper parameter selection, and rapid selection of hidden parameters through its evaluation function, thus improving the forecasting efficiency. Therefore, SCNs are used to forecast USTPLs with high accuracy and speed requirements. SCNs are random-weighted neural networks with a supervision mechanism proposed by Wang and Li, (2017). Their structure includes an input layer, a variable hidden layer, and an output layer. Unlike the traditional feedforward neural network, SCNs can start from a small network with minimal human intervention, randomly select import weights and thresholds, gradually increase the number of hidden layer neuron nodes, and use the least squares method to calculate the output weights and thresholds until the training accuracy of the network meets the termination conditions. In addition, SCNs add an evaluation function for random parameters and adaptively select the range of random parameters.

Suppose we build an SCNs model with L-1 hidden layer nodes, and its basic mapping relationship is

$$f_{L-1}(X) = \beta^T H = \sum_{j=1}^{L-1} \beta_j g_j\left(w_j^T X + b_j\right)\left(L = 1,2,\ldots,m; f_0 = 0\right) \tag{2}$$

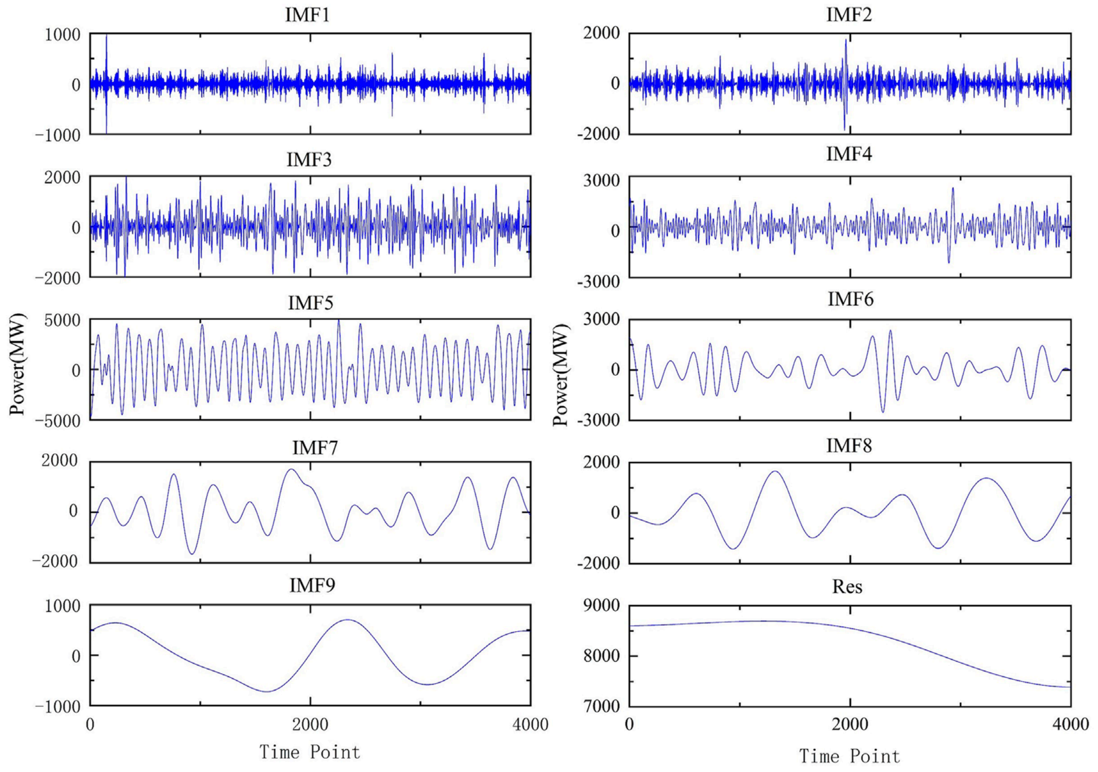

FIGURE 6
IMFs and Res after load data decomposition.

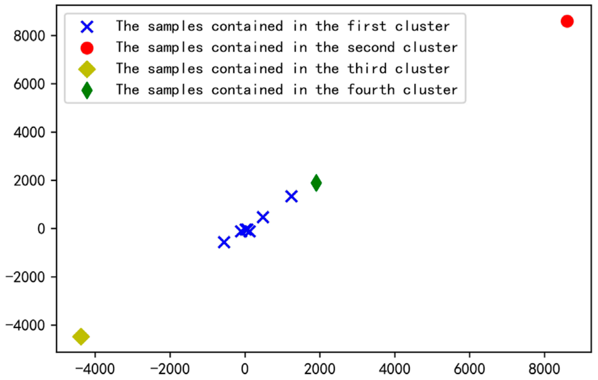

FIGURE 7
Effect of the clustering of each component.

where β_j is the output weight matrix of the jth hidden layer node; $X = \{X_1, X_2, \ldots, X_N\}$ is the import characteristic matrix, e.g., $X_1 = [x_1, x_2, \cdots x_M]^T$; w_j and b_j are the import weight and threshold matrix of the jth hidden layer node, respectively; g_j is the sigmoid activation function.

$$g_j = g\left(w_j^T X + b_j\right) = \frac{1}{1 + \exp\left(-w_j^T X + b_j\right)} \tag{3}$$

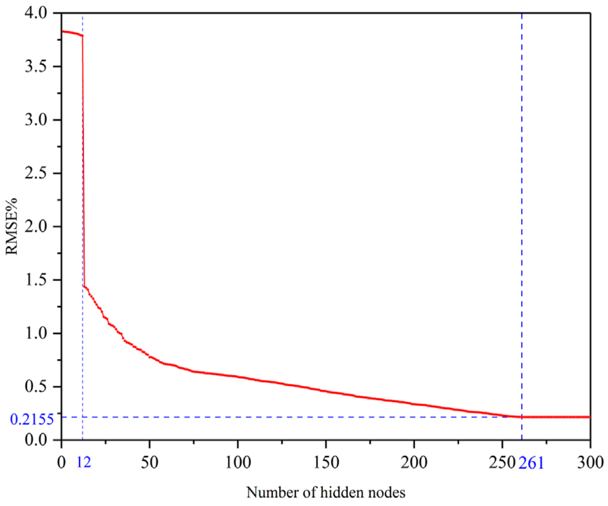

FIGURE 8
Training error value corresponding to the number of hidden layer nodes.

When the model is calculated for the first time, the difference between the model output and the real value is defined as

$$e_{L-1} = f - f_{L-1} = \left[e_{L-1,1}, e_{L-1,2}, \ldots, e_{L-1,m}\right] \tag{4}$$

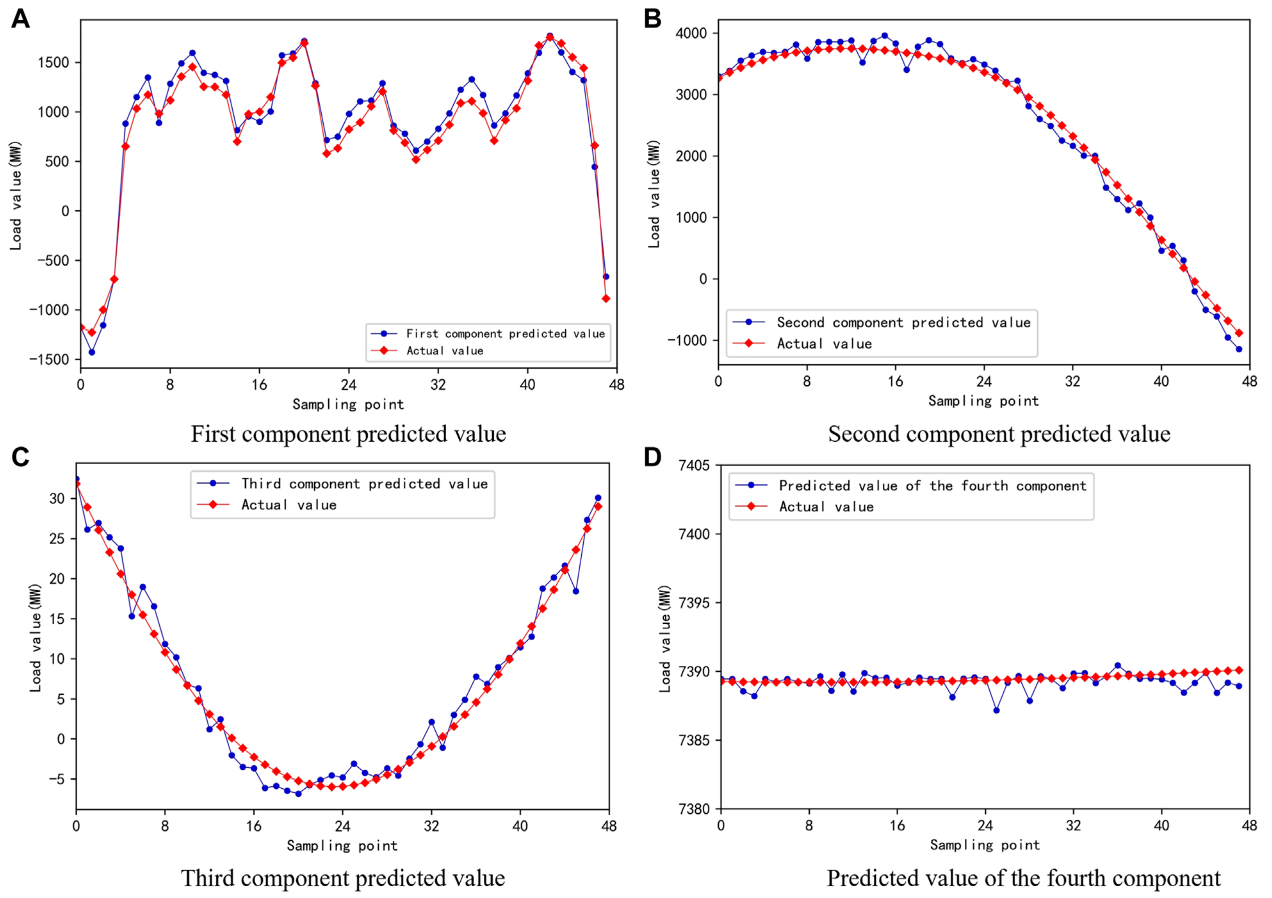

First component predicted value

Second component predicted value

Third component predicted value

Predicted value of the fourth component

FIGURE 9
Comparison between predicted and actual values of four components. **(A)** First component predicted value. **(B)** Second component predicted value. **(C)** Third component predicted value. **(D)** Predicted value of the fourth component.

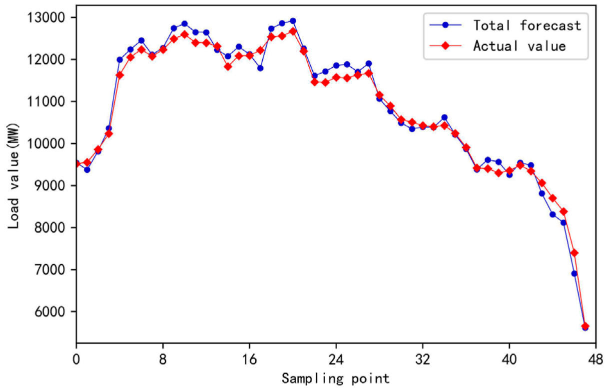

FIGURE 10
Comparison between total predicted value and actual value.

where e_{L-1} represents the difference between the number of different nodes, and $e_{L-1,K}$ is the difference of corresponding characteristics of different nodes.

When the error does not meet the set value, g_L and b_g are randomly generated in accordance with Formula (5)–Formula (7), and the updated output weight value β_L is calculated. A hidden layer node is added, and the model output is updated to $f_L(X) = f_{L-1}(X) + \beta_L g_L$ to achieve the purpose of correcting the residual. As a result, the output predicted value is closer to the real value, and the update process is until the error meets the set value. The update function is

$$\left\langle e_{L-1,q}, g_L^2 \right\rangle \geq b_g^2 \delta_{L,q}, q = 1, 2, \cdots m \tag{5}$$

$$\beta_{L,q} = \frac{\left\langle e_{L-1,q}, g_L \right\rangle}{\|g_L\|^2}, q = 1, 2, \ldots, m \tag{6}$$

$$\begin{cases} \delta_L = \sum_{q=1}^{m} \delta_{L,q} \\ \delta_{L,q} = (1 - r - \mu_L)\|e_{L-1,q}\|^2 \end{cases} \tag{7}$$

The evaluation function is defined as follows:

$$\xi_{L,q} = \frac{\left(e_{L-1,q}(X)^T \bullet g_L(X)\right)^2}{g_L(X)^T \bullet g_L(X)} - (1 - r - \mu_L) e_{L-1,q}(X)^T \bullet e_{L-1,q}(X) \tag{8}$$

where $g_L(X) = g_L\left(w_L^T X + b_L\right)$; $0 < r < 1$; μ_L is a sequence of non-negative real numbers. The larger the value of the evaluation

TABLE 2 MAE, MAPE, and RMSE of the four methods.

Prediction method	MAE/MW	MAPE/%	RMSE/MW
EKSCNs	178.94	1.69	216.34
SCNs	569.74	5.71	687.97
EKSVM	389.01	3.63	473.37
EKLSTM	389.53	4.20	558.07

function $\xi_{L,q}$, the better the model parameter configuration, and the faster the convergence of the stochastic configuration networks.

The construction of the SCNs ultra-short-term load forecasting model is shown in Figure 5. The model comprises 144 neurons in the input layer, 261 neurons in the hidden layer, and 48 neurons in the output layer. The algorithm starts with initialization and enters a while loop. In each iteration, it performs nested loops to randomly assign weights and calculate the evaluation function and error. If the evaluation function meets certain criteria, the weights are stored. If the stored set is not empty, the algorithm finds the weights that maximize the evaluation function and generates a matrix. Otherwise, it randomly fetches weights and continues the process. After the iterations, the algorithm calculates the optimal output weight and output error. It then updates the weights and continues the loop until the specified conditions are met. Finally, the algorithm returns the predicted value of load series components in the time period to be predicted. The detailed steps of the SCNs ultra-short-term load forecasting model are given in **Algorithm 2**.

7 Example analysis

7.1 Dataset description

This study adopts Shenzhen's power load data set from June 2 to 13 July 2017, with a total of 42 days of load data. The sampling interval of load data is 15 min, with a total of 4,032 data points. The time period to be predicted is 12:00–24:00 on July 13.

The power load data set is checked. If there is a missing value, it is filled with the average value. The data in this dataset are complete, and whether to fill in missing values is optional.

7.2 Performance evaluation index

MAE, MAPE, and RMSE are used as evaluation indicators of prediction methods. The calculation formulas are as follows:

$$\mathrm{MAE} = \frac{1}{N}\sum_{i=1}^{N}\left|y_i' - y_i\right| \tag{9}$$

$$\mathrm{MAPE} = \frac{1}{N}\sum_{i=1}^{N}\left|\frac{y_i' - y_i}{y_i}\right| \times 100 \tag{10}$$

$$\mathrm{RMSE} = \sqrt{\frac{1}{N}\sum_{i=1}^{N}\left(y_i' - y_i\right)^2} \tag{11}$$

where y_i' is the predicted load value, and y_i is the actual load value.

```
Input: Power load sequence component $X=\{X_1,X_2,\ldots,X_N\},N=21$; Expected output corresponding to the power load sequence component $T=\{t_1,t_2,\ldots,t_N\}$; Number of neurons in the maximum hidden layer of SCNs $L_{\max}$; Error tolerance $\varepsilon$; Maximum number of random configurations $T_{\max}$; Value range of random weight $\Upsilon=\{\lambda_{\min},\ldots,\lambda_{\max}\}$;
Output: Predicted value of load series components in the time period to be predicted $P=(P_1,P_2,\cdots,P_m),m=48$
1:  Initialization: $e_0=[t_1,t_2,\ldots,t_N]^T, 0<r<1, \Omega, W=\phi$;
2:  while $L \le L_{\max}$ and $\|e_0\|_F > \varepsilon$, do
3:    for $\lambda \in \Upsilon$, do
4:      for $k=1,2,\ldots,T_{\max}$, do
5:        Randomly assign $w_L$ and $b_L$ from intervals $[-\lambda,\lambda]^M$ and $[-\lambda,\lambda]$, respectively;
6:        Calculate $g_L(X)=\left[g_L\left(w_L^T x_1+b_L\right),g_L\left(w_L^T x_2+b_L\right),\ldots,g_L\left(w_L^T x_N+b_L\right)\right]$;
7:        Calculate the evaluation function $\xi_{L,K}$;
8:        Calculate $\mu_L=(1-r)/(L+1)$;
9:        if $\min\{\xi_{L,1},\xi_{L,2},\ldots,\xi_{L,K}\} \ge 0$ then
10:         Store $w_L$ and $b_L$ in $W$ and $\xi_L=\sum_{k=1}^{K}\xi_{L,k}$ in $\Omega$;
11:       else
12:         go to step 7
13:       end if
14:     end for
15:     if $W$ is not an empty set then
16:       Find the $w_L^*$ and $b_L^*$ that make $\xi_L$ the largest in $\Omega$, and then generate the matrix $\left[g_1^*,g_2^*,\ldots,g_L^*\right]$
17:       Break (go to step 24)
18:     else
19:       Randomly fetch $\tau \in (0,1-r)$, update $r$: $r=r+\tau$, go back to step 7
20:     end if
21:   end for
22:   Calculate the optimal output weight $\left[\beta_1^*,\beta_2^*,\ldots,\beta_L^*\right]=\mathrm{argmin}\beta\left\|f-\sum_{j=1}^{L}\beta_j g_j\left(w_j^T X+b_j\right)\right\|$
23:   Calculate output error $e_L=e_{L-1}-\beta_L^{*T}g_L^*$;
24:   To update $e_0$: $e_0=e_{L-1}$; $L$: $L=L+1$;
25: end while
26: Return $\beta_1^*,\beta_2^*,\ldots,\beta_L^*$; $w^*=\left[w_1^*,w_2^*,\ldots,w_L^*\right]$; $b^*=\left[b_1^*,b_2^*,\ldots,b_L^*\right]$
```

Algorithm 2. SCNs

7.3 Historical load data decomposition

The EMD method is used to decompose the historical power load data, and a total of 10 components are obtained, including 9 IMFs and 1 residual, which are recorded as $e1$–$e10$. The decomposed load series is shown in Figure 6. The frequency of each IMF component is relatively stable and shows evident periodicity.

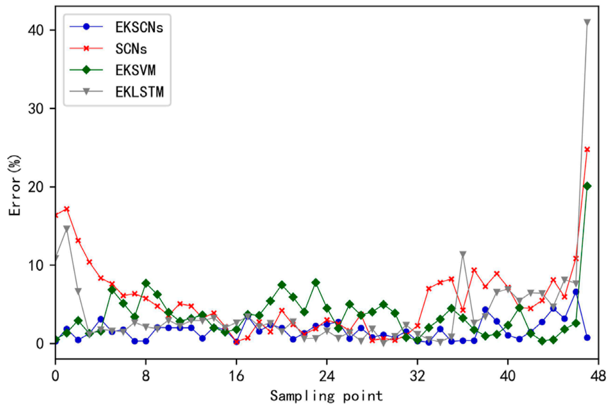

FIGURE 11
Comparison of errors of the four measures.

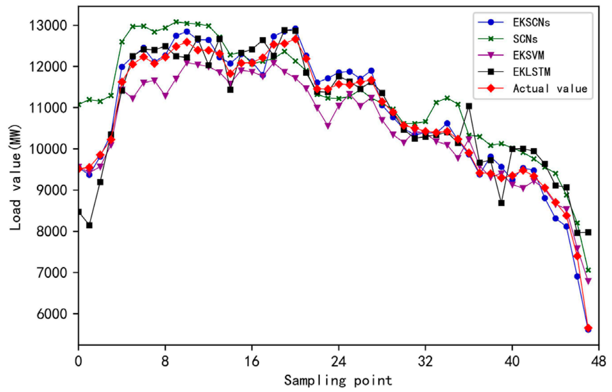

FIGURE 12
Comparison between the predicted values of the four methods and the real values.

Through its periodicity, the characteristics of the load series can be mined.

From Figure 6, the EMD decomposes the historical power load data into 10 components. If these 10 components are imported into the SCNs as import data for training, the calculation amount and prediction time of the model will increase. Therefore, to enhance the prediction speed, K-means is used to integrate all components, which are then used as import data for prediction. The center point is set to 4, and the effect of clustering each IMF component and Res is shown in Figure 7. Each component is divided into four categories. The components in the same category are added to obtain the new load series components d1–d4. The new components d1–d4 are predicted as the import data of the stochastic configuration networks model, and the sum of the four prediction results is the USTPLF result.

7.4 Parameter settings of stochastic configuration networks

Before USTPLF, the SCNs should be trained. The evaluation index used in training is the RMSE of the load forecast value and the actual value. The relationship between the training error of SCNs and the number of hidden layer nodes is shown in Supplementary Appendix SA1 and Figure 8.

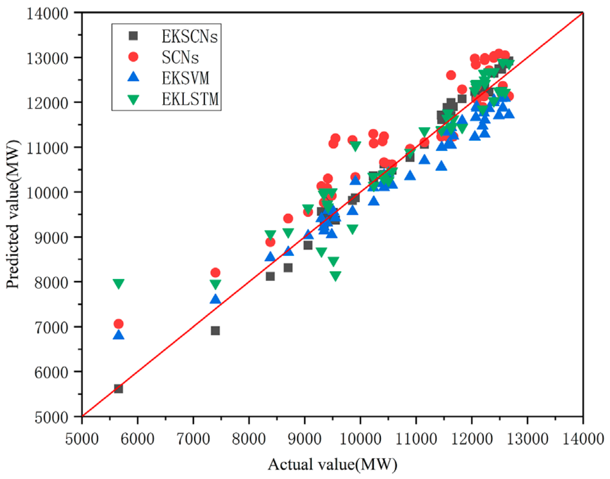

FIGURE 13
Scatter chart of the predicted values of the four methods and the actual values.

From the figure, when the number of hidden layer nodes is small, the training error of SCNs is significant and does not change as the number of nodes increases. When the number of hidden layer nodes increases to 13, the training error of SCNs decreases significantly, continues to decrease as the number of nodes increases, and finally tends to stabilize. At this time, the training RMSE of SCNs is 0.2155%.

The specific parameter settings of SCNs are as follows: number of neurons in the maximum hidden layer $L_{\max} = 300$, error tolerance $\varepsilon = 0.001$, random weight range $\Upsilon = [\ 0.1, 0.15, 0.2, \ldots, 8]$, and maximum number of random configurations $T_{\max} = 50$.

7.5 Load forecasting and analysis

This study sets every 3 days as a sample, having a total of 39 groups of samples. Of them, 80% are taken as the training set, with a total of 32 groups of samples; 20% are taken as the test set, with a total of 7 groups of samples. The import data of each group of samples are the load data of the first and second days of the sample and the load data of the third day from 00:00 to 11:45, a total of 144 data; the output data are the load data of the third day from 12:00 to 23:45, a total of 48 data. The first load series component d1, the second load series component d2, the third load series component d3, and the fourth load series component d4 are imported into the SCNs for training. The predicted values are compared. The actual load values in the 12:00–24:00 time period of each load series component to be predicted are shown in Figure 9. The predicted values of the four components are added to determine the load values of the period from 12:00 to 24:00 on the day. The comparison with the actual value is shown in Figure 10.

The four methods are programmed separately, and the numerical examples are analyzed.

(1) Method 1: The historical power load data without EMD and K-means processing are taken as the import data to build the SCNs model, which is called SCNs.
(2) Method 2: The four load series components obtained after EMD and K-means processing are taken as import data, four SVM models are constructed, the prediction results are summed, and the method is called EKSVM.
(3) Method 3: The four load series components obtained after EMD and K-means processing are taken as import information, four LSTM models are set, the prediction results are summed, and the method is called EKLSTM.
(4) The proposed measure in this thesis is to construct four SCNs models and sum the prediction results by using the four load series components obtained after EMD and K-means processing as import data. The method is named EKSCNs.

The MAE, MAPE, and RMSE of the four measures are shown in Table 2. The error between the predicted value and the real value at 48 time points in the time period from 12:00 to 24:00 on 12 July 2017 is shown in Figure 11. Figure 12 presents a comparison between the predicted loads of the four methods and the real loads at 48 time points. The scatter plots between the predicted values of the four methods and the actual values are given in Figure 13. The smaller the difference between the predicted and actual values, the closer the point in the figure is to the diagonal line.

From Figures 11–13; Table 2, when SCNs are also used, the load series components obtained after EMD and K-means processing and used as import data show reductions of 390.8 MW, 4.02%, and 471.63 MW in MAE, MAPE, and RMSE, respectively, compared with the historical load data that are not preprocessed. This result verifies the effectiveness of using EMD and K-means in preprocessing historical load data. In the same case of EMD and K-means processing, EKSCNs is the closest to the slant, without abnormal points, and its MAE, MAPE, and RMSE are smaller than those of EKSVM and EKLSTM. The curve trend is closer to the real load, which verifies the effectiveness of using SCNs.

8 Conclusion

In this study, EMD is used to decompose the historical load data into various components. K-means is employed to sum the decomposed components by category to establish the EKSCNs USTPLF model. Finally, the load forecasting value of the 12:00–24:00 period of the day to be predicted is obtained. An example proves the effectiveness of the proposed method.

(1) Through EMD, the historical load data are decomposed into various IMFs and residuals, and the inherent characteristics of the load series are mined to enhance the prediction accuracy.
(2) The decomposed components are added by K-means, which reduces the number of import data and avoids the problem of increasing workload and slowing down prediction speed caused by importing all components into stochastic configuration networks for training.
(3) Compared with the SVM and the LSTM, the SCNs has the advantage of fewer parameters set manually and avoids the trouble of forecast precision decline on account of improper parameter selection.

Data availability statement

The original contributions presented in the study are included in the article/Supplementary Material, further inquiries can be directed to the corresponding author.

Author contributions

Conceptualization, XP, HL, and WL; formal analysis, XP and WS; investigation, XP and WS; resources, XP and HL; writing—original draft preparation, XP and WS; writing—review and editing, YM and XM. All authors contributed to the article and approved the submitted version.

Funding

This work was partly supported by the National Natural Science Foundation of China (61773269 and 62073226), China Scholarship Council (CSC 202008210181), the Natural Science Foundation of Liaoning Province of China (2022-MS-306), and Department of Education of Liaoning Province of China (LJKZ1110, LJKMZ20221716, and LJKMZ20221718).

Conflict of interest

Author WS was employed by Fuxin Power Supply Company and State Grid Liaoning Electric Power Co., Ltd.

The remaining authors declare that the research was conducted in the absence of any commercial or financial relationships that could be construed as a potential conflict of interest.

Publisher's note

Supplementary material

The Supplementary Material for this article can be found online at: https://www.frontiersin.org/articles/10.3389/fenrg.2023.1182287/full#supplementary-material

References

Ageng, D., Huang, C.-Y., and Cheng, R.-G. (2022). A short-term household load forecasting framework using LSTM and data preparation. *IEEE Access* 9, 167911–167919. doi:10.1109/ACCESS.2021.3133702

Bouktif, S., Fiaz, A., Ouni, A., and Serhani, M. (2018). Optimal deep learning LSTM model for electric load forecasting using feature selection and genetic algorithm: Comparison with machine learning approaches. *Energies* 11, 1636. doi:10.3390/en11071636

Bukhari, A. H., Raja, M. A. Z., Sulaiman, M., Islam, S., Shoaib, M., and Kumam, P. (2020). Fractional neuro-sequential ARFIMA-LSTM for financial market forecasting. *IEEE Access* 8, 71326–71338. doi:10.1109/ACCESS.2020.2985763

Chen, X. F., Chen, W. R., Venkata, D., Liu, Y. Q., and Feng, J. L. (2023). Short-term load forecasting and associated weather variables prediction using ResNet-LSTM based deep learning. *IEEE Access* 11, 5393–5405. doi:10.1109/ACCESS.2023.3236663

da Silva, I. N., and de Andrade, L. C. M. (2016). Efficient neurofuzzy model to very short-term load forecasting. *IEEE Lat. Am. Trans.* 14, 721–728. doi:10.1109/TLA.2016.7437215

Ding, Y., Su, H., Kong, X. F., and Zhang, Z. Q. (2020). Ultra-short-term building cooling load prediction model based on feature set construction and ensemble machine learning. *IEEE Access* 8, 178733–178745. doi:10.1109/ACCESS.2020.3027061

Gloersen, P., and Huang, N. (2003). Comparison of interannual intrinsic modes in hemispheric sea ice covers and other geophysical parameters. *IEEE Trans. Geoscience Remote Sens.* 41, 1062–1074. doi:10.1109/TGRS.2003.811814

Guan, C., Luh, P. B., Michel, L. D., and Chi, Z. Y. (2013). Hybrid kalman filters for very short-term load forecasting and prediction interval estimation. *IEEE Trans. Power Syst.* 28, 3806–3817. doi:10.1109/TPWRS.2013.2264488

Gunawan, J., and Huang, C.-Y. (2021). An extensible framework for short-term holiday load forecasting combining dynamic time warping and LSTM network. *IEEE Access* 9, 106885–106894. doi:10.1109/ACCESS.2021.3099981

Guo, Y. X., Li, Y., Qiao, X. B., Zhou, W. F., Mei, Y. J., Lin, J. J., et al. (2022). BiLSTM multitask learning-based combined load forecasting considering the loads coupling relationship for multienergy system. *IEEE Trans. Smart Grid* 13, 3481–3492. doi:10.1109/TSG.2022.3173964

He, Y., Luo, F. J., and Ranzi., G. (2022). Transferrable model-agnostic meta-learning for short-term household load forecasting with limited training data. *IEEE Trans. Power Syst.* 37, 3177–3180. doi:10.1109/TPWRS.2022.3169389

HuangZhao, Y. R. X., Zhou, Q. Y., and Xiang, Y. X. (2022). Short-term load forecasting based on A hybrid neural network and phase space reconstruction. *IEEE Access* 10, 23272–23283. doi:10.1109/ACCESS.2022.3154362

Jiang, H. Y., Wu, A. J., Wang, B., Xu, P. Z., and Yao, G. (2020). Industrial ultra-short-term load forecasting with data completion. *IEEE Access* 8, 158928–158940. doi:10.1109/ACCESS.2020.3017655

Kim, N., Park, H., Lee, J., and Choi, J. K. (2022). Short-term electrical load forecasting with multidimensional feature extraction. *IEEE Trans. Smart Grid* 13, 2999–3013. doi:10.1109/TSG.2022.3158387

Kong, Z. M., Zhang, C. G., Lv, H., Xiong, F., and Fu, Z. l. (2020). Multimodal feature extraction and fusion deep neural networks for short-term load forecasting. *IEEE Access* 7, 185373–185383. doi:10.1109/ACCESS.2020.3029828

Li, B. W., Zhang, J., He, Y., and Wang, Y. (2017). Short-term load-forecasting method based on wavelet decomposition with second-order gray neural network model combined with ADF test. *IEEE Access* 5, 16324–16331. doi:10.1109/ACCESS.2017.2738029

Li, W. W., Shi, Q., Sibtain, M., Li, D., and Eliote Mbanze., D. (2020). A hybrid forecasting model for short-term power load based on sample entropy, two-phase decomposition and whale algorithm optimized support vector regression. *IEEE Access* 8, 166907–166921. doi:10.1109/ACCESS.2020.3023143

Liang, J. K., and Tang, W. Y. (2022). Ultra-short-term spatiotemporal forecasting of renewable resources: An attention temporal convolutional network-based approach. *IEEE Trans. Smart Grid* 13, 3798–3812. doi:10.1109/TSG.2022.3175451

Lin, Y. H., Tang, H. S., Shen, T. Y., and Hsia, C. H. (2022). A Smart home energy management system utilizing Neuro computing-based time-series load modeling and forecasting facilitated by energy decomposition for Smart home automation. *IEEE Access* 10, 116747–116765. doi:10.1109/ACCESS.2022.3219068

Liu, M. P., Qin, H., Cao, R., and Deng, S. H. (2022). Short-term load forecasting based on improved TCN and DenseNet. *IEEE Access* 10, 115945–115957. doi:10.1109/ACCESS.2022.3218374

Madhukumar, M., Sebastian, A., Liang, X. D., Jamil, M., and Shabbir, M. N. S. K. (2022). Regression model-based short-term load forecasting for university campus load. *IEEE Access* 10, 8891–8905. doi:10.1109/ACCESS.2022.3144206

Mir, A. A., Khan, Z. A., Abdullah, A., Badar, M., Ullah, K., Imran, M., et al. (2021). Systematic development of short-term load forecasting models for the electric power utilities: The case of Pakistan. *IEEE Access* 9, 140281–140297. doi:10.1109/ACCESS.2021.3117951

Pham, C. H., Minh, N. Q., Tien, N. D., and Anh, T. T. Q. (2022). Short-term electricity load forecasting based on temporal fusion transformer model. *IEEE Access* 10, 106296–106304. doi:10.1109/ACCESS.2022.3211941

Shahid, F., Zameer, A., Mehmood, A., and Raja, M. A. Z. (2020). A novel wavenets long short term memory paradigm for wind power prediction. *Appl. Energy* 269, 115098. doi:10.1016/j.apenergy.2020.115098

Shahid, F., Zameer, A., and Muneeb, M. (2021). A novel genetic LSTM model for wind power forecast. *Energy* 223, 120069. doi:10.1016/j.energy.2021.120069

Sun, Q., and Cai, H. F. (2022). Short-term power load prediction based on VMD-SG-LSTM. *IEEE Access* 10, 102396–102405. doi:10.1109/ACCESS.2022.3206486

Tan, M., Yuan, S. P., Li, S. H., Su, Y. X., Li, H., and He, F. (2020). Ultra-short-term industrial power demand forecasting using LSTM based hybrid ensemble learning. *IEEE Trans. Power Syst.* 35, 2937–2948. doi:10.1109/TPWRS.2019.2963109

Tang, X. L., Dai, Y. Y., Liu, Q., Dang, X. Y., and Xu, J. (2019). Application of bidirectional recurrent neural network combined with deep belief network in short-term load forecasting. *IEEE Access* 7, 160660–160670. doi:10.1109/ACCESS.2019.2950957

Wang, D., and Li, M. (2017). Stochastic configuration networks: Fundamentals and algorithms. *IEEE Trans. Cybern.* 47, 3466–3479. doi:10.1109/TCYB.2017.2734043

Xuan, Y., Si, W. G., Zhu, J., Zhao, J., Xu, M. J., Xu, S. L., et al. (2021). Multi-model fusion short-term load forecasting based on random forest feature selection and hybrid neural network. *IEEE Access* 9, 69002–69009. doi:10.1109/ACCESS.2021.3051337

Yan, J. C., Hu, L., Zhen, Z., Wang, F., Qiu, G., Li, Y., et al. (2021). Frequency-domain decomposition and deep learning based solar PV power ultra-short-term forecasting model. *IEEE Trans. Industry Appl.* 57, 3282–3295. doi:10.1109/TIA.2021.3073652

Yang, M., Chen, X. X., Du, J., and Cui, Y. (2018). Ultra-short-term multistep wind power prediction based on improved EMD and reconstruction method using run-length analysis. *IEEE Access* 6, 31908–31917. doi:10.1109/ACCESS.2018.2844278

Zhao, B., Wang, Z. P., Ji, W. J., Gao, X., and Li, X. B. (2019). A short-term power load forecasting method based on attention mechanism of CNN-GRU. *Power Syst. Technol.* 43, 4370–4376. doi:10.13335/j.1000-3673.pst.2019.1524

Frontiers in
Energy Research

Advances and innovation in sustainable, reliable and affordable energy

Explores sustainable and environmental developments in energy. It focuses on technological advances supporting Sustainable Development Goal 7: access to affordable, reliable, sustainable and modern energy for all.

Discover the latest Research Topics

See more →

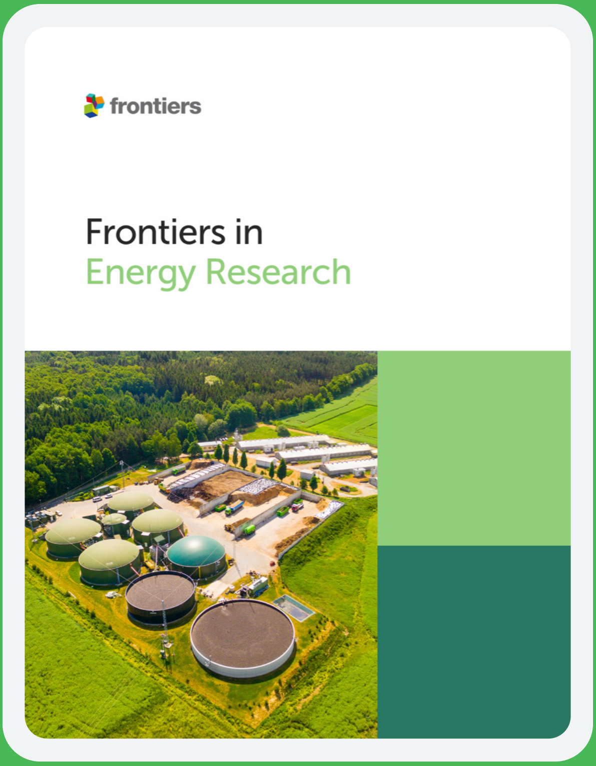

frontiers

Frontiers in
Energy Research

Frontiers

Avenue du Tribunal-Fédéral 34
1005 Lausanne, Switzerland
frontiersin.org

Contact us

+41 (0)21 510 17 00
frontiersin.org/about/contact